Editors

M. Terasawa

S. Kubono

T. Kishida

T. Kajino

T. Motobayashi

K. Nomoto

Origin of Matter & Evolution of Galaxies

2003

Origin of Matter & Evolution of Galaxies

2003

This page intentionally left blank

Editors

M. Terasawa
CNS, University of Tokyo, Japan

S. Kubono
CNS, University of Tokyo, Japan

T. Kishida
RIKEN, Japan

T. Kajino
National Astronomical Observatory, Japan

T. Motobayashi
RIKEN, Japan

K. Nomoto
University of Tokyo, Japan

Origin of Matter & Evolution of Galaxies

2003

World Scientific

NEW JERSEY • LONDON • SINGAPORE • BEIJING • SHANGHAI • HONG KONG • TAIPEI • CHENNAI

Published by

World Scientific Publishing Co. Pte. Ltd.

5 Toh Tuck Link, Singapore 596224

USA office: 27 Warren Street, Suite 401-402, Hackensack, NJ 07601

UK office: 57 Shelton Street, Covent Garden, London WC2H 9HE

British Library Cataloguing-in-Publication Data
A catalogue record for this book is available from the British Library.

ORIGIN OF MATTER AND EVOLUTION OF GALAXIES 2003

ISBN 981-238-824-9

Printed in Singapore by World Scientific Printers (S) Pte Ltd

International Symposium on

The Origin of Matter and Evolution of Galaxies 2003

RIKEN, Wako, Saitama, Japan

November 17-19, 2003

Local Organizing Committee

M. Terasawa	Center for Nuclear Study, University of Tokyo
S. Kubono	Center for Nuclear Study, University of Tokyo
T. Kishida	RIKEN Accelerator Research Facility
T. Kajino	National Astronomical Observatory of Japan
T. Motobayashi	RIKEN Accelerator Research Facility
K. Nomoto	Department of Astronomy, University of Tokyo

Hosted by: Center for Nuclear Study, University of Tokyo (CNS)
RIKEN Accelerator Research Facility (RARF)
National Astronomical Observatory of Japan (NAOJ)

This page intentionally left blank

PREFACE

This book is the proceedings of the International symposium on Origin of Matter and Evolutions of Galaxies 2003 (OMEG03) which was held in RIKEN, Japan, during November 17 - 19 in 2003. This was the 8th meeting of this series, started back in 1988 in Japan. We had 105 participants including 26 scientists from outside Japan.

The main purpose of this meeting was to exchange new development of many topics among theoretical and experimental scientists from various science fields, i.e. nuclear physics, nuclear astrophysics, cosmic-ray physics, particle physics, cosmology, astronomy, geophysics, and others. Furthermore, we tried to make opportunities for young people to participate actively as much as possible. Therefore, 24 invited talks, 23 oral talks, and 27 posters with a three-minute oral talk were presented within 3 days! A lot of interesting experimental and observational results which were made by the recent development of new instrumentations and techniques were presented. Many theoretical efforts were also reported. Lively and hot discussions have proven that nuclear astrophysics has a flourishing future.

The OMEG03 was co-hosted and sponsored by the Center for Nuclear Study, University of Tokyo (CNS), RIKEN Accelerator Research Facility (RARF), and National Astronomical Observatory, Japan (NAOJ). We thank all those sponsors listed above. We wish to thank Ms. K. Takeuchi and T. Iwanami for their secretariat works. We are grateful to all members at CNS and RARF as well as students who worked for this symposium.

We believe that all the participants enjoyed to discuss and could identify new problems for future collaborations. Finally, we would like to express many thanks all the participants, speakers, and chairpersons for making the symposium successful.

M. Terasawa and S. Kubono

This page intentionally left blank

CONTENTS

This page intentionally left blank

Review and Scope

This page intentionally left blank

ORIGIN AND EVOLUTION OF MATTER IN BRANE-WORLD COSMOLOGY

G. J. MATHEWS, T. ASHENFELTER, P. M. GARNAVICH, D. MENZIES

University of Notre Dame, Center for Astrophysics
Notre Dame, IN 46556, USA
E-mail: gmathews@nd.edu, tashenfe@nd.edu, pgarnavi@nd.edu, demenzies@nd.edu

K. ICHIKI, T. KAJINO

National Astronomical Observatory, 2-21-1, Osawa,
Mitaka, Tokyo 181-8588, Japan
E-mail: ichiki@th.nao.ac.jp. kajino@th.nao.ac.jp

M. YAHIRO

Department of Physics and Earth Sciences, University of the Ryukyus,
Nishihara-chou, Okinawa 903-0213, Japan
E-mail: yahiro@sci.u-ryukyu.ac.jp

The brane-world paradigm is based upon the premise that our universe could be a submanifold embedded in a higher-dimensional spacetime. In the currently popular Randall-Sundrum model, the universe is described as a three-space (3-brane) embedded in a five-dimensional anti-de Sitter spacetime with a large (infinite) extra dimension. This concept is motivated by the D-brane solution found in ten-dimensional superstring theory and eleven dimensional M-theory/supergravity. If correct, this notion significantly alters our views on the origin of matter and origin of galaxies. This talk summarizes some possible observational consequences of brane-world cosmology. For example, a new "dark radiation" term arises in the cosmic evolution equations which can affect the radiation dominated epoch. Moreover, matter may literally disappear into (or reemerge from) the extra dimension. This suggests a new interpretations for dark matter, dark energy and their evolution. Further possible consequences of brane-world cosmology are time-varying physical constants and the existence of a sub-horizon compact dimension. Constraints on these possibilities arise from big-bang and stellar nucleosynthesis, observations of high redshift supernovae, galaxy-clusters, X-ray gas in galactic clusters, and the cosmic microwave background. So far, all of the available constraints are consistent with (and may even slightly favor) the existence of a large extra dimension.

1. INTRODUCTION

This is an exciting time in the study of the origin of matter and evolution of galaxies. With the recent accumulation of high-resolution microwave background data,[1] together with observations of high-redshift supernovae,[2] high-resolution abundance measurements[3,4] in quasar absorption line systems, and both optical [5] and X-ray [6] observations of galactic clusters at high redshift, we now have values of cosmological parameters obtained with unprecedented precision. As with any other time in the history of science, we can anticipate that such a breakthrough in measurement precision should be accompanied by new breakthroughs in our understanding of the nature of the universe. It is time therefore to look for where new insights might be found.

In this regard, it is of value to the theme of this conference to review some of the insight to be realized from recent developments in string theory. Not long ago it was realized that the many proposed varieties of string theories could be unified into a single M-theory by the addition of one extra dimension. In the low-energy limit,[7] heterotic M-theory is an eleven dimensional supergravity coupled to two ten-dimensional E_8 gauge theories. The universe then appears as two smooth ten-dimensional manifolds (10-branes) embedded in a bulk dimension. Six dimensions compactify on each brane. Physical particles and gauge fields are strings trapped on the branes, while gravitons reside in both the bulk dimension and the branes. This unification of string theory and supergravity seem to suggest the possibility of a large extra dimension.

The next breakthrough in this regard was the realization[8] that the 10-dimensional branes could be more simply represented as thin 3-brane embedded in an infinite five-dimensional bulk anti-de Sitter spacetime (AdS_5). In such Randall-Sundrum (RSII) models, physical particles are trapped on a three-dimensional brane via curvature in the bulk dimension. This representation of large extra dimensions is an alternative to the standard Kaluza-Klein (KK) compactification, and it has led to a flood of papers dealing with various aspects of brane-world cosmology. Our focus in this paper is to review some aspects of the brane world which might reveal themselves in observational cosmology. These consequences include the disappearance of matter into the bulk dimension, time variation of physical constants, and the existence of a sub-horizon scale compact dimension.

2. Brane-World Cosmology

The five-dimensional Einstein equation for the brane world can be reduced to an effective set of four-dimensional equations on the brane [9,10,11] by decomposing the five-dimensional Riemann tensor into a Ricci tensor plus the five dimensional Weyl tensor. For the five-dimensional metric one writes,

$$ds^2 = \exp^{-2|z|L} \eta_{\mu\nu} dx^\mu dx^\nu + dz^2 \quad , \tag{1}$$

where z is the bulk dimension and the bulk curvature parameter is, $L = \sqrt{-\Lambda_5/6}$, where, Λ_5 is the negative bulk cosmological constant.

The four-dimensional effective energy-momentum tensor contains the usual $T_{\mu\nu}$ term of ordinary (and dark matter) plus a new term quadratic in $T_{\mu\nu}$, and a residual term containing the five-dimensional Weyl tensor with two of its indices projected along a direction normal to the brane. The (0,0) component of the effective four-dimensional Einstein equation reduces to a new generalized Friedmann equation[12,13] for the Hubble expansion as detected by an observer on the three brane,

$$H^2 = \left(\frac{\dot{a}}{a}\right)^2 = \frac{8\pi G_{\rm N}}{3}(\rho + \rho_{DR}) - \frac{k}{a^2} + \frac{\Lambda_4}{3} + \frac{\kappa_5^4}{36}\rho^2 \quad . \tag{2}$$

Here, $a(t)$ is the usual scale factor at cosmic time t, and $\rho = \rho_B + \rho_\gamma + \rho_{DM}$, with ρ_B and ρ_γ the usual contributions from nonrelativistic (mostly baryons) and relativistic particles, respectively and ρ_{DM} is the contribution from cold dark matter. The first term on the right hand side is obtained by relating the four-dimensional gravitational constant $G_{\rm N}$ to the five-dimensional gravitational constant, κ_5. Specifically, $G_{\rm N} = M_4^{-2} = \kappa_5^4 \tau/48\pi$, where τ is the brane tension and $\kappa_5^2 = M_5^{-3}$. where M_5 the five-dimensional Planck mass. Secondly, the four-dimensional cosmological constant Λ_4 is related to its five-dimensional counterpart Λ_5, $\Lambda_4 = \kappa_5^4 \tau^2/36 + \Lambda_5/6$. A negative Λ_5 (and $\kappa_5^4\tau^2/36 \approx |\Lambda_5/6|$) is required for Λ_4 to obtain its presently observed small value.

Standard big-bang cosmology does not contain the ρ_{DR} and ρ^2 terms of Eq. (2). The ρ^2 term arises from the imposition of a junction condition for the energy-momentum tensor on the surface of the brane. This term decays rapidly as a^{-8} in the early radiation dominated universe and is not of interest here.

In the present formulation, ρ_{DR} includes two contributions, $\rho_{DR} = \rho_E + \rho_{GW}$. One is the ρ_E term which derives from the electric part of the Bulk Weyl tensor. The second (ρ_{GW}) includes the possibility of residual gravity waves left on the brane [16]. Since these gravity waves are associated

with the disappearing particles, their dynamics can be formally absorbed together with ρ_E into a Bianchi identity for the effective four-dimensional Einstein equation. This leads to, $\dot{\rho}_{DR} + 4H\rho_{DR} = \Gamma\rho_{DM}$. In its simplest form, $\Gamma = 0$, ρ_{DR} scales as a^{-4} like normal radiation (hence, the name 'dark radiation') even though it has nothing whatsoever to do with electromagnetic radiation. Upper and lower limits on such dark radiation can be deduced from big-bang nucleosynthesis [14]. In this simplest form, the dark radiation can significantly affect the radiation-dominated epoch. Of particular interest in this regard[14] primordial nucleosynthesis can be made in better accord with observed abundances by allowing for a slightly negative dark radiation term. In essence, the dark radiation term relaxes the tension between the observed ^{4}He and ^{7}Li abundances and deuterium. A negative dark radiation slows the expansion rate and reduces primordial lithium and helium consistent with the baryon-to-photon ratio required by the deuterium and CMB determinations.

Since this term represents the projection of curvature in the bulk into our 3-brane, the introduction of negative dark radiation is allowed, but it implies interesting curvature in the bulk. Even so, this is not the end of the story, as a significant alteration of the simple dark radiation term occurs if one allows for the possibility that massive particles may not be entirely trapped on the brane. Also, the possibility that particles may tunnel onto the brane from the bulk allows for a new interpretation of dark energy.

3. Disappearing Dark Matter

Although massive particles can indeed be trapped on the brane, they may also be metastable [15]. That is, for both scalar and fermion fields, the quasi-normal modes are metastable states that can decay into continuum KK modes in the higher dimension. From the viewpoint of an observer on the three-brane, massive particles will appear to propagate for some time and then may literally disappear into the bulk fifth dimension.

In the RSII model, curvature in the bulk dimension is introduced as a means to suppress the interaction of massless particles with the continuum of KK states in the bulk dimension. However, introducing a mass term into the higher-dimensional action leads to nonzero coupling to that KK continuum. The mathematical realization of this decay is simply that the eigenvalues for the mass modes of the field theory are complex, $m = m_0 - i\Gamma$, with a width Γ generally proportional to some power of the particle mass for either scalar or fermion fields.[13] Thus, the comoving density of massive

particles may decay over time with a rate, $(\rho a^3)\exp[-\Gamma t]$, where a is the scale factor. We thus argue that a heavy ($\gtrsim$ TeV) dark matter particle [e.g. the lightest supersymmetric particle, (LSP)] may have the shortest lifetime to tunnel into the bulk. In [13], we analyzed cosmological constraints on this scenario, which we now summarize.

The apparent brightness of the Type Ia supernova standard candle with redshift is given [17] by a simple relation which we slightly modified[13] to incorporate the brane-world cosmology given in Eq. (2). We analyzed this relation using recent combined data from the High-Z Supernova Search Team [2,18] and the Supernova Cosmology Project [19]. Of particular interest are the highest redshift points which constrain the redshift evolution during the important dark-matter dominated decelerating phase during which disappearing matter is most relevant.

We note that the highest redshift data are consistently brighter than the best-fit standard flat $S\Lambda CDM$ cosmology in the epoch at $z > 0.9$. This analysis, thus, slightly favors the disappearing dark matter ($\Lambda DCDM$) cosmology, although we caution that a more recent analysis [20] based upon data from *HST* may not exhibit this trend.

The contours labeled SNIa of Figure 1 show 1σ, 2σ, and 3σ confidence limit regions of constant goodness of fit to the $z > 0.01$ data of [18] in the parameter space of disappearance lifetime Γ^{-1} versus Ω_Λ plane.

The SNIa data imply a shallow minimum for $\Gamma^{-1} \approx 0.3$ Gyr and $\Omega_\Lambda = 0.78$. The reduced χ^2 per degree of freedom at this minimum is $\chi^2_r = 0.94$ for 171 degrees of freedom. This is to be compared with compared with $\chi^2_r = 0.96$ for a standard ΛCDM cosmology [18]. The 1σ confidence limit corresponds to $\Gamma^{-1} \leq 10$ Gyr, but the 2σ region is consistent with a broad range of Γ as long as $\Omega_\Lambda = 0.75 \pm 0.15$.

Another interesting cosmological probe comes from galaxy cluster mass-to-light ratios as also shown on Figure 1. This is the traditional technique to obtain the total universal matter content Ω_M. A recent average [5] value of $\Omega_M = 0.17 \pm 0.05$ has been determined based upon 21 galaxy clusters out to $z \approx 1$ corrected for their color and evolution with redshift. The very fact that the nearby cluster data seem to prefer a smaller value of Ω_M than the value of $\Omega_M = 0.27 \pm 0.02$ deduced [1] from the distant microwave background surface of photon last scattering is consistent with the notion of disappearing dark matter.

In the present disappearing dark matter paradigm, the dark matter content diminishes with time, while the normal baryonic luminous matter remains mostly confined to the brane. Therefore, the M/L ratio should

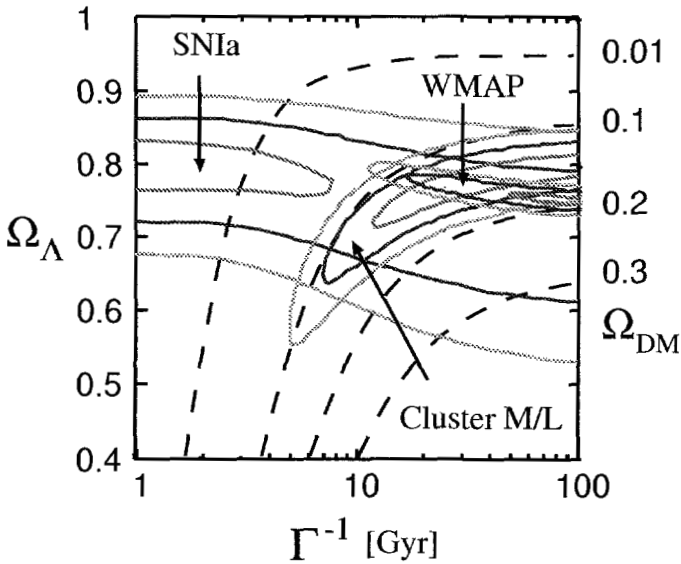

Figure 1. Contours of constant χ^2 in the Γ^{-1} vs. Ω_Λ plane. Lines drawn correspond to 1, 2, and 3σ confidence limits for fits to the magnitude-redshift relation for Type Ia supernovae, the mass-to-light ratios of galaxy clusters, and constraints from the CMB. The dashed lines indicate contours of constant Ω_{DM} as labeled. The dark radiation contribution can be deduced from the figure, via $\Omega_{DR} = 1 - \Omega_\Lambda - \Omega_{DM} - \Omega_B$.

increase with look-back time. Our fits to the data [5] supports this possibility. Contours of constant χ^2 goodness of fit are labeled as Cluster M/L on Figure 1. We find a minimum χ^2 per degree of freedom of $\chi^2_r = 0.61$ for $\Gamma^{-1} = 34$ Gyr as shown on Figure 1. This is an improvement over the fit with a fixed M/L. The 2σ (95% confidence level) limits from the galaxy cluster data correspond to $\Gamma^{-1} \geq 7$ Gyr which is concordant with the previously discussed Type Ia supernova analysis.

There complementary data [6] from *BeppoSax* and the *ROSAT* X-ray observations of rich clusters at high redshift. In this case, the X-ray emitting gas mass can be determined from the X-ray luminosity and the total mass deduced from the gravitational mass required to maintain the X-ray gas in hydrostatic equilibrium. There is, however, uncertainty in this method due to the model dependence of the inferred gas fractions [6] due to the need to introduce a bias parameter. Nevertheless, the observations clearly exhibit a trend of diminishing gas fraction for systems with $z > 1$.

We have done calculations [13] of the CMB power spectrum for the disap-

pearing dark matter cosmology described in Eq. (2). As noted above, the matter content ($\Omega_M = 0.27 \pm 0.02$) deduced from the recent high-resolution *WMAP* analysis [1] of the cosmic microwave background is larger than that deduced ($\Omega_M = 0.17 \pm 0.05$) from nearby galaxy cluster mass-to-light ratios [5]. This in itself is suggestive of the disappearing dark matter paradigm proposed here. However, this cosmology can also involve a shorter look back time and different expansion history between now and the epoch of photon last scattering. In particular there will be more dark matter at earlier times leading to earlier structure formation. There is also a smaller integrated Sachs-Wolf effect (ISW) at early times, and a larger ISW effect at late times as photons propagate to the present epoch. Thus, the amplitudes and locations of the peaks in the power spectrum of microwave background fluctuations [21] can in principle be used[13] to constrain this cosmology under the assumption that fluctuations in the dark radiation contribute insignificantly to the power spectrum at the surface of photon last scattering, a straight forward study of the CMB constraints on the disappearing dark matter cosmology is possible.

A finite Γ still fits the *WMAP* data. As an illustration of this, we have simultaneously varied Γ and Ω_Λ, and marginalized over the parameters of the matter power spectrum, while maintaining other cosmological parameters at the best fit *WMAP* values. The likelihood functions [22] were used to generate contours of 1, 2, and 3σ confidence limits for fits to the *WMAP* power spectrum [23,24] as shown on Figure 1.

Equivalent fits to that of the best-fit *WMAP* parameters [1] can be obtained for a broad range of values for Γ and Ω_Λ. This means that the CMB does not rule out this paradigm. On the contrary, the 2σ CMB contours nicely overlap the region allowed by the cluster M/L ratios. A 2σ concordance region of $15 \leq \Gamma^{-1} \leq 80$ Gyr survives this constraint. The essential requirements to fit the CMB in this model is that the matter content during photon decoupling be at the (higher) *WMAP* value, and that the dark radiation be an insignificant contributor to the background energy density during that epoch.

4. Time Varying α vs. Galactic Chemical Evolution

Values of the physical constants can be connected to the size of the extra dimensions in the brane-world cosmology. Hence, there has recently been considerable excitement over the prospect that a time variation in the fine structure constant may have been observed ($\frac{\delta\alpha}{\alpha} = (0.54 \pm 0.12) \times 10^{-5}$

over a redshift range of $0.5 < z < 3$) in quasar absorption systems.[4,26,27,28] Nevertheless, in view of the importance if this result it is important to carefully scrutinize sources of systematic errors.

The sources of systematic errors in this method have been well documented.[27,28,29,30,31] Recently, we have considered[25] one of these sources of systematic error for which there is recent evidence of a new interpretation, namely the isotopic abundances of Mg assumed in the analysis. The analyses in [4,26,27,28] assumed terrestrial ratios for the three Mg isotopes. They have also shown that had they neglected the presence of the neutron rich Mg isotopes, the case for a varying α would only be strengthened. They further argued, based upon the galactic chemical evolution studies available at that time, that the ratio of $^{25,26}Mg/^{24}Mg$ is expected to decrease at low metallicity making their result a robust and conservative one.

We have proposed [25] that the $^{25,26}Mg/^{24}Mg$ ratio was sufficiently *higher* at low metallicity to account for the apparent variation in α due to isotope shifts. This analysis applies only to the 'low-z' $z < 1.8$ systems considered in [4,26,27,28] which are sensitive to Mg isotopic ratios. There is some evidence from observations that Mg isotopes could have been different in the past based upon observed abundances in globular clusters.[32,33,34] These observations reveal Mg isotopic ratios which range from ^{24}Mg:^{25}Mg+^{26}Mg = 84:18 (slightly poor in the heavies) to 44:56 (greatly enriched in ^{26}Mg). The terrestrial value is ^{24}Mg:^{25}Mg:^{26}Mg = 79:10:11.[35] According to,[28] raising the heavy isotope concentration to ^{24}Mg:$^{25,26}Mg$ = 63:37 would sufficiently shift the multiplet wavelengths to eliminate the need for a varying fine structure constant.

Recently, it has been recognized [37,38,39] that intermediate mass stars of low metallicity can also be efficient producers of the heavy Mg isotopes during the thermal-pulsing AGB phase. Heavy magnesium isotopes (and to some extent silicon isotopes as well) are synthesized via two mechanisms both of which are particularly robust in 2.5-6 $M_\odot$ stars with low metallicity.

One process is that of hot-bottom burning. During the AGB phase, stars develop an extended outer convective envelope. Material in this convective envelope is mixed downward to regions of high temperature at the base. The base of the envelope is more compact and of higher temperature in low metallicity stars than in stars of solar composition. This can be traced to the decreased opacity of these objects. These stars would also have a shorter lifetime because they are hotter. Hence, AGB stars at low metallicity could contribute to the enrichment of the interstellar medium considerably sooner than their higher metallicity counterparts.

Because these stars become sufficiently hot ($T \geq 7 \times 10^7$ K), proton capture processes in the Mg-Al cycle become effective. Proton capture on ^{24}Mg then leads to the production of ^{25}Mg (from the decay of ^{25}Al) and to ^{26}Al (which decays to ^{26}Mg).

A second contributing process occurs deeper in the star during thermal pulses of the helium-burning shell. The helium shell experiences periodic thermonuclear runaways when the ignition of the triple-alpha reaction occurs under electron-degenerate conditions. Due to electron degeneracy, the star is unable to expand and cool. Hence, the temperature rapidly rises until the onset of convection to transport the energy away. During these thermal pulses, ^{22}Ne is produced by α captures on ^{14}N which itself is left over from the CNO cycle. Heavy magnesium isotopes are then produced via the ^{22}Ne(α,n)^{25}Mg and ^{22}Ne(α,γ)^{26}Mg reactions. It was argued recently[38] that in intermediate mass stars which experience a 3rd dredge-up, significantly greater amounts of ^{25,26}Mg are produced.

For our purposes a simple recalculation of the results of Timmes et al.[36] with and without the contribution from intermediate-mass AGB stars is sufficient. Our chemical evolution model is based upon exponential infall and a Schmidt star formation rate. We utilize a slightly modified supernova rate [41] and updated yields.[40]

The yields of heavy magnesium isotopes in AGB stars is extremely temperature sensitive, and hence rather sensitive to detailed physics of the stellar models. Moreover, there are reasons to expect that the initial mass function at low metallicity could be biased toward intermediate-mass stars. One argument for this is simply that with fewer metals, the cooling is less efficient in the protostellar cloud, so that a more massive cloud is required to form a star. Hence, we allow yields to be enhanced by a modified IMF.

Figure 2 shows a comparison of our calculated magnesium isotope ratio vs iron abundance. The solid curve shows the result of the model described above including the AGB contribution. The QSO absorption-line systems in question have metallicities in the range from 0 to -2.5 with a typical iron abundance of [Fe/H]~ -1.5. The mean isotopic ratio needed to account for the data of [4-28] is ^{25,26}Mg/^{24}Mg $= 0.58$ (shown by the solid horizontal line) with a 1σ lower limit of 0.47 (dashed horizontal line). This figure clearly demonstrates that a plausible model is possible in which a sufficient abundance of heavy Mg isotopes can be produced to both explain the observed globular-cluster data and the apparent trends in the many-multiplet data or QSO absorption-line systems at high redshift.

The behavior in the evolution of the heavy isotopes can be explained

as follows: Initially, the production of ^{25,26}Mg in the ejecta of intermediate mass stars is delayed by their relatively long lifetime (compared to very massive stars). Initial contributions to the chemical enrichment of the interstellar medium comes from the most massive and shortest lived stars. In this model, the burst of intermediate mass stars begins to produce ^{25,26}Mg at [Fe/H] ≥ -2.5. At this stage, during the intermediate mass burst, ^{25}Mg and ^{26}Mg are copiously produced relative to ^{24}Mg as per the yields [39]. At higher metallicity, the ejecta from the standard population of (massive) stars which is poor in ^{25,26}Mg begins to dilute the ratio relative to ^{24}Mg, thereby producing the noticeable bump in ^{25,26}Mg/^{24}Mg around [Fe/H] ~ -1.5. At late times, the effect of the early generation of intermediate mass stars is largely washed away. The dashed curve excludes the AGB yields and the intermediate mass component. It gives a result similar to that of Timmes et al.[36]

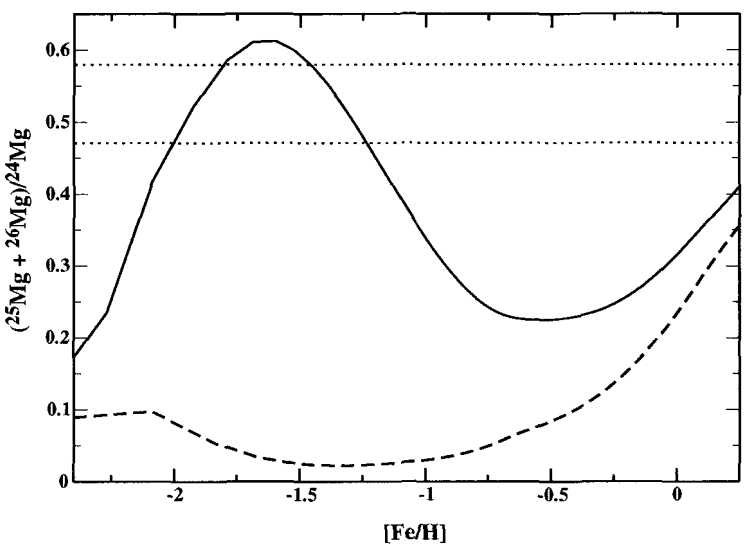

Figure 2. The chemical evolution of the ^{25,26}Mg isotopes relative to ^{24}Mg. The solid curve is our result based on the AGB Mg yields [39] and an enhanced IMF for intermediate-mass stars. The dashed curve is the result of turning off the AGB contribution and excluding the burst of intermediate mass stars. The horizontal lines indicate the ratio of ^{25,26}Mg/^{24}Mg necessary to explain the shifts seen in the many-multiplet analysis.

5. The Search for a Compact Dimension

It is a fundamental notion in brane-world cosmology that the universe was born out of a multidimensional cosmic chaos in which different dimensions are not infinite, but wrapped up onto themselves. Indeed, such compact dimensions are crucial features of theories (such as superstrings) which seek to explain the fundamental forces in nature. The three large dimensions we see today have grown out of this cosmic chaos. Hence, it seems natural that even the large distances of space are compactified. One wishes to look for observational evidence of this.

If a dimension in space is compact then it could have some very distinct observational features. There are 10 possible compact configurations the universe could be in [43]. The simplest one to visualize is the three-torus. If one looks along the smallest compact dimension, multiple images of the same galaxy or cluster should line up like holding up one looking glass to another. The stretching out of a flat would produce a covering space in which multiple images of objects repeat in each box. In fact, along the exact direction of the compact dimension we would be looking at our own galaxy sometime in the past. These simple features, however, will be obscured by the fact that objects move and evolve in time making it is difficult to discern whether one is viewing the same object multiple times. Even without these complexities, one is also limited by the fact that one does not know where to look.

Recently, however, analysis [44,45] of the WMAP microwave background data has suggested the possibility of a suppression of the largest sized fluctuations in the microwave background temperature along an axis directed roughly toward the constellation Virgo. The simplest interpretation [46] may be that of the Sunyaev-Zeldovich effect due to scattering of CMB photons with X-ray gas in the Virgo cluster. However a more intriguing explanation is that the a universe contains a topologically compact dimension within the cosmic horizon. The scale of this structure, however, suggests that a repeat along this dimension will not occur until at least a redshift of $z > 3$. This would mean that nearby galaxies could, in principle, be seen again some eight billion years ago in their past.

Previous studies have searched for compact dimensions by directly looking for multiple images of objects. The most sensitive test [47] looks for multiple images of 3 dimensional groups of objects, allowing for the possibility rotation and translation. Redshift measurements are used to determine radial distances. These depend on the history of cosmological evolution, and

are also sensitive to radial peculiar velocity.[47]

Shortcomings in previous searches have prompted us to develop a new test which is not so reliant on redshift, and does not require groups of nearby objects. This new method is based upon geometrically correlating distant astrophysical objects in the current data base of galaxies, clusters and QSOs at high redshift. If one dimension is short enough to lie within the observable universe, then multiple occurrences of an astrophysical object can be seen. Corresponding images are collinear with the central axis. The axis can therefore be found by the intersection of lines constructed between images in this view. Images behind the observer can mapped to the front and the same test applied.

To search the furthest distances, pairs of images (e.g. galaxies, clusters, QSOs) from opposite sides of the axis are matched, for example, 2 images in front and 2 behind. To reduce the number of false intersections caused by pairs of unrelated objects, some more tests are applied. Distance and look-back times are estimated from redshift using the latest likely cosmological model parameters. Distant observed objects, mainly quasars, have an estimated upper lifetime of one billion years, so we exclude images that differ in estimated age by more than this. The angles of the images relative to the axis are related to the distances. Pairs of images falling outside this constraint can be excluded, making sure all uncertainties are allowed for. Once an image pair passes all the above tests, the compact dimension distance can be estimated. The results are collected in a set of distance bins, to further improve signal to noise. To determine whether a bin count is significant, the original data is decorrelated and processed multiple times to generate an estimate of the average peak count and its variance in each bin. The decorrelation is performed by randomly swapping z data between objects.

Up to now, we have searched a 30 by 20 degree region, using all known objects with $z > 1$ and within about a 60 degree cone from the candidate axis. The sensitivity is now such that even a peak count of a few is significant in simulations with densities of objects comparable to those observed. However, sky coverage in the desired direction is incomplete. This means that the probability of a matching object of an observed object being itself observed is greatly reduced, even at lower z, hence the need for maximizing sensitivity. The number of objects falls nearly to zero for $z > 4$, which limits the maximum detectable dimension to about 0.5 the diameter of the observable universe. The catalog of high-z objects is growing fast, so the test can be reapplied in the future. For now, it must be concluded that

there is no evidence yet for a compact sub-horizon dimension.

6. Conclusion

We have shown that there are many ways in which the study of the origin of matter and evolution of galaxies can be used to probe brane-world cosmology. Obviously, there is great need for better Type Ia supernova data in the crucial $z > 1$ regime as well as more galactic cluster mass-to-light ratios at high redshifts. Although the evidence for disappearing dark matter is of marginal statistical significance at the present time, we emphasize the importance of future studies aimed at determining the decay width. Such evidence would constitute the first observational indication for noncompact extra dimensions. It would also provide valuable insight into the physical parameters of the higher-dimensional space.

The current evidence for a time variation of the fine structure constant is of extreme significance. However, previous analysis for the apparent broadening of the Mg multiplet in QSO absorption-line systems may have left out an important contribution to heavy magnesium isotopes low-metallicity intermediate-mass AGB stars. We have proposed that a simple, galactic chemical evolution model can explains both the large abundances of heavy Mg isotopes observed in globular clusters and the large abundance necessary to explain the many-multiplet data with $z < 1.8$. This model, however, requires enhanced yields either from the hot bottom burning nucleosynthesis or from an IMF enhanced in intermediate-mass stars. Obviously more detailed work is warranted to clarify the ability of this mechanism to account for the data.

We have also emphasized here that a search for a compact sub-horizon dimension is well worth further investigation and have proposed a new way by which this might be done. Although there is as of yet no evidence for a compact dimension, additional studies in the redshift range $z \geq 3$ is well worth doing.

Work at the University of Notre Dame was supported by the U.S. Department of Energy under Nuclear Theory Grant DE-FG02-95-ER40934. Work at NAOJ has been supported in part by the Sasakawa Scientific Research Grant from the Japan Science Society, and also by the Ministry of Education, Science, Sports and Culture of Japan through Grants-in-Aid for Scientific Research (12047233, 13640313, 14540271), and for Specially Promoted Research (13002001). The work of K.A.O. was partially supported by DOE grant DE–FG02–94ER–40823

References

1. D. Spergel, et al. (*WMAP Collab*), Astrophys. J., Suppl., 148, 175 (2003).
2. P. M. Garnavich, et al., Astrophys. J., **509**, 74 (1998).
3. D. Kirkman, D. Tytler, N. Suzuki, J. M. O'Meara and D. Lubin, s Q1243+3047," arXiv:astro-ph/0302006.
4. J. K. Webb, V. V. Flambaum, C. W. Churchill, M. J. Drinkwater and J. D. Barrow, Phys. Rev. Lett. **82** (1999) 884
5. N. Bahcall and J. M. Comerford, Astrophys. J. Lett., **565**, L5 (2002).
6. S. Ettori, P. Tozzo, and P. Rosati, Astron. Astrophys., **398**, 879 (2003).
7. P. Horava and E. Witten, Nucl. Phys. B475 (1996) 94.
8. L. Randall and R. Sundrum, Phys. Rev. Lett. **83**, 3370 (1999); **83**, 4690 (1999).
9. T. Shiromizu, K.I. Maeda, and M. Sasaki, Phys. Rev. **D62**, 024012(2000).
10. J. Yokoyama and Y. Himemoto, Phys. Rev., **D64**, 083511(2001).
11. T. Tanaka and Y. Himemoto, (gr-qc/0301010) (2003).
12. D. Langlois, R. Maartens, M. Sasaki and D. Wands, Phys. Rev. **D63**, 084009 (2001); J. D. Barrow and R. Maartens, Phys. Lett., **B532**, 155 (2002). P. Binétruy, C. Deffayet, U. Ellwanger, and D. Langlois, Phys. Lett. **B477**, 285 (2000); P. Binétruy, C. Deffayet, and D. Langlois, Nucl. Phys. **B565**, 269 (2000).
13. K. Ichiki, P. M. Garnavich, T. Kajino, G. J. Mathews, and M. Yahiro, Phys. Rev. **D68** , 083518, (2003).
14. K. Ichiki, M. Yahiro, T. Kajino, M. Orito and G. J. Mathews, Phys. Rev. **D66**, 043521 (2002).
15. S. L. Dubovsky, V. A. Rubakov and P. G. Tinyakov, Phys. Rev. **D62**, 105011 (2000).
16. R. Gregory, V. Rubakov and S. Sibiryakov, Class. Quant. Grav., **17**, 4437 (2000).
17. S. M. Carroll, W. H. Press, and E. L. Turner, Ann. Rev. Astron. Astrophys., **30**, 499 (1992).
18. J. L. Tonry, et al. Astrophys. J., 594, 1 (2003).
19. S. Perlmutter, et al. Nature, **391**, 51 (1998).
20. A. G. Riess, et al., Astrophys. J., **602**, 571 (2004).
21. W. Hu, D. Scott, N. Sugiyama, and M. White, Phys. Rev. **D52**, 5498 (1995).
22. L. Verde, et al. (*WMAP Collab.*), Astrophys. J Suppl., 148, 195 (2003).
23. G. Hinshaw, et al. (*WMAP Collab.*), Astrophys. J Suppl., 148, 135 (2003).
24. A. Kogut, et al. (*WMAP Collab.*), Astrophys. J Suppl., 148, 161 (2003).
25. T. Ashenfelter, G. J. Mathews, and K. A. Olive, Phys. Ref. Lett., 92, 041102 (2004).
26. M. T. Murphy *et al.*, Mon. Not. Roy. Astron. Soc. **327** (2001) 1208 [arXiv:astro-ph/0012419]. J. K. Webb *et al.*, Phys. Rev. Lett. **87** (2001) 091301 [arXiv:astro-ph/0012539].
27. M. T. Murphy, J. K. Webb, V. V. Flambaum, C. W. Churchill and J. X. Prochaska, Mon. Not. Roy. Astron. Soc. **327** (2001) 1223 [arXiv:astro-

ph/0012420].
28. M. T. Murphy, J. K. Webb and V. V. Flambaum, arXiv:astro-ph/0306483.
29. J. P. Uzan, Rev. Mod. Phys. **75** (2003) 403 [arXiv:hep-ph/0205340].
30. V. A. Dzuba, V. V. Flambaum, and J. K. Webb, Phys. Rev. A **59** (1999) 230; Phys. Rev. Lett. **82** (1999) 888.
31. J. N. Bahcall, C. L. Steinhardt and D. Schlegel, arXiv:astro-ph/0301507.
32. D. Yong, F. Grundahl, D. L. Lambert, P. E. Nissen and M. Shetrone, Astron. Astrophys. **402** (2003) 985 [arXiv:astro-ph/0303057].
33. P. Gay and D. L. Lambert, Astrophys. J. **533** (2000) 260 [arXiv:astro-ph/9911217].
34. D. Yong, D.L. Lambert, and I.I.Ivans, astro-ph/0309/079.
35. K.J.R. Rosman and P.D.P. Taylor, J. Phys. Chem. Ref. Data, **27** (1998) 1275.
36. F. X. Timmes, S. E. Woosley and T. A. Weaver, Astrophys. J. Suppl. **98** (1995) 617 [arXiv:astro-ph/9411003].
37. M. Forestini and C. Charbonnel, Astron. Astrophys. Supp. **123** (1996) 241.
38. L. Siess, M. Livio, and J. Lattanzio, Astrophys. J. **570** (2002) 329 [arXiv:astro-ph/0201284].
39. A.I. Karakas and J.C. Lattanzio, PASA **20** (2003) 279 and arXiv:astro-ph/0305011.
40. P. Marigo, Astron. Astrophys. **370** (2001) 194; L.Portinari, C. Chiosi, and A. Bressan, Astron. Astrophys. **334** = (1998) 505.
41. C. Kobayashi, T. Tsujimoto, and K. Nomoto, Ap. J. **539** (2000) 26.
42. B. D. Fields, K. A. Olive, J. Silk, M. Casse and E. Vangioni-Flam, Ap. J. **563** (2001) 653, [arXiv:astro-ph/0107389].
43. Levin, J., Phys. Rept. 365 (2002) 251, gr-qc0108043
44. Tegmark, M., et al., Phys.Rev. D68 (2003) 123523, astro-ph/0302496
45. de Oliveira-Costa, A., et al., astro-ph0307282
46. L. R. Abramo and J. Sodre, Phys. Rev., (2003) submitted, astro-ph/0312124.
47. Roukema B.F, A&A (2004) submitted, astro-ph/0402608, astro-ph 9603052; astro-ph 0201092

This page intentionally left blank

I. Big Bang Cosmology and Primordial Nucleosynthesis

This page intentionally left blank

UPDATED BIG–BANG NUCLEOSYNTHESIS COMPARED TO WMAP RESULTS

ALAIN COC
CSNSM, CNRS/IN2P3/UPS, Bât. 104, 91405 Orsay Campus, France

ELISABETH VANGIONI-FLAM
IAP/CNRS, 98bis Bd. Arago, 75014 Paris France

PIERRE DESCOUVEMONT
Physique Nucléaire Théorique et Physique Mathématique, CP229, Université Libre de Bruxelles, B-1050 Brussels, Belgium

ABDERRAHIM ADAHCHOUR*
Physique Nucléaire Théorique et Physique Mathématique, CP229, Université Libre de Bruxelles, B-1050 Brussels, Belgium

CARMEN ANGULO
Centre de Recherche du Cyclotron, UcL, Chemin du Cyclotron 2, B-1348 Louvain-La-Neuve, Belgium

*permanent address: lphea, fssm, université caddi ayyad, marrakech, morocco

From the observations of the anisotropies of the Cosmic Microwave Background (CMB) radiation, the WMAP satellite has provided a determination of the baryonic density of the Universe, $\Omega_b h^2$, with an unprecedented precision. This imposes a careful reanalysis of the standard Big–Bang Nucleosynthesis (SBBN) calculations. We have updated our previous calculations using thermonuclear reaction rates provided by a new analysis of experimental nuclear data constrained by *R*-matrix theory. Combining these BBN results with the $\Omega_b h^2$ value from WMAP, we deduce the light element (^4He, D, ^3He and ^7Li) primordial abundances and compare them with spectroscopic observations. There is a very good agreement with deuterium observed in cosmological clouds, which strengthens the confidence on the estimated baryonic density of the Universe. However, there is an important discrepancy between the deduced ^7Li abundance and the one observed in halo stars of our Galaxy, supposed, until now, to represent the primordial abundance of this isotope. The origin of this discrepancy, observational, nuclear or more fundamental remains to be clarified. The possible role of the up to now neglected ^{7}Be(d,p)2α and ^{7}Be(d,α)^{5}Li reactions is considered.

1. Introduction

Big–Bang nucleosynthesis used to be the only method to determine the baryonic content of the Universe. However, recently other methods have emerged. In particular the analysis of the anisotropies of the cosmic microwave background radiation has provided $\Omega_b h^2$ values with ever increasing precision. (As usual, Ω_b is the ratio of the baryonic density over the critical density and h the Hubble constant in units of 100 km·s^{-1}·Mpc^{-1}.) The baryonic density provided by WMAP[1], $\Omega_b h^2 = 0.0224 \pm 0.0009$, has indeed dramatically increased the precision on this crucial cosmological parameter with respect to earlier experiments: BOOMERANG, CBI, DASI, MAXIMA, VSA and ARCHEOPS. It is thus important to improve the precision on SBBN calculations. Within the standard model of BBN, the only remaining free parameter is the baryon over photon ratio η directly related to $\Omega_b h^2$ [$\Omega_b h^2 = 3.6519 \times 10^7\ \eta$]. Accordingly, the main source of uncertainties comes from the nuclear reaction rates. In this paper we use the results of a new analysis[2,3] of nuclear data providing improved reaction rates which reduces those uncertainties.

2. Nuclear reaction rates

In a previous paper[4] we already used a Monte–Carlo technique, to calculate the uncertainties on the light element yields (^4He, D, ^3He and ^7Li) related to nuclear reactions. The results were compared to observations that are thought to be representative of the corresponding primordial abundances. We used reaction rates from the NACRE compilation of charged particles

reaction rates[5] completed by other sources[6,7,8] as NACRE did not include all of the 12 important reactions of SBBN. One of the main innovative features of NACRE with respect to former compilations[9] is that uncertainties are analyzed in detail and realistic lower and upper bounds for the rates are provided. However, since it is a general compilation for multiple applications, coping with a broad range of nuclear configurations, these bounds had not always been evaluated through a rigorous statistical methodology. Hence, we assumed a simple uniform distribution between these bounds for the Monte–Carlo calculations. Other works [10,11] have given better defined statistical limits for the reaction rates of interest for SBBN. In these works, the astrophysical S–factors (see definition in Ref. [4]) were either fitted with spline functions[10] or with NACRE S–factor fits and data but using a different normalization[11]. In this work, we use a new compilation[2] specifically dedicated to SBBN reaction rates using for the first time in this context nuclear theory to constrain the S–factor energy dependences and provide statistical limits. The goal of the R-matrix method[12] is to parametrize some experimentally known quantities, such as cross sections or phase shifts, with a small number of parameters, which are then used to interpolate the cross section within astrophysical energies. The R-matrix theory has been used for many decades in the nuclear physics community (see e.g. Ref. [13,14] for a recent application to a nuclear astrophysics problem) but this is the first time that it is applied to SBBN reactions. This method can be used for both resonant and non-resonant contributions to the cross section. (See Ref. [2] and references therein for details of the method.) The R-matrix framework assumes that the space is divided into two regions: the internal region (with radius a), where nuclear forces are important, and the external region, where the interaction between the nuclei is governed by the Coulomb force only. The physics of the internal region is parameterized by a number N of poles, which are characterized by energy E_λ and reduced width $\tilde{\gamma}_\lambda$. Improvements of current work on Big Bang nucleosynthesis essentially concerns a more precise evaluation of uncertainties on the reaction rates. Here, we address this problem by using standard statistical methods [15]. This represents a significant improvement with respect to NACRE [5], where uncertainties are evaluated with a simple prescription. The R-matrix approach depends on a number of parameters, some of them being fitted, whereas others are constrained by well determined data, such as energies or widths of resonances. As usual, the adopted parameter set is obtained from the minimal χ^2 value. The uncertainties on the parameters are evaluated as explained in Ref.[15]. The range of acceptable p_i values is such that

$\chi^2(p_i) \leq \chi^2(p_i^{min}) + \Delta\chi^2$, where p_i^{min} is the optimal parameter set. In this equation, $\Delta\chi^2$ is obtained from $P(\nu/2, \Delta\chi^2/2) = 1-p$, where ν is the number of free parameters p_i, $P(a,x)$ is the Incomplete Gamma function, and p is the confidence limit ($p = 0.683$ for the 1σ confidence level)[15]. This range is scanned for all parameters, and the limits on the cross sections are then estimated at each energy. As it is well known, several reactions involved in nuclear astrophysics present different data sets which are not compatible with each other. An example is the ^{3}He$(\alpha,\gamma)^7$Be reaction where data with different normalizations are available. In such a case, a special procedure is used[2].

This new compilation[2] provides 1–σ statistical limits for each of the 10 rates: ^{2}H(p,γ)^{3}He, ^{2}H(d,n)^{3}He, ^{2}H(d,p)^{3}H, ^{3}H(d,n)^{4}He ^{3}H(α,γ)^{7}Li, ^{3}He(n,p)^{3}H, ^{3}He(d,p)^{4}He, ^{3}He(α,γ)^{7}Be, ^{7}Li(p,α)^{4}He and ^{7}Be(n,p)^{7}Li. The two remaining reactions of importance, n$\leftrightarrow$p and ^{1}H(n,γ)^{2}H come from theory and are unchanged with respect to our previous work[4].

3. SBBN calculations

We performed Monte-Carlo calculations using Gaussian distributions with parameters provided by the new compilation and calculated the ^4He, D, ^3He and ^7Li yield range as a function of η, fully consistent with our previous analysis[4]. The differences with Ref. [11] on the ^7Li yield is probably due to their different normalization procedure of the NACRE S–factors. Figure 1 displays the resulting abundance limits (1-σ) [it was 2-σ in Fig.4 of Ref. [4]] from SBBN calculations compared to primordial ones inferred from observations. Using these results and the WMAP $\Omega_b h^2$ range (quoted WMAP+SBBN in the following), it is now possible to infer the primordial ^4He, D, ^3He and ^7Li abundances.

We obtain (WMAP+SBBN) a deuterium primordial abundance of D/H = $(2.60^{+0.19}_{-0.17}) \times 10^{-5}$ [ratio of D and H abundances by number of atoms] which is in perfect agreement with the average value $(2.78^{+0.44}_{-0.38}) \times 10^{-5}$ of D/H observations in cosmological clouds[16]. These clouds at high redshift on the line of sight of distant quasars are expected to be representative of primordial D abundances. The exact convergence between these two independent methods is claimed to reinforce the confidence in the deduced $\Omega_b h^2$ value.

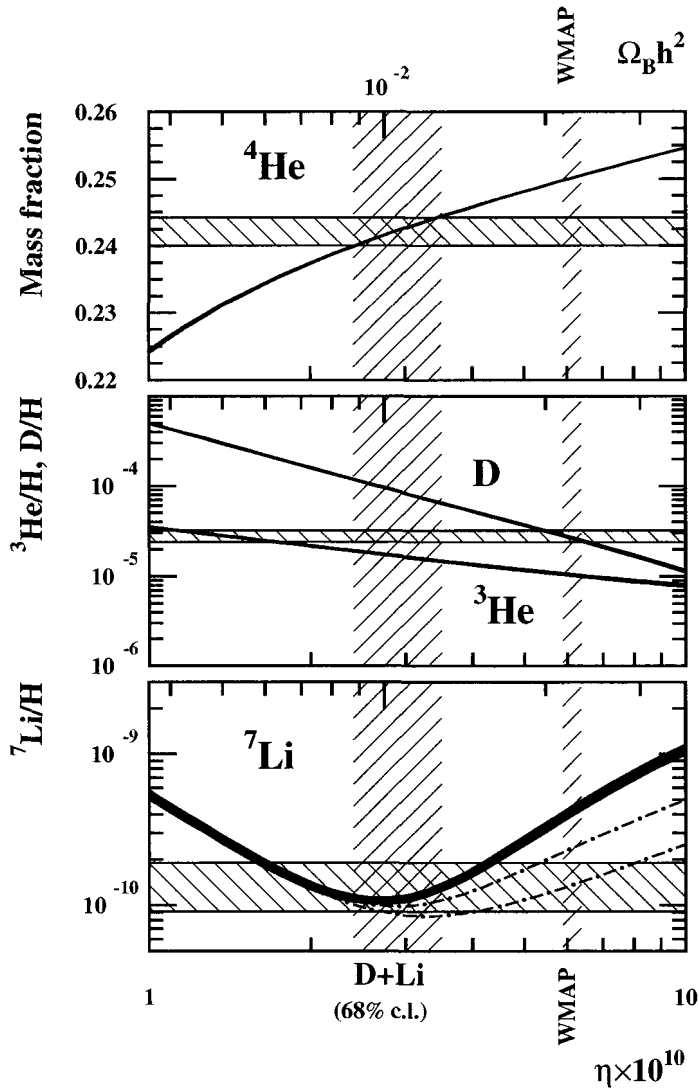

Figure 1. Abundances of ^4He (mass fraction), D, ^3He and ^7Li (by number relative to H) as a function of the baryon over photon ratio η or $\Omega_b h^2$. Limits (1-σ) are obtained from Monte Carlo calculations. Horizontal lines represent primordial ^4He, D and ^7Li abundances deduced from observational data (see text). The vertical stripes represent the (68% c.l.) $\Omega_b h^2$ limits provided by WMAP[1] or deduced from ^7Li and ^4He observations and SBBN calculations. For the dash-dotted lines in the bottom panel: see text.

The other WMAP+SBBN deduced primordial abundances are $Y_P = 0.2457 \pm 0.0004$ for the ^4He mass fraction, $^3\mathrm{He/H} = (1.04 \pm 0.04) \times 10^{-5}$ and $^7\mathrm{Li/H} = (4.15^{+0.49}_{-0.45}) \times 10^{-10}$. We leave aside ^3He whose primordial abundance cannot be reliably determined because of its uncertain rate of stellar production and destruction[17].

The ^4He primordial abundance, Y_p (mass fraction), is derived from observations of metal–poor extragalactic, ionized hydrogen (H II) regions. Recent evaluations gave a relatively narrow ranges of abundances: $Y_p = 0.2452 \pm 0.0015$ (Izotov et al.[18]), 0.2391 ± 0.0020 (Luridiana et al.[19]). However, recent observations by Izotov and Thuan[20] on a large sample of 82 H II regions in 76 blue compact galaxies have lead to the value of $Y_p = 0.2421 \pm 0.0021$ that we adopt here. With this range, WMAP and SBBN results are hardly compatible. Nevertheless, as systematic uncertainties may prevail due to observational difficulties and complex physics[21] ^4He alone is unsufficient to draw a conclusion.

The ^7Li abundance measured in halo stars of the Galaxy is considered up to now as representative of the primordial abundance as it display a plateau[32] as a function of metallicity (see definition in Ref. [4]). Recent observations[31] have lead to (95% c.l.) $\mathrm{Li/H} = (1.23^{+0.68}_{-0.32}) \times 10^{-10}$. These authors have extensively studied and quantified the various sources of uncertainty : extrapolation, stellar depletion and stellar atmosphere parameters. This Li/H value, based on a much larger number of observations than the D/H one was considered[4] as the most reliable constraint on SBBN and hence on $\Omega_b h^2$. However, it is a factor of 3.4 lower than the WMAP+SBBN value. Even when considering the corresponding uncertainties, the two Li/H values differ drastistically. This confirms our[4] and other[11,22] previous conclusions that the $\Omega_b h^2$ range deduced from SBBN of ^7Li are only marginally compatible with those from the CMB observations available by this time (BOOMERANG, CBI, DASI and MAXIMA experiments). It is strange that the major discrepancy affects ^7Li since it could a priori lead to a more reliable primordial value than deuterium, because of much higher observational statistics and an easier extrapolation to primordial values.

Fig. 2 shows a comparison between $\Omega_b h^2$ ranges deduced either from SBBN or WMAP. The curves represent likelihood functions obtained from our SBBN calculations and observed deuterium[16], helium[20] and lithium[31] primordial abundances. These were obtained as in our previous analysis[4] except for the new reaction rates and new D and ^4He primordial abundances. The incompatibility between the D and ^7Li likelihood curves is more obvious than before due to the lower D/H adopted value (Kirkman

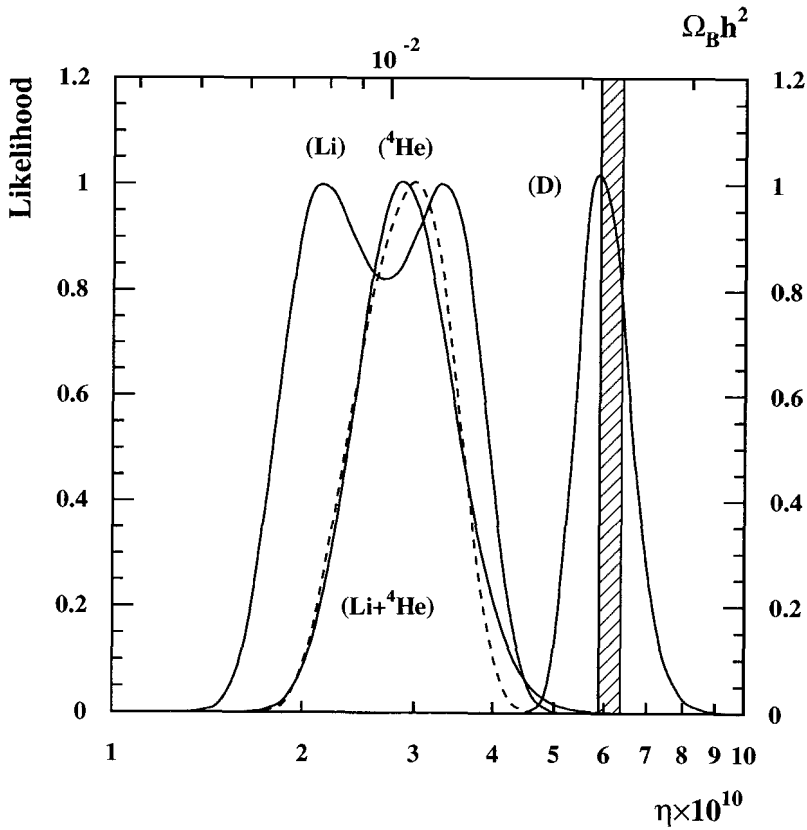

Figure 2. Likelihood functions for D, ^4He and ^7Li (solid lines) obtained from our SBBN calculations and Kirkman et al.[16], Izotov and Thuan[20], and Ryan et al.[31] data for D, ^4He and ^7Li respectively. The dashed curve represent the likelihood function for ^4He and ^7Li while the verical stripe shows the WMAP $\Omega_b h^2$ range[1].

et al., averaged value). On the contrary, the new ^4He adopted value[20] is perfectly compatible with the ^7Li one as shown on Fig. 2 (likelihood curves) and Fig. 1 (abundances). Putting aside, for a moment, the CMB results on the baryonic density, we would deduce the following 68% c.l. intervals: $1.85 < \eta_{10} < 3.90$ [$0.007 < \Omega_b h^2 < 0.014$] from ^7Li only or $5.4 < \eta_{10} < 6.6$ [$0.020 < \Omega_b h^2 < 0.024$] from D only. If we now consider ^4He together with ^7Li, we obtain $2.3 < \eta_{10} < 3.5$ [$0.009 < \Omega_b h^2 < 0.013$]. Hence, including these

new ^4He observations favors a low $\Omega_b h^2$ interval as proposed in our previous work[4]. The WMAP result on the contrary definitively favors the upper (D) one. If we now assume that the ^4He constrain is not so tight, because e.g. of systematic errors on this isotope whose weak sensitivity to $\Omega_b h^2$ requires high precision abundance determinations, the origin of the discrepancy on ^7Li remains a challenging issue very well worth further investigations.

4. Possible origins of ^7Li discrepancy between SBBN and CMB

4.1. *Stellar*

Both observers and experts in stellar atmospheres agree to consider that the abundance determination in halo stars, and more particularly that of lithium requires a sophisticated analysis. The derivation of the lithium abundance in halo stars with the high precision needed requires a fine knowledge of the physics of stellar atmosphere (effective temperature scale, population of different ionization states, non LTE (Local Thermodynamic Equilibrium) effects and 1D/3D model atmospheres[35]. However, the 3D, NLTE abundances are very similar to the 1D, LTE results, but, nevertheless, 3D models are now compulsory to extract lithium abundance from poor metal halo stars[36].

Modification of the surface abundance of Li by nuclear burning all along the stellar evolution has been discussed for a long time in the literature. There is no lack of phenomena to disturb the Li abundance: rotational induced mixing, mass loss,...[37,38]. However, the flatness of the plateau over three decades in metallicity and the relatively small dispersion of data represent a real challenge to stellar modeling. In addition, recent observations of ^6Li in halo stars (an even more fragile isotope than ^7Li) constrain more severely the potential destruction of lithium[39].

4.2. *Nuclear*

Large systematic errors on the 12 main nuclear cross sections are excluded[2,3]. However, besides the 12 reactions classically considered in SBBN, first of all the influence of *all* nuclear reactions needs to be evaluated[3]. It is well known that the valley shaped curve representing Li/H as a function of η is due to two modes of ^7Li production. One, at low η produces ^7Li directly via $^3\mathrm{H}(\alpha,\gamma)^7\mathrm{Li}$ while ^7Li destruction comes from $^7\mathrm{Li(p,}\alpha)^4\mathrm{He}$. The other one, at high η, leads to the formation of ^{7}Be

through ^{3}He$(\alpha,\gamma)^7$Be while ^{7}Be destruction by ^{7}Be(n,p)^{7}Li is inefficient because of the lower neutron abundance at high density (^7Be later decays to ^7Li). Since the WMAP results point toward the high η region, a peculiar attention should be paid to ^{7}Be synthesis. In particular, the ^{7}Be+d reactions could be an alternative to ^{7}Be(n,p)^{7}Li for the destruction of ^7Be, by compensating the scarcity of neutrons at high η. Fig. 1 shows (dash–dotted lines) that an increase of the ^{7}Be(d,p)2^4He reaction rate by factors of 100 to 300 would remove the discrepancy. The rate for this reaction[9] can be traced to an estimate by Parker[40] who assumed for the astrophysical S–factor a constant value of 10^5 kev.barn. based on the single experimental data available[41]. To derive this S–factor, Parker used this measured differential cross section at 90° and assumed isotropy of the cross section. Since Kavanagh measured only the p_0 and p_1 protons (i.e. feeding the ^{8}Be ground and first excited levels), Parker introduced an additional but arbitrary factor of 3 to take into account the possible population of higher lying levels. Indeed, a level at 11.35 MeV is also reported[42]. This factor should also include the contribution of another open channel in ^{7}Be+d: ^{7}Be(d,α)^{5}Li for which no data exist. In addition, one should note that *no* experimental data for this reaction is available at energies relevant to ^{7}Be Big Bang nucleosynthesis (Fig. 3), taking place when the temperature has dropped below 10^9 K. A seducing possibility[3] to reconciliate, SBBN, ^7Li and CMB observations would then be that new experimental data below $E_d = 700$ keV ($E_{cm} \approx 0.5$ MeV) for ^{7}Be(d,p)2^4He [and ^{7}Be(d,α)^{5}Li] would lead to a sudden increase in the S–factor as in ^{10}B(p,α)^{7}Be[43,5]. This is not supported by known data, but considering the cosmological or astrophysical consequences, this is definitely an issue to be investigated and an experiment is planned in 2004 at the Cyclotron Research Centre in Louvain-la-Neuve.

4.3. *Cosmology*

Recent theories that could affect BBN include the variation of the fine structure constant[44], the modification of the expansion rate during BBN induced by quintessence[45], modified gravity[46], or leptons asymmetry[47]. However, their effect is in general more significant on ^4He than on ^7Li.

It may not be excluded that some bias exists in the analysis of CMB anisotropies. For instance, it has been argued[48] that a contamination of CMB map by blazars could affect the second peak of the power spectrum on which the CMB $\Omega_b h^2$ values are based.

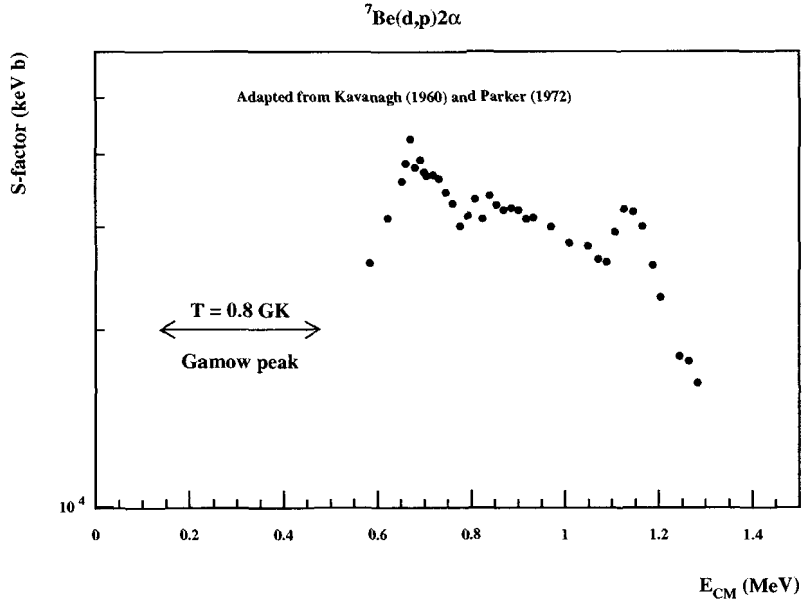

Figure 3. The only experimental data available for the ^{7}Be(d,p)2^{4}H reaction from Kavanagh (1960). The displayed S–factor is calculated as in Parker (1972) from the differential cross section at 90° ($\times 4\pi$) leading to the ground and first ^{8}Be excited states. Note that no data is available at SBBN energies as shown by the Gamow peak for a typical temperature of $T_9 = 0.8$

4.4. *Pregalactic evolution*

We note that between the BBN epoch and the birth of the now observed halo stars, $\approx$1 Gyr have passed. Primordial abundances could have been altered during this period. For instance, cosmological cosmic rays, assumed to have been born in a burst at some high redshift, could have modified these primordial abundances in the intergalactic medium[49]. This would increase the primordial ^7Li and D abundances trough spallative reactions, increasing in the same time the discrepancy between SBBN calculations and observations instead to reconciliate them.

Another source of alteration of the primordial abundances could be the contribution of the first generation stars (Population III). However, it seems difficult that they could reduce the ^7Li abundance without affecting the D one, consistent with CMB $\Omega_b h^2$.

5. Conclusions

The baryonic density of the Universe as determined by the analysis of the Cosmic Microwave Background anisotropies is in very good agreement with Standard Big–Bang Nucleosynthesis compared to D primordial abundance deduced from cosmological cloud observations. However, it strongly disagrees with lithium observations in halo stars (Spite plateau) and possibly ^4He new observations. The origin of this discrepancy, if not nuclear, is a challenging issue.

References

1. D.N. Spergel, L. Verde, H.V. Peiris, E. Komatsu, M.R. Nolta, C.L. Bennett, M. Halpern, G. Hinshaw, N. Jarosik, A. Kogut, M. Limon, S.S. Meyer, L. Page, G.S. Tucker, J.L. Weiland, E. Wollack and E.L. Wright, *Astrophys. J. S.* **148**, 175 (2003).
2. P. Descouvemont, A. Adahchour, C. Angulo, A. Coc and E. Vangioni–Flam, preprint, http://pntpm.ulb.ac.be/bigbang.
3. A. Coc, E. Vangioni-Flam, P. Descouvemont, A. Adahchour and C. Angulo, *Astrophys. J.*, in press, ArXiv:astro-ph/0309480
4. A. Coc, E. Vangioni–Flam, M. Cassé and M. Rabiet, *Phys. Rev.* **D65**, 043510 (2002).
5. C. Angulo, M. Arnould, M. Rayet et al., *Nucl. Phys.* **A656**, 3 (1999).
6. M.S. Smith, L.H. Kawano, and R.A. Malaney, *Astrophys. J. S.* **85**, 219 (1993).
7. C.R. Brune, K.I. Hahn, R.W. Kavanagh and P.W. Wrean, *Phys. Rev.* **C60**, 015801 (1999).
8. J.-W. Chen, and M.J. Savage, *Phys. Rev.* **C60**, 065205 (1999).
9. G.R. Caughlan and W.A. Fowler, *Atomic Data and Nuclear Data Tables* **40**, 283 (1988).
10. K.M. Nollett and S. Burles (NB), *Phys. Rev.* **D61**, 123505 (2000).
11. R.H. Cyburt, B.D. Fields, and K.A. Olive (CFO), *New Astronomy* **6**, 215 (2001).
12. A.M. Lane and R.G. Thomas, Rev. Mod. Phys. **30**, 257 (1958)
13. F.C. Barker and T. Kajino, Aust. J. Phys. **44** (1991) 369.
14. C. Angulo and P. Descouvemont, *Nucl. Phys.* **A639** 733 (1998).
15. Particle Data Group, K. Hagiwara et al., *Phys. Rev.* **D66**, 010001 (2002)
16. D. Kirkman, D. Tytler, N Suzuki, J.M. O'Meara, and D. Lubin, submitted to *Astrophys. J. S.*, ArXiv:astro-ph/0302006.
17. E. Vangioni–Flam, K.A. Olive, B.D. Fields and M. Cassé, *Astrophys. J.* **585**, 611 (2003).
18. Y.I. Izotov, F.H. Chaffee, C.B. Foltz, R.F. Green, N.G. Guseva, and T.H. Thuan, *Astrophys. J.* **527**, 757 (1999).
19. V. Luridiana et al., *Astrophys. J.* **592**, 846 (2003).
20. Y.I. Izotov and T.X. Thuan, *Astrophys. J.*, in print, ArXiv:astro-ph/0310421.

21. B.D. Fields and K.A. Olive, *Astrophys. J.* **506**, 177 (1998).
22. R.H. Cyburt, B.D. Fields, and K.A. Olive, *Phys. Lett.* **B567**, 227 (2003).
23. S. Burles and D. Tytler, *Astrophys. J.* **499**, 699 (1998).
24. S. Burles and D. Tytler, *Astrophys. J.* **507**, 732 (1998).
25. D. Tytler, X.-M. Fan and S. Burles, S., *Nature* **381** 207 (1996).
26. J.M. O'Meara D. Tytler, D. Kirkman, N. Suzuki, J.X. Prochaska, D. Lubin and A.M. Wolfe, *Astrophys. J.* **552**, 718 (2001).
27. M. Pettini, and D.V. Bowen, 2001, *Astrophys. J.* **560**, 41 (2001).
28. S. D'Odorico, M. Dessauges-Zavadsky, and P. Molaro, *Astron. Astrophys.* **368**, L21 (2001).
29. S.G. Ryan, T. Kajino, T.C. Beers, T.K. Suzuki, D. Romano, F. Matteucci and K. Rosolankova, *Astrophys. J.* **549**, 55 (2001).
30. S.G. Ryan, J. Norris, and T.C. Beers, *Astrophys. J.* **523**, 654 (1999).
31. S.G. Ryan, T.C. Beers, K.A. Olive, B.D. Fields, and J.E. Norris, *Astrophys. J.* **530** L57 (2000).
32. F. Spite, and M. Spite, *Astron. Astrophys.* **115**, 357 (1982).
33. F. Thévenin, C. Charbonnel, J.A. de Freitas Pacheco, T.P. Idiart, G. Jasniewicz, P. de Laverny, B. Plez, *Astron. Astrophys.* **373**, 905 (2001).
34. P. Bonifacio, L. Pasquini, F. Spite, et al., *Astron. Astrophys.* **390**, 91 (2002).
35. M. Asplund, M. Carlsson and A.V. Botnen, *Astron. Astrophys.* **399**, L31 (2003).
36. P.S. Barklem, A.K. Belyaev, and M. Asplund, 2003, astro-ph 0308170.
37. S. Theado and S. Vauclair, *Astron. Astrophys.* **375**, 86 (2001).
38. M.H. Pinsonneault et al., *Astrophys. J.* **574**, 411 (2002).
39. E. Vangioni-Flam, et al., *New Astronomy* **4**, 245 (1999).
40. P.D. Parker, *Astrophys. J.* **175**, 261 (1972).
41. R.W. Kavanagh, *Nucl. Phys.* **18**, 492 (1960).
42. F. Ajzenberg-Selove, *Nucl. Phys.* bf A490, (1988) 1 and TUNL Nuclear Data Evaluation Project, http://www.tunl.duke.edu/nucldata/fas/88AJ01.shtml.
43. C. Angulo, S. Engstler, G. Raimann, C. Rolfs, W.H. Schulte, and E. Somorjai, *Z. Phys.* **A345**, 231 (1993).
44. K.M. Nollett and R.E. Lopez, *Phys. Rev.* **D66**, 063507 (2002).
45. P. Salati, *Phys. Lett.* **B571**, 121 (2003).
46. A. Navarro, A. Serna and J.-M Alimi, Classical and Quantum Gravity, **19**, 4361 (2002).
47. M. Orito, T. Kajino, G.J. Mathews and Y. Wang, *Phys. Rev.*, **D65** 123504 (2002).
48. P. Giommi, S. Colafrancesco, submitted to *Astron. Astrophys.*, ArXiv:astro-ph/0306206.
49. T. Montmerle, *Astrophys. J.* **216**, 620 (1977).

DECAYING COLD DARK MATTER COSMOLOGY AND CMB ANISOTROPIES

K. ICHIKI *

University of Tokyo, Department of Astronomy,
7-3-1 Hongo, Bunkyo-ku,
Tokyo, 113-0033, Japan

National Astronomical Observatory,
2-21-1 Osawa, Mitaka,
Tokyo, 181-8588, Japan
E-mail: ichiki@th.nao.ac.jp

K. TAKAHASHI †, M. OGURI AND K. KOTAKE

University of Tokyo, Department of Physics,
7-3-1 Hongo, Bunkyo-ku,
Tokyo, 113-0033, Japan

We re-formulate the theory of cosmological perturbations in decaying cold dark matter cosmology and calculate cosmological microwave background anisotropies. By comparing with recent observation we derive a new bound on the life time of such decaying particles. We show that the data of CMB anisotropies alone do not prefer the decaying cold dark matter models to the standard cold dark matter ones, and constrained to $\Gamma^{-1} \geq 43$ Gyr at 3σ.

1. Introduction

The existence of cold dark matter (CDM) is now strongly believed from numerous kinds of astronomical phenomena, such as rotation curves in galaxies, anisotropies in cosmic microwave background (CMB), and x-ray emitting clusters of galaxies, combined with the low cosmic baryon density predicted by big bang nucleosynthesis. The nature of CDM, however, is still one of the biggest mysteries in cosmology. Moreover, some discrepan-

*Work partially supported by the Sasakawa Scientific Research Grant from the JSS
†Work is supported by Grant-in-Aid for JSPS Fellows

cies on galactic and sub-galactic scales in standard CDM cosmology have stimulated numerous proposals for the alternative CDM candidate [2].

Phenomenologically, decaying cold dark matter (DCDM) cosmology has been extensively studied in various contexts. Among them, DCDM model which Cen proposed could solve both over-concentration problem of the dark matter halos and overproduction problem of small dwarf galaxies in the standard CDM models [3]. The authors showed in previous papers [4,5] that introducing DCDM can improve the fits of observational data sets of Type Ia SN, mass-to-light ratios and X-ray gas fraction of clusters of galaxies, and evolution of cluster abundance. It is also suggested that the decay of super-heavy dark matter particle can be the origin of ultra-high energy cosmic rays above the Greisen-Zatsepin-Kuzmin cut-off of the spectrum [6].

Theoretical candidates for DCDM have been proposed by many authors and their predictions for lifetime of such particles cover a large range of values $10^{-2} < \tau < 10^{11}$ Gyr [7,8,9]. Although DCDM attracts strong phenomenological interests, such particles with lifetime around the age of the universe may have dangerous observational signals and should thus be tightly constrained if it decays into visible particles. The most stringent constraint on such particles may come from the diffuse gamma ray background observations [10]. However, realistic simulation which takes all energy dissipation processes into account showed that even the particles with lifetime as short as a few times of the age of the universe still are not ruled out by recent observations [11]. Moreover, as long as we have not identified what dark matter is, the decay channel cannot escape some uncertainties.

On the other hand, cosmological constraint derived from CMB in the present paper is different from those from diffuse gamma ray background in the point that it does not depend on the details of the decay products. Here we assume only that dark matter particles decay into relativistic particles and put a new bound on the life time of such decaying particles.

2. CMB and DCDM

To make theoretical predictions of CMB anisotropies in DCDM cosmology, we review and formulate cosmological perturbation theory.

2.1. *Background Equations*

The equations of background energy densities for DCDM particles and its relativistic daughter particles are given by

$$\dot{\rho}_{DM} = -3H\rho_{DM} - a\Gamma\rho_{DM} \ , \tag{1}$$

$$\dot{\rho}_{DR} = -4H\rho_{DR} + a\Gamma\rho_{DM} \ . \tag{2}$$

Here dot denotes conformal time derivative and Γ is the decay width of the dark matter. The equation of state parameters $w = P/\rho$ are

$$w_{DM} = 0 \ , \quad w_{DR} = 1/3 \ , \tag{3}$$

respectively. We also define effective equation of state,

$$w_{eff}^{DM} = \frac{a\Gamma}{3H} \ , \tag{4}$$

$$w_{eff}^{DR} = \frac{1}{3} - w_{eff}^{DM}\left(\frac{\rho_{DM}}{\rho_{DR}}\right) \ , \tag{5}$$

which are defined by the evolution of energy density, $\dot{\rho}_i = -3H(1+w_{eff})\rho_i$.

2.2. *Perturbation Equations*

In the conformal Newtonian gauge, the line element is given by

$$ds^2 = a(\tau)^2\left[-(1+2\psi)d\tau^2 + (1+2\Phi)\delta_{ij}dx^i dx^j\right] \ . \tag{6}$$

The perturbed Einstein equations in this metric are described as [12],

$$a^2\bar{\rho}\bar{\delta} = 2\mathrm{M_P^2}\left\{k^2\Phi + 3\frac{\dot{a}}{a}\left(\dot{\Phi} - \frac{\dot{a}}{a}\psi\right)\right\} \ , \tag{7}$$

$$a^2\bar{v}(\bar{\rho}+\bar{p}) = 2\mathrm{M_P^2}k\left(\frac{\dot{a}}{a}\psi - \dot{\Phi}\right) \ , \tag{8}$$

$$a^2\bar{p}\Pi = -\mathrm{M_P^2}k^2(\Phi+\psi) \ . \tag{9}$$

where $\mathrm{M_P}$ is Planck mass, δ, v and Π are perturbations of density, velocity, and anisotropic stress, respectively.

The conservation of energy-momentum is a consequence of the Einstein equations. The perturbed part of energy-momentum conservation equations $T^{\mu\nu}_{\ \ ;\mu} = 0$ yields the following equations of motion,

$$\begin{aligned}\dot{\delta\rho}_{DM}^{g} = &-3H\delta\rho_{DM}^{g} - \rho_{DM}kv_{DM} + 3w_{eff}^{DM}\rho_{DM}\dot{\Phi} + 3\dot{w}_{eff}^{DM}\rho_{DM}\Phi \\ &-9Hw_{eff}^{DM}(1+w_{eff}^{DM})\rho\Phi - a\Gamma\delta\rho_{DM}^{g} \ ,\end{aligned} \tag{10}$$

$$\dot{v}_{DM} = (3w_{eff}^{DM} - 1)Hv_{DM} + k\psi - 3Hw_{eff}^{DM}v_{DM} \ , \tag{11}$$

and

$$\delta\dot{\rho}^g_{DR} = (3w^{DR}_{eff} - 1)\rho_{DR}\dot{\Phi} + 3\dot{w}^{DR}_{eff}\rho_{DR}\Phi + 3H(1 - 2w^{DR}_{eff} - 3w^{DR\,2}_{eff})\rho\Phi$$
$$-\frac{4}{3}\rho_{DR}kv_{DR} - 4H\delta\rho^g_{DR} + a\Gamma\delta\rho^g_{DM} \ , \tag{12}$$

$$\dot{v}_{DR} = (3w^{DR}_{eff} - 1)Hv_{DR} + k\psi - \frac{1}{6}k\Pi_{DR} + \frac{k}{4}\frac{\delta\rho^g_{DR}}{\rho_{DR}} - \frac{3}{4}(1 + w^{DR}_{eff})k\Phi$$
$$+\frac{3\rho_{DM}}{4\rho_{DR}} \times 3Hw^{DM}_{eff}v_{DM} \ . \tag{13}$$

Here gauge invariant density perturbation is defined by

$$\delta\rho^g_i = \delta\rho^{Newton}_i + 3(1 + w^i_{eff})\rho_i\Phi \ . \tag{14}$$

Note that we subtracted and added the decaying term $a\Gamma\delta\rho^g_{DM}$ from the equation of dark matter to that of daughter radiation. As for the velocity perturbation, we subtracted $3Hw^{DM}_{eff}v_{DM}$ from the equation of dark matter and added $\frac{3\rho_{DM}}{4\rho_{DR}} \times 3Hw^{DM}_{eff}v_{DM}$ to that of daughter radiation to express the momentum flux between them. These terms are analogous to baryon - photon momentum transfer by Compton scattering in the standard CMB theory.

2.3. *Boltzmann Hierarchy for Daughter Radiation*

Further, we need Boltzmann hierarchy for $l \geq 2$ moments of daughter radiation, where l stands for multipole moment in a Legendre expansion of perturbed distribution function. We begin with the Boltzmann equation in the Newtonian gauge [12],

$$f^{DR}_0\frac{\partial\Psi^{DR}}{\partial\tau} + \frac{\partial f^{DR}_0}{\partial\tau}(1 + \Psi^{DR}) + i(\vec{k}\cdot\hat{n}) + \frac{df^{DR}_0}{dq}(q\dot{\Phi} - iq(\vec{k}\cdot\hat{n})\psi) = \left(\frac{\partial f}{\partial\tau}\right)_c \ , \tag{15}$$

where $\vec{q} = q\hat{n}$ is the comoving 3-momentum with $n^i n_i = 1$, and we write the distribution function of daughter radiation as $f^{DR}(x^i, q, n_j, \tau) = f^{DR}_0(q, \tau)(1 + \Psi^{DR}(x^i, q, n_j, \tau))$. We should note that, unlike the standard CDM, f^{DR}_0 is now time *dependent* in DCDM. To describe the decay process, let us consider the collision term in the form,

$$\left(\frac{\partial f}{\partial\tau}\right)_c = a\Gamma\frac{m_{DM}}{q}f^{DM}_0(1 + \Psi^{DM}) \ . \tag{16}$$

where $f^{DM} = f^{DM}_0(1 + \Psi^{DM})$ and m_{DM} are the distribution function and mass of DCDM, respectively. Then we get

$$\frac{\partial f^{DR}_0}{\partial\tau} = a\Gamma\frac{m_{DM}}{q}f^{DM}_0 \ , \tag{17}$$

and

$$\frac{\partial \Psi^{DR}}{\partial \tau} + \frac{1}{f_0^{DR}} \frac{\partial f_0^{DR}}{\partial \tau} \Psi^{DR} + i(\vec{k} \cdot \hat{n}) \Psi^{DR} + \frac{d \ln f_0^{DR}}{d \ln q} (\dot{\Phi} - i(\vec{k} \cdot \hat{n}) \psi) = a \Gamma \frac{m_{DM}}{q} \frac{f_0^{DM}}{f_0^{DR}} \Psi^{DM} \ , \quad (18)$$

in linear perturbation theory. The 3rd and 4th terms in l.h.s of Eq.(18) lead standard stream and gravitational scattering terms, respectively. We define,

$$F^{DR}(\vec{k}, \hat{n}, \tau) \equiv \frac{\int q^2 dq \ q f_0^{DR} \Psi^{DR}}{\int q^2 dq \ q f_0^{DR}} = \frac{\int q^2 dq \ q f_0^{DR} \Psi^{DR}}{\frac{1}{4\pi} a^4 \rho_{DR}} \ , \quad (19)$$

then Eq.(18) can be written as

$$\frac{\partial}{\partial \tau} F^{DR} + ik\mu F^{DR} - 4(\dot{\Phi} - ik\mu\psi) = -a\Gamma \frac{\rho_{DM}}{\rho_{DR}} F^{DR} + \frac{a \Gamma m_{DM} \int q^2 dq \ f_0^{DM} \Psi^{DM}}{\frac{1}{4\pi} a^4 \rho_{DR}} \ . \quad (20)$$

The two terms in r.h.s of Eq.(20) are new ones in DCDM cosmology. The second term of them corresponds to the flow from the dark matter to daughter radiation in first order perturbation. Unfortunately, the calculation of this term is complicated in general [14], but in a fluid approximation, it can be easily described. (see Eq. (12) and Eq.(13) for $l = 0$ and $l = 1$, respectively.) For higher multipoles ($l \geq 2$) this term vanishes since the perturbation in the dark matter (Ψ^{DM}) does have only $l = 0, 1$ perturbations which correspond to density and velocity perturbation, respectively. Finally, we have hierarchy for daughter radiation,

$$\dot{M}_l = k \left(\frac{l}{2l-1} M_{l-1} - \frac{l+1}{2l+3} M_{l+1} \right) + (3 w_{eff}^{DR} - 1) H M_l \ , \quad (21)$$

where M_l is the coefficient in a Legendre expansion,

$$F^{DR} = \sum (-i)^l M_l(\tau, \vec{k}) P_l(\mu) \ . \quad (22)$$

3. CMB Constraint and Discussions

Recent high-resolution measurement of CMB anisotropies by the Wilkinson Microwave Anisotropy Probe (WMAP) has become one of the most stringent test for cosmology [15,16,17]. The standard procedure based on a Bayesian statistics gives us the posterior probability distribution from which we obtain the optimal set of cosmological parameters and their confidence levels.

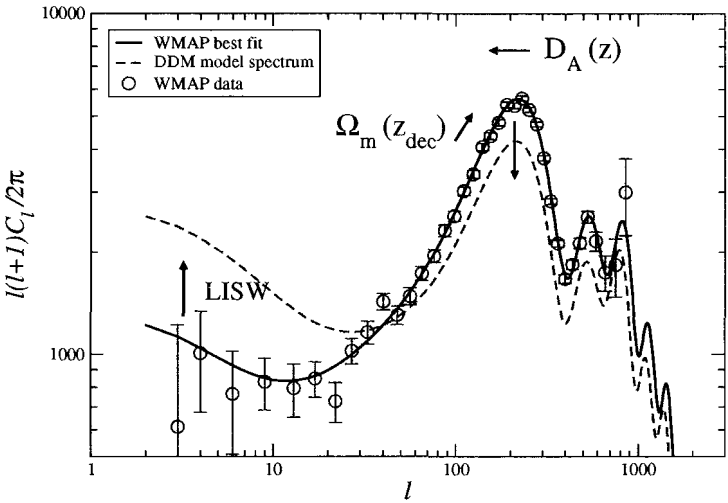

Figure 1. CMB angular power spectrum with and without decay of cold dark matter particles. For both theoretical lines, all the other standard parameters are fixed to WMAP optimal values to demonstrate how decay of the dark matter particles modify the spectrum. Observational data from WMAP are also shown in the figure.

The likelihood functions we calculate are given by the combination of Gaussian and lognormal distribution of Verde et al.[18]. To include the decay of dark matter particles described above, we calculate theoretical angular power spectrum of CMB fluctuation ($l(l+1)C_l/(2\pi)$) using a modified Boltzmann code of CAMB [19], which is based on a line of sight integration approach [20].

The decay of the CDM particles modify the CMB spectrum in some ways. The modified evolution of dark matter will change the expansion history of the universe and generally cause the shorter look back time to the photon last scattering surfaces than that of standard CDM cosmology. This will push the acoustic peaks in the CMB spectrum toward the larger scales. There will be also a decay of gravitational potential at later epochs due to that of dark matter particles leading to a larger integrated Sachs-Wolfe effect (LISW) and thus larger anisotropies at low multipoles. Thus, the amplitudes and locations of the peaks in the power spectrum of microwave background fluctuations [21] can in principle be used to constrain this cosmology. An Illustration of CMB power spectrum in DCDM cosmology is shown in Fig. 1.

It is well known, however, that there are another cosmological parameters which also modify the CMB spectrum. Therefore, we have to generate the full probability distribution function and marginalize over nuisance parameters to obtain the constraint on parameter(s) which we are interested in. To realize this, we followed the Markov Chain Monte Carlo (MCMC) approach [22] and explore the likelihood in seven dimensional parameter space (six WMAP standard parameters, $\Omega_b h^2$, $\Omega_c h^2$, h, $z_{\rm re}$, n_s, A_s, and one DCDM parameter Γ). Our results are shown in Fig. 2.

An interesting point is that the parameter of DCDM cosmology, Γ, dose not degenerate with other parameters very much as one can see in the left side of Fig. 2. This means that the change in the CMB spectrum from Γ can not be mimicked by other standard parameters. This is the reason why CMB can put constraint on the life time of DCDM particle effectively. The right side of Fig. 2 shows marginalized likelihood of the life time of DCDM particle and it is limited by $\Gamma^{-1} \geq 43$ Gyr at 3σ. One does not find any signal to prefer DCDM to standard CDM cosmology.

4. Conclusion

We showed that even the current CMB data alone put constraint on the life time of cold dark matter to $\Gamma^{-1} \geq 43$ Gyr at 3σ. Although this result is comparable to that from the diffuse gamma ray background of Zeaeepour [11], it is completely different in a sense that CMB constraint is purely gravitational, i.e, it is independent from the details of decay channels.

References

1. M. Barranco and J. R. Buchler, *Phys. Rev.* **C34**, 1729 (1980).
2. J. P. Ostriker, and P. Steinhardt, *Science*, **300**, 1909 (2003).
3. R. Cen, *ApJ*, 546, L77 (2001).
4. M. Oguri, K. Takahashi, H. Ohno, and K. Kotake, *ApJ*, **597**, 645 (2003)
5. K. Ichiki, P. M. Garnavich, T. Kajino, G. J. Mathews, and M. Yahiro, *Phys. Rev.* **D68**, 083518, (2003).
6. V. A. Kuzmin, and I. I. Tkachev, *JETP Lett.*, **68**, 271 (1998).
7. D. J. H. Chung, E. W. Kolb, and A. Riotto, *Phys. Rev. Lett.*, **81**, 4048 (1998).
8. K. Benakli, J. R. Ellis, and D. V. Nanopoulos, *Phys. Rev.* **D59**, 047301 (1999).
9. H. B. Kim, and J. E. Kim, *Phys. Lett.* B, 527 18 (2002).
10. A. D. Dolgov, and Y. B. Zeldovich, *Rev. Mod. Phys.*, **53**, 1, (1981).
11. H. Ziaeepour, *Astropart. Phys.*, **16**, 101 (2001).
12. C. P. Ma and E. Bertschinger, Astrophys. J. **455**, 7 (1995).
13. M. Doran, arXiv:astro-ph/0302138.
14. M. Kaplinghat, R. E. Lopez, S. Dodelson and R. J. Scherrer, *Phys. Rev.* **D60**, 123508 (1999).

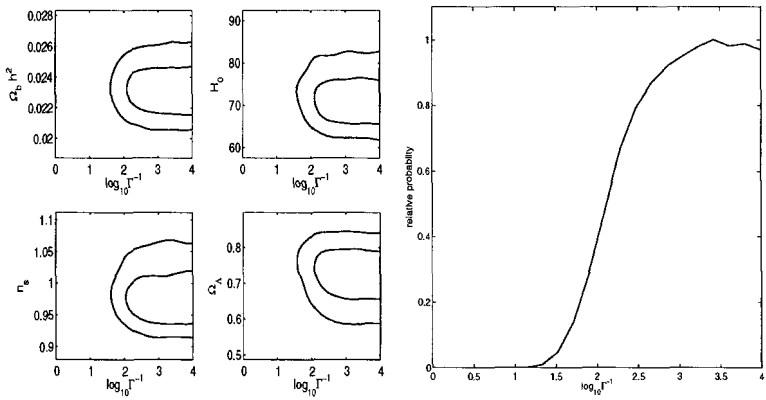

Figure 2. *left:* Contours of constant relative probabilities in two dimensional parameter plane. Lines correspond to 1σ and 2σ confidence limits. *right:* Probability distribution of the decay parameter Γ^{-1}.

15. D. N. Spergel *et al.*, *Astrophys. J. Suppl.* **148**, 175 (2003).
16. G. Hinshaw *et al.*, *Astrophys. J. Suppl.* **148**, 135 (2003).
17. A. Kogut *et al.*, *Astrophys. J. Suppl.* **148**, 161 (2003).
18. L. Verde *et al.*, *Astrophys. J. Suppl.* **148**, 195 (2003).
19. A. Lewis, A. Challinor, and A. Lasenby, *Astrophys. J.*, **538** 473 (2000).
20. U. Seljak, and M. Zaldarriago, *Astrophys. J.*, **469** 437 (1996).
21. W. Hu, D. Scott, N. Sugiyama, and M. White, *Phys. Rev.* **D52**, 5498 (1995).
22. A. Lewis and S. Bridle, *Phys. Rev.* **D66**, 103511 (2002).

HADRONIC DECAY OF SUSY PARTICLE AND DESTRUCTION OF LIGHT ELEMENTS

KAZUNORI KOHRI

Department of Earth and Space Science, Graduate School of Science Osaka University, Toyonaka OSAKA 560-0043

MASAHIRO KAWASAKI

Research Center for the Early Universe (RESCEU), School of Science, The University of Tokyo, 7-3-1 Hongo, Bunkyo-ku, Tokyo 113-0033, Japan

TAKEO MOROI

Department of Physics, Tohoku University, Sendai 980-8578, Japan

In this talk, we consider the effects on big bang nucleosynthesis (BBN) of the hadronic decay of a long-lived massive particle in supergravity. If high-energy hadrons are emitted during/after the BBN epoch ($t \sim 10^{-2} - 10^{12}$ sec), they may change the abundances of the light elements through the destruction processes caused by such high energy hadrons, which may result in a significant discrepancy between standard BBN and observation. So far, these types of hadronic decay process in BBN have not been studied well without a few papers whose treatments were simple, because of severe shortage of hadron experimental data. However, recently the experiments of the high energy physics have been widely developed. Now we can obtain a lot of experimental informations of the hadron fragmentation in the high energy region and also simulate the process even in the higher energies where we have no experimental data by executing the numerical code of the hadron fragmentation, e.g. JETSET 7.4 Monte Carlo event generator. In addition, we have more experimental data of the hadron-nucleon cross sections. One of the candidates of the long-lived massive particle would be gravitino which appears in supergravity. If we consider general particle physics models in supergravity, it possibly decays during/after big-bang nucleosynthesis epoch. Compared with observational light element abundances, for the successful nucleosynthesis, we can obtain severe upper bound on reheating temperature after the primordial inflation which controls the primordial abundance of gravitinos. We discuss the implications of that result for cosmology, particle physics and nuclear physics.

Big bang nucleosynthesis (BBN) is one of the most important tools to probe the early universe because it is sensitive to the condition of the universe from 10^{-2} sec to 10^{12} sec, for the review, see Ref. [1]. Therefore, from the theoretical predictions we can indirectly check the history of the universe in such an early epoch and impose constraints on hypothetical particles by observational light element abundances. Now we have a lot of models of modern particle physics beyond the standard model, e.g., supergravity or superstring theory, which predict unstable massive particles with masses of $O(100)$ GeV – $O(100)$ TeV, such as gravitinos, Polonyi fields, or moduli. They have long lifetimes because their interactions are suppressed by inverse powers of the gravitational scale ($\propto 1/M_{\rm pl}$). These exotic particles may necessarily decay during/after the BBN epoch ($T \lesssim O(1)$ MeV) if they have already existed in earlier stages.

If the massive particles X decay into quarks or gluons, during/after the BBN epoch $10^{-2} \lesssim t \lesssim 10^{12}$ sec. it is expected that non-standard effects are induced. If once the high-energy quarks or gluons are emitted, they quickly fragment into a lot of hadrons. Then, such high-energy hadrons are injected into the electromagnetic thermal bath which is constituted by photons, electrons, and nucleons (protons and nucleons) at that time.

For relatively short lifetime ($\lesssim 10^4$ sec), the emitted high-energy hadrons scatter off the background photons and electrons because they are more abundant than the background nucleons. Then, almost all kinetic energy of the hadrons are transfered into the thermal bath through the electromagnetic interaction. As a result, they are completely stopped and reach to the kinetic equilibrium. After that time, they scatter off the background p or n through the strong interaction, and they inter-convert the background p and n each other even after the normal freeze-out time of the neutron to proton ratio n/p of the weak interaction. This effect extraordinarily tends to increase n/p. Therefore, the produced ^{4}He would be increased in the hadron injection scenario compared to standard big-bang nucleosynthesis (SBBN) [2].

On the other hand, for relatively longer lifetime ($\gtrsim 10^4$ sec), the other important effects occur. The emitted high-energy nucleons are no longer stopped in the electromagnetic plasma and directly scatter off the background nuclei such as proton or ^{4}He. Then ^{4}He is destroyed through strong interactions and produces many lighter nuclei and nucleons. The produced nuclei and nucleons still have high energies and induce the further hadronic showers. Namely this hadron showers produce a lot of light elements, and that may result in a significant discrepancy between SBBN and observa-

tions.

In this situation, we have obtained upper bounds on the abundance n_X/s as a function of the lifetime τ_X to agree with the observations for the wide range of the mass m_X = 100 GeV - 100 TeV which are relevant for various models of supergravity or superstring theory. We have also applied the results obtained by a generic hadronic decaying particle to gravitino $\psi_{3/2}$. Then we have got the upper bound on the reheating temperature after primordial inflation as a function of the mass. The details will be shown in Ref. [3].

References

1. K. Hagiwara *et al.* [Particle Data Group Collaboration], Phys. Rev. D **66**, 010001-162 (2002).
2. K. Kohri, Phys Rev D**64**, 043515 (2001) [astro-ph/0103411], and references therein.
3. M. Kawasaki, K. Kohri and T. Moroi, in preparation.

This page intentionally left blank

II. Observations: X-Rays, Cosmic Rays and Meteoritic Anomalies

This page intentionally left blank

NUCLEAR ASTROPHYSICS WITH THE INTEGRAL OBSERVATORY

ROLAND DIEHL

Max-Planck-Institut für extraterrestrische Physik
Postfach 1312, D-85741 Garching, Germany
E-mail: rod@mpe.mpg.de

With gamma-ray measurements from the decay of radioactive isotopes of intermediate lifetimes, nucleosynthesis in stars, supernovae, and novae may be constrained. ESA's INTEGRAL observatory with its Ge spectrometer SPI is now in orbit for one year, and at least four more years are scheduled. The INTEGRAL satellite and instruments show excellent performance. Instrumental background, higher than, estimated, limits current gamma-ray line results. Nevertheless, first results on annihilation radiation and ^{26}Al demonstrate the potential of this mission for nuclear astrophysics. The ^{26}Al line is narrow, casting doubt on previously-reported broadening which would require typical ^{26}Al decay at $\simeq$ 500 km s^{-1}; the annihilation of e^+ appears concentrated in the inner Galaxy, more extended than what would correspond to the Galactic bulge, but without a significant Galactic-disk component. After its first successful mission year with emphasis on hard-X-ray sources, the second mission year is aimed more at the study of nucleosynthesis sources, with their required long exposures.

1. Introduction

Radioactive isotopes are common by-products of nucleosynthesis in cosmic sources. Gamma-rays from their decay can be measured with satellite-borne telescopes, and thus provide direct constraints to the physics of nuclear burning regions inside these sources. In comparison, other measurements of cosmic nucleosynthesis are less direct (e.g. the isotopic analysis of presolar grains found in meteorites, or the analysis of X-ray line emission from ionized-gas portions of supernova remnants and galactic-halo gas). Yet, the technique of gamma-ray telescopes is complex, and less precise than such alternatives for abundance measurements, with spatial resolutions of $\simeq$ degrees and signal-to-background ratios of $\simeq$ %. Only nearby sources in the Galaxy (up to 10 Mpc for SNIa ^{56}Ni sources) are sufficiently bright for such isotopic measurements; but these are unaffected by physical conditions in/around the source such as temperature or density, and not attenuated

along the line-of-sight due to the penetrating nature of gamma-rays (attenuation length $\simeq$ few g cm^{-2}).

Candidate sources are supernovae and novae, but also the winds from massive stars. Freshly-produced nuclei from explosive layers near the surface of compact stars and from stellar interiors are ejected into interstellar space, where gamma-rays from their decay can be observed directly. Radioactivity which is still embedded within the source will lead to X-ray/low-energy gamma-ray continuum emission due to Comptonization, and early radioactive energy is completely thermalized in novae and supernovae. This allows indirect measurements of radioactivity, where bolometric measurements are converted to original radioactive energy through radiation transport models. In outer envelopes, where densities are still sufficiently high for collisions, and temperatures are low enough for dust formation from refractory species, characterisic isotopic samples of the nuclosynthesis source may be conserved in "presolar dust grains"; some fraction of those survives interstellar transport and processings by interstellar shocks, and have been found inside meteorites. Even though the transport and processing history of such grains is uncertain, isotopic anomalies detected in precision laboratory measurements are sufficiently large (factors 10–1000) to allow significant nucleosynthesis inferences, in particular on AGB stars, but more recently even on supernovae and novae.

Before INTEGRAL, gamma-ray studies established this new window for the study of cosmic nucleosynthesis[6]: (1) Interstellar ^{26}Al has been mapped along the plane of the Galaxy, confirming that nucleosynthesis is an ongoing process [7,35,33]. (2) Characteristic Ni decay gamma-rays have been observed from SN1987A [44,27,24], directly confirming supernova production of fresh isotopes up to iron group nuclei. (3) ^{44}Ti gamma-rays have been discovered[13,39] from the young supernova remnant Cas A, confirming models of α-rich freeze-out for core collapse supernovae. (4) A diffuse glow of positron annihilation gamma-rays has been recognized from the direction of the inner Galaxy[36,17], consistent with nucleosynthetic production of β^+-decaying radioactive isotopes from supernovae, novae and massive stars.

But these positive results are accompanied by new questions and open issues, which should be addressed through better new measurements and through theoretical studies: (1) Which fraction of radioactive energy is converted into other forms of energy in supernovae? This adresses the absolute normalization of indirectly-inferred radioactive amounts (^{56}Ni in SNIa, and ^{44}Ti in core-collapse SNe[22], and the positron leakage from supernovae[29]),

and the morphology of expanding supernova envelopes[4] ("bullets", filaments, jets). (2) How good are our (basically one-dimensional) models for nova and supernova nucleosynthesis, in view of important 3D effects such as rotation and convective mixing? This adresses the amount of ^{44}Ti ejected from regions near the mass cut between compact remnant and ejected supernova envelope[43], and also the seed compositions for explosive hydrogen burning in novae, leading to predicted production of ^{22}Na in novae which is yet to be directly observed[12,15]. (3) Which variety of physical conditions is expected for nucleosynthesis events, from above effects, but also from clustering of events in space and time? This adresses stellar mass distributions and supernova rates in massive-star clusters, self-enrichment, triggered star formation in dense, active nucleosynthesis regions, but also the very different stellar evolution of the first stellar generations when metallicity was extremely low. (4) How are ejecta and energy from nucleosynthesis events fed back into the interstellar medium on all scales and over the time of the chemical evolution of interstellar gas, i.e., how is cosmic nucleosynthesis related to the morphology of the interstellar medium, to the spatial pattern of star formation, to nucleation of dust and its processing by interstellar shocks, and to the acceleration of cosmic rays? Different methods of measuring cosmic nucleosynthesis can be related, in particular connecting models for chemical evolution on different scales of time and space.

With ESA's INTEGRAL[48], now a new step is taken with two coded-mask telescopes, improving sensitivities by $\simeq$ an order of magnitude, and resolutions in spatial and spectral domains significantly over previous experiments. INTEGRAL's spectrometer substantially improves the measurement of characteristic gamma-ray lines through their unique identification in energy, and through the prospect of observing kinematic signatures from Doppler-shifted energy values in expanding/accelerated radioactive material from sources of cosmic nucleosynthesis.

2. INTEGRAL and its Spectrometer

The INTErnational Gamma-Ray Astrophysics Laboratory (INTEGRAL) of ESA has been launched into a highly-excentric 72-h orbit by a Russian Proton rocket on October 17, 2002. With an apogee of $\simeq$ 150000 km and a perigee of $\simeq$ 8000 km, most of the time is spent above the radiation belts, thus minimizing local background generation from charged-particle interactions with spacecraft material. Main instruments are the Imager and Spectrometer coded-mask telescopes; these are supplemented by two moni-

tor detectors, one microstrip gas scintillation detector coded mask telescope for soft X-rays, and one CCD camera for optical emission, both with larger fields of views. INTEGRAL data are collected by ESA ground stations in Belgium and in Australia, and pre-processed in Versiox/Switzerland at the INTEGRAL Science Data Center (ISDC) for distribution to observers.

The INTEGRAL mission has a nominal duration of 2 years, but at this time ESA has approved already the envisaged 3-year extension because of the high-quality performance and success of the mission. The Core Program is conducted by the INTEGRAL Science Working Team (which consists of the instrument teams and data center scientistrs, space agency representatives from the US and Russia, and the ESA mission and project scientists). The percentage of Core Program reduces from initially 35% through 30 to 25% at and beyond the 3rd year, leaving most of the observing time to the "Open Program", which is open to the international scientific community with proposal rounds at one-year intervals (AO-2 for Dec 2003 – Dec 2004 just approved at the time of this conference).

The spectrometer SPI on INTEGRAL[45,38] is based on 19 hexagonal Ge detector modules, each one 7 cm thick and 5.5 cm wide (flat-to-flat along their hexagonal shape), arranged in a densely packed detector plane of 500 cm^2 total. It is illuminated through a 127-element coded mask made of tungsten 3 cm thick and 2.5 times dimensions of the camera, about half the area as open pixels, with a mask/camera separation of 171 cm. This geometry defines a field-of-view of 16 degrees opening angle ("fully-coded"), beyond which the shadow pattern of the mask cast by a point source at infinite distance falls outside the camera elements ("partially-coded field-of-view", out to 35 degrees, beyond which there is no coding at all). The camera and mask are surrounded by BGO scintillation detectors to shield it from low-energy photons, and to detect and veto charged-particle induced events. Exposures are typically days to weeks. In order to improve the mask pattern recognition also for extended and diffuse sources, the INTEGRAL satellite pointing is varied during such exposures in steps of two degrees on a regular "dithering" pattern around the target position, typically every 2200 s. The Ge detector temperature is maintained at $\simeq$ 90 K by stirling coolers. The accumulated damage from cosmic-ray bombardement in the detector crystals leads to $\simeq$ 10% degradation of spectral resolution and an asymmetric response; this is cured every $\simeq$ 6 months by heating up the camera to $\simeq$ 105 C for $\simeq$ 1.5 days ("annealing"); this procedure has been exercised successfully in orbit two times already, and re-establishes the original spectral response and resolution of $\simeq$ 3 keV at 2 MeV.

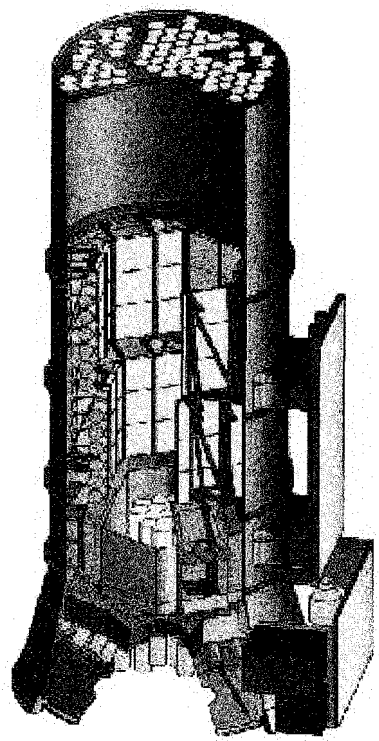

Figure 1. The SPI Spectrometer on INTEGRAL

3. First Science Results

In its first mission year, INTEGRAL observations have already demonstrated the useful complement of such measurements of high-energy photons:

- Many gamma-ray bursts have been measured, helping to constrain, in particular, the spectrum at the high-energy end, and the time profile towards short-time variability and structure[28,1,46].
- High-energy sources such as accreting binaries including black-hole candidates have been observed, where several outbursts and transient events provide rich material to constrain the accretion process near black holes (e.g. Cyg X-1[34], GRS1915+105[10]).
- New transient gamma-ray sources have been found in the inner Galaxy, and are suggested to be accreting binaries deeply embed-

ded into interstellar clouds which absorb lower-energy radiation and thus have hidden these sources up to now (e.g. IGR J16318-4848[47]).

- The gamma-ray line sources of ^{26}Al and positron annihilation have been detected (details are presented in the following Sections).

3.1. *Interstellar ^{26}Al*

The precision followup measurements of 1809 keV emission from Galactic ^{26}Al has been one of the design goals of the INTEGRAL mission[48], after the COMPTEL sky survey [33,21,32,7] had demonstrated that structured emission extended along the plane of the Galaxy. Modelling of ^{26}Al emission from the Galaxy and specific source regions based on knowledge about the massive-star populations suggests that such stars dominate ^{26}Al production in the Galaxy [35,19,20].

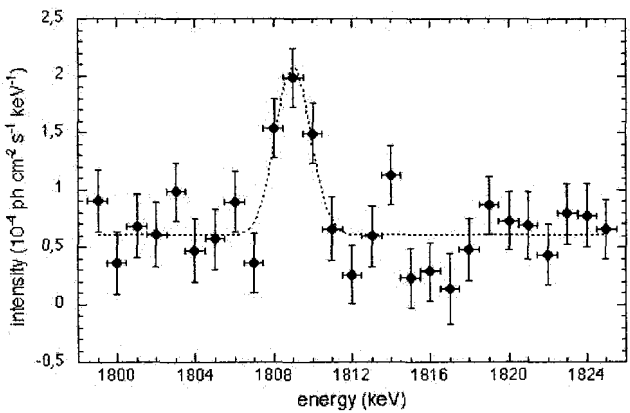

Figure 2. SPI measurement of the ^{26}Al gamma-ray line from the inner Galaxy

The high spectral resolution of Ge detectors of 3 keV (FWHM) at the ^{26}Al line energy of 1808.7 keV is expected to reveal more information about the sources and their location through Doppler broadenings and shifts, from Galactic rotation and from dynamics of the ^{26}Al gas ejected into the interstellar medium[8,23]. In particular after the GRIS balloon experiment and their report of a significantly-broadened line[31], alternative measurements of the ^{26}Al line shape were of great interest. GRIS's value translates into

an intrinsic line width of 5.4 keV, equivalent to a Doppler broadening of 540 km s^{-1}. Considering the 1.04×10^6 y decay time of ^{26}Al such a large line width is hard to understand[3,42].

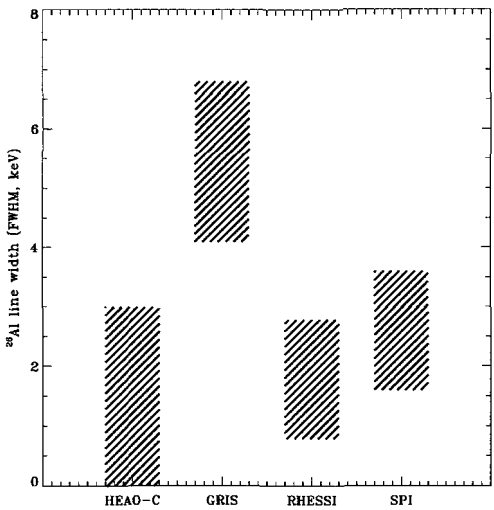

Figure 3. Line width measurements for ^{26}Al

From spectral analysis of a subset of the first-year's inner-Galaxy deep exposure ("GCDE"), the SPI team obtained a clear detection of celestial ^{26}Al emission at the level of 5–7σ, through fitting of adopted models for the ^{26}Al skymap over an energy range around the ^{26}Al line[5]. Values derived for ^{26}Al flux, as well as details of the spectral signature, however, vary significantly with parameters of the analysis, and thus indicate the levels of uncertainty at this initial stage of these observations and their analysis; statistical uncertainties are negligable, in comparison. Figure 2 shows a spectrum derived from all event types (single and multiple detector hits), using the COMPTEL Maximum-Entropy map from 9 years of measurements as a model for the spatial distribution of the sky emission [33]. Given the rather modest spatial resolution of SPI, the particular choice of such distribution is not critical, as long as the dynamic range of fluxes and spatial distribution are approximately correct; any choice of good source tracers, such as the warm dust or free electron distributions[19], produce very

similar results.

Derived sky intensity values from the inner ±30° of the Galaxy are (3–5)×10^{-4} ph $cm^{-2}s^{-1}$. These are within the range suggested by previous observations: SMM[40]: $4.0 \pm 0.x \times 10^{-4}$ ph $cm^{-2}s^{-1}$, COMPTEL[32]: $2.8 \pm 0.15 \times 10^{-4}$ ph $cm^{-2}s^{-1}$, RHESSI[41]: $5.7 \pm 0.54 \times 10^{-4}$ ph $cm^{-2}s^{-1}$.

Line width results are consistent with SPI's instrumental resolution of 3 keV (FWHM). Therefore, these initial and preliminary SPI results already support RHESSI's recent finding[41] that the broad line reported by GRIS[31] probably *cannot* be confirmed (Figure 3).

3.2. *Positron Annihilation*

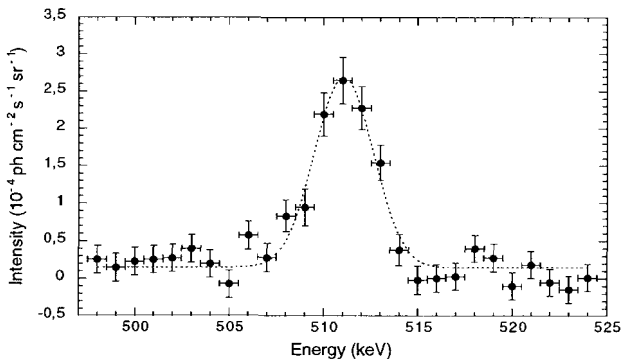

Figure 4. SPI measurement of the positron annihilation gamma-ray line from the inner Galaxy. The line is confirmed to be instrinsically broadened.

Positrons are produced upon β^+-decay of radioactive isotopes with excess protons, hence may be expected to trace nucleosynthesis of such isotopes. Other positron sources have been proposed, however, so that the nucleosynthesis connection is not unique: Plasma jets ejected from pulsars[49,16] or microquasars[30] as a consequence of rotational magnetosphere discharges and accretion, respectively, will produce positron beams, and annihilation of dark-matter particles attracted by the gravitational potential of the Galaxy may produce distributed e^-e^+ pairs[2]. The fractional contribution from nucleosynthesis sources to the positron budget within the inner Galaxy regions is estimated to range from $\simeq$ 30% to 100%, most probably from novae and SNIa (^{19}F and ^{56}Co being the dominating radioactive sources, respectively). Substantial uncertainty arises from the unknown escape fractions of

positrons from these sources. A lower limit is placed from the contributions of the observed ^{26}Al , at $\simeq$ 25%. Positrons with high energies have a low probability for annihilation. Ejected by their source processes with typically MeV energies, they will thermalize along their trajectories in the ISM, and annihilate preferentially through the formation of intermediate positronium atoms. The two possible spin orientations in positronium atoms (antiparallel/parallel; para/ortho positronium) result in annihilation either from a singlet or from a triplet state, thereby producing either two annihilation photons at 511 keV energy, or a photon continuum made up from three annihilation photons, with a maximum energy of 511 keV for any one of the three photons. The ratio between the line and continuum gamma-ray intensities thus allows to measure the physical conditions in the annihilation region, i.e., its density, temperature, and ionization state[9]. This ratio has been measured to be rather low, only $\simeq$ 1/4 of annihilation emission is contained in the 511 keV line[17]. Nevertheless, line measurements are an important diagnostic, (a) because its measurement is easier than constraining the spectrally-distributed continuum, and (b) the details of the annihilation line shape will encode kinematics and thermal properties of the annihilation regions. As a complication, the lifetime of $\simeq$ MeV positrons in interstellar space can be substantial[9], up to 10^5y, so that positrons may travel significant (few 100 pc) distances between their sources and the locations of their annihilation. A diffuse nature of the source is expected from radioactive (and from dark matter) sources, while localized emission / hot spots would be expected if annihilation near compact sources (microquasars, pulsars) is significant. Therefore, models which have been used to interpret previous measurements with instruments of rather modest (few degrees) imaging resolution have been composed from disk contributions (diffuse radioactivity from bulge and disk novae and other sources, or latitudinally more-extended warm or hot ISM gas models) and from point sources for candidate e^-e^+ producers such as 1E 1740.7-2942.

From OSSE scans of the inner Galaxy with its field-of-view of 11.4 x 3.8°, the spatial distribution was found to be best represented by a Gaussian with an extent of $\simeq 5^o$ (FWHM) in longitude and latitude[17,29]. Surprisingly no clear disk-like component was observed, and the "bulge" component appeared rather extended; furthermore, there was indication of asymmetry[36], with an excess of annihilation emission in the northern hemisphere towards latitudes of $\simeq 10^o$. Yet, no mapping of annihilation emission is available along the disk of the Galaxy outside this inner region; this is one of the projects for the SPI instrument on INTEGRAL.

The intensity in the annihilation line, derived from first analysis of SPI data from a part of the inner-Galaxy deep exposure (GCDE) of the first mission year[14] (see Fig.4 from Jean et al., 2003[14]), is $9.9^{+4.7}_{-2.2} \times 10^{-4}$ ph cm^{-2}s^{-1}, consistent with previous measurements and theoretical predictions. This corresponds to a positron production rate in the inner Galaxy on the order of 10^{43}s^{-1} for an assumed steady state [37].

The line is found to be significantly broadened, from deconvolution with the instrumental resolution after subtraction of the (strong) instrumental background. The SPI value of 2.95(±0.6) keV (FWHM) is on the high side of values measured by previous instruments (HEAO-C[26]: 1.6 ± 1.3; GRSI[25]: 2.5 ± 0.4; TGRS[11]: 1.81 ± 0.54).

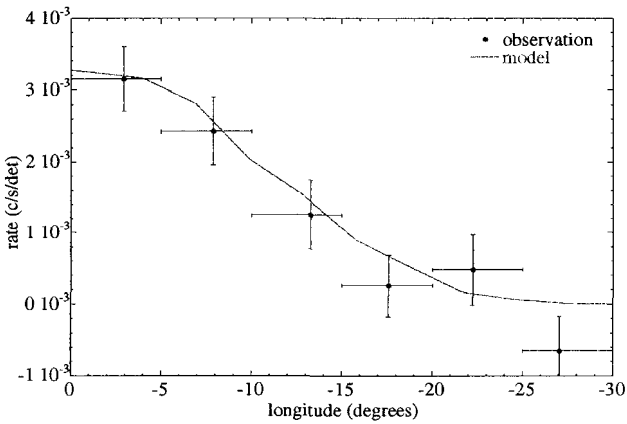

Figure 5. The positron annihilation gamma-ray line intensity in the inner Galaxy as observed with SPI, compared to the longitude distribution expected from a Gaussian-distributed model.

The spatial extent of the annihilation emission is not (yet) well constrained from these first studies[14,18]. But preliminary inspections of the 511 keV line flux as it varies for different exposures successively pointed along the plane of the Galaxy (Fig. 5, from Jean et al., 2003[14]) suggests that diffuse emission extends over a large volume. A preliminary constraint is given by a Gaussian distribution with an extent (FWHM) of 6^o–18^o[14]. First imaging attempts do not show hints for asymmetry, but confirm the extended and rather smoothly-distributed emission, both in longitude and latitude[18]. This suggests that annihilation near localized sources (in particular microquasars) does not dominate the positron bud-

get in the inner Galaxy, and rather a large number of sources distributed over a larger region, or distributed source processes, provide the origin of positrons. But e^+ propagation issues remain complex, and a deconvolution of the observed emission into the above candidate source categories remains a formidable challenge, including presently unknown parameters of the inner-Galaxy ISM.

4. Summary and Outlook

The measurement of characteristic gamma-rays from radioactive isotopes provides a useful complement to other means of the study of cosmic nucleosynthesis. With INTEGRAL, a spectrometer has been put in space, which is capable to measure details of the characteristic gamma-ray lines with sufficient precision to directly constrain abundances and kinematic of freshly-produced isotopes. First results on ^{26}Al and 511 keV emission confirm these perspectives. INTEGRAL is scheduled to observe the gamma-ray sky for at least five years. Its survey of the plane of the Galaxy, but also LMC observations and the study of SNIa from nearby galaxies, promises to significantly advance our understanding of supernovae and novae, and of the interstellar medium embedding the sources of nucleosynthesis.

Acknowledgments

The results reported here have been obtained through collaborative efforts of the team of SPI scientists, based on the excellent performance which resulted from the dedication of SPI detector and subsystem experts, and ESA with the Russian launch vehicle. SPI has been completed under the responsibility and leadership of CNES. We are grateful to ASI, CEA, CNES, DLR, ESA, INTA, NASA and OSTC for support.

References

1. Beckmann V., Borkowski J., Courvoisier T. J.-L. *et al. A&A*, **411**, L327 (2003).
2. Boehm C., Hopper D., Silk J., *et al.*, *astro/ph* 0309686 (2003).
3. Chen W., Diehl R., Gehrels N., *et al.*, *ESA-SP*, **382**, 105 (1997).
4. Chevalier R., *NewAstRev*,**46**, 449, (2002).
5. Diehl R., Knödlseder J., Lichti G.G., *et al.*, *A&A*, **411**, L451 (2003).
6. Diehl R., and Timmes F.X., *PASP*, **110, 748**, 637 (1998).
7. Diehl R., Dupraz C., Bennett K., *et al.*, *A&A*, **298**, 445 (1995).
8. Gehrels N., and Chen W., *A&AS*, **120**, 331 (1996).
9. Guessoum N., Ramaty R., Lingenfelter R.E. , *ApJ*, **378**, 170 (1991).

10. Hannikainen D. C., Vilhu O., Rodriguez J. , *et al.*, *A&A*, **411**, L415 (2003).
11. Harris M.J., Teegarden B.J., Cline T.L., et al. , *ApJ*, **501**, L55 (1998).
12. Iyudin A. F., Bennett K., Bloemen H., *et al.*, *A&A*,**300**, 422 (1994).
13. Iyudin A. F., Diehl R., Bloemen H., *et al.*, *A&A*,**284**, L1 (1994).
14. Jean P., Vedrenne G., Roques J.-P., *et al.*, *A&A*, **407**, L55 (2003).
15. Jose J., and Henrnanz M., *ApJ*, **494**, 680 (1998).
16. Kennel C.F., and Coroniti F.V., *ApJ*,**283**, 694 (1984).
17. Kinzer R. *et al.*, *ApJ*, **559**, 705 (1999).
18. Knödlseder J., Lonjou V., Jean P., *et al.*, *A&A*, **411**, L457 (2003).
19. Knödlseder J., Bennett K., Bloemen H., *et al.*,*A&A*, **344**, 68 (1999).
20. Knödlseder J. , *ApJ*, **510**, 915 (1999).
21. Knödlseder J., Dixon D., Bennett K., *et al.* , *A&A*, **345**, 813 (1999).
22. Kozma C., and Fransson C., *ApJ*, **497**, 431 (1998).
23. Kretschmer K., Diehl R., Hartmann D.H., *A&A*,**412**, 47 (2003).
24. Kurfess J. D., Johnson W. N., Kinzer R. L., *et al.*, *ApJL*, **399**, L137 (1992).
25. Leventhal M., Barthelmy S.D., Gehrels N., et al. , *ApJ*, **405**, L25 (1993).
26. Mahoney W. A., Ling J.C., Wheaton W.A., Lingenfelter R.E. , *ApJS*, **92**, 387 (1994)
27. Matz S. et al., *Nat.*, **331**, 416, (1988).
28. Mereghetti S., Gtz D., Beckmann V., *et al. A&A*, **411**, L311 (2003).
29. Milne P., Kurfess J., Kinzer R.E., *et al. AIP Conf. Proc.*, **587**, 11 (2001).
30. Mirabel I.F., Rodriguez L.F., Cordier B., *et al.*, *Nat.*, **358**, 215 (1992).
31. Naya J. E., Barthelmy S.D., Bartlett L.M., *et al.*, *Nat*, **384**, 44 (1996).
32. Oberlack, U., *Ph. D. Thesis, Technische Universität München* (1997).
33. Plüschke, S., Diehl, R., Schönfelder, V., *et al.*, *ESA SP*, **459**, 55 (2001).
34. Pottschmidt K., Wilms J., Chernyakova M., *et al. A&A*, **411**, L383 (2003).
35. Prantzos, N., and Diehl, R., *Phys. Rep.*, **267**, 1, (1996).
36. Purcell W.R., Cheng L.-X., Dixon D.D., *et al.*, *ApJ*, **491**, 725 (1997).
37. Ramaty R., Skibo J., Lingenfelter R.E., *ApJS*, **92**, 393 (1994).
38. Roques J.-P., Schanne S., von Kienlin A., *et al.*, *A&A*, **411**, L91 (2003).
39. Schönfelder V., Bloemen H., Collmar W., *et al.*, *AIP Conf Proc*, **510**, 54 (2000).
40. Share G.H., Leising M.D., Messina D.C., *et al.*, *ApJ*, **385**, L45 (1990).
41. Smith, D. , *ApJ*, **589**, L55 (2003).
42. Sturner S. J., and Naya J. E., *ApJ*, **526**, 200 (1999).
43. Timmes F.X., Woosley, S.E., Hartmann, D.H., *et al.*, *ApJ*, **464**, 332 (1996).
44. Tueller J., Barthelmy S., Gehrels N., *et al.*, *ApJ*, **351**, L41 (1990).
45. Vedrenne G., Roques J.-P., Schönfelder V., *et al.*, *A&A*, **411**, L63 (2003).
46. von Kienlin A., Beckmann V., Rau A., *et al.*, *A&A*, **411**, L299 (2003).
47. Walter R., Rodriguez J., Foschini L. , *et al. A&A*, **411**, L427 (2003).
48. Winkler C., Courvoisier T. J.-L., Di Cocco G. *et al. A&A*, **411**, L1 (2003).
49. Zhu T., and Ruderman M, *ApJ*,**48**, 701 (1987).

PROBING THE GALACTIC CHEMICAL EVOLUTION OF SI AND TI WITH PRESOLAR SIC GRAINS

SACHIKO AMARI[†], ERNST ZINNER[†]
Laboratory for Space Sciences and the Physics Department, Washington University, St. Louis, Missouri 63130, USA

ROBERTO GALLINO*
Dipartimento di Fisica Generale dell'Universita' di Torino, 10125 Torino, Italy
Centre for Stellar and Planetary Astrophysics, School of Mathematical Sciences, Monash University 3800 Victoria, Australia

MARIA LUGARO*
Institute of Astronomy, University of Cambridge, Cambridge, CB3 0HA, UK

OSCAR STRANIERO
INAF-Osservatorio Astronomico di Teramo, I-64100 Teramo, Italy

INMA DOMÍNGUEZ
Departmento de Física Teórica y del Cosmos, Universidad de Granada, E-18071 Granada, Spain

Presolar SiC grains of the types mainstream, Y, and Z are believed to have formed in thermally pulsing asymptotic giant branch stars with a range of metallicity: mainstream grains in stars of close-to-solar metallicity, Y grains in stars of around half-solar metallicty, and Z grains in stars of around one-third solar metallicity. From their Si and Ti isotopic ratios, it is possible to obtain information on both neutron capture processes that take place in the He intershell and initial compositions of the parent stars of the grains. Since Z grains formed in stars with the lowest metallicity, their study will likely provide insight into the Galactic chemical evolution of these elements as well as nuclear processes in low-metallicity stars. A preliminary comparison of data on Z grains with models of AGB stars confirms that Z grains formed in low-metallicity stars ($Z \leq 0.006$). The $^{12}C/^{13}C$ ratios of the Z grains indicate that in these stars cool bottom processing operates during the third dredge-up.

1. Introduction

Our solar system formed from a collapsing molecular cloud 4.6 billion years ago. Until the late sixties, it was believed that solid material in the molecular

[†] This work is supported by NASA grant NAG5-11545.
* This work is supported by Italian FIRB Project "Astrophysical Origin of the Heavy Elements Beyond Fe".

cloud completely evaporated during this event and thus the solar system was isotopically homogenized. This notion had been widely accepted since isotopic ratios of bulk meteorites, the only extra-terrestrial object available at that time, were identical to those of terrestrial material.

The first indication of the preservation of extra-solar material came from isotopically anomalous noble gases in primitive meteorites. When Black and Pepin [1] heated six carbonaceous chondrites in incremental temperature steps and analyzed isotopic ratios of Ne released in each step, in the temperature fractions between 900 and 1000°C they observed low ratios ($^{20}Ne/^{22}Ne$ down to 3.4, $^{20}Ne/^{22}Ne_{air}$=9.8) that had previously not been seen in meteorites. Later, this Ne-rich component was named Ne-E [2]. It has been proposed that the low $^{20}Ne/^{22}Ne$ ratio is due to ^{22}Na that decays to ^{22}Ne with half life of 2.6 years [3]. As this component is observed in only a few temperature steps, the fraction of the anomalous noble gas relative to the total ^{22}Ne in meteorites is very small ($\sim 7\times10^{-4}$ in the Orgueil meteorite). Isotopically anomalous components have been also observed for Kr and Xe. The Kr and Xe components that are enriched in even-number isotopes are called Kr-S and Xe-S, respectively, because this pattern is the signature of the *s*-process [4]. Xenon that is enriched in both *l*ight and *h*eavy isotopes has been named Xe-HL; it most likely originated from supernovae [5].

The minerals that contained the anomalous noble gases are what we now call presolar grains. Presolar grains formed in stellar outflows or stellar ejecta, and were incorporated into meteorites where they retained their distinct isotopic ratios. At the time these anomalous noble gas components were discovered, the carrier minerals were not known although subsequent studies indicated that they seemed to be carbonaceous. Thus, Edward Anders, Roy S. Lewis and their colleagues at the University of Chicago, the group that finally succeeded in isolating the minerals, temporarily gave the carriers alphabetical names such as Cα and Cβ during their search [6]. In 1987, diamonds, which carry Xe-HL were finally isolated from a meteorite [7], followed by SiC [8, 9] and graphite [10].

Presolar grains that do not contain anomalous noble gases have been identified by secondary ion mass spectrometry (SIMS) single-grain isotopic analysis. Oxide grains were located in acid resistant residues from meteorites because of their anomalous O isotopic ratios [11-13]. Recently, advances in SIMS instrumentation [14] have made it possible to identify presolar silicate grains in interplanetary dust particles [15] and the Acfer094 meteorite [16] by their anomalous O isotopic ratios. Other mineral types of presolar grains identified up to date include refractory carbides [17, 18] and silicon nitride [19].

2. Silicon carbide grains of an AGB star origin

2.1. *Carbon, N and Si isotopic ratios of SiC grains*

Of the types of presolar grains, SiC has been most extensively studied. The reason is that the extraction procedure of SiC is straightforward compared with that of graphite [20]. Furthermore, SiC grains occur in various kinds of meteorites [21] with relatively high abundances (6ppm in the Murchison meteorite). Most data on single SiC grains have been obtained by ion probe isotopic analysis. In Figure 1, which shows C and N isotopic ratios of SiC grains, the data points cluster in specific regions. This fact led to the classification of SiC grains into populations according to their C, N and Si isotopic ratios (Figs. 1 and 2).

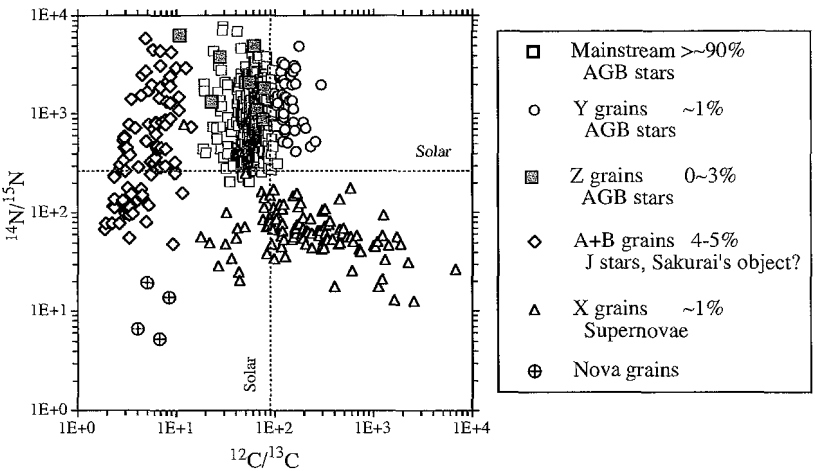

Figure 1. Carbon and N isotopic ratios of SiC grains. The grains have been classified into several populations based on their C, N and Si isotopic ratios. Abundances and proposed stellar sources of the populations are shown in the legend. Error bars are smaller than the symbols. Data are from [19, 22-28].

Mainstream grains, making up more than 90% of presolar SiC, have lower $^{12}C/^{13}C$ and higher $^{14}N/^{15}N$ ratios than the sun [22]. We note that grains of the minor populations, which comprise the rest, are overrepresented in Figs. 1 and 2 because they were preferentially studied after having been identified by a technique called ion imaging (their abundances are shown in the legend of Fig. 1). A+B grains are defined as having $^{12}C/^{13}C$ ratios lower than 10 with a range of $^{14}N/^{15}N$ ratios. Since it is difficult to explain the spread of the $^{14}N/^{15}N$ ratios by one type of stellar source, at least two types of stellar sources seem to exist

for this population [25]. X grains are characterized by ^{28}Si excesses up to 5 times solar in addition to higher-than-solar $^{12}C/^{13}C$, and lower-than-solar $^{14}N/^{15}N$ ratios. They most likely formed in supernovae [29]. Only a handful of putative nova grains with low $^{12}C/^{13}C$ and $^{14}N/^{15}N$ ratios have been identified [30].

Grains of type Y and Z exhibit higher-than-solar $^{14}N/^{15}N$ ratios, similar to mainstream grains. Y grains are defined as having $^{12}C/^{13}C>100$ [23], while Z grains show $^{12}C/^{13}C$ ratios similar to those of mainstream grains [24]. Silicon isotopic ratios in mainstream, Y and Z grains show a systematic trend. First, average $^{29}Si/^{28}Si$ ratios systematically decrease from mainstream to Y to Z grains ($\delta^{29}Si/^{28}Si$ = 55±46, 18±36, and −76±57‰, where $\delta^{i}Si/^{28}Si(‰) \equiv [(^{i}Si/^{28}Si)_{grain}/(^{i}Si/^{28}Si)_{solar}-1]\times1000$). Second, the spread of $\delta^{30}Si/^{28}Si$ values systematically becomes larger: average $\delta^{30}Si/^{28}Si$ values with standard deviations are 44±36, 67±43, and 91±170‰ for mainstream, Y and Z grains, respectively. Grains of the three populations are believed to have formed in asymptotic giant branch (AGB) stars of a range of metallicity [31]: mainstream grains in AGB stars of close-to-solar metallicity [32], Y grains of around half solar metallicity [23], and Z grains of around one-third of solar metallicty [24].

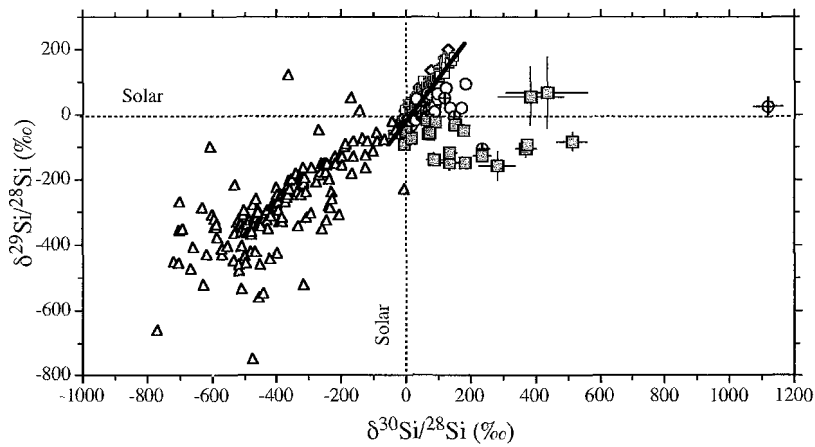

Figure 2. Silicon isotopic ratios of SiC grains expressed as δ values, which are deviations from the solar ratios in parts per thousand. Data are from [19, 22-28]. Symbols are the same as in Fig. 1. The correlation line for the mainstream grain data is shown.

2.2. *AGB star origin of mainstream, Y and Z grains*

The strongest proof of an AGB star origin of the mainstream grains came from isotopic measurements of heavy elements on bulk samples (=aggregates of grains) and later on single grains. Since >90% of the SiC grains are mainstream grains, bulk analyses can be regarded as representative of mainstream grains.

s-Process isotopic ratios inferred from the grain analyses agree quite well with average ratios predicted for low-mass (1-3$M_{\odot}$) AGB stars with solar metallicity [32], as shown in Fig. 3 in the case of Xe [33]. A good agreement is also observed for Kr, Sr, Xe, Ba, Nd, and Sm (bulk analyses) [32] as well as Zr and Mo (single grain analyses) [34, 35].

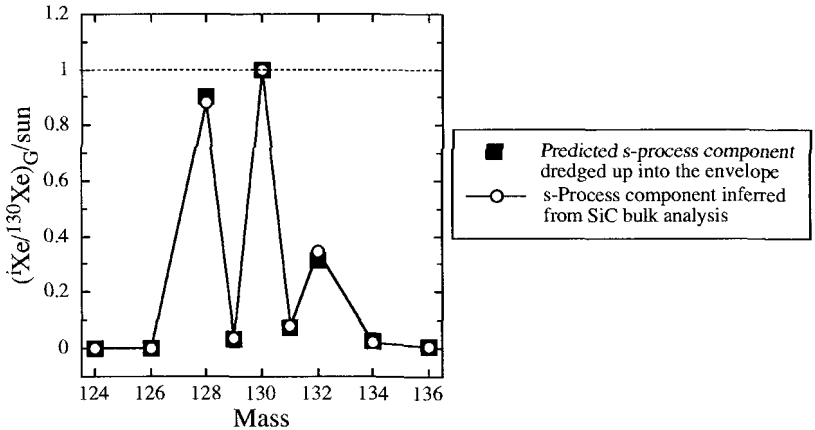

Figure 3. *s*-Process Xe inferred from noble gas analysis of aggregates of SiC grains (open circles) [36, 37] agrees with theoretical predictions of cumulative *s*-process Xe that is dredged up into the envelope during third dredge up episode (denoted as "G" in the ordinate) in low-mass AGB stars with solar metallicity [33].

An AGB star origin of Y and Z grains has been concluded from the similarity of isotopic ratios of light elements to those of mainstream grains and comparison with model calculations [23, 24].

Silicon isotopic ratios of the mainstream grains bear the signature of both, the original composition of the grains' parent stars and neutron-capture that took place inside stars. However, the latter is not as pronounced as the *s*-process signature in the heavy elements. Silicon data of the mainstream grains plot along a line in a Si 3-isotope plot (Fig. 2). Expected isotopic shifts due to neutron capture (27‰ in $\delta^{30}Si/^{28}Si$ in 2$M_{\odot}$ stars of solar metallicity) are much smaller than the whole range observed in the grains (–50 to 100‰). Furthermore, the slope due to neutron capture process (0.11) is expected to be much smaller than the slope of the mainstream correlation line (1.31). Thus the linear trend has been interpreted as representing the initial compositions of parent stars of the mainstream grains, which in turn are determined by the Galactic chemical evolution.

2.3. *Silicon and Ti*

The fact that Si in mainstream grains reflects two factors, neutron-capture in stars and the Galactic chemical evolution, can be well understood if we consider grain formation in AGB stars. Condensation temperatures of SiC depend on the total pressure. For assumed pressures of 10^{-5} to 10^{-3} bars (10–1000 dyn/cm^2) and C/O=1.05, SiC grains are expected to condense at ~1900 to 1500 K [38]. Thus, they formed in the stellar outflow, far away from the photosphere (where the temperature is estimated to be 2650 K). For SiC to condense the gas has to be C-rich. Otherwise, all C combines with O to form CO, which is a very stable molecule, and C is not available for the formation of carbonaceous grains. Meanwhile, in the He-rich region located between the H shell and He shell (He intershell) convective instabilities are episodically triggered by the thermal instability occurring periodically in the He shell (thermal pulses). After the quenching of a pulse, material from the He intershell, enriched in ^{4}He, ^{12}C and *s*-process elements, is mixed with material in the convective envelope (third dredge-up) when the convective envelope penetrates in the upper region of the He-intershell, which eventually makes the envelope C-rich [39]. The conditions of low temperature and C>O require that the SiC grains formed in the stellar outflow during and/or after third dredge-up. The composition of the envelope during that period is the result of mixing between two components, the initial composition of the star and that of the burnt material in the He shell and He intershell.

It is estimated that overproduction factors of ^{28}Si and ^{48}Ti that are processed in the He intershell and dredged up into the envelope (averages of 1.5 and $3M_\odot$ stars of half solar metallicity), so-called the G-component, are 1.09 and 0.77, respectively, while those of *s*-process only isotopes such as ^{96}Mo and ^{138}Ba are 1000, which for the heavy elements results in a complete domination of the nucleosynthesis component in the mix.

It should be pointed out that, of the trace elements found in SiC, Ti is the third most abundant element after N and Al and this enables us to make Ti isotopic measurements with relatively small errors.

2.4. *Z grains*

Among the three SiC populations with an AGB star origin, Z grains are of a particular interest, since they formed in stars of the lowest metallicity [24]. The Z grains that were studied were analyzed for isotopic ratios of only one or two elements in addition to Si. This is because they are more abundant among small grains (<1μm) and most studies on SiC have been performed for grains larger

than 1μm. Two grains were analyzed for Ti isotopic ratios (Fig. 4) [40] with a new type of ion probe, the NanoSIMS [14].

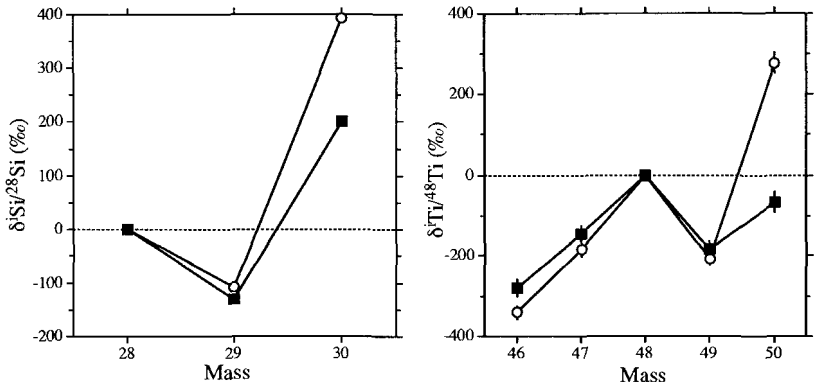

Figure 4. Silicon and Ti isotopic ratios of two Z grains. The grains show strikingly similar isotopic patterns except for $^{30}Si/^{28}Si$ and $^{50}Ti/^{48}Ti$ ratios. The dotted lines represent solar isotopic ratios.

The two Z grains have relatively high $^{12}C/^{13}C$ ratios (93.5±0.6 and 81.1±0.5) but exhibit the typical Si isotopic signature of Z grains with ^{29}Si depletions and ^{30}Si enhancements. Their Ti isotopic patterns are striking. Titanium-46, ^{47}Ti and ^{49}Ti are depleted relative to ^{48}Ti to the same extent in the two grains, while their $^{50}Ti/^{48}Ti$ ratios are quite different. One grain has a ^{50}Ti excess ($\delta^{50}Ti/^{48}Ti$ = 276±26‰), while the other one has a deficit ($\delta^{50}Ti/^{48}Ti$ = -66±25‰). These $^{50}Ti/^{48}Ti$ ratios are positively correlated with the $^{30}Si/^{28}Si$ ratios of these two grains. During the third dredge-up, the $^{30}Si/^{28}Si$ and $^{50}Ti/^{48}Ti$ ratios in the envelope are expected to increase more than the other Si and Ti isotopic ratios, leading to relative ^{30}Si and ^{50}Ti excesses. The correlation thus reflects the result of nuclear processes in the He-intershell. After the addition of the material from the He-intershell that is enriched in neutron-rich Si and Ti isotopes, the isotopic ratios of the grains (except $^{30}Si/^{28}Si$ ratios and a $^{50}Ti/^{48}Ti$ ratio of one of the grains) are still lower than solar. This indicates that all original Si and Ti isotopic ratios in the parent stars of the two Z grains were lower than solar, suggesting stars of low metallicity.

3. Models of AGB stars

We have made a comparison between the Z grain data and predicted ratios in models of AGB stars. To model the nucleosynthesis in the He intershell, a post-processing code that computes neutron captures on nuclei from He to Bi [41] was used. The evolution of the nuclear abundances at the stellar surface is

subsequently calculated by mixing He intershell material by third dredge-up with a mass-losing envelope. Stellar structure features such as the envelope mass, the dredged-up mass, the temperature and density at the base of the convective pulse, as well as their trends in time and in mass during the convective thermal pulse, are needed as inputs in the post-processing code. The stellar structure parameters for a large number of models were obtained from the analytic formulas for AGB stars of masses $\leq 3M_{\odot}$ provided by Straniero et al. [42]. These formulas were generated by interpolating the results of a set of stellar models which were previously evolved using the Frascati Raphson Newton Evolutionary Code (FRANEC) [43]. The model grid covers the following masses: M=1.5 and $3M_{\odot}$ and metallicities: Z=0.01, 0.006 and 0.003. Mass loss during the AGB phase is included by following the prescription of Reimers as expressed by the parameter η [44].

For the C/O ratio of solar metallicity, we used a revised value of 0.50 ± 0.07 from newly acquired spectroscopic data of the solar photosphere [45, 46]. Alpha enhancement, the linear enrichment of α elements with decreasing [Fe/H] down to –1, was taken into account for ^{12}C as well as ^{28}Si and ^{48}Ti based on the observation by Reddy et al. [47]. The adopted ^{16}O enhancement is based on the observation by Abia et al. [48]. The initial Si isotopic ratios are assumed to be –175‰ for Z=0.003, –115‰ for Z=0.006, and –70‰ for Z=0.01, and the initial Ti isotopic ratios to be –380‰ for Z=0.003, and –260‰ for Z=0.006.

3.1. *Comparison between the grain data and the models*

3.1.1. *Silicon*

The Si isotopic ratios of the Z grains and several cases of the model calculations are shown in a Si 3-isotope plot (Fig. 5). The spread of Si isotopic ratios in the models depends on both mass that is dredged up into the envelope and the maximum temperature at the bottom of the convective He-flash zone. The former increases with increasing mass, decreasing metallicity, and decreasing Reimers mass loss parameter η, whereas the latter increases with decreasing metallicity. The Z=0.003 and Z=0.006 models cover the data points fairly well. Since the Z=0.01 cases cover only a small range of the grain data, the Z grains more likely have formed in lower metallicity stars.

A point where the models do not agree with the data is the $^{12}C/^{13}C$ ratios. Whereas C isotopic ratios of the Z grains are in the same range as those of mainstream grains, the models predict that at the end of third dredge up, $^{12}C/^{13}C$ ratios in the envelope are high in low-metallicity stars (855 for $3M_{\odot}$ stars of Z=0.006). In order to explain the $^{12}C/^{13}C$ ratios of the Z grains, Hoppe et al.

[24] invoked cool bottom processing (CBP) after the first dredge up and before the AGB phase [49-52], which is considered to take place in stars with mass of less than $2.3M_{\odot}$.

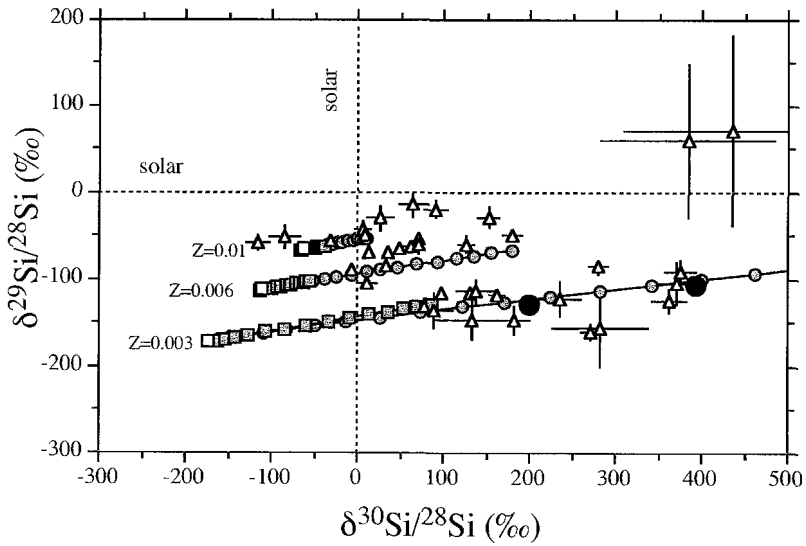

Figure 5. Triangles represent Z grain data obtained by [24, 53-55]. The two solid circles are the grains for which Ti isotopic ratios had been measured [40]. Squares indicate $M=1.5M_{\odot}$ models, while circles $M=3M_{\odot}$ models. Reimers mass loss parameter η is 0.3 for all cases. Open symbols indicate ratios when the envelope is O-rich and filled symbols when it is C-rich.

Nollett et al. [56] proposed that cool bottom processing (CBP) occurs also during the thermally pulsing phase of AGB stars. Hot bottom burning (HBB) that takes place in intermediate mass stars also produces low $^{12}C/^{13}C$ ratios, but also high $^{26}Al/^{27}Al$ ratios. The ratios of two Z grains ($<2.9\times10^{-3}$, $1.9\pm0.9\times10^{-3}$) [24] are lower than those predicted form models of HBB, indicating that CBP is a more likely process.

3.1.2. *Titanium*

With only two data points, it is not possible to see any trend. One piece of important information is that the initial $^{47}Ti/^{48}Ti$ ratios are lower than the assumed values. Initial compositions may vary depending on a better fine-tuning for the choice of the α-enhancement. There is uncertainty of a factor of two on the Galactic chemical evolution inferred from spectroscopic observations. It should be also noted that Ti cross sections have uncertainties of about 10%

(1σ). New measurements of the Ti cross sections are expected to improve the precision of the model calculations.

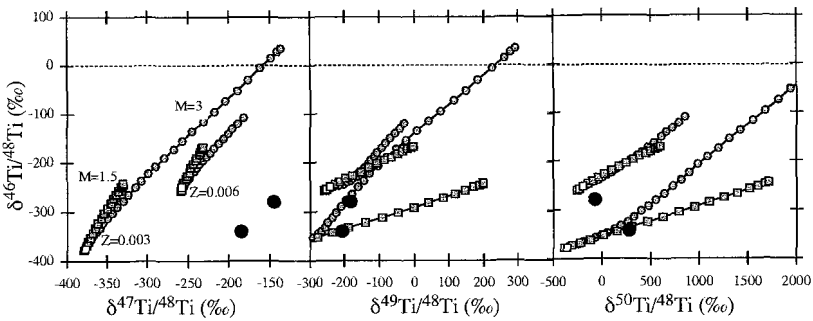

Figure 6. Titanium isotopic ratios of two Z grains and predicted ratios in the envelope. The symbols are the same as those in Fig. 5. The dotted lines indicate solar isotopic ratios.

4. Future work

Obviously it is highly desirable to find more Z grains, analyze their Ti isotopic ratios and have a larger data set for Z grains. As for the other populations of grains of an AGB star origin, Ti isotopic ratios of Y grains have previously been analyzed [23]. However, the large errors of these measurements did not allow to detect a systematic difference between the Ti isotopic ratios of Y grains and mainstream grains [23]. Thus, it would also be helpful to reanalyze Ti isotopic ratios of Y grains with the NanoSIMS.

References

1. D. C. Black and R. O. Pepin, *Earth Planet. Sci. Lett.*, **6**, 395 (1969).
2. D. C. Black, *Geochim. Cosmochim. Acta,* **36**, 377 (1972).
3. D. D. Clayton, *Nature,* **257**, 36 (1975).
4. B. Srinivasan and E. Anders, *Science,* **201**, 51 (1978).
5. R. S. Lewis, B. Srinivasan and E. Anders, *Science,* **190**, 1251 (1975).
6. E. Anders In *Meteorites and the Early Solar System,* (J. F. Kerridge and M. S. Matthews) 927 University of Arizona Press, (1988).
7. R. S. Lewis, M. Tang, J. F. Wacker, E. Anders and E. Steel, *Nature,* **326**, 160 (1987).
8. T. Bernatowicz, G. Fraundorf, M. Tang, E. Anders, B. Wopenka, E. Zinner and P. Fraundorf, *Nature,* **330**, 728 (1987).
9. M. Tang and E. Anders, *Geochim. Cosmochim. Acta,* **52**, 1235 (1988).
10. S. Amari, E. Anders, A. Virag and E. Zinner, *Nature,* **345**, 238 (1990).
11. I. D. Hutcheon, G. R. Huss, A. J. Fahey and G. J. Wasserburg, *Astrophys. J.,* **425**, L97 (1994).

12. G. R. Huss, A. J. Fahey, R. Gallino and G. J. Wasserburg, *Astrophys. J.*, **430**, L81 (1994).
13. L. R. Nittler, C. M. O'D Alexander, X. Gao, R. M. Walker and E. Zinner, *Astrophys. J.*, **483**, 475 (1997).
14. F. J. Stadermann, R. M. Walker and E. Zinner, *Lunar Planet. Sci.*, **XXX**, Abstract #1407 (1999).
15. S. Messenger, L. P. Keller, F. J. Stadermann, R. M. Walker and E. Zinner, *Science*, **300**, 105 (2003).
16. A. N. Nguyen and E. Zinner, *Science*, in revision (2004).
17. T. J. Bernatowicz, S. Amari, E. K. Zinner and R. S. Lewis, *Astrophys. J.*, **373**, L73 (1991).
18. T. J. Bernatowicz, R. Cowsik, P. C. Gibbons, K. Lodders, B. Fegley, Jr., S. Amari and R. S. Lewis, *Astrophys. J.*, **472**, 760 (1996).
19. L. R. Nittler et al., *Astrophys. J.*, **453**, L25 (1995).
20. S. Amari, R. S. Lewis and E. Anders, *Geochim. Cosmochim. Acta*, **58**, 459 (1994).
21. G. R. Huss and R. S. Lewis, *Geochim. Cosmochim. Acta*, **59**, 115 (1995).
22. P. Hoppe, S. Amari, E. Zinner, T. Ireland and R. S. Lewis, *Astrophys. J.*, **430**, 870 (1994).
23. S. Amari, L. R. Nittler, E. Zinner, R. Gallino, M. Lugaro and R. S. Lewis, *Astrophys. J.*, **546**, 248 (2001).
24. P. Hoppe et al., *Astrophys. J.*, **487**, L101 (1997).
25. S. Amari, L. R. Nittler, E. Zinner, K. Lodders and R. S. Lewis, *Astrophys. J.*, **559**, 463 (2001).
26. S. Amari, P. Hoppe, E. Zinner and R. S. Lewis, *Astrophys. J.*, **394**, L43 (1992).
27. P. Hoppe, R. Strebel, P. Eberhardt, S. Amari and R. S. Lewis, *Meteorit. Planet. Sci.*, **35**, 1157 (2000).
28. S. Amari, X. Gao, L. Nittler, E. Zinner, J. José, M. Hernanz and R. Lewis, *Astrophys. J.*, **551**, 1065 (2001).
29. S. Amari and E. Zinner In *Astrophysical Implications of the Laboratory Study of Presolar Materials*, (T. J. Bernatowicz and E. Zinner) 287 AIP, New York (1997).
30. S. Amari, X. Gao, L. Nittler, E. Zinner, J. José, M. Hernanz and R. S. Lewis, *Astrophys. J.*, **551**, 1065 (2001).
31. E. Zinner, S. Amari, R. Gallino and M. Lugaro, *Nuclear Physics A*, **A688**, 102 (2001).
32. R. Gallino, M. Busso and M. Lugaro In *Astrophysical Implications of the Laboratory Study of Presolar Materials*, (T. J. Bernatowicz and E. Zinner) 115 AIP, New York (1997).
33. M. Pignatari, R. Gallino, R. Reifarth, F. Käppeler, S. Amari, A. M. Davis and R. S. Lewis, *Meteorit. Planet. Sci.*, **38**, A152 (2003).
34. G. K. Nicolussi, A. M. Davis, M. J. Pellin, R. S. Lewis, R. N. Clayton and S. Amari, *Science*, **277**, 1281 (1997).
35. G. K. Nicolussi, M. J. Pellin, R. S. Lewis, A. M. Davis, S. Amari and R. N. Clayton, *Geochim. Cosmochim. Acta*, **62**, 1093 (1998).
36. R. S. Lewis, S. Amari and E. Anders, *Nature*, **348**, 293 (1990).

37. R. S. Lewis, S. Amari and E. Anders, *Geochim. Cosmochim. Acta,* **58**, 471 (1994).
38. K. Lodders and B. Fegley Jr., *Meteoritics,* **30**, 661 (1995).
39. M. Busso, R. Gallino and G. J. Wasserburg, *Ann. Rev. Astron. Astrophys.,* **37**, 239 (1999).
40. S. Amari, E. Zinner, R. Gallino and C. S. Lewis, *Meteorit. Planet. Sci.,* **38**, A66 (2003).
41. R. Gallino et al., *Astrophys. J.,* **497**, 388 (1998).
42. O. Straniero, I. Domínguez, S. Cristallo and R. Gallino, *Publ. Astron. Soc. Australia,* **20**, 389 (2003).
43. O. Straniero, A. Chieffi, M. Limongi, M. Busso, R. Gallino and C. Arlandini, *Astrophys. J.,* **478**, 332 (1997).
44. D. Reimers In *Problems in stellar atmospheres and envelopes,* 229 Springer-verlag, New York (1975).
45. C. Allende Prieto, D. L. Lambert and M. Asplund, *Astrophys. J.,* **556**, L63 (2001).
46. C. Allende Prieto, D. L. Lambert and M. Asplund, *Astrophys. J.,* **573**, L137 (2002).
47. B. E. Reddy, J. Tomkin, D. L. Lambert and C. A. Prieto, *Mon. Not. R. Astron. Soc.,* **340**, 304 (2003).
48. C. Abia, M. Busso, R. Gallino, I. Domínguez, O. Straniero and J. Isern, *Astrophys. J.,* **559**, 1117 (2001).
49. D. S. P. Dearborn, P. P. Eggleton and D. N. Schramm, *Astrophys. J.,* **203**, 455 (1976).
50. A. V. Sweigart, L. Greggio and A. Renzini, *Astrophys. J. Suppl.,* **69**, 911 (1989).
51. C. Charbonnel, *Astron. Astrophys.,* **282**, 811 (1994).
52. A. I. Boothroyd and I.-J. Sackmann, *Astrophys. J.,* **510**, 232 (1999).
53. C. M. O'D Alexander, *Geochim. Cosmochim. Acta,* **57**, 2869 (1993).
54. X. Gao and L. R. Nittler, *Lunar Planet. Sci.,* **XXVIII**, 393 (1997).
55. E. Zinner, S. Amari, R. Guinness and C. Jennings, *Meteorit. Planet. Sci.,* **38**, A60 (2003).
56. K. M. Nollett, M. Busso and G. J. Wasserburg, *Astrophys. J.,* **582**, 1036 (2003).

XMM OBSERVATIONS OF METAL ABUNDANCES IN THE INTRACLUSTER MEDIUM

KYOKO MATSUSHITA

Tokyo University of Science, 1-3 Kagurazaka, Shinjyuku, Tokyo, 162-8601, Japan E-mail: matusita@rs.kagu.tus.ac.jp

HANS BÖHRINGER, ALEXIS FINOGUENOV

Max-Planck-Institut für Extraterrestrische Physik, Postfach 1312, Garching, D85748, Germany

YASUSHI IKEBE

Joint center for Astrophysics, University of Maryland, Baltimore County, 1000 Hilltop Circle, Baltimore, MD 21250, USA

Based on XMM-Newton observations of the X-ray halo of M 87 and the Centaurus cluster, abundance profiles of O, Mg, Si, and Fe of the intracluster medium (ICM) are derived. The abundances of Si and Fe show strong decreasing gradients. In contrast, the O and Mg abundances are about a half of the Si abundance at the center. From the gas mass to stellar mass ratio and the comparison of Mg abundance with the stellar metallicity, the stellar mass loss from the central galaxies is indiated to be the main source of the gas in the very central region of the clusters. The observed O, Si and Fe abundance pattern determines the contribution of supernova (SN) Ia and SN II, with the abundance pattern of ejecta of SN Ia. The most of Si and Fe of the ICM in the central region of the clusters come from SN Ia occured in the central galaxies. In order to explain the observed O/Si ratio of a half solar, SN Ia products should have similar abundances of Si and Fe, which may reflect dimmer SN Ia observed in old stellar systems. The Mg/O ratio are close to those of Galactic stars, which indicates that nucleosynthesis of these elements has no discrepancy between our Galaxy and early-type galaxies.

1. Introduction

The intracluster medium (ICM) contains a large amount of metals, which are mainly synthesized in early-type galaxies[2,24]. Thus, abundances of the metals are tracers of chemical evolution of galaxies and clusters of galaxies.

Based on the Si/Fe ratio observed with ASCA, a discussion on contri-

butions from SN Ia and SN II to the metals has commenced. In a previous nucleosynthesis model of SN Ia, the Fe abundance is much larger than the Si abundance in the ejecta of SN Ia (W7 model[19]). Observations of metal poor Galactic stars indicate that average products of SN II have a factor of 2–3 larger abundance of α-elements than Fe[9],[18], although this ratio may depend on the initial mass function (IMF) of stars. Fukazawa et al.[13] systematically studied 40 nearby clusters and found that the Si/Fe ratio is lower among the low-temperature clusters, which indicates that SNe Ia products are also important among these clusters. From the observed radial dependence of the abundances, Finoguenov et al.[11] found that the SNe II ejecta have been widely distributed in the ICM.

In addition to the Si and Fe abundances, the XMM-Newton observatory enables us to obtain α-element abundances such as for O and Mg, which are not synthesized by SN Ia. Böhringer et al.[5] and Finoguenov et al.[12] analyzed annular spectra of M 87 observed by XMM-Newton, and found a flatter abundance gradient of O compared to steep gradients of Si, S, Ar, Ca, and Fe. The stronger abundance increase of Fe compared to that of O indicates an enhanced SN Ia contribution in the central regions A similar abundance pattern of O, Si and Fe is observed around center of A 496[26].

In this paper, abundances of O, Mg, Si and Fe of M 87 and the Centaurus cluster are discussed. We adopt for the solar abundances the values given by Feldman[10], where the solar Fe abundances relative to H is 3.24×10^{-5} in number.

2. Observation

M 87 was observed with XMM-Newton on June 19th, 2000. The effective exposures of the EPN and the EMOS are 30ks and 40ks, respectively. The Centaurus cluster was observed on January 3rd, 2002. The effective exposures of the EPN and the EMOS are 29 ks and 32 ks, The details of the analysis of background subtraction, vignetting correction and deprojection technique are described in Matsushita et al.[21],[22],[23]. When accumulating spectra of M 87, we used a spatial filter, excluding regions with soft emission around radio structures[4],[3],[21].

3. Result

The abundances of Mg and Fe of the ICM of the X-ray halo of M 87 and the Centaurus cluster are shown in Figure 1. In addition, the Si/Fe ratio and the O/Fe ratio of the two clusters are summarized in Figure 2.

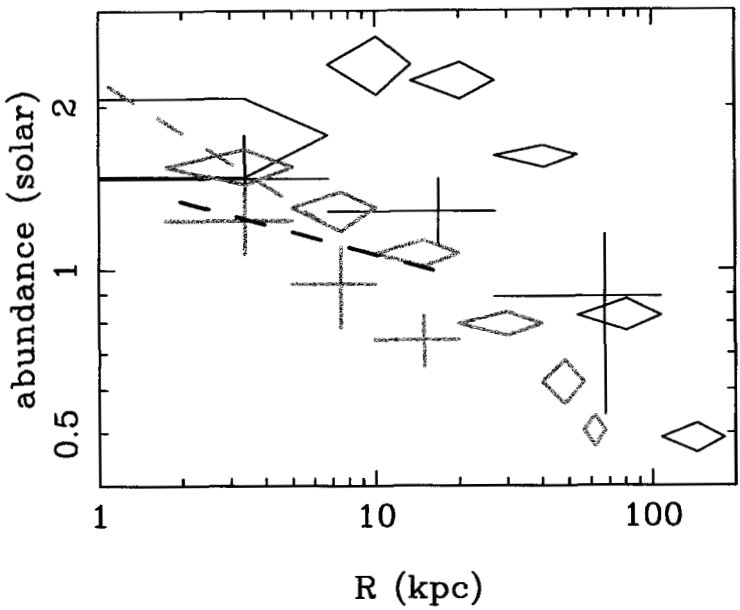

Figure 1. Abundance profiles of Fe (diamonds) and Mg (crosses) of M 87 (gray) and the Centaurus cluster (black). The dashed line represents the stellar metallicity derived from Mg_2 index[17].

These clusters have similar abundance patterns. The gradients of the Fe abundance profiles of these two clusters are steep at outer regions, while they become flatter in central regions. The Si abundance have similar profiles with those of Fe. In contrast, the O abundances are a factor of 2 smaller than the Fe and Si abundances, and have a flatter gradient. The Mg abundance is similar to the O abundance at the central region, while it is not obtained at the outer regions due to the instrumental Al line.

However, there are small discrepancies between the Centaurus cluster and M 87. The central Fe abundance of the Centaurus cluster, 2.2 solar, is significantly larger than 1.6 solar of M 87. The Si/Fe ratio of the former is 20% smaller than that of the latter. We have checked uncertainties in the temperature structure, and in the the background subtraction, and in the spectral model and found that their effects on the central Fe abundance and the Si/Fe ratio are smaller than the differences between the two clusters.

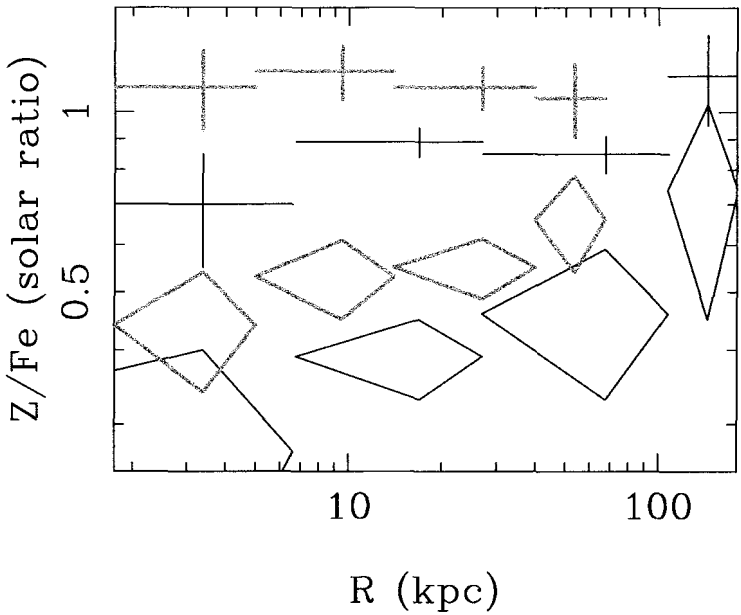

Figure 2. The Si/Fe ratio (crosses) and O/Fe ratio (diamonds) of M 87 (gray) and the Centaurus cluster (black).

4. Comparison with stellar metallicity and SN II abundance pattern

The gas within the cD galaxy is a mixture of the ICM and gas ejected from the cD galaxy recently. The O and Mg of the latter come from stellar mass loss and their abundances reflect the stellar metallicity, since they do not synthesized by SN Ia.

Figure 1 compares the observed Mg profiles with the stellar metallicity profiles from the Mg_2 index[17]. The Mg abundance profiles of the ICM are consistent within 20~30% with the stellar metallicity profile at the same radius.

The observed Mg/O ratios of the two clusters are consistent or slightly larger than the solar ratio, and also close to [Mg/O] of the Galactic stars[9]. The Mg/O ratio does not depends on uncertainties in temperature structure very much since the line ratio of Kα lines of these two elements is nearly constant above 1.1 keV[22]. The observed Mg/O ratio means that at least for the Mg/O ratio, the products of the Galactic SN II and those trapped

in stars in the cD galaxy have the same value.

The Mg_2 index depends not only Mg abundance but also total metallicity where O contributes most, although it also depends on age of stellar system. Therefore, we can conclude that the O and Mg abundances of the ICM are close to the stellar metallicity of the cD galaxy derived from the Mg_2 index. Since we are comparing abundances in two distinct media, stars and ISM, which could have very different histories, the abundance results do not have to agree in general. But this agreement indicate that the ICM in this region should be dominated by the accumulation of gas lossed from the central galaxy.

5. The Fe abundance profile and SN Ia contribution

The Fe in the gas at core of clusters is also a mixture of Fe in the ICM and the recent supply of Fe ejected from the cD galaxy. The latter contains Fe synthesized by recent SN Ia and that comes from stars through stellar mass loss, since Fe is synthesized by both SN Ia and SN II. The Fe abundance profiles of M 87 and the Centaurus cluster have negative radial gradients (Figure 1). This gradient should reflect the metal supply from the cD galaxy. The gradients become flatter within the effective radius of the cD galaxies, where, the O and Mg abundances of these clusters are close to the stellar metallicity derived from the Mg_2 index. These results indicate that the ICM in this region should be dominated by the accumulation of gas lossed from the central galaxy.

The Fe abundance of the ICM of the Centaurus cluster is systematically higher than that around M 87 at a same distance from the cluster center. For example, within the effective radius of these clusters, The peak Fe abundance of the Centaurus cluster is 2.2 solar. This value is significantly higher than that of M 87, which is 1.5 solar. Subtracting the SN II contribution, assuming that the O/Fe ratio of SN II is 3, the central Fe abundances from SN Ia of the Centaurus cluster and M 87 become 1.8 and 1.3 solar, respectively. The Fe abundance of gas from SN Ia in an elliptical galaxy is proportional to $M_{\rm SN}^{\rm Fe}\theta_{\rm SN}/\alpha_*$ [22]. Here, $M_{\rm SN}^{\rm Fe}$ is the mass of Fe synthesized by one SN Ia, $\theta_{\rm SN}$ is SN Ia rate, and α_* is stellar mass loss rate. Therefore, $M_{\rm SN}^{\rm Fe}\theta_{\rm SN}/\alpha_*$ of the Centaurus cluster is 40% higher than that of M 87, or the gas of M 87 is more diluted than the Centaurus cluster, which is opposit to the standard cooling flow model as described in Section 7.

One of major difference between M 87 and the Centaurus cluster is gas mass to stellar mass ratio (Figure 3). Within the effective radius of the

cDs, the ratio of M 87 is only 1%, while that of the Centaurus cluster is several %. Considering that within the radius the gas is dominated by that comes from the cD galaxies, it may need a higher accumulation time in the Centaurus cluster than M87, although we do not know the actual gas flow rate due to the cooling flow problem as will discussed in §7. Integrating the stelar mass loss rate by Ciotti et al.[7], within the effective radius, the accumulation time scale of the Centaurus cluster is nearly 10 Gyr, while that of the M 87 is a few Gyr. This result suggests that $M_{\rm SN}^{\rm Fe}\theta_{\rm SN}/\alpha_*$ was higher in the past. Therefore, Fe mass synthesized by a SN Ia was higher in the past or the ratio of SN Ia rate to stellar mass loss rate was higher in the past as suggested in Renzini et al[24].

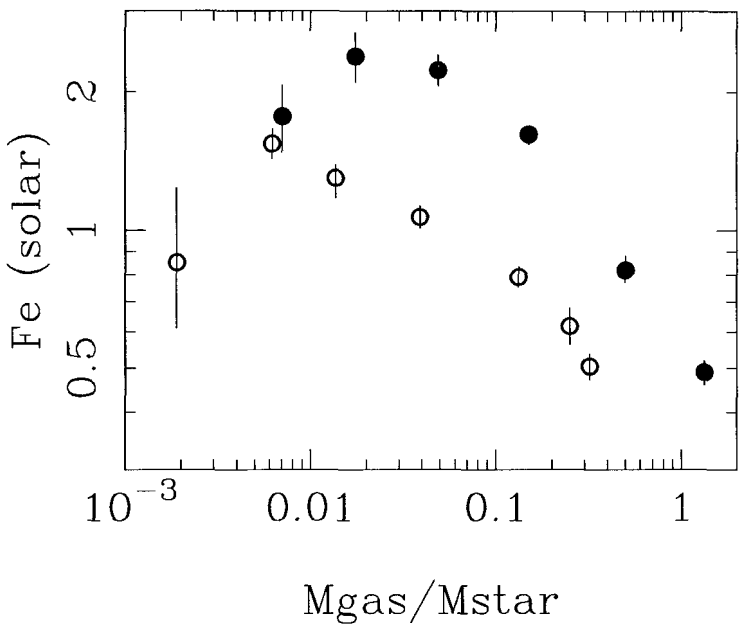

Figure 3. The Fe abundances of the ICM of the M 87 (open circles) and the Centaurus cluster (closed circles) are plotted against the integrated gas mass to stellar mass

6. The abundance ratios of O,Si and Fe and abundance pattern of SN Ia

The Si/Fe ratios of the two clusters are determined to be close to unity. For M 87, the Si/Fe ratio is ~1.1 solar ratio, and for the Centaurus cluster, it is ~ 0.9 solar ratio. In contrast, the O/Fe ratio is less than 0.5 solar at the center and increases with radius.

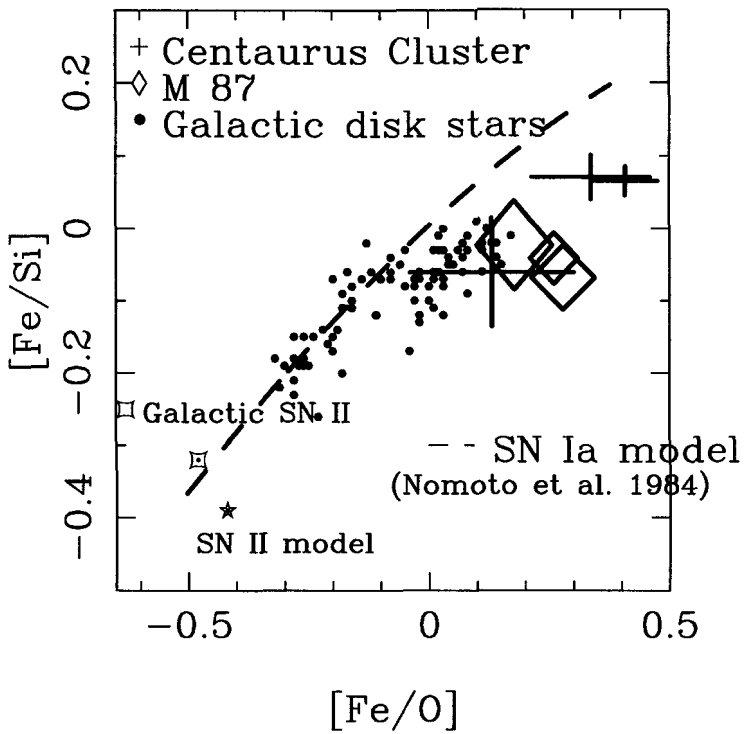

Figure 4. [Fe/Si] of the ICM of the Centaurus cluster (crosses;[23]) and M 87 (diamonds;[22]) are plotted against [Fe/O]. The average value of Galactic metal poor stars and the abundance ratio of SN II model using the nucleosynthesis model (asterisk) derived in Nomoto et al.[19], assuming Salpeter's IMF[15]. The dashed line represents the relation of the abundance pattern synthesized by SN Ia of W7 model[19]

Figure 4 summarizes the abundance pattern of O, Si, and Fe of the ICM. Although the abundance pattern of ejecta of SN II may differ between early-type and late-type galaxies, and that of SN Ia also may not be a

constant[27],[12], for a first attempt we have assumed $(Fe/Si)_{SNIa}$, $(Si/O)_{SNII}$, and $(Fe/O)_{SNII}$ to be constants. Here, $(Fe/Si)_{SNIa}$ is the Fe/Si ratio of ejecta of SN Ia, and $(Si/O)_{SNII}$ and $(Fe/O)_{SNII}$ are the Si/O ratio and the Fe/O ratio of the ejecta of SN II, respectively.

The classical deflagration model of SN Ia, W7[19], expects the Fe/Si ratio of 2.6 solar ratio. When we adopt the abundance pattern of the Galactic metal poor stars by Clementini et al.[8] as that of SN II, $(Fe/Si)_{SNIa}$ of M 87 is determined to be ~ 1 solar. That of the center of the Centaurus cluster is slightly larger than M 87, but still smaller than the W7 ratio. Thus, these values are much smaller than W7 model[19], and in the range of the ratio derived from the WDD models[15], which considers slow deflagration.

The light curves of observed SN Ia are not identical but display a considerable variation[14]. In SN Ia, the mass of synthesized Ni^{56} determines the luminosity of each SN. Since the mass of the progenitor should be constant at 1.4 $M_{\odot}$, the ratio of mass of intermediate group elements from Si to Ca, to the mass of Fe and Ni, should depend on the luminosity of SN Ia. The observed luminosity of SN Ia correlates with the type of the host galaxy, and is suggested to be related to the age of the system; SNe Ia in old stellar system may have smaller luminosities[16], and hence are suggested to yield a smaller Fe/Si ratio[27].

We note that the observed abundance patterns of the ICM are located at a extension of that of Galactic stars, although the observed [Fe/O] range of the ICM is systematically larger (Figure 4). The metal poor Galactic stars, i.e. those with lower [Fe/O], tend to be located around larger $(Fe/Si)_{SNIa}$ values. In contrast, the O/Si/Fe pattern of metal rich Galactic stars favor lower $(Fe/Si)_{SNIa}$ values. The difference of metal rich and metal poor Galactic stars are difference of age of the system when the stars were born. This result suggests that the SN Ia products trapped in the metal poor Galactic stars were dominated by those with larger $(Fe/Si)_{SNIa}$ when the Galaxy was a young stellar system.

In conclusion, as discussed in Finoguenov et al.[12], Matsushita et al.[22],[23] the smaller Fe/Si ratio observed for the ICM around M 87 and the Centaurus cluster may reflect the fact that M 87 and the cD galaxy of the Centaurus cluster are old stellar systems.

7. The failure of the cooling flow model

The Fe abundance profiles of M 87 and the Centaurus cluster contradicts the standard cooling flow model, consistent with the recent finding of the

missing of the cooling gas[20,25,6,21]. From the standard cooling flow model, the mass deposition rates of the Centaurus cluster and M 87 within 10 kpc and 27 kpc are determined to be $15M_{\odot}$ and 4 $M_{\odot}$, respectively[1,21], using a Hubble constant of 70 M pc/km/s. These values are much larger than the stellar mass loss rate within the radii, $\sim 0.4M_{\odot}$ and $\sim 1M_{\odot}$ for M 87 and NGC 4696, respectively. Even from the whole galaxy, the stellar mass loss rate of M 87 and NGC 4696 are only $1M_{\odot}$ and $2M_{\odot}$, respectively. Therefore, if a cooling flow with this mass deposition rate exists, the fraction of gas from the central galaxy must be low, and the central abundance of Mg and Fe of the Centaurus cluster should be smaller than that of M 87.

References

1. Allen, S. W., & Fabian, A.C., 1994, MNRAS, 269, 409
2. Arnaud M., Rothenflug R., Boulade O., et al. 1992, A&Ap, 254, 49
3. Belsole E., Sauvageot, J.L., Böhringer, H., et al. 2001, A&Ap, 365, L188
4. Böhringer H., Nulsen P.E.J., Braun R., & Fabian A.C., 1995, MNRAS, 274, 67
5. Böhringer, H., Belsole, E., Kennea, J., et al. 2001, A&Ap, 365, L181
6. Böhringer, H., Matsushita, K., Churazov, E., Ikebe, Y., & Chen, Y., 2002, A&Ap, 382,804
7. Ciotti L., Pellegrini S., Renzini A., & D'Ercole A. 1991, ApJ, 376, 380
8. Clementini, G., Gratton, R.G., Carretta, E. et al., 1999, MNRAS, 302, 22
9. Edvardsson, E., Andersen, J., Gustafsson B., et al. A&Ap,1993, 275, 101
10. Feldman, U., 1992, Physica Scripta 46, 202
11. Finoguenov, A., David, L.P., & Ponman, T.J, 2000, ApJ, 544, 188
12. Finoguenov A., Matsushita, K., Böhringer, H., et al. 2002, A&Ap, 381, 21
13. Fukazawa, Y., Makishima, K., Tamura, T., et al. 1998, PASJ, 50, 187
14. Hamuy, M., Philips, M.M., Suntzeff, N.B., et al. 1996, AJ 112, 2438
15. Iwamoto, K., Brachwitz, F., Nomoto, K., et al. 1999, ApJS, 125,439
16. Iwanov, V., Hamuy, M., & Pinto, P.A., 2000, ApJ, 542,588
17. Kobayashi, C., & Arimoto, N., 1999, ApJ, 527, 573
18. Nissen, P.E., Gustafsson, B., Edvardsson, B., et al. 1994, A&Ap, 285, 440
19. Nomoto, K., Thielemann, F-K., & Wheeler, J.C., 1984, ApJ, 279, 23
20. Makishima K., Ezawa H., Fukazawa Y., et al. 2001, PASJ, 53, 401
21. Matsushita, K., Belsole, E., Finoguenov, A., & Böhringer, H., 2002, A&Ap, 386, 77
22. Matsushita K., Finoguenov A., Böhringer H., 2003, A&Ap, 401, 443
23. Matsushita K., Böhringer H., Takahashi I., & Ikebe Y., 2004, submitted to A&Ap
24. Renzini A., Ciotti, L., D'Ercole, A., & Pellegrini, S. 1993, ApJ, 419, 52
25. Tamura T., et al. 2001a, A&Ap, 365, L87
26. Tamura, T., Bleeker, J.A.M., Kaastra, J.S, et al. 2001b, A&Ap, 379, 107
27. Umeda H., Nomoto K., & Kobayashi C. 1999, ApJ, 522, L43

RECENT ADVANCES IN THE STUDY OF EXTREMELY METAL-POOR STARS

F. PRIMAS

European Southern Observatory
KarlSchwarzschildstr. 2,
D-85748 Garching bei München, Germany
E-mail: fprimas@eso.org

The advent of 8-10m class telescopes equipped with very efficient and high resolution spectrographs has strongly boosted the study of chemical patterns in the Galactic halo, allowing us to derive very accurate abundances in the most metal-poor stars. Here, the tremendous progress recently achieved in this field of research is presented and critically reviewed.

1. Introduction: The Role of Metal-Poor Stars

The history of the chemical composition of the Galaxy is dominated by the nucleosynthesis occurring in many generations of stars. In each generation, a fraction of the gas will be transformed into metals and returned to the interstellar medium (ISM). What is important to know is how the environment dictated the kind of stars that formed and enriched the Galactic gas, and how the enriched gas mixed with the interstellar medium to form subsequent stellar generations.

A first step is to derive the halo metallicity distribution function which provides direct information about the initial stages of galaxy formation, being sensitive to the bulk chemical properties of the interstellar gas from which the earliest generations of stars were born. Comparisons between the relative numbers of low metallicity stars in the halo and models for Galactic chemical evolution can then be used to place constraints on the primordial rate of Type II supernovae (SNe), the star formation rate (SFR), and the timescale for the re-distribution of elements in the early Galaxy. Another key ingredient is to assemble a large, representative sample of the early Galactic halo, *i.e.* a large sample of the most metal-poor[a] and oldest stars.

[a]with a metal content [m/H] lower than 1/1000 solar (where $[m/H] = \log(m/H)_\star -$

Very metal-poor stars have now become one of the main diagnostic tools as they exhibit the products of nucleosynthesis from the first high-mass, zero-metallicity objects to evolve and pollute the proto-galaxy. Elemental abundance ratios observed in these low-mass stars allow us to probe the ejecta of the earliest SNe and determine the nature of the stars and sites of nucleosynthesis that existed during the first epochs of star formation in the Galaxy. Any variation in the elemental abundance ratios observed at different metallicites can then be compared with the yields derived from SNe of different masses to determine which ones have contributed to the Galactic chemical enrichment and when.

2. Metal-Poor Stars: Searches and Findings

Since the 50s, when the first two metal-poor stars were analysed (HD 19445 and HD 140283, Chamberlain & Aller, 1951) more than 8,000 metal-poor stars have been identified through a variety of techniques, the most successful of which have been proper-motion (*e.g.* Ryan & Norris 1991 and Carney et al. 1994) and objective-prism surveys (*e.g.* the HK survey of Beers et al. 1985, and the exploitation of the stellar content, by Christlieb et al. 1999, of the more recent HES survey).

The HK survey takes its name from the Ca II H and K lines falling in the 150 Å bandpass selected via an interference filter near the focal plane of the 61cm Curtis Schmidt telescope at CTIO. Because of its earlier start (compared to the HES), it has had a very strong impact on this field: it has produced a list of 10,000 candidate metal-poor stars, the identification of which is based on a calibration of the Ca II K line at 3933 Å as a function of metallicity and broad-band B-V colour. It is complete in the 11-15 B mag interval and the sky coverage is on the order of 7000 deg^2 (including also the Northern hemisphere fields, surveyed at the Burrell Schmidt telescope at KPNO). Approximately 100 stars with a metal content less than 1/1000 solar have been identified.

The other very successful survey is the more recent Hamburg-ESO Survey (Wisotzki et al. 2000), an objective-prism survey targeting primarily bright QSOs and covering the full southern extra-galactic sky (*i.e.* at Galactic latitudes $|b|$ >30°, ~10,000 deg^2). It is based on plates taken at the ESO Schmidt telescope, using a 4° prism. Because it is based on un-widened prism spectra it gains two magnitudes with respect to the HK survey (down

$\log(m/H)_\odot$, and m usually refers to the iron content)

to B=17.5). More than 8,700 metal-poor candidates have already been identified. Medium-resolution spectroscopic follow-ups of approximately 2/3 of these candidates have yielded ~200 stars with [Fe/H]≤ -3.0 (*cf* Christlieb et al. 2004).

Thanks to these efforts, we now have a large sample of extremely metal-poor stars representative of the early evolutionary phases of our Galaxy. In the following sections, I will address in some more detail the main outcomes of these surveys, namely: 1. which is the most metal-poor object ever detected ? 2. the most recent high-resolution spectroscopic follow-ups of large samples of the most metal-poor stars currently known; 3. the surprisingly high percentage of carbon-rich objects found among the most metal-poor population; 4. the discovery of few very metal-poor stars characterised by a peculiar abundance pattern in the n-capture elements.

2.1. *HE 0107−5240: the most metal-poor star ever found*

The halo giant HE 0107−5240 was discovered by Christlieb et al. (2002) during a medium-resolution spectroscopic follow-up of metal-poor candidates selected from the HES survey. From a high resolution spectrum taken at the VLT with UVES, it has been confirmed to have the lowest metallicity ever detected: [Fe/H]=−5.3. Therefore, the star is clearly important in the debate about the first mass function (*i.e.* top-heavy, or if both high- and low-mass stars played a role).

The star is characterised by large over-abundances of carbon, nitrogen, and oxygen, but no radial velocity variations have been detected so far. This implies that the mass transfer scenario (in which an AGB star produced the CNO observed today in HE 0107−5240 before evolving to a white dwarf) is not the most obvious explanation (though it cannot yet be excluded it, as the the radial velocity monitoring needs to be extended). The global abundance pattern of the star (in total there are 8 detections and 12 upper limits, Christlieb et al. 2004) can be accounted for if pre-enrichment from a zero-metallicity Type II supernova with a progenitor mass around 20-25$M_{\odot}$ is considered. Other possible scenarios include the mixing of the products ejected by two Pop III SNe (with masses of 35$M_{\odot}$ and 15$M_{\odot}$ respectively, *cf* Limongi et al. 2003) or a 25$M_{\odot}$ Pop III star exploding as a sub-luminous supernova ($E_{exp} \approx 3 \times 10^{50}$ erg) with mixing and fallback (Umeda & Nomoto 2003). However, the O abundance recently determined by Bessell et al. (2004) does not seem to support either one.

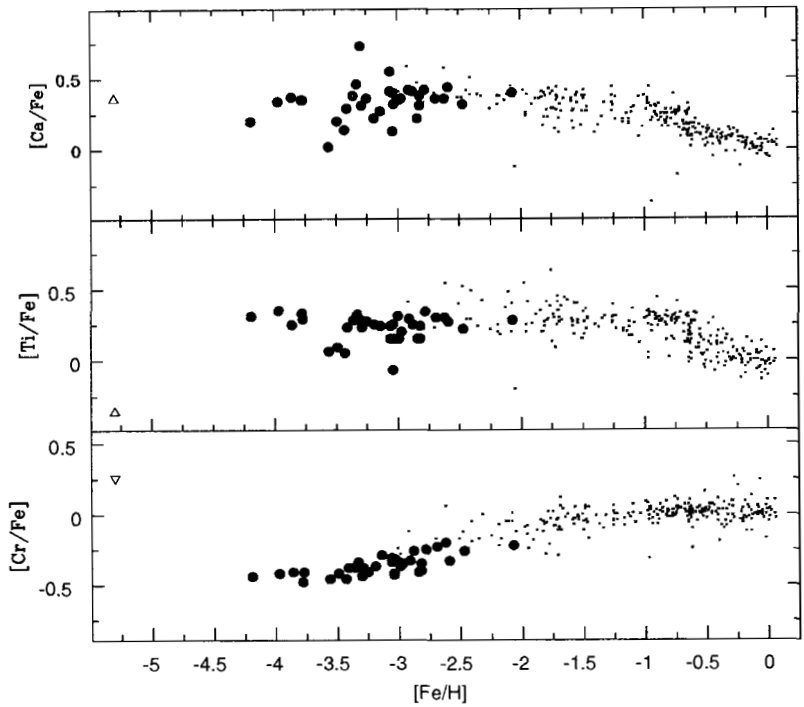

Figure 1. A selection of abundance ratios (Ca, Ti, and Cr) in the sample of giant stars analysed by Cayrel et al. (2004, filled circles). Typical errors are of the order of 0.10 dex or smaller. The open triangles represent abundances in *HE* 0107 − 5240 (Christlieb et al. 2004 - the Cr abundance is an upper limit). Small dots are abundance results for more metal-rich stars from Chen et al. (2000) and Fulbright et al. (2000).

2.2. *Chemical Signatures of the First Stellar Generations*

Thanks to the advent of 8-10m class telescopes equipped with efficient high-resolution spectrographs like UVES at the VLT (Dekker et al. 2000), HIRES at Keck I (Vogt et al. 1994), and HDS at Subaru (Noguchi et al. 2002) several observational campaigns have been devoted in recent years to high resolution studies of very metal-poor stars. The Pilot Program at Keck I (led by J. Cohen) analysed 8 metal-poor candidates selected from the HES survey, two of which have been confirmed to be extremely metal-deficient ([Fe/H]< -3.5, Carretta et al. 2003). During this meeting, we learned about the abundance results recently obtained at Subaru (Aoki, Ishimaru et al., Honda et al.; *this volume*). At the VLT, the Large Pro-

gram "The First Stars" (led by R. Cayrel) focused on the analysis of 65 objects (30 dwarfs and 35 giants), the majority of which has a metallicity lower than 1/1000 solar.

One of the most important outcomes of this work (Cayrel et al. 2004) is the finding of very well defined abundance trends, with very little dispersion down to the lowest metallicites (*cf* Fig. 1). Compared to previous works (*e.g.* McWilliam et al. 1995) these results are in agreement with the trends and slopes already found, but they disagree with the significant scatter previously found in the early Galaxy. This has clearly challenged again the debate about the number of SNe that polluted the early Galaxy and the size of the clouds undergoing independent chemical evolution in the first epochs of halo formation. The new abundance trends could imply that these stars have been pre-enriched by single burst events, or that mixing was very efficient already at those early epochs.

Another interesting result is the finding of a plateau at the lowest metallicity end in most of the elemental trends when abundances are plotted *vs* magnesium, instead of iron (*cf* Fig. 13 in Cayrel et al. 2004). Because these could tell us something about the primordial yields of the first supernovae to go off, they clearly deserve further investigation, especially on the theoretical side.

2.3. *C-rich, Very Metal-Poor Stars*

One unexpected result of the HK survey is the high percentage ($\approx$15%) of very metal-poor stars found to exhibit anomalously strong CH bands. This is certainly not a negligible fraction of the early halo, especially since inspections of the HES stellar database have shown that this number may be as high as 25-30%. Figure 2 shows the run of [C/Fe] ratios as a function of metallicity (see caption for references).

Chemical peculiarities in cool stars ($B - V > 0.4$) are often interpreted as a result of mixing nucleosynthesis products to the stellar surface. The nucleosynthesis may have taken place either in the star itself or in an evolved companion from which mass has been accreted either through Roche-Lobe overflow or through stellar winds. However, the first high-resolution analyses of some of these C-rich, very metal-poor stars have challenged such a straightforward scenario by finding each star to exhibit quite different abundance patterns.

Barbuy et al. (1997) and Norris et al. (1997) found that the C-enhancement in their respective samples was associated to over-abundances

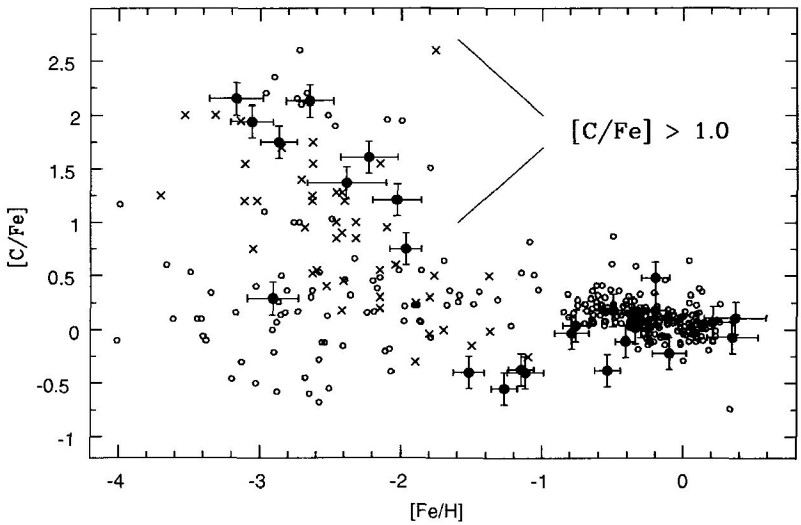

Figure 2. [C/Fe] vs [Fe/H] for a large sample of stars, assembled from: Rossi et al. (1999, crosses); Gustafsson et al. (1999) and Aoki et al. (2002a) and references therein (open circles). Filled circles are from Masseron et al. (2003), and they represent preliminary results from an on-going program at the VLT.

in the *s*-process elements (indicative of classical CH and Ba stars). The star CS 22892-052 (Sneden et al. 1994) was found to be characterised by a unique signature of enhanced *r*-process elements, whereas under-abundant *s*-process elements were detected in another very metal-poor, C-enhanced object studied by Bonifacio et al. (1998). Moreover, an 8-years radial velocity monitoring of seven metal-poor stars with abnormally strong CH G bands (Preston & Sneden 2001) found no variation (at least not exceeding 0.5 km/s) for approximately half of them.

Except for LP 625-44, which is one of the best studied examples (with 16 heavy elements detected, Aoki et al. 2002b) and which has been shown to be a binary (thus strongly supporting the mass-transfer scenario), the other stars remain very challenging. Fujimoto et al. (2000) suggested that extremely metal-poor stars may in fact be transformed into C-rich stars due to extensive mixing at the initiation of He-core burning. According to Abia et al. (2001) the IMF at zero metallicity must peak at intermediate mass in order to account for the C and N enhancements observed. Preston & Sneden (2001) proposed that the C-enhancement may come from

an enhanced mixing event at the end of the giant branch evolution that recycled the stars to the base of the sub-giant branch because of increased H-mixing into their cores. From extensive analyses of C-rich metal-poor stars, Aoki et al. (2002a) proposed that the origin of those stars characterised by enhanced *s*-process elements is likely to be in a binary system, whereas those objects found to have a normal *n*-capture signature could be low mass stars in which C and N have been self-enhanced during the AGB evolution phase, or they could be companions of slightly higher mass (0.8-1.0 $M_{\odot}$) stars from which C-rich material without excess of *n*-capture elements has been accreted.

Because of the clear challenge these stars represent to our understanding of the nucleosynthesis responsible for their abundance anomalies and of their role and influence in the evolution of the early Galaxy, several systematic analyses are under way, both at Subaru (*cf* Honda et al.; Aoki; and Ishimaru, *this volume*) and at the VLT (Masseron et al. 2003, Sivarani et al. 2004).

2.4. *n-capture Nucleosynthesis in the Early Galaxy*

The dominant isotopes of the elements with atomic numbers Z>30 are synthesised in neutron bombardment reactions during late stellar evolution phases. The work by Gilroy et al. (1988) has been one of the first large surveys of heavy elements abundances in metal-poor stars, which confirmed the operation of *r*-process (*rapid n*-captures) at low metallicity (theoretically predicted by Truran 1981), and revealed significant star-to-star scatter. The occurrence of *r*-process elements all the way up to the actinides in these very metal-deficient (and presumably very old) stars seem to demand massive stars of short lifetime.

Recently, the finding of few extremely metal-poor stars with very enhanced *r*-process signatures (factor of 50 or more, *cf* Sneden et al. 1994, 2003; Hill et al. 2002) has opened the path to new discoveries and challenges. First of all, thanks to the large enhancement factor, it has become possible to detect almost the entire range of the heavy elements, from germanium (Z=32) up to uranium (Z=92), thus including the 1^{st}, 2^{nd}, and 3^{rd} *n*-capture peaks. Transitions that otherwise would be too weak are in these stars of measurable strength. Furthermore, these stars have the advantage that some elemental abundances, usually determined from one transition only, can now be measured more reliably, combining a larger number of lines. One such example is thorium, whose abundance in

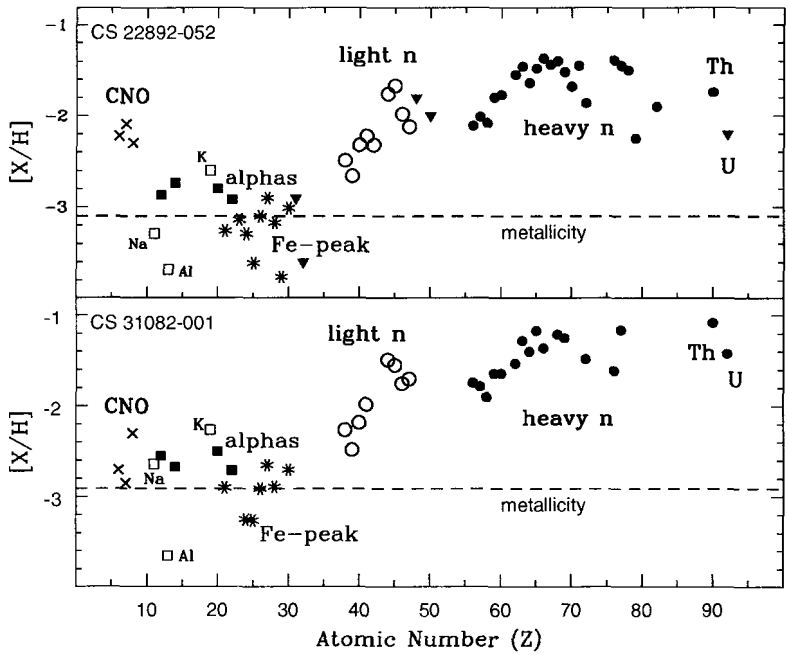

Figure 3. Detailed abundance analyses of two of the most metal-poor and n-capture rich stars known to date: CS 22892-052 (*top*, Sneden et al. 2003) and CS 31082-001 (*bottom*, Hill et al. 2002).

the spectrum of CS 31082-001 (Hill et al. 2002) has been derived from 11 absorption lines!

Because of their chemical peculiarities, these stars have been studied in very detail, and are now among the best studied stars apart from the Sun. Figure 3 shows the impressively complete abundance patterns of CS 22892-052 and CS 31082-001. Sneden et al. (1994, 2003) were the first ones to make a detailed analysis of a metal-poor star with a very distinctive mark of r-process nucleosynthesis: CS 22892-052, a K giant with $Fe/H] \simeq -3.0$, was found to be characterised by enormous over-abundances of all n-capture elements, reaching a maximum with [Dy/Fe]=+1.7. This demonstrated not only the occurrence of r-process nucleosynthesis in a stellar generation preceding that of the halo stars, but also it strongly argued for a single local prior SN event in a largely unmixed early Galactic halo.

The importance of CS 31082-001 (Hill et al. 2002, $[Fe/H] = -2.9$)

extends even further: its enhancement in heavy element abundances and a normal carbon abundance (thus minimising blending problems) have allowed the first detection of uranium in such a metal-poor object (Cayrel et al. 2001). Moreover, it has provided the first evidence that variations in progenitor mass, explosion energy, distance to dense interstellar clouds, and/or other intrinsic or environmental effects may produce significantly different r-process abundance patterns from star-to-star in the actinide region (Z>90).

2.4.1. *Cosmo-chronometry: Dating Very Metal-Poor Stars*

One of the basic assumptions behind what has been discussed so far is that the most metal-poor stars we observe today are also very old: if elements are continuously formed in stars, then a low metal content implies an old stellar population. The discovery of n-capture rich stars, among the most metal-deficient stars of the halo, has offered us a way to empirically confirm this, taking advantage of some of the heaviest isotopes. Nuclei in the actinides region are radioactively unstable but long-lived on astrophysically interesting (many Gyr) timescales. Therefore, comparisons of their abundances to some other stable n-capture element (such as Nd or Eu – Eu should be preferred because of its almost pure r-process origin in solar system material) have allowed the first stellar age estimates based on their radioactive decay.

This technique (similar to the ^{14}C dating for archaeological finds) was first applied to CS 22892-052 (Cowan et al. 1997) using the [Th/Eu] ratio, from which an age of 15.2 Gyr $\pm$ 3.7 Gyr was derived based on the assumption of a universal r-process pattern. The biggest uncertainty of this technique lies in the assumption of the initial Th/r production ratio, thus far determined by fitting theoretical nucleosynthesis results to the solar r-process pattern. The assumed universality of the r-pattern in all astrophysical environments was extrapolated from the finding of a broad agreement between the heavier n-capture elements and the scaled solar system r-process curve observed in CS 22892-052.

However, actinides and lower-mass r-nuclei have been found to vary strongly in CS 31082-001 (Hill et al. 2002), despite the abundance constancy for all nuclei with Z=56-82 (*cf* also Honda et al. *this volume*), thus raising some doubts about the universality of the r-process in the early Galaxy. An important consequence of these variations is the failure of the conventional [Th/Eu] chronometer: assuming an initial production ratio

similar to CS 22892-052, a negative age is derived. Instead, by taking advantage of the detection of U in CS 31082-001, a new abundance ratio useful for age-dating has become available: [U/Th]. The major advantage of using U and Th lies in their similar ionisation and excitation potentials (thus making errors largely to cancel out), and their closeness in the n-capture chain, which may help in making them more robust against variations in n-exposure. From this ratio, an age of 14 Gyr $\pm$ 2.4 Gyr was derived (Cayrel et al. 2001).

3. Concluding Remarks

The traditional explanation for the chemical evolution of the Galactic halo is based on the differing products of the two main types of SNe. Type Ia SNe produce mainly Fe-group elements, while Type II SNe produce lighter elements as well as some of the Fe-group and some of the heavies. Since the time between star formation and explosion differs significantly between them (SN II need 10^7 yr, while SN Ia typically need 10^9 yr), there is a time in which the enrichment is exclusively from SN II.

The enrichment of the halo then depends on how many SN II explode and how effectively the ejected gas is mixed with the surrounding ISM. If the ejected metals are distributed over a large volume, a spatially homogeneous enrichment takes place. If the mixing volume is small, the ISM in the vicinity of a core-collapse SN is highly enriched, while the rest of halo gas remains metal-poor. In this way the ISM is chemically very inhomogeneous and newly formed stars are of different chemical composition, depending on where they formed.

The well defined abundance trends emerged from recent analyses of halo stars contrast a chaotic halo-formation mechanism (*e.g.* Searle & Zinn 1978), where independently evolving fragments coalesce into the modern Galactic halo over a period of the order of 10^9 yr. The very small dispersion found for almost all elements (from C to Zn) by Cayrel et al. (2004) is difficult to reconcile with the interpretation that the chemical patterns observed in these stars may represent the products of single supernovae events. On the contrary, it seems to suggest that mixing of stellar ejecta was already quite efficient, by the time these stars formed. New clues on the primordial yields may still come from a closer inspection and analysis of the *plateau*-like behaviours observed in these stars when several elemental abundances are plotted *vs* magnesium.

The higher data-quality, now routinely achieved on the largest tele-

scopes, has clearly provided us with a much more accurate picture of the chemical evolution of the early stellar generations. It is now fundamental that these new results (as well as the ones to come) are fed back into theoretical models, in order to further constrain the number and masses of supernovae required to reproduce the observed trends. The availability of higher quality data has also strongly pushed the field to evolve into a multi-disciplinary field, in which stellar spectroscopists, atomic physicists, stellar evolution studies, 3D NLTE analyses and modellers of the physics of SNe, all benefit from each other's work and progress. The OMEG03 meeting has clearly shown and reinforced how important this is.

Acknowledgements

The author would like to thank the organisers for a very successful meeting, that brought together scientist with different but complementing expertise, and in particular Prof. Kajino for his kind invitation to visit NAOJ.

References

1. J.W. Chamberlain and L.H. Aller, *ApJ* **114**, 52 (1951).
2. S.G. Ryan and J.E. Norris, *AJ* **101**, 1865 (1991).
3. B.W. Carney, D.W. Latham, J.B. Laird, and L.A. Aguilar, *AJ* **107**, 2240 (1994).
4. T.C. Beers, S.A. Shectman, and G.W. Preston, *AJ* **90**, 2089 (1985).
5. N. Christlieb, L. Wisotzki, D. Reimers, T. Gehren, J. Reetz, and T.C. Beers, *ASP Conference Series* **Vol.165**, 259 (1999).
6. L. Wisotzki, N. Christlieb, N. Bade, V. Beckmann, T. Köhler, C. Vanelle, and D. Reimers, *A&A*, **358**, 77 (2000)
7. N. Christlieb, B. Gustafsson, A. Korn, P.S. Barklem, T.C. Beers, M.S. Bessell, T. Karlsson, and M. Mizuno-Wiedner, *ApJ* **in press**, (2004).
8. N. Christlieb, M.S. Bessell, T.C. Beers, B. Gustafsson, A. Korn, P.S. Barklem, T. Karlsson, M. Mizuno-Wiedner, and S. Rossi, *Nature* **419**, 904 (2002).
9. M. Limongi, A. Chieffi and P. Bonifacio, *ApJ* **594**, L123 (2003).
10. H. Umeda and K. Nomoto *Nature*, **422**, 871 (2003).
11. M.S. Bessel, N. Christlieb, and B. Gustafsson, *astro-ph* **0401450**, submitted to ApJL (2004).
12. H. Dekker, S. D'Odorico, A. Kaufer, B. Delabre and H. Kotzlowski, *SPIE* **Vol. 4008**, 534 (2000).
13. S. Vogt et al., *SPIE* **Vol. 2198**, 362 (1994).
14. K. Noguchi et al., *PASJ* **54**, 855 (2002).
15. W. Aoki, *this volume* (2004).
16. S. Honda, W. Aoki, T. Kajino, H. Ando, and T.C. Beers, *this volume* (2004).
17. Ishimaru, *this volume* (2004).

18. E. Carretta, R. Gratton, J.G. Cohen, T.C. Beers, and N. Christlieb, *AJ* **124**, 481 (2002).
19. R. Cayrel, E. Depagne, M. Spite, V. Hill, F. Spite, P. François, B. Plez, T. Beers, F. Primas, J. Andersen, B. Barbuy, P. Bonifacio, P. Molaro, and B. Nordström, *A&A* **in press**, (2004).
20. Y.Q. Chen, P.E. Nissen, G. Zhao, H.W. Zhang, and T. Benoni, *A&AS* **141**, 491 (2000).
21. J.P. Fulbright, *AJ* **120**, 1841 (2000).
22. A. McWilliam, G.W. Preston, C. Sneden, and L. Searle, *AJ* **109**, 2757 (1995).
23. B. Gustafsson, T. Karlsson, E. Olsson, B. Edvardsson, and N. Ryde, *A&A* **342**, 426 (1999).
24. S. Rossi, T.C. Beers, and C. Sneden, *ASP Conf. Series* **Vol. 165**, 264 (1999).
25. W. Aoki, J.E. Norris, S.G. Ryan, T.C. Beers, and H. Ando, *ApJ* **567**, 1166 (2002a).
26. T. Masseron, B. Plez, F. Primas, S. Van Eck and A. Jorissen, *SF2A-2003* **EdP-Sciences Conf. Series**, 227 (2003).
27. B. Barbuy, R. Cayrel, M. Spite, T.C. Beers, F. Spite, B. Nordström, and P.E. Nissen, *A&A* **317L**, 63 (1997).
28. J.E. Norris, S.G. Ryan, and T.C. Beers, *ApJ* **489**, L169 (1997).
29. C. Sneden, G.W. Preston, A. McWilliam, and L. Searle, *ApJ* **431**, L27 (1994).
30. P. Bonifacio, P. Molaro, T.C. Beers, and G. Vladilo, *A&A* **332**, 672 (1998).
31. G. Preston and C. Sneden, *AJ* **122**, 1545 (2001).
32. W. Aoki et al., *PASJ* **54**, 427 (2002b).
33. M.Y. Fujimoto, Y. Ikeda, and I. Iben, *ApJ* **529**, L25 (2000).
34. C. Abia, I. Domínguez, O. Straniero, M. Limongi, A. Chieffi, and J. Isern, *ApJ* **557**, 126 (2001).
35. T. Sivarani, P. Bonifacio, P. Molaro, R. Cayrel, M. Spite, F. Spite, B. Plez, J. Andersen, B. Barbuy, T.C. Beers, E. Depagne, V. Hill, P. François, B. Nordström, and F. Primas, *A&A* **413**, 1073 (2004)
36. K.K. Gilroy, C. Sneden, C.A. Pilachowski, and J.J. Cowan, *ApJ* **327**, 298 (1988).
37. J.W. Truran, *A&A* **97**, 391 (1981).
38. C. Sneden, J.J. Cowan, J.E. Lawler, I.I. Ivans, S. Burles, T.C. Beers, F. Primas, V. Hill, J.W. Truran, G.M. Fuller, B. Pfeiffer, and K.-L. Kratz, *ApJ* **591**, 936 (2003).
39. V. Hill, B. Plez, R. Cayrel, T.C. Beers, B. Nordström, J. Andersen, M. Spite, F. Spite, B. Barbuy, P. Bonifacio, E. Depagne, P. François, and F. Primas, *A&A* **387**, 560 (2002).
40. R. Cayrel, V. Hill, T.C. Beers, B. Barbuy, M. Spite, F. Spite, B. Plez, J. Andersen, P. Bonifacio, P. François, P. Molaro, B. Nordström, and F. Primas, *Nature* **409**, 691 (2001).
41. J.J. Cowan, A. McWilliam, C. Sneden, D.L. Burris, *ApJ* **480**, 246 (1997).
42. L. Searle and R. Zinn, *ApJ* **225**, 357 (1978).

WHAT DO METAL-POOR STARS TELL?: ORIGIN OF O–ZN AND *R*-PROCESS ELEMENTS

Y. ISHIMARU[1], S. WANAJO[2], N. PRANTZOS[3], W. AOKI[4], S. G. RYAN[5]

[1] *Dept. of Physics, Ochanomizu Univ., 2-1-1 Otsuka, Bunkyo, Tokyo 112-8610, Japan; E-mail: ishimaru@phys.ocha.ac.jp*

[2] *Dept. of Physics, Sophia Univ., 7-1 Kioi-cho, Chiyoda, Tokyo 102-8554, Japan.*

[3] *IAP, 98 bis, Boulevard Arago, 75014, Paris, France.*

[4] *NAO, Mitaka, Tokyo 181-8588 Japan.*

[5] *Dept. of Physics and Astronomy, The Open Univ., Walton Hall, Milton Keynes, MK7 6AA, UK.*

Observed large dispersions in chemical abundances of metal-poor stars may indicate that the inter-stellar gas was not mixed enough at the early epoch. We construct an inhomogeneous chemical evolution model, and compare predicted stellar abundance distributions with observations, using statistical method. We take several supernova yields; the data of Nomoto et al. (1997) and Woosley & Weaver (1995), and discuss consistency of these yield sets with observations. In particular, we discuss the origin of *r*-process, from the point of view of enrichment of europium. Using the *Subaru* HDS, we have estimated Eu abundances of three extremely metal-poor stars with [Fe/H] $\lesssim -3$. Comparison with our Galactic evolution model implies the dominant source of Eu to be the low-mass end of the supernova mass range.

1. Introduction

Recent abundance analysis of metal-poor halo stars reveals the presence of large dispersions in heavy elements. This may be interpreted as a result of incomplete mixing of the interstellar medium (ISM) at the beginning of the Galaxy[1]. Each type of element shows a unique dispersion, which cannot be simply explained by spatial inhomogeneity of the ISM[2]. One of the possible explanations is that the ISM was not mixed well, and metal-poor stars contain products of only one or a few supernovae (SNe). If star formations are mainly triggered by SNe, the composition of the formed star must be a mixture of the ISM and the individual SNe ejecta, and the scatter possibly reflects variation in the yields of SNe from different mass progenitors.

In particular, the abundances of neutron-capture elements like Sr, Ba, and Eu show large dispersions in excess of observational errors[3,4]. This implies that r-process yields are highly dependent on the masses of SN progenitors.

However, the origins of r-process elements are still uncertain. Although a few scenarios such as neutrino winds[5] in core-collapse supernovae (SNe), the collapse of O-Ne-Mg cores resulting from $8-10M_{\odot}$ stars[6], and neutron star mergers[7] show some promise, no consensus has been achieved.

In this study, we construct a Galactic chemical evolution model, taking into account of inhomogeneous gas mixing. We take several known SN yields and examine their consistency with observational dispersions in stellar chemical compositions. Especially, we discuss the enrichment of europium, using an inhomogeneous chemical evolution model based on induced star formations. In addition, we report on three extremely metal-poor stars which we show to have very low Eu abundances. These data are compared with our chemical evolution models to distinguish between the proposed r-process sites.

2. Inhomogeneous Chemical Evolution

We have constructed a Galactic chemical evolution model, assuming star formations are induced by individual SNe. Since a new star is formed from a mixture of a supernova remnant (SNR) and the ISM gathered by expansion of the SNR, its chemical composition can be calculated from the mass average of that of the SNR and the ISM. We take two sets of yields given by known SN models; Nomoto et al.[8] (hereafter N97) and Woosley & Weaver[9] (hereafter WW95). The yields of WW95 take into account dependency of yields on stellar metallicity, whereas N97 assumes constant yields irrespective of metallicity. Thus, differences in predictions by two SN models must reveal effect of metallicity dependency of yields on chemical evolution and scatters in [X/Fe] [a] of metal-poor stars.

2.1. *[X/Fe] vs. [Fe/H] predicted by different SN models*

We calculate stellar distributions on diagrams of relative abundance ratios of [O–Zn/Fe] vs. [Fe/H], and compare dispersions predicted from both two models with observational data by statistical method. Figure 1 shows

[a] $[X_i/X_j] \equiv \log(N_i/N_j) - \log(N_i/N_j)_{\odot}$, where N_i indicates abundance of i-th element X_i.

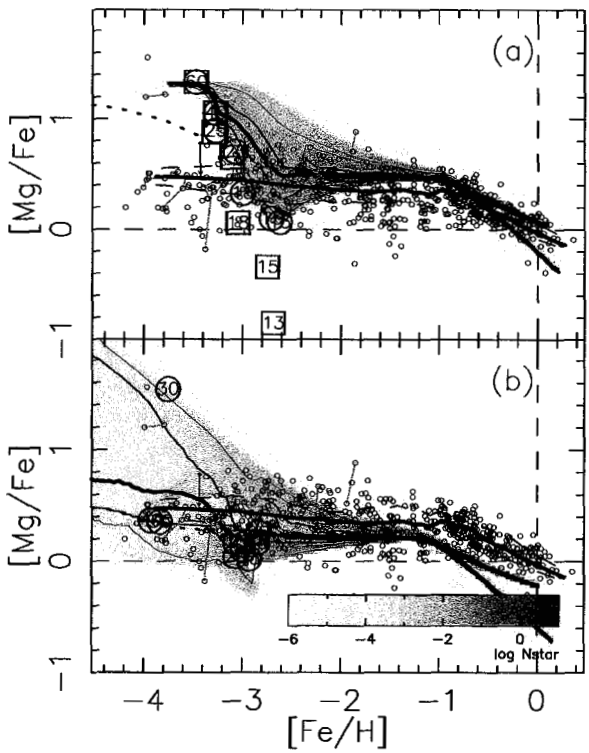

Figure 1. [Mg/Fe] vs. [Fe/H] relations predicted from N97 (left panel) and WW95 (right panel). Predicted distributions of stellar fraction (gray scales) are compared to observational data (small circles). Large symbols indicate stars formed from the SNe of the first generation stars (N97) and from SNe of $10^{-4} Z_{\odot}$ stars(WW95). The numbers in the circles indicate progenitor masses in a unit of the solar mass. The average lines and 50% confidence regions of observations are given by thick solid and thin dashed lines, respectively. Those of model predictions are also given by gray thick solid, solid, and thin thin (90%) lines.

examples of [Mg/Fe] vs. [Fe/H] relations predicted by N97 and WW95. Obviously, we can see the predicted number density of stars per unit area (gray-scales) shrinks with increasing of metallicity. We also put several stars formed via SNe of the first generation stars (large symbols). It is shown that the widths of stellar distributions are determined by variations in yields of different progenitor mass. Stellar distribution shows extremely large dispersion, if SN products of the first generation stars are mixed with *zero-metal gas* (large squares in N97). But if ISM is already enriched

efficiently by higher mass stars when lower mass progenitors explode (large circles in N97), a predicted scatter is smaller. Thus, since the efficiency of gas mixing has some uncertainties, actual stars can distribute between these two extreme cases. A similar result is obtained also by WW95 (right panel), which shows stars formed by SNe of 10^{-4} $Z_{\odot}$ stars. We also put the average stellar abundance distributions (thick solid gray lines) and the 50% and 90% confidence intervals (solid and thin-solid gray lines). They are compared with observational values of average (thick solid lines) and 50% confidence intervals (solid lines)[2].

2.2. *Statistical analysis of dispersions and SN yields*

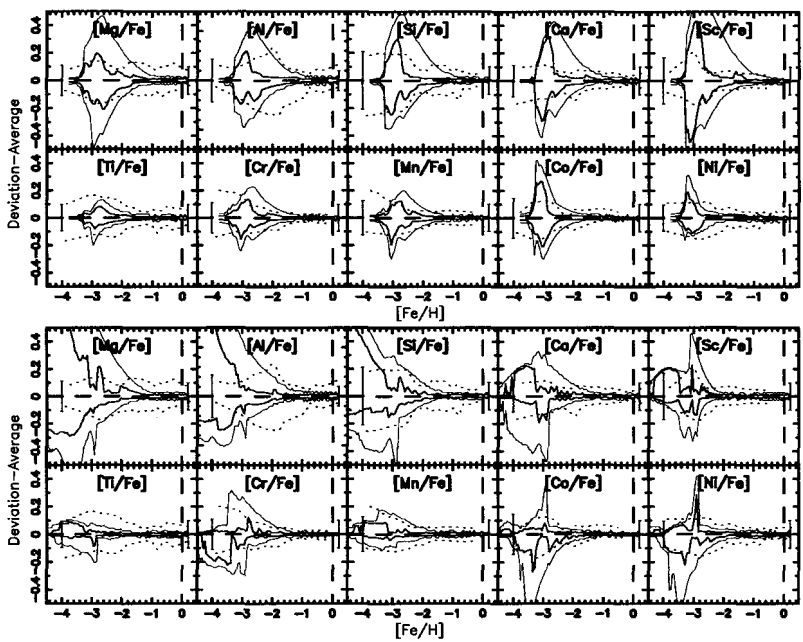

Figure 2. Relation between [Fe/H] and width of scatters. The upper and lower panels are given by N97 and WW95, respectively. Gray thick solid and thin solid lines indicate predicted 50% and 90% intervals, respectively. Black dotted lines are given from observations of Norris et al. (2001).

Concerning the average trends of [X/Fe], several elements such as Na, Al, Sc, Cu, Zn, etc. are already known to show clear differences between

two yield sets, while some elements such as α-elements are believed to be rather stable and show similar trends irrespective of models. However, as shown in Fig. 1, the width of scatters in metal-poor stars shows clear difference of two models even in α-elements. Thus, we take 50% confidence intervals and compare them with observational values. Figure 2 shows the ratios of predictions over observations of width of 50% confidence intervals. Although both of two models seem to predict underestimated dispersions in [Fe/H]> -2, it can be understood if we take into account observational errors which are comparable to dispersions in higher metallicity stars. On the other hand, dispersions by N97 seem small especially in [Fe/H]< -3, since few stars are predicted in this area. The distributions of lower metallicity stars are affected also by the efficiency of gas mixing. In our model, a parameter for gas mixing is given by the expansion radius of SNR, which is calculated from an analytical function of density of the ISM [10]. If SNR radius has 1.5σ uncertainty in logarithmic scale, some stars are formed from the gas more diluted by the ISM. As a result, stellar dispersions are elongated towards lower metallicity and show better agreements with observations. However, the maximum width of 50% confidence interval is affected little. Therefore, if predicted dispersion exceeds observational value significantly, the inconsistency comes from the SN model rather than gas dynamics. Figure 2 shows overestimates of dispersions in Mg and Al of WW95 and in Ca and Co in N97. Both models predict too large dispersions in Sc. These elements suggest problems in supernova models.

3. The site of r-process inferred from Eu abundances

3.1. *Enrichment of Eu in the Halo*

We investigate the enrichment of Eu, as a representative of r-process elements, in the Galactic halo[11]. The r-process elements are supposed to be produced only in Type II SNe. We examine the following two cases in which the r-process elements are produced from the stars: (a) $8-10M_{\odot}$, and (b) $\geq 30M_{\odot}$. Yields for Type II and Type Ia SNe are taken from Nomoto et al. [8,12]. The $8-10M_{\odot}$ stars are assumed to produce no iron, since their contribution to the enrichment of iron-peak elements in the Galaxy is negligible[6]. The mass of produced Eu is assumed to be constant over the stellar mass range. The requirement that the model reproduces the solar values [Eu/Fe] = [Fe/H] = 0 implies ejected Eu masses 3.1×10^{-7} and $7.8 \times 10^{-7}M_{\odot}$ for cases (a) and (b), respectively.

Figures 3a and 3b show the enrichment of Eu in the halo by cases a

and b, respectively. The observable differences between the cases appear at [Fe/H]$\lesssim -3$. In case (b), most of the stars are expected to have [Eu/Fe]> 0, owing to Eu production solely by massive, short-lived stars. In cases (a), significant numbers of stars having [Eu/Fe] < 0 are predicted at [Fe/H] $\lesssim -3$ owing to the delayed production of Eu by lower mass SN progenitors. However, most previous observational data (small circles) distribute between the 90% confidence lines for both cases, which has made it difficult to determine the mass range of the r-process site.

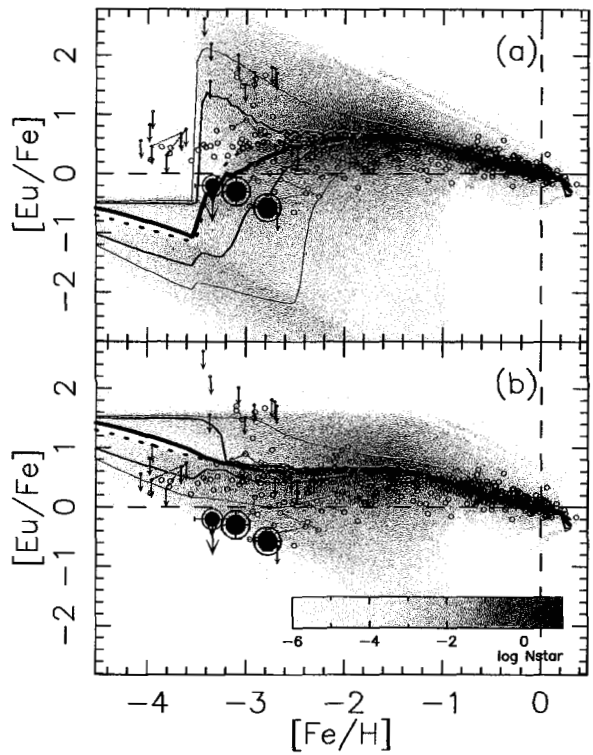

Figure 3. Comparison of the observed data of [Eu/Fe] with the model predictions. The r-process site is assumed to be SNe of (a) $8-10M_{\odot}$ and (b) $> 30M_{\odot}$ stars. The predicted number density of stars per unit area is gray-scaled. The average stellar abundance distributions are indicated by thick-solid lines with the 50% and 90% confidence intervals (solid and thin-solid lines, respectively). The average abundances of the ISM are denoted by the thick-dotted lines. The current observational data are given by large double circles, with other previous data (small circles).

3.2. *Detection of low Eu abundances*

Although [Ba/Fe] in metal-poor stars decreases towards lower metallicity, it has been uncertain whether [Eu/Fe] shows a similar trend, because almost no data of Eu abundance has been available for such low metallicity stars. Thus we selected three very metal-poor ([Fe/H] $\lesssim -3$) giants, HD 4306, CS 22878–101, and CS 22950–046, which were known from previous studies[3,13] to have [Ba/Fe] ~ -1, typical for their metallicities. Observations were made with the High Dispersion Spectrograph (HDS) of the 8.2m *Subaru* Telescope in 2001 July, at a resolving power $R = 50,000$. The detailed analysis and estimated abundances are seen in Ishimaru et al.[14].

The newly obtained data are represented by large double circles in Fig. 3ab. Our data add the lowest detections of Eu, at [Fe/H] $\lesssim -3$, and help distinguish between the two cases. The best agreement can be seen in case (a), in which the three stars, and most other stars from previous observations are located between the 50% confidence lines at [Fe/H] $\lesssim -3$. On the other hand in case (b), these stars are located outside the 90% confidence region. We suggest, therefore, that case (a) is most likely to be the r-process site, i.e. SNe from low-mass progenitors such as $8 - 10M_{\odot}$ stars.

Our analysis gives [Ba/Eu] values consistent with the solar r-process [15] when estimated errors are included (see Table 3 of Ishimaru et al. 2004). Hence our result may hold for heavy r-process elements with $Z \geq 56$, not just $Z \simeq 63$. The values of [Sr/Ba], however, are significantly higher than for the solar r-process, implying that these three stars exhibit light r-process elements ($Z < 56$) produced in more massive SNe ($> 10M_{\odot}$).

The discussion above suggests that the production of the r-process elements is associated with a small fraction of SNe near the low-mass end of the range. Neutrino winds in the explosions of massive stars may face difficulties in being a dominant source of the r-process elements. Wanajo et al.[16] have demonstrated that an r-process in the neutrino winds proceeds from only very massive proto-neutron stars, which might result from massive progenitors such as $\gtrsim 20 - 30M_{\odot}$ stars. Hypernovae ($> 20 - 25M_{\odot}$)[17] or pair-instability supernovae ($140 - 260M_{\odot}$)[18], resulting from stars near the high mass-end of the SN progenitors, similar to case (b), are clearly excluded as the major r-process site.

We suggest, therefore, that the dominant r-process site is SN explosions of collapsing O-Ne-Mg cores from $8 - 10M_{\odot}$ stars [19]. Recently, Wanajo et al.[6] have demonstrated that the prompt explosion of the collapsing O-Ne-

Mg core from a $9M_{\odot}$ star reproduces the solar r-process pattern for nuclei with $A > 130$, and is characterized by a lack of α-elements and only a small amount of iron-peak elements. This clearly differs from more massive SNe with iron cores ($> 10M_{\odot}$) that eject both these elements, and is consistent with the fact that the abundances of heavy r-process elements in stars with [Fe/H] ~ -3 are not related with those of iron-peak elements or of elements with lower atomic numbers [20].

This study shows the importance of detecting Eu in extremely metal-poor stars to explore the origin of r-process elements. Further observations are needed to confirm the origin.

4. Conclusions

We constructed a chemical evolution model, assuming SN induced star formation. Predicted dispersions in [O–Zn/Fe] are compared with observational data. The differences between two sets of yields; N97 and WW95, clearly appear in dispersions. The widths of 50% and 90% confidence regions are determined by stellar mass dependency of SN yields, but are not affected significantly by the mixing length of SNR. Thus, the overestimate in dispersions suggests problems for SN models; Mg and Al for WW95, Ca and Co for N97, and Sc for both models.

The abundances of neutron-capture elements like Sr, Ba, and Eu show large dispersions in excess of observational errors. This implies that r-process yields are highly dependent on the masses of SN progenitors. Using the *Subaru* HDS, we have estimated Eu abundances of three extremely metal-poor stars with [Fe/H] $\lesssim -3$ to determine the r-process site. All are found to have sub-solar values of [Eu/Fe]. Comparison with our chemical evolution model of the Galactic halo implies the dominant source of Eu to be the low-mass end of the supernova mass range. Future studies of stars with low Eu abundances will be important to determine the r-process site.

References

1. Gilroy, K. K., Sneden, C., Pilachowski, C. A., & Cowan, J. J. 1988, ApJ, 327, 298
2. Norris, J. E., Ryan, S. G., & Beers, T. C. 2001, ApJ, 561, 1034
3. McWilliam, A., Preston, G. W., Sneden, C., & Searle, L. 1995, AJ, 109, 2757
4. Ryan, S. G., Norris, J. E., & Beers, T. C. 1996, ApJ, 471, 254
5. Woosley, S. E., Wilson, J. R., Mathews, G. J., Hoffman, R. D., & Meyer, B. S. 1994, ApJ, 433, 229
6. Wanajo, S., Tamamura, M., Itoh, N., Nomoto, K., Ishimaru, I., Beers, T. C., & Nozawa, S. 2003, ApJ, 593, 968

7. Freiburghaus, C., Rosswog, S., & Thielemann, F. -K. 1999, ApJ, 525, L121
8. Nomoto, K., Hashimoto, M., Tsujimoto, T., et al. 1997a, Nucl. Phys. A, 616, 79
9. Woosley, S. E. & Weaver, T. A. 1995, ApJS, 101, 181
10. Cioffi, D. F., McKee, C. F., & Bertschinger, E. 1988, ApJ, 334, 252
11. Ishimaru, Y. & Wanajo, S. 1999, ApJ, 511, L33
12. Nomoto, K., et al. 1997b, Nucl. Phys. A, 621, 467
13. McWilliam, A. 1998, AJ, 115, 1640
14. Ishimaru, Wanajo, Aoki, & Ryan, 2004, ApJ, 600, L47
15. Arlandini, C., Käppeler, F., Wisshak, K., Gallino, R., Lugaro, M., Busso, M., & Straniero, O., 1999, ApJ, 525, 886
16. Wanajo, S., Kajino, T., Mathews, G. J., & Otsuki, K. 2001, ApJ, 554, 578
17. Maeda, K. & Nomoto, K. 2003, ApJ, in press
18. Heger, A. & Woosley, S, E. 2002, ApJ, 567, 532
19. Wheeler, J. C., Cowan, J. J., & Hillebrandt, W. 1998, ApJ, L493, 101
20. Qian, Y. -Z. & Wasserburg, G. J. 2003, ApJ, 588, 1099

III. Weak Interaction, Neutrinos, dark matter

This page intentionally left blank

NEUTRINO EXPERIMENTS AND THEIR IMPLICATIONS

A. B. BALANTEKIN
University of Wisconsin, Department of Physics
Madison, WI 53706, USA
E-mail: baha@nucth.physics.wisc.edu

Recent developments in solar, reactor, and accelerator neutrino physics are reviewed. Implications for neutrino physics, solar physics, nuclear two-body physics, and r-process nucleosynthesis are briefly discussed.

1. Introduction

Solar neutrino experiments, especially with the announcement of recent results from the Sudbury Neutrino Observatory (SNO) [1], have reached the precision stage. An analysis of the data from SNO as well as data from other solar neutrino experiments (Super-Kamiokande [SK] [3], Chlorine [4], and Gallium [5,6,7]), combined with the data from the reactor experiment KAMLAND [2], place severe constraints on the neutrino parameters, especially mixing between first and second generations [8,9,10]. The neutrino parameter space obtained from such a global analysis, including the neutral-current results from the SNO salt phase, is shown in Fig. 1 [10].

The mixing angle between first and second generations of the neutrinos dominates the solar neutrino oscillations whereas the mixing angle between second and third generations dominates the oscillations of atmospheric neutrinos. There are several puzzles in the data. Both mixing angles seem to be close to maximum, very unlike the mixing between quarks. Also the third mixing angle, between first and third generations, seems to be very small, even possibly zero. It is especially important to find out if this mixing angle is indeed different from zero since in the mixing matrix it multiplies a CP-violating phase. Such a CP-violation may have far reaching consequences. To explain the baryon excess (over antibaryons) in the Universe, Sakharov pointed out that it may be sufficient to satisfy three conditions: i) Baryon number non-conservation (which is readily satisfied by the grand unified theories), ii) CP-violation, and iii) Non-equilibrium conditions. It

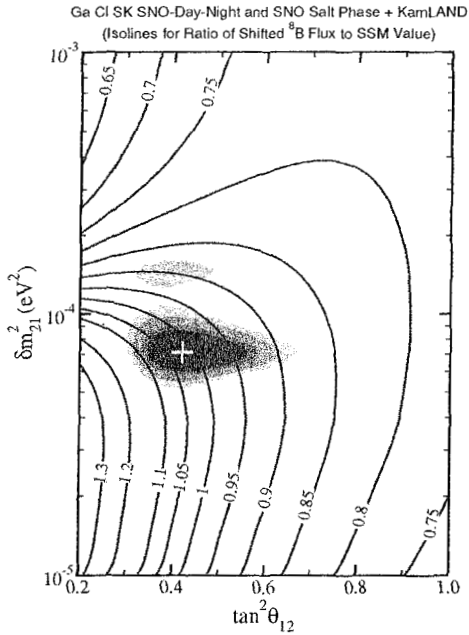

Figure 1. Allowed confidence levels from the joint analysis of all available solar neutrino data (chlorine, average gallium, SNO and SK spectra and SNO salt phase) and KamLAND reactor data The isolines are the ratio of the shifted ^{8}B flux to the SSM value. At best fit (marked by a cross) the value of this ratio is determined to be 1.02 (from Reference 10).

is entirely possible that the CP-violation necessary for the baryogenesis is hidden in the neutrino sector.

It is worth pointing out that high-precision solar-neutrino data have potential beyond exploring neutrino parameter space. Here we discuss two such applications to solar physics and to nuclear physics.

2. Limits on Solar Density Fluctuations

It was suggested that solar neutrino data can be inverted to extract information about the density scale height [11] in a similar way the helioseismological information is inverted to obtain the speed of the sound throughout the Sun. Even though the precision of the data has not yet reached to a point where such an inversion is possible, one can obtain rather strong limits on *fluctuations* of the solar density using the current solar neutrino data.

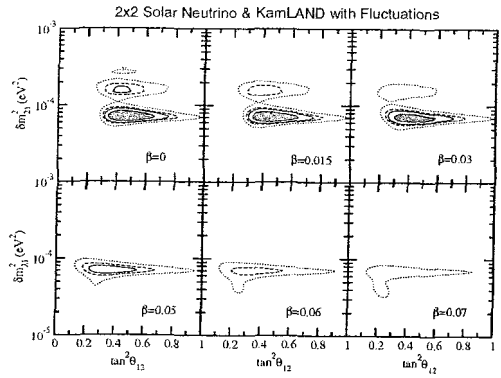

Figure 2. Allowed regions of the neutrino parameter space with solar-density fluctuations when the data from the solar neutrino and KamLAND experiments are used. The SSM density profile of Reference 14 and the correlation length of 10 km are used. The case with no fluctuations ($\beta = 0$) are compared with results obtained with the indicated fractional fluctuation. The shaded area is the 70 % confidence level region. 90 % (solid line), 95 % (dashed line), and 99 % (dotted line) confidence levels are also shown (From Reference 15).

To do so one assumes [12] that the electron density N_e fluctuates around the value, $\langle N_e \rangle$, predicted by the Standard Solar Model (SSM) [14]

$$N_e(r) = (1 + \beta F(r))\langle N_e(r)\rangle, \tag{1}$$

and that the fluctuation $F(r)$ takes the form of white-noise. It turns out that the effect of the fluctuations is more dominant when the neutrino parameters and the average density are such that neutrino evolution in the absence of fluctuations is adiabatic. There are two constraints on the value of the correlation length. One is a restriction in the applicability of our analysis. In averaging over the fluctuations we assumed that the correlation function is a delta function. In the Sun it is more physical to imagine that the correlation function is like a step function of size τ. Assuming that the logarithmic derivative is small, which is accurate for the Sun, delta-correlations are approximately the same as step-function correlations if the condition

$$\tau \ll \left(\sin 2\theta \frac{\delta m^2}{2E}\right)^{-1} \tag{2}$$

is satisfied [13]. A second constraint on the correlation length is provided by the helioseismology. Density fluctuations over scales of $\sim$ 1000 km seem

to be ruled out. On the other hand current helioseismic observations are rather insensitive to density variations on scales close to $\sim$ 100 km [16].

The neutrino parameter space for various values of the parameter β was calculated in Reference 15 and is shown in Figure 2. These results, in agreement with the calculations of other authors [17,18], show that the neutrino data constrains solar density fluctuations to be less than $\beta = 0.05$ at the 70 % confidence level when τ is about 10 km. It is important to emphasize that the best fit to the combined solar neutrino and KamLAND data is given by $\beta = 0$ (exact SSM). Neutrinos interact with dense matter not only in the Sun (and other stars) but also in several other sites such as the early universe, supernovae, and newly-born neutron stars and neutrino interactions with a stochastic background may play an even more interesting role in those sites.

3. Two-Body Axial Current

In the effective field theory approach to nuclear interactions, nonlocal interactions at short distances are represented by effective local interactions in a derivative expansion. Since the effect of a given operator on low-energy physics is inversely proportional to its dimension, an effective theory valid at low energies can be written down by retaining operators up to a given dimension. It turns out that the deuteron break-up reactions

$$\nu_e + d \rightarrow e^- + p + p \tag{3}$$

and

$$\nu_x + d \rightarrow \nu_x + p + n, \tag{4}$$

observed at SNO, are dominated by a ${}^3S_1 \rightarrow {}^3S_0$ transition, hence one only needs the coefficient of the two-body counter term, commonly called L_{1A}, to parameterize the unknown isovector axial two-body current [19]. Chen, Heeger, and Robertson, using the SNO and SK charged-current, neutral current, and elastic scattering rate data, found [20] $L_{1A} = 4.0 \pm 6.3$ fm^3. In order to obtain this result they wrote the observed rate in terms of an averaged effective cross section and a suitably defined response function. One can explore the phenomenology associated with the variation of L_{1A}. For example the variation of the neutrino parameter space, which fits the SNO data, as L_{1A} changes was calculated in [21] and is shown in Figure 3. In Reference 21 the most conservative fit value with fewest assumptions is found to be $L_{1A} = 4.5^{+18}_{-12}$ fm^3. (One should point out that if the neutrino parameters were better known one can get a much tighter limit). It was also

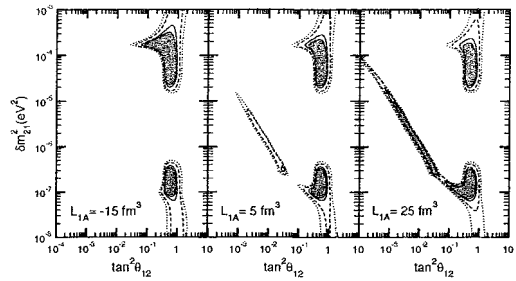

Figure 3. The change in the allowed region of the neutrino parameter space using solar neutrino data measured at SNO as the value of L_{1A} changes. The shaded areas are the 90 % confidence level region. 95 % (solid line), 99 % (log-dashed line), and 99.73 % (dotted-line) confidence levels are also shown (From Reference 21).

shown that the contribution of the uncertainty of L_{1A} to the analysis and interpretation of the solar neutrino data measured at the Sudbury Neutrino Observatory is significantly less than the uncertainty coming from the lack of having a better knowledge of θ_{13}, the mixing angle between first and third generations.

4. Implications for r-process Nucleosynthesis

There is another puzzling experimental result. The Los Alamos Liquid Scintillator Neutrino Detection (LSND) experiment has reported an excess of $\bar{\nu}_e$-induced events above known backgrounds in a $\bar{\nu}_\mu$ beam with a statistical significance of 3 to 4 σ [22,23]. The mass scale indicated by the LSND experiment is drastically different than the mass scales implied by the solar and atmospheric neutrino experiments. Since to get three different differences one needs four numbers, a confirmation of the LSND result by the mini-BooNE experiment represents evidence for vacuum neutrino oscillation at a new δm^2 scale. Discovery of such a mixing would imply either CPT-violation in the neutrino sector, or the existence of a light singlet sterile neutrino which mixes with active species. The latter explanation may signal the presence of a large and unexpected net lepton number in the universe. The existence of a light singlet complicates the extraction of a neutrino mass limit from Large Scale Structure data. It may also have implications for core-collapse supernovae, which is one of the leading candidates for the site of r-process nucleosynthesis [24]. A sterile neutrino scale implied by the LSND experiment may resolve some outstanding problems preventing a successful nucleosynthesis. Formation of too many alpha par-

ticles in the presence of a strong electron neutrino flux coming from the cooling of the proto-neutron star, known as the alpha effect [25,26], may be prevented by transforming active electron neutrinos into sterile neutrinos [27,28,29,30]. One can find the appropriate mass scale to achieve this goal [27,30] which seems to overlap with the LSND mass scale.

R-process nucleosynthesis requires a neutron-rich environment, i.e., the ratio of electrons to baryons, Y_e, should be less than one half. Time-scale arguments based on meteoritic data suggests that one possible site for r-process nucleosynthesis is the neutron-rich material associated with core-collapse supernovae [31,32]. In one model for neutron-rich material ejection following the core-collapse, the material is heated with neutrinos to form a "neutrino-driven wind" [33,34]. In outflow models freeze-out from nuclear statistical equilibrium leads to the r-process nucleosynthesis. The outcome of the freeze-out process in turn is determined by the neutron-to-seed ratio. The neutron to seed ratio is controlled by the expansion rate, the neutron-to-proton ratio, and the entropy per baryon. Of these the neutron-to-proton ratio is controlled by the flavor composition of the neutrino flux coming from the cooling of the proto-neutron star. Hence understanding neutrino properties (including the impact of neutrino-neutrino scattering in neutrino propagation [35]) could significantly effect our understanding of the r-process nucleosynthesis.

I thank G. Fuller, G. McLaughlin, and H. Yüksel for many useful discussions and the organizers of the OMEG03 conference for their hospitality. This work was supported in part by the U.S. National Science Foundation Grant No. PHY-0244384 and in part by the University of Wisconsin Research Committee with funds granted by the Wisconsin Alumni Research Foundation.

References

1. S. N. Ahmed *et al.* [SNO Collaboration], arXiv:nucl-ex/0309004.
2. K. Eguchi *et al.* [KamLAND Collaboration], Phys. Rev. Lett. **90** (2003) 021802 [arXiv:hep-ex/0212021].
3. S. Fukuda *et al.* [Super-Kamiokande Collaboration], Phys. Lett. B **539**, (2002) 179 [arXiv:hep-ex/0205075].
4. B. T. Cleveland *et al.*, Astrophys. J. **496** (1998) 505.
5. J. N. Abdurashitov *et al.* [SAGE Collaboration], J. Exp. Theor. Phys. **95** (2002) 181 [Zh. Eksp. Teor. Fiz. **122** (2002) 211] [arXiv:astro-ph/0204245].
6. W. Hampel *et al.* [GALLEX Collaboration], Phys. Lett. B **447** (1999) 127.
7. M. Altmann *et al.* [GNO Collaboration], Phys. Lett. B **490** (2000) 16 [arXiv:hep-ex/0006034].

8. A. B. Balantekin and H. Yuksel, J. Phys. G **29** (2003) 665 [arXiv:hep-ph/0301072].
9. P. C. de Holanda and A. Y. Smirnov, arXiv:hep-ph/0309299; M. Maltoni, T. Schwetz, M. A. Tortola and J. W. F. Valle, arXiv:hep-ph/0309130; G. L. Fogli, E. Lisi, A. Marrone and A. Palazzo, arXiv:hep-ph/0309100.
10. A. B. Balantekin and H. Yuksel, Phys. Rev. D **68** (2003) 113002 [arXiv:hep-ph/0309079].
11. A. B. Balantekin, J. F. Beacom and J. M. Fetter, Phys. Lett. B **427** (1998) 317 [arXiv:hep-ph/9712390]; see also A. B. Balantekin, Phys. Rept. **315** (1999) 123 [arXiv:hep-ph/9808281].
12. F. N. Loreti and A. B. Balantekin, Phys. Rev. D **50** (1994) 4762 [arXiv:nucl-th/9406003].
13. A. B. Balantekin, J. M. Fetter and F. N. Loreti, Phys. Rev. D **54** (1996) 3941 [arXiv:astro-ph/9604061].
14. J. N. Bahcall, M. H. Pinsonneault and S. Basu, Astrophys. J. **555** (2001) 990 [arXiv:astro-ph/0010346].
15. A. B. Balantekin and H. Yuksel, Phys. Rev. D **68** (2003) 013006 [arXiv:hep-ph/0303169]; see also A. B. Balantekin, arXiv:hep-ph/0109163.
16. C. Burgess, N. S. Dzhalilov, M. Maltoni, T. I. Rashba, V. B. Semikoz, M. Tortola and J. W. Valle, arXiv:hep-ph/0209094.
17. C. P. Burgess, N. S. Dzhalilov, M. Maltoni, T. I. Rashba, V. B. Semikoz, M. A. Tortola and J. W. F. Valle, arXiv:hep-ph/0310366.
18. M. M. Guzzo, P. C. de Holanda and N. Reggiani, Phys. Lett. B **569** (2003) 45 [arXiv:hep-ph/0303203].
19. M. Butler and J. W. Chen, Nucl. Phys. A **675** (2000) 575 [arXiv:nucl-th/9905059]; M. Butler, J. W. Chen and X. Kong, Phys. Rev. C **63** (2001) 035501 [arXiv:nucl-th/0008032].
20. J. W. Chen, K. M. Heeger and R. G. H. Robertson, Phys. Rev. C **67** (2003) 025801 [arXiv:nucl-th/0210073].
21. A. B. Balantekin and H. Yuksel, Phys. Rev. C **68** (2003) 055801 [arXiv:hep-ph/0307227].
22. C. Athanassopoulos *et al.* [LSND Collaboration], Phys. Rev. Lett. **77**, 3082 (1996) [arXiv:nucl-ex/9605003].
23. A. Aguilar *et al.* [LSND Collaboration], Phys. Rev. D **64**, 112007 (2001) [arXiv:hep-ex/0104049].
24. A. B. Balantekin and G. M. Fuller, J. Phys. G **29**, 2513 (2003) [arXiv:astro-ph/0309519].
25. G. M. Fuller and B. S. Meyer, Astrophys. J. **453** (1995) 792.
26. B. S. Meyer, G. C. McLaughlin and G. M. Fuller, Phys. Rev. C **58** (1998) 3696 [arXiv:astro-ph/9809242].
27. G. C. McLaughlin, J. M. Fetter, A. B. Balantekin and G. M. Fuller, Phys. Rev. C **59** (1999) 2873 [arXiv:astro-ph/9902106].
28. D. O. Caldwell, G. M. Fuller and Y. Z. Qian, Phys. Rev. D **61** (2000) 123005 [arXiv:astro-ph/9910175].
29. M. Patel and G. M. Fuller, arXiv:hep-ph/0003034.
30. J. Fetter, G. C. McLaughlin, A. B. Balantekin and G. M. Fuller, Astropart.

Phys. **18**, 433 (2003) [arXiv:hep-ph/0205029].
31. Y. Z. Qian, P. Vogel and G. J. Wasserburg, Astrophys. J. **494** (1998) 285.
32. Y. Z. Qian, P. Vogel and G. J. Wasserburg, Astrophys. J. **506** (1998) 868 [arXiv:astro-ph/9803300].
33. S. E. Woosley, J. R. Wilson, G. J. Mathews, R. D. Hoffman and B. S. Meyer, Astrophys. J. **433** (1994) 229.
34. K. Takahashi, J Witti, and H.-Th. Janka, Astron. Astrophys. **286** (1994) 857.
35. Y. Z. Qian and G. M. Fuller, Phys. Rev. D **51** (1995) 1479 [arXiv:astro-ph/9406073].

PERSPECTIVES OF NEUTRINO STUDIES BY NEUTRINO-LESS DOUBLE BETA DECAYS

H. EJIRI

JASRI, SPring-8, Mikazuki-cho, Hyogo, 679-5198, Japan
Research Center for Nuclear Physics,
Osaka University, Ibaraki, Osaka 567-0047, Japan
E-mail: ejiri@spring8.or.jp

Future experiments of double beta decays(DBD) for studying neutrino masses are briefly reported. Neutrino-less double beta decays($0\nu\beta\beta$ decays) provide an evidence for the Majorana nature of neutrinos and an absolute ν mass scale. In view of recent ν oscillation studies, high sensitive studies of $0\nu\beta\beta$ decays with mass sensitivities of the solar and atmospheric ν masses are of great interest. Future $0\nu\beta\beta$ experiments with a mass sensitivity of $m_\nu = 10 \sim 50$ meV have been proposed, and their R&D works are under progress. International cooperatiive works are encouraged for new generation $0\nu\beta\beta$ experiments.

1. Majorana neutrino masses and double beta decays

Double beta decays are second order weak processes, and are used to study fundamental properties of neutrinos. Double beta decays with two ν's, which conserve the lepton number, are within the standard model(SM), while those without ν violate the lepton number conservation law by $\Delta L = 2$ and thus are beyond SM. The decay rates for the two neutrino double beta decay($2\nu\beta\beta$) and the neutrino-less double beta decay($0\nu\beta\beta$) are expressed as

$$T^{2\nu} = G^{2\nu} \, |M^{2\nu}|^2, \qquad T^{0\nu} = G^{0\nu} \, |M^{0\nu}|^2 \, |m_\nu|^2, \tag{1}$$

where $G^{2\nu}$ and $M^{2\nu}$ are the phase space factor and the nuclear matrix element(response) for $2\nu\beta\beta$, and $G^{0\nu}$ and $M^{0\nu}$ are those for $0\nu\beta\beta$. $m_\nu =< m_\nu >$ is the effective Majorana ν mass term. Here we discuss mainly the $0\nu\beta\beta$ via a massive Majorana neutrino.

The $0\nu\beta\beta$ may be caused also by the right-handed weak current, the ν-Majoron coupling, ν-SUSY coupling, and others, which are beyond the standard electroweak theory. Recent experimental and theoretical works on $\beta\beta$ decays are given in review articles and references therein [1] [2] [3] [4]. The

present report is a brief review of future $\beta\beta$ experiments. Some of them have been presented at a recent workshop [5].

The effective ν-mass term involved in the $0\nu\beta\beta$ decay is written as a sum of the three mass terms as

$$m_\nu = |u_{e1}|^2 m_1 + |u_{e2}|^2 m_2 e^{i\phi_2}| + |u_{e3}|^2 m_3 e^{i\phi_3+\delta}. \quad (2)$$

Here m_i, u_{ei}, and ϕ_i are the mass eigen value, the mixing coefficient for the electron neutrino and the Majorana phase with $\imath$ = 1,2,3, respectively.

The $2\nu\beta\beta$ transition rate is observed, and thus it gives experimentally $M^{2\nu}$, which is used to check the nuclear structure calculation and to evaluate the GT component involved in $M^{0\nu}$.

Nuclear matrix elements $M^{0\nu}$ for the ν-mass term includes spin-isospin and isospin components of

$$M^{0\nu}(\tau\sigma) = \sum_c < 0_f^+ | h_+(r, E_c)\tau\tau\sigma\sigma | 0_i^+ >, \quad (3)$$

$$M^{0\nu}(\tau) = \sum_c < 0_f^+ | h_+(r, E_c)\tau\tau | 0_i^+ >, \quad (4)$$

where $h_+(r, E_c)$ is the ν potential with the intermediate energy E_c

Since the ν potential term $h_+(r_{nm}, E)$ is effectively given by the Coulomb term of $kR/|\mathbf{r_n} - \mathbf{r_m}|$, $M^{0\nu}$ is expressed approximately by a separable form as in case of $M^{2\nu}$ [2],

$$M^{0\nu} \sim \Sigma_J [M_S(J) M_{S'}(J)/\Delta_S(J)], \quad (5)$$

where $M_S(J)$ and $M_{S'}(J)$ are single β matrix elements through the intermediate single particle-hole states $|S_J >$ with spin J. Then $M_S(J)$ and $M_{S'}(J)$ are obtained experimentally from charge exchange reactions and/or single β decay rates. In particular, charge exchange (^{3}He, t) and (t, ^{3}He) reactions with charged particles in both the initial and final channels are very useful for studying $M_S(J)$ and $M_{S'}(J)$, respectively [2].

2. Effective neutrino mass and neutrino mass spectrum

The ν mass can be expressed in terms of the solar and atmospheric mass-square differences, δm_s^2 and δm_a^2, for normal(NH) and inverted (IH) hierarchy mass spectra.

The mass differences are $\delta m_s^2 = m_2^2 - m_1^2$ for NH, $\delta m_s^2 = m_3^2 - m_2^2$ for IH, and $\delta m_a^2 = m_3^2 - m_1^2$. The ν masses of m_1, m_2, and m_3 are given in Table 1.

The effective ν mass is expressed for the mass spectra of the normal hierarchy(NH) and the inverted hierarchy(IH) [6] as,

$$m_\nu^N = c_2^2 c_3^2 m_1 + c_2^2 s_3^2 e^{i\phi_2}(\delta m_s^2 + m_1^2)^{1/2} + s_2^2 e^{i\phi_3}(\delta m_a^2 + m_1)^{1/2}, \quad (6)$$

$$m_\nu^I = s_2^2 m_1 + c_2^2 c_3^2 e^{i\phi_2}(\delta m_a^2 - \delta m_s^2 + m_1^2)^{1/2} + c_2^2 s_3^2 e^{i\phi_3+\delta}(\delta m_a^2 + m_1)^{1/2}, \quad (7)$$

where c_i and s_i are $cos\theta_i$ and $sin\theta_i$. According to the recent ν oscillation data, the mass differences are $\delta m_s \sim 8$ meV and $\delta m_a \sim 50$meV, and the mixing angles are approximately expressed as $\theta_1 \sim \pi/4$, $\theta_2 \sim 0$, and $\theta_3 \sim \pi/6$. Then the mixing coefficients are simply given by $c_1 \sim s_1 \sim 1/\sqrt{2}, c_2 \sim 1, s_2 \sim 0, c_3 \sim \sqrt{3}/2, s_3 \sim 1/2$.

Then the effective mass is approximately expressed by using these mass differences and the mixing parameters as given in Table 1.

The effective neutrino mass m_ν depends on the mass m_1, the phases, and the mass spectrum. The effective masses for the mass regions of $m_1 \gg \delta m_a$, $m_1 \sim \delta m_a$, $m_1 \ll \delta m_a$, and $m_1 \ll \delta m_s$ are approximately written as shown in Table 2 for cases of NH $e^{i\phi_2} = \pi_{21} = +$, NH $\pi_2 = -$, IH $e^{i\phi_3+\delta} = \pi_3 = +$ and NH $\pi_3 = -$.

In case of the quasi-degenerate mass spectrum of $m_3 \sim m_2 \sim m_1 \geq 100$ meV, one gets $m_\nu = (0.5 \sim 1.0)\ m_1 \geq 50$ meV. On the other hand, one gets $m_\nu = (0.5 \sim 1.0)\ \delta m_a = 25 \sim 50$ meV in case of IH with $m_1 \ll \delta m_a \sim 50$ meV, and $m_\nu \sim 0.25\ \delta m_s \sim 2$ meV in case of NH with $m_1 \ll \delta m_s \sim 8$ meV. Thus it is crucial for ν mass studies to build detectors with the mass sensitivity of $20 \sim 30$ meV, and to develop future detectors with the ultra high sensitivity of $1 \sim 2$ meV.

Table 1. Neutrino masses of m_1, m_2, m_3 and the effective ν mass of m_ν.

Neutrino mass	NH	IH
m_1	m_1	m_1
m_2	$\sqrt{\delta m_s^2 + m_1^2}$	$\sqrt{\delta m_a^2 + m_1^2}$
m_3	$\sqrt{\delta m_a^2 + m_1^2}$	$\sqrt{\delta m_a^2 + m_1^2}$
m_ν	$\frac{3}{4}m_1 + \frac{1}{4}\pi_2\sqrt{\delta m_s^2 + m_1^2}$	$\frac{1}{4}\sqrt{\delta m_a^2 + m_1^2}\ (3 + \pi_3\ )$

Note: $\pi_i = +1$ or -1 is the neutrino phase for ν_i with respect to ν_1.

The sum of the neutrino masses is interesting from cosmology. It is expressed in terms of the effective mass and the mass differences. The values for for the mass regions of $m_1 \gg \delta m_a$, $m_1 \sim \delta m_a$, $m_1 \ll \delta m_a$, and

Table 2. Effective neutrino mass $m_\nu =< m_\nu >$ and m_1.

	NH $\pi_2 = +$	NH $\pi_2 = -$	IH $\pi_3 = +$	NH $\pi_3 = -$
m_1 scale	m_ν	m_ν	m_ν	m_ν
$m_1 \gg \delta m_a$	m_1	$0.5m_1$	m_1	$0.5m_1$
$m_1 \sim \delta m_a$	m_1	$0.5m_1$	$\sqrt{m_1^2 + \delta m_a^2}$	$0.5\sqrt{m_1^2 + \delta m_a^2}$
$m_1 \ll \delta m_a$	m_1	$0.5\ m_1$	δm_a	$0.5\ \delta m_a$
$m_1 \ll \delta m_s$	$0.25\ \delta m_s$	$0.25\ \delta m_s$	δm_a	$0.5\ \delta m_a$

$m_1 \ll \delta m_s$ are approximately written as given in Table 3. In case of $m_1 \sim \delta m_a$, the sum is $2m_\nu + \sqrt{\delta m_a^2 + m_\nu^2}$ for NH $\pi_2 = +$, $4m_\nu + \sqrt{\delta m_a^2 + 4m_\nu^2}$ for NH $\pi_2 = -$, $2m_\nu + \sqrt{m_\nu^2 - \delta m_a^2}$ for IH $\pi_3 = +$, and $4m_\nu + \sqrt{4m_\nu^2 - \delta m_a^2}$, for NH $\pi_3 = -$, respectively. Thus the effective mass, together with the mass differences, constrains the sum and vice versa.

Table 3. Sum of Σm_i.

	NH $\pi_2 = +$	NH $\pi_2 = -$	IH $\pi_3 = +$	NH $\pi_3 = -$
m_1 scale	Σm_i	Σm_i	Σm_i	Σm_i
$m_1 \gg \delta m_a$	$3m_\nu$	$6m_\nu$	$3m_\nu$	$6m_\nu$
$m_1 \sim \delta m_a$	$3.4\delta m_a$	$6.3\delta m_a$	$2\delta m_a$	$5.7\delta m_a$
$m_1 \ll \delta m_a$	δm_a	δm_a	$2\delta m_a$	$2\delta m_a$

3. Sensitivity of $\beta\beta$ Experiments to the effective neutrino mass

The $0\nu\beta\beta$ decay is studied by high sensitive detectors at low background underground laboratories. The decay rates are of the orders of 10^{-25}, 10^{-27}, and 10^{-29} per year for $m_\nu \sim$100, 10, 1 meV, respectively. Detector sensitivity S can be expressed by the inverse of the minimum mass to be measured,

$$S = (m_\nu(min))^{-1} = M^{0\nu} G(ZQ_{\beta\beta})^{1/2} N_{\beta\beta}^{1/2} [\Delta E N_{BG}]^{-1/4} \qquad (8)$$

where $G(ZQ_{\beta\beta}), N_{\beta\beta}$, and $\Delta E N_{BG}$ are the phase space factor, the total number of the $\beta\beta$ isotopes, and the BG rate in the energy window of ΔE. The phase space is nearly proportional to $Q_{\beta\beta}^5$.

Double beta decays have been studied by using various types of detectors. The details are found in recent reviews [1] $\sim$ [4]. There are two types of detectors, one is a calorimetric method(C) to measure the total energy

of the two β rays, and other is a spectroscopic method to measure energy and angular correlations of two β rays. Here the correlations are used to identify the $0\nu\beta\beta$ process due to the ν mass term and to reject BG signals.

So far $\beta\beta$ decays of ^{76}Ge, ^{116}Cd, ^{130}Te, and others have been studied by using detectors of the type C, where detectors include $\beta\beta$ isotopes internally. Merits of ^{76}Ge experiments by Ge detectors and ^{130}Te ones by cryogenic bolometers are the very good energy resolution of the order of $\Delta E = 3 \sim 8$ keV to reduce BG rates and the high detection efficiency to increase the signal rate.

Double beta decays of ^{82}Se, ^{100}Mo and others have been studied by detectors of the type S. Detectors used are β ray tracking detectors with $\beta\beta$ sources separated from detectors. Merits of these detectors are to choose $\beta\beta$ isotopes with a large Q value to enhance the phase space volume and the signal rate and to get the $0\nu\beta\beta$ signal beyond most BG signals.

Double beta decay experiments with calorimetric detectors(Ge detectors, Te bolometers) give upper limits of $0.3 \sim 1.3$ eV, while those with the type S detectors(ELEGANTs, NEMO) give upper limits of around $1 \sim 3$ eV depending on $M^{0\nu}$ used. Recently NEMO III with large tracking chambers has started $\beta\beta$ experiments of ^{100}Mo, ^{82}Se, ^{150}Nd and others [7].

The neutrino mass to be studied by the present detectors are limited by their mass sensitivities of $0.3 \sim 1$ eV. Among them NEMO and CUORECINO are expected to reach the mass region of $0.2 \sim 0.5$ eV [7 3 4].

New generation experiments with higher sensitivity of $20 \sim 30$ meV are crucial to study the ν mass and the mass spectrum as suggested by ν oscillation experiments. Such detectors necessarily involve large amounts of $\beta\beta$ isotopes of the order of 1 ton in order to get statistically significant signals, and stringent ways to reduce all BG events and to separate true signals from BG ones.

Nuclei used for $\beta\beta$ experiments are selected by taking into accounts the matrix element, the phase space, the Q value, the isotopic abundance(a) and the feasibility of isotope separation. The large Q value helps improve signal to BG ratios since the phase space is proportional to Q^5 and most BG RI signals are below 3 MeV. Using enriched isotopes are effective to improves the signal to BG ratio.

The energy resolution (ΔE) is a key element to search for a small $0\nu\beta\beta$ peak among RI and $2\nu\beta\beta$ BG's. RI BG's and $2\nu\beta\beta$ BG's in the $0\nu\beta\beta$ window are proportional to ΔE and ΔE^6, respectively. Calorimetric semiconductor and cryogenic detectors with $\Delta E \sim 5$ keV are almost free from $2\nu\beta\beta$ BG's, while spectroscopic tracking detectors for $Q_{\beta\beta} \geq 2.9$ MeV can

be almost free from RI BG's.

Reduction of RI BG signals in the $0\nu\beta\beta$ window is crucial for high sensitive studies of rare $0\nu\beta\beta$ decays. External RI BG's may be reduced by proper passive shields such as old lead and/or high purity cupper bricks. Internal RI BG's can be reduced partly by using high purity detector components. The purity level required for the mass sensitivity of $20 \sim 30$ meV is around or higher than 10^{-3}Bq per ton or 0.1 ppt of Ur-Th chain isotopes. Signal selection by soft ware analyses are effective for separation of true signals from BG ones as given in next section.

4. Rare nuclear decay measurements with signal selection by spatial and time correlation analyses

Natural and cosmogenic RI impurities are serious BG sources. Many of them are associated with γ - X rays and/or with pre- (post-) $\beta - \alpha$ decays. They are reduced by $1 \sim 2$ orders of magnitudes by SSSC (Signal Selection by Spatial Correlation) and SSTC(Signal Selection by Time Correlation).

Since γ rays pass through the detector for about 10gr/cm^2, β rays associated with γ rays are eliminated by measuring the spatial correlation of the energy deposits. Thus SSSC with position sensitive detectors is effective for reducing β rays followed by γ rays, Compton electrons followed by Compton γ rays, and conversion electrons followed by X rays. The spatial resolution Δx required for SSSC is $\Delta x \ll l$, where l is the mean absorption length of the γ ray.

There are many long lived RI's (B), which are decay products of preceding β decays of parent nuclei (A) with a half life ($T_{1/2}$) in the range of $10^{-2} \sim 10^{-4}$ y. SSTC is used to identify and eliminate BG signals from the decay of B $\rightarrow$ C by measuring the time-correlated preceding decay of A $\rightarrow$ B in the time range of $\Delta T = 10^{-2} \sim 10^{-4}$ y. The two decays of A $\rightarrow$ B and B $\rightarrow$ C are spatially correlated provided that B stays in the same spot for the time interval of ΔT. Preceding decays used for SSTC can be α, β, γ decays and X rays from EC decays. If the decay of B$\rightarrow$ C is followed by a post decay of C $\rightarrow$ D, one can use the post decay to identify and eliminate the BG from the decay of B $\rightarrow$ C.

SSTC is essentially BG rejection by anti-coincidence with correlated pre- and/or post-decays. The efficiency of the BG reduction is given by $\epsilon = \epsilon_t \epsilon_s$, where ϵ_t is the probability of the preceding decay in the time interval of ΔT and ϵ_s is the detection efficiency of the decay of A $\rightarrow$ B. Using the time window of $\Delta T = 5\ T_{1/2}$, one gets $\epsilon_t = 97$ %. For β, α and

X rays with energies well above the detector threshold, one gets $\epsilon_s \geq 95$ %. Thus the BG reduction efficiency can be $\epsilon \geq 90$ %.

In general SSTC cuts a little true $0\nu\beta\beta$ signals by accidental coincidence with the decay of A $\rightarrow$ B in the time interval of ΔT. The loss is given by the ratio of the accidental coincidence rate($R(AC)$) to the true signal rate($R(T)$),

$$\eta = R(AC)R(T)^{-1} = R(A)\epsilon\Delta T K^{-1}, \tag{9}$$

where $R(A)$ is the A $\rightarrow$ B rate / t y and K^{-1} is the position resolution in unit of ton. K is the number of segments per ton in case of segmented detectors. Using a modest RI impurity of $R(A) \sim 10^{-2}$ Bq / t = 3 10^5/ y t and a typical time interval of $\Delta T = 3\ 10^{-3}$ y (1 day) and $K = 10^5$, η is an order of 1 %. Thus the loss is almost negligible.

5. Perspectives of $\beta\beta$ experiments

Details of the present and future $\beta\beta$ experiments are given in recent review papers [2] [3], [4]. Extensive works of R&D and tests with proto-type detectors are now going on for future $\beta\beta$ experiments with sensitivities of 20 $\sim$200 meV. Some of them are listed in Table 4. Here brief comments are given on some of future $\beta\beta$ experiments. Future experiments are described in refs [3,4,6-13] and refs therein.

5.1. *MAJORANA for double beta decays of ^{76}Ge*

MAJORANA is based on the IGEX $\beta\beta$ decay experiment of ^{76}Ge [8]. It uses an array of segmented intrinsic Ge detectors with a total mass of 500 kg of Ge isotropically enriched to 86 % in ^{76}Ge. Each detector with 1 kg is divided into 12 segments. Pulse shape discrimination (PSD) and segmentation of detector (SED), together with stringent material selection and electro forming of cupper, make it possible to reduce all kinds of BG's to get high sensitive $0\nu\beta\beta$ studies.

Major BG's are β and γ rays from cosmogenic ^{68}Ge and ^{60}Co produced in the Ge detectors. Since their decays involve γ rays, their contributions are much reduced by SSSC with PSD and SED. In fact PSD reduces the BG rate to 26.5 %, and SEG to 15.8 %, and the net reduction is 3.8 %.

An expected sensitivity for an experimental run over 10 years is $T_{1/2}$ = 4 $\times 10^{27}$ y, which corresponds to a mass sensitivity of 30 $\sim$ 40 meV by using the recent QRPA matrix element.

^{68}Ge with $T_{1/2}$ = 271 d decays by EC to ^{68}Ga with 67.6 min., which decays mainly by β^+ to the ground state of ^{68}Zn. The EC is followed by the 11 keV X ray. Thus the BG contribution from ^{68}Ga can be reduced by SSTC, i.e. by measuring the preceding X ray in the time interval of $\Delta T \sim$ 5 hours. The ^{68}Ge BG rate is reduced further to $\sim$ 5 % by the SSTC. The efficiency loss of the true signal is less than 1 %.

The β^- decay of ^{60}Co with $T_{1/2}$ = 5.27 y is followed by 1.173 MeV and 1.333 MeV γ rays. Thus the BG contribution from ^{60}Co in one segment(detector) can be reduced by SSSC, i.e. by measuring Compton scattered γ rays in active shields surrounding the segment. In case of a Ge detector array with close-packed 500 Ge detectors, outer segments of the outermost detectors may be used as active shields. The segments/detectors in the inner region are well self-shielded. The reduction factor of around 10 may be expected by the SSSC. The active shield is very effective to reduce external BG's from Cu, Rn, and lead shields.

5.2. *MOON for double beta decays of ^{100}Mo*

MOON (Molybdenum Observatory Of Neutrinos) is based on ELEGANYT V [9]. It is a "hybrid" $\beta\beta$ and solar ν experiment with ^{100}Mo. It aims at studies of Majorana ν masses with a sensitivity of $m_\nu \sim$ 30 meV by measuring $0\nu\beta\beta$ decays of ^{100}Mo and the pp and ^{7}Be solar ν's by inverse β decays of ^{100}Mo.

The β_1 and β_2 with the large energy sum of $E_1 + E_2$ are measured in prompt coincidence for the $0\nu\beta\beta$ studies, while the inverse β-decay induced by the solar ν and the successive β decay are measured sequentially in an adequate time window for the low energy solar-ν studies.

The large Q value of $Q_{\beta\beta}$=3.034 MeV gives a large phase-space factor $G^{0\nu}$ to enhance the $0\nu\beta\beta$ rate and a large energy sum of $E_1 + E_2 = Q_{\beta\beta}$ to place the $0\nu\beta\beta$ energy signal well above most BG.

MOON is a spectroscopic study of two β-rays (charged particles). The energy and angular correlations for the two β-rays identify the ν-mass term for the $0\nu\beta\beta$. The tight localization of β-β events in space and time windows is very effective for selecting $0\nu\beta\beta$ and solar-ν signals and for reducing correlated and accidental BG's by means of SSSC and SSTC.

MOON has ^{100}Mo isotopes of the order of 1 ton to get adequate signal rate, the energy resolution of $\sigma \sim 0.03\ /\sqrt{E(MeV)}$ to reduce the $2\nu\beta\beta$ tail in the $0\nu\beta\beta$ window, and the position resolution of 10^{-9} per ton to reduce

$2\nu\beta\beta$ and RI accidental coincident BG events and modest RI impurities of the order of or less than 10^{-3} Bq /ton (0.1 ppt of U and Th). Enriched ^{100}Mo isotopes with 85-90 % enrichment are obtained by centrifugal separation.

A possible option of MOON detectors is a super module of hybrid plate and fiber scintillators. One module consists of a plate scintillator and two sets of X-Y fiber scintillator planes, between which a thin ^{100}Mo film is interleaved. The fiber scintillators coupled with multi-anode photomultiplier tubes (PMT's) enable one to get the necessary position resolution of $\sim 10^{-9}$ ton and the scintillator plate (X-Y plane) with multi PMT's at both X and Y sides provides an adequate energy resolution to satisfy the physics goals. Another option is an array of Mo bolometers.

MOON with $\beta\beta$ source $\neq$ detector may be used to study other $\beta\beta$ isotopes such as ^{82}Se, ^{150}Nd and ^{116}Cd as well by replacing Mo isotopes with other isotopes.

Table 4. Isotopes used for $\beta\beta$ decays and $\beta\beta$ detectors. Refs [6-13].

Isotope	Abundance %	$Q_{\beta\beta}$ MeV	$G_1\ 10^{-25} y^{-1}\ (\mathrm{eV})^{-2}$	Detectors
^{48}Ca	0.187	4.271	2.44	CANDLES
^{76}Ge	7.8	2.039	0.244	Majorana
^{82}Se	9.2	2.992	1.08	NEMO
^{100}Mo	9.6	3.034	1.75	MOON
^{116}Cd	7.5	2.804	1.89	CAMEO
^{130}Te	34.5	2.528	1.70	CUORE,COBRA
^{136}Xe	8.9	2.467	1.81	EXO, XMASS
^{150}Nd	5.6	3.368	8.00	DCBA

5.3. *CUORE for double beta decays of* ^{130}*Te*

The cryogenic bolometer has been developed for $\beta\beta$ experiments by the Milano group [3,4]. CUORE(Cryogenic Underground Detector for Rare Events) uses a calorimetric method to measure the total $\beta\beta$ energy with the extremely good energy resolution. The group has started the $0\nu\beta\beta$ experiment of ^{130}Te with $Q = 2.528$ MeV by means of CUORECINO. The detector consists of a TeO_2 crystal array with the total mass of 41 kg.

Merits of studying the ^{130}Te $\beta\beta$ decay is the large natural abundance of 34 % and the large ratio of Te in the TeO_2 crystal. The Q value is just in between the photo and Compton peaks of the ^{208}Tl 2.615 MeV γ ray.

The major BG's are due to surface contamination of RI's, and the expected BG' rate is 0.23 per keV kg per y. The energy resolution in FWHM

is about 8 keV. Then the expected sensitivity for the 3 y run is around $T_{1/2} \sim 1.5\ 10^{25}$ y, and the corresponding mass sensitivity is of the order of 200 meV, depending on the nuclear matrix element used.

CUORE is a scale-up of CUORECINO. It consists of 1K of 0.75 kg TeO_2 crystals. The net ^{130}Te mass is 203 kg. They expect to reduce the BG rate to 0.01 $\sim$ 0.001 per keV kg y and improve the energy resolution to 5 keV. Then the goal of CUORE is to achieve the sensitivity of $T_{1/2} \sim 7\ 10^{26}$ y, corresponding to the mass sensitivity of the order of 30 meV.

5.4. *EXO for double beta decays of ^{136}Xe*

EXO (Enriched Xenon Observatory) is a $\beta\beta$ experiment of ^{136}Xe with $Q = 2.467$ MeV [12]. It uses a large scale Xe detector with Xe enriched to 90 % in ^{136}Xe to measures the total energy of the $\beta\beta$ rays.

The unique feature of EXO is to reduce BG's by identifying the decay product of ^{136}Ba by means of a laser spectroscopy technique. Excitation of ^{136}Ba ($6\ ^2S_{1/2}$) by the 493 nm laser leads to the excited state of $6\ ^2P_{1/2}$, which decays with a 30 % branch by emitting the 650 nm light to the metastable state of $5\ ^4D_{3/2}$. Then the metastable state feeds the initial state of ^{136}Ba by 650 nm laser absorption and 493 nm laser emission. Thus the laser tagging technique selects ^{136}Ba and suppress all kinds of BG's. The overall detection efficiency is estimated to be 70 %.

Then the major BG is the high energy tail of the continuum $2\nu\beta\beta$ spectrum. Assuming no BG's except the $2\nu\beta\beta$ tail in the $0\nu\beta\beta$ window, a 1 ton enriched Xe detector with the energy resolution of $\sigma = 2.8$ % gives a sensitivity of $T_{1/2} \sim 8.3\ 10^{26}$ y for a 5 y run. A 10 ton Xe with the improved energy resolution of $\sigma = 2$ % will give the sensitivity of $1.3\ 10^{28}$ y. The ν mass sensitivities are 51 - 150 meV and 13 - 37 meV, respectively, depending on the nuclear matrix elements.

6. Summary and remarks

1. Neutrino-less double beta decays ($0\nu\beta\beta$) are sensitive to the Majorana ν mass, the right-handed weak current, and other ν properties beyond SM. High sensitive studies of $0\nu\beta\beta$ decays with ν mass sensitivities of the order of 10 meV are crucial for studying the Majorana mass scale and the mass spectrum as suggested by the recent ν oscillation data.

2. Future experiments with different detection methods (calorimetric and spectroscopic methods) for several $\beta\beta$ isotopes are indispensable to

identify the $0\nu\beta\beta$ signal among other BG's ones and to establish the Majorana nature of the neutrinos and the ν mass spectrum. SSSC and SSTC are very powerfull to select $0\nu\beta\beta$ signals and to eliminate other BG ones.

3. Nuclear matrix elements of $M^{0\nu}$ are necessary for extracting the effective ν mass from the $0\nu\beta\beta$ rate. Theoretical calculations of $M^{0\nu}$ within $20 \sim 30$ % are highly appreciated. Experimental study of nuclear structures relevant to $0\nu\beta\beta$ decays are important as well. Since $M^{0\nu}$ may be expressed as a separable form, experimental data of β^- and β^+ strengths for $1^+, 2^-, 3^+$ and others are useful.

4. In view of the importance and scale of new generation $\beta\beta$ experiments, internationally collaborative works in both experiments and theories are quite important. Accordingly, experimental and theoretical physicists working currently for DBD have agreed to promote international collaborative works for future DBD experiments and theories as given in the international statements on neutrinoless double-beta decays [15]. The points are

1). Fundamental ν properties to be studied by DBD include the Majorana nature and the lepton number non-conservation, the mass spectrum, the ν mass scale, possibly the CP violation, and others. Actually, DBD is the only practical method for studying all these important properties in the foreseeable future.

2). Next-generation DBD experiments with the sensitivities of the order of $10 \sim 1$meV should discover non-zero effective Majorana electron ν mass if the mass spectrum is IH $\sim$ NH.

3). A coordinated approach to and international collaboration for executing next-generation DBD experiments are indispensable. We form an international DBD network to promote collaborative works for BDD experiments and theories.

References

1. J. D. Suhonen and Civitarese, Phys. Rep. **300** (1998) 123.
   A. Faessler and F. Simcovic, J. Phys. **G 24** (1998) 2139.
   J.D. Vergados, Phys. Rep. **361** (2002) 1.
2. H. Ejiri, Phys. Rep. C 338 (2000) 265.
3. E. Fiorini, Nucl. Phys., **B110** (2002) 233.
   E. Fiorini and T.O. Niinikoski, Nucl.Instr. Meth. **224** (1984) 83.
4. O. Cremonesi, Nucl. Phys. **B118** (2003) 287.
5. H. Ejiri Proc. MEDEX, July 2003, Praque, ed. J. Suhonen, et al. Ceckslovak Jounal of Physics 2004.
6. V. Barger, et al., Phys. Lett. **B532** (2002) 15.

S. Pascoli and S. T. Petcov, Phys. Rev. D arXiv: hep-ph/0205022.
7. L. Simard, et al., Nucl. Phys., **B110** (2002) 372; X. Sarazin et al., hep-exp/0006031.
8. C.E. Aalseth et al., Phys. Rev. **65** (2002) 092007
C.E. Aalseth et al., hep.exp/0201038; Proc. Dubna03 July 2003.
9. H. Ejiri, J. Engel, R. Hazama, P. Krastev, N. Kudomi, and R.G.H. Robertson, Phys. Rev. Lett. **85** (2000) 2917; H. Ejiri, Phys. Rev. C 63 (2001) 065501 1.
10. K. Zuber, Phys. Lett., **B519** (2001) 1.
G. Bellini et al., Eur. Phys. J. **C19** (2001) 43.
11. S. Moriyama et al., Proc. XENON01 workshop, Dec. 2001, Tokyo.
12. M. Danilov et al., Phys. Lett. **B480** (2000) 12; M. Moe, Phys. Rev. **C40** (1991) 931.
13. N. Ishihara et al., Nucl. Instr. Method. **A443** (2000) 101.
14. I. Ogawa et al., Proc. Neutrinos and Dark Matters in Nuclear Physics, June 2003, Nara Japan, ed. H. Ejiri and I. Ogawa.
15. DBD(Double Beta Decay) collaboration, 2002,
http://www.rcnp.osaka-u.ac.jp/ ejiri/DBD-Lett

CURRENT STATUS OF TOKYO DARK MATTER EXPERIMENT

Y. INOUE
International Center for Elementary Particle Physics, University of Tokyo

H. SEKIYA, M. MINOWA, Y. SHIMIZU, W. SUGANUMA
Department of Physics, School of Science, University of Tokyo

K. MIUCHI, A. TAKEDA
Cosmic-Ray Group, Department of Physics, Faculty of Science, Kyoto University

We, the Tokyo group, have performed some dark matter search experiments at an underground cell in the Kamioka Observatory (2700 m.w.e). Two cryogenic detectors, a 168-g lithium fluoride (LiF) bolometer and a 176-g sodium fluoride (NaF) bolometer, are aimed at the direct detection of nuclear recoils caused by elastic scattering of weakly interacting massive particles (WIMPs) through a spin-dependent interaction. The LiF bolometer run at Kamioka was performed from 2001 through 2002 with the total exposure of 4.1 kg days, and the NaF bolometer run was performed from 2002 through 2003 with the total exposure of 3.38 kg days. From these experiments, we derived limits on WIMP-nucleon couplings in the a_p–a_n parameter plane which is complementary to other existing limits. We are also developing a direction-sensitive detector using organic crystal scintillator in order to sense the wind of WIMP dark matter. It exploits the anisotropic scintillation efficiency of organic crystals with respect to the direction of nuclear recoils relative to crystallographic axes. A variation of about 7% was observed in the scintillation efficiency of carbon recoils in a stilbene crystal for recoil energy of 30 keV to 1 MeV using neutrons from $^7\mathrm{Li}(p,n)^7\mathrm{Be}$ and $^{252}\mathrm{Cf}$. We are now performing a pilot experiment at Kamioka to prove the feasibility of this method.

1. Introduction

It is widely believed that the universe is filled with a large mass fraction of invisible stuff — so-called dark matter. In 1933, F. Zwicky pointed out the presence of dark matter in the Coma cluster[1]. The presence is most evidently inferred from the rotation velocity of spiral galaxies[2]. The inferred mass to explain the gravitational potential must be much more than that

can be expected from the luminous stuff. The mass to light ratio tend to increase as the scale of the system get larger such as in galaxy clusters or superclusters. In the largest scale, the recent precision observation of the cosmic microwave background radiation by WMAP combined with other measures of large scale structure is supporting an inflationary universe composed of 73% of dark energy, 22% of cold dark matter, and only 4.4% of baryons[3].

Cold dark matter is a type of dark matter consisting of particles which were moving in non-relativistic velocity at the time of matter–radiation equality. Hypothetical weakly interacting massive particles are generally called WIMPs. The lightest supersymmetric particles in the SUSY model often called neutralinos are one of the most promising candidates among them. It is a superposition of photino, Z-ino, and Higgsinos:

$$\chi = a_1\tilde{B} + a_2\tilde{W}_3 + a_3\tilde{H}_1^0 + a_4\tilde{H}_2^0, \tag{1}$$

with a mass less than 1 TeV.

Current WIMP search experiments detect the nuclear recoils produced by the elastic scattering of WIMPs off detector nuclei. The nuclear recoils are detected as scintillation, eg. DAMA(NaI)[20], UKDMC(NaI)[15]; ionization; phonon, eg. CRESST(Al_2O_3)[19], Tokyo(LiF, NaF)[7]; the combination of them, eg. CDMS(Ge)[21]; or others, eg. SIMPLE(C_2ClF_5)[18].

The WIMP–nucleus cross section is a sum of the spin-dependent (SD) and spin-independent (SI) terms. The SD interaction is dominant if dark

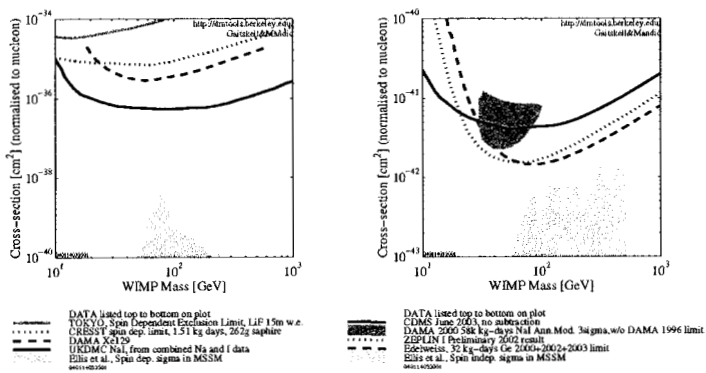

Figure 1. Current sensitivity to the SD WIMP-proton cross section $\sigma_{\chi p}^{\mathrm{SD}}$ and the SI WIMP-nucleon cross section $\sigma_{\chi p,n}^{\mathrm{SI}}$. Note the cross section is shown in a unit of cm^2 ($1\,\mathrm{cm}^2 = 10^{36}$pb). These figures are generated by SUSY Dark Matter/Interactive Direct Detection Limit Plotter[27].

matter neutralino is gaugino-like, and vise versa. Since we don't know the composition of WIMPs yet, searches through both the SD and SI interactions are complementary.

Recent experimental limits on the SD WIMP-proton and SI WIMP-nucleon cross section are shown in Fig. 1. The values predicted by the minimal standard supersymmetric model (MSSM) are $\sigma^{\rm SI}_{\chi p,n} < O(10^{-6}{\rm pb})$ and $\sigma^{\rm SD}_{\chi p} < O(10^{-2}{\rm pb})$, respectively[4].

The fluorine is expected to be one of the best nuclei for detecting SD interacting WIMPs[5]. In addition, it posseses spin property complementary to that of widely used sodium and iodine when the WIMP-model independent WIMP-nucleon couplings are discussed[6]. We have developed lithium fluoride (LiF) and sodium fluoride (NaF) bolometers. Bolometers are phonon-type detectors which detects nuclear recoils as heat pulses. The results from the dark matter search experiment with these bolometers at Kamioka Observatory will be presented in the first half of this paper[7].

Another dark matter detector being developed by us is the direction-sensitive stilbene scintillators[8,9]. The earth is revolving in the solar system at about 30 km/s, and the solar system is revolving in our galaxy at about 230 km/s. This should provide an annual modulation of about 3% in the energy spectrum of dark matter assuming an isothermal spherical halo of WIMPs, however, this is prone to many systematic errors.

The most convincing signature of the WIMPs would appear in the bias in the direction of nuclear recoils. It is known that the scintillation efficiency of some organic crystals depends on the direction of nuclear recoils relative to the crystallographic axes[10,11]. This property could be applied to a direction-sensitive dark matter detector[12,13].

We adopted stilbene crystal scintillator, because of its relatively high light yield (30% of NaI), and the modest anisotropy — known to be about 20% for 6.5-MeV α particles[11]. However, the recoil energy given by WIMPs is much lower. In the second half of this paper, the result of the measurement of the anisotropy in scintillation efficiency for the low-energy carbon recoils by neutrons, and the pilot experiment being performed at Kamioka Observatory will be presented.

2. LiF/NaF bolometer

2.1. *Experimental set-up*

The detector is located at the Kamioka Observatory under a 2700 m.w.e rock overburden at Mozumi Mine of the Kamioka Mining and Smelting Co.

in Kamioka-cho, Gifu, Japan. The detector is an array of eight LiF or NaF bolometers with a total mass of 168 g or 176 g, respectively. Each bolometer consists of a $2 \times 2 \times 2\,\mathrm{cm}^3$ crystal and a neutron transmutation doped (NTD) germanium thermistor. The bolometer array is encapsulated in a 2-cm thick low radio-active lead (older than 200 years). They are suspended with three Kevlar cords from the bottom of a dilution refrigerator, and are cooled at about 10 mK by the dilution refrigerator through four annealed copper ribbons. The schematic drawing of the bolometer array as well as the radiation shield is shown in Fig. 2.

2.2. *Measurement and Result*

The measurement was performed from 22 November 2001 through 12 January 2002 for LiF bolometers and 23 December 2002 through 24 January

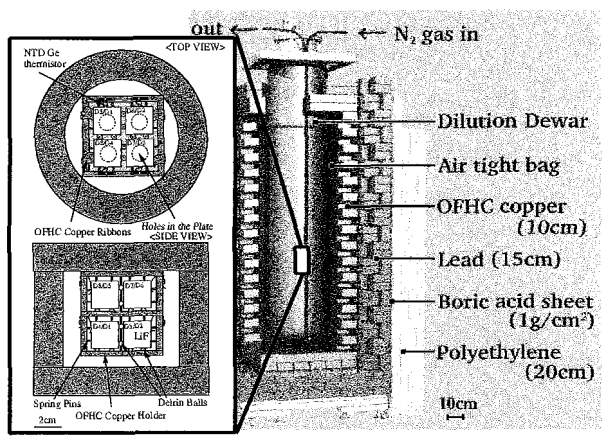

Figure 2. Bolometer array and radiation shield

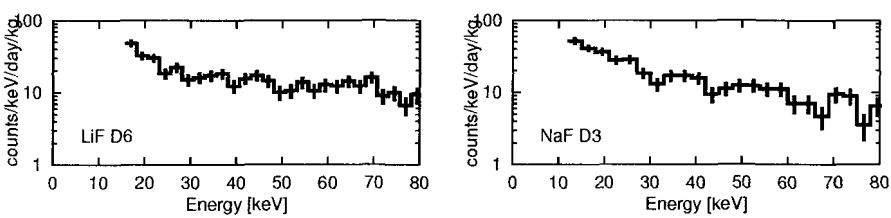

Figure 3. Low energy spectra obtained with a LiF bolometer (D6) and a NaF bolometer (D3).

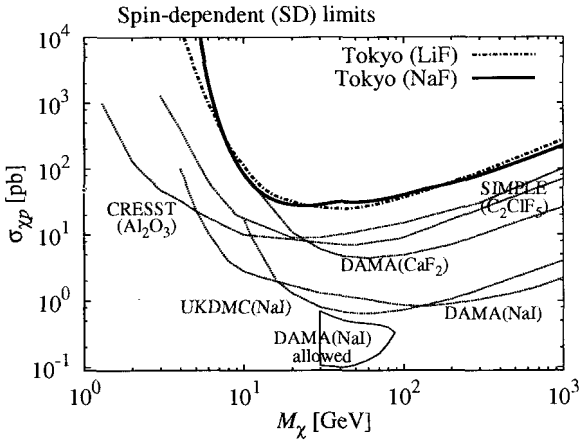

Figure 4. Combined 90% C.L. $\sigma_{\chi p}^{\rm SD}$ limits for NaF and LiF as a function of M_χ are shown in a thick solid line and a thick dash-dotted line, respectively. Limits from other experiments[15,16,17,18,19] and DAMA's allowed region investigated in a mixed coupling framework shown as "case c" in Ref. 20 are also shown for comparison.

2003 for NaF bolometers. The total exposure of 4.1 kg days for LiF and 3.38 kg days for NaF was analysed. In both run, two bolometers out of the eight are not used for analysis because of their poor signal to noise ratio.

The energy spectra obtained with one of LiF bolometers (D6) and one of NaF bolometers (D3) are shown in Fig. 3 by way of example.

From the spectra, we derived the limits on the SD WIMP-proton elastic scattering cross section $\sigma_{\chi p}^{\rm SD}$ following the conventional method as used in Ref. 14. The limits are shown in Fig. 4. The spherical isothermal halo of WIMPs is assumed with the local dark matter density of $\rho_D = 0.3\,{\rm GeV/cm^3}$, the velocity dispersion of $v_0 = 220\,{\rm km/s}$, the escape velocity of $v_{\rm esc} = 650\,{\rm km/s}$, and the velocity of the earth in our galaxy of $v_E = 217\,{\rm km/s}$. Values for the spin factor, $\lambda^2 J(J+1)$, of ^{7}Li, ^{23}Na, and ^{19}F is taken from Ref. 5.

However, these $\sigma_{\chi p}^{\rm SD}$ limits are fraught with potentially significant WIMP model dependence. We derived the limits on the model-independent WIMP-nucleon couplings following the notation in Ref. 22. The SD WIMP-nucleus cross section $\sigma_{\chi N}^{\rm SD}$ is given by:

$$\sigma_{\chi N}^{\rm SD} = 4G_F^2\mu_{\chi N}^2 \times \frac{8}{\pi}(a_p\langle S_p\rangle + a_n\langle S_n\rangle)^2\frac{J+1}{J}, \qquad (2)$$

where G_F is the Fermi coupling constant, $\mu_{\chi N}$ is the WIMP-nucleus re-

duced mass, a_p and a_n are the effective WIMP-proton and WIMP-neutron couplings, $\langle S_p \rangle$ and $\langle S_n \rangle$ are the expectation values of the proton and neutron spins within the nucleus, and J is the total nuclear spin. $\langle S_p \rangle$ and $\langle S_n \rangle$ calculated with recent shell models are shown in Table 1. The limits derived in the a_p–a_n plane for WIMPs with mass of 10 GeV, 50 GeV and 100 GeV are shown in Fig. 5. It is clearly seen that our results obtained with LiF or NaF detectors has successfully excluded a large portion of parameter space which has been allowed by the limits obtained with NaI detectors of UK Dark Matter Collaboration (UKDMC) experiment[15] for $M_\chi \leq 50$ GeV. This is owing to the large spin factor of ^{19}F and the fact that the sign of $\langle S_p \rangle / \langle S_n \rangle$ of ^{19}F is opposite to those of ^{7}Li, ^{23}Na, and ^{127}I.

The remaining background in the energy region between 10 and 90 keV restricting the current sensitivity is supposed to be due to the uranium and thorium contamination. A use of more radio-pure materials around the detector including the crystal holder would help reducing the background. A use of active shields between the crystals would also be helpful.

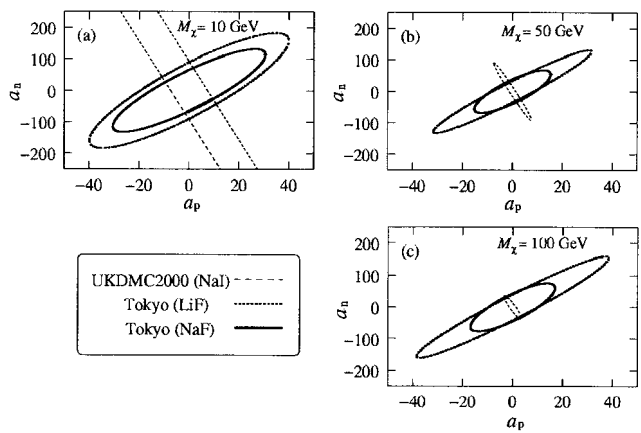

Figure 5. Exclusion plots in the a_p–a_n plane for WIMPs with mass M_χ of (a) 10 GeV, (b) 50 GeV, and (c) 100 GeV. The region inside the solid and dotted lines are allowed by the results with NaF and LiF bolometers. The exclusion regions by the data from UKDMC[15] are shown in thin dashed lines.

Table 1. Nuclear parameters $\langle S_p \rangle$ and $\langle S_n \rangle$ for various nuclei.

Nucleus	Abundance	J	$\langle S_p \rangle$	$\langle S_n \rangle$	Reference
^{7}Li	92.5%	3/2	0.497	0.004	[23]
^{19}F	100%	1/2	0.441	−0.109	[23]
^{23}Na	100%	3/2	0.248	0.020	[24]
^{127}I	100%	5/2	0.309	0.075	[24]

3. Direction-sensitive organic crystal scintillator

3.1. *Measurement of anisotropic scintillation response*

We measured the angle and energy dependence of the scintillation response of carbon recoils in a stilbene crystal in the low energy region with nuclear recoil events caused by elastic scattering of neutrons. In order to obtain high statistics and wide neutron energy range, two neutron sources, ^{7}Li$(p,n)^{7}$Be and ^{252}Cf, were employed. The ^{7}Li$(p,n)^{7}$Be source run was performed at 3.2-MV Pelletron accelerator of the Research Laboratory for Nuclear Reactors at Tokyo Institute of Technology. Pulsed proton beam interacted with a thin lithium target, and pulsed neutrons were produced by the ^{7}Li$(p,n)^{7}$Be reaction. Details of the experimental setup are given in Ref. 9.

Stilbene crystals form monoclinic systems and the crystallographic axes are called a, b and c as shown in Fig. 6. The axis perpendicular to a–b plane is called c' which can be easily known since the crystal is cleaved along a–b plane. We measured the recoil angle dependence by changing the angle of the recoil direction with respect to c' axis named θ, and the angle around the c' axis named ϕ. The origin of ϕ was determined arbitrarily.

A $2 \times 2 \times 2\,\mathrm{cm}^3$ stilbene crystal was used as the neutron target. Two opposite faces were cleaved (a–b plane) and other four faces (arbitrary plane) were polished. Two Hamamatsu H6411 photomultipliers (PMT) were attached to both cleaved faces, and the left faces were covered with GORE-TEX. Self coincidence between two PMTs was required to reduce dark current events. Scattered neutrons were detected by $\phi 2" \times 2"$ Saint-Gobain BC501A-MAB liquid scintillator with a PMT (H6411). The energies of incident and scattered neutrons were measured by the time-of-flight (TOF) method, and the recoil energy E_R was determined by kinematics.

The scintillation efficiency for carbon recoils relative to that for electrons with $\theta = 0°$ and 90° are shown in Fig. 6. The variation of the scintillation efficiency is about 7% over the measured energy region, $E_R = 30\,\mathrm{keV}$–$1\,\mathrm{MeV}$. The scintillation efficiency is maximal in the direction perpendicular to c' axis namely at $\theta = 90°$, and is minimal in the direction parallel to c' axis

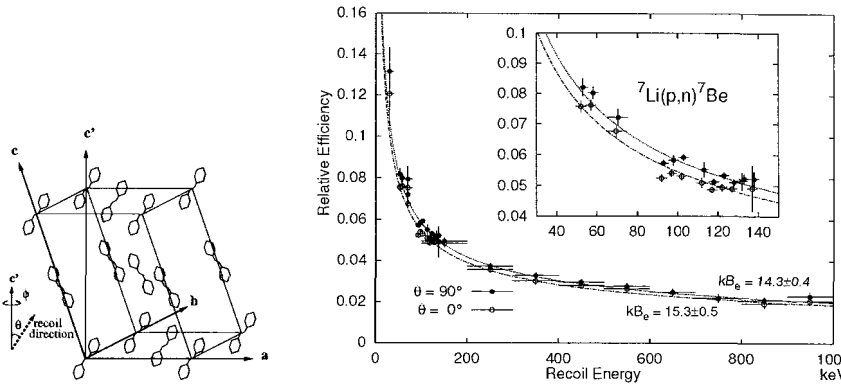

Figure 6. The measured scintillation efficiency relative to that for electrons with $\theta = 0°$ and $90°$ recoils ($\phi = 0°$). The inset is the results of the ^{7}Li$(p,n)^7$Be source run. Horizontal error bars represents selected recoil energy region for calculating the efficiency. The definition of the recoil angles θ and ϕ are shown in the left along with the schematic drawing of the stilbene crystalline lattice where a stilbene molecule is drawn smaller than reality. θ is the angle with respect to the c' axis and ϕ is the angle around the c' axis.

namely $\theta = 0°$. Any significant ϕ-dependence is not observed. This behavior is consistent with the result of proton recoils[8] and of high energy charged particles[11].

3.2. *Kamioka pilot experiment*

A pilot dark matter search experiment to prove the feasibility of the method is being carried out at Kamioka Observatory. A ϕ50 mm × 50 mm (100 g) cylindrical stilbene crystal is viewed by two Hamamatsu 8778MOD low background PMTs through two Horiba low background NaI(Tl) active shields. Self coincidence of two PMTs are required again, and both PMTs are cooled at about −7℃ by Peltier coolers to reduce dark current further.

In this pilot experiment, c' axis of the crystal is laid horizontally to north. In the heliocentric frame, the WIMP wind comes from Cygnus (RA 22^h 12^m, dec. +48° 19' (J2000.0)). Thus, at Kamioka Observatory at 36° 25' 30" N and 137° 18' 32"E, the incident angle of the WIMP wind with respect to c' axis varies between 5° and 78° within a sidereal daily period neglecting the effect of aberration of WIMPs for simplicity.

The WIMP signal as of 1 December 2003 in the visible energy spectrum of the stilbene crystal scintillator expected by the Monte Carlo method is shown in Fig. 7. The effect of the motion of the earth is fully taken into

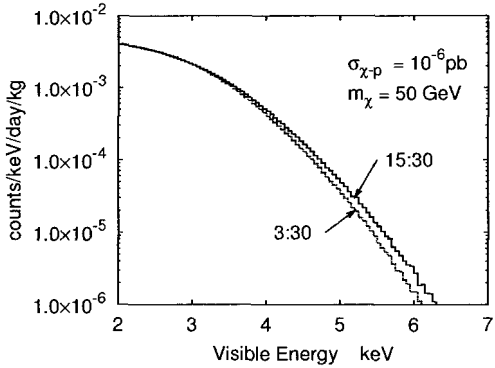

Figure 7. The expected signal of WIMP induced carbon recoils as of 1 December 2003. The lower line is the count rate expected at 3:30 JST ($\theta_0 = 5.4°$) and the upper line is the one at 15:30 JST ($\theta_0 = 71.5°$), where θ_0 is the angle between c' axis and the topocentric apparent direction of the WIMP wind.

account using NOVAS[25]. In order to express the scintillation efficiency as a function of the recoil energy, we assumed a modified Birks' empirical model[26] for the light yield dL/dx as

$$\frac{dL}{dx} = \frac{S_e(\frac{dE}{dx})_e + S_n(\frac{dE}{dx})_n}{1 + kB_e(\frac{dE}{dx})_e + kB_n(\frac{dE}{dx})_n} \tag{3}$$

with $kB_e/kB_n = 3250$, where electric energy loss $(dE/dx)_e$ and nuclear energy loss $(dE/dx)_n$ are assumed to contribute differently to the quenching and scintillating process. The lines in Fig. 6 are the best fits to the data with three parameters; $kB_e(\theta = 90°)$, $kB_e(\theta = 0°)$, and S_e/S_n. θ-dependence of the scintillation efficiency between 0° and 90° is assumed to be trigonometric. The modulation seen in Fig. 7 is about the same order as that of annual modulation.

Now, data taking is ongoing and the result will appear elsewhere. We are also planning to examine other organic crystal scintillators in parallel in pursuit of larger sensitivity to the WIMP wind.

4. Summary

We have performed dark matter search experiments at Kamioka Observatory with LiF and NaF bolometers. With the 4.1 kg days exposure of LiF and the 3.38 kg days exposure of NaF, we derived limits in the a_p–a_n plane which excluded a part of the parameter space which had not been excluded by the data of UKDMC.

We are also developing a direction-sensitive detector for dark matter search experiment. The anisotropic scintillation response of carbon recoils in a stilbene crystal was investigated using neutrons from $^{7}\mathrm{Li}(p,n)^{7}\mathrm{Be}$ and $^{252}\mathrm{Cf}$. A variation of about 7% was observed for recoil energy of 30 keV to 1 MeV depending on the recoil angle with respect to c' axis. A pilot experiment with a 100-g stilbene crystal is running at Kamioka Observatory. The estimated sidereal daily modulation in the recoil energy spectrum is about the same as that of annual modulation.

References

1. F. Zwicky, Helv. Phys. Acta 6 (1933) 110.
2. S. M. Kent, Astron. J. 93 (1987) 816; A. Bosma, Astron. J. 86 (1981) 1825.
3. C. L. Bennet *et al.*, Astrophys. J. Suppl. 148 (2003) 1.
4. J. Ellis, A. Ferstl, K. A. Olive, Phys. Rev. D 63 (2001) 065016.
5. J. Ellis, R. A. Flores, Nucl. Phys. B 400 (1993) 25.
6. K. Miuchi *et al.*, Astropart. Phys. 19 (2003) 135.
7. A. Takeda *et al.*, Phys. Lett. B 572 (2003) 145.
8. Y. Shimizu *et al.*, Nucl. Instr. Meth. A 496 (2003) 347.
9. H. Sekiya *et al.*, Phys. Lett. B 571 (2003) 132.
10. J. B. Birks, The Theory and Practice of Scintillation Counting, 1964.
11. P. H. Heckmann, H. Hansen, and A. Flammersfeld, Z. Phys. 162 (1961) 84.
12. P. Belli *et al.*, Nuovo Cimento C 15 (1992) 475.
13. N.J.C Spooner *et al.*, Int. Workshop on Identification of Dark Matter, World Scientific (1997) 481.
14. J. D. Lewin and P. F. Smith, Astropart. Phys. 6 (1996) 87.
15. N.J.C Spooner *et al.*, Phys. Lett. B 473 (2000) 330.
16. R. Bernabei *et al.*, Nucl. Phys. B 389 (1996) 757.
17. P. Belli *et al.*, Nucl. Phys. B 563 (1999) 97.
18. J. I. Collar *et al.*, Phys. Rev. Lett. (2000) 3083.
19. G. Angloher *et al.*, Astropart. Phys. 18 (2002) 43.
20. R. Bernabei *et al.*, Phys. Lett. B 509 (2001) 197.
21. CDMS Collaboration, Phys. Rev. Lett. 84 (2000) 5699.
22. J. Jungman, M. Kamionkowski, K. Griest, Phys. Rep. 267 (1996) 195.
23. A. F. Pacheco and D. Strottman, Phys. Rev. D 40 (1989) 2131.
24. M. T. Ressell and D. J. Dean, Phys. Rev. C 56 (1997) 535.
25. G. H. Kaplan *et al.*, Astron. J. 97 (1989) 1197; `http://aa.usno.navy.mil/AA/software/novas/`
26. J. Hong *et al.*, Astropart. Phys. 16 (2002) 333.
27. R. Gaitskell, V. Mandic, `http://dmtools.berkeley.edu/limitplots/`

HIGH-ENERGY NEUTRINOS PRODUCED BY INTERACTIONS OF RELATIVISTIC PROTONS IN SHOCKED PULSAR WINDS

S. NAGATAKI

Research Center for the Early Universe (RESCEU), School of Science, The University of Tokyo, 7-3-1 Hongo, Bunkyo-ku, Tokyo 113-0033, Japan
E-mail: nagataki@utap.phys.s.u-tokyo.ac.jp

We have estimated fluxes of neutrinos and gamma-rays that are generated from decays of charged and neutral pions from a pulsar surrounded by supernova ejecta in our galaxy, including an effect that has not been taken into consideration, that is, interactions between high energy cosmic rays themselves in the nebula flow, assuming that hadronic components are the energetically dominant species in the pulsar wind. Bulk flow is assumed to be randomized by passing through the termination shock and energy distribution functions of protons and electrons behind the termination shock are assumed to obey the relativistic Maxwellians. We have found that fluxes of neutrinos and gamma-rays depend very sensitively on the wind luminosity, which is assumed to be comparable to the spin-down luminosity. In the case where $B = 10^{12}$G and $P = 1$ms, neutrinos should be detected by km^3 high-energy neutrino detectors such as AMANDA and IceCube. Also, gamma-rays should be detected by Cherenkov telescopes such as CANGAROO and H.E.S.S. as well as by gamma-ray satellites such as GLAST.

1. Introduction

It has been long time since the possibility that a baryonic component is present and may be energetically dominant in pulsar winds was pointed out. Based on this scenario, many works on the emissivity of high energy gamma-rays and neutrinos have been reported. Beall and Bednarek (2002) pointed out the possibility that the baryons interact with the thermal radiation field in the supernova cavity. Amato et al. (2003) calculated the flux of high-energy gamma-rays and neutrinos produced from the interactions of the winds with the supernova remnant.

On the other hand, Hoshino et al. (1992) studied the properties of relativistic, transverse, magnetosonic collisionless shock waves in electron-positron-heavy ion plasma. They found that the proton spectra in downstream of the MHD shock which connects the pulsar wind with the su-

pernova remnant is well fitted by a Maxwellian distribution function with temperature $k_B T_p/m_p c^2\gamma \sim 0.34$. where γ is the bulk Lorenz factor in the upstream of the pulsar wind.

Based on this study, we consider another possibility to produce high-energy gamma-rays and neutrinos in the downstream of MHD shock. The study presented by Hoshino et al. (1992) suggests the possibility that the distribution of the accelerated protons in the pulsar winds becomes the thermalized one and interact with each other. Thus we calculate the emissivity of high-energy gamma-rays and neutrinos that are produced in the downstream from the decays of neutral and charged pions. This picture is interesting and new one which should be investigated. As a model of the nebular flow, we adopt the formulation presented by Kennel and Coroniti (1984), although we assume in this study that protons are energetically dominant in the pulsar winds.

After calculating the flux of high-energy neutrinos from a pulsar with the amplitude of the magnetic field around the polar region $B \sim 10^{12}$G, we discuss the detectability of these signals at the Earth with km^3 high-energy neutrino detectors such as IceCube.

2. Method of Calculation

2.1. *Nebular Flow*

As stated in section 1, we adopt the model presented by Kennel and Coroniti (1984), assuming that protons are energetically dominant. In their model, the pulsar's spin down luminosity L just ahead of the shock is divided between particle and magnetic luminosity as follows:

$$L = 4\pi n\gamma r_s^2 m_p c^3(1+\sigma), \tag{1}$$

where n is the proper density of proton, u is the radial four speed of the flow, $\gamma^2 = 1+u^2$, r_s is the radial distance of the shock from the pulsar, m_p is the proton mass, c is the speed of light, *sigma* is the ratio of the magnetic plus electric energy flux to the particle energy flux,

$$\sigma = \frac{B^2}{4\pi nu\gamma m_p c^2}, \tag{2}$$

and B is the observer frame magnetic field. The maximum energy of the protons just ahead of the shock is estimated by the potential difference between the equatorial plane and pole of the rotating neutron star.

$$m_p c^2 \gamma_{\max} = 3\times 10^{12} R_6 B_{12}/P^2 \quad \text{eV}, \tag{3}$$

where R_6 is the radius of the neutron star in 10^6 cm, B_{12} is the amplitude of the magnetic field at pole of the neutron star, and P is the period of rotation of the pulsar in second. We adopt $\gamma_{\max}$ for the bulk velocity of the pulsar wind in the upstream.

The upstream flow is connected to the downstream via the Rankine-Hugoniot relations for perpendicular shock. As for the downstream flow, the steady state equation of motion is adopted. Position of the termination shock is determined so as to achieve the pressure balance between the supernova remnant and downstream of the pulsar wind at the inner-edge of the supernova remnant. We estimate the pressure in the supernova remnant by assuming that the ratio of the thermal energy relative to the kinetic energy is about 0.02 in the supernova remnant. Total explosion energy of a supernova is taken to be 10^{51} erg. The velocity of the inner-edge of the supernova remnant is set to be 2000 km s^{-1}. As for the distribution of the protons in the downstream, the Maxwellian with the temperature that gives the required pressure at each position is adopted.

2.2. *Emissivity of High Energy Gamma-rays and Neutrinos*

Next, we calculate the emissivity of high-energy gamma-rays and neutrinos using the formulation as follows:

$$F(E_\pi) = 2\pi c \int R^2 dR \int_1^\gamma d\gamma_1 \int_\gamma^\infty \gamma_2 \int_{-1}^1 d\cos\theta \frac{d\sigma(\gamma_1, \gamma_2, \cos\theta)}{dE_\pi} n(R, \gamma_1) n(R, \gamma_2) \times \sqrt{(\vec{\beta_1} - \vec{\beta_2})^2 - (\vec{\beta_1} \times \vec{\beta_2})^2} \ [\text{particles erg}^{-1}\ \text{s}^{-1}], \quad (4)$$

where γ_1, γ_2 are the respective Lorenz factors of the two protons, $\cos\theta = \vec{\beta_1} \cdot \vec{\beta_2} / \left|\vec{\beta_1}\right| \left|\vec{\beta_2}\right|$, R is the radius with respect to the neutron star, $n(R, \gamma)$ is the differential number density of protons at position R, and $d\sigma(\gamma_1, \gamma_2, \cos\theta)/dE_\pi$ is the differential cross section of proton-proton interaction.

The energy spectrum of gamma-rays produced through the decays of neutral pions in the fluid-rest frame is obtained as

$$F(E_\gamma) = 2 \int_{E_{\pi,\min}}^\infty dE_\pi \frac{F(E_\pi)}{\sqrt{E_\pi^2 - m_\pi^2}} \ [\text{photons s}^{-1}\ \text{erg}^{-1}], \quad (5)$$

where $E_{\pi\,\min}$ is the minimum pion energy required to produce a gamma-ray with energy E_γ. In the observer's frame, the energy spectrum of photons

are expressed as

$$\frac{F'(E'_\gamma)}{d\Omega'} = \sum_{\Delta V} \frac{F(E_\gamma)}{\Gamma^2(1-\beta\cos\theta')} \frac{1}{4\pi} \quad [\text{photons s}^{-1}\ \text{erg}^{-1}\ \text{sr}^{-1}], \qquad (6)$$

where Γ is the bulk Lorenz factor of the fluid element at each position in the observer's frame, θ' is the angle between the line of sight and direction of the flow, and ΔV is the volume of the each fluid element. The dashes($'$) represent the quantum for the observer's frame. The flux of neutrinos and pions can be obtained as a result of pion decays. although $\mu^\pm \rightarrow e^\pm + \nu_e(\bar{\nu}_e) + \bar{\nu}_\mu(\nu_\mu)$ is a 3-body process and slightly complicated. As for the differential cross section of pion production, we adopted the formulation presented by Badhwar et al. (1977).

3. Results

In figure 1, we show spectrum of energy fluxes of neutrinos from a pulsar which is located 10kpc away from the earth. The amplitude of the magnetic field and period of the pulsar is assumed to be 10^{12}G and 1ms. The detection limits of the energy flux for AMANDA-B10, AMANDA II (1yr), and IceCube are represented by horizontal lines. The atmospheric neutrino energy fluxes for a circular patch of 1° are also shown. The upper panel represents the case that the age of the pulsar is 1yr, while lower panel represent the case that the age is 10^2yr. From this figure, we can find that there is a possibility to detect the signals of neutrinos from pulsar winds in our galaxy.

In figure 2, integrated gamma-ray fluxes from the neutral pion decays are shown assuming that the supernova ejecta has been optically thin for gamma-rays. The amplitude of the magnetic field and period of the pulsar are assumed to be 10^{12}G and 1ms. The upper panel represents the case that the age of the pulsar is 1yr, while the lower panel shows the case that the age of the pulsar is 10^2 yr. The detection limits of integrated fluxes for GLAST, STACEE, CELESTE, HEGRA, CANGAROO, MAGIC, VERITAS, and H.E.S.S. are also shown. From these figures, we can find that there is a possibility to detect gamma-rays from decays of neutral pions by these telescopes.

4. Conclusion

In this study, we have estimated fluxes of neutrinos and gamma-rays that are generated from decays of charged and neutral pions from a pulsar surrounded by supernova ejecta in our galaxy, including an effect that has not

been taken into consideration, that is, interactions between high energy cosmic rays themselves in the nebula flow, assuming that hadronic components be the energetically dominant species in the pulsar wind. Bulk flow is assumed to be randomized by passing through the termination shock and energy distribution functions of protons and electrons behind the termination shock obey the relativistic Maxwellians.

We have found that fluxes of neutrinos and gamma-rays depend very sensitively on the wind luminosity, which is assumed to be comparable with the spin-down luminosity. In the case where $B = 10^{12}$G and $P =$ 1ms, neutrinos should be detected by km^3 high-energy neutrino detectors such as AMANDA and IceCube. Also, gamma-rays should be detected by Cherenkov telescopes such as CANGAROO and H.E.S.S. as well as by gamma-ray satellites such as GLAST.

We have found that interactions between high energy cosmic rays themselves are so effective that this effect can be confirmed by future observations. Thus, we conclude that it is worth while investigating this effect further in the near future.

References

1. Amato E., Guetta D., Blasi P., astro-ph/0302121.
2. J. H. Beall, W. Bednarek, *Astrophys. J.* **569**, 343 (2002).
3. P. Goldreich, W. H. Julian, *Astrophys. J.* **157**, 869 (1969).
4. M. Hoshino, J. Arons, Y. A. Gallant, A. B. Langdon, *Astrophys. J.* **390**, 454 (1992).
5. C. F. Kennel, F. V. Coroniti, *Astrophys. J.* **283**, 694 (1984).
6. R. Mahadevan, R. Narayan, J. Krolik, *Astrophys. J.* **486**, 268 (1997).
7. S. Nagataki, *Astrophys. J.* in press (astro-ph/0309715)

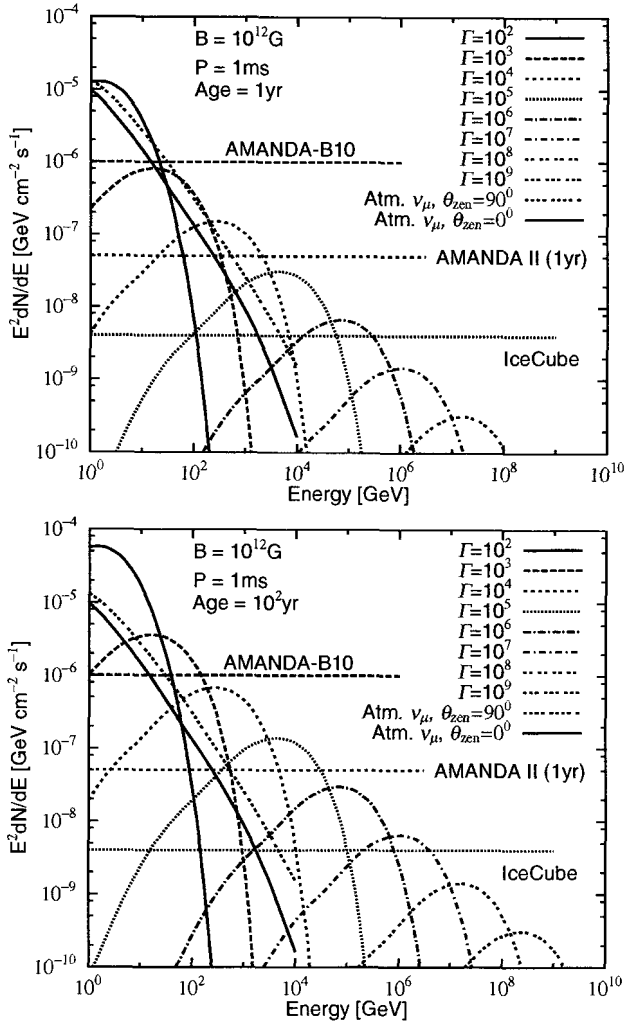

Figure 1. Spectrum of energy fluxes of neutrinos from a pulsar which is located 10 kpc away from the earth. The amplitude of the magnetic field and period of the pulsar is assumed to be 10^{12}G and 1ms. The minimum detectable energy flux of AMANDA-B10, AMANDA II (1yr), and IceCube is represented by horizontal lines. The atmospheric neutrino energy fluxes for a circular patch of 1° are also shown. The upper panel represents the case that the age of the pulsar is 1yr, while lower panel represent the case that the age is 10^2yr.

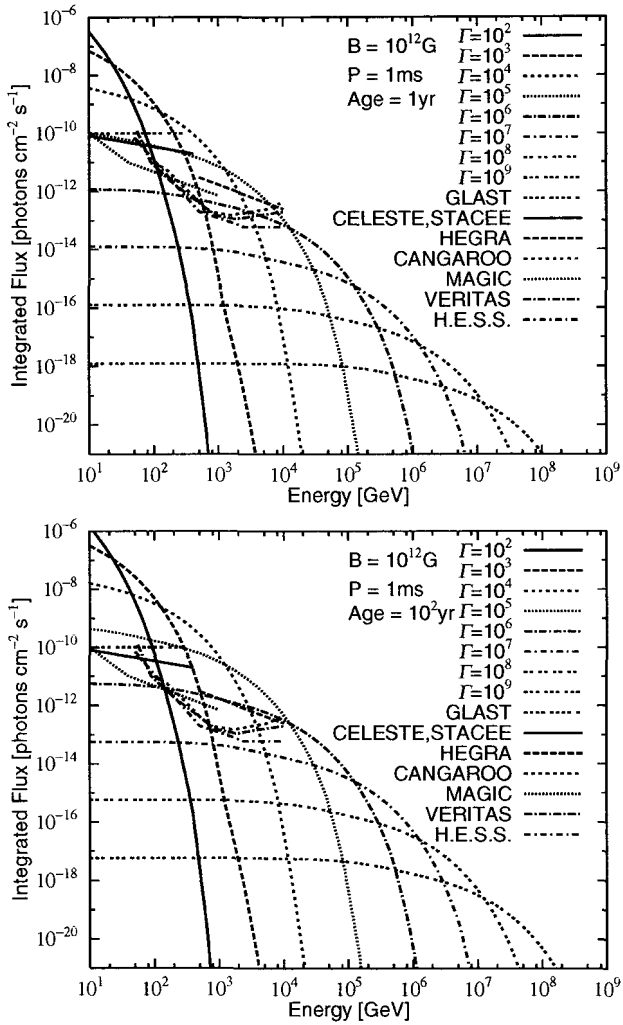

Figure 2. Integrated gamma-ray fluxes from the neutral pion decays are shown. The amplitude of the magnetic field and period of the pulsar are assumed to be 10^{12}G and 1ms. The upper panel represents the case that the age of the pulsar is 1yr, while the lower panel shows the case that the age of the pulsar is 10^2 yr. The minimum detectable integrated fluxes of GLAST, STACEE, CELESTE, HEGRA, CANGAROO, MAGIC, VERITAS, and H.E.S.S. are also shown.

This page intentionally left blank

IV. Evolution and Nucleosynthesis in Stars, and cross sections - hydro static burning

This page intentionally left blank

RECENT RESULTS FOR PROTON CAPTURE S FACTORS FROM MEASUREMENTS OF ASYMPTOTIC NORMALIZATION COEFFICIENTS

R.E. TRIBBLE, A. AZHARI, C. FU, C.A. GAGLIARDI, A.M. MUKHAMEDZHANOV, F. PIRLEPESOV, X. TANG, L. TRACHE

Cyclotron Institute, Texas A&M University, College Station, Texas 77843

P. BEM, V. BURJAN, V. KROHA, J. NOVÁK, Š. PIŠKOŘ, E. ŠIMEČKOVÁ, J. VINCOUR

Institute for Nuclear Physics, Czech Academy of Sciences, Prague-Řež, Czech Republic

F. CÂRSTOIU

Institute for Atomic Physics, Bucharest, Romania

Asymptotic normalization coefficients (ANCs) have proven to be useful for determining reaction rates of interest in nuclear astrophysics. These coefficients, which provide the normalization of the tail of the overlap function, determine S factors for direct capture reactions at astrophysical energies. They also can be related to resonance capture rates and are particularly useful for determining proton-capture reaction rates that involve subthreshold resonance states. During the past eight years, many ANCs have been measured by peripheral transfer reactions. Recent proton transfer reaction measurements have yielded ANCs for $^{14}\mathrm{O} \rightarrow {}^{13}\mathrm{N} + p$, $^{15}\mathrm{O} \rightarrow {}^{14}\mathrm{N} + p$ and $^{21}\mathrm{Na} \rightarrow {}^{20}\mathrm{Ne} + p$. These results have been used to find S factors for $^{13}\mathrm{N}(p,\gamma)^{14}\mathrm{O}$, $^{14}\mathrm{N}(p,\gamma)^{15}\mathrm{O}$ and $^{20}\mathrm{Ne}(p,\gamma)^{21}\mathrm{Na}$. Using mirror symmetry, the $^{13}\mathrm{C}(^{7}\mathrm{Li},^{8}\mathrm{Li})^{12}\mathrm{C}$ reaction has been used to obtain a new measurement of the ANC that defines the S factor for $^{7}\mathrm{Be}(p,\gamma)^{8}\mathrm{B}$. Following an introduction to ANCs, the recent experiments are discussed along with the astrophysical implications of these measurements.

1. Introduction

Stellar evolution is a complex process involving an interplay between nuclear burning, hydrodynamics, plasma physics and gravity. Nuclear burning provides the energy that ultimately dictates the fate of a star. The burning process is itself complicated, involving sequences of capture and transfer

reactions and beta decays, and depends on the density, temperature and nuclear abundances. Reaction and decay cycles, beginning with the p-p chain and extending to the CNO, Ne-Na, etc., cycles, process the nuclear fuel, primarily through hydrogen and helium burning, yielding increasingly massive nuclei and producing energy. Predicting the evolution of a star requires knowing the important reaction rates and half lives.

Direct proton-capture reactions of astrophysical interest usually involve systems where the binding energy of the captured proton is low. Hence at stellar energies, the capture proceeds through the tail of the nuclear overlap function. The shape of the overlap function in this tail region is completely determined by the Coulomb interaction, so the amplitude of the overlap function alone dictates the rate of the capture reaction. The asymptotic normalization coefficient (ANC), C, for $A + p \leftrightarrow B$ specifies the amplitude of the tail of the overlap function for the system. In previous communications[1,2], we have pointed out that astrophysical S factors for peripheral direct radiative capture reactions can be determined through measurements of ANC's using traditional nuclear reactions such as peripheral nucleon transfer. In many systems, resonant and nonresonant capture compete. We have shown[3] that the ANC can be used to determine the external part of Γ_γ. Thus the ANC is connected to both the resonant and nonresonant capture amplitudes. Also the ANC can be used to determine astrophysical S factors when the capture occurs through a subthreshold resonance state[3].

Below we describe the ANC technique citing a test that has been carried out to verify it. We then discuss four recent measurements, present their results and discuss their astrophysical implications.

2. Introduction to ANCs

It is well known that proton capture at stellar energies occurs at distances that are large compared to the nuclear radius. Direct capture rates depend on the normalization of the overlap function which is fixed by the appropriate ANCs. The connection between ANCs and the direct proton capture rate at low energies is straightforward to obtain. The cross section for the direct capture reaction $A + p \rightarrow B + \gamma$ can be written as

$$\sigma = \lambda | < I^B_{Ap}(\mathbf{r}) \mid \hat{O}(\mathbf{r}) \mid \psi_i^{(+)}(\mathbf{r}) > |^2, \qquad (1)$$

where λ contains kinematical factors, I^B_{Ap} is the overlap function for $B \rightarrow A + p$, $\hat{O}$ is the electromagnetic transition operator, and $\psi_i^{(+)}$ is

the scattering wave in the incident channel. If the dominant contribution to the matrix element comes from outside the nuclear radius, the overlap function may be replaced by

$$I^B_{Ap}(r) \approx C\frac{W_{-\eta,l+1/2}(2\kappa r)}{r}, \tag{2}$$

where C defines the amplitude of the tail of the radial overlap function I^B_{Ap}, W is the Whittaker function, η and l are the Coulomb parameter and orbital angular momentum for the bound state $B = A+p$, and κ is the bound state wave number. The required C's are just the ANCs; the direct capture cross sections are directly proportional to the squares of these ANCs. The ANC can also be related to the external or channel part of the resonance width for resonant capture[3]. The internal part of the width, however, depends on the strength of the overlap function in the nuclear interior. If resonance parameters are known either from measurements or calculations and ANCs are known, the resonant and nonresonant components can be used together in an R-matrix calculation to obtain capture cross sections.

Peripheral transfer reactions provide an excellent way to determine ANCs. Consider the proton transfer reaction $a + A \rightarrow c + B$, where $a = c + p$, $B = A + p$. As was previously shown[4] we can write the DWBA cross section in the form

$$\frac{d\sigma}{d\Omega} = \sum_{j_B j_a} \frac{(C^B_{Apl_B j_B})^2}{b^2_{Apl_B j_B}} \frac{(C^a_{cpl_a j_a})^2}{b^2_{cpl_a j_a}} \tilde{\sigma}^{DW}_{l_B j_B l_a j_a}, \tag{3}$$

where $\sigma^{DW}_{l_B j_B l_a j_a}$ is the reduced DWBA cross section and j_i, l_i are the total and orbital angular momenta of the transferred proton in nucleus i. The factors $b_{cpl_a j_a}$ and $b_{Apl_B j_B}$ are the ANC's of the bound state proton wave functions in nuclei a and B. which are related to the corresponding ANC of the overlap function by

$$(C^a_{cpl_a j_a})^2 = S^a_{cpl_a j_a} b^2_{cpl_a j_a}, \tag{4}$$

where $S^a_{cpl_a j_a}$ is the spectroscopic factor. If the reaction under consideration is peripheral, the ratio

$$R_{l_B j_B l_a j_a} = \frac{\tilde{\sigma}^{DW}_{l_B j_B l_a j_a}}{b^2_{Apl_B j_B} b^2_{cpl_a j_a}} \tag{5}$$

is independent of the single particle ANC's $b_{Apl_B j_B}$ and $b_{cpl_a j_a}$. Thus for surface reactions the DWBA cross section is best parametrized in terms of the product of the square of the ANCs of the initial and final nuclei

$(C^B)^2(C^a)^2$. The ANCs are just those needed in Eq. 1 to determine the capture reaction cross section.

We have measured ANCs in ^{16}O(^{3}He,d)^{17}F and compared them to radiative capture measurements to test our technique. The ^{16}O(^{3}He,d)^{17}F reaction was measured previously at a beam energy of 25 MeV[5]. We repeated the measurement at 29.75 MeV in order to obtain better angular coverage and to have a measurement at a second energy, both of which were necessary for extracting reliable ANC's. Data at laboratory scattering angles between 6.5° and 25° were obtained using Si solid state detectors and a ^{3}He beam, incident on a 134 μg/cm^2 Mylar target, from the U-120M isochronous cyclotron of the Nuclear Physics Institute (NPI) of the Czech Academy of Sciences. Additional data at laboratory angles between 1° and 11° were obtained using the MDM magnetic spectrometer and a molecular (^{3}He–d)$^+$ beam, incident on a 540 μg/cm^2 Mylar target, from the Texas A&M University K500 superconducting cyclotron. Absolute cross sections were determined at the NPI using their detection system which has been well calibrated for (^{3}He,d) reaction studies. The data obtained at TAMU were normalized to the data from the NPI measurement in the region where the two data sets overlapped. ANC's were extracted using finite-range DWBA calculations. Details of the experiment and the DWBA analysis can be found elsewhere[6].

Good agreement between predictions for S factors based on ANCs and experimental results were obtained. From these comparison we have verified that the ANC technique works to better than 10%. The largest uncertainty came from optical model parameters used to calculate the DWBA cross section.

3. Recent ANC Measurements

We have measured ANCs for ^{15}O $\rightarrow$ ^{14}N + p and ^{21}Na $\rightarrow$ ^{20}Ne + p using the ^{14}N(^{3}He,d)^{15}O and ^{20}Ne(^{3}He,d)^{21}Na reactions. The experiments were carried out with ^{3}He beams supplied by the U-120M isochronous cyclotron of the NPI. A 26.3 MeV beam was used with a 260 μg/cm^2 melamine target ($C_3H_6N_6$) to measure the ^{14}N(^{3}He,d)^{15}O. Reaction products were measured in a ΔE-E Si detector telescope. A second Si detector telescope fixed at 19° was used to monitor the target for degradation during the experiment. ANCs were obtained for the ground and five excited states in ^{15}O. The state that dominates the reaction rate at stellar energies, through an s-wave capture, is a subthreshold state at E_x = 6.79 MeV. The angular

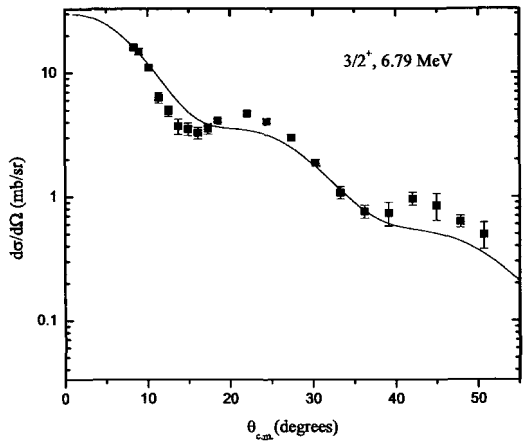

Figure 1. Angular distribution for the excited state at E_x = 6.79 MeV in ^{15}O from the ^{14}N(^{3}He,d)^{15}O reaction. The solid line is a DWBA fit to the data.

distribution for the important subthreshold state is shown in Fig. 1 along with a DWBA prediction. More details are given elsewhere[7].

A gas target cell filled with isotopic ^{20}Ne gas (99.99%) was bombarded by a 25.83 MeV ^{3}He beam in order to study the ^{20}Ne(^{3}He,d)^{21}Na reaction. The gas cell had entrance and exit windows of 3.05 μm havar and was operated at a pressure of 195 mbar. Both the temperature and pressure of the gas cell were continuously monitored during the experiment to verify that the target thickness remained constant. Also a Si monitor detector was set at 19° to act as an additional check on the system. A cooled ΔE-E Si detector telescope was used to observe the outgoing reaction products. A double collimating system was used to carefully define the detector solid angle. The stellar capture rate below T_9 of 0.2 is dominated by a subthreshold state at E_x = 2.425 MeV which is only 7 keV below the proton threshold. The ANC for the subthreshold state has been extracted from the angular distribution following the same procedure described above for the ^{14}N(^{3}He,d)^{15}O reaction.

The ANCs for ^{14}O → ^{13}N + p have been extracted from the ^{14}N(^{13}N,^{14}O)^{13}C reaction. The experiment was carried out at Texas A&M University. A beam of ^{13}C at 15 MeV/A from the K500 superconducting cyclotron was used to bombard a 9 cm long gas target filled with 2 atmospheres of H_2 gas cooled to LN_2 temperature. Recoil ions were collected by the MARS recoil spectrometer to produce a pure (>99%) secondary

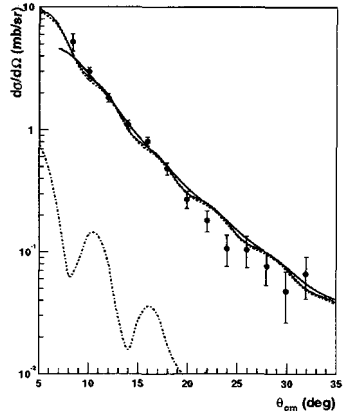

Figure 2. Angular distribution for ^{14}N(^{13}N,^{14}O)^{13}C$_{g.s.}$. The dashed curve is the DWBA prediction. The solid curve is the smeared prediction taking into account the finite size of the secondary beam spot and the angular spread in the beam. The upper and lower dashed-dotted lines represent the ^{14}N($p_{1/2}$) $\rightarrow$ ^{14}O($p_{1/2}$) and ^{14}N($p_{3/2}$) $\rightarrow$ ^{14}O($p_{1/2}$) proton transfer reactions, respectively.

beam of ^{13}N at 11.8 MeV/A. A 1.5 mg/cm^2 melamine target was placed at the focal plane of the recoil spectrometer and reaction products from the ^{14}N(^{13}N,^{14}O)^{13}C reaction were observed in 5 cm $\times$ 5 cm ΔE-E Si detector telescopes. The ΔE counters were 60 μm thick strip detectors and the E counters were 500 μm thick solid Si. A plastic scintillator detector was used to measure the beam particles. The angular distribution for ^{14}O reaction products populating the ground state of ^{13}C is shown in Fig. 2. The ANCs for ^{14}O $\rightarrow$ ^{13}N + p have been extracted and used to predict the direct capture contribution to the ^{13}N$(p,\gamma)^{14}$O reaction as described below. More details about the experiment can be found elsewhere[8].

In addition to the three proton transfer reactions discussed above, we have measured the ANCs for ^{8}Li $\rightarrow$ ^{7}Li + n from the neutron transfer reaction ^{13}C(^{7}Li,^{8}Li)^{12}C. By mirror symmetry, these ANCs can be related to those for the ^{8}B $\rightarrow$ ^{7}Be + p system[9]. Thus the neutron transfer reaction can be used to determine the S factor for ^{7}Be$(p,\gamma)^{8}$B. The ^{13}C(^{7}Li,^{8}Li)^{12}C reaction was carried out at Texas A&M University with a ^{7}Li beam at 9 MeV/A from the K500 superconducting cyclotron bombarding a 300 μg/cm^2 ^{13}C target. After passing through the beam analysis system, the primary beam was focused at the target chamber of the MDM magnetic spectrometer. Reaction products from the ^{13}C target were observed in the focal plane of

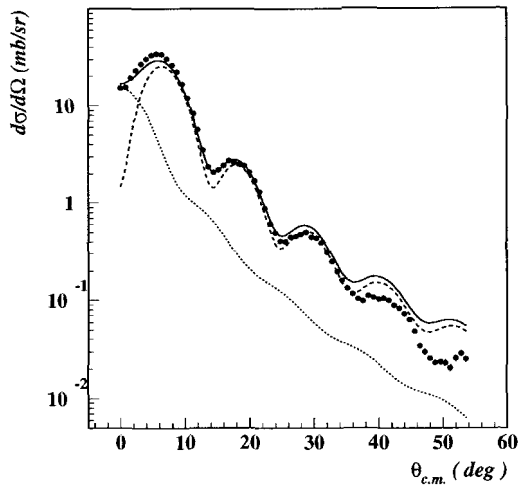

Figure 3. The angular distribution for the ^{13}C(^{7}Li,^{8}Li)^{12}C reaction. The data are shown as points and the solid line is the best fit. The $p_{1/2} \rightarrow p_{1/2}$ component is shown as the dotted line, and the $p_{1/2} \rightarrow p_{3/2}$ component is the dashed line.

the spectrometer. The high-quality beam from the analysis system allowed us to measure the angular distribution for the reaction to 0°. This made it possible to separate the $1p_{1/2}$ and $1p_{3/2}$ components in the transfer. In previous measurements of the mirror (^{7}Be,^{8}B) reaction[10], we were not able to separate the two components and had to rely on microscopic model calculations to fix the ratio. The angular distribution for the reaction and the DWBA fit are shown in Fig. 3. Optical model parameters were taken from an analysis of the ^{7}Li elastic scattering on ^{13}C. The resulting ANCs for the neutron transfer reaction are $C^2_{p_{3/2}}(^8Li) = 0.384 \pm 0.038$ fm^{-1} and $C^2_{p_{1/2}}(^8Li) = 0.048 \pm 0.006$ fm^{-1}. The ratio of the two ANCs is 0.13(2) which is in excellent agreement with the model calculations[11]. More details can be found elsewhere[12].

4. *S* factors from the ANCs and their astrophysical importance

The ^{14}N$(p,\gamma)^{15}$O reaction is one of the most important reactions in the CNO cycle. As the slowest reaction in the cycle, it defines the rate of energy production[13] and, hence, the lifetime of stars that are governed by hydrogen burning via CNO processing. The most recent measurement of the ^{14}N$(p,\gamma)^{15}$O reaction was carried out[14] in 1987 and a total astrophys-

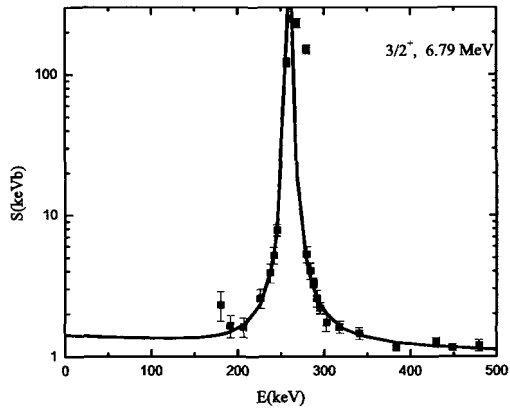

Figure 4. The $^{14}N(p,\gamma)^{15}O$ S factor for the important subthreshold state. The squares are the data points and the solid line is the best fit R-matrix solution.

ical factor $S(0) = 3.20 \pm 0.54$ keV b was deduced. This measurement led to a new understanding of the reaction, however, since it was found that $^{14}N(p,\gamma)^{15}O$ capture at low energies is dominated by capture through the first resonance at $E_{R1} = 259.5$ keV (the resonance energy in the c.m.) and a subthreshold state at $E_s = -504$ keV. At very low energies appropriate for stellar burning, the reaction was found to be dominated by a combination of direct and resonant capture and interference from the tail of the subthreshold resonance and the first resonance. Recently the first measurement of the radiative width of the subthreshold state in ^{15}O to the ground state was reported[15]. The new result for the width, $0.41^{+0.34}_{-0.13}$ eV, is about 15 times smaller than the value used by Schröder *et al.* in the analysis of their data. Consequently only direct capture to the subthreshold state in ^{15}O is important for the S factor. The ANC to the subthreshold state thus determines the reaction rate at stellar energies.

The ANCs that we determined from the transfer reaction have been used in an R-matrix analysis to determine the S factor for $^{14}N(p,\gamma)^{15}O$. The result for the transition to the subthreshold state is shown in Fig. 4. Extrapolating to stellar energies, we find $S(0) = 1.40 \pm 0.20$ keVb for the contribution from the subthreshold state. Including all contributions, we find the total calculated astrophysical factor at zero energy to be $S(0) = 1.70 \pm 0.22$ keV b[7]. This rate is about a factor of 2 smaller than that obtained from the analysis of Schröder *et al.* and makes the energy production in the CNO cycle smaller than previously estimated.

With increasing temperature, the rates of the proton capture reactions in the cold CNO cycle exponentially increase. Eventually the reaction rate for $^{13}N(p,\gamma)^{14}O$ exceeds the rate of ^{13}N β decay ($t_{1/2}$=9.965 min) and the hot (β limited) CNO-cycle takes over. But $^{14}N(p,\gamma)^{15}O$ is still the slowest reaction and it controls the energy generation rate. As the temperature continues to increase, all of the proton capture reaction rates in the hot CNO cycle exceed the β-decay rates of ^{14}O and ^{15}O (with half lifes $t_{1/2}$=70.6 s and 122s, respectively). The energy generation rate of the hot CNO cycle will remain constant until some break out processes begin to occur. Indeed the thermonuclear runaway in novae is driven by the energy release of the hot CNO cycle. Because the peak temperature in the thermonuclear runaway is typically below 3.5×10^8 K, break out processes are inhibited by their limited reaction rates. Observation of the abundance distribution in nova ejecta indicate large over abundances of nitrogen produced by the β-decay of the bottleneck nuclei, ^{14}O and ^{15}O, in the hot CNO cycle[16].

For T_9=0.2, the Gamow window for the $^{13}N(p,\gamma)^{14}O$ reaction is located at 148 keV with a width of 117 keV. At this energy the reaction is dominated by the low-energy tail of the s-wave capture on the broad 1^- resonance at E_r=0.529 MeV[17]. The direct capture contribution is significantly smaller than that due to the tail of the resonance within the Gamow window. But since both resonant and nonresonant capture proceed via s waves and then decay by E1 transitions, there is an interference between the two components. Thus the resonant tail can be enhanced through constructive interference or reduced through destructive interference.

The cross section for direct capture and resonant capture through the broad first excited state was calculated from the measured ANC and the experimental resonance parameters using the R-matrix approach[8]. In the calculation, the same parameters ($E_R^{c.m.} = 527.9 \pm 1.7$ keV, $\Gamma_{total} = 37.3 \pm 0.9$ keV and $\Gamma_\gamma = 3.36 \pm 0.72$ eV) as Magnus *et al.*[18] adopted were used for the first resonance. A theoretical calculation by Descouvemont[19] suggested that constructive interference occurs between the resonant and nonresonant amplitudes for the low energy tail, but there is no experimental confirmation of this so far. Thus both constructive and destructive interference were calculated and are shown, together with the result from Decrock *et al.*[17], in Fig. 5. The relatively flat lower solid line, which is our result for direct capture alone, is about 30% larger than the result obtained by Decrock *et al.* which is shown as the lowest dash-dotted line in Fig. 5. The two results just agree within the quoted uncertainties. At $E_{c.m.}$ = 140 keV where the Gamow peak is located for T_9=0.2, our updated result with constructive

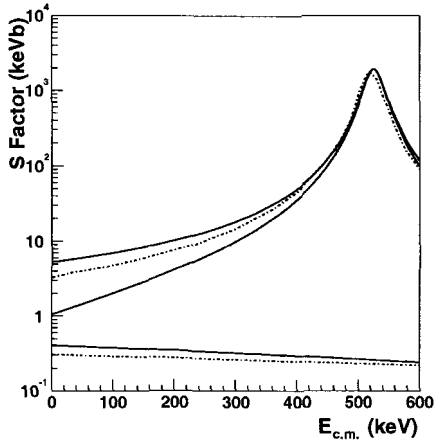

Figure 5. S factor for $^{13}N(p,\gamma)^{14}O$. The relatively flat solid line is the direct capture contribution determined from the ANC. This result is about 30% higher than that obtained by Decrock *et al.* which is shown as the lowest dash-dotted line.

interference, shown as the upper solid line, is about 38% higher than the previous result, which is shown as the upper dash-dotted line in Fig. 5. This is due to the larger direct capture contribution from the ANC measurement. In Decrock's calculation, the resonance energy was taken as 526 keV which is smaller than Magnus's recommendation[18] ($E_R^{c.m.} = 527.9 \pm 1.7$ keV). Therefore the peak of the resonance is shifted upward slightly with a higher resonance energy. The estimated destructive interference, shown as the lower solid line in Fig. 5 is smaller than the constructive interference result by a factor of 3 at $E_{c.m.} = 140$ keV. Verifying by a direct measurement that constructive interference is indeed correct would be quite useful.

As material leaks out of the CNO cycle, the Ne-Na cycle can begin. The $^{20}Ne(p,\gamma)^{21}Na$ reaction is one of the reactions in the Ne-Na cycle. Its reaction rate is extremely hard to measure since, like the $^{14}N(p,\gamma)^{15}O$ reaction, it is dominated by a subthreshold state. The important state in ^{21}Na at $E_x = 2.425$ MeV is only 7 keV below threshold. Thus even a small Γ_γ will result in a substantial resonant contribution to the reaction rate. The reaction rate at stellar energies was estimated previously to be about 3500 keV b[20]. The ANC that we have determined for this state fixes the direct capture through the subthreshold state. Figure 6 shows a preliminary R-matrix fit to the data from direct measurements[20]. At proton energies below about 150 keV, the resonant capture through the subthreshold state dominates the S factor. Based on the present information available about

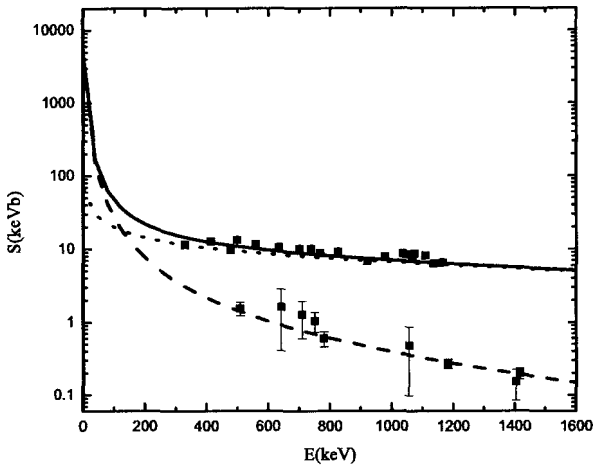

Figure 6. S factor for ^{20}Ne$(p,\gamma)^{21}$Na. The upper data points are the total capture rate and the lower ones are for capture through the subthreshold state. The solid line shows the total S factor. The dashed and dotted line give the resonant- and direct-capture rate through the subthreshold state, respectively.

the γ width of the state, we find $S(0) = 5700 \pm 800$ keV b. A new measurement of the width of this state, would substantially reduce the uncertainty in this result.

Previously, we used (^{7}Be,^{8}B) proton transfer reactions to measure the ANCs for the $^8\mathrm{B} \rightarrow {}^7\mathrm{Be} + p$ process, from which we determined the astrophysical factor $S_{17}(0)$[10]. This reaction is a very small branch in the $p-p$ chain but the resulting ^{8}B produces essentially all of the high-energy neutrinos from the sun. And it is these neutrinos that are detected in the water based solar neutrino detectors. Thus knowing the rate of ^{8}B production in the sun is quite important.

^{8}B and ^{8}Li are mirror nuclei, and charge symmetry implies that the spectroscopic amplitudes for the proton single particle orbitals entering the ^{8}B wave function are nearly the same as those of the neutron single particle orbitals in the ^{8}Li wave function. This leads to a proportionality between the asymptotic normalization coefficients in $^8\mathrm{B} \rightarrow {}^7\mathrm{Be} + p$ and $^8\mathrm{Li} \rightarrow {}^7\mathrm{Li} + n$. Thus the neutron transfer reaction allows us to determine the ANCs for $^8\mathrm{B} \rightarrow {}^7\mathrm{Be} + p$ and, consequently, the astrophysical factor S_{17}. This is a new variation of the ANC approach that will also be useful in other nuclear systems.

Using the ANCs in ^{8}Li, we find those for the mirror nucleus ^{8}B to be[12]

$C^2_{p_{3/2}}(^8B) = 0.405 \pm 0.041\,\mathrm{fm}^{-1}$ and $C^2_{p_{1/2}}(^8B) = 0.050 \pm 0.006\,\mathrm{fm}^{-1}$. These values are in good agreement with those obtained from proton transfer reactions at 12 MeV/u[10], where the average of the values extracted in two similar experiments on two different targets was found to be $C^2_{p_{3/2}}(^8B) = 0.388 \pm 0.039\,\mathrm{fm}^{-1}$. The two spin-orbit components could not be separated in the proton transfer reactions, as mentioned above. The value of 0.157 for the ratio, as predicted from a microscopic model calculation[11], was used to extract the ANCs from the (^{7}Be,^{8}B) reactions. Changing this ratio to 0.13 changes the value of $S_{17}(0)$ extracted from the proton transfer reactions by only 0.7%. Based on the results from the mirror neutron reaction, we find $S_{17}(0) = 17.6 \pm 1.8$ eV b.

This work was supported in part by the U.S. Department of Energy under Grant number DE-FG05-93ER40773, the U.S. National Science Foundation under Grants No. INT-9909787, PHY-0140343, ME 385(2000) project NSF and MSMT, CR, grant GACR 202/01/0709 and by the Robert A. Welch Foundation.

References

1. H.M. Xu *et al.*, Phys. Rev. Lett. **73**, 2027 (1994).
2. A.M. Mukhamedzhanov and N.K. Timofeyuk, JETP Lett. **51**, 282 (1990).
3. A.M. Mukhamedzhanov and R.E. Tribble *Phys. Rev.* **C59**, 3418 (1999).
4. A.M. Mukhamedzhanov *et al.*, Phys. Rev. C **56**, 1302 (1997).
5. J. Vernotte *et al.*, Nucl. Phys. **A571**, 1 (1994).
6. C.A. Gagliardi *et al.*, Phys. Rev. C **59**, 1149 (1999).
7. A.M. Mukhamedzhanov *et al.*, Phys. Rev. C **67**, 065804 (2003).
8. X. Tang *et al.*, Phys. Rev. C (submitted).
9. N. Timofeyuk, R.C. Johnson and A.M. Mukhamedzhanov, Phys. Rev. Lett. **91**, 232501 (2003).
10. A. Azhari *et al.*, Phys. Rev. C **63**, 055803 (2001).
11. A.M. Mukhamedzhanov and N. Timofeyuk, Yad. Fiz. **51**, 679 (1990) (Soviet J. Nucl. Phys. **51**, 431 (1990)).
12. L. Trache *et al.*, Phys. Rev. C **67**, 062801 (2003).
13. C. Rolfs, W. S. Rodney, Cauldrons in the Cosmos. (The University of Chicago Press, 1988).
14. U. Schröder *et al.*, Nucl. Phys. **A 467**, 240 (1987).
15. P. F. Bertone *et al.*, Phys. Rev. Lett. **87**, 152501 (2001).
16. M. Wiescher, J. Gorres and H. Schatz, J. Phys. G **25**, R133 (1999).
17. P. Decrock *et al.*, Phys. Rev. C **48**, 2057 (1993).
18. P.V. Magnus, E.G. Adelberger and A. Garcia, Phys. Rev. C **49**, R1755 (1994).
19. P. Descouvemont, Nucl. Phys. **A646**, 261 (1999).
20. C. Rolfs and W.S. Rodney, Nucl. Phys. **A241**, 460 (1975).

NEUTRON CAPTURE CROSS SECTION OF ^{14}C STUDIED BY INTERMEDIATE-ENERGY COULOMB DISSOCIATION

T. NAKAMURA

Department of Physics, Tokyo Institute of Technology,
2-12-1 O-Okayama, Meguro, Tokyo 152-8551, Japan,
E-mail: nakamura@phys.titech.ac.jp

N. FUKUDA

The Institute of Physical and Chemical Research (RIKEN),
2-1 Hirosawa, Wako, Saitama 351-0198, Japan
E-mail: nfukuda@riken.go.jp

The neutron capture reaction on ^{14}C leading to the ^{15}C ground state, which is important in the nucleo-synthesis processes in the universe, has been studied by using the Coulomb dissociation of ^{15}C on a Pb target at 68 MeV/nucleon. The dissociation cross sections at large impact parameters over 20 fm has been translated into the energy spectrum of the neutron capture by using the principle of the detailed balance. The energy spectrum shows the typical p-wave capture characteristics, which is understood by the fact that the ground state of ^{15}C is a loosely bound halo state. The present study suggests that such a p-wave neutron capture may often occur at the very neutron rich regions, where important nucleo-synthesis paths are expected.

1. Introduction

The neutron capture reaction of ^{14}C has been drawn much attention due to its importance in the nucleo-synthesis processes in the universe. M. Wiescher *et al.* [1] discussed the neutron induced CNO cycle, ^{14}C(n,γ) ^{15}C(β^-) ^{15}N(n,γ) ^{16}N(β^-) ^{16}O(n,γ) ^{17}O(n,α) ^{14}, which occurs in the burning zone of 1–3 $M_\odot$ asymptotic giant branch (AGB) stars. The ^{14}C$(n,\gamma)^{15}$C is the slowest in those reactions, and thus controls the cycle.

Recently, M. Terasawa proposed the r-process which starts from ^{4}He, and thus contains the light neutron rich nuclei in the path. This process is expected due to the similarity of the nuclear abundance patterns for the metal-deficient halo stars to those for the ordinary ones. The neutron capture of ^{14}C lies in the critical reaction flows. Another possible important

site for the neutron capture of ^{14}C has been suggested in the inhomogeneous big bang models , where the neutron-rich zone to induce the nucleosynthesis paths in the light neutron-rich nuclear regions can appear. In this scenario, the $^{14}C(n,\gamma)^{15}C$ reaction is considered to be one of the key reactions.

In the viewpoint of the nuclear structure, the ground state of ^{15}C, i.e., the final state of the capture reaction, is intriguing in that it has a moderate-sized halo state with a neutron separation energy of only 1.218 MeV. The main configuration of ^{15}C is $^{14}C(0^+)\otimes 2s_{1/2}$, which facilitates the formation of the halo due to no centrifugal barrier for the s-wave neutron. The p-wave neutron capture is then expected to become dominant for the present case since the final state occupies predominantly s orbital and the γ ray is E1 dominant. This is rather exceptional case as a stellar nuclear reaction since usually neutron captures in the stellar reactions occur as an s-wave n capture which follows the $1/v$ law. The p-wave neutron capture is a characteristic feature for the reaction having a halo state as a final channel.

The $^{14}C(n,\gamma)^{15}C$ reaction rate was once extracted directly by measuring the neutron capture cross section on ^{14}C [3]. Their extracted cross section of 1.1±0.28 μ barn at kT=23 keV was, however, about a factor of five smaller than those predicted by the p-wave direct neutron capture [4]. Recently, A. Horváth *et al.* measured the Coulomb dissociation of ^{15}C at 35 MeV/nucleon, where the energy spectrum of the inverse capture reaction is very different from the p wave characteristics. Their extracted capture cross section at 23 keV was 2.6(9) μ barn. More recently, at higher energy of 600 MeV/nucleon in GSI, the Coulomb dissociation of ^{15}C has been measured [6]. They show a typical direct breakup spectrum, unlike the MSU experiment, which indicates that the p-wave direct neutron capture is dominant for the inverse reaction. Here, we aim at resolving this controversial situation by measuring the Coulomb dissociation of ^{15}C. In particular, we introduce here the analysis of using a large impact parameter cut to select the dissociation induced by the Coulomb interaction.

2. Characteristics of Coulomb Dissociation of Halo Nuclei and Neutron Capture Reaction

Coulomb breakup can be used as a useful substitute for the (γ, n) reaction. The Coulomb breakup cross section is expressed by the product of the E1

virtual photon flux $N_{\rm E1}(E_{\rm x})$ and the photo-absorption cross section $\sigma_{\gamma n}$.

$$\frac{d\sigma_{\rm CD}}{dE_{\rm rel}} = \frac{16\pi^3}{9\hbar c} N_{\rm E1}(E_{\rm x}) \frac{dB({\rm E1})}{dE_{\rm rel}} \tag{1}$$

$$= N_{\rm E1}(E_{\rm x}) \frac{\sigma_{\gamma n}(E_\gamma)}{E_\gamma}, \tag{2}$$

Where $\frac{dB({\rm E1})}{dE_{\rm rel}}$ E1 stands for the reduced matrix element, and E_γ the γ ray energy which is equal to $E_{\rm x}$, i.e., the excitation energy in the Coulomb dissociation. This simple relation based on the first-order perturbation allows us to extract the $\sigma_{\gamma n}$ from the energy spectrum, which is obtained by measuring the momentum vectors of all the outgoing particles and thus by reconstructing the invariant mass of the excited intermediate state. The $\sigma_{\gamma n}$ is then translated into $\sigma_{n\gamma}$ by using the principle of the detailed balance as in,

$$\sigma_{n\gamma}(E_{\rm CM}) = \frac{2I_A + 1}{2I_{A-1} + 1} \frac{E_\gamma}{2\mu c^2} \sigma_{\gamma n}(E_\gamma), \tag{3}$$

where $I_A = 1/2$, and $I_{A-1} = 0$ for the present case. $E_{\rm CM}$ denotes the neutron energy in c.m. system of ^{14}C and neutron, which is equivalent to $E_{\rm rel}$ between neutron and ^{14}C in the breakup reaction. By this detailed balance, one can easily see that the $\sigma_{\gamma n}$ is 10^3–10^4 larger than $\sigma_{n\gamma}$ in the present case. In addition we have a gain factor due to the large number of the virtual photons. We can also take advantage of the kinematic focusing and the availability of the thick target of the order of 100 mg/cm^2. Owing to these factors, one can achieve higher yield for the Coulomb dissociation than the case of the neutron capture reaction even for the secondary beam experiment.

An intriguing feature for the Coulomb breakup of a halo nucleus is the strong E1 transition of the order of Weisskopf unit appearing at very low excitation energies of about 1 MeV [8,7,9,10,11,12]. This large E1 strength was explained successfully by the direct breakup mechanism as shown by our previous ^{11}Be experiment [8], where a halo nucleus breaks up without forming a resonance. The B(E1) distribution is then given simply by the transition matrix element as in,

$$\frac{dB({\rm E1})}{dE_{\rm rel}} \propto |< \mathbf{q} \mid \frac{Ze}{A} r Y_m^1 \mid R(\mathbf{r}) >|^2, \tag{4}$$

where $R(\mathbf{r})$ stands for the radial wave function of the halo nucleus in the ground state. The final state $< \mathbf{q} \mid$ describes a neutron in the continuum. The matrix element is then approximately described as a Fourier transform

of $rR(r)$. Hence, the B(E1) distribution at low excitation energy is an amplified image of the density distribution at large r. Namely, the Coulomb breakup probes exclusively the halo part of the wave function. With this feature, one can determine the amplitude of the tail part of the wave function. For instance, the spectroscopic factor of $^{10}\mathrm{Be}(0^+) \otimes 2s_{1/2}$ component was extracted for ^{11}Be as shown in the previous work [8,13]. This method was also successfully applied to the case of ^{19}C [12].

In the inverse reaction of the neutron capture, this large E1 strength is nothing but a p-wave direct capture. The above mechanism to enhance the breakup cross section holds for the inverse capture reaction. In fact, such an enhancement of the p-wave capture was shown for the $^{12}\mathrm{C}(n,\gamma)^{13}\mathrm{C}(1/2^+)$ reaction, where this excited ^{13}C state represents a loosely bound halo system with one neutron separation energy of 1.86 MeV [14,15,16].

3. Experimental Procedure

The experiment was performed at the RIPS facility [17] at RIKEN. The secondary beam of ^{15}C was produced by fragmenting ^{18}O at 100 MeV/nucleon on 1.1 g/cm^2 thick Be target. The secondary beam bombarded the Pb target with thickness of 220 mg/cm^2. The mean energy in the target was 68 MeV/nucleon. The energy of the ^{15}C ion was obtained event-by-event by the time of flight (TOF) measurement by using two thin plastic scintillators, which were located 4.57 m apart. The trajectory of ^{15}C incident on the target was determined by four sets of multi-wire proportional counters.

The breakup particles, ^{14}C and n, emerged in a narrow cone at forward angles with velocities close to that of the ^{15}C projectile. The neutron was detected by two layers of neutron hodoscope arrays with an effective area of 2.14(W)$\times$0.90(H) m^2 placed at 4.60 m and 4.99 m, respectively, downstream of the target. Each array consisted of 15 plastic scintillator rods with 6 cm thickness. The angular coverage ranged from $-7.0°$ to $19.0°$ in the horizontal direction, and from $-5.5°$ to $5.5°$ in the vertical direction. The neutron momentum vector was determined from the TOF and hit position information in the arrays. The intrinsic detection efficiency 7.2% for the threshold energy 6.0 MeVee (electron-equivalent energy) was obtained from a separate experiment using the $^7\mathrm{Li}(p,n)^7\mathrm{Be}$ reaction at 65 MeV.

The corresponding ^{14}C particle was analyzed by a magnetic spectrometer equipped with a drift chamber and plastic scintillator hodoscopes. Particle identification was performed by combining ΔE, TOF data from the

hodoscopes and magnetic rigidity information from the tracking of the particle. The momentum vector of ^{14}C was deduced by combining the TOF information with the tracking analysis.

4. Results and Discussions

By reconstructing the invariant mass of the intermediate ^{15}C state from the momentum vectors of neutron and ^{14}C, we have obtained a relative energy spectrum for ^{15}C as shown in Fig. 1. In the figure, we show the $E_{\rm rel}$ spectrum integrated for the scattering-angle θ of ^{14}C+n c.m. system ranging up to 6 degrees (solid square symbols), and the one with $\theta \leq$ 2.1 degrees (open circle symbols). Experimentally, this scattering angle was obtained as an opening angle between the incident momentum vector ($\boldsymbol{P}(^{15}\mathrm{C})$) and that of the outgoing ^{14}C+n system ($\boldsymbol{P}(^{14}\mathrm{C}) + \boldsymbol{P}(n)$) in the c.m frame of the ^{15}C + Pb. Since this ^{14}C+n c.m. system follows the classical Rutherford trajectory in the Coulomb dissociation, the impact parameter b, which is related to θ by b=$a\cot(\theta/2)$, can be obtained event by event. The cut at 2.1 degrees then corresponds to the impact parameter larger than 20 fm, which is far off the range of nuclear force in this nucleus.

From this figure, one can see clearly an excellent agreement with the first-order perturbation theory with the direct breakup model, as shown by the solid curve for the data with the impact parameter cut. Note that the selection of the large impact parameter region assures almost pure Coulomb dissociation. By comparing the amplitude with the calculation, the spectroscopic factor for the halo configuration ($^{14}\mathrm{C}(0^+) \otimes 2s_{1/2}$) was extracted to be 0.74(4) (preliminary), which is consistent with the GSI experiment [6], but not with the MSU experiment [5]. We apply this spectroscopic factor to calculate the case for $\theta \leq 6$ degrees. The overall agreement is obtained except the slight deviation at $E_{\rm rel} \sim$ 1-3 MeV. This can be due to the higher order effects and nuclear breakup contributions. The treatment of these effects will be discussed by using the ^{11}Be Coulomb breakup data elsewhere.

By using the data for $\theta \leq 2.1$ degrees, we have extracted the $\sigma_{n\gamma}$ cross sections as a function of $E_{\rm CM}$(=$E_{\rm rel}$), as shown in Fig.2. The overall agreement is obtained to the p-wave capture up to $E_{\rm CM} \sim$ 3 MeV. From this curve, we have extrapolated to the capture cross section at kT=23keV to be 4.1μb (preliminary), which is about 4 times larger than the previous direct capture experiment [3]. It is clearly seen that this curve follows the typical energy dependence of the p-wave direct capture, where the cross section is

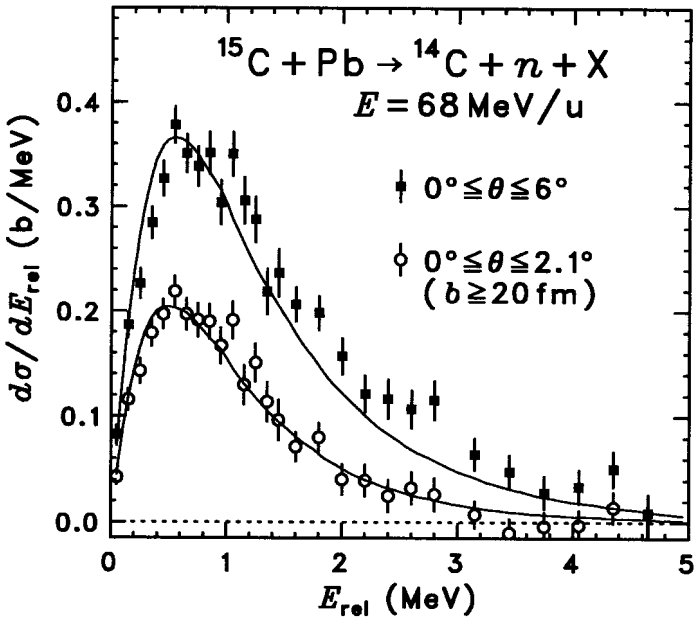

Figure 1. Relative energy spectra of the ^{15}C+Pb reaction for the scattering angle up to 2.1 degrees (open circles), and for the scattering angle up to 6 degrees (solid square). These are compared to the first-order perturbation calculation with the direct breakup mechanism.

roughly proportional to $\sqrt{E_{CM}}$ for low E_{CM}.

Here it should be noted that the Coulomb dissociation does not cover all the reaction channels of the neutron capture reaction since Coulomb dissociation is only applicable to the ground state. In fact, in the present case, we did not extract the cross section for the neutron capture of ^{14}C leading to the first excited state of ^{15}C located at E_x=0.74 MeV, which is the only bound excited state of ^{15}C. However, since for the n capture to this state a higher partial wave for neutron or γ ray is necessary, this cross section is to be negligible compared with the current reaction channel, as pointed out theoretically [4].

5. Summary

We have studied the Coulomb dissociation of ^{15}C to extract the ^{14}C(n,γ) cross section to resolve the controversial situations. We have found that

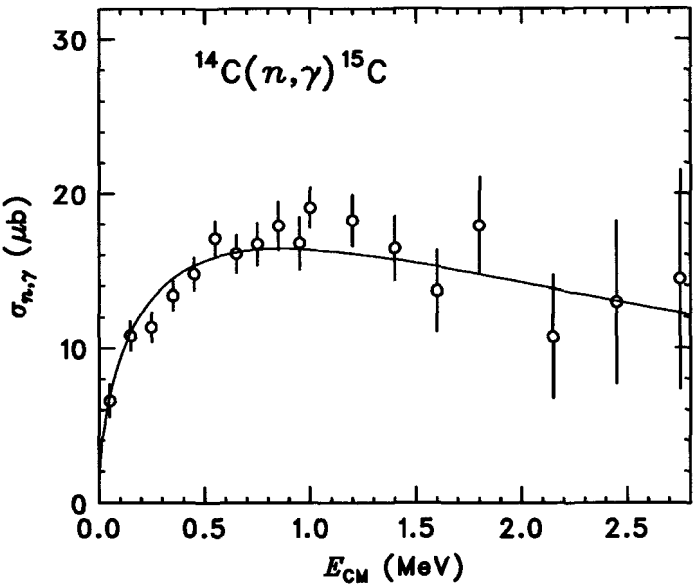

Figure 2. Neutron capture cross section on ^{14}C leading to ^{15}C ground state.

the $\sigma_{n\gamma}$ follows the typical p-wave direct capture characteristics of the dependence of $\sqrt{E_{\rm CM}}$. Our data shows that the capture cross section is larger by about a factor of four compared to the value obtained from the direct neutron capture experiment. The spectral shape is consistent with the GSI data, but not with the MSU data. We conclude here that this is a typical example of the p-wave direct capture due to the loosely bound halo state for the final state. This study shows that in the neutron-rich regions, where important nucleo-synthesis paths such as r-process locate, the p-wave capture reaction may often be dominant over the ordinary s-wave neutron capture.

Acknowledgement

The current experiment was done in collaboration with T. Kobayashi, H. Otsu, N. Aoi, H. Iwasaki, M. Notani, H. Sakurai, S. Shimoura, T. Teranishi, Y.X. Watanabe, K. Yoneda, T. Kubo, A. Mengoni, Y. Yanagisawa, N. Imai, and M. Ishihara.

References

1. M. Wiescher, J. Görres, and H. Schatz J. Phys. G: Nucl. Part. Phys., **25**, R133 (1999).
2. M. Terasawa *et al.*, Astrophys. J.**562**, 470 (2001).
3. H. Beer *et al.*, Astrophys. J.**387**, 258 (1992).
4. P. Descouvemont, Nucl. Phys. A bf 675, 559 (2000).
5. Á. Horváth *et al.*, Astrophys. J. **570**, 926 (2002).
6. U. Datta Pramanik *et al.*, Phys. Lett. B **551**, 63 (2003).
7. T. Kobayashi *et al.*, Phys. Lett. B **232**, 51 (1989).
8. T. Nakamura *et al.*, Phys. Lett. B **331**, 246 (1994).
9. K. Ieki *et al.*, Phys. Rev. Lett. **70**, 730 (1993). ; D. Sackett *et al.*, Phys. Rev. C **48**, 118 (1993).
10. S. Shimoura *et al.*, Phys. Lett. B **348**, 29 (1995).
11. M. Zinser *et al.*, Nucl. Phys. A **619**, 151 (1997).
12. T. Nakamura et al., Phys. Rev. Lett. **83**, 1112 (1999).
13. A. Mengoni *et al.*, *Proc. of the International Symp. on Capture gamma-ray and Related topics*, edited by G.L. Molnar, T. Belgya and Zs. Revay, (Springer, 1997), p. 416.
14. Y. Nagai *et al.*, Astrophys. J.**372**, 683 (1991).
15. T. Ohsaki *et al.*, Astrophys. J. **422**, 912 (1994).
16. T. Kikuchi *et al.*, Phys. Rev. C **57**, 2724 (1998).
17. T. Kubo et al., Nucl. Instrum. and Methods., B **70**, 309 (1992).

NUCLEOSYNTHESIS IN MASSIVE CORE-COLLAPSE SUPERNOVAE AS THE ORIGIN OF ABUNDANCES IN EXTREMELY METAL-POOR STARS *

H. UMEDA, N. TOMINAGA, T. OHKUBO, AND K. NOMOTO

Dept. of Astronomy, School of Scienece, University of Tokyo, Tokyo, 113-0033, Japan

E-mail: umeda@astron.s.u-tokyo.co.jp, ntominaga@astron.s.u-tokyo.co.jp, ohkubo@astron.s.u-tokyo.co.jp, nomoto@astron.s.u-tokyo.co.jp

We calculate nucleosynthesis in Population (Pop) III supernovae (SNe) and compare the yields with various abundance patterns of extremely metal-poor (EMP) stars. We assume that the observed EMP stars are the second generation stars, which have the metal-abundance pattern of the Pop III SNe. Previous theoretical yields and observations do not match well, suggesting that the simplest supernova model cannot account for the observations. In this paper we consider high energy explosions, "low-density" explosions, and mixing-fallback models. We show that the abundance patterns of both C-normal and C-rich EMP stars with [Fe/H] $\lesssim -2.5$ can be well reproduced with the yield of core-collapse SNe of $M \sim 20 - 130 M_{\odot}$. The abundance patterns of the [Fe/H] ~ -2.5 stars correspond to supernova yields with normal explosion energies, while those of the C-normal ([C/Fe] < 1) stars with [Fe/H] $\simeq -4 \sim -3$ correspond to high-energy supernova yields. The abundance pattern of C-rich ([C/Fe] $\gtrsim 2$) low [Fe/H] ($\simeq -5 \sim -3.5$) stars can be explained with the faint SN yield with little ^{56}Ni ejection, which is similar to SN1997D. Even we vary parameters, we still need a large explosion energy to obtain the large Co/Fe and Zn/Fe ratios observed in typical EMP stars.

1. Introduction

In the early universe, where the metal content of gas is very low, the enrichment by a single supernova (SN) can dominate the pre-existed metal contents. Low mass stars formed in the gas survives until today, and observed as extremely metal-poor (EMP) stars. Since EMP stars may preserve abundance patterns synthesized by a single or few SNe, the abundance patterns of those stars may be used to test SN explosion and nucleosynthesis

*Supported in part by the grant-in-aid for coe scientific research (14047206, 14540223, 15204010) of the ministry of education, science, culture, sports & technology in japan.

theories and to infer the nature of the first generation stars and SNe.

Previously, we have shown that the interesting trends in the abundance patterns of Fe-peak elements (Mn - Zn) in EMP stars with [Fe/H] $\lesssim -2.5$ (e.g., [15] [19]) can be explained with the nucleosynthesis in massive core-collapse supernovae (SNe) ([16], Umeda & Nomoto[26], UN02 hereafter). On the contrary, pair-instabillity supernovae, which are the explosion of $130 - 300 M_{\odot}$ stars, cannot explain the abundance of EMP stars, because of too small Co/Fe and Zn/Fe ratios (UN02).

In UN02 we also showed that the large Zn/Fe ratio typically observed in EMP stars ([19] [3]) which cannot be explained with conventional supernova yields, can be explained by core collapse SNe with large explosion energies (or "Hypernovae", e.g., [17]). Although Zn may be produced in the neutrino-powered wind just after the shock is launched in the deepest layers of stars where Y_e is very low [9], it is not clear the Zn production is really possible without over-producing unwanted elements, such as Ni, because no realistic yields have been published yet for the model.

In this paper, we compare our models with not only the Fe-peak elements but also with other elements observed in various (C-normal & C-rich) EMP stars, and discuss whether the observed abundances can be explained by the core-collapse SNe.

2. Nucleosynthesis calculations

The calculation method and other assumptions are the same as described in [29], UN02 and Umeda & Nomoto[28](UN03 hereafter). Presupernova progenitor models are first exploded by using the 1D hydrodynamical PPM code with the α-reaction networks and then the detailed explosive nucleosynthesis is calculated by post-processing with much larger reaction networks.

In UN02, we calculated the post-processing using the same distribution of Y_e, the electron mole fraction, as pre-supernova models. However, the Y_e during explosion may be affected by the neutrino process [11] [10]. Since the yields of Mn and Co are quite sensitive to Y_e, we varied the value of Y_e to find a better matching to the observations.

2.1. *Trends in the iron peak elements and hypernovae*

We have shown in previous papers (UN02, [27]) that the trends in the abundance ratios of Fe-peak elements, [(Zn, Co, Mn, Cr)/Fe] vs [Fe/H] (see Figure 2), can be understood by the variations of deepness of mass-cut

in the explosive nucleosynthesis of SNe II. We also have suggested that the large Zn/Fe and Co/Fe ratios in typical EMP stars are well-reproduced by hypernova nucleosynthesis.

For a larger explosion energy, the supernova shock is stronger and the temperature after the shock passage is higher. The post-shock region is radiation dominant, so that the peak temperature is approximately related to the stellar radius r and the deposited energy E^* as

$$T_9 = (E^*_{51})^{1/4}(r/3.16 \times 10^4\mathrm{km})^{-3/4}, \quad (1)$$

where T_9 is the peak temperature in 10^9 K and E^*_{51} is the deposited energy in 10^{51} erg. Complete Si-burning, which burns Si completely, occurs for $T_9 > 5$. In this region, elements such as ^{56}Ni, ^{64}Ge (decaying into ^{64}Zn) and ^{59}Cu (decaying into ^{59}Co) are produced. Incomplete Si-burning occurs for $4 < T_9 < 5$. In this region elements such as ^{56}Ni, ^{52}Fe (decaying into ^{52}Cr) and ^{55}Co (decaying into ^{55}Mn) are produced. For a larger explosion energy, the complete Si-burning region is enlarged in mass more than the incomplete Si-burning region (see Figure 1 and its caption). As a result, the mass ratio between the complete and incomplete Si-burning regions is larger in a more energetic explosion if the mass-coordinate of the mass-cut does not change significantly. Therefore, increasing the energy causes similar effect as making the mass-cut deeper without actually changing the mass coordinate of mass-cut.

The large energy is also consistent with the observation of [Zn/Fe] in EMP stars. For a typical EMP star, Zn is quite abundant, i.e., [Zn/Fe] $\sim$ 0.3 - 0.8 [19] [3]. We have shown that such large Zn/Fe ratio is difficult to produce by SNe with normal explosion energy ($\sim 10^{51}$ erg), but possible by energetic core collapse SNe with 10^{52} erg or more (UN02).

As an example, we show in Figure 2 the yield ratios for the ($15M_\odot$, $E_{51} = 1$) and ($25M_\odot$, E_{51}=30) models compared with the observations. This figure shows that the observed trends can be explained if [Fe/H] $\sim$ -3.5 stars are made of the gas of normal supernova while [Fe/H] $\sim$ -2.5 stars are made of that of hypernovae.

In this figure the [Fe/H] is assumed to be determined by the equation [Fe/H] = $\log_{10}$(Mg/E_{51}) + constant by the following reason. In the supernova-induced star formation model, [Fe/H] (or [Mg/H]) of a star formed in the SN ejecta is determined by the Fe (or Mg) mass ejected from a SN, divided by the hydrogen mass in circum stellar matter swept by the SN shock. It is estimated that the swept hydrogen mass is roughly proportional to the explosion energy [20] [23]. Thus we may write that

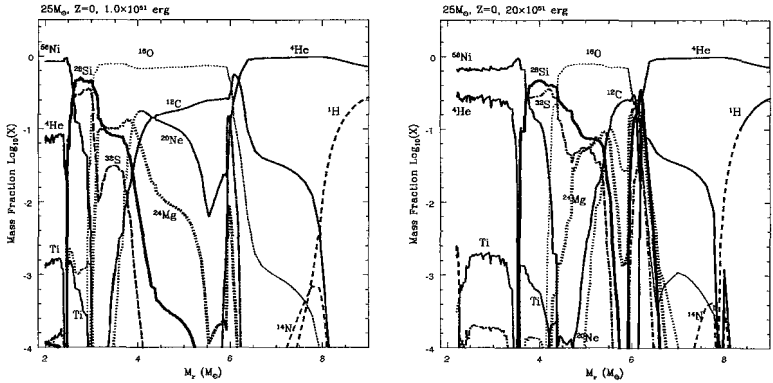

Figure 1. Abundance distribution after SN explosion of a 25 $M_\odot$ star with $E_{51} = 1$ (left panel) and $E_{51} = 20$ (right panel), where E_{51} is the explosion energy in 10^{51} erg. Complete Si-burning regions, here it is estimated by $X(^{28}Si) < 10^{-3}$, are $M_r < 2.5M_\odot$ for $E_{51} = 1$ and $M_r < 3.5M_\odot$ for $E_{51} = 20$. Incomplete Si-burning regions, here their upper edges are estimated by $X(^{56}Ni) < 10^{-3}$, are $2.5M_\odot < M_r < 3.0M_\odot$ for $E_{51} = 1$ and $3.5M_\odot < M_r < 4.3M_\odot$ for $E_{51} = 20$. For a larger explosion energy, complete Si-burning region is extended outside. Incomplete Si-burning region is also enlarged, however, the mass ratio between complete and incomplete Si-burning regions becomes larger for a larger explosion energy with a fixed mass-cut.

[Mg/H] = $\log_{10}$(Mg/E_{51}) + C. Here Mg and H represent mass fraction of Mg and H, respectively; E_{51} is the explosion energy in 10^{51} erg. 'C' is a constant if we assume spherically symmetric full mixing case. In reality, it depends on how much metal is actually mixed with the star-forming gas, and should depend on detailed hydrodynamical mixing, turbulent motion, local inhomogeneities and some other factors. Since we do not know how to determine the number exactly, here we simply assume that the number is constant. Since in the observations, [Mg/Fe] $\sim 0.3 - 0.5$ for typical EMP stars and roughly independent of [Fe/H], for simplicity we assume that [Fe/H] = [Mg/H] + constant = $\log_{10}$(Mg/E_{51}) + constant.

Unlike the similar results we showed previously (UN02, [27]), in this figure not only the trends but also the absolute value of [Co/Fe] and [Mn/Fe] agree with observations. This is because here we modify the Y_e in the Si-burning region as follows: $Y_e = 0.5001$ in the complete Si-burning region and $Y_e = 0.4997$ in the incomplete Si-burning. In our previous works, we have assumed that the pre-supernova value of Y_e is preserved during the explosive burning. In the Z=0 progenitor models, $Y_e \simeq 0.5000$ above the pre-supernova oxygen layer and decreases gradually toward the Fe core (UN02).

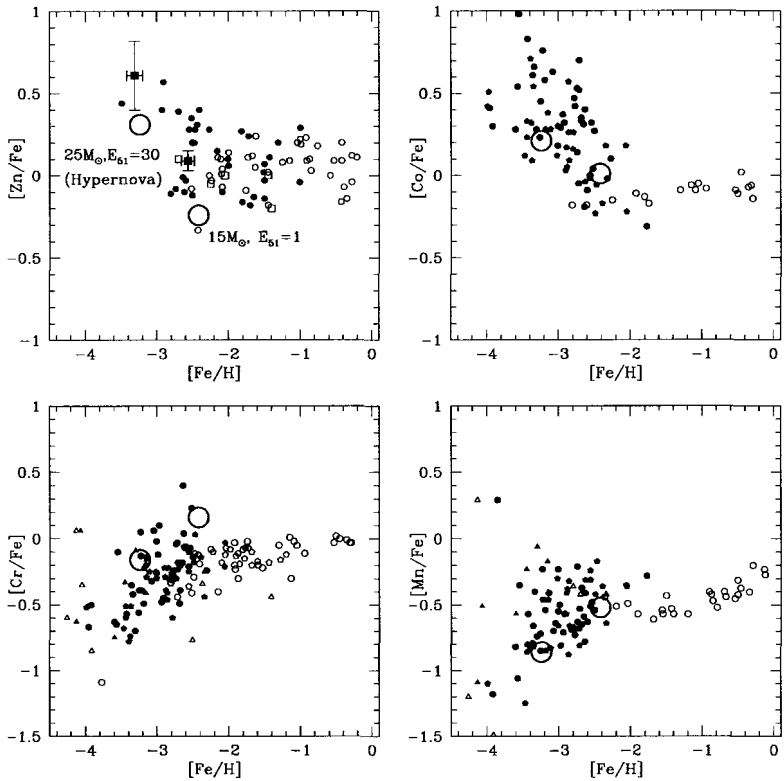

Figure 2. Observed abundance ratios of [(Zn, Co, Cr, Mn)/Fe] vs [Fe/H] compared with ($15M_\odot$, $E_{51} = 1$) and ($25M_\odot$, E_{51}=30) models (shown by large open circles). In these models, it is assumed that $Y_e = 0.5001$ in the complete Si-burning region and $Y_e = 0.4997$ in the incomplete Si-burning region.

However, recent detailed simulations of neutrino transport in core-collapse SNe show that Y_e may be significantly affected by the neutrino process during explosion [11] [10]. It is interesting that in the deep core $Y_e > 0.5$ may be realized, for such Y_e nucleosynthesis has not been systematically studied before. We show in Figure 3 how the abundances of Fe-peak elements depend on the value of Y_e. More detailed discussion and explanations about these models are given in [28].

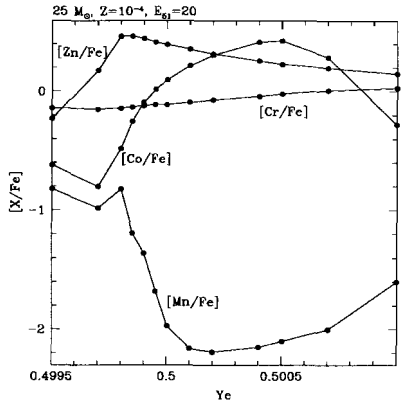

Figure 3. The abundance of Fe-peak elements as a function of Y_e in the Si-burning region. Here, we change the Y_e inside the incomplete Si-burning region to the value shown in the figure, and the mass-cut is chosen to maximize the Zn/Fe ratio. The supernova model is a $Z = 10^{-4}$, 25 $M_\odot$ model with explosion energy $E_{51} = 20$.

3. EMP Stars with Typical (C-normal) Abundance Pattern

In this section, we compare the typical abundance pattern of EMP stars with core-collapse SNe yields. The observed points shown in Figure 4 are the "averaged" abundances of three stars CD-38°245, CS22172-002 and CS22885-096 given in Norris et al.[18] (NRB01 hereafter). The NRB01 data do not include the Zn point. However, the over-abundance of Zn is quite common in EMP stars [19] [3], [Zn/Fe] is roughly homogeneous for [Fe/H] < -3.6, and the point is crucial to estimate the explosion energy, therefore, we add the value in the figure: specifically, [Zn/Fe]$= 0.3 \sim 0.8$ from [3]. The theoretical yield in Figure 4(a) is obtained for a zero metallicity (Pop III) $25M_\odot$ star after explosion with E_{51}=1.

In this model, the mass-cut is located at mass coordinate $M_r = M_{\rm cut} = 2.01\ M_\odot$. This mass-cut is chosen to maximize the Zn/Fe ratio in the original Y_e models (UN03 for detail). The fit in Figure 4(a) is not very good because of the underabundances of Mg, Sc, Ti, Co, Zn and over-abundance of Cr. The failure of the simplest model is also reported in [4].

The underabundances of Mg will be resolved if larger $M_{\rm cut}$ is chosen, for which Fe (decay products of ^{56}Ni) ejection is smaller. The overabundance of Cr and underabundances of Co are, on the other hand, improved for

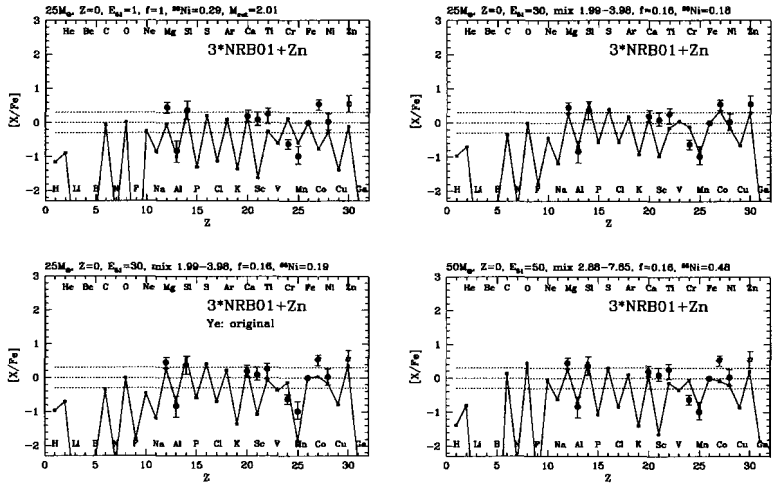

Figure 4. Elemental abundances of typical EMP stars at [Fe/H] ~ -3.7 (solid circles with error bars) compared with theoretical supernova yield (solid lines). In the panel (a), a $25M_\odot$, E_{51}=1 model is shown. This model does not assume mixing-fallback. In (b:"best" fitting model) a higher energy ($E_{51} = 30$) with a proper degree of mixing-fallback is assumed: 'mix 1.99–3.98' in the figure represents that $M_{\rm cut}$(ini) $= 1.99M_\odot$ and $M_{\rm mix}$(out) $= 3.98M_\odot$. This fits much better to the observation. In all models but (c), Y_e during the explosion is assumed to be $Y_e = 0.5001$ in the complete Si-burning and $Y_e = 0.4997$ in the incomplete Si-burning region. The model in (c) shows the model with the unmodified Y_e distribution. Similar goodness of the fitting may be obtained by more massive more energetic models as shown in (d), though the under-abundance of [Co/Fe] may suggest that a higher energy model might be better for this mass.

smaller $M_{\rm cut}$ (e.g., [16]). Therefore, these problems cannot be solved just by changing the mass-cut. In UN02, we proposed a solution, the mixing-fall back mechanism. If the inner part of the ejecta is mixed with the outer materials, and later some of the mixed matter is fallen-back to the central remnant, the ratio of the lighter elements, such as Mg and Al, to Fe increases without changing the abundance ratios in the Fe-peak elements.

We also note that the differences of the progenitor mass cannot resolve the problems. The mass-dependence on the yields are not so large, and especially the under-abundance of Co/Fe and Zn/Fe are not solved by the mass difference (see e.g., UN02).

In the mixing-fallback model, we define the following locations of M_r, and a function f:

- $M_{\rm cut}$(ini): the "initial mass-cut" which means that the matter above which is ejected even a fraction
- $M_{\rm mix}$(out): the outer boundary of the mixing region.
- f: a fraction of matter ejected from the mixed region of $M_{\rm cut}$(ini) $\leq M_r \leq M_{\rm mix}$(out).

Here, the inner most matter is first mixed between $M_{\rm cut}$(ini) and $M_{\rm mix}$(out), and some fraction of the matter, $1-f$, is fallen-back later on to the central remnant. The final mass-cut can be calculated by $M_{\rm cut}$(fin) = $M_{\rm mix}$(out) + $f\times$($M_{\rm mix}$(out) - $M_{\rm cut}$(ini)). Those parameters are shown at the top of Figure 4 (see its caption). In Figure 4, $M_{\rm mix}$(out) roughly corresponds to the outer boundary of the Si-burning region.

As shown in UN02, the Zn/Fe and Co/Fe ratios are significantly enhanced if the explosion energy is larger. In Figure 4(b), we show such a high-energy model with E_{51}=30. This is the "best" fitting model among the four models shown in Figure 4. We would like to stress here that the high-energy models agree with the observed data much better than the low-energy models.

In the model of Figure 4(b), all the elements but Sc, Ti and Cr fit well with the observation. For a comparison, we show in Figure 4(c) the same model as in Figure 4(b) but with the original Y_e distribution. We find that with the original Y_e distribution, [Mn/Fe] and [Co/Fe] fit much worse than the model in Figure 4(b).

The fit with similar goodness can be obtained by more massive and more energetic SNe. One such example, a $50M_\odot$ model with E_{51}=50, is shown in Figure 4(d). Looking at closely, the abundances of [Ti/Fe] and [Co/Fe] are smaller than the $25M_\odot$ model, but this would be remedied with larger explosion energy and/or asphericity or in the low density model (see next paragraph). This means that from the abundances of EMP stars, it is difficult to constrain the mass of the progenitor. We can constrain only the set of mass and explosion energy. At least we can say from the present SNe observations that the progenitors of energetic core-collapse SNe are more massive than $\sim 20M_\odot$. The upper mass limit is unknown, but should be lower than $\sim 140M_\odot$ because above which the stars would explode as pair-instability SNe (PISNe) and nucleosynthesis patterns are quite different from EMP stars (e.g., UN02, [8]).

Among these four models, the model in Figure 4(b) best agree with the observations: all the elements but Sc, Ti and Cr fit well. Currently we have no explanations about the over-production of Cr/Fe, but Sc and

Ti abundance may be explained if we consider a "low-density" model as shown in Figure 5 (UN03 for detail). In this model, the density of the progenitor model is artificially reduced, then the explosive burning takes place in a lower density. This makes the α-rich freezeout more efficient, enhancing the Sc/Fe and Ti/Fe ratios. We do not specify the reason for the low-density, but it may be related to the jet-like explosion (e.g., [13] [14]). If the jet is discontinuous and the inner part of the progenitor is expanded by weak-jets before strong jet explodes the star completely, a low density explosion may be realized.

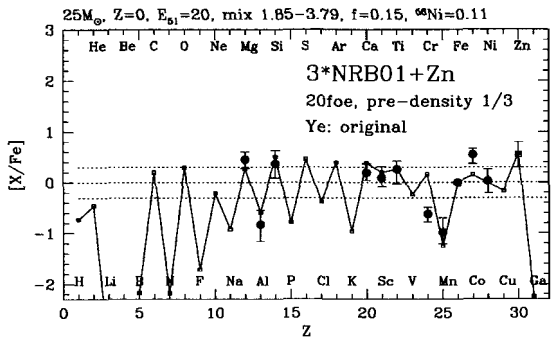

Figure 5. Elemental abundances of typical EMP stars at [Fe/H] ~ -3.7 given by NRB01 compared with yield of a low-density model. In this model, the density of the pre-supernova progenitor is reduced to 1/3 with keeping total stellar mass.

4. C-rich Fe-poor stars

4.1. *The most Fe-poor star: HE 0107-5240*

Recently discovered this star has the lowest [Fe/H] ($\simeq -5.3$) among the observed EMP stars [5]. Understanding the origin of this star has special importance, because it has been argued that low mass star formation is prohibited below a certain metallicity (e.g., below [Fe/H] ~ -4 [21]) due to inefficient gas cooling.

In [28] we discussed that this star is the second generation star, whose abundance pattern can be understood by the enrichment of population III core-collapse supernovae as is similar to other EMP stars discussed in Section 3. For HE0107-5240, the ejecta is Fe-poor but C-rich, then the low mass star formation can be possible with the C, N, O cooling.

In the supernova ejecta, the large C/Fe ratio is realized if the Fe ejection is small, because Fe is produced inner side of the star than C. This star has extremely high C/Fe ratio, [C/Fe] $\simeq 4$, which requires very small ^{56}Ni ejection, e.g., $M_{^{56}\mathrm{Ni}} \simeq 8 \times 10^{-6} M_\odot$ in the $25 M_\odot$ SN model. Such SNe have been actually observed, and the prototype is SN1997D [25]. Contrary to the large C/Fe ratio, Mg/Fe ratio is almost solar. This requires that large fraction of Mg needs to be fallen-back. Then the mixing region needs to be extended to the entire He-core, and only tiny fraction of the matter, 0.002%, is ejected from this region. The explosion energy of this SN model is assumed to be relatively low, $E_{51} = 0.3$, to reproduce the subsolar ratios of [Ti/Fe] $\simeq -0.4$ and [Ni/Fe] $\simeq -0.4$. The underabundances of N and Na may be explained by the production during the EMP star evolution (UN03). In Figure 6 we compare the model with the updated observed abundance pattern [6]. The model is basically the same as adopted in UN03. We note again that similar abundance pattern with the 1D mixing-fallback model may be obtained in the jet-like explosion as same as the case for the C-normal EMP stars.

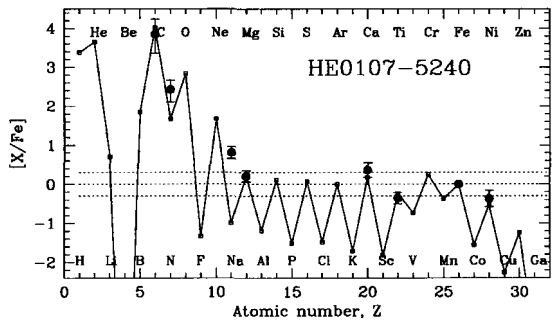

Figure 6. Elemental abundances of HE0107-5240, compared with a theoretical supernova yield. HE0107-5240 (filled circles) is the most Fe-deficient, C-rich star yet observed, with [Fe/H]= −5.3 and very large ratios of [C/Fe]=4.0 and [N/Fe] =2.3. Here the supernova model is the population III $25 M_\odot$ core collapse, with relatively small explosion energy $E_{51} = 0.3$. In this model, only a small fraction of the matter, 0.002% (f=0.00002), is ejected from the mixing region. The ejected Fe (or ^{56}Ni) mass, $8 \times 10^{-6} M_\odot$, is so small that the large C/Fe ratio can be realized.

For the abundance of this star, some other explanations have also been proposed [22] [12] [24]. These models assume that elements heavier than Na come from a supernova, but CNO elements come from either by another supernova or by a binary companion, though there is no evidence for the

existence of the binary companion so far. The abundance pattern in the two-supernovae model ([12]) may be hard to distinguish from ours unless the SN, which provides heavy elements is different from our model.

4.2. *Other C-rich EMP stars*

In addition to HE 0107-5240, several other C-rich EMP stars have been discovered. Interestingly, there are large variations in the abundance pattern for these stars. Some stars are Mg and Si rich :[Mg/Fe] & [Si/Fe] $\gtrsim 1$, e.g., CS22949-037 (NRB01, [7]) and CS29498-043 ([2]) while some of them are not: [Mg/Fe] & [Si/Fe] ~ 0.5, e.g., CS22957-027 and CS31062-012 [1]. Our model can explain these variations by the differences in the extent of the mixing region and the amount of fallback (e.g., Figure 7 for a Mg & Si rich star CS29498-043). On the other hand, the over-abundance of Mg and Si is hard to explain in the binary mass-transfer models.

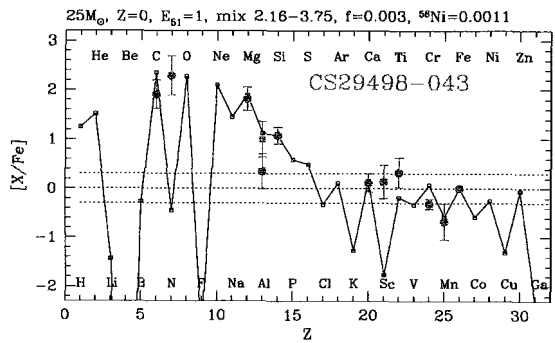

Figure 7. Elemental abundances of CS29498-043 compared with a theoretical supernova yield.

In summary, we have shown that the large variations in the abundance pattern in the EMP stars could be explained by the core-collapse SNe (20-130$M_{\odot}$) with various energies and various degree of mixing and fall-back. On the other hand, there is no evidence for PISNe in EMP stars.

References

1. Aoki, W., Ryan, S. G., Beers, T. C. & Ando, H. 2002a, ApJ, 567, 1166
2. Aoki, W., Norris, J. E., Ryan, S. G., Beers, T. C. & Ando, H. 2002b, ApJ, 576, L141
3. Cayrel, R. et al. 2004, A&A, in press (astro-ph/0311082)

4. Chieffi, A., & Limongi, M. 2002, ApJ, 577, 281
5. Christlieb, N., et al. 2002, Nature, 419, 904
6. Christlieb, N., Gustafsson, B., Korn, A.J., Barklem, P.S., Beers, T.C., Bessell, M.S., Karlsson, T., & Mizuno-Wiedner, M. 2003, preprint (astro-ph/0311173)
7. Depagne, E., et al. 2002, A&A, 390, 187
8. Heger, A., & Woosley, E. 2002, ApJ, 567
9. Hoffman, R.D., Woosley, E., Fuller, G.M., & Meyer, B.S. 1996, ApJ, 460, 478
10. Janka, H.-Th., Buras, R., & Rampp, M. 2003, Nucl. Phys. A, 718, 269
11. Liebendörfer, M., Mezzacappa, A., Messer, O. E. B., Martinez-Pinedo, G., Hix, W. R., & Thielemann, F.-K. 2002, Nucl. Phys. A., 719, 144
12. Limongi, M., Chieffi, A. & Bonifacio, P. 2003, ApJ, 594, L123
13. Maeda, K., & Nomoto, K. 2003a, ApJ, 598, 1163
14. Maeda, K., & Nomoto, K. 2003b, Prog. Theor. Phys. Suppl., in press (astro-ph/0305183)
15. McWilliam, A., Preston, G. W., Sneden, C., & Searle, L. 1995, AJ, 109, 2757
16. Nakamura, T., Umeda, H., Nomoto, K., Thielemann, F.-K., & Burrows, A. 1999, ApJ, 517, 193
17. Nomoto, K., Maeda, K., Umeda, H., Tominaga, N., Ohkubo, T., Deng, J., & Mazzali, P. A. 2003, to appear in Carnegie Observatories Astrophysics Series, Vol. 4: Origin and Evolution of the Elements, ed. A.McWilliam & M.Rauch (Pasadena: Carnegie Observatories) (http://www.ociw.edu/ociw/symposia/series/symposium4/proceedings.html)
18. Norris, J. E., Ryan, S. G., & Beers, T. C. 2001, ApJ, 561, 1034 (NRB01)
19. Primas, F., Brugamyer, E., Sneden, C., King, J. R., Beers, T. C., Boesgaard, A. M., & Deliyannis, C. P. 2000, in The First Stars, ed. A. Weiss, T. Abel, & V. Hill (Berlin: Springer), 51
20. Ryan, S. G., Norris, J. E., & Beers, T. C. 1996, ApJ, 471, 254
21. Schneider, R., Ferrara, A., Natarajan, P. & Omukai, K. 2002, ApJ, 571, 30
22. Schneider, R., Ferrara, A., Salvaterra, R., Omukai, K., & Bromm, V. 2002, Nature, 422, 869
23. Shigeyama, T. & Tsujimoto, T. 1998, ApJ, 507, L135
24. Shigeyama, T., Tsujimoto, T., & Yoshii, Y. 2003, ApJ, 586, L57
25. Turatto, M. et al. 1998, ApJ, 498, L122
26. Umeda, H., & Nomoto, K. 2002a, ApJ, 565, 385 (UN02)
27. Umeda, H., & Nomoto, K. 2002b, in proc. of the 11th Workshop on Nuclear Astrophysics, ed. W.Hillebrandt & E.Müller (Max-Planck-Institut fr Astrophysik), 164 (astro-ph/0205365)
28. Umeda, H., & Nomoto, K. 2003, Nature, 422, 871
29. Umeda, H., & Nomoto, K. 2003, ApJ, submitted (astro-ph/0308029) (UN03)
30. Umeda, H., Nomoto, K., & Nakamura, T. 2000, in The First Stars, ed. A. Weiss, T. Abel, & V. Hill (Berlin: Springer), 150 (astro-ph/9912248)

EVOLUTION, EXPLOSION AND NUCLEOSYNTHESIS OF POP III SUPER-MASSIVE STARS.

TAKUYA OHKUBO, HIDEYUKI UMEDA, AND KEN'ICHI NOMOTO
Department of Astronomy, School of Science, University of Tokyo.,
Hongo 3 chome 7-3-1,
Bunkyo-ku, Tokyo, JAPAN
E-mail: ohkubo@astron.s.u-tokyo.ac.jp

TAKASHI YOSHIDA
Astronomical Data Analysis Center, National Astronomical Observatory.,
Osawa 2-21-1,
Mitaka, Tokyo, Japan

We calculate evolution, explosion and nucleosynthesis of population III very-massive stars with 500 and $1000 M_{\odot}$. Then we compare the results of nucleosynthesis with the abundance patterns of hot gases in M82, intracluster matter (ICM), and extremely metal-poor stars in the Galactic halo. The patterns of nucleosynthesis match the observational data in M82, that is, undersolar [O/Fe], [Ne/Fe] and solar values or oversolar [Mg/Fe], [Si/Fe], and [S/Fe] if the contribution of the jet material is not so large. For the halo stars, [O/Fe] in our models are smaller than the observational abundances, but more detailed observations at [Fe/H] $\lesssim$ -3 are needed to judge whether pop III very-massive stars contributes to the early Galactic chemical evolution or not.

1. Introduction

One of the important problems in astronomy is to investigate the typical mass and the properties of the first generation stars — called "poplation III stars" (pop III stars). It is suggested that for pop III stars the Initial Mass Function (IMF), which indicates how many stars with a certain mass are formed, might be different from the present one. It has been suggested that there might exist very-massive stars in the early universe which are not observed at present. The reason is as follows. The early universe is metal free, therefore, radiation pressure is small and cooling is inefficient in the star forming gas clouds. That prevents the segmentation of the gas cloud. Numerical simulation has shown that very-massive stars over $300 M_{\odot}$ can be

formed from a massive cloud ($\sim 10^6 M_\odot$) in the zero-metal environment [1]. If such massive stars actually existed, they must have released a large amount of heavy elements into space by mass loss and/or supernova explosion. If so, they might have significantly contributed to the early Galactic chemical evolution.

The question if such very-massive stars over $300 M_\odot$ actually existed is very important to understand the origin of intermediate-mass black holes ($\sim 10^3 M_\odot$, IMBHs). Some IMBHs have been found recently. [2]. If very-massive stars actually existed, they could be considered as progenitor stars of IMBHs.

Motivated by these backgrounds, we calculate evolution, explosion, and nucleosynthesis of very-massive stars over $300 M_\odot$. Previously such calculations have not been carried out for such massive stars. These stars will form black holes directly during core-collapse, and it is unknown if they explode as SNe. However, if stars are rotating, the whole stars do not become black holes at once. They form accretion disks around their central remnants [3]. After forming accretion disks, jet-like explosions may occur by extracting energy from accretion disks or black holes [4, 5, 6].

We compare the results of nucleosynthesis with the observational abundance patterns in M82, intracluster medium, and extremely metal-poor stars in Galactic halo.

we describe the calculations of evolution of such massive stars in section 2. We describe the models and assumptions in the calculations of the explosion in section 3, and give the results of hydrodynamics and nucleosynthesis in sections 4 and 5, respectively. The predicted abundance patterns of the models and comparison with observations are described in section 6.

2. Stellar Evolution

2.1. *Models and Assumptions*

We calculate evolution of very-massive stars, $500 M_\odot$ and $1000 M_\odot$, with initially containing no-metal. In this study, for simplicity, we assume that these stars have 500 and $1000 M_\odot$ already on the zero-age main sequence. We also neglect radiative mass loss because of metal free [7]. We use stellar evolution code based on the Henyey method [8]. We calculate the evolution from zero-age main sequence to iron-core collapse where the central densities reach as high as $2 \times 10^{10} \mathrm{g/cm^3}$.

2.2. *Presupernova Evolution*

The time scale of evolution from the zero-age main sequence to core-collapse is $\sim 2 \times 10^6$ years for such massive stars, that is $1/3 \sim 1/10$ of ordinal massive stars ($13 \sim 25 M_\odot$) [9]. The left panel in figure 1 shows evolutionary tracks of the central density - temperature of $500 M_\odot$ and $1000 M_\odot$ stars. We also plot the track of the $300 M_\odot$ star for comparison, which results in a pair-instability supernova. Although each star passes through the region of electron-positron pair-instability, the $500 M_\odot$ and $1000 M_\odot$ stars proceed to iron-core collapse, unlike the $300 M_\odot$ star. The 500 and $1000 M_\odot$ star do not become Pair-Instability Supernovae, though they pass through the pair-instability region, because the energy released at this stage is less than the gravitational binding energy of the star [10, 11, 12, 13].

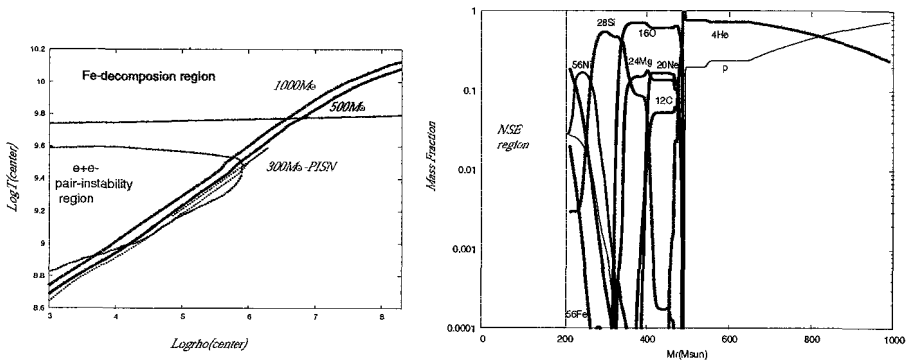

Figure 1. (left)Evolutionary tracks of the stars with $300 M_\odot$ (thin dotted line), $500 M_\odot$ (thick solid line), and $1000 M_\odot$ (thick dashed line). (right)Chemical compositon just before the explosion of the $1000 M_\odot$ star. The iron core occupies more than 20% of the total mass.

The right panel in figure 1 shows the chemical composition for the $1000 M_\odot$ star. In the region labeled as "NSE region" NSE is realized. For this region, we calculate the evolutions changes in terms of (Y_e, ρ, T) to obtain the NSE abundances. One can see the onion-like structure from the center to the surface: iron-core, silicon layer, oxygen layer, helium layer, and hydrogen layer. Here we define the iron-core as the region where the mass fraction of Si is less than 10%. The iron-core occupies up to $130 M_\odot$ from the center for the $500 M_\odot$ star, and $250 M_\odot$ for the $1000 M_\odot$ star. For both cases, they occupy a quarter of the total mass. This fraction is much

larger than those in ordinary massive stars, such as $25M_\odot$. For the $25M_\odot$ star, iron-core is about $1.6M_\odot$ [14], less than 10% of the total mass. The reason is the diffenrence in the density and temperature structures. In figure 2, we show the density and temperature structures of the two stars just before the explosion, compared with the $25M_\odot$ model. The density and temperature gradients for the 500 and $1000M_\odot$ stars are smaller than those of $25M_\odot$ [15], so the regions with high temperature and density are larger. Then the fraction of iron-core is larger.

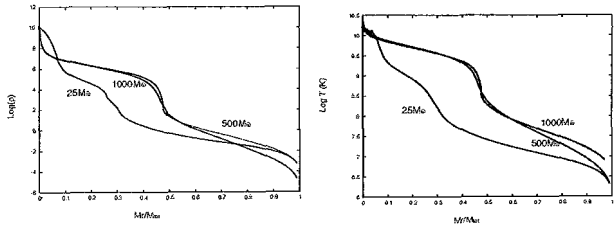

Figure 2. Density structure (left panel) and temperature structure (right panel) of $25M_\odot$, $500M_\odot$, $1000M_\odot$ models. The horizontal axis is the mass fractions M_r/M_{total}.

3. Explosion

3.1. *Hydrodynamics*

In hydrodynamical simulation, we use 2-dimentional Newtonian hydrodynamical code [6].

The models we examine are summarized in table 1. We consider jets as the energy souce of the explosion, which is injected from the accretion disk. We first set the initial black hole mass, and the outer matter accretes toward the central object. Because our hydrodynamical code includes gravitational force, the final black hole mass (and the ejected mass) are determind as a result of calculation with a set of given parameters [6].

For the jet injection, we set the parameter, θ_{jet}, which expresses the range of angle from the polar axis the jet is injected. The jet is injected into the direction of $0 \leq \theta \leq \theta_{jet}$. The energy and mass injected by the jets per unit time are connected with the properties of accreting matter as follows [6]:

$$\dot{E}_{jet} = \epsilon \dot{M}_{acc} c^2 = E_{thermal} + (\frac{1}{2}\rho_{jet} {v_{jet}}^2) v_{jet} A_{jet} \qquad (1)$$

$$\dot{M}_{\rm jet} = \mu \dot{M}_{\rm acc} = \rho_{\rm jet} v_{\rm jet} A_{\rm jet} \tag{2}$$

where $\dot{M}_{\rm acc}$ is accretion rate, $\dot{E}_{\rm jet}$ is injected energy per unit time, $\dot{M}_{\rm jet}$ is mass injected per unit time, ϵ is the efficiency of energy transformation, μ is the mass fraction of the jets to accreted matter, $\rho_{\rm jet}$ is the jet density, $v_{\rm jet}$ is the jet velocity, and $A_{\rm jet}$ is the area that jet is injected, respectively.

We consider two cases for the form of the injected energy. One is that almost all the energy of jets is given as kinatic energy (case A). The other is that almost all the energy is given as thermal energy (case B). We introduce a parameter $F_{\rm thermal}$ defined as follows:

$$F_{\rm thermal} = \frac{\dot{E}_{\rm thermal}}{\dot{E}_{\rm jet}} \tag{3}$$

i.e., the ratio of thermal energy in the jet to the total jet energy per unit time. By using the equations (1), (2), and (3), we obtain the jet velocity:

$$v_{\rm jet} = \left[\frac{2\epsilon(1 - F_{\rm thermal})}{\mu}\right]^{1/2} c \tag{4}$$

For case A, we set the ratio between the two parameters, ϵ / μ, to 0.1. Because we perform the Newtonian calculation, the larger we set ϵ, the larger we need to set μ in order that jet material do not exceed or approach to the speed of light. For case B, we set larger ϵ for the same μ compared with case A.

3.2. *Nucleosynthesis*

We calculate explosive nucleosynthesis by using temporal histories of density and temperature stored during hydrodynamical calculation. At high temperature $T_9 > 5$ — here we define T_9 as $T/10^9$ K —, NSE state are realized. We use "NSE" code [16] for $T_9 > 6$.

3.3. *Treatment of Jet Matter*

Jet matter should be included in the ejected matter and we need to calculate nucleosynthesis of it. However, we do not follow the history of jet matter since it has originally accreted, but only after it is injected, because we do not calculate the dynamics in the accretion disk. For simplicity, We make the following assumptions in this study:

(1):Because jet matter is injected through the inner region (from the accretion disk), it should have experienced high temperature at which NSE

state is realized ($T_9 > 5$). (2):The value of Y_e is also uncertain, we assume $0.48 \leq Y_e \leq 0.52$. Based on these assumptions above, we start the calculation of nucleosynthesis of jet matter from $T_9 = 6$, using the temperature and density historical data of the first test particle of jet (injected at the first stage of explosion) in model A-2 (history A), and the changed entropy data (twice (history B) or treble (history C) the density at the same temperature). Y_e and entropy of jet materials can change on when it is ejected. So here we consider the conbination of the jets with different values of these parameters.

Table 1. Models used in this study.

Models	progenitor($M_\odot$)	$M_{\rm BH0}(M_\odot)$	$\theta_{\rm jet}{}^\circ$	ϵ	μ	$F_{\rm thermal}$	$v_{\rm jet}$(c)
A-1	1000	100	15	0.01	0.1	0.01	0.45
A-2	1000	100	15	0.005	0.05	0.01	0.45
A-3	1000	100	15	0.002	0.02	0.01	0.45
A-4	1000	100	30	0.01	0.1	0.01	0.45
A-5	1000	50	15	0.005	0.05	0.01	0.45
A-6	1000	200	15	0.01	0.1	0.01	0.45
A-7	500	50	15	0.01	0.1	0.01	0.45
B-1	1000	100	15	0.01	0.02	0.9	0.32
B-2	1000	100	15	0.005	0.01	0.9	0.32
B-3	1000	100	15	0.01	0.005	0.95	0.45
B-4	1000	100	15	0.005	0.0025	0.95	0.45

4. Results of Hydrodynamics

4.1. *Explosion Energy and Ejected Mass*

In table 2, we summarize the total explosion energy, final black hole mass, and mass of the jet for each model. Total explosion energy is the order of 10^{54}erg for most cases.

There are several models in which explosion ends up as 'failure'. Figure 3 shows the models in which explosion occurs or not, depending on the two parameters $\theta_{\rm jet}$ and ϵ. One can see that the minimum ϵ needed for the successful explosion becomes higher if $\theta_{\rm jet}$ is larger.

The final black hole mass and ejected mass are also important. For the $1000M_\odot$ models, these values are $500 \pm 50M_\odot$ for most cases.

5. Explosive Nucleosynthesis

Figures 4 and 5 show the distribution of elements after explosive nucleosynthesis for models A-1, B-3. In each figure, the left panel shows Fe-group

Table 2. Explosion energy E, final black hole mass $M_{\rm BH}$, ejected mass excluding jet material $M_{\rm Ej0}$, mass of jet $M_{\rm jet}$, and total ejected mass $M_{\rm Ej}$ for the models in table 1.

Models	E (erg)	$M_{\rm BH}(M_\odot)$	$M_{\rm Ej0}(M_\odot)$	$M_{\rm jet}(M_\odot)$	$M_{\rm Ej}(M_\odot)$
A-1	1.2×10^{55}	4.9×10^2	4.7×10^2	43	5.1×10^2
A-2	4.0×10^{54}	5.3×10^2	4.5×10^2	23	4.7×10^2
A-3	5.2×10^{53}	5.6×10^2	4.3×10^2	9.5	4.4×10^2
A-4	2.7×10^{54}	4.5×10^2	5.1×10^2	39	5.5×10^2
A-5	3.0×10^{54}	5.1×10^2	4.5×10^2	45	4.9×10^2
A-6	8.2×10^{54}	5.1×10^2	4.6×10^2	34	4.9×10^2
A-7	6.1×10^{54}	2.4×10^2	2.4×10^2	21	2.6×10^2
B-1	6.4×10^{54}	4.6×10^2	5.3×10^2	7.4	5.4×10^2
B-2	1.8×10^{54}	4.7×10^2	5.3×10^2	3.7	5.3×10^2
B-3	7.2×10^{54}	4.7×10^2	5.3×10^2	1.9	5.3×10^2
B-4	1.9×10^{54}	4.8×10^2	5.2×10^2	0.95	5.2×10^2

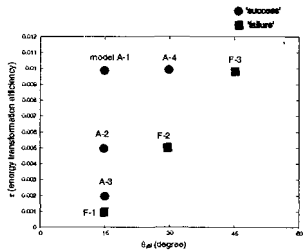

Figure 3. Models in which explosion occurs (filled circles) or not (filled squares), depending on two parameters $\theta_{\rm jet}$ and ϵ for $1000M_\odot$ models. The other parameters are set at $\mu = 10\epsilon$, $M_{\rm BH0} = 100M_\odot$, $f = 0.01$.

elements for the polar direction. The middle panel shows α - elements for the polar direction, the right shows α - elements at $\theta = 15^o$. In each model, complete silicon burning region shows strong α-rich freezeout. The left panel (polar direction) in each figure shows that ^{56}Ni is synthesized dominantly up to $400M_\odot$ from the center. Compared with figure 1, one can see that oxygen is consumed in the region of 350 - 400 $M_\odot$.

For the direction $\theta = 15^o$, silicon and oxygen layers considerably accretes for the model A-1. On the other hand, in model B-3, complete silicon burning region still remains for $\theta = 15^o$. This is because the shock is diffused to the equatrial directions for the model B-3 more than for the model A-1.

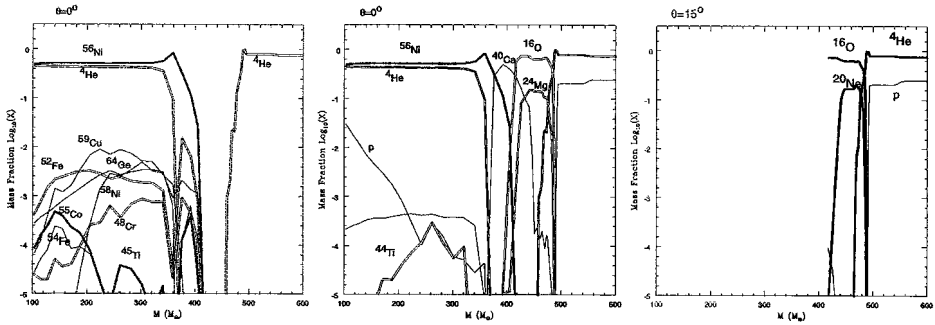

Figure 4. Destributions of elements: Fe-group elements for $\theta = 0^\circ$ (left), α-elements for $\theta = 0^\circ$ (middle), α-elements for $\theta = 15^\circ$ (right), for the model A-1.

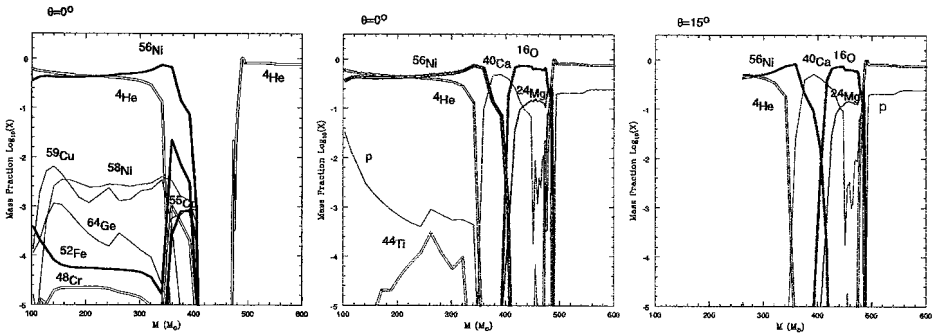

Figure 5. Same as figure 4, but for the model B-3.

6. Integrated Abundance Patterns and Comparison with Observation

Figure 6 shows the total abundance patterns for several models, compared with the observational data in M82 and intracluster matter (ICM). Their results are that (1) the ratio O/Fe is smaller than the solar value, (2) Ne/Fe is about the solar value, and (3) the intermediate-mass α - elements such as Mg, Si, S are oversolar abundance, that is, [Mg/Fe], [Si/Fe], [S/Fe] ~ 0.5.For the ICM gas (the bars), undersolar [O/Fe] and slightly oversolar [Si/Fe] tendencies are also reported. These data are not explained by a standard type II SN or pair-instability SN nucleosynthesis models.

The results of our nucleosynthesis calculation are summarized as follows. For case A, all models result in very underabundant values of $[\alpha/\mathrm{Fe}] \lesssim -1$

because the masses ^{56}Ni synthesized in the jet matter are much larger than those synthesized in the matter which does not accrete. On the other hand, in case B models we obtain the abundance patterns close to the observations of M82, that is, underabundance of [O/Fe], [Ne/Fe] and the oversolar values of [Mg/Fe], [Si/Fe], [S/Fe].

We also compare the yields of case B models with extremely metal-poor (EMP) stars in Galactic halo. It has been reported that [O/Fe] is generally oversolar for EMP stars, but there is little data of [O/Fe] at [Fe/H] $\lesssim$ -3 and the uncertainty is too large to make conclusive statemant. On the other hand, [Mg/Fe] in the EMP stars is oversolar for a wide range of metallicity, which is consistent with our very-massive star models. So whether metal-free very-massive stars could contribute to the enrichment at [Fe/H] < -3, we need more accurate observational data of [O/Fe].

For iron-peak elements, the main feature of the yields of very massive stars is that [Cr/Fe] and [Mn/Fe] are small while [Co/Fe] and [Zn/Fe] are large. This is consistent with the observed ratios in the extremely metal-poor stars.

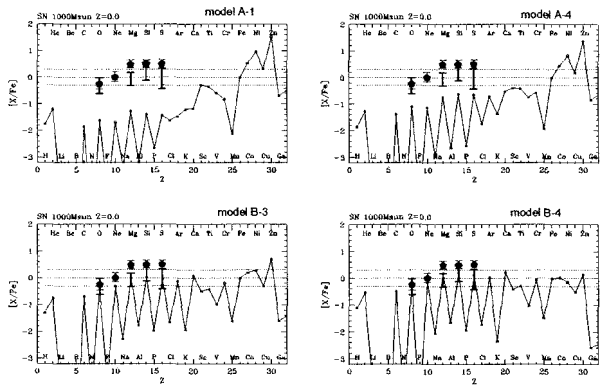

Figure 6. Total abundance patterns including jet contribution.

7. Conclusions

We calculate the evolution of population III very massive stars of $500M_{\odot}$ and $1000M_{\odot}$ and their explosion and nucleosynthesis for the bipolar jet models. Our findings are summarized as follows:

[1] The region which experiences silicon burning to produce iron-peak

elements is more than 20 % of the total masses, much larger than those of ordinary massive stars such as the $25M_{\odot}$ star model. In the metal-free $25M_{\odot}$ star model, this fraction is less than 10 %.

[2] Black hole masses are $\sim 500M_{\odot}$ for the $1000M_{\odot}$ star models. Such a mass of black hole is similar to those of intermediate-mass black holes (e.g. $\sim 700M_{\odot}$) recently found in M82. It is possible that very-massive stars over $300M_{\odot}$ could be the progenitors of such black holes.

[3] Our results of nucleosynthesis have similar patterns of [α/Fe] to the abundance pattern of the hot gas in M82 if the contribution of the jet is small (case B). For case B, resulting small [O/Fe], [Ne/Fe] and large [Mg/Fe], [Si/Fe], [S/Fe] are consistent with the observational data of M82.

[4] For iron-peak elements, the main feature of the yields of very-massive stars is that [Cr/Fe] and [Mn/Fe] are small while [Co/Fe] and [Zn/Fe] are large. This is consistent with the observed ratios in the extremely metal-poor stars. The oversolar ratios of [Mg/Fe] and [Si/Fe] are consistent with the extremely metal-poor stars. We need more data of [O/Fe] in extremely metal-poor stars to see whether very-massive stars can contribute to the early Galactic chemical evolution.

References

1. K. Omukai and F. Palla, *ApJ* **546**, 635 (2003).
2. H. Matsumoto et al., *ApJ* **547**, L25 (2001).
3. M. Shibata and S. L. Shapiro *ApJ* **572**, L39 (2002).
4. A. M. Khokhlov et al., *ApJ* **524**, L107 (1999).
5. A. I. MacFadyen et al., *ApJ* **550**, 410 (2001).
6. K. Maeda and K. Nomoto, *ApJ* **598**, 1163 (2003).
7. R.-P. Kudritzki, in *The First Stars* eds. A, Weiss, T. G. Abel, and V. Hill (Berlin:Springer), 127 (2000)
8. H. Umeda and K. Nomoto, *ApJ* **565**, 385 (2002).
9. H. Umeda et al. in *The First Stars* eds. A. Weiss., T. G. Abel., V. Hill (Springer)
10. G. Rakavy et al., *ApJ* **150**, 131 (1967).
11. J. R. Bond et al., *ApJ* **280**, 825 (1984).
12. W. Glatzel et al., *A&A* **149**, 413 (1985).
13. S. E. Woosley, in *Nucleosynthesis and Chemical Evolution* (1986) eds. B. Hauck, A. Maeder, and G. Meynet (Switzerland:Geneva Obs.), 1
14. H. Umeda et al., *astro-ph* 9912248.
15. H. Umeda and K. Nomoto, *Nature* **422**, 6934, 871 (2003)
16. W. R. Hix and F.-K. Thielemann, *ApJ* **460**, 869 (1996).
17. L. Origlia et al., *astro-ph* 0401361 (2004).
18. W. H. Baumgartner et al., *ApJ* submitted (2004).
19. I. R. Peterson et al., *ApJ* **590**, 207 (2003).

THE TROJAN HORSE METHOD IN NUCLEAR ASTROPHYSICS

C. SPITALERI, A. MUSUMARRA, M.G. PELLEGRITI, S. ROMANO AND A. TUMINO

Dipartimento di Metodologie Fisiche e Chimiche per l'Ingegneria - Università di Catania and Laboratori Nazionali del Sud-INFN, Catania, Italy

P. FIGUERA AND R.G. PIZZONE

Laboratori Nazionali del Sud-INFN, Catania, Italy

S. CHERUBINI

Ruhr-Universität, Bochum, Germany and Laboratori Nazionali del Sud-INFN, Catania, Italy

The basic features of the Trojan Horse Method are discussed together with a review of recent applications aimed to extract the bare $S_b(E)$ astrophysical factor for several two body processes. In this framework information on electron screening potential U_e was obtained from comparison with the direct experiments of fusion reactions.

1. INTRODUCTION

The main problem for charged particle induced reactions at astrophysical energies is the presence of the Coulomb barrier E_{CB} ([1,2]), usually of the order of MeV, much higher than the Gamow energy E_G, thus implying the reaction taking place via tunnel effect with an exponential decrease of the cross section , $\sigma(E) \sim exp(-2\pi\eta)$ (where η is the Sommerfeld parameter). Owing to the strong Coulomb suppression, the behavior of the cross section at astrophysical energies is in general extrapolated from the higher energies by using the definition of the smoother astrophysical factor S(E):

$$S(E) = E\sigma(E)exp(2\pi\eta) \tag{1}$$

where the inverse of the Gamow factor $exp(2\pi\eta)$ removes the dominant energy dependence of $\sigma(E)$.

Although the S(E)-factor allows for an easier extrapolation, large uncertainties on $\sigma(E_G)$ may be introduced due, for instance, to the presence of unexpected resonances. In order to avoid the extrapolation procedure, a number of solutions were proposed in direct measurements for enhancing the signal-to-noise ratio at astrophysical energies ([3]).

However for nuclear reactions studied in laboratory, the electron clouds surrounding the interacting nuclei lead to a screened cross section $\sigma_s(E)$ larger than the "bare" nucleus one, $\sigma_b(E)$ ([3,4,5,6,7,8,9]). This effect is usually described by introducing an enhancement factor f_{lab}(E) defined by the relation ([4])

$$f_{lab}(E) = \sigma_s(E)/\sigma_b(E) \approx exp(\pi\eta U_e/E) \tag{2}$$

where U_e is the electron screening potential energy in the laboratory which is different from the one present in the stellar environment. In order to extract the effective cross section for stellar plasma $\sigma_{pl}(E)$, the bare nucleus cross section $\sigma_b(E)$ must be known and multiplied for the stellar electron screening enhancement factor f_{pl}, estimated within the framework of the Debye-Hückel theory.

Then, although it could be possible to measure cross sections in the Gamow energy range, the bare cross section σ_b is extracted by extrapolating the direct data behavior at higher energies where a negligible electron screening contribution is expected.

Experimental studies of reactions involving light nuclides ([8]) have shown that the expected enhancement of the cross section at low energies was in all cases significantly larger than what could be accounted for by available atomic-physics models. This aspect deserves special attention because one may have a chance to predict the effects of electron screening in an astrophysical plasma only if it is preliminarily understood under laboratory conditions.

In order to overcome the experimental difficulties, arising from the small cross-sections involved and from the presence of the electron screening, additional information related to these processes is required.

In particular new methods to obtain independent measurements of the electron screening potential U_e, when ultra-low energy measurements are available, are needed.

In this context a number of indirect methods, e.g. the Coulomb dissociation ([10,11])(to study radiative capture reactions), the Asymptotic Normalization Coefficient ([12,13,14,15]) (an useful method for extracting direct capture cross sections using peripheral transfer reactions), and the Trojan-

horse method (THM) ([16,17,18,19,20,21,22,23,24,25,26,27,28,29,30,31,32]) (to extract charged particle induced reaction cross sections using the quasi-free mechanism) were developed. Some of them make use of direct reaction mechanisms, such as transfer processes (stripping and pick-up) and quasi-free reactions (knock-out reactions). In particular, the THM is a powerful tool which selects the quasi-free (QF) contribution of an appropriate three-body reaction performed at energies well above the Coulomb barrier to extract a charged particle two-body cross section at astrophysical energies free of Coulomb suppression and electron screening effects (see Table I).

2. THE PRINCIPLE OF THE METHOD

2.1. *Quasi-Free mechanism*

The quasi-free $A + a \rightarrow c + C + S$ reaction, a having a strong $x \oplus S$ cluster structure, can be described by a Pseudo-Feynmam diagram (Fig.1), where only the first term of the Feynman series is retained. The upper pole in the figure describes the virtual break-up of the target nucleus a into the clusters x and S; S is then considered to be spectator to the $A + x \rightarrow c + C$ reaction which takes place in the lower pole.

This description is called Impulse Approximation (IA)[33].

In Plane Wave Impulse Approximation (PWIA) the cross section of the three body reaction can be factorized into two terms corresponding to the two poles of Fig.1 ([34,35]) and it is given by:

$$\frac{d^3\sigma}{dE_c d\Omega_c d\Omega_C} \propto KF \left(\frac{d\sigma}{d\Omega}_{cm}\right)^{off} \cdot |\Phi(\vec{p}_s)|^2 \tag{3}$$

where:

- $[(d\sigma/d\Omega)_{cm}]^{off}$ is the off-energy-shell differential cross section for the two body A(x,c)C reaction at the center of mass energy E_{cm} given in post collision prescription by:

$$E_{cm} = E_{c-C} - Q_{2b} \tag{4}$$

  where Q_{2b} is the two body Q-value of the $A + x \rightarrow c + C$ reaction and E_{c-C} is the relative energy between the outgoing particles c and C;

- KF is a kinematical factor containing the final state phase-space factor and it is a function of the masses, momenta and angles of

the outgoing particles:

$$KF = \frac{\mu_{Aa} m_c}{(2\pi)^5 \hbar^7} \frac{p_C p_c^3}{p_{Aa}} \left[\left(\frac{\vec{p}_{Bx}}{\mu_{Bx}} - \frac{\vec{p}_{Cc}}{m_c} \right) \cdot \frac{\vec{p}_c}{p_c} \right]^{-1} \tag{5}$$

- $\Phi(\vec{p}_s)$ is the Fourier transform of the radial wave function $\chi(\vec{r})$ for the $x - S$ inter-cluster motion, usually described in terms of Hänkel, Eckart and Hultheń functions depending on the $x - S$ system properties. Besides the PWIA approach the Distorted Wave Impulse Approximation (DWIA) treatment was sometimes applied in the analysis of QF reactions and QF scattering experimental data.

However in some cases such as the ^{11}B(d,α_o^{8}Be)n reaction ([26]), the validity conditions of the IA appear to be fulfilled. Indeed in that experiment the quite high beam energy for ^{11}B of 27 *MeV* (740 MeV/c in momentum) corresponds to an associated de Broglie wavelength of 0.26 fm, much smaller than the deuteron effective radius of 4.5 fm.

We stress that in view of the various approximations involved in the THM and in particular of the assumption that off-energy-shell effects are negligible, one cannot extract the absolute value of the two-body cross section. However, the absolute value can be extracted through normalization to the direct data available at energies above the Coulomb barrier. Thanks to this, since we select the region of low momentum p_s for the spectator (in general $p_s < 40$ MeV/c), where PWIA and DWIA wave functions have very similar shapes ([36]), the PWIA approach was used for the analysis of the experimental results, in some cases where it is possible. Before going on with the discussion of some experimental results, details concerning the validity tests of the IA approach are given. If $|\Phi(\vec{p}_s)|^2$ is known and KF is calculated, it is possible to derive $[(d\sigma/d\Omega)_{cm}]^{exp}$ from a measurement of $d^3\sigma/dE_c d\Omega_c d\Omega_C$ by using Eq. 3.

$$\left(\frac{d\sigma}{d\Omega} \right) \propto \left[\frac{d^3\sigma}{dE_c d\Omega_c d\Omega_C} \right] \cdot [KF|\Phi(\vec{p}_s)|^2]^{-1} \tag{6}$$

2.2. *From Quasi Free Reactions to the Trojan Horse Method*

The application of the quasi-free mechanism to the study of reactions at astrophysically relevant energies ([27,37]), derives from previous researches on the quasi-free mechanism at very low energies

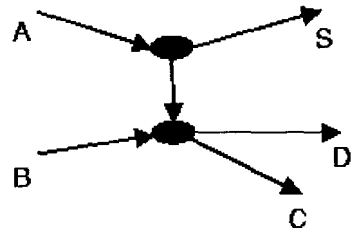

Figure 1. Pole diagram for quasi-free reaction A(B,cd)S. The first pole virtual decay of nucleus $A \rightarrow x + S$ second pole to the virtual reaction $B + x \rightarrow C + c$. In this picture the A nucleus must present a strong cluster structure: A = x + S. The x cluster interacts with the nucleus B $B + x \rightarrow C + c$. The S cluster acts as a spectator (it doesn't take part to the reaction).

([38,39,40,41,42,43,44,45,46,47,48,49]). In particular it is an extension, of the indirect excitation function measurements for the two body cross section of the ^{7}Li(p,α)α and ^{6}Li(p,α)^{3}He reactions([38,39]) at low energies.

This phenomenological approach derives from the theory of the *THM* proposed by Baur ([16]), whose basic idea is to extract an $A+x \rightarrow C+c$ two-body reaction cross section, at low energies from a suitable $A+a \rightarrow C+c+s$ three-body reaction.

Under appropriate kinematical conditions, the three-body reaction is considered as the decay "of the Trojan Horse" a into the clusters x and S with a subsequent interaction of A with x inside the nuclear region, whereby the nucleus S can be considered as a spectator during the reaction.

If the bombarding energy E_A is chosen high enough to overcome the Coulomb barrier E_C in the entrance channel of the three-body reaction, both Coulomb Barrier and electron screening effects are negligible.

Thus the two-body reaction can be induced at very low (even vanishing) relative energy. Moreover the role of the cutoff in the momentum distribution consists in fixing the accessible astrophysical energy region([25]), as given by:

$$\Delta E_{qf} = E_{Ax} - B_{xs} \pm E_{xs} \tag{7}$$

where E_{Ax} is the beam energy in the center-of-mass of the two-body A-x system, B_{xs} represents the binding energy for the x-b system and E_{xs}

describes their inter-cluster motion within the chosen cutoff in momentum.

In this way it is possible to extract the two-body cross section from Eq.(6) after inserting the appropriate penetration function P_l in order to account for the penetrability effects affecting the direct data below the Coulomb barrier ([17,18]) . The complete formula is given by:

$$\left(\frac{d\sigma}{d\Omega}\right) \propto \left[\frac{d^3\sigma}{dE_c d\Omega_c d\Omega_C}\right] \cdot [KF|\Phi(\vec{p}_s)|^2]^{-1} \cdot P_l \tag{8}$$

When the projectile energy is not very high and off-energy-shell effects are not negligible, a more sophisticated approach based on a Modified Plane Wave Born Approximation ($MPWBA$) ([31,32]), turned out to be useful since Coulomb and off-energy-shell distortions in the two body entrance channel are included ([21,22,23,24,25]).

In this approximation the differential two-body cross-section of Eq.3 is expressed by:

$$\left(\frac{d\sigma}{d\Omega}\right) = \sum_l C_l P_l \left(\frac{d\sigma_l}{d\Omega}\right) \tag{9}$$

where $d\sigma_l/d\Omega$ represents the on-shell two body cross section in partial wave l, C_l is a constant and P_l is the penetrability factor given in terms of regular and irregular Coulomb wave functions ([21,24,25]), which compensates for the Coulomb suppression of $d\sigma_l/d\Omega$ at low energies.

The MPWBA expression of the cross section ([31,32]) strongly resembles the factorization resulting from the PWIA, with the further correction for the Coulomb penetration. As already mentioned, the THM data are not affected by electron screening effects. Therefore, once the behavior of the absolute bare $S_b(E)$ factor from the two-body cross-section is extracted, a model-independent estimate of the screening potential U_e can be obtained from comparison with the direct screened S(E)−factor. Then, after the normalization of indirect data, the comparison between the two data sets can be performed down to the low energy region.

3. VALIDITY TEST FOR THE POLE APPROXIMATION

In order to select the region where the QF mechanism is dominant, coincidence events with spectator momenta close to zero were considered in the analysis.

Monte Carlo calculations were then performed to extract the ($KF \cdot |\Phi(\vec{p}_s)|^2$) product.

The momentum distribution entering the calculation was that given in [21,27]. The geometrical efficiency of the experimental setup as well as the detection thresholds of the PSD's were taken into account.

Following the PWIA prescription of eq.6, the two-body cross-section $d\sigma/d\Omega_{cm}$ was derived dividing the selected three-body coincidence yield by the result of the Monte Carlo calculation.

As already mentioned, since this approach provides the off-energy-shell two-body cross section, it is necessary to perform the appropriate validity tests for the adopted IA.

In order to test the basic assumptions of the polar description in the QF reaction it was suggested ([53,54,55]) that:
-the behavior of the angular distribution $\sigma(\theta)_{THM}$ indirectly extracted must be the same of that of the direct $\sigma(\theta)_{DIR}$ angular distribution;
-and/or the behavior of the excitation function $\sigma(E)_{THM}$ must be the same of the direct one.

It has to be stressed, however, that a good agreement of the two trends (direct and indirect cross sections) is a necessary condition (test of applicability of the approximation) to be fulfilled before extracting the astrophysical S(E) factor by means of the THM.

4. RESULTS

In the cases considered hereby and reported in Table 1 together with the related references, the behavior of the indirectly extracted excitation function, after normalization, is similar to the direct one in the whole investigated range except below 100-200 keV were electron screening effect is no longer negligible in the direct data.

The astrophysical S(E) factors and electron screening potential U_e, extracted via the THM for the $^7Li + p \rightarrow \alpha + \alpha$ (Fig.2), $^6Li + d \rightarrow \alpha + \alpha$ (Fig.3), $^6Li + p \rightarrow \alpha + ^3He$ (Fig.4), $^{11}B + p \rightarrow \alpha_o + ^8Be$ (Fig.5) and $^3He + d \rightarrow \alpha + p$ (Fig.6) reactions in the astrophysical energy range, are shown in Fig.2-6 together with direct data (Table 2). The quoted errors include statistical as well as systematic uncertainties (of about 10-15%) due to the normalization procedure (for details see references reported in Table 1).

Table 1. Two-body reactions studied via Trojan Horse Method.

	Direct reaction	Indirect reaction	E_{inc} (MeV)	Ref.
[1]	$^7Li + p \rightarrow \alpha + \alpha$	$^7Li + d \rightarrow \alpha + \alpha + n$	19-22	[19,20,22,23]
[2]	$^6Li + d \rightarrow \alpha + \alpha$	$^6Li + {}^6Li \rightarrow \alpha + \alpha + \alpha$	5.9	[18,24,25]
[3]	$^6Li + p \rightarrow {}^3He + \alpha$	$^6Li + d \rightarrow {}^3He + \alpha + n$	14,25	[26,27]
[4]	$^{11}B + p \rightarrow {}^8Be + \alpha$	$^{11}B + d \rightarrow {}^8Be + \alpha + n$	27	[28]
[5]	$d + {}^3He \rightarrow p + \alpha$	$^6Li + {}^3He \rightarrow p + \alpha + \alpha$	5-6	[30]
[6]	$p + {}^9Be \rightarrow \alpha + {}^6Li$	$d + {}^9Be \rightarrow \alpha + {}^6Li + n$	22	[31]
[7]	$d + d \rightarrow t + p$	$^6Li + d \rightarrow t + p + \alpha$	14	[32]
[8]	$\alpha + {}^{12}C \rightarrow \alpha + {}^{12}C$	$^6Li + {}^{12}C \rightarrow \alpha + {}^{12}C + d$	20	[21]

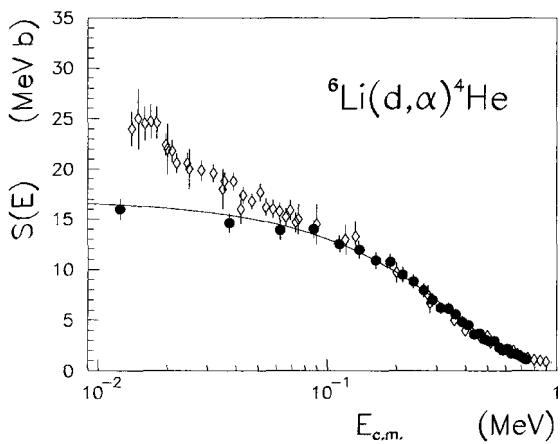

Figure 2. ^{6}**Li+ d** $\rightarrow \alpha + \alpha$. Astrophysical S(E)-factor for the reaction ^{6}Li + ^{6}Li $\rightarrow \alpha + \alpha + \alpha$ as obtained by THM (full dots) ([21]) and direct measurements (open dots) ([6]). The solid line represents a polynomial fit to the indirect S(E).

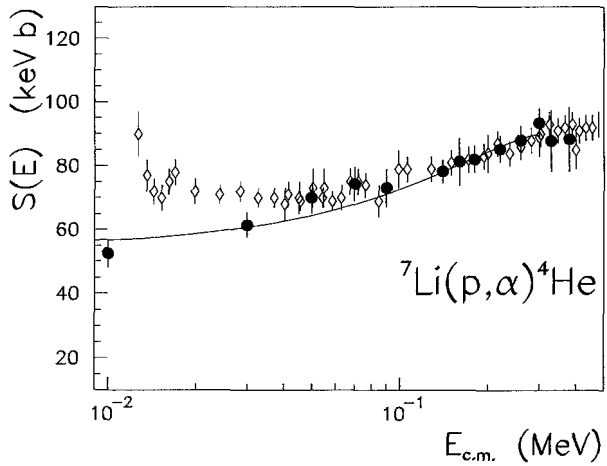

Figure 3. ^{7}Li + p$\rightarrow \alpha + \alpha$. The S(E)-factor extracted with the Trojan Horse method (full dots)([23]) is compared with the direct data from Ref([6])(open dots); a fit to the indirect data with a second-order polynomial is also shown as a solid line.

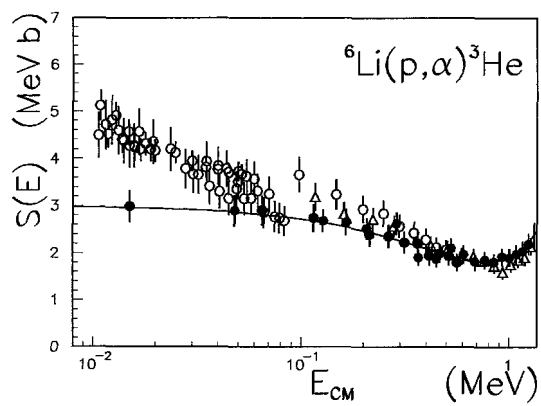

Figure 4. Astrophysical S(E)-factor for the reaction ^{6}Li + d$\rightarrow \alpha + {}^3$He + n as obtained by THM (full dots) ([25]) compared with the direct one (open dots) ([6]). The solid line represents a second order polynomial fit to the indirect data between 0.04 and 1 MeV.

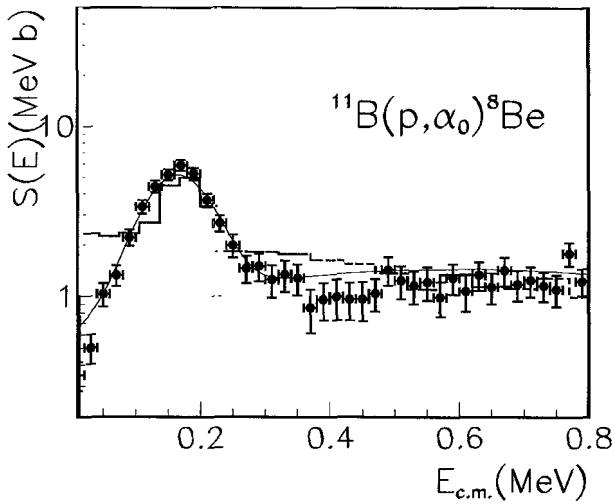

Figure 5. ^{11}B + p$\rightarrow$ α_o +^{8} *Be*. Astrophysical S(E)-factor for the reaction ^{11}B + p$\rightarrow$ α_o+^{8} *Be* as obtained by THM (full dots) ([26]) and direct measurements (open dots) ([56]). The dashed line represents a polynomial fit to the indirect S(E).

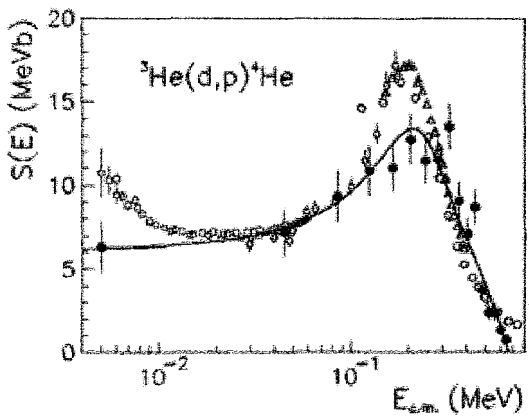

Figure 6. ^{3}**He** +**d** $\rightarrow$ $\alpha + p$. Astrophysical S(E)-factor (right) for the reaction ^{3}He +d $\rightarrow$ $\alpha + p$ as obtained by THM (full dots) ([28]) and direct measurements (open dots). The dashed line represents a polynomial fit to the indirect S(E).

Table 2. Astrophysical factor S(0) and electron screening potential U_e.

	Reaction	$U_e^{Adiab.}$ (eV)	U_e^{Dir} (eV)	U_e^{THM} (eV)	$S(0)^{Dir}$ (MeVb)	$S(0)^{THM}$ (MeVb)
[1]	$^7Li + p \rightarrow \alpha + \alpha$	186	300±160	330±40	0.059	0.055±0.003
[2]	$^6Li + d \rightarrow \alpha + \alpha$	186	330±120	340±50	17.4	16.9±0.5
[3]	$^6Li + p \rightarrow ^3He + \alpha$	186	440±150	450±100	2.86	3.0±0.3
[4]	$^{11}B + p \rightarrow ^8Be + \alpha$	304	430±80	—	2.1	0.31±0.05
[5]	$d + ^3He \rightarrow p + \alpha$	115	219±7	180±40	6.51	6.08±1.42

5. CONCLUSIONS

The present paper reports the basic features of the THM together with a general review of recent applications to several astrophysically relevant reactions. In particular these results show the possibility to extract the bare nucleus two-body cross section via the THM. The THM has proven to be a powerful tool for measuring nuclear reaction cross sections at sub-Coulomb energies.

However, a lot remains to do in the future to achieve reliable information for many key reactions and processes, especially for the electron screening effects in fusion reactions where new theoretical developments are strongly needed to meet progress in the application field.

References

1. C. Rolfs, W.S. Rodney, Cauldrons in the cosmos, University of Chicago Press, Chicago (1988)
2. C. Rolfs, Prog. Part. Nucl. Phys., **153** , 23 (2001)
3. F. Streider et al., Naturwissenschaften **88**, 461, (2001)
4. H.J. Assenbaum et al., Z. Phys. **A327**, 461 (1987)
5. S. Engstler et al., Phys. Lett.**B 202** (1988) 179
6. S. Engstler et al., Phys. Lett.**B 279**(1992)20
7. Luna Collaboration, Nucl. Phys., **A706**,203 (2002)
8. R. Bonetti et al., Phys. Rev.Lett., **82**, 5205 (1999)
9. M. Junker et al., Phys. Rev., C **57** ,2700 (1998)
10. G. Baur and H. Rebel, J. Phys. G **20**, 1 (1994) and references therein
11. G. Baur and H. Rebel, Annu. Rev. Nucl. Part. Sci. **46**, 321 (1996)
12. X.D. Tang et al., Phys. Rev. C **67**, art.n.015804 (2003)

13. A.M. Mukhamedzhanov et al., Phys. Rev. C **56**, 1302 (1997)
14. A.M. Mukhamedzhanov et al. Phys. Rev. C**63**, art.n.024612 (2001)
15. C.A. Gagliardi, et al. Eur. Phys. J A **13**, 227 (2002)
16. G. Baur, Phys. Lett. B **178**, 135 (1986)
17. S. Cherubini et al. Ap. J. **457**, 855 (1996)
18. C. Spitaleri et al., Phys. Rev. C **60**, 055802 (1999)
19. C. Spitaleri et al., Eur. Phys. J **A7**, 181 (2000)
20. A. Aliotta et al. Eur.Phys. J., A9, 435(2000)
21. M. Lattuada et al. Ap.J. **562**, 1076 (2001)
22. C. Spitaleri et al. Phys. Rev. C **63**, 005801 (2001)
23. A. Musumarra et al. Phys. Rev., **C64** , 068801 (2001)
24. A. Tumino et al. Nucl.Phys. **A718** 499 (2003)
25. A. Tumino et al. Phys. Rev. C**67), 065803 (2003)**.
26. C. Spitaleri et al., Phys. Rev. C (2004) in press
27. C. Spitaleri et al. Nucl. Phys. A **719**,99 (2003)
28. M. La Cognata et al., Proc. to Cluster 2003 conference, Nara, Japan
29. R.G. Pizzone et al., Proc. to Cluster 2003 conference, Nara, Japan
30. A. Rinollo et al. Report INFN-LNS, 2002
31. S. Typel and. H. Wolter, Few Body Syst.**29**, 7 (2000)
32. S. Typel and G. Baur, Ann. Phys. **305**, 228 (2003)
33. G.F. Chew, Phys. Rev. C **80**, 196(1950)
34. U.G.Neudatchin, Y.F.Smirnov, At. Energy Rev., **3** , 157 (1965)
35. G. Jacob et al., Rev. Mod. Phys. **38**, 121 (1966)
36. N.S. Chant , P.G. Roos, Phys. Rev. C **15**, 57 (1977) and referencences therein
37. C. Spitaleri, Problems of Fundamental Modern Physics II, World Scientific,p. 21- 35, 1990
38. M. Zadro et al., Phys. Rev. C **40**, 181 (1989)
39. G. Calvi et al., Phys. Rev. C **41**, 1848 (1990)
40. M.Furic et al., Phys. Lett. **39 B**, 629 (1972)
41. Dj. Miljanić et al., Phys. Lett. **50 B**, 330 (1974)
42. J. Kasagi et al., Nucl. Phys. **A239**, 233 (1975)
43. I. Slaus et al., Nucl. Phys. **A286**, 67 (1977)
44. N. Arena et al., Nuovo Cimento **45**, 405 (1978)
45. M. Lattuada et al., Nuovo Cimento **69**, 1 (1982)
46. M. Zadro et al., Nucl. Phys. **A474**, 373 (1987)
47. M. Lattuada et al., Z. Phys. A-Atomic Nuclei **330**,183 (1986)
48. S. Blagus et al., Z. Phys. A-Atomic Nuclei **337**, 297 (1990)
49. V. Soic, et al., Eur. Phys. J. **A 3**, 303 (1998)
50. S.B. Treiman and C.N. Yang, Phys. Lett.**8**, 140 (1962) 140
51. I.S. Shapiro et al., **61** , 353 (1965)
52. V.M. Kolybasov et al. Nucl. Phys. **14**, 330 (1972)
53. A. Guichard et al., Phys. Rev., C **4**, 493 (1986)
54. M. Jain et al., Nucl.Phys. **A153**, 49, (1970)
55. M. Chevalier et al., Nucl. Phys., **A216**, 519 (1973)
56. H.W. Becker et al., Z. Phys. A-Atomic Nuclei, **327**, 341 (1987)
57. F.C. Barker Nucl. Phys. **A707**, 277 (2002)

THE s-PROCESS NUCLEOSYNTHESIS IN MASSIVE METAL-POOR STARS*

NOBUYUKI IWAMOTO

Department of Astronomy, University of Tokyo, Hongo, Bunkyo-ku, Tokyo 113-0033, JAPAN

E-mail: niwamoto@astron.s.u-tokyo.ac.jp

We present the s-process nucleosynthesis in massive stars with a wide range of metallicity, using the recent sets of reaction rates and stellar input physics. The decreasing metallicity makes poisoning effects of primary ^{16}O larger at the late phase of core He burning, at which the s-process occurs actively in solar metallicity stars, and prevents the synthesis of heavy elements from being efficient. However, we find that the s-process proceeds very efficiently via neutron source reaction of ^{13}C(α,n)^{16}O at the end of core H burning phase when the metallicity decreases below $Z \sim 10^{-8}$. These massive, extremely low metallicity stars may have an important contribution of light s-elements to observed extremely metal-poor stars.

1. Introduction

The slow neutron-capture process (s-process) is one of the processes to produce elements heavier than iron. This heavy-element synthesis occurs under low neutron density conditions where neutron-capture timescales are longer than typical β-decay lifetimes of newly synthesized unstable nuclei. Accordingly, the s-process proceeds along the β-stability line. The main sites of the s-process are considered to be in He shell burning phase of low-mass, thermally pulsing asymptotic giant branch (AGB) stars and in core He burning and C shell burning phases of massive stars.

The AGB stars contribute to the production of heavy elements with mass number $A \simeq$ 90-209.[1-5] The $^{13}C(\alpha,n)^{16}O$ reaction is the main neutron source reaction and is activated efficiently above $T_9 \simeq 0.09$, where T_9 is the temperature in units of 10^9 K.[1,2] The seed nuclei for the s-process are considered to be iron group nuclei, whose abundances de-

*This work is supported by the fellowship of the Japan Society for Promotion of Science (JSPS).

crease with decreasing metallicity. However, within a scenario accepted for the s-process nucleosynthesis ^{13}C is produced as primary nuclide via ^{4}He$(2\alpha,\gamma)^{12}$C$(p,\gamma)^{13}$N$(\beta^+\nu)^{13}$C at the top of the helium layer where protons are diffusively injected into ^{4}He and ^{12}C-rich region after the completion of third dredge-up. In other words, the abundance of this isotope has no metallicity dependence. The above two characteristics indicate that the production of heavier nuclei (i.e., Pb and Bi) is favored as metallicity becomes lower. This is because the number of neutrons captured per seed nuclei (equivalently, ^{13}C/seed ratio) increases as metallicity decreases. Recent observations of very metal-poor stars show clear evidence that heavy-s (Ba, La, Ce and Nd) to light-s (Sr, Y and Zr) ratio is high relative to solar[6] and Pb is detected abundantly.[7–11] However, the relatively large spread of [Pb/(Ba,La,Ce)][a] is also observed.[9,10] This might be responsible for reduced efficiency invoked by stellar rotation.[12] Moreover, this scenario suggests that a zero metallicity star may exhibit large enhancements of heavy elements from seed nuclei of much lighter C-Ne elements.[13]

The s-process in massive stars mainly occurs at the late phase of core He burning, during which the central temperature exceeds $T_9 \sim 0.25$. The main neutron source reaction ^{22}Ne$(\alpha$,n$)^{25}$Mg efficiently produces neutrons. The neutron density averaged over convective core is typically $N_n \simeq 10^6$ cm^{-3}. In this site the synthesis of heavy elements is confined to the mass number range $A \simeq$ 60-90.[14–21] Previous investigations have shown that the efficiency of heavy-element production decreases with decreasing metallicity[14,17,20] due to a decreasing abundance of ^{22}Ne and an increasing importance of neutron poisoning effects of the primary ^{16}O produced by ^{12}C$(\alpha,\gamma)^{16}$O. In the C shell burning phase s-process nucleosynthesis takes place under relatively high neutron density conditions ($N_n \sim 10^{11}$ cm^{-3}), and thus may change dramatically in spite of short irradiation timescales. It has been known that nuclei sensitive to neutron density are significantly affected.[17,19] As the metallicity reduces to [Fe/H][b]~ -3, the effects of the s-process in C shell burning is not important due to the almost complete destruction of ^{22}Ne during the central He burning phase.[17]

In this paper, we re-consider the metallicity dependence of the s-process nucleosynthesis over metallicity range wider than investigated before, and follow the s-process from zero-age main sequence through the central H and

[a][A/B]$= \log(N_A/N_B)_{\rm star} - \log(N_A/N_B)_\odot$, where N_A and N_B are the number abundances of elements A and B.

[b]Metallicity [Fe/H] is roughly related with heavy element abundance Z as follows; [Fe/H]$\simeq \log Z/Z_\odot$.

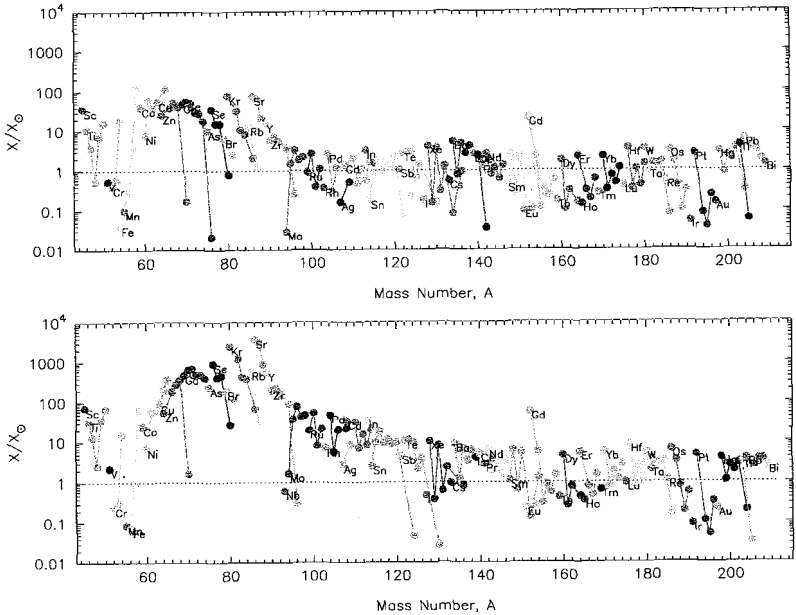

Figure 1. Comparison of overabundances in $25M_{\odot}$, solar metallicity models for different ^{22}Ne(α,n)^{25}Mg rate. Top panel represents the result with the recommended rate of Jaeger et al. Bottom panel shows the result with their rate multiplied by 10.

He burning phases up to the end of central C burning phase.

2. The Models

Models with initial masses of $M = 15$, 25, and $40M_{\odot}$ and various metallicities from $Z = Z_{\odot}(= 0.02)$ to 0 are followed from zero-age main sequence to the end of the central carbon burning phase. The nuclear network includes nuclides from neutron to sulfur in stellar evolution code. We include 564 nuclei in the s-process nucleosynthesis network and take into account many important branches along neutron-capture paths. The charged particle reaction rates are mostly taken from NACRE compilation,[22] but the important reactions relevant to the s-process nucleosynthesis, ^{12}C(α,γ)^{16}O, ^{13}C(α,n)^{16}O and ^{22}Ne(α,n)^{25}Mg, are taken from recent evaluations by Kunz et al.[23], Kubono et al.[24], and Jaeger et al.[25], respectively. We adopt ^{12}C(n,γ)^{13}C and ^{16}O(n,γ)^{17}O rates from Ohsaki et al.[26] and Igashira et al.[27], respectively, and most of the other neutron-capture rates are from

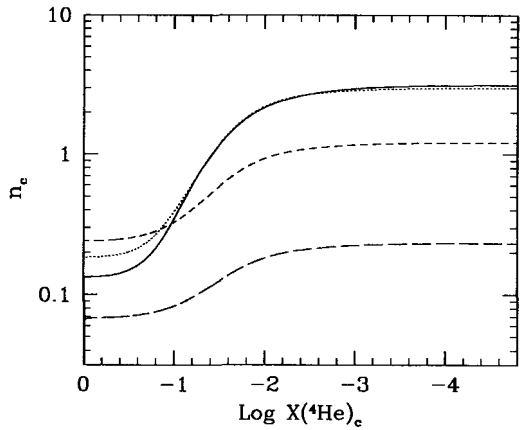

Figure 2. The number of neutrons captured per iron seed nucleus as a function of central He abundance. Solid, dotted, short-dashed, and long-dashed lines represent the results of $25M_\odot$ models with metallicity $Z = 1, 10^{-1}, 10^{-2}$ and $10^{-3}Z_\odot$, respectively.

Bao et al.[28] and REACLIB[29]. Moreover, we include recent experimental and theoretical rates.

The initial composition for elements heavier than He are scaled to the appropriate metallicity from the solar abundance to calculate lower metallicity models. We take into account α-enhancements of [O/Fe]=+0.8 for oxygen and [α/Fe]=+0.4 for other α elements in models with $Z \leq 10^{-3}Z_\odot$.

The condition for convective stability is the Schwarzschild criterion. We treat convective mixing diffusively by adopting diffusion coefficient.[30] The mass loss prescription[31] with metallicity dependence[32] is adopted. Further details of our stellar evolution code are found in Iwamoto et al.[33].

3. Results

3.1. $^{22}Ne(\alpha,n)^{25}Mg$ reaction and the s-process

First, we investigate the influence of different sets of neutron source reaction ^{22}Ne(α,n)^{25}Mg on the s-process nucleosynthesis in Figure 1. These panels in Fig. 1 show results with the rate taken from Jaeger et al.[25] (*top panel*) and the 10 times higher rate[34] (*bottom panel*). As expected from previous investigations,[35,36] solar metallicity models are very sensitive to the variation of this rate. We can see that significant overproduction of nuclei with the mass number of 60-90 is realized due to the efficient production

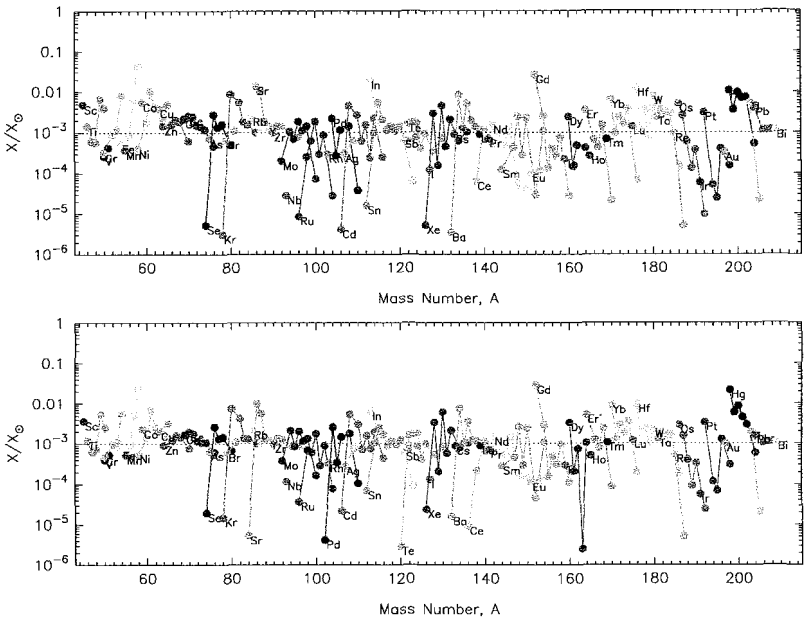

Figure 3. Comparison of overabundances in $Z = 10^{-3} Z_{\odot}$ models with masses of 40 (*top panel*) and $15 M_{\odot}$(*Bottom panel*).

of neutrons at the late phase of central He burning and large amounts of seed nuclei. However, our adopted set of reaction rates shows that the production of A = 60-90 nuclei is significantly suppressed, in comparison with recent detailed calculations.[19] These differences may be responsible for the higher rate of their used ^{22}Ne(α,n)^{25}Mg in the temperature below $T_9 = 0.30$, while differences in stellar input physics are also important. If 10 times higher rate is adopted, large enhancements of light s-elements can be obtained.

In Figure 2 the variations of the number of neutrons captured per iron seed nucleus n_c for $25 M_{\odot}$ models of various metallicities are shown as a function of central He abundance. n_c is defined as

$$n_c = \frac{\sum_{A>56}(A-56)(Y_A - Y_A^{\rm ini})}{Y_{56}^{\rm ini}}, \qquad (1)$$

where Y_A is the number abundance of nuclide with mass number A, and $Y_A^{\rm ini}$ is its initial value. We can see that the large contribution to the production of heavy nuclei is obtained during the late phase of the central

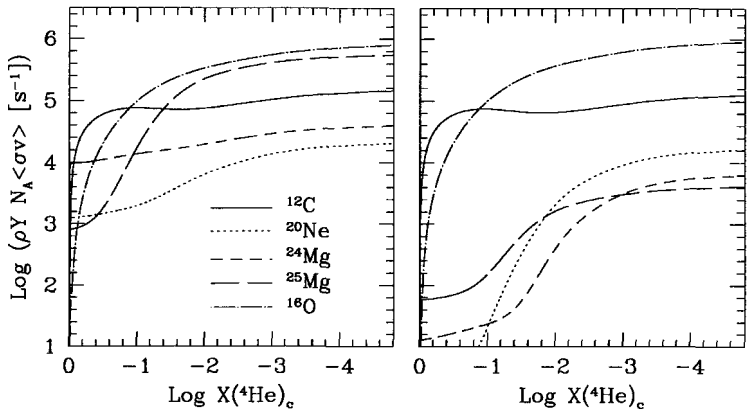

Figure 4. Interaction rate of each nuclide with neutrons as a function of central He abundance in $25M_\odot$ models of $Z/Z_\odot = 1$ (*left panel*) and 10^{-3} (*right panel*).

He burning[14,15,19]. As metallicity decreases, the n_c becomes small. This is because the poisoning effects of ^{16}O is much more important to absorb neutrons released from ^{22}Ne(α,n)^{25}Mg. This results in insignificant s-process nucleosynthesis in low metallicity models.[17,20] Therefore, in contrast to solar metallicity models, we cannot obtain the large enhancement of nuclei with A = 60-90 in $Z = 10^{-3}Z_\odot$ models, even if we adopt the higher rate of ^{22}Ne(α,n)^{25}Mg. At the early phase of the core He burning non-zero values of n_c are attributed to the s-process by the operation of ^{13}C(α,n)^{16}O reaction, but its contribution is negligible at the metallicity above $Z \sim 10^{-1}Z_\odot$.

The results of $Z = 10^{-3}Z_\odot$ models with different masses are shown in Figure 3. In these metallicity models we cannot see a large difference in abundance distributions, resulting from different central temperatures, in contrast to the solar metallicity models in which higher mass models show larger enhancements in the range of A = 60-90. This is also due to poisoning effects of ^{16}O in these low metallicity models.[17,37] This makes the production of heavy nuclei inefficient. Accordingly, the determination of the ^{16}O(n,γ)^{17}O rate is important to fix the efficiency of the s-process in low metallicity stars,[17,20,37] and to evaluate the contribution of weak s-component to the early Galaxy[38] and the solar system abundance[14,16,17]. However, metal-rich stars cannot greatly influence the variation of this rate because there exists the other efficient neutron poison of ^{25}Mg(n,γ)^{26}Mg reaction in Fig. 4. By comparing interaction rates ($\rho Y N_A < \sigma v >$, where

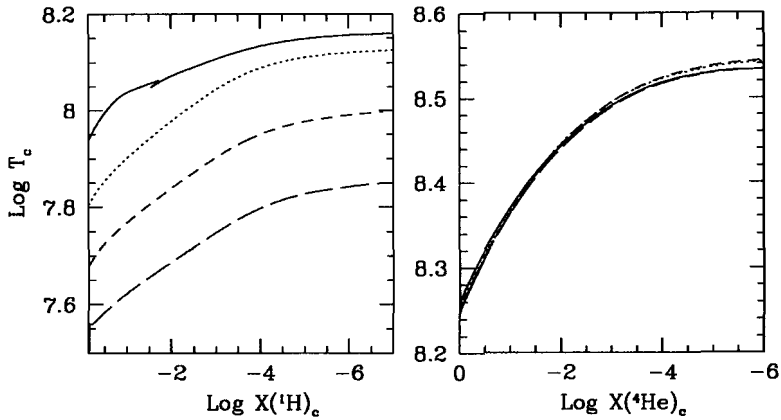

Figure 5. Evolution of central temperature as a function of central abundance of H (*left panel*) and He (*right panel*). Solid, dotted, short-dashed, and long-dashed lines represent the $25M_\odot$ models with $Z/Z_\odot = 10^{-7}, 10^{-5}, 10^{-3}$, and 1, respectively.

ρ is the density, Y the number abundance of nuclide, $N_A < \sigma v >$ the reaction rate) for two metallicity cases, we found the similar variation for ^{16}O and ^{12}C, and ^{20}Ne at very low He abundance. This is because (1) these nuclides are primary and (2) the central temperature evolution is insensitive to change of metallicity during central He burning phase as shown in Figure 5. On the contrary, Figure 5 also shows that there exists the strong metallicity dependence of the central temperature during core H burning phase. We will discuss this effect on the *s*-process nucleosynthesis below.

3.2. *The s-Process in Extremely Low Metallicity Stars*

As metallicity decreases from $Z = 10^{-3}$ to $10^{-5}Z_\odot$, iron seed abundance becomes much lower than the primary oxygen abundance at the late phase of the central He burning. Therefore, oxygen absorbs most of neutrons available. As a consequence, the *s*-process nucleosynthesis is highly suppressed and heavy nuclides are not created as shown in Figure 6 (*top and middle panels*).

However, the *s*-process efficiency dramatically changes at the metallicity range $Z = 10^{-5}$-$10^{-6}Z_\odot$. We find that models with extremely low metallicity ($Z = 10^{-7}Z_\odot$) can produce significant amounts of heavy nuclei in Figure 6 (*bottom panel*). The previous investigation[20] for the metal-

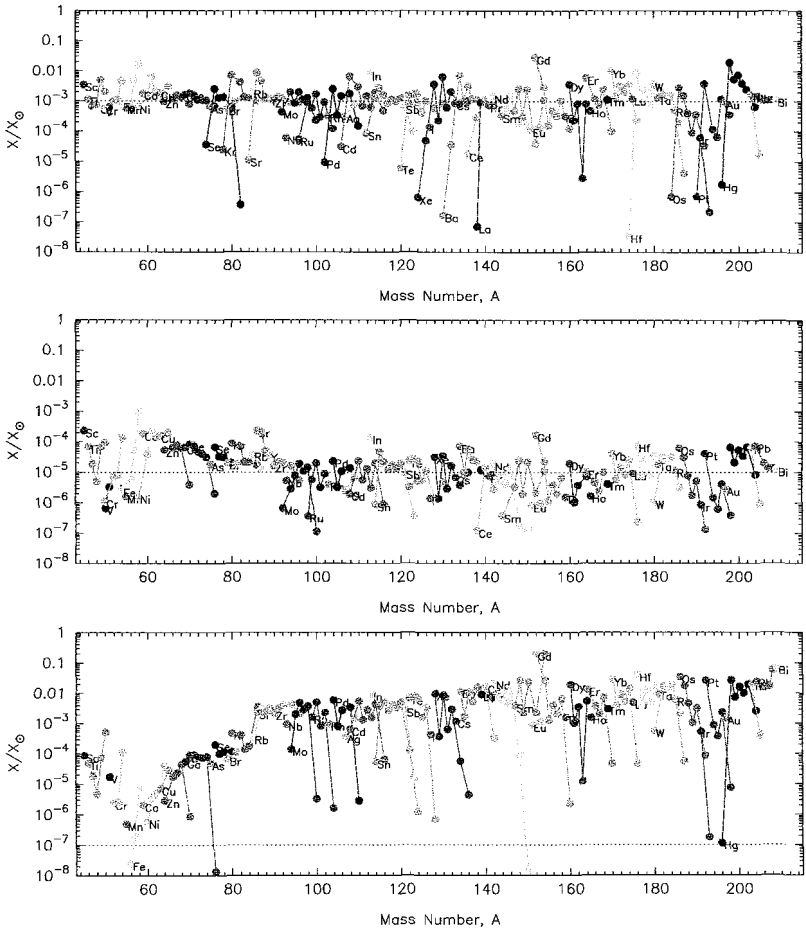

Figure 6. Distribution of heavy nuclei in $25M_{\odot}$ models with metallicity of $Z/Z_{\odot} = 10^{-3}$ (*top panel*), 10^{-5} (*middle panel*), 10^{-7} (*bottom panel*) after the end of central He burning phase.

licity $Z = 10^{-8}$ found that the *s*-process proceeds via the activation of $^{13}C(\alpha,n)^{16}O$ reaction at the late phase of central H burning, and showed that nuclear flow reaches nuclei with $A \sim 90$ and makes a peak around $A = 80$-85.

In a massive star with such extremely low metal contents, energy supply by central H burning is not enough, and thus stars shrink and heat up

stellar interior to compensate low CNO abundances with high temperature in the burning region. The $Z \lesssim 10^{-5} Z_{\odot}$ models show that the temperature exceeds over $\sim 10^8$ K (Figure 5), at which 3α reaction occurs and creates ^{12}C. The produced ^{12}C is transmuted into ^{13}C and ^{14}N through CN cycle. At these temperatures the averaged neutron density reaches $\sim 10^8$ cm^{-3} or higher. Such large amounts of neutrons are released via ^{13}C(α,n)^{16}O at the late phase of the central H burning.

At this phase neutron absorption by ^{16}O and ^{12}C is not yet efficient due to low abundances, compared with the s-process during core He burning phase in Figure 4. ^{14}N(n,p)^{14}C, the most dominant reaction for neutron capture in this phase, and other neutron capture reactions (including ^{16}O(n,γ) and ^{12}C(n,γ) reactions) play a role in producing seed nuclei, in variation with higher metallicity stars. Even in the case of a zero metallicity star we find the production of heavy elements whose overabundances are of a factor of ~ 10 lower than in the $Z = 10^{-7} Z_{\odot}$ model. This nucleosynthetic process is primary process, and thus this site may contribute to the abundance patterns, in particular light s-elements (Sr, Y and Zr), in extremely metal-poor stars observed.[39]

4. Conclusion

We calculate the s-process nucleosynthesis in massive stars with a wide range of metallicity from $Z = Z_{\odot}$ to 0. We find the well-known characteristics that the production of heavy elements is less efficient as the metallicity decreases down to $Z/Z_{\odot} \sim 10^{-6}$ due to low seed abundances and large poisoning effects of mainly ^{16}O. However, in very low metallicity stars below $Z/Z_{\odot} = 10^{-6}$ the central temperature already exceeds $\sim 10^8$ K during the central H burning phase. The α-capture on the newly synthesized ^{13}C leads to the release of neutrons to create seed nuclei via neutron capture reactions on neutron poisons ^{14}N, ^{12}C and ^{16}O, as well as proton capture reactions. The s-process occurs actively from seed nuclei of C-Si elements, different from more metal-rich cases, in which the seed nuclei are iron group elements.

References

1. O. Straniero, R. Gallino, M. Busso, A. Chieffi, C. M. Raiteri, M. Limongi and M. Salaris, *ApJL* **440**, L85 (1995)
2. R. Gallino, C. Arlandini, M. Busso, M. Lugaro, C. Travaglio, O. Straniero, A. Chieffi, and M. Limongi, *ApJ* **497**, 388 (1998)
3. S. Goriely and N. Mowlavi, *A&A* **362**, 599 (2000)

4. M. Busso, R. Gallino and G. J. Wasserburg, *ARA&A* **37**, 239 (1999)
5. M. Lugaro, F. Herwig, J. C. Lattanzio, R. Gallino and O. Straniero, *ApJ 586*, 1305 (2003)
6. M. Busso, R. Gallino, D. L. Lambert, C. Travaglio and V. V. Smith, *ApJ* **557**, 802 (2001)
7. W. Aoki, J. E. Norris, S. G. Ryan, T. C. Beers and H. Ando, *ApJL* **536**, L97 (2000)
8. S. Van Eck, S. Goriely, A. Jorissen and B. Plez, *Nature* **412**, 793 (2001)
9. W. Aoki, S. G. Ryan, J. E. Norris, T. C. Beers, H. Ando and S. Tsangarides, *ApJ* **580**, 1149 (2002)
10. S. Van Eck, S. Goriely, A. Jorissen and B. Plez, *A&A* **404**, 291 (2003)
11. J. A. Johnson and M. Bolte, *ApJL* **579**, L87 (2002)
12. F. Herwig, N. Langer and M. Lugaro, *ApJ* **593**, 1056 (2003)
13. S. Goriely and L. Siess, *A&A* **378**, L25 (2001)
14. N. Prantzos, M. Hashimoto and K. Nomoto, *A&A* **234**, 211 (1990)
15. C. M. Raiteri, M. Busso, G. Picchio, R. Gallino and L. Pulone, *ApJ* **367**, 228 (1991)
16. C. M. Raiteri, M. Busso, G. Picchio and R. Gallino, *ApJ* **371**, 665 (1991)
17. C. M. Raiteri, R. Gallino and M. Busso, *ApJ* **387**, 263 (1992)
18. C. M. Raiteri, R. Gallino, M. Busso, D. Neuberger and F. Kaeppeler, *ApJ* **419**, 207 (1993)
19. L.-S. The, M. F. El Eid and B. S. Meyer, *ApJ* **533**, 998 (2000)
20. I. Baraffe, M. F. El Eid and N. Prantzos, *A&A* **258**, 357 (1992)
21. R. D. Hoffman, S. E. Woosley and T. A. Weaver, *ApJ* **549**, 1085 (2001)
22. C. Angulo et al., *Nucl. Phys.* A**656**, 3 (1999)
23. R. Kunz, M. Fey, M. Jaeger, A. Mayer, J. W. Hammer, G. Staudt, S. Harissopulos and T. Paradellis, *ApJ* **567**, 643 (2002)
24. S. Kubono et al., *Phys. Rev. Lett.* **90**, 062501 (2003)
25. M. Jaeger, R. Kunz, A. Mayer, J. W. Hammer, G. Staudt, K. L. Kratz and B. Pfeiffer, *Phys. Rev. Lett.* **87**, 202501 (2001)
26. T. Ohsaki, Y. Nagai, M. Igashira, T. Shima, K. Takeda, S. Seino and T. Irie, *ApJ* **422**, 912 (1994)
27. M. Igashira, Y. Nagai, K. Masuda, T. Ohsaki and H. Kitazawa, *ApJL* **441**, L89 (1995)
28. Z. Y. Bao, H. Beer, F. Käppeler, F. Voss, K. Wisshak and T. Rauscher, *Atomic Data and Nuclear Data Tables* **76**, 70 (2000)
29. F. -K. Thielemenn, private communication (1995)
30. H. C. Spruit, *A&A* **253**, 131 (1992)
31. C. de Jager, H. Nieuwenhuijzen and K. A. van der Hucht, *A&AS* **72**, 259 (1988)
32. R. P. Kudritzki, A. Pauldrach, J. Puls and D. C. Abbott, *A&A* **219**, 205 (1989)
33. N. Iwamoto, T. Kajino, G. J. Mathews, M. Y. Fujimoto and W. Aoki, *ApJ* **602**, 377 (2004)
34. P. E. Koehler,*Phys. Rev.* C**66**, 055805 (2002)
35. V. Costa et al., *A&A* **358**, L67 (2000)

36. T. Rauscher, *Nucl. Phys.* A**719** 73 (2003)
37. M. Rayet and M. Hashimoto, *A&A* **354**, 740 (2000)
38. I. Baraffe and K. Takahashi, *A&A* **280**, 476 (1993)
39. H. Umeda and K. Nomoto, astro-ph/0308029 (2003)

^{186}RE ISOMER CONTRIBUTION TO ^{187}RE-^{187}OS COSMOCHRONOMETER

T. HAYAKAWA

Japan Atomic Energy Research Institute, Tokai, Ibaraki 319-1195, Japan
and National Astronomical Observatory, Mitaka, Tokyo 181-8588, Japan
E-mail: hayakawa@jball4.tokai.jaeri.go.jp

T. SHIZUMA

Japan Atomic Energy Research Institute, Tokai, Ibaraki 319-1195, Japan

T. ARIMA

Tohoku University, Sendai 980-8578, Japan

T. KAJINO

National Astronomical Observatory, Mitaka, Tokyo 181-8588, Japan
and Japan Atomic Energy Research Institute, Tokai, Ibaraki 319-1195, Japan

S. CHIBA AND N. SHINOHARA

Japan Atomic Energy Research Institute, Tokai, Ibaraki 319-1195, Japan

H. UTSUNOMIYA

Konan University, Higashinada, Kobe 658-8501, Japan

A ^{187}Os-^{187}Re pair has been known to be a good cosmochronometer for the r-process nucleosynthesis. The radioactivity ^{187}Re decays to a daughter nucleus ^{187}Os with a half-life of 2.0×10^5 years. The ^{187}Re has been considered to be synthesized predominantly by the r-process, whereas the ^{187}Os has been produced by both the radioactive decay of ^{187}Re and the s-process nucleosynthesis. The s-process contaminations to ^{187}Re and ^{187}Os must be subtracted for an estimation of the passing time from a r-process episode to the present time with an accuracy. An s-process path through a ^{186}Re isomer has been ignored up to now because the neutron capture cross section of the ^{185}Re(n,γ)^{186m}Re reaction at a thermal energy as well as a quasi-stellar energy has not been measured by experimental techniques with an estimation of uncertainty. In order to estimate this s-process contamination through the isomer, a production ratio of the isomer to the ground state in ^{186}Re has been measured through an activation technique with a thermal neutron provided by a nuclear reactor.

1. Introduction

Nuclear cosmochronometers of nucleosynthesis processes are very useful for investigations of the astronomical chronology of the solar system and the Galaxy. Almost nuclei heavier than the iron group were produced by two neutron capture processes. The first one is a rapid neutron capture process (r-process) considered to occur in supernova explosions. The other is a slow neutron capture process (s-process) in low-mass asymptotic giant branch (AGB) stars or massive stars. The general idea of the nuclear cosmochronometer was originally proposed by Rutherford about 70 years ago [1]. A major advance of the study of the ^{238}U-^{232}Th chronometer for the r-process was made by BBFH [2,3].

A ^{187}Re-^{187}Os pair is proposed to be as a nuclear cosmochronometer of the r-process [4]. The ground state of the ^{187}Re nucleus decays to a daughter nucleus ^{187}Os by β^--decay with a half-life of 4.35×10^{10} years [5]. Figure 1 shows a nuclear chart neighboring the ^{187}Re nucleus and flows of nucleosynthesis processes. The ^{187}Re nucleus is dominantly produced by the β^--decay after the freezeout of the r-process, while ^{186,187}Os isotopes are synthesized by the s-process because they are shielded by stable isobars against the post r-process. The ^{187}Os nucleus is also produced by the cosmoradiogeneric β^--decay of ^{187}Re. The time passed from a r-process episode to the present can be calculated by a present abundance ratio of ^{187}Os and ^{187}Re if s-process contributions to these nuclei can be subtracted. This chronometer has an advantage that it does not depend on initial abundances calculated by r-process models. Although the initial abundance of, in particular, the ^{187}Os should be calculated by s-process models, the uncertainty of the calculated abundances is generally lower than that by the r-process models. This chronometer was applied to the study of the chronology of the chemical evolution of the Galaxy[6,7,8] and an estimation of the age of the solar system by analyzing meteorites[9,10,11]. Recent progress in spectroscopic studies of extremely metal-poor stars, which compositions are enhanced by elements produced by the r-process nucleosynthesis in the first generation, has enabled isotope separation of several heavy elements, for example, Ba[14], Eu[12,13]. Analysis of pre-solar grains in primitive meteorites provides a sample affected strongly by a single or a few nucleosynthesis episode. Heavy elements such as Sr, Mo and Ba in the pre-solar grains have already been successfully separated into isotopes, whose origins are considered to be ejecta of core collapse SN explosions[15,16]. Measurements of Os and Re isotopes are, thus, desirable. Although ^{187}Re is pro-

duced predominantly by the r-process, it is also synthesized through weak s-process branches. The s-process contributions via two known weak paths of ^{185}W(n,γ)^{186}W(n,γ)^{187}W(ν,e$-$)^{187}Re and ^{186}Re(n,γ)^{187}Re$_{g.s.}$(n,γ)^{187}Re were studied by Käppeler through a measurement of neutron capture cross sections of ^{184}W and ^{185}Re [17,18].

We here would like to point out a possibility that ^{187}Re may be produced via a new weak branch of the s-process which is the path though the isomeric state in ^{186}Re [19] from ^{185}Re. This path has been ignored because there is no absolute data of the neutron capture cross section with uncertainty at any energy [21]. The neutron capture cross section from ^{185}Re to the ^{186}Re isomer may be small relative to that to the ground state. However, the s-process contribution to ^{187}Re may be large, which may give a large shift to the passing time estimated using the Re-Os chronometer, because the isomer has a half-life of 2.0×10^5 years which is enough longer than a time scale of a typical s-process. Seegmiller *et al.* measured the half-life of the isomer by a mass-spectrometric analysis and γ-ray spectroscopy of samples after neutron irradiation [20]. The only relative production ratio of the isomer to the ground state in ^{186}Re without an estimation of the experimental uncertainty was reported in the paper [20]. Although the neutron capture cross section to ^{186}Re isomer could be estimated by using this ratio and the neutron capture cross section to ^{186}Re$_{gs}$, there is no data at a thermal energy in the Table of Isotopes [21]. In this paper, we report the possibility that ^{187}Re would be produced by the new weak s-process path through the isomer with the long half-life in ^{186}Re. It is considered that the neutron capture ratio of the isomer to the ground state is important for the calculation of the contamination of the s-process. In order to estimate the contamination by the new s-process path, we measured the neutron capture cross-section ratio and calculated the contamination of the s-process by using the classical steady-flow model.

2. Measurement of the neutron capture ratio of the isomer to the ground state in ^{186}Re

We carried out the measurement of the neutron capture cross-section ratio of the isomer to the ground state in ^{186}Re at the thermal energy using an activation method. Two thin natural Re foils and two Al-Co wires were irradiated with the thermal neutron provided by the nuclear reactor JRR-4 at the Japan Atomic Energy Research Institute (JAERI). The weights of the Re foils were 43.8 mg and 58.1 mg. The Al-Co wires had weights of 1.74

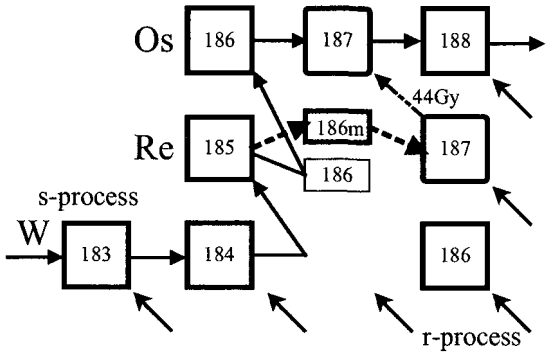

Figure 1. Nuclear chart and nucleosynthesis flow around the ^{187}Re.

mg and 4.58 mg and the Co element in the Al-Co wires accounted for 0.475 % of all. The total neutron flux was evaluated by measurements of decay γ-rays after β-decay from the activated Co, which was about 4.37×10^{13} n/cm^{2}s. Although the ^{28}Al produced by the ^{27}Al(n, γ)^{28}Al reaction is also useful for the evaluation of the neutron flux, the decay γ-rays of the ^{28}Al could not be measured in the experiment because the cooling time from the irradiation to the first measurement was much longer than the half-life of ^{28}Al. Since the natural Re sample consists of two stable isotopes ^{185}Re (37.4% of all) and ^{187}Re (62.6%), two unstable isotopes of ^{186}Re and ^{188}Re were mainly produced by the n+^{nat}Re reaction with the thermal energy. The half-lives of the ground states of these isotopes are $T_{1/2} = 91h$ (^{186}Re) and $T_{1/2} = 17h$ (^{188}Re).

The samples were irradiated by the thermal neutron for six hours, and subsequently they were cooled in a water pool for about four mounts in order to reduce the background produced by unstable isotopes with short half-lives. Four and eight months later, γ-rays irradiated from the activated samples were measured by two HPGe detectors. In addition sixteen months later, γ-rays from one sample was measured by one HPGe detector. Total efficiency of the HPGe detectors is about 20% relative to $3''\times3''$ NaI detector. The energy dependence of the efficiency was calibrated by the standard sources of ^{152}Eu and ^{133}Ba. The energy resolution is about 2.2 keV at 1.3 MeV γ-ray. The γ-rays from the samples were measured

at a 5 cm or 3 cm distance from the end cap of the detectors at the first or second measurement, respectively, with low-background environment by lead shields. The isomer feeds the ground state through only internal decay. The γ-ray transitions from the isomer to the ground state could not be distinguished from other γ-rays in this measurement because there are many strong γ-rays originated from ^{184}Re ($T_{1/2}$=38 day) produced by the ^{185}Re(n,2n)^{184}Re reaction with a fast neutron (see Fig. 2). Although the flux of the fast neutron is small, the intensities of the ^{184}Re γ-rays were enhanced since the half-life is suitable to the cooling time. We observed a 137 keV transition in ^{186}Os irradiated after the β-decay of the ground state in ^{186}Re. The γ-ray is most strong in the decay scheme of the isomer. It should be noted that the decay of both the ground state produced directly by the ^{185}Re(n, γ)^{186}Re$_{gs}$ reaction and the isomer contributed to the yield of the 137 keV γ-ray because the isomer decays to ^{186}Os through the ground state in ^{186}Re.

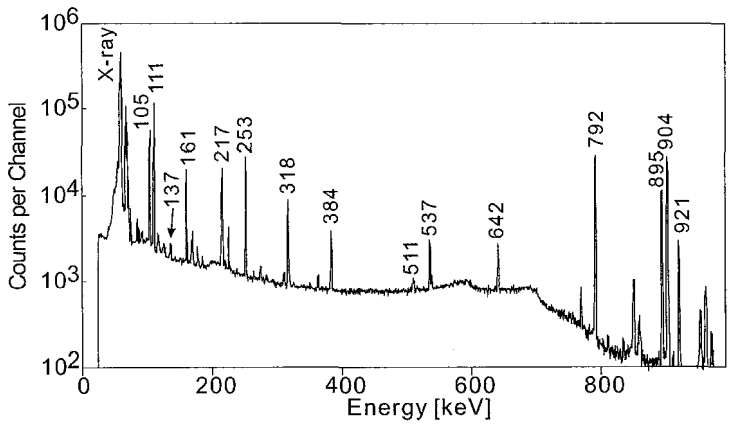

Figure 2. A typical spectrum.

In order to measure the neutron capture cross section ratio between the isomer and the ground state, we selected a cooling time of four months after the irradiation for the first measurement. At this measurement, the unstable ground state of ^{186}Re with $T_{1/2}$=91 hours produced directly was

still alive because the neutron capture cross section to the ground state is much larger than that to the isomer. In contrast the ground state did not alive at second and third measurements because cooling times of eight and sixteen months are enough larger than the half-life. We could thus obtain the average neutron capture cross section to the isomer by analyzing the yields of the 137 keV γ-ray at the second and third measurements.

A number of β decay of unstable nucleus produced by a neutron capture reaction was evaluated from γ-ray intensities in a measured spectra by applying the following equation,

$$N_{total} = \cdot \frac{n_{peak}}{R \cdot \epsilon \cdot f_{decay}},$$

where N_{total} means the total number produced by the activation, n_{peak} means the peak count corresponding to the decay γ-ray, R means the emission probability of the measured γ-ray per decay, ϵ is the efficiency of HPGe detectors and f_{decay} is correction of the β-decay with measurement time. The f_{decay} is expressed by,

$$f_{decay} = exp(-t_1 \cdot \lambda) - exp(-t_2 \cdot \lambda),$$

where t_1 and t_2 are start and stop time for measurements, respectively. Experimental uncertainty consists mainly of the statistical error of the peak count and the uncertainty of the efficiency of the HPGe detectors. The energy of the γ ray of interest is 137 keV, which is located near the peak of the efficiency curve of the detectors. We evaluated the efficiency uncertainty to be about 7% from deviations between an efficiency curve fitted by checking sources and intensities of individual γ-rays. A pileup effect of γ rays was negligible because the absolute efficiency that is lower than 5% is very small.

We obtained a result that an average neutron capture cross section derived from the second and third measurements is 0.74±0.05 [mb]. The γ-ray yield at the first measurement consists of contributions from the ground-state decay as well as the isomer. The average neutron capture cross section to the ground state could be evaluated by subtracting the contribution of the isomer from the total count, and thereby the average value of 137 ± 26 [b] was obtained. Finally we obtained the production ratio of 0.54±0.11%. This value is about twice larger than the value of 0.3 % reported previously [20]. We note that these neutron capture cross-sections include contribution of a neutron higher than a thermal energy.

3. Estimation using the steady-flow model

In order to estimate the contribution of the weak s-process through the ^{186}Re isomer to ^{187}Re, a calculation using the classical steady-flow model [2,4] was carried out. The steady-flow model extended by Ward, Newman and Clayton can be applied to a branching point where a neutron capture reaction and beta decay compete[22]. An s-process nucleus was produced by a neutron capture and/or a feeding of β-decay of a parent nucleus, and was also destroyed by a neutron capture and/or β-decay. The abundance of the residual nucleus can be calculated by the following equation,

$$\frac{dN}{dt} = \sum_i \lambda_i(A)N_i(A) - \sum_j \lambda_j(A')N(A'), \tag{1}$$

where λ means $n{\cdot}\sigma$ or β-decay rate, N means an isotope abundance ratio, A and A' are atomic numbers which have the relationship, $A{=}A'$ or A'-1. The equation in the limit of the steady flow is expressed by the following equation,

$$\sum_i \lambda_i(A)N_i(A) = \sum_j \lambda_j(A')N(A'). \tag{2}$$

If other weak s-process paths are ignored, the initial conditions in the W-Re-Os region are given by the following equations,

$$\lambda N(^{187}Re) = \lambda N(^{186m}Re), \tag{3}$$

$$\lambda(to^{186m}Re)N(^{185}Re) = \lambda N(^{186m}Re), \tag{4}$$

$$\lambda(to^{186}Re)N(^{185}Re) = (\lambda_{\beta^-} + \lambda_{EC/\beta^+})N(^{186}Re_{gs}), \tag{5}$$

$$\lambda_{\beta^-} N(^{186}Re_{gs}) = \lambda N(^{186}Os). \tag{6}$$

The final equation is given by

$$N(^{187}Re) = \frac{N(^{186}Os){\cdot}\lambda(^{187}Os)}{A{\cdot}\lambda(^{188}Re)} \cdot \frac{\lambda(^{186m}Re)}{\lambda(^{186}Re)}, \tag{7}$$

where A is a branching ratio of β-decay, namely $A = \lambda_{\beta^-}/(\lambda_{\beta^-}+\lambda_{EC/\beta^+})$.

It should be noted that the s-process abundance of ^{187}Re via the ^{186}Re isomer is proportional to the production ratio of the isomer to the ground state in ^{186}Re. Thus the s-process abundance can be calculated by the production ratio and neutron capture cross sections of Os and Re isotopes.

The production ratio with a thermal energy was measured in the present experiment but the ratio may depend on the neutron energy. The neutron capture cross section to the ^{186}Re isomer and the production ratio were seen at the Japan Evaluation Nuclear Data Library activation files (JENDL) [23,24]. The calculated ratio with a kT=30 keV energy in JENDL is larger than the thermal energy. We thus estimated the ratio with kT= 30 keV by multiplying the values of 8.3. The neutron capture cross section with kT=30 keV for the Re and Os isotopes were taken from a previous study[17], where the best set of the Maxwellian average capture cross section for these isotopes was evaluated. The values are 1160 and 418 [mb] for ^{187}Re and ^{186}Os, respectively. Substituting these values and the production ratio measured in the present experiment for the equation (7), we obtained about 1.7% as the s-process abundance of the ^{187}Re relative to ^{186}Os.

4. Summary

We point out that an weak s-process path to ^{187}Re which is a nuclear cosmochronometer for the r-process has been ignored up to now. The reason is that there is no neutron capture cross section with experimental uncertainty at any energy. In order to estimate the contamination of the s-process through the isomer, the neutron capture cross section ratio of the isomer to the ground state in ^{186}Re was measured with a thermal energy. Two natural Re foils was irradiated by the thermal neutron provided by a nuclear reactor at JAERI. The ^{186}Re isomer decays to the ground state with a half-life of 2.0 $\times$ 10^5 years. After four, eight and sixteen months later from the irradiation, the γ-rays following the decay of the ^{186}Re isomer were measured by two HPGe detectors. We finally obtained the isomer production ratio of 0.54±0.11%.

References

1. E. Rutherford, Nature, **123**, 313 (1929).
2. E. M. Burbidge, *et al.*, Rev. Mod. Phys. **29**, 548 (1957).
3. W.A. Fowler and F. Hoyle. Ann. Phys. **10**, 280 (1960).
4. D.D. Clayton, ApJ, **139**, 637 (1964).
5. M. Lindner, et al., Nature, **320**, 256 (1986).
6. D. D. Clayton, Nature, **224**, 56 (1969).
7. M. Arnould, K. Takahashi and K. Yokoi, A&A, **137**, 51 (1984).
8. K. Yokoi, K. Takahashi and M. Arnould, A&A, **117**, 65 (1983).
9. J.M. Luck, J.L. Brich and C.J. Allegre,, Nature, **283**, 256 (1980).
10. J. M. Luck and C. J. Allegre, Nature, **302**, 130 (1983).

11. J. L. Birck and C. J. Allegre, , Meto. & Plan. Sci., **33**, 647 (1998).
12. C. Sneden, *et al.*, *Astrophys. J.* **566**, L25 (2002).
13. W. Aoki, *et al.*, *Astrophys. J.* **592**, L67 (2003).
14. D.L. Lambert, C.A. Prieto, *Mon. Not. R. Astron. Soc.* **335**, 325 (2002).
15. M.J. Pellin, *et al.*, *Lunar and Planet. Sci.* **31**, 1917 (2000).
16. Q. Yin, S.B. Jacobsen, K. Yamashita, *Nature* **415**, 881 (2002).
17. F. Käppeler, et al., ApJ, **366**, 605 (1991).
18. K. Sonnabend, et al. ApJ, **583**, 506 (2003).
19. M. Lindner, Phys. Rev., **84**, 240 (1951).
20. D. W. Seegmiller, et al., Nucl. Phys. A, **185**, 94 (1972).
21. R. B. Firestone, et al. , Table of Isotopes, Eighth Edition, Wiley Interscience, 1998.
22. R.A. Ward, M.J. Newman and D.D. Clayton, ApJ, 31, 33 (1976).
23. Nuclear Data Center, Japan Atomic Energy Research Institute: "Chart of the Nuclides 2000," http://wwwndc.tokai.jaeri.go.jp/CN00/index.html (2001.12.16).
24. Y. Nakajima, JNDC WG on Activation Cross Section Data: "JENDL Activation Cross Section File," Proc. the 1990 Symposium on Nuclear Data, JAERI-M 91-032, p. 43, 1991

DIRECT MEASUREMENT OF THE E1 AND E2 CROSS SECTIONS OF THE $^{12}C(\alpha,\gamma)^{16}O$ REACTION AT $E_{c.m.}$ =1.3~1.5MeV*

T. SHIMA, H. MAKII, K. MISHIMA, Y. NAGAI, M. SEGAWA, H. UEDA, T. MASAKI

Research Center for Nuclear Physics, Osaka University, 10-1 Mihogaoka, Ibaraki, Osaka 567-0047, Japan

M. IGASHIRA, T. OHSAKI

Research Laboratory for Nuclear Reactors, Tokyo Institute of Technology, 2-12-1, O-okayama, Meguro, Tokyo 152-8550, Japan

I. SUGAI, Y. TAKEDA

Accelerator Laboratory, High Energy Accelerator Research Organization, 1-1, Oho, Tsukuba, Ibaraki 305-0801, Japan

The E1 and E2 transition cross sections at the center-of-mass energies of 1.3~1.5MeV have been measured by directly detecting the prompt γ ray from the capture state of the ^{16}O nucleus. Using a pulsed α beam, major background due to the $^{13}C(\alpha,n)^{16}O$ reaction were efficiently reduced, and the cross sections were determined with very good statistical accuracy of 4~10%.

1. Introduction

The $^{12}C(\alpha,\gamma)^{16}O$ reaction is the key in stellar evolution and stellar nucleosynthesis during the He-burning phase [1,2]. It governs the $^{12}C/^{16}O$ ratio and the abundances of intermediate-mass nuclei produced by the He-burning, and the iron core mass of the type-II supernova explosion [2,3]. Therefore precise data of the reaction rate at the center-of-mass energy $E_{c.m.}$~300keV is highly demanded, where $E_{c.m.}$~300keV corresponds to the "Gamow energy" of the He-burning region. The reaction rate at $E_{c.m.}$~300keV, however, is expected to be as small as $<10^{-2}$fb, being far below the sensitivities of the current experimental methods for the direct measurement. Therefore the reaction rate should anyhow be estimated by using reliable theoretical models and the

* This work was supported by a Grant-in-Aid for Scientific Research (B) of Japan Society for the Promotion of Science.

experimental data obtained in a higher energy region, say, $E_{c.m.}$> 1MeV. Unfortunately, there has been a large discrepancy among the previous experimental data [4-9], and the estimated reaction rate still suffers from a large uncertainty. In fact, the astrophysical S-factors S_{E1} for the E1 transition, S_{E2} for E2, and $S_{cascade}$ for the cascade transition at 300keV are estimated using R-matrix theory as 79 }21keVb, 4~140keVb and 0~30keVb, respectively, and thus the total S-factor was estimated as 62~270keVb, which contains an ambiguity of a factor of ~4 [10]. Therefore a more precise measurement is necessary, especially for the E2 cross section, and thus we performed a new measurement for both the E1 and E2 cross sections of the $^{12}C(\alpha,\gamma)^{16}O$ reaction. In this paper we will show our experimental method, and will report a preliminary result on S_{E1} and the ratio of the E2 cross section to the E1 cross section at $E_{c.m.}$= 1.3MeV and 1.5MeV.

2. Experimental Method

Since the $^{12}C(\alpha,\gamma)^{16}O$ reaction cross section is quite small at low energies, it is necessary to use a high intensity of the incident beam and a high efficiency of the γ-ray detector are useful. Also it is essential to suppress the backgrounds as small as possible. Therefore we employed a pulsed α beam and the prompt γ-ray detection method. Fig. 1 shows a schematic drawing (top view) of our experimental setup.

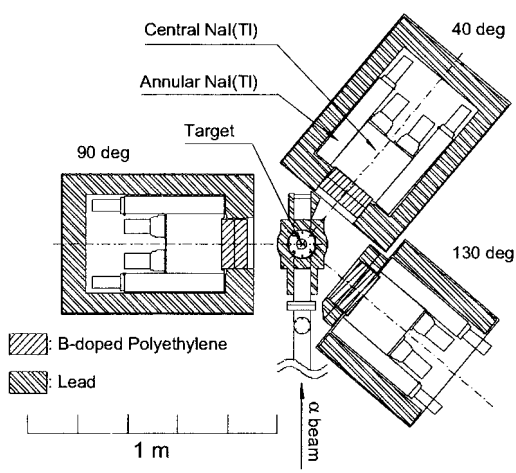

Figure 1. Experimental setup (top view).

One of the important points in the measurement of the $^{12}C(\alpha,\gamma)^{16}O$ reaction cross section at low energies is the suppression of the backgrounds induced by the MeV neutrons from the $^{13}C(\alpha,n)^{16}O$ reaction, whose Q-value is as high as +2.216MeV, and the cross section is about 10^6 times larger than that of $^{12}C(\alpha,\gamma)^{16}O$ at the same incident energy of the α particle [11]. Here the ^{13}C nuclei are possibly contained in the target material. To get rid of the neutron-induced backgrounds, we employed a pulsed α beam provided from the 3.2MV Pelletron accelerator at the Research Laboratory for Nuclear Reactors (RLNR) in Tokyo Institute of Technology. The beam current was ~7μA, which was measured with a Faraday cup placed at the beam stopper. The time width and the repetition rate of the beam pulse were 2.5ns (FWHM) and 4MHz, respectively. The true signals of the α-capture γ ray are discriminated from the backgrounds according to the time interval between the detected signal and the beam pulse.

To reject the background neutrons further, we used a self-supported graphite target foil, made of 99.95% enriched ^{12}C. The effective thickness of the foils was typically 350μg/cm^2, which was monitored during the measurement by means of the Rutherford backscattering spectroscopy (RBS) method, as shown later.

The capture γ rays were detected using three NaI(Tl) detectors with Compton suppressors, which were located at the angles of $\theta = 40°$, 90° and 130° with respect to the direction of the incident beam. Each NaI(Tl) detectors has the dimension of 22.9cm in diameter and 20.3cm in length. To reduce the background γ rays from the surroundings, the γ-ray detectors were shielded with 10cm thick lead. To attenuate fast neutrons from the carbon target, 10cm thick borated polyethylene walls were placed in front of the γ-ray detectors. The data of the timing and the pulse height of the γ-ray signals were acquired with a Linux-based personal computer event by event in a list mode, and analyzed offline.

3. Data Analysis

Fig. 2 shows an example of the pulse height spectra for all the signals observed with γ-ray detectors. It was found that the main background is caused by the neutron-capture reactions on ^{127}I contained in NaI(Tl) crystals. Those background events are distributed more than 10ns after the prompt signals in the time-of-flight spectrum as shown in Fig. 3. Therefore the true signal can be separated from the background due to the fast neutron-capture on iodine by setting a time window for the foreground as shown in Fig. 3.

Furthermore, in order to subtract time-independent background, a time window for such background was used. By subtracting the pulse height spectrum for the background from the one for the foreground, a net γ-ray pulse height spectrum was obtained as shown in Fig. 4. As shown in the figure, the net spectrum can be well reproduced with the calculated response function of the γ-ray detector, and contributions from residual background γ rays are almost negligible. Thus the γ-ray yields from the $^{12}C(\alpha,\gamma)^{16}O$ reaction have been obtained accurately.

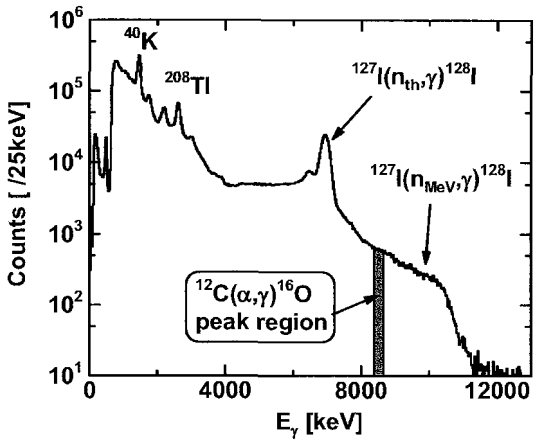

Figure 2. A pulse height spectrum for $E_{c.m.}$=1.5MeV measured with a γ-ray detector at θ=90°.

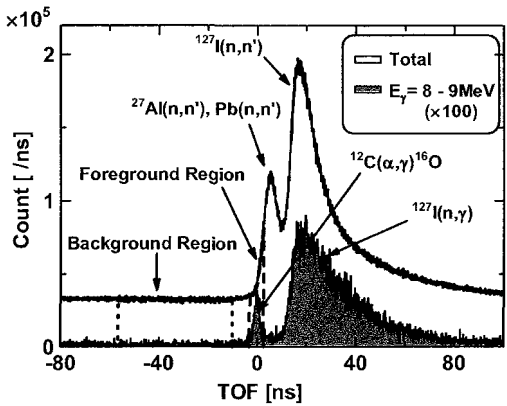

Figure 3. Time of flight spectra observed for $E_{c.m.}$=1.5MeV and θ=90°. The shaded histogram is for E_γ=8MeV to 9MeV. The dashed lines and the dotted lines indicate the time windows for the foreground and the background, respectively.

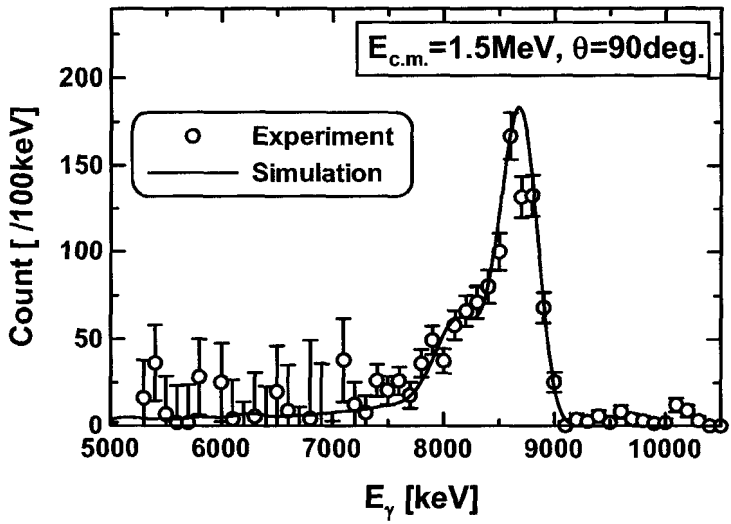

Figure 4. Net γ-ray pulse height spectrum for $E_{c.m.}$=1.5MeV and θ=90°. The open circles indicate the experimental data. The solid curve is the Monte Carlo calculated response function of the γ-ray detector.

4. Target Monitor

Since the condition of the carbon target changes rapidly due to damage by the bombardment with the α beam, it is monitored using the Rutherford backscattering spectroscopy (RBS) method. An incident α particle passes through the target, and is backscattered at the backing plate made of gold. Then the scattered α particle passes through the target, and is detected with a Si(Li) solid-state detector, located 32cm distant from the target in the direction with the scattering angle of 177°. Typical RBS spectra are shown in Fig. 5. The edge of the spectrum with the carbon target is shifted to ~1.1MeV, while the one without carbon (i.e. gold backing only) is ~2.1MeV. The shift corresponds to the total energy loss of the α particles in the carbon layer, and therefore it indicates the effective thickness of the target. Fig. 6 shows the distribution of the target thickness obtained from the energy spectrum shown in Fig. 5. In this case the thickness was determined as 370 }20μg/cm^2.

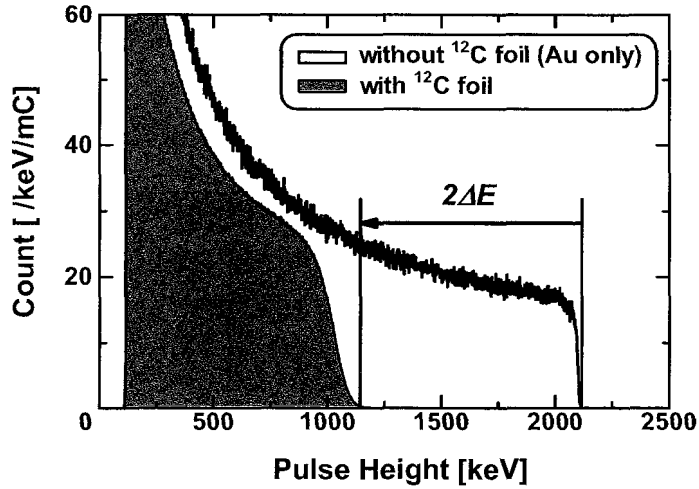

Figure 5. RBS spectra with (shaded) and without (open) ^{12}C foil.

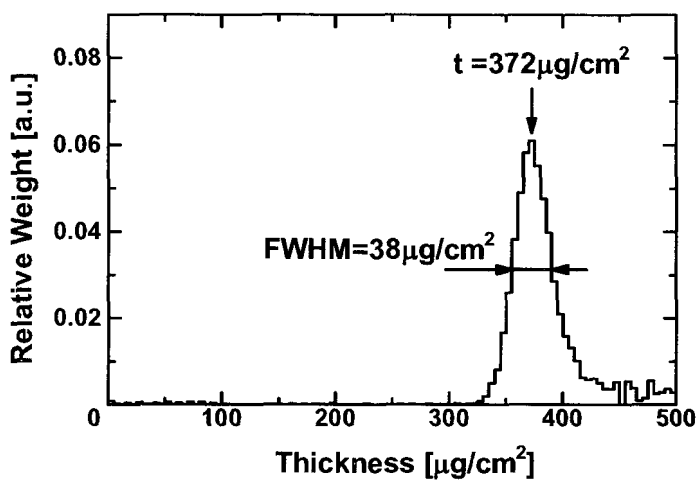

Figure 6. Distribution of target thickness obtained from the RBS spectrum shown in Fig. 5.

5. Result

The preliminary result on the differential cross sections of the $^{12}C(\alpha,\gamma)^{16}O$ reaction were obtained as shown in Fig. 7.

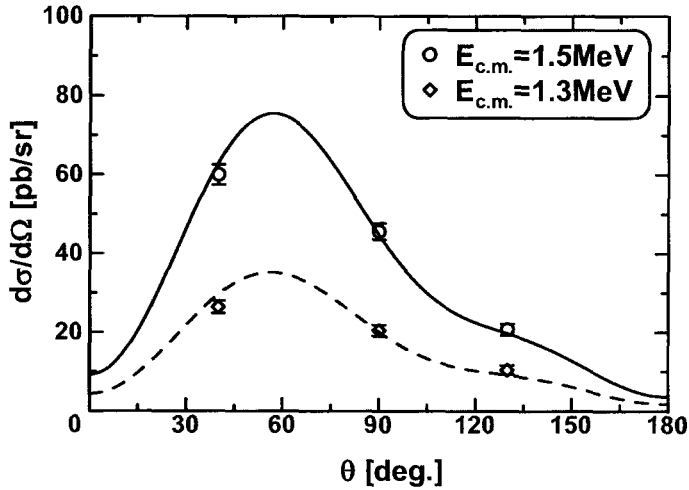

Figure 7. Experimental differential cross sections of the $^{12}C(\alpha,\gamma)^{16}O$ reaction. Circles; $E_{c.m.}$=1.5MeV, diamonds; $E_{c.m.}$=1.3MeV. Solid and dashed curves are the fittings for the data for 1.5MeV and 1.3MeV, respectively.

To determine the E1 and E2 transition strengths, we fitted the present data with Eq. (1) :

$$\frac{d\sigma}{d\Omega} = \frac{1}{4\pi}\left[\sigma_{E1}(1 - P_2(\theta)) + \sigma_{E2}\left(1 + \frac{5}{7}P_2(\theta) - \frac{12}{7}P_4(\theta)\right) + 6\cos\Phi\sqrt{\frac{\sigma_{E1}\sigma_{E2}}{5}}(P_1(\theta) - P_3(\theta))\right] \quad (1)$$

Here σ_{E1} and σ_{E2} stand for the E1 and E2 cross sections, respectively. $P_l(\theta)$ denotes the l-th order Legendre polynomial $P_l(\cos\theta)$. Φ is the phase of the interference between E1 and E2, and have been determined as $\cos\Phi$= 0.56 and 0.60 at 1.3MeV and 1.5MeV, respectively, from the previous measurement of the α-elastic scattering on ^{12}C [12]. Using the present differential cross section and the previous data of $\cos\Phi$, we obtained preliminary results on σ_{E1} and σ_{E2} as listed in Table 1.

Table 1. Total cross sections for E1 and E2 transitions (preliminary). The errors are the statistical and systematic ones.

$E_{c.m.}$ [MeV]	σ_{E1} [pb]	σ_{E2} [pb]
1.3	170 }10 }19	80 }8 }10
1.5	370 }15 }41	170 }10 }22

6. Summary and Discussion

In this work the E1 and E2 cross sections of the $^{12}C(\alpha,\gamma)^{16}O$ reaction have been measured very accurately by means of a pulsed α beam. Our preliminary values of the astrophysical S-factor S_{E1} and the ratio σ_{E2}/σ_{E1} are consistent with most of the previous works, while the uncertainty is much improved, as shown in Fig. 8 and Fig. 9. A detailed analysis is now in progress.

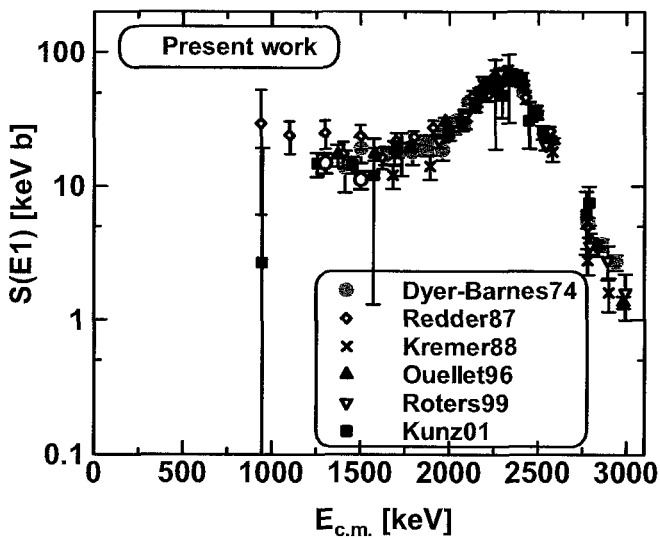

Figure 8. Astrophysical S-factor S_{E1} for the E1 transition of the $^{12}C(\alpha,\gamma)^{16}O$ reaction. Open circles; present, gray circles; Ref. 4, open diamonds; Ref. 5, diag. crosses; Ref. 6, filled triangles; Ref. 7, open reversed triangles; Ref. 8, and filled squares; Ref. 9.

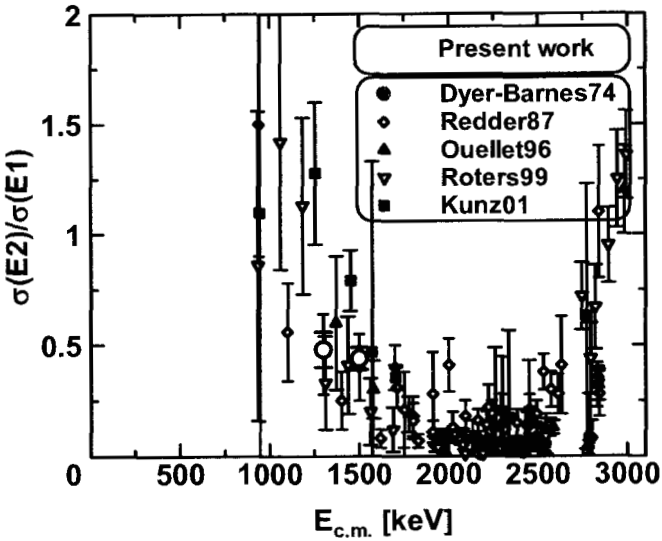

Figure 9. Ratio of the E2 cross section to the E1 cross section. Open circles; present, gray circles; Ref. 4, open diamonds; Ref. 5, filled triangles; Ref. 7, open reversed triangles; Ref. 8, and filled squares; Ref. 9.

Acknowledgments

We would like to thank Mr. K. Tosaka for operation of the T.I.T. Pelletron accelerator.

References

1. W.A. Fowler, Rev. Mod. Phys. **56**, 149 (1984).
2. T.A. Weaver and S.E. Woosley, Phys. Rep. **227**, 65 (1993).
3. M. Hashimoto, Prog. Theor. Phys. **94**, 663 (1995).
4. P. Dyer and C.A. Barnes, Nucl. Phys. **A233**, 495 (1974).
5. A. Redder *et al.*, Nucl. Phys. **A462**, 385 (1987).
6. R.M. Kremer *et al.*, Phys. Rev. Lett. **60**, 1475 (1988).
7. J.M.L. Ouellet *et al.*, Phys. Rev. **C54**, 198 (1996).
8. G. Roters *et al.*, Eur. Phys. J. **A6**, 451 (1999).
9. R. Kunz *et al.*, Phys. Rev. Lett. **86**, 3244 (2001).
10. L. Buchmann *et al.*, Phys. Rev. **C54**, 393 (1996).
11. H.W. Drotleff *et al.*, ApJ. **414**, 735 (1993).
12. C.R. Brune, Phys. Rev. **C64**, 055803 (2001).

This page intentionally left blank

V. Nuclear data and Nuclear Physics

This page intentionally left blank

MICROSCOPIC NUCLEAR STRUCTURE RELEVANT TO NUCLEAR ASTROPHYSICS

W. NAZAREWICZ

Department of Physics and Astronomy, The University of Tennessee, Knoxville, Tennessee 37996

Institute of Theoretical Physics, Warsaw University, ul. Hoża 69, PL-00681, Warsaw, Poland

Physics Division, Oak Ridge National Laboratory, P.O. Box 2008, Oak Ridge, Tennessee 37831

Structure of exotic radioactive nuclei having extreme neutron-to-proton ratios is different from that around the stability line. Those nuclei are crucial astrophysically; they pave the highway along which the nuclear material is transported up in the proton and neutron numbers during the complicated synthesis processes in stars. Their structure is also crucial for our understanding of how the stars tick. This short review discusses the progress in microscopic nuclear modeling relevant to nuclear astrophysics.

1. Introduction

The goal of nuclear structure theory is to build a unified microscopic framework in which bulk nuclear properties (including masses, radii, and moments, structure of nuclear matter), nuclear excitations (including a variety of collective phenomena), and nuclear reactions can all be described. While this goal is extremely ambitious, it is no longer a dream. Indeed, hand in hand with developments in radioactive nuclear beam (RNB) experimentation, a qualitative change in theoretical modeling is taking place. Due to the influx of new ideas and the progress in computer technologies and numerical algorithms, nuclear theorists have been quite successful in solving various pieces of the nuclear puzzle. In addition to nuclear structure interest, the nuclear "Terra Incognita" is important for astrophysics and cosmology. Since radioactive nuclei are produced in many astrophysical sites, knowledge of their properties is crucial to the understanding of the underlying processes.

During recent years, we have witnessed substantial progress in many areas of theoretical nuclear structure. The Effective Field Theory (EFT) has

enabled us to construct high-quality NN and NNN bare interactions consistent with the chiral symmetry of QCD[1,2]. New effective interactions in the medium have been developed that, together with a powerful suite of *ab-initio* approaches, provide a quantitative description of light nuclei[3,4,5,6,7]. For heavy systems, *global* modern shell-model approaches[8,9,10,11] and self-consistent mean-field methods[12,13,14] offer a level of accuracy typical of phenomenological approaches based on parameters *locally* fitted to the data. By exploring connections between models in various regions of the chart of the nuclides, nuclear theory aims to develop a comprehensive theory of the nucleus across the entire nuclear landscape.

From a theoretical point of view, short-lived exotic nuclei far from stability offer a unique test of those aspects of the many-body theory that depend on the isospin degrees of freedom[15]. The challenge to microscopic theory is to develop methodologies to reliably calculate and understand the origins of unknown properties of new physical systems, physical systems with the same ingredients as familiar ones but with totally new and different properties.

2. The Territory of Nucleonic Matter

Figure 1 shows the vast territory of various domains of nuclear matter characterized by the neutron excess, $(N-Z)/A$, and the isoscalar nucleonic density ($\rho = \rho_n + \rho_p$). In this diagram, the region of finite (i.e., particle-bound) nuclei extends from the neutron excess of about -0.2 (proton drip line) to 0.5 (neutron drip line).

The very neutron-rich drip-line nuclei cannot be reached experimentally under present laboratory conditions. On the other hand, these systems are the building blocks of the astrophysical r-process; their separation energies, decay rates, and neutron capture cross sections are the basic quantities determining the results of nuclear reaction network calculations. The link between RNB physics and astrophysics runs even deeper than this since, as indicated in Fig. 1, the study of neutron-rich nuclei provides the tools for understanding physics of such important objects as neutron stars and the physics of nuclear phase evolution in the realm of extreme densities.

3. Towards the Universal Nuclear Energy Density Functional

For medium-mass and heavy nuclei, a critical challenge is the quest for the universal energy density functional, which will be able to describe properties

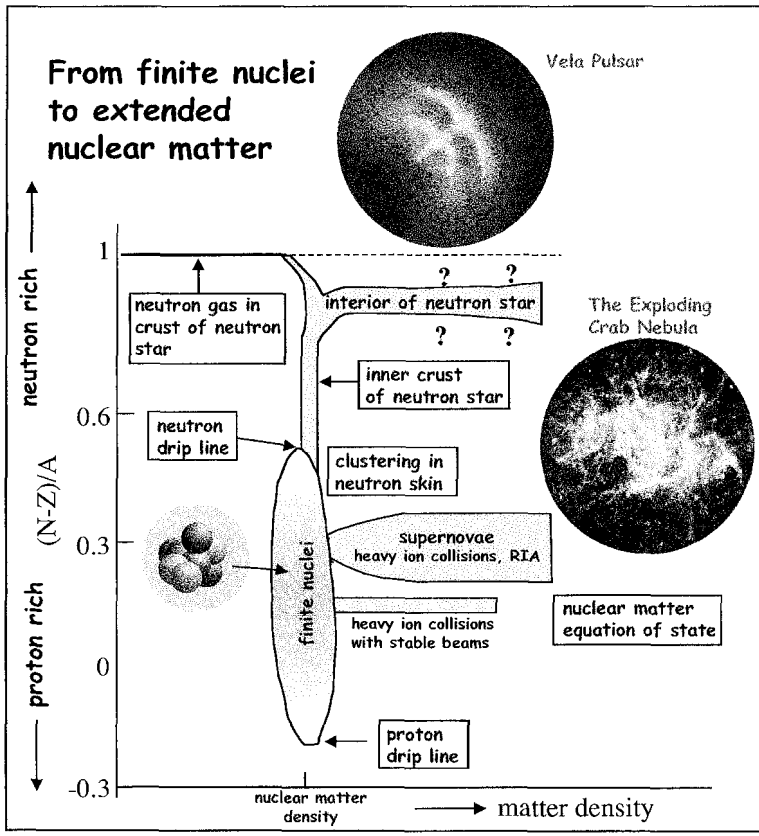

Figure 1. Diagram illustrating the range of nucleonic densities and neutron excess of importance in various contexts of the low- and intermediate-energy nuclear many-body problem. The territory of various domains of nucleonic matter is characterized by the neutron excess and the nucleonic density. The full panoply of bound nuclei comprises the vertical ellipse. Densities accessible with different reactions, and the properties of neutron star layers, are indicated. The new-generation RNB facilities will provide a unique capability for accessing very neutron-rich nuclei – our best experimentally accessible proxies for the bulk neutron-rich matter in the neutron star crust. They will also enable us to compress neutron-rich matter in order to explore the nuclear matter equation of state – essential for the understanding of supernovae and neutron stars. (Based on Ref. [16].)

of finite nuclei (static properties, collective states, large-amplitude collective motion) as well as extended asymmetric nucleonic matter (e.g., as found

in neutron stars). Self-consistent methods based on the density functional theory (DFT) have already achieved a level of sophistication and precision which allows analyses of experimental data for a wide range of properties and for arbitrarily heavy nuclei. For instance, self-consistent Hartree-Fock (HF) and Hartree-Fock-Bogoliubov (HFB) models are now able to reproduce measured nuclear binding energies with an impressive rms error of $\sim$700 keV[12,17,18]. However, much work remains to be done. Developing a universal nuclear density functional will require a better understanding of the density dependence, isospin effects, and pairing, as well as an improved treatment of symmetry-breaking effects and many-body correlations.

3.1. *Density Functional Theory and Skyrme HFB*

The density functional theory[19,20] has been an extremely successful approach for the description of ground-state properties of bulk (metals, semiconductors, and insulators) and complex (molecules, proteins, nanostructures) materials. It has also been used with great success in nuclear physics[21,22,23,24]. The main idea of DFT is to describe an interacting system of fermions via its densities and not via its many-body wave function. The energy of the many body system can be written as a density functional, and the ground state energy is obtained through the variational procedure.

The nuclear energy density functional appears naturally in the Skyrme-HFB theory[25,26], or in the local density approximation (LDA)[23,27], in which the functional depends only on local densities, and on local densities built from derivatives up to the second order. In practice, a number of local densities are introduced: nucleonic densities, kinetic densities, spin densities, spin-kinetic densities, current densities, tensor-kinetic densities, and spin-current densities. If pairing correlations are considered, the number of local densities doubles since one has to consider both particle and pairing densities.

In the case of the Skyrme effective interaction, as well as in the framework of the LDA, the energy functional is a three-dimensional spatial integral of local energy density that is a real, scalar, time-even, and isoscalar function of local densities and their first and second derivatives. In the case of no proton-neutron mixing, the construction of the most general energy density that is quadratic in one-body local densities can be found in Ref.[28]. With the proton-neutron mixing included, the construction can be performed in an analogous manner[29].

3.2. *From Finite Nuclei to Bulk Nucleonic Matter*

In the limit of the infinite nuclear matter, the density functional is reduced to the nuclear equation of state (EOS). The EOS plays a central role in nuclear structure and in heavy-ion collisions. It also determines the static and dynamical behavior of stars, especially in supernova explosions and in neutron star stability and evolution. Unfortunately, our knowledge of the EOS, especially at high densities and/or temperatures, is very poor. Many insights about the density dependence of the EOS, in particular the density dependence of the symmetry energy, can be obtained from microscopic calculations of neutron matter using realistic nucleon-nucleon forces[30,31,32]. Those results will certainly be helpful when constraining realistic energy density functionals. Another constraint comes from measurements of neutron skin and radii[33,34]. Recently, a correlation between the neutron skin in heavy nuclei and the derivative of the neutron equation of state has been found[35,34,36], which provides a way of giving a stringent constraint on the EOS if the neutron radius of a heavy nucleus is measured with sufficient accuracy.

Unfortunately, the theoretical knowledge of EOS of pure neutron matter is poor; the commonly used energy-density functionals give different predictions for neutron matter. Figure 2 illustrates difficulties with making theoretical extrapolations into neutron-rich territory. It shows the two-neutron separation energies for the even-even Sn isotopes calculated in several microscopic models based on different effective interactions. Clearly, the differences between forces are greater in the neutron-rich region than in the region where masses are known. Therefore, the uncertainty due to the largely unknown isospin dependence of the effective force (in both particle-hole and particle-particle channels) gives an appreciable theoretical "error bar" for the position of the drip line. Unfortunately, the results presented in Fig. 2 do not tell us much about which of the forces discussed should be preferred since one is dealing with dramatic extrapolations far beyond the region known experimentally. However, a detailed analysis of the force dependence of results may give us valuable information on the relative importance of various force parameters.

Another serious difficulty when extrapolating from stable nuclei to the neutron-rich territory and to extended nuclear matter is due to the diffused neutron surface in neutron-rich nuclei. As discussed in Ref. [37], the nuclear surface cannot simply be regarded as a *layer of nuclear matter at low density*. In this zone the gradient terms are as important in defining the energy

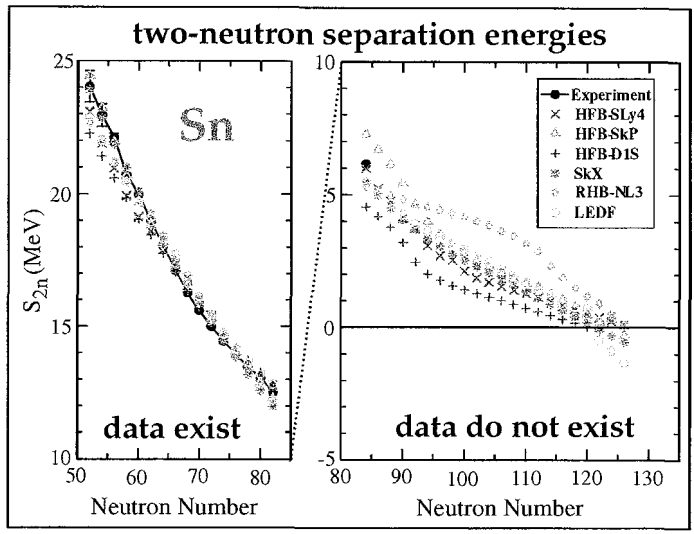

Figure 2. Predicted two-neutron separation energies for the even-even Sn isotopes using several microscopic models based on effective nucleon-nucleon interactions and obtained with phenomenological mass formulas (shown in the inset at top right).

relations as those depending on the local density.

3.3. *Microscopic Mass Table*

Microscopic mass calculations require a simultaneous description of particle-hole, pairing, and continuum effects – the challenge that only very recently could be addressed by mean-field methods. A new development[14] is the solution of deformed HFB equations by using the local-scaling point transformation[38,39]. A representative example of deformed HFB calculations, recently implemented using the parallel computational facilities at ORNL, is given in Fig. 3. By creating a simple load-balancing routine that allows one to scale the problem to 200 processors, it was possible to calculate the entire deformed even-even mass table in a single 24 wall-clock hour run (or approximately 4,800 processor hours).

Future calculations will take into account a number of improvements, including (i) implementation of the exact particle number projection before variation[40]; (ii) better modeling of the density dependence of the effective interaction by considering corrections beyond the mean-field and three-

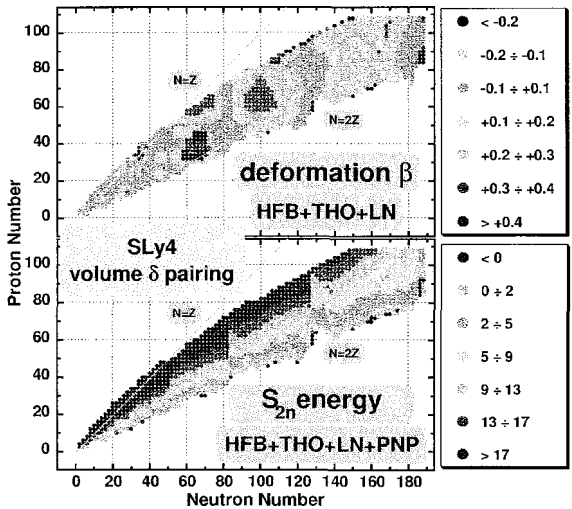

Figure 3. Quadrupole deformations β (upper panel) and two-neutron separation energies S_{2n} in MeV (lower panel) of particle-bound even-even nuclei calculated within the HFB+THO method with Lipkin-Nogami correction followed by exact particle number projection. The Skyrme SLy4 interaction and volume contact pairing were used. (From Ref. [14].)

body effects[41], the surface-peaked effective mass[42,18], and better treatment of pairing[37]; (iii) proper treatment of the time-odd fields[43]; and (iv) inclusion of dynamical zero-point fluctuations associated with the nuclear collective motion[44,45,46]. As far as the density dependence is concerned, many insights can be obtained from the EFT[47]. The resulting universal energy density functional will be fitted to nuclear masses, radii, giant vibrations, and other global nuclear characteristics.

These microscopic mass calculations are also important for providing the proper input for studies of nuclear decays and excited states within the quasiparticle random phase approximation (QRPA). The recent QRPA work includes investigations of the Gamow-Teller strength in r-process nuclei[48,43,49] and studies of exotic isocalar dipole vibrations and pygmy modes[50,51,52]. The QRPA formalism can also be used to calculate the competition between the low-energy E1 strength and radiative neutron capture for r-process nuclei[53] and neutrino and electron capture rates[54,55].

4. Continuum Shell Model

The major theoretical challenge in the microscopic description of nuclei, especially weakly bound ones, is the rigorous treatment of both the many-body correlations and the continuum of positive-energy states and decay channels. The importance of continuum for the description of resonances is obvious. Weakly bound states cannot be described within the closed quantum system formalism since there always appears a virtual scattering into the continuum phase space involving intermediate scattering states. The consistent treatment of continuum in multi-configuration mixing calculations is the domain of the continuum shell model (CSM) (see Ref.[56] for a review). In the following, we briefly mention one recent development in the area of the CSM, the so-called Gamow Shell Model.

4.1. *Gamow Shell Model*

Recently, the multiconfigurational CSM in the complete Berggren basis, the so-called Gamow Shell Model (GSM), has been formulated[57,58,59,60]. The single-particle basis of GSM is given by the Berggren ensemble[61] which contains Gamow states (or resonant states and the non-resonant continuum). The resonant states are the generalized eigenstates of the time-independent Schrödinger equation which are regular at the origin and satisfy purely outgoing boundary conditions. They correspond to the poles of the S matrix in the complex energy plane lying on or below the positive real axis.

There exist several completeness relations involving resonant states[62]. In the heart of GSM is the Berggren completeness relation:

$$\sum_n |u_n\rangle\langle\tilde{u}_n| + \int_{L_+} |u_k\rangle\langle\tilde{u}_k| dk = 1 \quad , \tag{1}$$

where $|u_n\rangle$ are the Gamow states (both bound states and the decaying resonant states lying between the real k-axis and the complex contour L_+) and $|u_k\rangle$ are the scattering states on L_+. As a consequence of the analytical continuation, the resonant states are normalized according to the squared radial wave function and not to the modulus of the squared radial wave function. In practical applications, one has to discretize the integral in (1). Such a discretized Berggren relation is formally analogous to the standard completeness relation in a discrete basis of L^2-functions and, in the same way, leads to the eigenvalue problem $H|\Psi\rangle = E|\Psi\rangle$. However, as the formalism of Gamow states is non-hermitian, the matrix H is complex symmetric.

In the shell-model calculations with Gamow states, the angular momentum and isospin algebra do not change in the GSM. However, expectation values of operators in the many-body GSM states have both real and imaginary parts. As discussed in Refs.[63,64,65], the imaginary part gives the uncertainty of the average value. It is also worth noting that, in most cases, the real part of the matrix element is influenced by the interference with the non-resonant background.

Contrary to the traditional shell model, the effective interaction of GSM cannot be represented as a single matrix calculated for all nuclei in a given region. The GSM Hamiltonian contains a real, effective two-body force expressed in terms of space, spin, and isospin coordinates. The matrix elements involving continuum states are strongly system-dependent, and they fully take into account the spatial extension of s.p. wave functions.

In the first applications of the GSM, a schematic zero-range surface delta force was taken as a residual interaction. As a typical example, the calculated level scheme of ^{19}O is displayed in Fig. 4 together with the selected E2 transition rates. It is seen that the electromagnetic transition rates involving unbound states are complex.

The first applications of the GSM to the oxygen, lithium, and helium isotopes look very promising[57,58,66]. The beginning stages of a broad research program has begun which involves applications of GSM to halo nuclei, particle-unstable nuclear states, reactions of astrophysical interest, and a variety of nuclear structure phenomena. The important step will be to develop effective finite-range interactions to be used in the GSM calculations. One would also like to optimize the path of integration representing the non-resonant continuum.

5. Conclusions

The main objective of this presentation was to discuss the opportunities in nuclear structure that have been enabled by studies of exotic nuclei with extreme neutron-to-proton ratios. New-generation data will be crucial in pinning down a number of long-standing questions related to the effective Hamiltonian, nuclear collectivity, and properties of nuclear excitations.

One of the major challenges for nuclear theory is to develop the "universal" nuclear energy density functional that will describe properties of finite nuclei as well as extended asymmetric nucleonic matter as found in neutron stars. Another major task is to tie nuclear structure directly to nuclear reactions within a coherent framework applicable throughout the

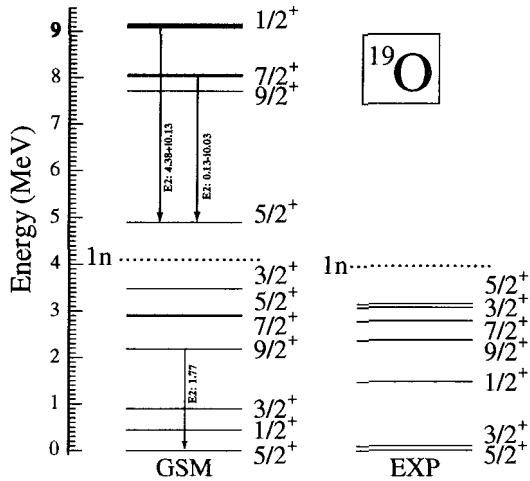

Figure 4. The GSM level scheme of ^{19}O calculated in the full *sd* space of Gamow states and employing the discretized (10 points) $d_{3/2}$ non-resonant continuum. The dashed lines indicate experimental and calculated one-neutron emission thresholds. As the number of states becomes large above the one-neutron emission threshold, only selected resonances are shown. Selected E2 transitions are indicated by arrows and the calculated E2 rates (all in W.u.) are given (from Ref. [58]).

nuclear landscape. From the nuclear structure perspective, the continuum shell model is the tool of choice that will be able to describe new phenomena in discrete/continuum spectroscopy of exotic nuclei.

Finally, it is important to recognize that solving the nuclear many-body problem also entails extensive use of modern parallel computing systems and the development of powerful new computational algorithms both for nuclear structure calculations and for modeling cataclysmic stellar explosions. Thus, a three-way synergy exists among the many-body problem, astrophysics, and computational science.

Acknowledgments

This work was carried out in collaboration with Jacek Dobaczewski, Nicolas Michel, Marek Płoszajczak, and Mario Stoitsov. This work was supported in part by the U.S. Department of Energy under Contract Nos. DE-FG02-96ER40963 (University of Tennessee) and DE-AC05-00OR22725 with UT-Battelle, LLC (Oak Ridge National Laboratory), by the Polish Committee

for Scientific Research (KBN), and by the National Science Foundation Contract No. 0124053 (U.S.-Japan Cooperative Science Award).

References

1. D.R. Entem and R. Machleidt, Phys. Rev. C **68**, 041001 (2003).
2. W. Gloeckle et al., nucl-th/0312063.
3. S.C. Pieper, K. Varga, and R.B. Wiringa, Phys. Rev. C **66**, 044310 (2002).
4. R.B. Wiringa and S.C. Pieper, Phys. Rev. Lett. **89**, 182501 (2002).
5. B.R. Barrett, P. Navratil, and J.P. Vary, Nucl. Phys. A **704**, 254c (2002).
6. P. Navratil and W.E. Ormand, Phys. Rev. C **68**, 034305 (2003).
7. K. Kowalski et al., nucl-th/031008.
8. E. Caurier, F. Nowacki, and A. Poves, Eur. Phys. J. A **15**, 145 (2002).
9. M. Honma et al., Phys. Rev. C **65**, 061301 (2002); Nucl. Phys. A **704**, 134c (2002).
10. K. Langanke and G. Martinez-Pinedo, Nucl. Phys. A **704**, 154c (2002).
11. K. Langanke, D.J. Dean, and W. Nazarewicz, Nucl. Phys. A **728**, 109 (2003).
12. S. Goriely et al., Phys. Rev. C **66**, 024326 (2002).
13. M. Bender, P.-H. Heenen, and P.-G. Reinhard, Rev. Mod. Phys. **75**, 121 (2003).
14. M.V. Stoitsov et al., Phys. Rev. C **68**, 054312 (2003).
15. J. Dobaczewski and W. Nazarewicz, Phil. Trans. R. Soc. Lond. A **356**, 2007 (1998).
16. C.J. Pethick and D.G. Ravenhall, Annu. Rev. Nucl. Part. Sci. **45**, 429 (1995).
17. M. Samyn et al., Nucl. Phys. A **700**, 142 (2002).
18. S. Goriely et al., Phys. Rev. C **68**, 054325 (2003).
19. P. Hohenberg and W. Kohn. Phys. Rev. B **76**, 6062 (1964); M. Levy. Proc. Nat. Acad. Sci. **76**, 6062 (1979).
20. W. Kohn and L.J. Sham, Phys. Rev. A **140**, 1133 (1965).
21. A.B. Migdal, *Theory of Finite Fermi Systems and Applications to Atomic Nuclei* (Interscience, New York, 1967).
22. J.W. Negele, Phys. Rev. C **1**, 1260 (1970).
23. J.W. Negele and D. Vautherin, Phys. Rev. C **5**, 1472 (1972).
24. M. Brack and R.K. Bhaduri, *Semiclassical Physics* (Addison Wesley, Reading 1997).
25. T.H.R. Skyrme, Nucl. Phys. **9**, 615 (1959).
26. D. Vautherin and D.M. Brink, Phys. Rev. C **5**, 626 (1972).
27. P. Ring and P. Schuck, *The Nuclear Many-Body Problem* (Springer-Verlag, Berlin, 1980).
28. J.Dobaczewski and J.Dudek, Acta Phys. Pol. **B27**, 45 (1996).
29. E. Perlińska et al., Phys. Rev. C **69**, 014316 (2004).
30. B.A. Friedman and V.R. Pandharipande, Nucl. Phys. A **361**, 502 (1981).
31. J. Morales, V.R. Pandharipande, and D.G. Ravenhall, Phys. Rev. C **66**, 054308 (2002).
32. J. Carlson et al., Phys.Rev. C **68**, 025802 (2003).
33. C. Horowitz and J. Piekarewicz, Phys. Rev. Lett. **86**, 5647 (2001).

34. R.J. Furnstahl, Nucl. Phys. A **706**, 85 (2002).
35. S. Typel and B.A.Brown, Phys. Rev. C **64**, 027302 (2001).
36. A.E.L. Dieperink, D. Van Neck, Y. Dewulf, and V. Rodin, nucl-th/0312012.
37. J. Dobaczewski, W. Nazarewicz, and M. V. Stoitsov, Eur. Phys. J. A **15**, 21 (2002).
38. M.V. Stoitsov, W. Nazarewicz, and S. Pittel, Phys. Rev. C **58**, 2092 (1998).
39. M.V. Stoitsov et al., Phys. Rev. C **61**, 034311 (2000).
40. J.A. Sheikh and P. Ring, Nucl. Phys. A **665**, 71 (2000); J.A. Sheikh et al., Phys. Rev. C **66**, 044318 (2002).
41. T. Duguet and P. Bonche, Phys. Rev. C **67**, 054308 (2003).
42. M. Farine, J.M. Pearson, and F. Tondeur, Nucl. Phys. A **696**, 396 (2001).
43. M. Bender et al., Phys. Rev. C **65**, 054322 (2002).
44. P.-G. Reinhard, Z. Phys. A **285**, 93 (1978).
45. P.-G. Reinhard and K. Goeke, Rep. Prog. Phys. **50**, 1 (1987).
46. P.-G. Reinhard et al., Phys. Rev. C **60**, 014316 (1999).
47. S.J. Puglia, A. Bhattacharyya, and R.J. Furnstahl, Nucl. Phys. A **723**, 145 (2003).
48. J. Engel et al., Phys. Rev. C **60**, 014302 (1999).
49. I.N. Borzov, Phys. Rev. C **67**, 025802 (2003).
50. M. Matsuo, Prog. Theor. Phys. Suppl. **146**, 110 (2002).
51. D. Vretenar et al., Phys. Rev. Lett. **91**, 262502 (2003).
52. N. Paar, P. Ring, T. Niksic, and D. Vretenar, Phys. Rev. C **67**, 034312 (2003).
53. S. Goriely and E. Khan, Nucl. Phys. A **706**, 217 (2002).
54. I.N. Borzov, Nucl. Phys. A **688**, 382c (2001).
55. E. Kolbe, K. Langanke, G. Martinez-Pinedo, and P. Vogel, J. Phys. G **29**, 2569 (2003).
56. J. Okołowicz, M. Płoszajczak, and I. Rotter, Phys. Rep. **374**, 271 (2003).
57. N. Michel et al., Phys. Rev. Lett. **89**, 042502 (2002).
58. N. Michel et al., Phys. Rev. C **67**, 054311 (2003).
59. R. Id Betan et al., Phys. Rev. Lett. **89**, 042501 (2002).
60. R. Id Betan et al., nucl-th/0307060.
61. T. Berggren, Nucl. Phys. A**109**, 265 (1968).
62. P. Lind, Phys. Rev. C **47**, 1903 (1993).
63. T. Berggren, Phys. Lett. B **373**, 1 (1996).
64. C.G. Bollini et al., Phys. Lett. B **382**, 205 (1996).
65. O. Civitarese, M. Gadella, and R.I. Betan, Nucl. Phys. A **660**, 255 (1999).
66. N. Michel et al., Proc. XXVII Symposium on Nuclear Physics, Jan. 5-8, 2004, Taxco, Guerrero, Mexico; nucl-th/0401036 .

THEORETICAL MODELS FOR NUCLEAR ASTROPHYSICS

PIERRE DESCOUVEMONT

Physique Nucléaire Théorique et Physique Mathématique, C.P. 229,
Université Libre de Bruxelles, B-1050 Brussels, Belgium
Email: pdesc@ulb.ac.be

We review and compare some theoretical models used in nuclear astrophysics: the R-matrix method, the DWBA method, and microscopic cluster models. Applications are presented. The R-matrix theory is illustrated by results of a recent compilation of reactions involved in the Big-Bang nucleosynthesis. The DWBA method is tested with the ^{13}C(α,n)^{16}O reaction, and is shown to be quite sensitive to the conditions of the calculation. Finally, we apply a microscopic model to the ^{7}Be(p,γ)^{8}B reaction, and update previous results obtained within this framework.

1. Introduction

Nuclear astrophysics plays a crucial role in the understanding of nucleosynthesis in the universe [1]. Nuclear reactions determine stellar evolution and are the major energy source in stars. Current modelisations of star evolution require a very large amount of data, which remains a challenge for nuclear physicists. Experimental investigations meet two main limitations. (*i*) For charged-particle reactions, relevant energies are much lower than the Coulomb barrier, which makes the cross sections too small to be measured. Recent technological developments allow measurements at stellar energies for some reactions with low charges, such as ^{3}He(^{3}He,2p)α [2], but for most important reactions the experimental lower limit is far above the Gamow energy. (*ii*) Investigations of explosive burning are fairly sensitive to reactions involving unstable nuclei. Development of radioactive ion beams [3] in many laboratories provides useful information on such reactions, but much work remains to be carried out, more especially for the rp-process which runs through the proton-rich unstable region.

In view of these limitations, theoretical models of nuclear reactions appear to be a necessary complement to experimental studies. Theoretical calculations can be done at any energy, and are not restricted by instability of the nuclei. However, they face many other problems. Transfer

and radiative-capture reactions involved in stellar nucleosynthesis are often difficult to treat, and no systematics can be applied. It is of course impossible for any model to cover the thousands of reactions involved in modern codes of stellar evolution. However, a limited number of reactions, especially in the low-mass range, play a major role, and deserve special attention. Typical examples are ^{7}Be(p,γ)^{8}B for the solar-neutrino problem [4], ^{12}C(α, γ)^{16}O for He burning [1], or ^{22}Ne(α,n)^{25}Mg in the *s* process [5]. Here we review different models often used in low-energy reactions [6].

2. Theoretical models

2.1. *General discussion*

Theoretical models can be roughly classified in three categories:

(*i*) Models involving adjustable parameters, such as the *R*-matrix [7] or the *K*-matrix [8] methods; parameters are fitted to the available experimental data and the cross sections are extrapolated down to astrophysical energies. These fitting procedures of course require the knowledge of data, which are sometimes too scarce for a reliable extrapolation.

(*ii*) "Ab initio" models, where the cross section is determined from the wave functions of the system. The potential model [9], the Distorted Wave Born Approximation (DWBA) [10], and microscopic models [11] are, in principle, independent of experimental data. More realistically, these models depend on some physical parameters, such as a nucleus-nucleus or a nucleon-nucleon interaction which can be reasonably determined from experiment only. The microscopic Generator Coordinate Method (GCM) provides a "basic" description of a *A*-nucleon system, since the whole information is obtained from a nucleon-nucleon interaction. Since this interaction is nearly the same for all light nuclei, the predictive power of the GCM is important.

(*iii*) Models (*i*) and (*ii*) can be used for low level-density nuclei only. This condition is fulfilled in most of the reactions involving light nuclei ($A \leq 20$). However when the level density near the threshold is large (i.e. more than a few levels per MeV), statistical models are better adapted. Statistical models, such as the Hauser-Feschbach theory [12] can be used in a systematic way, but are not expected to provide more than a rough estimate of the reaction rates.

2.2. *The R-matrix method*

Owing to the very low cross sections, one of the main problems in nuclear astrophysics is to extrapolate the available data down to stellar energies[1,6].

Several models, such as the potential model or microscopic approaches, are widely used for that purpose. However, they are in general not flexible enough to account for the data with a high accuracy. A simple way to extrapolate the data is to use a polynomial approximation as, for example, in Ref.[13]. This is usually used to investigate electron screening effects, where the cross section between bare nuclei is derived from a polynomial extrapolation of high-energy data. This polynomial approximation, although very simple, is not based on a rigorous treatment of the energy dependence of the cross section. In the R-matrix method, the energy dependence of the cross sections is obtained from Coulomb functions, as expected from the Schrödinger equation. The goal of the R-matrix method [7] is to parameterize some experimentally known quantities, such as cross sections or phase shifts, with a small number of parameters, which are then used to extrapolate the cross section down to astrophysical energies.

The R-matrix framework assumes that the space is divided into two regions: the internal region (with radius a), where the nuclear force is important, and the external region, where the interaction between the nuclei is governed by the Coulomb force only. Although the R-matrix parameters do depend on the channel radius a, the sensitivity of the cross section with respect to its choice is quite weak. The physics of the internal region is parameterized by a number N of poles, which are characterized by energy E_λ and reduced width $\tilde{\gamma}_\lambda$. In a multichannel problem, the R-matrix at energy E is defined as

$$R_{ij}(E) = \sum_{\lambda=1}^{N} \frac{\tilde{\gamma}_{\lambda i}\tilde{\gamma}_{\lambda j}}{E_\lambda - E}, \tag{1}$$

which must be given for each partial wave J. Indices i and j refer to the channels. For the sake of simplicity we do not explicitly write indices $J\pi$ in the R matrix and in its parameters.

Definition (1) can be applied to resonant as well as to non-resonant partial waves. In the latter case, the non-resonant behavior is simulated by a high-energy pole, referred to as the background contribution, which makes the R-matrix nearly energy independent. The pole properties (E_λ, $\tilde{\gamma}_{\lambda i}$) are associated with the physical energy and width of resonances, but not strictly equal. This is known as the difference between "formal" parameters (E_λ, $\tilde{\gamma}_{\lambda,i}$) and "observed" parameters (E_λ^r, $\gamma_{\lambda,i}$), deduced from experiment. In a general case, involving more than one pole, the link between those two sets is not straightforward; recent works [14,15] have established a general formulation to deal with this problem.

We illustrate here the R-matrix formalism with a compilation of reactions involved in Big-Bang nucleosynthesis [16]. Recent work has been focusing on primordial nucleosynthesis and on its sensitivity with respect to nuclear reaction rates [17,18,13,19,20]. In these papers, the nuclear reaction rates are either reconsidered by the authors themselves [13], or taken from specific works [20] such as the Caltech [21] or NACRE [22] compilations. The goals of the present work are multiple. First, we analyze low-energy cross sections in the R-matrix framework which provides a more rigorous energy dependence, based on Coulomb functions. This approach is more complicated than those mentioned above, and could not be considered for broad compilations covering many reactions [21,22]. However, the smaller number of reactions involved in Big Bang nucleosynthesis makes the application of the R-matrix feasible. A second goal of our work is a careful evaluation of the uncertainties associated with the cross sections and reaction rates. The results are given in Ref.[16]. In Figs. 1 and 2 we show the S-factors derived in the R-matrix formalism for the ^{3}He(d,p)^{4}He and ^{7}Li(p,α)α reactions. The new reaction rates have been applied to improve Standard Big Bang Nucleosynthesis calculations by using a Monte–Carlo technique[23].

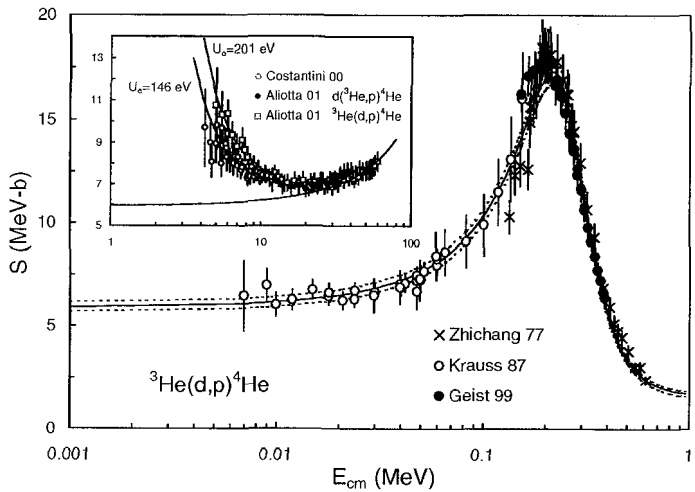

Figure 1. ^{3}He(d,p)^{4}He S factor. See Ref.[16] for the data. The insert shows the influence of electron screening with screening potential U_e (energies are given in keV). Dashed curves represent 1σ uncertainties.

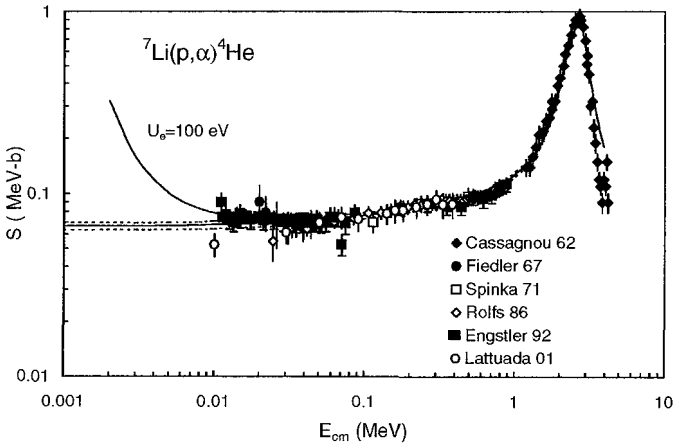

Figure 2. ^{7}Li(p,α)α S factor (see caption of Fig. 1). See Ref.[16] for the data.

2.3. *The DWBA method*

The Distorted Wave Born Approximation (DWBA) method is widely used in nuclear physics and in nuclear astrophysics [24]. It essentially deals with transfer reactions and relies upon the knowledge of nucleus-nucleus potentials in the entrance and exit channels, as well as of the spectroscopic factors of the colliding nuclei.

The main disadvantage of the DWBA is the need for parameters which are poorly known, or not known at all. This essentially occurs in reactions involving radioactive nuclei where the nucleus-nucleus potentials should be adapted from neighboring reactions. In addition, the spectroscopic factors are expected to be somewhat dependent on the potentials.

The aim of this work (see Ref.[25]) is to test the DWBA with the ^{13}C(α,n)^{16}O reaction, which plays an important role in nuclear astrophysics (see Ref. [26]). We compare the DWBA with a microscopic cluster model [27]. Our goal here is not to provide an optimized DWBA analysis, but to test its precision and sensitivity through a comparison with a previous microscopic study [28]. In Ref. [28], the cluster model was shown to provide a fair description of the available cross sections; it also pointed out the importance of the $1/2^+_2$ subthreshold state in ^{17}O. We apply the DWBA with conditions of the calculation as close as possible to those of the microscopic model. In

other words, the α+^{13}C and n+^{16}O potentials are fitted on the microscopic phase shifts, and the spectroscopic factors are taken from the model. The ^{13}C+α and ^{16}O+n phase shifts are given in Fig. 3.

The transition amplitude ϵ is then determined for some typical partial waves. We have chosen here $J^\pi = 1/2^+, 1/2^-$ and $3/2^-$, which present different behaviors: the $1/2^+$ partial wave involves a subthreshold state, $1/2^-$ a broad resonance near 2 MeV, and $3/2^-$ is non-resonant. The partial waves are chosen as a representative set of conditions occurring in low-energy reactions. We assume that the ^{13}C(α,n)^{16}O reaction proceeds through an exchange mechanism. The external neutron of ^{13}C and the incident α particle are exchanged during the collision.

The transition amplitudes ϵ are given in Fig. 4. In order to remove the strong energy dependence occurring at subcoulomb energies, we have divided ϵ by the penetration factor $\exp(-\pi\eta)$, where η is the Sommerfeld parameter. Figure 4 shows that the DWBA does reproduce the energy dependence. This is not surprising since the energy dependence is mainly given by the wave functions in the entrance channel, which are derived from a phase-equivalent potential. The normalization, however, is somewhat different. The DWBA overestimates the reference calculation. The overestimation factor is about 4 for $J = 1/2^-$ and 2 for $J = 3/2^-$. For $J = 1/2^+$, the low-energy part is essentially determined by the properties of the $1/2^+$ subthreshold state, which yield the low-energy enhancement.

One of the main goals of the present work is to evaluate the sensitivity of the DWBA against some inputs. As a first test, we have replaced the harmonic-oscillator wave functions of ^{13}C and ^{16}O by more realistic functions, deduced from a potential model. This approach is not fully consistent with the microscopic model, but provides an interesting way to evaluate the DWBA stability. We have used single-Gaussian potentials with the parameters fitted to the experimental binding energies (-4.95 MeV for ^{12}C+n and -7.16 MeV for ^{12}C+α). Two different sets have been used. Fig. 4 shows that the transition amplitude is rather sensitive to the ^{13}C and ^{16}O wave functions. These wave functions are very close to harmonic-oscillator functions, corresponding to the microscopic model, but the long-range part presents a more physical behavior, and slight changes in the inner part have a non-negligible effect on the transition amplitude.

A further test of the sensitivity of the DWBA has been carried out by replacing the ^{13}C+α and ^{16}O+n potentials by their supersymmetric partners. The supersymmetric transform [29] keeps the phase shifts unchanged, but deep potentials are replaced by equivalent potentials presenting a repul-

sive core. The corresponding wave functions do not have nodes associated with the forbidden states [29]. The results are shown in Fig. 4, where we find out that the DWBA is much closer to the microscopic results. The DWBA appears to be quite sensitive to the description of the scattering wave functions (up to a factor of 20 for $J^\pi = 1/2^-$), although the phase shifts are identical.

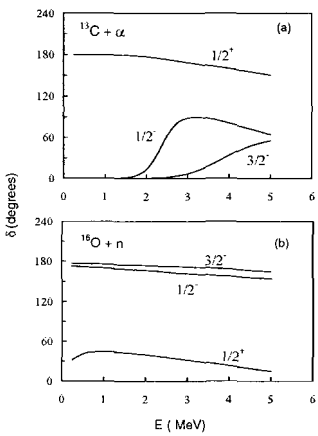

Figure 3. Microscopic α+^{13}C (a) and n+^{16}O (b) phase shifts.

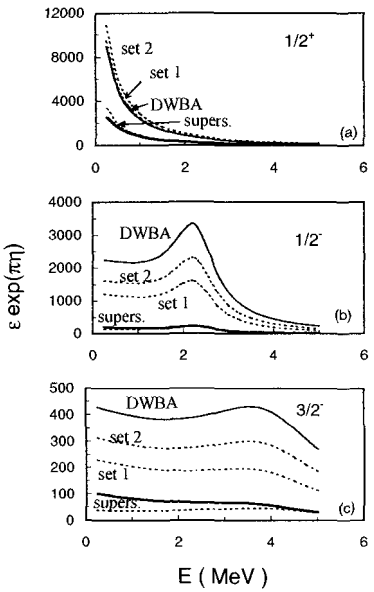

Figure 4. Transition amplitudes obtained in the exchange approximation for $J = 1/2^+$ (a), $J = 1/2^-$ (b), and $J = 3/2^-$ (c). Thick curves: reference microscopic calculation, solid curves: DWBA calculation, dotted curves: DWBA calculation with modifications of the conditions of the calculation (see text).

The conclusion drawn from this work is twofold. On one hand, the DWBA method turns out to be very sensitive to the conditions of the calculations: choice of the nucleus-nucleus potentials and, to a lesser extent, of the wave functions of the colliding nuclei. This sensitivity is due to

very basic properties, i.e. the short-range character of the DWBA matrix elements, which are quite sensitive to details of the wave functions. On the other hand, the difference between the DWBA and the reference microscopic method can be fairly large, and varies with angular momentum. This is most likely due to antisymmetrization effects which are approximately included in the DWBA through the choice of deep nucleus-nucleus potentials. This property should also occur in other systems and suggests that the DWBA method can only provide transfer cross sections with a non-negligible uncertainty.

2.4. *Microscopic models*

The information is derived from a A-body Hamiltonian

$$H = \sum_{i=1}^{A} T_i + \sum_{i<j}^{A} V_{ij} \tag{2}$$

where T_i is the kinetic energy of nucleon i, and V_{ij} a nucleon-nucleon interaction. In the cluster approximation, the wave functions are defined from the cluster wave functions ϕ_1 and ϕ_2 of the colliding nuclei. The total wave function reads, in a schematic notation

$$\Psi = \mathcal{A}\,\phi_1\,\phi_2\,g(\boldsymbol{\rho}) \tag{3}$$

where $g(\boldsymbol{\rho})$ is the relative function depending on the relative coordinate $\boldsymbol{\rho}$; it is determined from the Schrödinger equation. In (3), $\mathcal{A}$ is the antisymmetrization operator which ensures the Pauli principle to be satisfied. Projection over good quantun numbers is performed exactly. The reliability on the model mostly depends on the accuracy of the internal wave functions ϕ_1 and ϕ_2. Many efforts have been done to go beyond the simple shell model approximation: multicluster description [30], monopole distortion [31] and extended shell model developments [32] aim at improving the definition (3). Microscopic models are however uneasy to handle and require much computer time.

Here we illustrate microscopic models with the ^{7}Be(p,γ)^{8}B S-factor, which plays a crucial role in the solar-neutrino problem [4]. Many direct as well as indirect measurements have been performed in order to reduce the uncertainties on the S-factor at zero energy (see Ref.[33] for an overview). As a high precision is required for $S(0)$, the extrapolation down to astrophysical energies should be done very carefully. Current experiments are performed in a limited energy range, which requires the use of a theoretical

model to derive $S(0)$. The reliability of the model can be tested in the energy range where data exist, which provides some "confidence level" on the extrapolation. In most experiments, a microscopic cluster model [34] (hereafter referred to as DB94) is used for the extrapolation. This model takes account of the ^{7}Be deformation, of inelastic and rearrangement channels, and has been tested with spectroscopic properties of ^{8}B and ^{8}Li, as well as with the ^{7}Li(n,γ)^{8}Li mirror cross section.

The calculation of DB94 presents two shortcomings. First the ^{7}Be nucleus is assumed to be "frozen" during the collision. In other words, a single generator coordinate R_2 was used (see Fig. 5). On the other hand, the nucleon-nucleon interaction is the Volkov force (V2, Ref.[35]) only. These approximations are quite reasonable, but the $S(0)$ value of DB94 is 29 eV.b, which is significantly larger than current values. Although the main output of DB94 is the energy dependence, the conditions should be questioned owing to the high accuracy needed for the ^{7}Be(p,γ)^{8}B reaction. This prompted us to improve DB94 by allowing ^{7}Be to be distorted: the ^{7}Be nucleus is described here by five R_2 values (see Fig. 5). The ^{7}Be($3/2^-, 1/2^-, 7/2^-, 5/2^-$)+p and ^{5}Li+^{3}He channels are included. In addition, the analysis is complemented by the use of the Minnesota force (MN, ref. [36]), known to be better adapted to low-mass systems. We have computed spectroscopic properties of ^{8}B, which do not significantly differ from DB94.

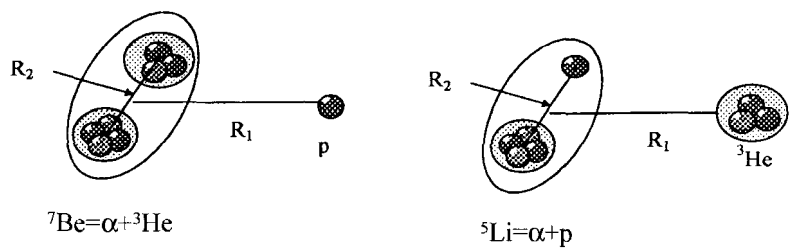

Figure 5. Three-cluster configuration of ^{8}B.

The ^{7}Be(p,γ)^{8}B S-factor is shown in Fig. 6 (non-resonant E1 component only). The role of the ^{7}Be distortion is illustrated by comparing DB94 with the present V2 result: the amplitude is reduced by 10%. With the MN force

we have, without any renormalization, $S(0) = 23$ eV.b.

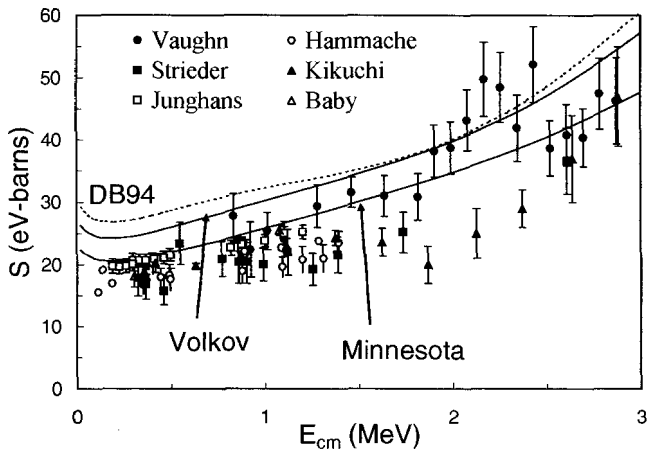

Figure 6. ^{7}Be(p,γ)^{8}B S-factor (E1 term) with data from refs. [37,38,39,40,41,42]. The results of DB94 are shown as a dashed line.

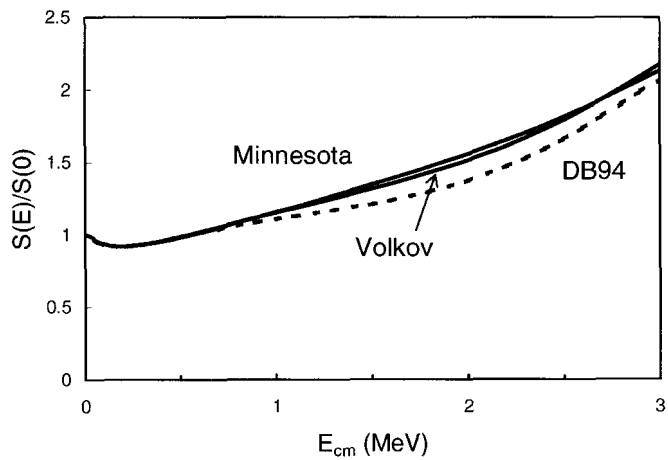

Figure 7. ^{7}Be(p,γ)^{8}B S-factor (E1 contribution) normalized at $E = 0$.

As discussed in DB94, a cluster model provides an upper bound of

the capture cross section. The "exact" ^{8}B wave function should contain many other configurations (other arrangements, 4 clusters, 5 clusters, etc.). Accordingly, the capture cross section which, up to the electromagnetic operator, is nothing but the overlap between the initial ^{7}Be+p and final ^{8}B wave functions, is in general overestimated by a cluster model. This overestimation factor decreases as the model is improved.

Even if the present MN calculation provides a significant improvement with respect to DB94, it is likely that the energy dependence is still more accurate than the normalization. Figure 7 shows the energy dependence, normalized to zero energy. The new calculations with V2 and MN are almost undistinguishable; below 0.6 MeV, DB94 gives the same results. However the difference with DB94 reaches about 10% near 2 MeV; the slope of the S-factor between 1.5 and 3 MeV is weaker than in DB94. Although this modification is minor, it may affect current extrapolations, especially for breakup experiments, usually performed above 1 MeV.

3. Conclusion

In this work, we have tried to give an overview of some models relevant for in nuclear astrophysics. We were only concerned with reactions, without discussing other aspects, such as masses, beta decays, etc. In general, charged-particle induced reactions occur at energies much lower than the Coulomb barrier, and the corresponding cross sections are therefore extremely small. An other characteristic is that there is almost no systematics. In the low-mass region, each reaction presents its own peculiarities and difficulties, in the theoretical as well as in the experimental viewpoints.

We have discussed different theoretical models often used in nuclear astrophysics. The DWBA and R-matrix methods are widely applied in this field; they are fairly simple and well adapted to low-energy reactions. A very impressive amount of work has been devoted to nuclear astrophysics in the last decades. Although most reactions involving light nuclei are sufficiently known, some reactions, such as ^{7}Be(p,γ)^{8}B still require much effort to reach the accuracy needed for stellar models. In the nucleosynthesis of heavy elements (s process, p process), further problems arise from the level densities and the cross sections should be determined from statistical models. A better knowledge of these cross sections represents a challenge for the future.

References

1. C. Rolfs and W.S. Rodney, *Cauldrons in the Cosmos*, University of Chicago Press, 1988.
2. C. Arpasella *et al.*, *Phys. Lett.* **B389**, 452 (1996).
3. J. Vervier, *Nucl. Phys.* **A616**, 97c (1997).
4. J.N. Bahcall *et al.*, *Phys. Lett.* **B433**, 1 (1998); *Astrophys. J.* **555**, 990 (2001).
5. M. Jaeger *et al.*, *Phys. Rev. Lett.* **87**, 202501 (2001)
6. P. Descouvemont, *Theoretical models for nuclear astrophysics*, Nova Science Publishers (New York, 2003).
7. A.M. Lane and R.G. Thomas, *Rev. Mod. Phys.* **30**, 257 (1958).
8. J. Humblet, *Nucl. Phys.* **A187**, 65 (1972).
9. D. Baye and P. Descouvemont, *Ann. Phys.* **165**, 115 (1985).
10. H. Oberhummer and G. Staudt, in "Nuclei in the Cosmos", ed. H. Oberhummer et al., Springer, Berlin, 1991, p.29.
11. P. Descouvemont, *J. Phys.* **G19**, S141 (1993).
12. F.-K. Thielemann, M. Arnould and J.W. Truran, in "Advances in Nuclear Astrophysics", eds. E. Vangioni-Flam *et al.*, 525 (1987).
13. M.S. Smith, L.H. Kawano, and R.A. Malaney, *Astrophys. J. S.* **85**, 219 (1993)
14. C. Angulo and P. Descouvemont, *Phys. Rev.* **C61**, 064611 (2000).
15. C.R. Brune, *Phys. Rev.* **C66**, 044611 (2002).
16. P. Descouvemont, A. Adahchour, C. Angulo, A. Coc and E. Vangioni-Flam, to be published.
17. L.M. Krauss and P. Romanelli, *Astrophys. J.* **358**, 47 (1990).
18. T.P. Walker, G. Steigman, D.N. Schramm, K.A. Olive, and H.-S. Kang, *Astrophys. J.* **376**, 51 (1991).
19. K.M. Nollett and S. Burles, *Phys. Rev.* **D61**, 123505 (2000).
20. R.H. Cyburt, B.D. Fields, and K.A. Olive , *New Astronomy* **6**, 215 (2001).
21. G.R. Caughlan and W.A. Fowler, *At. Data Nucl. Data Tables* **40**, 283 (1988).
22. C. Angulo *et al.*, *Nucl. Phys.* **A656**, 3 (1999).
23. A. Coc, E. Vangioni-Flam, P. Descouvemont, A. Adahchour, and C. Angulo, *Ap. J.*, in press.
24. G.R. Satchler, "Direct Nuclear Reactions", Oxford (1983).
25. A. Adahchour and P. Descouvemont, to be published.
26. S. Kubono *et al.*, *Phys. Rev. Lett.* **90**, 062501 (2003).
27. K. Wildermuth and Y.C. Tang, "A Unified Theory of the Nucleus", ed. by K. Wildermuth and P. Kramer, Vieweg, Braunschweig (1977).
28. P. Descouvemont, *Phys. Rev.* **C36**, 2206 (1987).
29. D. Baye, *Phys. Rev. Lett.* **58**, 2738 (1987).
30. M. Dufour and P. Descouvemont, *Nucl. Phys.* **A605**, 160 (1996).
31. D. Baye and M. Kruglanski, *Phys. Rev.* **C45**, 1321 (1992).
32. P. Descouvemont, *Nucl. Phys.* **A596**, 285 (1996).
33. A.R. Junghans *et al.*, nucl-ex/0308003.
34. P. Descouvemont and D. Baye, *Nucl. Phys.* **A567**, 341 (1994).
35. A.B. Volkov, *Nucl. Phys.* **74**, 33 (1965).
36. D.R. Thompson, M. LeMere, and Y.C. Tang, *Nucl. Phys.* **A286**, 53 (1977).

37. F.J. Vaughn *et al.*, *Phys. Rev.* **C2**, 1657 (1970).
38. F. Hammache *et al.*, *Phys. Rev. Lett.* **80**, 928 (1998); *Phys. Rev. Lett.* **86**, 3985 (2001).
39. T. Kikuchi *et al.*, *Eur. Phys. J.* **A3**, 213 (1998).
40. A.R. Junghans *et al.*, *Phys. Rev. Lett.* **88**, 041101 (2002).
41. F. Strieder *et al.*, *Nucl. Phys.* **A696**, 219 (2001).
42. L.T. Baby *et al.*, *Phys. Rev. Lett.* **90**, 022501 (2003); *Phys. Rev.* **C67**, 065805 (2003).

GLOBAL CALCULATIONS OF FISSION BARRIERS AND BETA-DECAY PROPERTIES OF NEUTRON-RICH NUCLEI

PETER MÖLLER AND ARNOLD J. SIERK

Theoretical Division, Los Alamos National Laboratory, Los Alamos, NM 87544

TAKATOSHI ICHIKAWA AND AKIRA IWAMOTO

Tokai Research Establishment, Japan Atomic Energy Research Institute(JAERI) Tokai-mura, Naka-gun, Ibaraki, 319-11 Japan

Recently we have performed large-scale calculations of fission barriers in the actinide region based on five-dimensional deformation spaces with more than 3 000 000 deformation points for each potential-energy surface. We have determined new model constants. We have also extended our model to axially asymmetric shapes. We apply these techniques to the calculations of fission barriers of heavy nuclei from the line of beta stability to the r-process line. The aim is to study fission near the end of the r-process. We have also extended our model of β-decay so that allowed Gamow-Teller transitions are treated in a quasi-particle random-phase approximation as earlier, but we now also consider first-forbidden transitions in the statistical gross theory. We discuss the properties of this enhanced model and present results of global calculations.

1. Introduction

Relative to other fields of physics, astrophysics is probably unique in its requirement that a very large number of physical environments be modeled to achieve a satisfactory description of the phenomena under study. The dynamics of the cosmos is governed by interactions that span a vast range, from subnucleon, nucleon and nuclear distances to distances affected by the gravitational interaction, which extends over the width of a galaxy and beyond, to the edge of the universe. It is the nuclear processes that provide much of the energy that drives the macroscopic behavior of the cosmos. Through this energy release the behavior on the very small scale is coupled to the very large-scale behavior.

On the nuclear level, cross sections, nuclear decay energies and nuclear decay paths are but a few examples of quantities that are of paramount importance in astrophysical models. Because nuclei of extreme composition,

quite different from what may be studied on earth, exist in stellar environments, an understanding of the nuclear structure properties of these nuclei may only be obtained through theoretical means. This presents a continuing, stimulating challenge to the nuclear-physics community.

In our macroscopic-microscopic approach[1,2] we can calculate a substantial number of nuclear-structure quantities for nuclei from ^{16}O to the heaviest known nuclei and also beyond. Examples of quantities that can be calculated are nuclear ground-state masses, nuclear ground-state shapes, single-particle levels, fission-barrier heights, and β-decay half-lives and β-delayed neutron-emission probabilities. It has been shown that for nuclear-mass-related quantities the model is about as reliable for recently observed nuclei that were not known when the model parameters were determined as it is in the region of nuclei where the model parameters were determined[1,2,3].

In our presentation here we focus on recent developments in the area of fission-barrier calculations and β-decay properties, with a special emphasis on astrophysical applications.

2. Fission-Barrier Studies

In nuclear fission the nucleus evolves from a single ground-state shape into two separated fission fragments. During the shape and configuration changes that occur during this process the total energy of the system initially increases up to a maximum, the fission-barrier height, then decreases. The transition configuration between a single shape and two separated fragments is the *scission* configuration. At this configuration the "neck" radius is zero. Beyond the scission configuration the separated fragments are accelerated by their mutual Coulomb repulsion and reach kinetic energies in the range 150–240 MeV for actinide fission.

Calculations of fission barriers involve the determination of the total nuclear potential energy for different nuclear shapes. Such a calculation defines an energy landscape as a function of a number of shape coordinates. The fission-barrier height is given by the energy relative to the ground state of the most favorable saddle point that has to be traversed when the shape evolves from a single shape to separated fragments. These landscapes are often displayed in terms of energy contour diagrams versus two shape coordinates with one shape coordinate corresponding to elongation and the other to the nuclear neck dimension, for example. However, in contrast to a geographical landscape the fission-energy landscape needs to be analyzed in terms of more than two coordinates. It is a difficult problem to identify

the relevant saddle points in these multidimensional spaces, and many incorrect approaches have appeared and still do appear in the literature. We use here a technique borrowed from the area of geographical topography studies, namely imaginary water flow[4,5,6,7], to determine the structure of multidimensional fission-energy landscapes.

A number of models for the total nuclear potential energy exist. We use here the FRLDM macroscopic-microscopic model to calculate fission and fusion potential-energy landscapes.

2.1. *Shape Parameterization*

Because fragment shell effects strongly influence the structure of the fission potential-energy surface long before scission, often in the outer saddle region, it is crucial to include in calculations the nascent-fragment deformations as two independent shape degrees of freedom. In addition, elongation, neck diameter, and mass-asymmetry shape degrees of freedom are required, at a minimum, to adequately describe the complete fission potential-energy surface. For nascent-fragment deformations we choose spheroidal deformations characterized by Nilsson's quadrupole ϵ parameter. This single deformation parameter is sufficient because higher-multipole shape-degrees of freedom are usually of lesser importance in the fission-fragment mass region below the rare earths.

The three-quadratic-surface parameterization (3QS) is ideally suited for the above description[8,1]. In the 3QS the shape of the nuclear surface is specified in terms of three smoothly joined portions of quadratic surfaces of revolution. We use here 15 points each in the neck diameter and left and right fragment deformations, 20 points in the mass asymmetry, and 41 points in the nuclear elongation. This leads to a space of 2767500 grid points. However, as explained elsewhere[7] some grid-point coordinate values do not correspond to physically realizable shapes; therefore the actual number of grid points considered are 2610885.

2.2. *Global Barrier Studies*

In general our calculated potential-energy surfaces exhibit a complex structure with multiple minima, maxima, saddle points and valleys. Structures significant in fission are extracted by use of the water immersion techniques outlined above. For nuclei in the radium through light actinide region we find consistently that beyond the second minimum the potential-energy surfaces are dominated by two valleys leading to symmetric and asymmetric

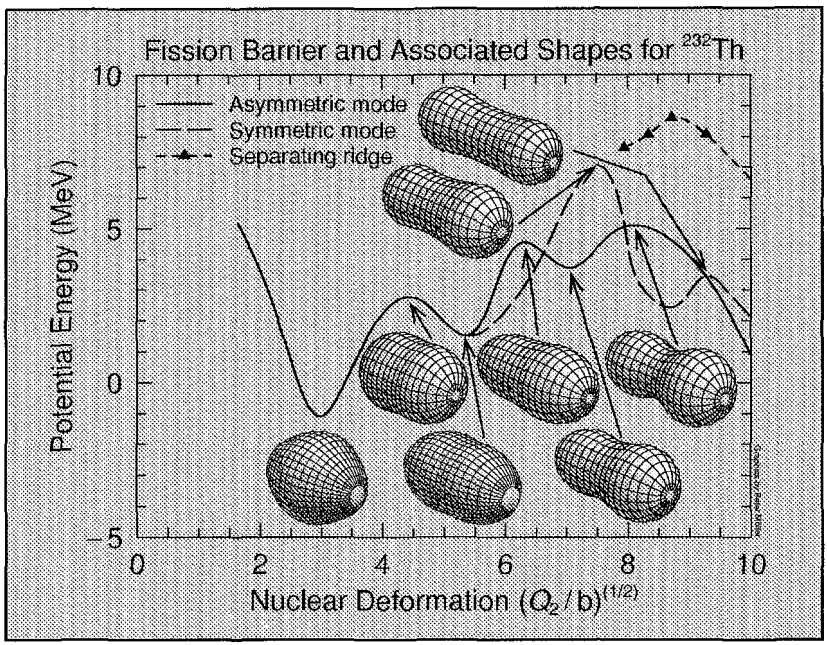

Figure 1. Fission barriers for symmetric and asymmetric fission modes for ^{232}Th. The ridge between the two valleys is also shown. The shapes shown correspond to saddle points and minima along the two fission barriers. The entry saddle point to the symmetric valley is 2.17 MeV higher than the entry saddle point to the asymmetric valley. The highest point on the separating ridge is 1.56 MeV higher than the symmetric saddle. All energies are given relative to the spherical macroscopic energy. The calculation was done with the FRLDM (1992) parameter set.

division into two fragments. The two valleys are separated from the second minimum by *different* saddle points and from each other by a ridge. We find that for ^{228}Ra the ridge peaks at 2.47 MeV above the entrance saddle to the symmetric valley, whereas for ^{232}Th it peaks at 1.56 MeV. For ^{234}U the ridge only rises marginally above the entrance saddle to the symmetric valley. For still heavier systems such as ^{240}Pu we find that the symmetric valley emerges as a "side valley" to the asymmetric valley at some point beyond a single outer saddle at the beginning of the asymmetric valley. Calculated features of the five-dimensional potential-energy surface for ^{232}Th are illustrated in Fig. 1.

Because fission saddle points in our five-dimensional deformation spaces are systematically lower than in earlier, lower-dimensional spaces a readjustment of the macroscopic-model constants is necessary to avoid systematic errors in the calculated fission-barrier heights. We have performed

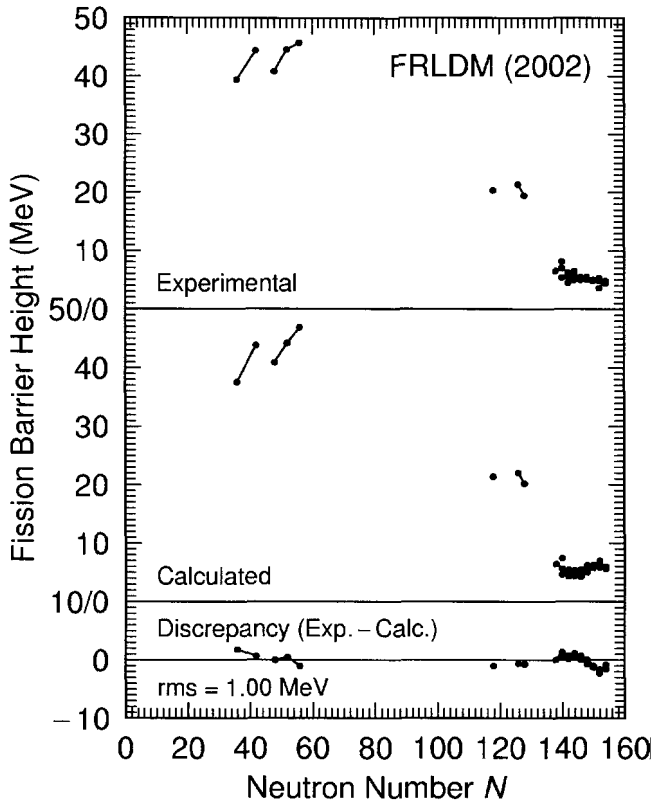

Figure 2. Comparison of calculated and experimental fission-barrier heights for nuclei throughout the periodic system, after a readjustment of the macroscopic model constants. It is assumed here that the saddle-point shapes are not affected by the readjustment. Experimental barriers are well reproduced by the calculations, the rms error is only 0.999 MeV for 31 nuclei. In the actinide region it is the outer of the two peaks in the "double-humped" barrier that is compared to experimental data.

such a readjustment[9] in a manner similar to how our FRLDM (1992) constants were determined[1]. Only 6 constants are varied; the others remain unchanged. In the FRLDM (1992) the mass-model error was 0.779 MeV, and the barrier rms error was 1.40 MeV. We now obtain a mass-model error of 0.752 MeV, and a barrier rms error of 0.999 MeV for the same experimental mass-data set but for a larger and slightly different barrier-data set. Calculated barriers for the 31 nuclei used in this constant determination are compared to experimental data in Fig. 2.

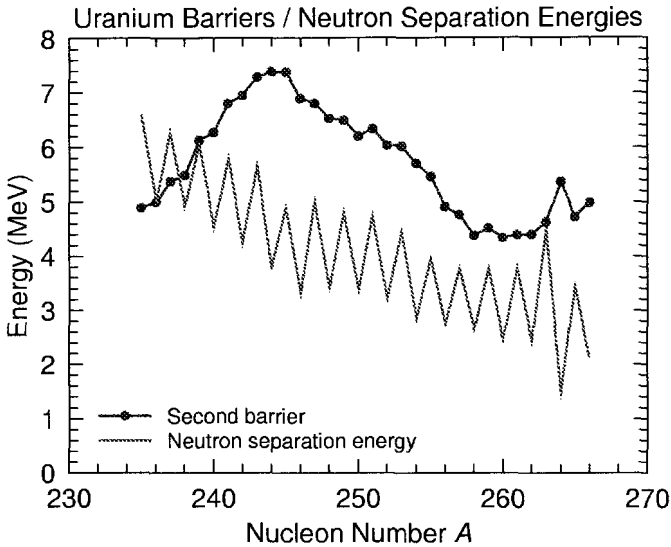

Figure 3. Calculated outer fission-barrier heights for a sequence of uranium isotopes. Also shown is the neutron separation energy for the $A+1$ system. When the separation energy is higher than the fission barrier, fission is possible when a neutron is captured during the r-process.

2.3. *Barriers of r-Process Nuclei*

In Fig. 3 we show for a sequence of uranium isotopes the calculated height of the *outer* peak in the barrier. In the vicinity of $A = 260$ the calculated outer barrier height is lower than 5 MeV. In a 3D calculation in a deformation grid appropriate for studies of the first peak in the fission barrier we find that its height is also below 5 MeV. Thus the r-process could be terminated here by neutron-induced fission. However, for a more complete description it is necessary to calculate barriers for the entire neutron-rich heavy-element region and follow β-decay to stability and determine the associated β-delayed neutron-emission and β-delayed fission branching ratios. These studies are in progress. However, we can already note that in thermonuclear explosions designed to generate particularly high neutron fluences only nuclei with mass number A up to $A = 257$ were produced with uranium targets[10]. This is in qualitative agreement with Fig. 3, where the calculated neutron separation energies become close to the calculated barrier heights just below $A = 260$. Calculations of all fission barriers above $A = 190$ are in progress.

3. β-Decay Properties

In β-decay nuclei decay from a parent nucleus to accessible states in the daughter. We have previously only considered Gamow-Teller β-decay and developed a model in which decay rates from mother ground states (or specified excited states) to accessible states in the daughter could be obtained. The decay rates were obtained as matrix elements of the Gamow-Teller operator between parent and daughter states in a quasi-particle random-phase approximation (QRPA). The model is extensively described in elsewhere[11,12,2]. Recently we have made two enhancements to this model. The new approach combines calculations within the quasi-particle random-phase approximation (QRPA) for the Gamow-Teller (GT) part with an empirical spreading of the QP-strength and the gross theory[13,14] for the first-forbidden (*ff*) part of β^--decay. Relative to the allowed Gamow-Teller strength which over a given energy range is represented by relatively few strong peaks, the first forbidden *ff* strength with its numerous small densely spaced peaks to a good approximation constitutes a "smooth background". It is therefore a reasonable approach to calculate the GT transitions in a microscopic QRPA approach and the *ff* transitions in a macroscopic statistical model, in analogy with the macroscopic-microscopic method in which the nuclear energy as a function of shape is calculated as a sum of a liquid-drop-type model that varies smoothly with proton number, neutron number, and deformation and a shell-correction part that exhibits rapid variation in these variables. Strictly speaking the Fermi function $f(Z, R, \epsilon_0)$ is different for allowed and first forbidden transitions. Here we use the same $f(Z, R, \epsilon_0)$ in both cases, contributing a negligible error in our statistical model of the first-forbidden decays.

We show in Fig. 4 for ^{92}Rb an example of the effect of our two model enhancements on the strength functions, half-lives and β-delayed neutron-emission probabilities . The top subplot shows the original model, the middle subplot the effect of spreading the transition strength, and the bottom subplot the effect of also including *ff* transitions.

We have chosen ^{92}Rb as an illustrative example for two reasons. First, in the standard model calculation, illustrated in the top subplot, S_{1n} sits just below the first major peak in the strength function, with some strength, not discernable on this plot occurring below the one-neutron separation energy. This leads to a very high delayed-neutron emission probability, in contradiction to experiment. Second, most of the strength occurring within the Q_β window lies *just below* Q_β. Therefore we obtain a half-life

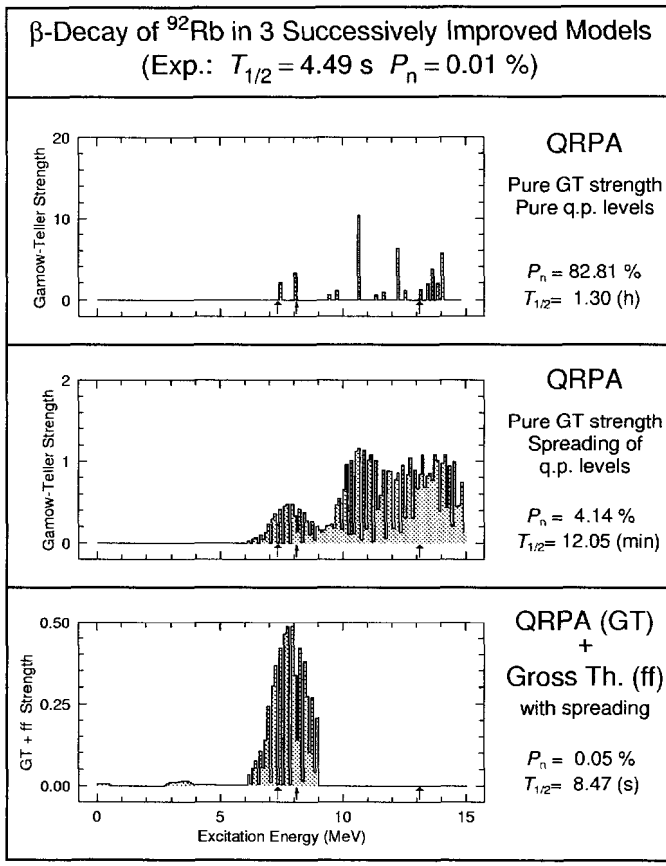

Figure 4. Calculated β-strength functions, corresponding half-lives and delayed-neutron emission probabilities for ^{92}Rb in three successively enhanced models. The narrow arrow indicates the Q_β value, the wide arrows successive neutron-separation energies; the lowest arrow S_{1n}, the second lowest S_{2n}, and so on.

in the order of hours, again in contradiction with experiment. Already after implementing the first model enhancement, the spreading of the GT strength the agreement with experiment improves considerably: the half-life is reduced by a factor of 6.5 and the delayed-neutron emission probability by a factor of 20! In the next step there are even more dramatic changes in the calculated half-life and neutron-emission probability and the agreement with experiment is now quite good.

It is not our aim here to make a detailed analysis of each individual nucleus, but instead to present an overview of the model performance in a calculation of a large number of β-decay half-lives and delayed neutron-

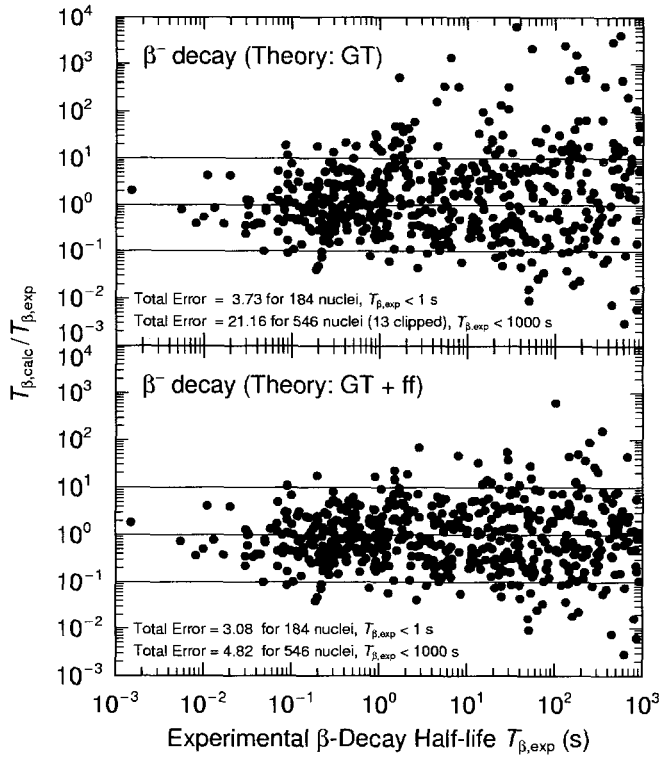

Figure 5. Ratio of calculated to experimental β^--decay half-lives for nuclei from ^{16}O to the heaviest known in our previous and current models. The β-decay rates of r-process nuclei are normally shorter than 150 ms.

emission probabilities. In Figs. 5 and 6 we compare measured β^--decay half-lives and β-delayed neutron-emission probabilities with calculations based on our two models, for nuclei throughout the periodic system. To address the reliability versus distance from stability, we present the ratio between the calculated and experimental quantity versus the experimental quantity, that is $T_{\beta,\mathrm{calc}}/T_{\beta,\mathrm{exp}}$ versus $T_{\beta,\mathrm{exp}}$ in Fig. 5 and $P_{\mathrm{n,calc}}/P_{\mathrm{n,exp}}$ versus $P_{\mathrm{n,exp}}$ in Fig. 6. Because the relative error in the calculated half-lives is more sensitive to small shifts in the positions of the calculated single-particle levels for decays with small energy releases, where long half-lives are expected, one can anticipate that half-life calculations are more reliable far from stability, where the β-decay Q-values are large, than close to β-stable nuclei.

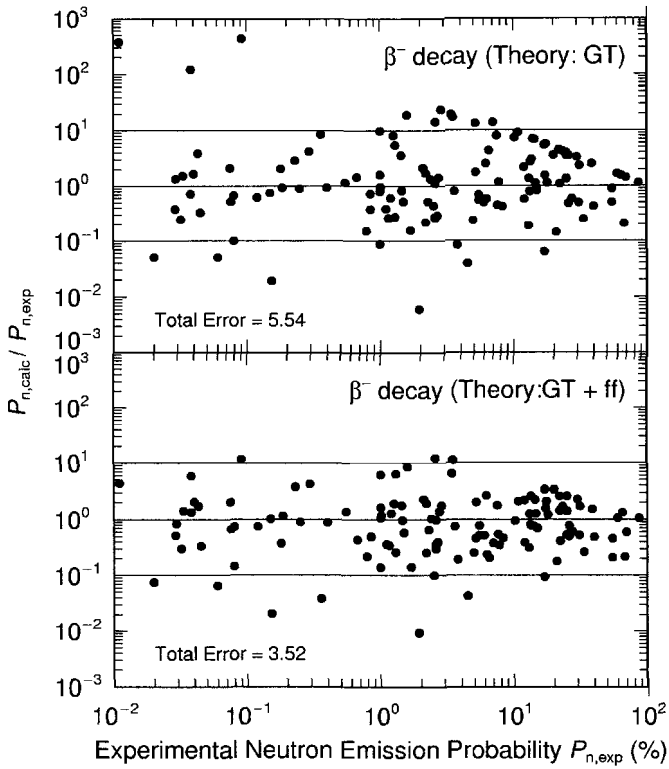

Figure 6. Ratio of calculated to experimental β-delayed neutron-emission probabilities $P_{\rm n}$ for nuclei in the fission-fragment region in our previous and current models.

Furthermore, because the Fermi function is dominated by the phase space factor $(Q_\beta - E_f)^5$ where E_f is the excitation energy of the final state in the daughter nucleus it is clear that the same absolute error ΔE in the calculated Q_β value, will result in a smaller error in $T_{1/2}$ for large Q_β than for small Q_β. Since Q_β increases quite rapidly with distance from β-stability (for example for ^{94}Sr Q_β is 2.36 MeV and for ^{100}Sr it is 6.86 MeV) we expect for this reason alone that the errors in the calculated half-lives will decrease with distance for stability even if Q_β were to develop somewhat increasing errors.

We briefly discuss what conclusions can be drawn from a simple visual inspection of Fig. 5. As functions of $T_{\beta,\rm exp}$ one would expect the average error to increase as $T_{\beta,\rm exp}$ increases. This is indeed the case in both of the model calculations. When, as in the lower part of the figure, *ff* transitions are included the agreement between calculations and experiment is better,

in particular for long half-lives, as expected, because for the small decay Q values here the *ff* transitions are relatively more important. In addition one is left with the impression that the errors in our calculation are fairly large. However, this is partly a fallacy, since for small errors there are many more points than for large errors. This is not clearly seen in the figures, since for small errors many points are superimposed on one another. A more extensive analysis of the error in the calculation is presented elsewhere[15].

For delayed-neutron emission there are fewer data points available than for β-decay half-lives. However, the more than 100 data points[16] are sufficient to allow us to draw several conclusions. First, just as for the half-lives we find that the calculations are more accurate for decays corresponding to large Q_β values, that is far from stability where data are often not available. Large Q_β values usually correspond to large P_n values. Second, we find also here that including *ff* transitions in the simple statistical gross theory model considerably improves the calculations.

The calculated half-lives and β-delayed neutron-emission probabilities in the enhanced model described here are available through a Los Alamos National Laboratory web location[17] on the T-16 site.

4. Summary and Conclusions

A comprehensive understanding of the r-process needs to include modeling of fission, β-decay half-lives, β-delayed neutron-emission probabilities, neutron separation energies, and β-decay Q values at the end of the r-process in the heavy-element region. Our macroscopic-microscopic model of the nuclear potential energy allows the calculation of all these quantities within a unified framework for all nuclei heavier than ^{16}O[1,2]. Comparisons between calculated masses and masses that were measured after the calculated mass tables were published show that the model is reliable for masses and associated Q values also far from stability[2,3]. Applications of our recently enhanced model of β-decay to studies of the r-process also yields encouraging results[15].

Over the years several fission-barrier calculations for r-process applications have been published[18,19,20,4,21]. However, none of these are based on mass/fission models that have been as extensively tested globally as our current fission model. Furthermore they all consider very limited deformation spaces. In contrast we have shown that our current model reproduces to within 1 MeV fission-barrier heights over the entire periodic system, and in detail many actinide fission properties[7]. Our first results here for neutron-

rich uranium isotopes are in qualitative agreement with isotope production in thermonuclear explosions. Because of these promising results we are proceeding with a large-scale calculation of the fission barriers of all nuclei with $A > 190$.

This research is supported by the US DOE.

References

1. P. Möller, J. R. Nix, W. D. Myers, and W. J. Swiatecki, Atomic Data Nucl. Data Tables **59** (1995) 185.
2. P. Möller, J. R. Nix, and K.-L. Kratz, Atomic Data Nucl. Data Tables **66** (1997) 131.
3. D. Lunney, J. M. Pearson, c. Thibault, Rev. Mod. Phys. **75** (2003) 1021.
4. A. Mamdouh, J. M. Pearson, M. Rayet, and F. Tondeur, Nucl. Phys. **A644** (1998) 389.
5. B. Hayes, Am. Sci. **88** (2000) 481.
6. P. Möller, D. G. Madland, and A. Iwamoto Kyoto University Research Reactor Institute Report, Proceedings of Specialists' Meeting on Interdisciplinary Approach to Nuclear Fission, 2000, January 18-19, 2000, Kyoto University Research Reactor Institute, Kumatori-cho, Osaka, Japan (LA-UR-001435), URL:http://t16web.lanl.gov/Moller/publications/kumatori2000.html.
7. P. Möller, D. G. Madland, A. J. Sierk, and A. Iwamoto, Nature **409** (2001) 785.
8. J. R. Nix, Nucl. Phys. **A130** (1969) 241.
9. P. Möller, A. J. Sierk, and A. Iwamoto, Phys. Rev. Lett., to be published (2004).
10. S. A. Becker, Carnegie Observatories Astrophysics Series, Vol 4, Origin and Evolution of the Elements, 2003, ed. A. McWilliam and M. Rauch (Pasadena: Carnegie Observatories, URL: http://www.ociw.edu/ociw/symposia/series/symposium4/proceedings.html).
11. J. Krumlinde and P. Möller, Nucl. Phys. **A417** (1984) 419.
12. P. Möller and J. Randrup, Nucl. Phys. **A514** (1990) 1.
13. K. Takahashi, Prog. Theor. Phys. **47** (1972) 1500.
14. K. Takahashi, M. Yamada, and T. Kondoh, Atomic Data Nucl. Data Tables **12** (1973) 101.
15. P. Möller and A. J. Sierk, Nature, **422** (2003) 485.
16. B. Pfeiffer, K.-L. Kratz, and P. Möller, Progr. Nucl. Energy **41/1–4** (2002) 39.
17. URL: http://t16web/Moller/publications/rspeed2002.html.
18. W. M. Howard and J. R. Nix, Proc. Third IAEA Symp. on the physics and chemistry of fission, Rochester, 1973, vol. I (IAEA, Vienna, 1974) p. 145.
19. W. M. Howard and J. R. Nix, Nature, **247** (1974) 17.
20. W. M. Howard and P. Möller, Atomic Data Nucl. Data Tables **25** (1980) 219.
21. A. Mamdouh, J. M. Pearson, M. Rayet, and F. Tondeur, Nucl. Phys. **A679** (2001) 337.

SYNTHESIS OF SUPERHEAVY ELEMENTS

KOSUKE MORITA

Cyclotron Center, RIKEN (The Institute of Physical and Chemical Research)
Hirosawa 2-1, Wako-shi, Saitama 351-0198, Japan

In RIKEN (The Institute of Physical and Chemical Research) productions and decays of isotopes ^{271}110 and ^{272}111 were studied using a gas-filled recoil ion separator GARIS. The isotopes were produced by ^{208}Pb + ^{64}Ni ¤ ^{271}110 + n and ^{209}Bi + ^{64}Ni ¤ ^{272}111 + n reactions, respectively. Fourteen α-decay chains have been assigned to be the decays originating from the isotope ^{271}110. We have observed 14 α-decay chains that can be assigned to subsequent decays from ^{272}111. The results have provided good confirmations of productions and decays of both the ^{271}110 and ^{272}111 reported by GSI group.

All elements find in nature was produced in the process of evolution of the universe. Many attempts have been made to find out elements whose atomic numbers are greater than 92 (Uranium) in nature. Although two elements, Z=93 (Neptunium) and Z=94 (Plutonium) were found in nature, experimental nuclear physicists and chemists produced those elements in laboratories before those were discovered in nature. The elements with atomic numbers greater than 94 were synthesized artificially as new elements. New elements whose atomic numbers were greater than 101 were synthesized by heavy-ion induced fusion reactions. To produce heavy system the fusion reaction should proceed by neutron evaporation not by fission process. Because the fissility of a heavy system increases with the increase of the atomic number, the production cross sections of the heavy system tend to decrease in logarithmic manner with the increase of the atomic number. The small cross section is limiting further research of nuclei with greater atomic numbers. To overcome the difficulty, more intense primary beams must be used for the production, and a recoil separator with high efficiency and high background reduction must be used.

In RIKEN a gas-filled recoil ion separator GARIS was installed in the experimental hall of RIKEN Linear Accelerator (RILAC) Facility for studies of heavy elements. The RILAC provides high intensity heavy ion beam with energy up to 6 AMeV. The maximum energy is suitable for study fusion reactions near Coulomb barieer. GARIS has a large transmissiopn and a high background reduction. As the first attempt of the system, we studied production and decay of an isotope ^{271}110. The isotopes were produced by ^{208}Pb + ^{64}Ni ¤ ^{271}110 + n reaction. The present work has confirmed the experimental results by GSI group, reported by S. Hofmann *et al.*, [1-3]. A presence of an isomeric

state in $^{271}110$ is firstly confirmed by the present work. An excitation function of the production cross section was measured. Results are reported in ref. [4].

Then we investigated the production and decay of $^{272}111$ using ^{209}Bi + ^{64}Ni ¤ $^{272}111$ + n reaction. The synthesis of this nuclide was reported by Hofmann *et al.*[5, 6] using the same reaction with the present work. The present result is the first clear confirmation for the discovery of $^{272}111$ and its α-decay products, ^{264}Bh and ^{268}Mt, reported previously by a GSI group. New information on their half-lives and decay energies as well as the excitation function was obtained. Results are reported in ref. [7].

References

1. S. Hofmann, *Rep. Prog. Phys.* **61** 639(1998).
2. S. Hofmann et al., *Z. Phys.* **A350** 277(1995).
3. S. Hofmann, *J. Nucl. Radiochem. Sci.* **4** ,R1 (2003).
4. K. Morita, K. Morimoto, D. Kaji, H. Haba, E. Ideguchi, R. Kanumgo, K. Katori, H. Koura, H. Kudo, T. Ohnishi, A. Ozawa, T. Suda, K. Sueki, I. Tanihata, H. Xu, A. V. Yeremin, A. Yoneda, A. Yoshida, Y.-L. Zhao, T. Zhen, *Eur. Phys. J.* (2004) in print.
5. S. Hofmann et al., *Z. Phys.* **A350** 281(1995).
6. S. Hofmann et al., *Eur. Phys. J.* **A14**, 147 (2002).
7. K. Morita, K. Morimoto, Kaji, H. Haba, E. Ideguchi, J. C. Peter, R. Kanungo, K. Katori, H. Koura, H. Kudo, T. Ohnishi, A. Ozawa, T. Suda, K. Sueki, I. Tanihata, H. Xu, A. V. Yeremin, A. Yoneda, A. Yoshida, Y.-L. Zhao, T. Zheng, S. Goto, F. Tokanai, *J. Jpn. Phys. Soc.* (2004) in print.

DETERMINATION OF S_{17} BASED ON CDCC ANALYSIS OF ^{8}B DISSOCIATION

K. OGATA*, T. MATSUMOTO, N. YAMASHITA AND M. KAMIMURA
Department of Physics, Kyushu University, Fukuoka 812-8581, Japan

Y. ISERI
Department of Physics, Chiba-Keizai College, Todoroki-cho 4-3-30, Inage, Chiba 263-0021, Japan

T. KAMIZATO AND M. YAHIRO
Department of Physics and Earth Sciences, University of the Ryukyus, Nishihara-cho, Okinawa 903-0213, Japan

Analysis of ^{8}B Coulomb dissociation with the Asymptotic Normalization Coefficient (ANC) method is proposed to determine the astrophysical factor $S_{17}(0)$ accurately. An important advantage of the analysis is that uncertainties of the extracted $S_{17}(0)$ coming from the use of the ANC method can quantitatively be evaluated, in contrast to previous analyses using the Virtual Photon Theory (VPT). Calculation of measured spectra in dissociation experiments is done by means of the method of Continuum-Discretized Coupled-Channels (CDCC). From the analysis of ^{58}Ni(^{8}B,^{7}Be+p)^{58}Ni at 25.8 MeV, $S_{17}(0) = 22.3 \pm 0.64$(theo) $\pm$ 2.23(expt) (eVb) is obtained; the ANC method turned out to work in this case within 1% of error.

1. Introduction

The solar neutrino problem is one of the central issues in the neutrino physics.[1] Nowadays, the neutrino oscillation is assumed to be the solution of the problem and the focus of the solar neutrino physics is to determine oscillation parameters: the mass difference among ν_e, ν_μ and ν_τ, and their mixing angles.[2] The astrophysical factor S_{17}, defined by $S_{17}(E) \equiv \sigma_{p\gamma}(E)E\exp[2\pi\eta]$ with $\sigma_{p\gamma}$ the cross section of the p-capture reaction ^{7}Be$(p,\gamma)^8$B and η the Sommerfeld parameter, plays an essential

*Electric address: kazu2scp@mbox.nc.kyushu-u.ac.jp

role in the investigation of neutrino oscillation, since the prediction value for the flux of the ^{8}B neutrino, which is intensively being detected on the earth, is proportional to $S_{17}(0)$. The required accuracy from astrophysics is about 5% in errors.

Because of difficulties of direct measurements for the p-capture reaction at very low energies, alternative indirect measurements were proposed: p-transfer reactions and ^{8}B Coulomb dissociation are typical examples of them. In the former the Asymptotic Normalization Coefficient (ANC) method[3] is used, carefully evaluating its validity, while in the latter the Virtual Photon Theory (VPT) is adopted to extract $S_{17}(0)$; the use of VPT requires the condition that the ^{8}B is dissociated through its pure E1 transition, the validity of which is not yet clarified quantitatively.

In the present paper we propose analysis of ^{8}B Coulomb dissociation by means of the ANC method, instead of VPT. An important advantage of the analysis is that one can evaluate the error of $S_{17}(0)$ coming from the use of the ANC method; the fluctuation of $S_{17}(0)$, by changing the ^{8}B single-particle wave functions, can be interpreted as the error of the ANC analysis.[4,5,6,7] For the calculation of ^{8}B dissociation cross sections, we use the method of Continuum-Discretized Coupled-Channels (CDCC),[8] which was proposed and developed by Kyushu group. CDCC is one of the most accurate methods being applicable to breakup processes of weakly-bound stable and unstable nuclei. As a subject of the present analysis, we here take up the Notre Dame experiment at 25.8 MeV and extract $S_{17}(0)$ by the CDCC + ANC analysis, quantitatively evaluating the validity of the use of the ANC method.

In Sec. 2 we give a quick review of the ANC method and discuss advantages of applying it to ^{8}B Coulomb dissociation. Calculation of ^{8}B breakup cross section by means of CDCC is briefly described in Sec. 3. In Sec. 4 numerical results for ^{58}Ni(^{8}B,^{7}Be+p)^{58}Ni at 25.8 MeV and the extracted value of $S_{17}(0)$ with its uncertainties are shown. Finally, summary and conclusions are given in Sec. 5.

2. The Asymptotic Normalization Coefficient method

The ANC method is a powerful tool to extract $S_{17}(0)$ indirectly. The essence of the ANC method is that the cross section of the ^{7}Be$(p,\gamma)^8$B at stellar energies can be determined accurately if the tail of the ^{8}B wave function, described by the Whittaker function times the ANC, is well determined. The ANC can be obtained from alternative reactions where pe-

ripheral properties hold well, i.e., only the tail of the ^{8}B wave function has a contribution to observables.

So far the ANC method has been successfully applied to p-transfer reactions such as ^{10}Be(^{7}Be,^{8}B)^{9}Be,[4] ^{14}N(^{7}Be,^{8}B)^{13}C,[5] and ^{7}Be$(d,n)^8$B.[7] Also Trache *et al.*[6] showed the applicability of the ANC method to one-nucleon breakup reactions; $S_{17}(0)$ was extracted from systematic analysis of total breakup cross sections of $^8\mathrm{B} \longrightarrow {}^7\mathrm{Be} + p$ on several targets at intermediate energies.

In the present paper we apply the ANC method to ^{8}B Coulomb dissociation, where $S_{17}(0)$ has been extracted by using the Virtual Photon Theory (VPT) based on the principle of detailed balance. In order to use VPT, the previous analyses neglected effects of nuclear interaction on the ^{8}B dissociation, which is not yet well justified. Additionally, roles of the E2 component, interference with the dominant E1 part in particular, need more detailed investigation, although recently some attempts to eliminate the E2 contribution from measured spectra have been made. On the contrary, the ANC analysis proposed here is free from these problems. We here stress that as an important advantage of the present analysis, one can evaluate quantitatively the error of $S_{17}(0)$ by the fluctuation of the ANC with different ^{8}B single-particle potentials.

Comparing with Ref. [6], in the present ANC analysis angular distribution and parallel-momentum distribution of the ^{7}Be fragment, instead of the total breakup cross sections, are investigated, which is expected to give more accurate value of $S_{17}(0)$. Moreover, our purpose is to make systematic analysis of ^{8}B dissociation at not only intermediate energies but also quite low energies. Thus, the breakup process should be described by a sophisticated reaction theory, beyond the extended Glauber model used in Ref. [6]. For that purpose, we use CDCC, which is one of the most accurate methods to be applicable to ^{8}B dissociation.

3. The method of Continuum-Discretized Coupled-Channels

Generally CDCC describes the projectile (c) + target (A) system by a three-body model as shown in Fig. 1; in the present case c is ^{8}B and 1 and 2 denote ^{7}Be and p, respectively. The three-body wave function Ψ_{JM}, corresponding to the total angular momentum J and its projection M, is

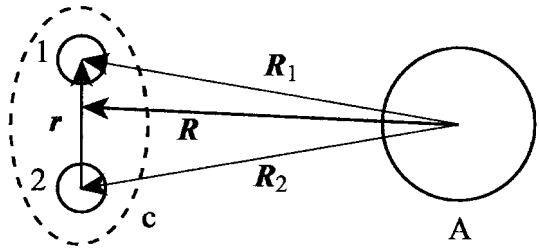

Figure 1. Schematic illustration of the system treated in the present paper.

given in terms of the internal wave functions φ of c:

$$\Psi_{JM} = \sum_{L} Y_{JM}^{\ell_0 L} \varphi_0(r) \frac{\chi_{\ell_0 L J}(P_0, R)}{R} + \sum_{\ell L} Y_{JM}^{\ell L} \int_0^\infty \varphi_\ell(k, r) \frac{\chi_{\ell L J}(P, R)}{R} dk; \tag{1}$$

$$Y_{JM}^{\ell L} \equiv [i^\ell Y_\ell(\Omega_r) \otimes i^L Y_L(\Omega_R)]_{JM}, \tag{2}$$

where ℓ is the total spin of c and L is the orbital angular momentum for the relative motion of c and A; the subscript 0 represents the initial state. For simplicity we here neglect all intrinsic spins of the constituents and also assume that c has only one bound state. The first and second terms in the r.h.s. of Eq. (1) correspond to the bound and scattering states of c, respectively. In the latter the relative momentum P between c and A is related to the internal one k of c through the total-energy conservation.

In CDCC the summation over ℓ and integration over k are truncated at certain values $\ell_{\max}$ and $k_{\max}$, respectively. For the latter, furthermore, we divide the k continuum into N *bin*-states, each of which is expressed by a discrete state $\hat{\varphi}_{i\ell}$ with i denote a certain region of k, i.e., $k_{i-1} \leq k < k_i$. After truncation and discretization, Ψ_{JM} is approximately expressed by $\{\hat{\varphi}_{i\ell}\}$ with finite number of channels:

$$\Psi_{JM}^{\mathrm{CDCC}} = \sum_{L} Y_{JM}^{\ell_0 L} \varphi_0(r) \frac{\chi_{\ell_0 L J}(P_0, R)}{R} + \sum_{\ell=0}^{\ell_{\max}} \sum_{i=1}^{N} \sum_{L} Y_{JM}^{\ell L} \hat{\varphi}_{i\ell}(r) \frac{\hat{\chi}_\gamma(\hat{P}_i, R)}{R} \tag{3}$$

with $\gamma = \{i, \ell, L, J\}$. The $\hat{P}_i$ and $\hat{\chi}_\gamma$ are the discretized P and $\chi_{\ell L J}$, respectively, corresponding to the ith bin state $\hat{\varphi}_{i\ell}$.

Inserting $\Psi_{JM}^{\mathrm{CDCC}}$ into a three-body Schrödinger equation, one obtains

the following (CC) equations:

$$\left[\frac{d^2}{dR^2} + \hat{P}_i^2 - \frac{L(L+1)}{R^2} - \frac{2\mu}{\hbar^2}V_{\gamma\gamma}(R)\right]\hat{\chi}_\gamma(\hat{P}_i, R) = \sum_{\gamma' \neq \gamma} \frac{2\mu}{\hbar^2}V_{\gamma\gamma'}(R)\hat{\chi}_{\gamma'}(\hat{P}_{i'}, R) \quad (4)$$

for all γ including the initial state, where μ is the reduced mass of the c + A system and $V_{\gamma\gamma'}$ is the form factor defined by

$$V_{\gamma\gamma'}(R) = \langle Y_{JM}^{\ell L}\hat{\varphi}_{i\ell}(r)|U|Y_{JM}^{\ell' L'}\hat{\varphi}_{i'\ell'}(r)\rangle_{\mathbf{r},\Omega_R}, \quad (5)$$

with U the sum of the interactions between A and individual constituents of c. The CDCC equations (4) are solved with the asymptotic boundary condition:

$$\hat{\chi}_\gamma(\hat{P}_i, R) \sim u_L^{(-)}(\hat{P}_i, R)\delta_{\gamma,\gamma_0} - \sqrt{\hat{P}_i/\hat{P}_0}\hat{S}_{\gamma,\gamma_0}u_L^{(+)}(\hat{P}_i, R), \quad (6)$$

where $u_L^{(-)}$ and $u_L^{(+)}$ are incoming and outgoing Coulomb wave functions. Thus one obtains the S-matrix elements $\hat{S}_{\gamma,\gamma_0}$, from which any observables, in principle, can be calculated; we followed Ref. [13] to calculate the distribution of ^{7}Be fragment from ^{8}B.

CDCC treats breakup channels of a projectile explicitly, including all higher-order terms of both Coulomb and nuclear coupling-potentials, which gives very accurate description of dissociation processes in a framework of three-body reaction dynamics. Detailed formalism and theoretical foundation of CDCC can be found in Refs. [8,14,15].

4. Numerical results and the extracted $S_{17}(0)$

In the present paper we take up the ^{8}B dissociation by ^{58}Ni at 25.8 MeV (3.2 MeV/nucleon) measured at Notre Dame,[12] for which VPT was found to fail to reproduce the data.[16] The extended Glauber model, used in Ref. [6], is also expected not to work well because of the low incident energy. Thus, the Notre Dame data is a good subject of our CDCC + ANC analysis.

Parameters of the modelspace taken in the CDCC calculation are as follows. The number of bin-states of ^{8}B is 32 for s-state, 16 for p- and d-states, and 8 for f-state. We neglected the intrinsic spin of ^{7}Be, while that of p is explicitly included. The maximum excitation energy of ^{8}B is 10 MeV, $r_{\max}$ ($R_{\max}$) is 100 fm (500 fm) and $J_{\max}$ is 1000. For nuclear interactions of p-^{58}Ni and ^{7}Be-^{58}Ni we used the parameter sets of Becchetti and Greenlees[17] and Moroz *et al.*,[18] respectively.

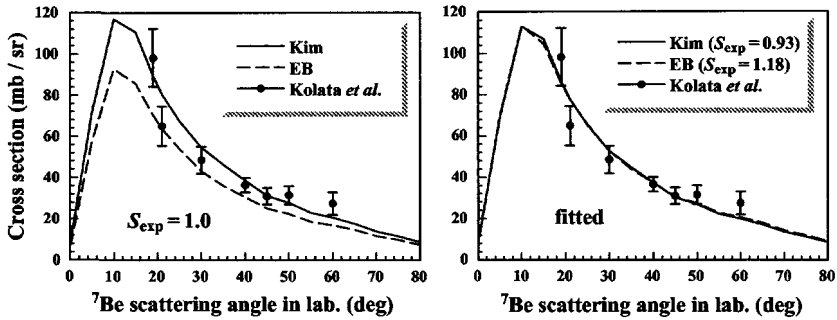

Figure 2. Angular distribution of the ^{7}Be fragment in the laboratory frame. The solid and dashed lines represent the results of CDCC calculation with the parameter set of Kim and Esbensen-Bertsch (EB), respectively, for ^{8}B single particle potential. Results in the left panel correspond to $S_{\rm exp} = 1$ and those with appropriate values of $S_{\rm exp}$, i.e., 0.93 for Kim and 1.18 for EB, are shown in the right panel. The experimental data are taken from Ref. [12].

In Fig. 2 we show the results of the angular distribution of ^{7}Be fragment, integrated over scattering angles of p and excitation energies of the ^{7}Be + p system. In the left panel the results with the ^{8}B wave functions by Kim *et al.*[19] (solid line) and Esbensen and Bertsch[16] (dashed line), with the spectroscopic factor $S_{\rm exp}$ equal to unity, are shown. After χ^2 fitting, one obtains the results in the right panel; one sees that both calculations very well reproduce the experimental data. The resultant $S_{\rm exp}$ is 0.93 and 1.18 with the ^{8}B wave functions by Kim and Esbensen-Bertsch, respectively, showing quite strong dependence on ^{8}B models. In contrast to that, the ANC C calculated by $C = S_{\rm exp}^{1/2} b$ with b the single-particle ANC, is found to be almost independent of the choice of ^{8}B wave functions, i.e., $C = 0.58 \pm 0.008$ (fm$^{-1/2}$). Thus, one can conclude that the ANC method works in the present case within about 1% of error.

Following Ref. [3] we obtained the following result:

$$S_{17}(0) = 22.3 \pm 0.31(\text{ANC}) \pm 0.33(\text{CDCC}) \pm 2.23(\text{expt}) \ \ (\text{eVb}),$$

where the uncertainties from the choice of the modelspace of CDCC calculation (1.5%) and the systematic error of the experimental data (10%) are also included. Although the quite large experimental error forbids one to determine $S_{17}(0)$ with the required accuracy (5%), the CDCC + ANC method turned out to be a powerful technique to determine $S_{17}(0)$ with small theoretical uncertainties. More careful analysis in terms of nuclear

optical potentials is being made and more reliable $S_{17}(0)$ will be reported in a forthcoming paper.

5. Summary and Conclusions

In the present paper we propose analysis of ^{8}B Coulomb dissociation with the Asymptotic Normalization Coefficient (ANC) method. An important advantage of the use of the ANC method is that one can extract the astrophysical factor $S_{17}(0)$ evaluating its uncertainties quantitatively, in contrast to the previous analyses with the Virtual Photon Theory (VPT).

In order to make accurate analysis of the measured spectra in dissociation experiments, we use the method of Continuum-Discretized Coupled-Channels (CDCC), which was developed by Kyushu group. The CDCC + ANC analysis was found to work very well for ^{58}Ni(^{8}B,^{7}Be+p)^{58}Ni at 25.8 MeV measured at Notre Dame, and we obtained $S_{17}(0) = 22.3 \pm 0.64(\text{theo}) \pm 2.23(\text{expt})$ (eVb), which is consistent with both the latest recommended value 19^{+4}_{-2} eVb[20] and recent results of direct measurements.[21,22]

In conclusion, the ANC + CDCC analysis of ^{8}B Coulomb dissociation is expected to accurately determine $S_{17}(0)$, with reliable evaluation of its uncertainties. An extracted $S_{17}(0)$ from the systematic analysis of RIKEN, MSU and GSI data, combined with that from the Notre Dame experiment shown here, will be reported in near future.

Acknowledgement

The authors wish to thank M. Kawai, T. Motobayashi and T. Kajino for fruitful discussions and encouragement. We are indebted to the aid of JAERI and RCNP, Osaka University for computation. This work has been supported in part by the Grants-in-Aid for Scientific Research of the Ministry of Education, Science, Sports, and Culture of Japan (Grant Nos. 14540271 and 12047233).

References

1. J. N. Bahcall *et al.*, Astrophys. J. **555**, 990 (2001) and references therein.
2. J. N. Bahcall *et al.*, JHEP **0108**, 014 (2001) [arXiv:hep-ph/0106258]; JHEP **0302**, 009 (2003) [arXiv:hep-ph/0212147].
3. H. M. Xu *et al.*, Phys. Rev. Lett. **73**, 2027 (1994).
4. A. Azhari et al., Phys. Rev. Lett. **82**, 3960 (1999).
5. A. Azhari et al., Phys. Rev. C **60**, 055803 (1999);
6. L. Trache et al., Phys. Rev. Lett. **87**, 271102 (2001).

7. K. Ogata *et al.*, Phys. Rev. C **67**, R011602 (2003).
8. M. Kamimura *et al.*, Prog. Theor. Phys. Suppl. **89** 1 (1986); N. Austern *et al.*, Phys. Rep. **154**, 125 (1987).
9. T. Motobayashi *et al.*, Phys. Rev. Lett. **73**, 2680 (1994); T. Kikuchi *et al.*, Eur. Phys. J. A **3**, 209 (1998).
10. N. Iwasa *et al.*, Phys. Rev. Lett. **83**, 2910 (1999).
11. B. Davids *et al.*, Phys. Rev. Lett. **86**, 2750 (2001); Phys. Rev. C **63**, 065806 (2001).
12. J. von Schwarzenberg *et al.*, Phys. Rev. C **53**, 2598 (1996); J. J. Kolata *et al.*, Phys. Rev. C **63**, 024616 (2001).
13. Y. Iseri *et al.*, Prog. Theor. Phys. Suppl. **89**, 84 (1986).
14. R. A. D. Piyadasa *et al.*, Phys. Rev. C **60**, 044611 (1999).
15. N. Austern *et al.*, Phys. Rev. Lett. **63**, 2649(1989); Phys. Rev. C **53**, 314 (1996).
16. H. Esbensen and G. F. Bertsch, Phys. Rev. C **59**, 3240 (1999).
17. F. D. Becchetti and G. W. Greenlees, Phys. Rev. **182**, 1190 (1969).
18. Z. Moroz *et al.*, Nucl. Phys. **A381**, 294 (1982).
19. K. H. Kim *et al.*, Phys. Rev. C **35**, 363 (1987).
20. E. G. Adelberger *et al.*, Rev. Mod. Phys. **70**, 1265 (1998).
21. A. R. Junghans *et al.*, Phys. Rev. Lett. **88**, 041101 (2002).
22. L. T. Baby *et al.*, Phys. Rev. C **67**, 065805 (2003).

This page intentionally left blank

VI. Novae, Supernovae, and Explosive Nucleosynthesis, GRB Models and Nuclearphysics parameters

This page intentionally left blank

THE r-PROCESS IN SUPERNOVA EXPLOSIONS FROM THE COLLAPSE OF ONeMg CORES

SHINYA WANAJO[1], NAOKI ITOH[1], KEN'ICHI NOMOTO[2], YUHRI ISHIMARU[3], AND TIMOTHY C. BEERS[4]

[1] *Department of Physics, Sophia University, 7-1 Kioi-cho, Chiyoda-ku, Tokyo, 102-8554; wanajo@sophia.ac.jp, n_itoh@sophia.ac.jp*

[2] *Department of Astronomy, School of Science, University of Tokyo, Bunkyo-ku, Tokyo, 113-0033; nomoto@astron.s.u-tokyo.ac.jp*

[3] *Department of Physics and Graduate School of Humanities and Sciences, Ochanomizu University, 2-1-1 Otsuka, Bunkyo-ku, Tokyo 112-8610; ishimaru@phys.ocha.ac.jp*

[4] *Department of Physics/Astronomy, Michigan State University, E. Lansing, MI 48824; beers@pa.msu.edu*

We examine r-process nucleosynthesis in a "prompt supernova explosion" from an $8 - 10M_{\odot}$ progenitor star. In the present model, the progenitor star has formed an oxygen-neon-magnesium core at its center. The core-collapse simulations are performed with a one-dimension, Newtonian hydrodynamic code. We simulate energetic prompt explosions by enhancement of the shock-heating energy, in order to investigate conditions necessary for the production of r-process nuclei in such events. The r-process nucleosynthesis is calculated using a nuclear reaction network code including relevant neutron-rich isotopes with reactions among them. The highly neutronized ejecta ($Y_e \approx 0.14 - 0.20$) leads to robust production of r-process nuclei; their relative abundances are in excellent agreement with the solar r-process pattern. Our results suggest that prompt explosions of $8 - 10M_{\odot}$ stars with oxygen-neon-magnesium cores can be a promising site of r-process nuclei.

1. Introduction

The astrophysical origin of the rapid neutron-capture (r-process) species has been a long-standing mystery. Recently, however, a number of important new clues have been provided by spectroscopic studies of extremely-metal-poor stars in the Galaxy. The appearance of neutron-capture elements in these oldest stars in the Galaxy, including the pure-r-process origin of elements such as thorium and uranium, strongly suggests that the r-process nuclei have come from core-collapse supernovae [17 5]. Ishimaru & Wanajo [9] have shown that the large star-to-star dispersion of the observed

abundances of neutron-capture elements relative to iron in very metal-poor stars is also naturally explained if the r-process elements originate from a limited mass range of core-collapse supernovae with little iron production ($8 - 10M_\odot$ or $\geq 30M_\odot$).

So far, the "neutrino wind" scenario, in which the free nucleons accelerated by the intense neutrino flux near the neutrino sphere of a core-collapse supernova assemble to heavier nuclei, has been believed to be the most promising astrophysical site of the r-process [24]. Even this scenario, however, encounters some difficulties [20] [21]. In addition, recent spectroscopic studies of extremely metal-poor stars in the Galactic halo indicate that the observed abundance patterns of the lighter ($Z < 56$) and heavier ($Z > 56$) neutron-capture elements cannot be explained by a single astrophysical site (e.g., neutrino winds); there must exist at least two different r-process sites [11] [10]. Hence, it is of special importance to consider alternative possibilities for the occurrence of the r-process in core-collapse supernovae.

The question of whether $8 - 10M_\odot$ stars that form O-Ne-Mg cores can explode hydrodynamically is still open [23]. The possibility that these stars explode promptly remains because of the smaller iron core present at the onset of the core bounce, as well as the smaller gravitational potential of their collapsing cores [18]. Hillebrandt et al. [7] have obtained a prompt explosion of a $9M_\odot$ star with a $1.38M_\odot$ O-Ne-Mg core [15], while others, using the same progenitor, have not [2] [1]. Mayle & Wilson [14] obtained an explosion, not by a prompt shock, but by late-time neutrino heating. The reason for these different outcomes is due, perhaps, to the application of different equations of state for dense matter, although other physical inputs may also have some influence. Thus, even if a star of $8 - 10M_\odot$ exploded, it would be difficult to derive, with confidence, the physical properties as well as the mass of the ejected matter. Given this highly uncertain situation it is necessary to examine the resulting r-process nucleosynthesis in explosions obtained with different sets of input physics.

The purpose of this study is to investigate conditions necessary for the production of r-process nuclei obtained in purely hydrodynamical models of prompt explosions of collapsing O-Ne-Mg cores, and to explore some of the consequences if those conditions are met [22]. The core collapse and the subsequent core bounce are simulated by a one-dimensional hydrodynamic code with Newtonian gravity (§ 2). The energetic explosions are simulated by artificial enhancements of the shock-heating energy, rather than by application of different sets of input physics, for simplicity. The r-process nucleosynthesis in these explosions is then calculated with the

use of a nuclear reaction network code (§ 3). The resulting contribution of the r-process material created in these simulations to the early chemical evolution of the Galaxy is discussed in § 4. A summary follows in § 5.

2. Prompt Explosion

A pre-supernova model of a $9M_\odot$ star is taken from Nomoto [15], which forms a 1.38 $M_\odot$ O-Ne-Mg core near the end of its evolution. We link this core to a one-dimensional implicit Lagrangian hydrodynamic code with Newtonian gravity. This core is modeled with a finely zoned mesh of 200 mass shells ($2\times10^{-2}M_\odot$ to $0.8M_\odot$, $5\times10^{-3}M_\odot$ to $1.3M_\odot$, and $5\times10^{-3}-1\times10^{-7}M_\odot$ to the edge of the core).

The equation of state of nuclear matter (EOS) is taken from Shen et al. [16], which is based on relativistic mean field theory. The equation of state for the electron and positron gas includes arbitrary relativistic pairs as well as arbitrary degeneracy. Electron and positron capture on nuclei, as well as on free nucleons, are included, along with the use of the up-to-date rates from Langanke & Martinez-Pinedo [13]. The capture is suppressed above the neutrino trapping density, taken to be 3×10^{11} g cm^{-3}, since the neutrino transport process is not taken into account in this study.

Nuclear burning is implemented in a simplified manner. The composition of the O-Ne-Mg core is held fixed until the temperature in each zone reaches the onset of oxygen-burning, taken to be 2×10^9 K, at which point the matter is assumed to be instantaneously in nuclear statistical equilibrium (NSE). The temperature is then calculated by including its nuclear energy release.

We begin the hydrodynamical computations with this pre-supernova model, which has a density of 4.4×10^{10} g cm^{-3} and temperature of 1.3×10^{10} K at its center. The inner $0.1M_\odot$ has already burned to NSE. As a result, the central Y_e is rather low, 0.37, owing to electron capture. The core bounce is initiated when $\sim$ 90 ms has passed from the start of the calculation. At this time the NSE core contains only $1.0M_\odot$, which is significantly smaller than the cases of collapsing iron cores ($\gtrsim 1.3M_\odot$). The central density is 2.2×10^{14} g cm^{-3}, significantly lower than that of Hillebrandt et al. [7], although the temperature ($=2.1\times10^{10}$ K) and Y_e ($=0.34$), are similar. This difference is perhaps due to the use of a relatively stiff EOS in this study.

We find that a very weak explosion results, with an ejected mass of $0.008M_\odot$ and an explosion energy of 2×10^{49} ergs (model Q0 in Table 1).

The lowest Y_e in the outgoing ejecta is 0.45, where no r-processing is expected given the entropy of $\sim 10 N_A k$. This is in contrast to the very energetic explosions, with ejected masses of $0.2 M_\odot$, explosion energies of 2×10^{51} ergs, and low Y_e of ~ 0.2 obtained by Hillebrandt et al [7]. This might be a consequence of the lower gravitational energy release owing to the EOS applied in this study.

Table 1. Results of Core-Collapse Simulations

Model	$f_{\rm shock}$	$E_{\rm exp}$ (10^{51} ergs)	$M_{\rm ej}$ ($M_\odot$)	$Y_{e,\rm min}$
Q0...	1.0	0.018	0.0079	0.45
Q3...	1.3	0.10	0.029	0.36
Q5...	1.5	1.2	0.19	0.30
Q6...	1.6	3.5	0.44	0.14

In order to examine the possible operation of the r-process in the explosion of this model, we artificially obtain explosions with typical energies of $\sim 10^{51}$ ergs by application of a multiplicative factor ($f_{\rm shock}$) to the shock-heating term in the energy equation (models Q3, Q5, and Q6 in Table 1). We take this simplified approach in this study, since the main difference between our result and that by Hillebrandt et al. [7] appear to be the lower central density in ours. If the inner core reached a higher density at the time of core bounce by applying, for example, a softer EOS, the matter would obtain higher shock-heating energy. This is clearly not a self-consistent approach, and a further study is needed to conclude whether such a progenitor star explodes or not, taking into account a more accurate treatment of neutrino transport, as well as with various sets of input physics (like EOSs).

Table 1 lists the multiplicative factor applied to the shock-heating term ($f_{\rm shock}$), explosion energy ($E_{\rm exp}$), ejected mass ($M_{\rm ej}$), and minimum Y_e in the ejecta obtained for each model. Energetic explosions with $E_{\rm exp} > 10^{51}$ ergs are obtained for $f_{\rm shock} \geq 1.5$ (models Q5 and Q6), in which deeper neutronized zones are ejected by the prompt shock, as can be seen in Figure 1 (model Q6). This is in contrast to the weak explosions with $E_{\rm exp} \leq 10^{50}$ ergs (models Q0 and Q3), in which only the surface of the core blows off. Note that the remnant masses for models Q5 and Q6 are $1.19 M_\odot$ and $0.94 M_\odot$, respectively, which are significantly smaller than the typical neutron star mass of $\sim 1.4 M_\odot$. We consider it likely that a mass of $\sim 1.4 M_\odot$ is recovered by fallback of the once-ejected matter, as discussed in § 4.

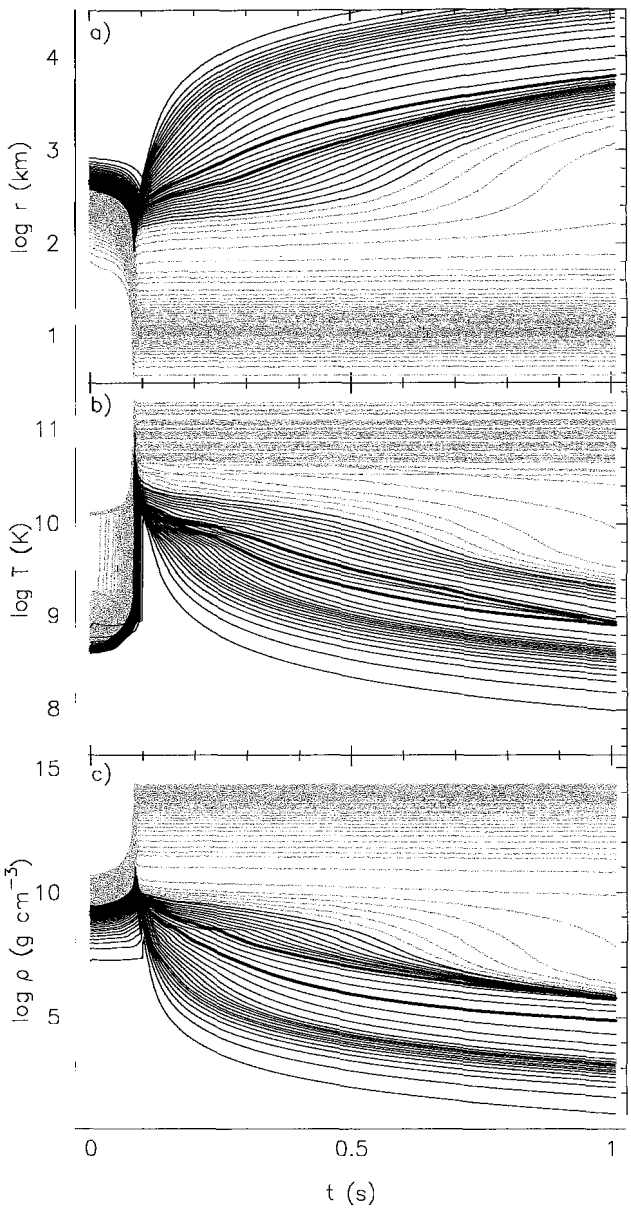

Figure 1. Time variations of (a) radius, (b) temperature, and (c) density for selected mass points (with roughly an equal mass interval) for model Q6. The ejected mass points are denoted in black, while those of the remnant are in grey.

In Figure 2 the electron fraction in the ejecta of each model is shown as a function of the ejected mass point, M_{ej}. For models Q0 and Q3, Y_e decreases steeply with M_{ej}, since the duration of electron capturing is long, owing to the slowly expanding ejecta (Figure 1). For models Q5 and Q6, on the other hand, Y_e decreases gradually with M_{ej}, owing to the fast expansion of the outgoing ejecta. Nevertheless, the inner regions approach very low Y_e, 0.30 and 0.14 for models Q5 and Q6, respectively, owing to their rather high density ($\sim 10^{11}$ g cm^{-3}) at the time of core bounce (Figure 1). Note that, for model Q6, Y_e increases again for $M_{ej} > 0.3M_\odot$. This is due to the fact that the positron capture on free neutrons overcomes the electron capture on free protons when the electron degeneracy becomes less effective in the high temperature matter.

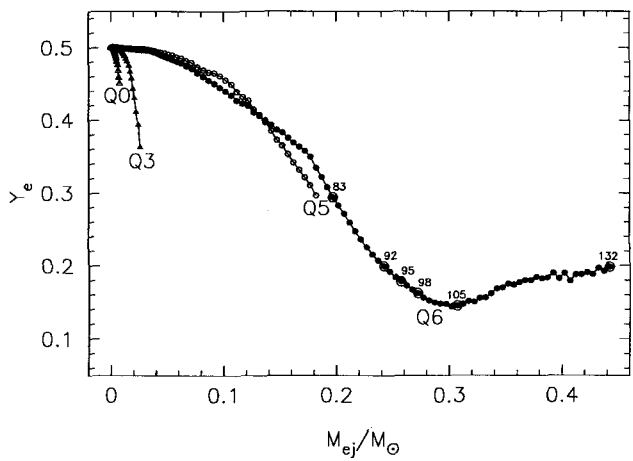

Figure 2. Y_e distribution in the ejected material in models Q0 (open triangles), Q3 (filled triangles), Q5 (open circles), and Q6 (filled circles). The surface of the O-Ne-Mg core is at mass coordinate zero. For model Q6, selected mass points are denoted by zone numbers.

The trend of the $Y_e - M_{ej}$ relation up to $M_{ej} \sim 0.2M_\odot$ is similar in models Q5 and Q6, although it is inverted at $M_{ej} \sim 0.14M_\odot$, owing to the slightly different contribution of the positron and electron capture on free nucleons (Figure 2). Hence, the $Y_e - M_{ej}$ relation between the surface and the innermost layer of the ejecta is expected to be similar to that of model Q6, as long as the explosion is sufficiently energetic ($\gtrsim 10^{51}$ ergs). In the subsequent sections, therefore, we focus only on model Q6, which is

taken to be representative of cases where r-process nucleosynthesis occurs. The ejected mass, $M_{\rm ej}$, is thus taken to be a free parameter, instead of simulating many other models by changing $f_{\rm shock}$.

3. The r-Process

The yields of r-process nucleosynthesis species, adopting the model described in § 2 for the physical conditions, are obtained by application of an extensive nuclear reaction network code. The network consists of $\sim$ 3600 species, all the way from single neutrons and protons up to the fermium isotopes ($Z = 100$). We include all relevant reactions, i.e., (n,γ), (p,γ), (α,γ), (p,n), (α,p), (α,n), and their inverses. Reaction rates are taken from Thielemann (1995, private communication) for nuclei with $Z \leq 46$ and from Cowan et al. [3] for those with $Z \geq 47$. The weak interactions, such as β-decay, β-delayed neutron emission (up to three neutrons), and electron capture are also included, although the latter is found to be unimportant.

Each calculation is started at $T_9 = 9$ (where $T_9 \equiv T/10^9$ K). The initial composition is taken to be that of NSE with the density and electron fraction at $T_9 = 9$, and consists mostly of free nucleons and alpha particles.

Table 2. Ejected Mass ($M_\odot$)

Model	$M_{\rm ej}$	$A \geq 120$	^{56}Ni	Fe	Eu
Q0 ..	0.0079	0.0	0.0018	0.0019	0.0
Q6a..	0.19	2.6×10^{-4}	0.018	0.020	0.0
Q6b..	0.24	0.035	0.018	0.020	2.4×10^{-4}
Q6c..	0.25	0.051	0.018	0.020	4.1×10^{-4}
Q6d..	0.27	0.064	0.018	0.020	4.3×10^{-4}
Q6e..	0.30	0.080	0.018	0.020	4.6×10^{-4}
Q6f..	0.44	0.21	0.018	0.020	0.0020

The mass-integrated abundances from the surface (zone 1) to the zones 83, 92, 95, 98, 105, and 132 are compared with the solar r-process abundances [12] in Figure 3 (models Q6a-f in Table 2). The latter is scaled to match the height of the first ($A = 80$) and third ($A = 195$) peaks of the abundances in models Q6a-b and Q6c-f, respectively. The ejecta masses of these models are listed in Table 2. As can be seen in Figure 3, a solar r-process pattern for $A \gtrsim 130$ is naturally reproduced in models Q6c-f, while

models Q6a-b fail to reproduce the third abundance peak. This implies that the region with $Y_e < 0.20$ must be ejected to account for production of the third r-process peak. Furthermore, to account for the solar level of thorium ($A = 232$) and uranium ($A = 235, 238$) production, the region with rather low Y_e (< 0.18) must be ejected.

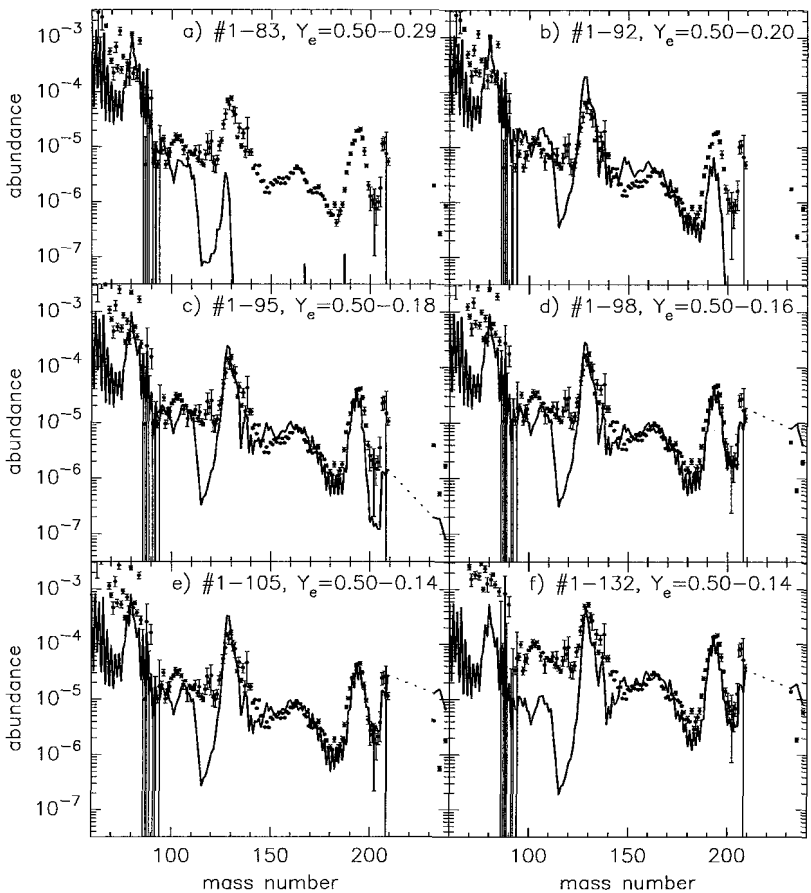

Figure 3. Final mass-averaged r-process abundances (line) as a function of mass number obtained from the ejected zones in (a) models Q6a, (b) Q6b, (c) Q6c, (d) Q6d, (e) Q6e, and (f) Q6f (see Table 2). These are compared with the solar r-process abundances (points), which is scaled to match the height of the first peak ($A = 80$) for (a)-(b) and the third peak ($A = 195$) for (c)-(f).

We find that, for models Q6c-e, the lighter r-process nuclei with $A < 130$ are somewhat deficient compared to the solar r-process pattern (Figure 3c-e). This trend can be also seen in the observational abundance patterns of the highly r-process-enhanced, extremely metal-poor stars CS 22892-052 [17] and CS 31082-001 [5]. In model Q6f, the deficiency is outstanding because of large ejection of the low Y_e matter (Figure 2). This is in contrast to the previous results obtained for the neutrino wind scenario, which significantly *overproduce* the nuclei with $A \approx 90$ [24] [20]. The nuclei with $A < 130$ can be supplied by slightly less energetic explosions, like models Q6a-b (Figures 3a-b). It is also possible to consider that these lighter r-process nuclei originate from "neutrino winds" in more massive supernovae ($> 10M_\odot$). The nuclei with $A < 130$ can be produced naturally in neutrino winds with a reasonable compactness of the proto-neutron star, e.g., $1.4M_\odot$ and 10 km [20].

Figure 3 implies that the production of thorium and uranium differs from model to model, even though the abundance pattern seems to be *universal* between the second and third r-process peaks, as seen in models Q6c-f. This is in agreement with recent observational results suggesting that the ratio Th/Eu may exhibit a star-to-star scatter, while the abundance pattern between the second and third peaks is in good agreement with the solar r-process pattern [8]. Thus, the use of Th/Eu as a cosmochronometer should be regarded with caution, at least until the possible variations can be better quantified; U/Th might be a far more reliable chronometer [21] [22].

4. Contribution to Chemical Evolution of the Galaxy

One of the essential questions raised by previous works is that, if prompt supernova explosions are one of the major sites of r-process nuclei, would in fact the r-process nuclei be significantly *overproduced* [6]. As far as the explosion is purely hydrodynamical, a highly neutronized deeper region must be ejected in order for a successful r-process to result. It seems inevitable, therefore, that one must avoid an ejection of large amounts of r-process matter, at least when assuming spherical symmetry. Our result shows that more than $0.05M_\odot$ of the r-process matter ($A \geq 120$) is ejected per event, which reproduces the solar r-process pattern (models Q6c-f in Table 2). This is about three orders of magnitude larger than the $5.8 \times 10^{-5}M_\odot$ in the neutrino-heated supernova ejecta from a $20M_\odot$ star obtained by Woosley et al [24].

It might be argued that this type of event is extremely rare, accounting

for only $0.01 - 0.1\%$ of all core-collapse supernovae. However, observations of extremely metal-poor stars ([Fe/H] ~ -3) in the Galactic halo show that at least two, CS 22892-052 and CS 31082-001, out of about a hundred studied at high resolution, imply contributions from highly r-process-enhanced supernova ejecta [5] [17]. Moreover, such an extremely rare event would result in a much larger dispersion of r-process elements relative to iron than is currently observed amongst extremely metal-poor stars. Ishimaru & Wanajo [9] demonstrated that the observed star-to-star dispersion of [Eu/Fe] over a range ~ -1 to 2 dex, was reproduced by their chemical evolution model if Eu originated from stars of $8 - 10 M_\odot$. Recent abundance measurements of Eu in a few extremely metal-poor stars with [Fe/H] $\lesssim -3$ by SUBARU/HDS further supports their result [10]. The requisite mass of Eu in their model is $\sim 10^{-6} M_\odot$ per event. The ejected mass of Eu in our result is more than two orders of magnitude larger (Table 2).

In order to resolve this conflict, we propose that the "mixing-fallback" mechanism operates in this kind of supernova [19]. If a substantial amount of the hydrogen and helium envelope remains at the onset of the explosion, the outgoing ejecta may undergo large-scale mixing by Rayleigh-Taylor instabilities. Thus a tiny amount, say, $\sim 1\%$, of the r-process material is mixed into the outer layers and then ejected, but most of the core material may fall back onto the proto-neutron star via the reverse shock arising from the hydrogen-helium layer interface. In this case, the typical mass of the proto-neutron star ($\sim 1.4 M_\odot$) is recovered. An asymmetric explosion mechanism, such as that which might arise from rotating cores, may have a similar effect as the ejection of deep-interior material in a small amount [25] [4]. This "mixing-fallback" scenario must be further tested by detailed multidimensional-hydrodynamic studies. However, it may provide us with a new paradigm for the nature of supernova nucleosynthesis.

5. Summary

We have examined the r-process nucleosynthesis obtained in the prompt explosion arising from the collapse of a $9 M_\odot$ star with an O-Ne-Mg core. The core collapse and subsequent core bounce were simulated with a one-dimensional, implicit, Lagrangian hydrodynamic code with Newtonian gravity. Neutrino transport was neglected for simplicity. We obtained a very weak explosion (model Q0) with an explosion energy of $\sim 2 \times 10^{49}$ ergs, and an ejected mass of $\sim 0.008 M_\odot$. No r-processing occurred in this model, because of the high electron fraction ($\gtrsim 0.45$) with low entropy ($\sim 10 N_A k$).

We further simulated energetic explosions by an artificial enhancement of the shock-heating energy, which might be expected from calculations with other sets of input physics, as well as with other pre-supernova models. This resulted in an explosion energy of $\gtrsim 10^{51}$ ergs and an ejected mass of $\gtrsim 0.2M_{\odot}$. Highly neutronized matter ($Y_e \approx 0.14$) was ejected, which led to strong r-processing (model Q6). Material arising from r-process nucleosynthesis was calculated with a nuclear reaction network code containing ~ 3600 isotopes with all relevant reactions. The result was in good agreement with the solar r-process pattern, in particular for nuclei with $A > 130$. Some of lighter r-process nuclei ($A < 130$) were deficient, which is consistent with the abundance patterns of the highly r-process enhanced, extremely metal-poor stars CS 22892-052 and CS 31082-001. This implies that the lighter r-process nuclei may originate from another site, which we suggest might be associated with the "neutrino wind" in core-collapsing supernovae of iron cores resulted from more massive stars ($> 10M_{\odot}$).

The large ejection of r-process material ($\gtrsim 0.05M_{\odot}$ per event) conflicts with the level of dispersion of r-process elements relative to iron observed in extremely metal-poor stars. We suggest, therefore, that only a small fraction ($\sim 1\%$) of the r-processed material is ejected, while the bulk of such material falls back onto the proto-neutron star by the "mixing-fallback" mechanism.

Acknowledgments

This work was supported by a Grant-in-Aid for Scientific Research (13640245, 13740129, 14047206, 14540223) from the Ministry of Education, Culture, Sports, Science, and Technology of Japan. T.C.B. acknowledges partial support from grants AST 00-98508 and AST 00-98549 awarded by the U.S. National Science Foundation.

References

1. Baron, E., Cooperstein, J., & Kahana, S. 1987, ApJ, 320, 300
2. Burrows, A. & Lattimer, J. M. 1985, ApJ, 299, L19
3. Cowan, J. J., Thielemann, F. -K., & Truran, J. W. 1991, Phys. Rep., 208, 267
4. Fryer, C. & Heger, A. 2000, ApJ, 541, 1033
5. Hill, et al. 2002, A&A, 387, 560
6. Hillebrandt, W., Takahashi, K., & Kodama, T. 1976, A&A, 52, 63
7. Hillebrandt, W., Nomoto, K., & Wolff, G. 1984, A&A, 133, 175
8. Honda, et al. 2003, ApJ, submitted
9. Ishimaru, Y. & Wanajo, S. 1999, ApJ, 511, L33

10. Ishimaru, Y., Wanajo, S., Aoki, W., & Ryan, S. G. 2004, ApJ, 600, L47
11. Johnson, J. A. & Bolte, M. 2002, ApJ, 579, 616
12. Käppeler, F., Beer, H., & Wisshak, K. 1989, Rep. Prog. Phys., 52, 945
13. Langanke, K. & Martinez-Pinedo, G. 2000, Nucl. Phys. A, 673, 481
14. Mayle, R. & Wilson, J. R. 1988, ApJ, 334, 909
15. Nomoto, K. 1984, ApJ, 277, 791
16. Shen, H., Toki, H., Oyamatsu, K., & Sumiyoshi, K. 1998, Nucl. Phys. A, 637, 435
17. Sneden, C., et al. 2003, ApJ, 591, 936
18. Sumiyoshi, K., Terasawa, M., Mathews, G. J., Kajino, T., Yamada, S., & Suzuki, H. 2001, ApJ, 562, 880
19. Umeda, H. & Nomoto, K. 2003, Nature, 422, 871
20. Wanajo, S., Kajino, T., Mathews, G. J., & Otsuki, K. 2001, ApJ, 554, 578
21. Wanajo, S., Itoh, N., Ishimaru, Y., Nozawa, S., & Beers, T. C. 2002, ApJ, 577, 853
22. Wanajo, S., Tamamura, M., Itoh, N., Nomoto, K., Ishimaru, Y., Beers, T. C., & Nozawa, S. 2003, ApJ, 593, 968
23. Wheeler, J. C., Cowan, J. J., & Hillebrandt, W. 1998, ApJ, 493, L101
24. Woosley, S. E., Wilson, J. R., Mathews, G. J., Hoffman, R. D., & Meyer, B. S. 1994, ApJ, 433, 229
25. Yamada, S. & Sato, K. 1994, ApJ, 434, 268

NUCLEOSYNTHESIS IN THE NEUTRINO-DRIVEN WINDS FROM ROTATING PROTO-NEUTRON STARS

T. YAMASAKI
Kyoto University,
Oiwake-cho,
Kitashirakawa, Sakyo-ku, Kyoto 606-8502, JAPAN
E-mail: yamasaki@kusastro.kyoto-u.ac.jp

S. YAMADA
Waseda University,
3-4-1 Ohkubo,
Shinjuku-ku, Tokyo 169-8555, JAPAN
E-mail: shoichi@heap.phys.waseda.ac.jp

We examine the effects of proto-neutron star rotation on r-process nucleosynthesis in the neutrino-driven winds. Finding steady, axisymmetric, rotating wind solutions, we argue the possibility that such a nucleosynthesis effectively takes place there.

About a half of the heavy element nuclei are believed to be synthesized by r-process. In particular, most nuclei heavier than lead are believed to be synthesized by this process [1]. This is indicated by existence of peaks of abundance slightly off the peaks at magic number.

The neutrino-driven wind from nascent neutron-star produced by gravitational collapse is one of the most plausible site for r-process nucleosynthesis, Neutron stars are believed to be formed by gravitational collapse of massive stars. Following the well recognized scenario of the gravitational collapse, about 1[ms] after the collapse, neutrinos trapped in the neutron star begin escaping from surface of neutron star, and radiation of neutrinos from neutron star last about 10[s]. When the neutrino radiates, hot outflow are driven from neutron star surface [2]. This outflow called neutrino-driven wind is a plausible site for r-process nucleosynthesis due to its neutron richness and explosive environment of short timescale and high entropy [3]. Indeed, in the case of neutrino-driven wind, the resulting abundance of the

r-process nucleosynthesis is characterized by entropy, dynamical time scale and electron fraction of flow. Higher entropy and shorter dynamical time scale of flow are favorable for nucleosynthesis of heavier elements [4].

Although many researchers have studied to verify this hypothesis of site for the r-process nucleosynthesis, it still remains unsettled. Many studies of spherically symmetric wind result in failure to achieve sufficient nucleosynthesis, except for Terasawa et al. [5]. However, the nascent neutron stars are not spherically symmetry in general, due to the rotation or magnetic field. In this paper, we examined the possibility of the r-process nucleosynthesis in the rotating neutrino-driven wind solving two dimensional axisymmetric and steady equations of fluid.

Our purpose of this paper is to examine the efficiency of the r-process nucleosynthesis in the neutrino-driven wind. In order to know the resulting abundance, we should perform reaction network calculations. In this paper, however, we go around such calculations and only estimate the efficiency of the r-process nucleosynthesis, by adopting the formula given by Hoffman et al. [4]. The yield of r-process is determined by the mass of elements synthesized by the α-process (that is, seed element) preceding the r-process, and the number ratio of neutron to the seed elements at the time α-process is frozen. These are dependent on dynamical time scale and entropy of the wind. We calculate these values and estimate the yield of the nucleosynthesis.

The results show that in the winds from rotating proto-neutron star, short dynamical time scale which is a reasonable condition so as to achieve successful r-process nucleosynthesis is realized around the poles of neutrino-driven wind.

References

1. Burbidge, E. M., Burbidge, G. R., Fowler, W. A., Hoyle, F., *Rev. Mod. Phys.* **29**, 547 (1957).
2. Duncan, R. C., Shapiro, S. L., and Wasserman, I. *Astrophysical Journal*, **309**, 141 (1986).
3. Woosley, S. E., and Hoffman, R. D. *Astrophysical Journal*, **395**, 202 (1992).
4. Hoffman, R. D., Woosley, S. E., and Qian, Y. -Z. *Astrophysical Journal*, **482**, 951 (1997).
5. Terasawa, M., Sumiyoshi, K., Yamada, S., Suzuki, H., and Kajino, T. *Astrophysical Journal Letters*, **578**, 137 (2002).

NEUTRINO EFFECTS BEFORE, DURING AND AFTER THE FREEZEOUT OF THE R-PROCESS*

MARIKO TERASAWA
Center for Nuclear Study, University of Tokyo, Hirosawa, Wako, Saitama 351-0198; mariko@cns.s.u-tokyo.ac.jp

K. LANGANKE
Institute for Physics and Astronomy, University of Aarhus DK-8000 Aarhus C, Denmark

G. J. MATHEWS
Center for Astrophysics, University of Notre Dame, Notre Dame, IN 46556, U.S.A.

T. KAJINO
National Astronomical Observatory, Osawa, Mitaka, Tokyo 181-8588, Japan

We study the effects of neutrino interactions before, during and after the operation of the r-process in a neutrino-driven wind model with a short dynamical timescale. We find that charged- and neutral-current interactions can have specific unique effects on the final abundances. Early on, charged-current interactions determine the electron fraction, while later on, neutrino-induced neutron emission can continue to provide a slight neutron exposure even after the freezeout of the r-process. We propose that observations of an enhanced odd-even effect in the final abundances and a suppression of light nuclei in r-process material might be used to identify the neutrino fluxes in operation near the freezeout of the r-process.

1. Introduction

The rapid capture of neutrons by heavy nuclei (the r-process) is responsible for roughly half of the abundance of nuclei heavier than iron. A popular current model [1] involves the flow of neutrino heated material into the high entropy bubble above a nascent proto-neutron star in a core-collapse supernova. The r-process occurs in the region between the surface of the neutron star and the outward moving shock wave [2]. In this region the entropy is so high that the nuclear statistical equilibrium (NSE) favors abundant free neutrons and protons rather than heavy nuclei. This is, therefore, an ideal r-process site which satisfies the requirement from observations that the yields be metallicity independent [3-9]. Woosley et al. [1] obtained an excellent fit to the Solar r-process abundance pattern.

* This work will be published in Terasawa et al. [43].

However, the required high entropy in their simulation has not been duplicated by other numerical calculations (e.g. Witti et al. [10], Takahashi et al. [11]). Furthermore, it was pointed out that the light-element reaction network used in those calculations may be too limited [12]. Of particular interest for the present paper, however, is that they did not consider all possible neutrino-nucleus interactions. Since neutrinos can completely dominate the environment just outside a newly born neutron star, their effects must be included in the nucleosynthesis calculations.

Neutrino-nucleus interaction processes during the r-process have been considered by several authors [13-17]. These studies have shown that, among other things, neutrino processes tend to hinder the r-process by decreasing the neutron-to-seed abundance ratio (although they were concluded to help to smooth the final abundance pattern). These results may restrict the supernova explosion model. However, Cardall and Fuller [18], Qian and Woosley [19], Otsuki et al. [20], and Sumiyoshi et al. [21] have shown that a short dynamical timescale model included general relativistic effects can lead to successful r-process nucleosynthesis. This is because the temperature and density decrease very rapidly. Hence, charged particle reactions to make seed nuclei do not proceed efficiently, and only a small amount of seed nuclei is produced. Moreover, since electron-neutrino interactions on neutrons (converting neutrons into protons) is diminished, the neutron density remains high (Terasawa [22, 42] and Fig. 30 in Langanke and Martinez-Pinedo [23]) and a robust r-process follows. Thus, the neutrino-heated bubble remains a plausible and likely model for the r-process. It is important to carefully identify the influence of these neutrino interactions on the final abundances, since this environment is dominated by neutrino interactions.

In this paper we attempt such a detailed exploration of the specific effects which the neutrino interactions can have on the final produced abundances. We show that some unique abundance signatures can be identified which may be used to characterize the neutrino influence during the r-process freezeout. Such specific effects could be used, for example, to unambiguously identify the supernova bubble as the r-process site. We use and partially provide new neutrino-induced reaction rates for nuclei heavier than alpha-particles [24-26] and consider detailed effects of both charged-current and neutral-current interactions in the context of a neutrino-driven wind model. We show that the effects of charged-current interactions in particular may be identifiable in the final r-process abundance distribution even after freezeout and decay back to the line of stability.

2. Calculations

2.1. *Neutrino-Driven Winds*

Our goal in this paper is to quantify particular effects on the final abundance pattern due to charged- and neutral-current neutrino interactions on nuclei by adopting the winds with a short dynamical timescale.

For this purpose, we will adopt the neutrino-driven wind model as described in Terasawa et al. [27]. They employed the implicit Lagrangian code for general relativistic and spherically symmetric hydrodynamics [28]. Their model has been modified to simulate the evolution of the bubble environment above the proto-neutron star. Neutrino heating and cooling process within the bubble were calculated. Instead of solving the Boltzmann equation, they set the neutrino distribution function at each Lagrangian mesh point as described in Sumiyoshi et al. [21]. In this model, they assumed that the mass of a neutron star is about 1.4 $M_{\odot}$ and the radius is 10 km. As for other parameters, the neutrino luminosity is set to $L_{\nu,i} = 10^{51}$ erg/s for each species (i = e, μ, τ, and their antineutrinos) and average neutrino energies of $\langle E_{\nu,i} \rangle$ = 10, 20, and 30 MeV are adopted for electron-, antielectron-, and muon/tau-neutrinos, respectively. A constant pressure of $P_{out} = 10^{20}$ dyn/cm^2 is maintained at the outer boundary. Because of this low boundary pressure, the asymptotic temperature becomes low, about $T_9 = 0.4$. These lead to a high neutron to seed ratio. Note that a dynamical time scale, τ_{dyn}, is about 23 ms and an entropy, S/k, is about 200.

This model gives a reasonable reproduction of the r-process abundance distribution between the second and third peaks for a single trajectory, though the entropy is rather lower than the successful model with a high entropy ($S/k \sim 400$ in Woosley et al.[1]) and the dynamical timescale is longer than the successful models with a short dynamical timescale ($\tau_{dyn} \sim 10$ ms in Otsuki et al. [20], Sumiyoshi et al. [21], and Thompson et al. [29]). The point for successful r-process in their model is to realize the lower asymptotic temperature, $T_9 \sim 0.4$. In the models with a low asymptotic temperature, alpha reactions for seed nuclei become slower and a neutron to seed ratio becomes higher than other models. As a result, heavy elements are synthesized.

2.2. *Neutrino-Nucleus Reactions and Network Calculations*

For the calculations of r-process nucleosynthesis, we employ the reaction network of Terasawa et al. [12] which includes over 3000 species from the stability line to the neutron drip-line. In the present study, we have added following neutrino-nucleus interactions.

The charged- and neutral-current reaction rates used in this study are based upon calculations of Langanke and Kolbe [25] and references therein. We have included the charged-current interactions, e.g.

$$\nu_e + {}_ZX_N \rightarrow {}_{Z+1}X^*_{N-1} + e^- . \quad (1)$$

Note that reactions of anti-electron neutrino with heavy nuclei were found to be negligible in this study and, therefore, were not included in the results discussed here. We also included neutral-current reactions,

$$\nu + {}_ZX_N \rightarrow {}_ZX^*_N + \nu' . \quad (2)$$

Most of the multipole transition strength for the neutrino-induced reactions studied here resides above the particle (i.e. neutron) emission threshold. Hence, the excited daughter state will decay by the emission of one or several neutrons. We calculate the partial cross sections for the emission of k neutrons as described in Hektor et al. [30]. In our neutral-current calculations, we allow $k \leqq 5$. Due to the rather large Q-values encountered for the heavy neutron-rich nuclei, we consider $k \leqq 8$ neutrons emitted in charged-current reactions. Again we use the compilation of Duflo and Zuker [31,32] to derive the relevant neutron thresholds for neutron-rich nuclei.

In our r-process network calculations we do not consider the emission of k neutrons as individual channels, but describe neutrino-induced neutron emission 'on average', i.e we determine for every reaction the average number $<k>$ of neutrons emitted and assume that the reaction on the nucleus (Z,N), where Z and N are the charge and neutron numbers of the parent nucleus, leads to the final nucleus $(Z,N-<k>)$ for neutral-current reactions and to $(Z+1,N-(<k>+1))$ for charged-current reactions.

For neutrino-alpha interactions, we consider only the ^{4}He$(\nu,\nu'n)^3$He and ^{4}He$(\nu,\nu'p)^3$H reactions, even though there are other possible spallation reactions on alpha-particles. The neutron and proton branching ratios are taken from Woosley et al. [33].

3. Results

3.1. *Effects of Neutral-Current Interactions*

As for neutral-current interactions, Meyer [13] has shown that neutral-current interactions with alphas can have a significant influence on the r-process yields. He found that elements heavier than the second peak can be greatly reduced even in the very high entropy environment $S/k \sim 400$ of Woosley et al. [1]). This effect is mainly caused by neutrino-induced proton spallation from alpha particles.

However, in the present models of a neutrino-driven wind, we find that there is little effect on the final abundances from neutral-current interactions with alphas. This is because the dynamical timescale of our model is much shorter than that of Woosley et al. [1]. Hence, neutrino interactions with alphas are suppressed in our model.

We also find that neutral-current interactions with nuclei heavier than alphas have little effect on the final abundance pattern. This is because the cross sections are much smaller than those of the charged-current interactions and the number of neutrons emitted by neutral-current interactions is smaller [24,25].

3.2. *Effects of Charged-Current Interactions*

We confirmed that the charged-current interactions hinder the synthesis of heavy elements, which has been previously pointed out [13-17].

We find that the dominant effect from charged current-interactions is just that due to neutrino interactions with free neutrons and protons. Furthermore, we note the dominant effect from neutrino-induced neutron emissions. It is generally known that β-delayed neutron emission smoothes out the final abundance pattern after freezeout [2,17,34]. From this fact, one might expect that neutrino-induced neutron emission may have the same smoothing effect. On the contrary, however, we find in our hydrodynamic model that there is a larger scatter in the abundance yields in the case when neutrino-induced neutron emission is included than for the other one in which it is excluded.

In Figure 1, the dotted line includes charged-current interactions and neutrino-induced neutron emission on all nuclei. In the solid line, neutrino-induced neutron emission has been removed. We observe effects near A = 125 and 185 previously noted in Qian et al. [17], but at a much reduced level. There are, however, two additional effects to emerge from our short timescale model. For one, the largest change of abundances (nearly a factor of two) occurs in the range A = 68-76. The other is an enhanced odd-even effect. The magnitude of these effects may be smaller than the uncertainty due to the use of nuclear mass models. Nevertheless, the observed universality of r-process abundances (e.g Cowan and Sneden [35] and references therein) significantly constrains the uncertainty due to the nuclear mass model [36] as discussed below. Hence, these abundance changes by neutrino-induced neutron emission may be significant when a comparison with observed abundances is made.

Regarding the observations of r-process abundances, heavy element abundances have been detected in a number of metal-poor stars. These observations have shown that excellent agreement with the Solar system r-process abundance pattern is obtained for elements with $56 \leqq Z \leqq 76$ [35]. More recently, Honda et al. [9] have also observed several stars using the SUBARU/HDS. Although they are in

reasonable agreement with the previous observations, they also found several interesting differences in the details. Some stars agree with the Solar r-process abundances within the observational error bar. Others, however, clearly exhibit some differences with Solar abundances for light nuclei ($10 < Z < 30$), and even in the region between $56 \leqq Z \leqq 69$. Especially, odd-Z nuclei tend to have a smaller abundance than the Solar abundance (when normalized to the Solar abundance of Eu with odd-Z). This is of particular interest in the present context, since we deduce that at least some of these light elements may be the ones most affected by neutrino interactions.

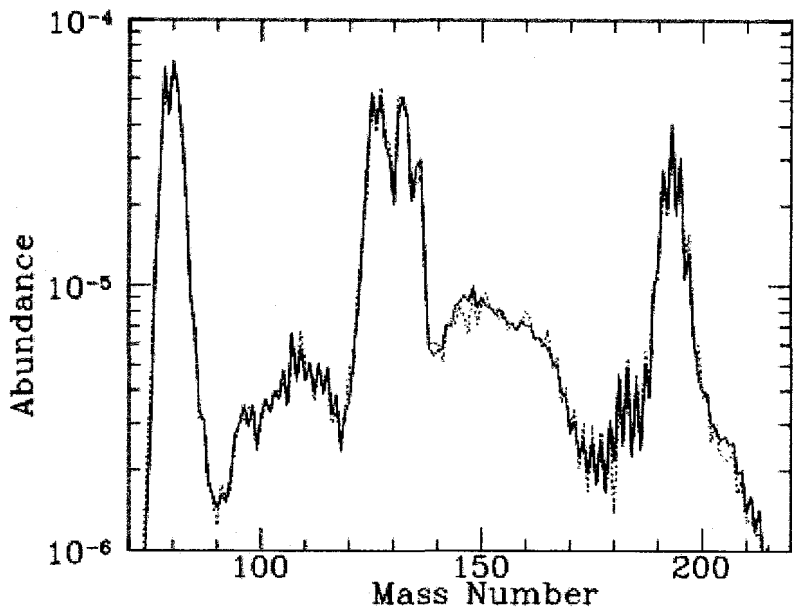

Figure 1. A comparison of final r-process yields for calculations with (dashed line) and without (solid line) neutrino-induced neutron-emissions.

As for numerical calculations of the r-process, studies of nucleosynthesis yields in a variety of different physical conditions for the r-process environment have been made [22,36-38]. It generally appears that an almost perfect universality can be theoretically realized as long as the 3rd r-process peak is reasonably produced regardless of how high the peak is [22,36]. Thus, the small changes of abundances in our present calculations are large enough to break the universality, though they are too small to explain the observational gaps. Terasawa [22,36] have also shown that there is a unique decay path for the r-process and the universality can be broken by changes in the β-decay path due to beta-delayed neutron emissions after the freezeout of the r-process. Therefore, an underproduction of odd nuclei

as suggested by the observations may be caused by changes in the decay path due to neutrino-induced neutron emission after the freezeout of the r-process. One would hope to constrain the neutrino emission model in supernovae by a detailed study of such effects on the final abundances. Therefore, we speculate that if precise observations of r-process abundance patterns can be obtained for many stars, it may be possible to unfold the relationship between the neutrino luminosity and the progenitor star.

As described before, a change of the β-decay path causes changes of abundances. The reason for this change can be traced to the availability of neutrons even after freezeout. Figure 2 displays neutron densities as a function of time. The solid and dotted lines correspond to these in the case with and the case without neutrino-induced neutron emissions, respectively. At early times ($t \leqq 1$ s) these two lines are nearly identical. These gradually show appreciable departure at late times as the dotted line rises above the solid line. This increase of neutron density is caused by neutrino-induced neutron emission.

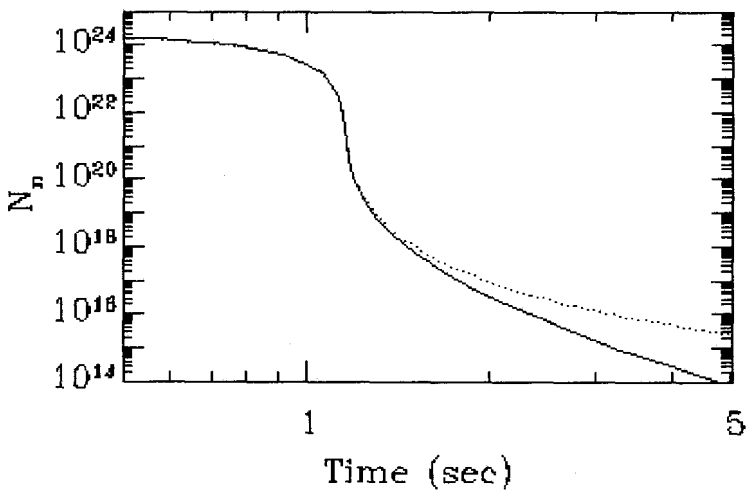

Figure2. Comparison of neutron density as a function of time for models with (dotted line) and without (solid line) neutrino-induced neutron emission in the case of $L_\nu = 10^{51}$ erg s^{-1}.

These late-time neutron captures alter the path of decay chains, since some nuclei more readily capture neutrons than others. The final abundance pattern therefore reflects differences in the neutron capture cross sections of nuclei near the stability line. When an odd-A nucleus captures a neutron, the resultant nucleus has an even-mass number. The cross section is determined by the level density of the resultant nuclei. Even-A nuclei typically have a lower density of states. Therefore, odd-A nuclei have a larger neutron capture cross section. This causes an enhancement of the odd-even effect in the final abundances. In other

words, when a strong neutrino flux continues even after freezeout, the neutron density can remain sufficiently high that an enhanced odd-even effect in the final abundance can emerge.

In the present calculations, we have adopted a neutrino luminosity of $L_\nu = 10^{51}$ erg s^{-1}. With this choice, the maximum difference in abundances between the cases with and without neutrino induced neutron emission is about factor of 1.9. However, if we adopted a larger neutrino luminosity of 10^{52} erg s^{-1}, the maximum gap also increases to over one order of magnitude. This is because the increased luminosity leads to a similar increase in the neutron density, about two orders of magnitude (Figure 3). In order to explain the gaps in the abundance patterns observed in Honda et al. [9], a neutrino luminosity greater than 10^{52} erg s^{-1} is probably needed. However, if the neutrino luminosity is too great, heavy elements are not synthesized. These facts combined lead us to conclude that these observations suggest that the r-process may be occurring in an environment with a neutrino flux about 10^{52} erg s^{-1} and that neutrino flux decreases slowly. This flux is consistent with the gravitational binding energy of the neutron star. This conclusion regarding the neutrino flux is also similar to that of Yoshida et al. [39]

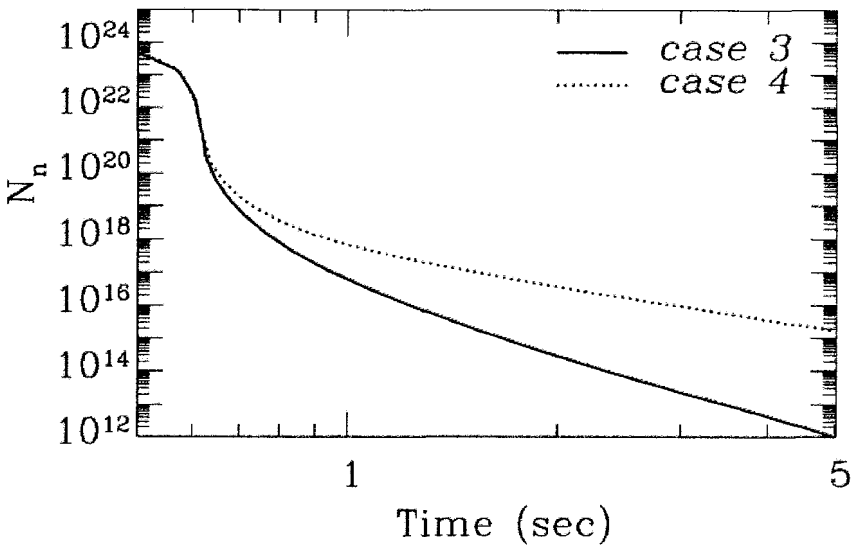

Figure 3. Comparison of neutron density as a function of time for models with (dotted line) and without (solid line) neutrino-induced neutron emission in the case of $L_\nu = 10^{52}$ erg s^{-1}.

who considered neutrino emission models which realize both the light (^{7}Li and ^{11}B) and r-process elements.

Finally, we also mention the effect of neutrino-induced neutron emission on nuclear cosmochronometry. Several studies [22,36,38,40,41] indicate that the Th-Eu chronometer may be uncertain because Th and Eu are positioned on either side of

the 3rd peak, and the initial Th-Eu ratio can vary widely. Both Th and U have an even proton number and they differ in atomic number by only two. Therefore, we expect from our calculations that both nuclei will be affected similarly by neutrino-processes. Hence, conclusions regarding the Th-U ratio may not change even when the effects of neutrino-process are large.

4. Summary

We have studied the effects of neutrino-interactions on the r-process nucleosynthesis in the context of a neutrino-driven wind model with a neutron star mass of 1.4 $M_{\odot}$. This model has a short expansion timescale, about 20 msec, and a moderately high entropy, about $S/k = 200$ [27].

In this short expansion timescale model, we find that the most important neutrino interactions are those involving free nucleons at an early phase of the expansion near the surface of the proto-neutron star. These reactions determine the initial electron fraction and the end point of synthesized elements by the r-process. Later, after alpha synthesis, these interactions unilaterally change neutrons into protons which quickly lock up into alphas. Therefore, the amount of heavy elements produced diminishes as these neutrino interactions increase.

We have also found that neutrino-induced neutron emission, especially by charged-current interactions, may have a significant role in explaining some differences between observational abundance patterns in metal-poor stars and the Solar system [9]. When neutrino-induced neutron emission is important, nuclei with smaller neutron-capture cross sections become more abundant. This is because the flux of neutrons generated by neutrino-induced neutron emission causes neutron captures in addition to β-decays after the freezeout of the r-process. This difference in capture cross section leads to an enhanced even-odd effect in the final abundances. From detailed studies of this effect, one may be able to constrain the neutrino spectrum in the neutrino-driven winds and deduce a relationship between the neutrino spectra and progenitor stars. For this, we need more studies of supernova explosions and more samples of the heavy-element abundance pattern in metal-poor stars.

The effects of neutral-current interactions are not as significant. However, we have found that they can increase the amount of light nuclei with $A \leqq 80$ and reduce the heavy nuclei ($A \geqq 200$). This tendency may help to solve the problem of the observed depletions of the lighter nuclei relative to Solar abundances [5].

For details see Terasawa et al. [43].

Acknowledgments

We thank Edwin Kolbe for his help providing the neutrino-nucleus cross sections. One of the authors (MT) wishes to acknowledge the fellowship of the Japan Society for Promotion of Science (JSPS). This work has been supported in part by Grants-in-Aid for Scientific Research (12047233, 13640313, 14540271) and for Specially Promoted Research (13002001) of the Ministry of Education, Science, Sports and Culture of Japan. Our work was partially supported by the Danish research Council. Work at the University of Notre Dame supported by the U.S. Department of Energy under Nuclear Theory Grant DE-FG02-95-ER40934.

References

1. S. E. Woosley, J. R. Wilson, G. J. Mathews, R. D. Hoffman, and B. S. Meyer, *ApJ*, **433**, 229 (1994)
2. B. S. Meyer, G. J. Mathews, W. M. Howard, S. E. Woosley, and R. D. Hoffman, *ApJ*, **399**, 656 (1992)
3. C. Sneden, A. McWilliam, G. Preston, J. J. Cowen, D. Burris, and B. J. Armosly, *ApJ*, **467**, 819 (1996)
4. C. Sneden, J. J. Cowen, L. B. Debra, and J. W. Truran, *ApJ*, **496**, 235 (1998)
5. C. Sneden, J. J. Cowen, I. I. Ivans, G. M. Fuller, S. Burles, T. C. Beers, and J. E. Lawler, *ApJ*, **133**, 139 (2000)
6. J. Westin, C. Sneden, B. Gustafsson, and J. J. Cowan, *ApJ*, **530**, 783 (2000)
7. J. A. Johnson, and M. Bolte, *ApJ*, **554**, 888 (2001)
8. R. Cayrel et al., *Nature*, **409**, 691 (2001)
9. S. Honda, W. Aoki, T. Kajino, H. Ando, T. C. Beers, H. Izumiura, K. Sadakane, and M. Takada-Hidai, *Accepted for publication in ApJ* (2004)
10. J. Witti, H.-Th. Janka, and K. Takahashi, *A & A*, **286**, 841 (1994)
11. K. Takahashi, J. Witti, and H.-Th. Janka, *A & A*, **286**, 857 (1994)
12. M. Terasawa, K. Sumiyoshi, T. Kajino, I. Tanihata, and G. J. Mathews, *ApJ*, **562**, 470 (2001)
13. B. S. Meyer, *ApJ. Lett.*, **449**, 55 (1995)
14. G. M. Fuller, and B. S. Meyer, *ApJ*, **453**, 792 (1995)
15. G. C. McLaughlin, and G. M. Fuller, *ApJ Lett.*, **464**, 143 (1996)
16. G. C. McLaughlin, and G. M. Fuller, *ApJ*, **489**, 766 (1997)
17. Y.-Z. Qian, W. C. Haxton, K. Langanke, and P. Vogel, *Phys. Rev. C*, **55**, 1532 (1997)
18. C.Y. Cardall, and G. Fuller, *ApJ Lett.*, **486**, L111 (1997)
19. Y.Z. Qian, and S.E. Woosley, *ApJ*, **471**, 331 (1996)
20. K. Otsuki, H. Tagoshi, T. Kajino, and S. Wanajo, *ApJ*, **533**, 424 (2000)

21. K. Sumiyoshi, H. Suzuki, H., K. Otsuki, M. Terasawa, and S. Yamada, *Publ. Astron. Soc. Japan,* **52**, 601 (2000)
22. M. Terasawa, *PhD Thesis, University of Tokyo* (2002)
23. K. Langanke and G. Martinez-Pinedo, *Rev. Mod. Phys*, **75**, 819 (2002)
24. K. Langanke and E. Kolbe, *At. Data Nucl. Data Tables*, **79** 293 (2001)
25. K. Langanke and E. Kolbe, *At. Data Nucl. Data Tables*, **82** 191 (2002)
26. E. Kolbe and K. Langanke (2003): kolbe@quasar.physik.unibas.ch, langanke@ifa.au.dk
27. M. Terasawa, K. Sumiyoshi, S. Yamada, H. Suzuki, T. Kajino, *ApJL*, **578**, L137 (2002)
28. S. Yamada, *ApJ*, **475**, 720 (1997)
29. T. A. Thompson, A. Burrows, and B. S. Meyer, *ApJ*, **562**, 887 (2001)
30. A. Hektor, E. Kolbe, K. Langanke and J. Toivanen, *Phys. Rev.*, **C61**, 055803 (2000)
31. J. Duflo and A. P. Zuker, *Phys. Rev.*, **C52**, R23 (1995)
32. J. Duflo and A. P. Zuker, *Phys. Rev.*, **C59**, R2347 (1999)
33. S. E. Woosley, D. H. Hartmann, R. D. Hoffman, and W. C. Haxton, *ApJ*, **356** 272 (1990)
34. T. Kodama and K. Takahashi, *Phys. Lett.*, **43B**, 167 (1973)
35. J. J. Cowan and C. Sneden, *ArXiv Astrophysics e-prints*, **0212149** (2002)
36. M. Terasawa, *Nucl. Phys.*, **A719**, 296 (2003)
37. H. Schatz, R. Toenjes, B. Pfeiffer, T. C. Beers, J. J. Cowan, V. Hill, and K. Kratz, *ApJ*, **579**, 626 (2002)
38. K. Otsuki, G. J. Mathews, and T. Kajino, *New Astronomy*, **8**, 767 (2003)
39. T. Yoshida, M. Terasawa, T. Kajino, K. Sumiyoshi, *ApJ*, **600**, 204 (2004)
40. B. S. Meyer and J. W. Truran, *Phys. Rep*, **333**, 1 (2000)
41. S. Goriely and M. Arnould, *A&A*, **379**, 1113 (2001)
42. M. Terasawa, *Master Thesis, University of Tokyo* (1999)
43. M. Terasawa, K. Langanke, T. Kajino and G. J. Mathews, *ApJ*, **10 June** (2004)

HALF-LIFE MEASUREMENT OF NEUTRON-RICH NUCLEI AND FUTURE AT RIBF

S. NISHIMURA *, Y. NISHI, M. KURATA-NISHIMURA, I. TANIHATA
RIKEN, Hirosawa 2-1, Wako, Saitama, 351-0198 JAPAN

M. A. FAMIANO
National Superconducting Cyclotron Laboratory, MI 48824, USA

M. E. HOWARD, D. REITZNER, E. E. SMITH, R. N. BOYD
Ohio State University, Columbus, OH 43210, USA

A new accelerator facility RI Beam Factory will be operated in 2006 at RIKEN. Its production capability enables us to study the characteristics of nuclei far from the stability. A new beta counting system has been developed to study the beta decay of rare isotopes produced by fast fragmentation. Our preliminary results on half-life measurement are presented as well as the expected performance of the upgraded system in future.

1. Introduction

Astrophysical rapid neutron-capture process (r-process) has been recognized to play an important role for the synthesis of approximately half of the nuclear species which are more massive than Fe [1,2,3]. Such neutron captures should happened through neutron-rich nuclei, where the reaction process should be faster than beta-decays under high neutron density environments. An accurate r-process calculation is expected not only to understand the location of such processes, but also for the application to chronometers of old stars through the relative abundances of some r-process nuclei such as ^{238}U and ^{232}Th.

Informative studies of the astrophysical network calculations in the r-process can be accomplished with a knowledge of nuclear physics properties, namely, the nuclear mass related to neutron separation energies Sn and

*E-mail: nishimu@rarfaxp.riken.go.jp

β-decay Q_β values, the β-decay half-lives $T_{1/2}$, and β-delayed neutron-emission probabilities P_n [4]. Furthermore, systematic measurement of these nuclear properties has a possibility to shed light on the new features of the nuclear properties such as the discovery of new magic number in N=16 [5]. The experimental difficulties, however, increases somehow exponentially with additional number of neutrons for the r-process nuclei toward the neutron-drip line due to its drastic reduction of production yield. Therefore, constructions of a new accelerator facility for intense radioactive beam is essential together with the development of an efficient beta counting system.

In this paper, a new accelerator facility at RIKEN will be briefly reported, mainly focused on the production capability of rare isotopes. In addition, our preliminary results on half-lives of neutron-rich nuclei will be presented as well as the overall performance of new detection system.

2. RIKEN RI Beam Factory (RIBF)

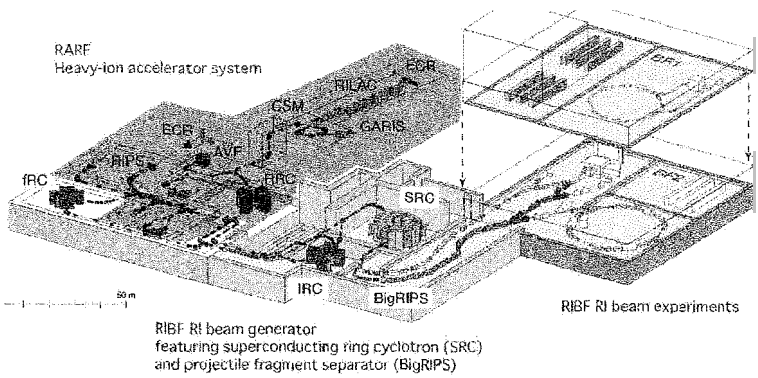

Figure 1. **Schematic view of accelerators for the RIBF at RIKEN. About** 1 pμA of uranium beam is expected after the Super-conducting Ring Cyclotron (SRC).

Production of radioactive isotope (RI) beams by means of an in-flight separation scheme provides opportunities to study reactions and properties of unstable nuclei far from stabilities. Recently, several new projects for the next-generation of accelerator facilities are planned for drastic extension of nuclear chart. The RI Beam Factory (RIBF), which is under construction at

RIKEN, will become the most powerful accelerator facility in the world and will be ready to produce highest intensity of RI beam in 2006 [6]. Figure 1 shows a schematic view of the RIBF including the existing facilities. The cascade of the cyclotrons can provide a wide range of heavy ion beams, boosting their energies up to 400 MeV/nucleon in the case of relatively light elements (A < 40) and 350 MeV/nucleon in the case of heavier elements up to uranium. Intense RI beam production will be performed via projectile fragmentation of energetic heavy ions or in-flight fission of massive ions including uranium. In the case of using the in-flight fission of ^{238}U ions,

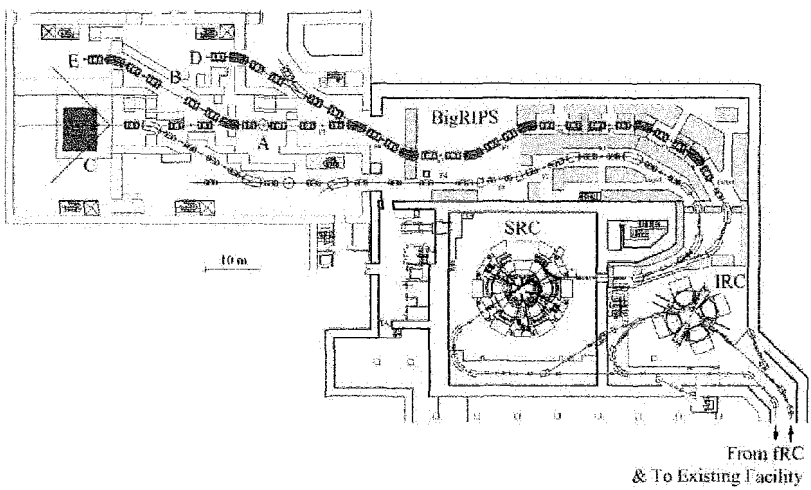

Figure 2. Part of planned layout of RIKEN-RIBF and experimental hall with the separator Big-RIPS.

for instance, the intensity of a doubly-magic neutron-rich nucleus ^{132}Sn is estimated to be in the order of 10^8 pps, which is almost 10^3 times larger than the projectile fragmentation of ^{136}Xe beam [7]. The in-flight fission, however, causes a much larger spread in both angle and momentum. Consequently, large aperture superconducting quadrupoles are chosen as components of the separator for the large acceptances.

Figure 2 shows a top view of the separator Big-RIPS. The first stage of the Big-RIPS serves to produce and separate RI beams. The second stage serves to identify RI-beam species as well as to measure their momentum in event-by-event basis. The particle tracking method is employed to de-

termine the momentum from Bρ value. The time-of-flight (TOF) and the energy loss will be measured for the determination of the ratio of mass number to charge number (A/q) and the atomic number (Z) in the transport beam line.

Figure 3 shows a nuclear chart with expected drip-lines[8]. The line near the neutron drip-line illustrates the resulting scientific reach of fast beams (one particle / day) assuming the maximum primary beam intensity of 1 pμA. Here, the target thickness and the charge states are optimized to provide the highest secondary beam intensity [9]. The produced RI beams are collected and separated by using the BigRIPS. Since, transit time of RI beams through the separator is expected to be below the order of μs, experiment with fast fragmentation beams offers the advantages that are beyond the reach of experiments with re-accelerated beams in terms of efficient beam transportation of short-lived nuclei. One may find that considerable amount of neutron-rich nuclei, which are important for the r-process path, will be possibly measured at the RIBF.

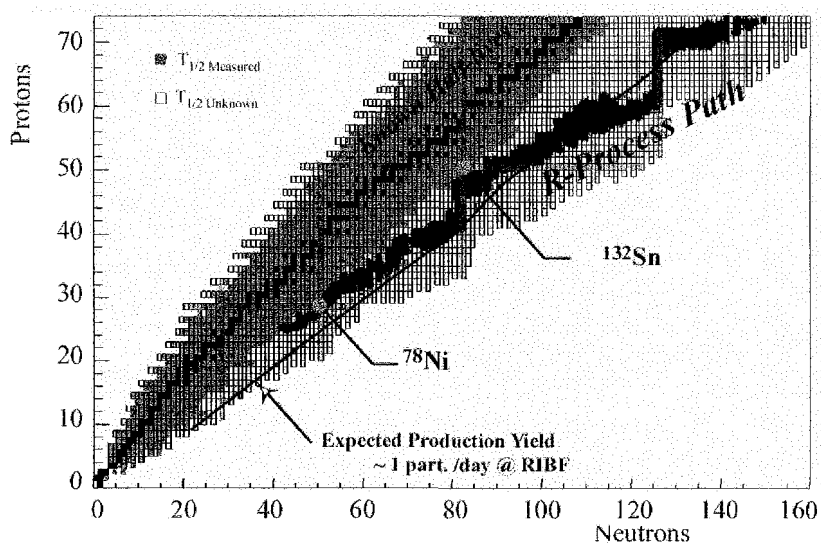

Figure 3. Nuclear chart with the status of half-life measurement. Filled boxes correspond to the known half-lives, and open is for the unknown ones. Most of the half-lives along the expected r-process path have not been measured yet. The production yield of about one particle per day at the RIBF is shown in the neutron-rich side.

3. Half-life measurement

As discussed in the previous section, the production capabilities at the RIBF is extremely high so that drastic improvement of the nuclear chart mapping is expected along the r-process path. As a result, new isotopes search would be an experiment with the first beam, and of course the half-life measurement related to astrophysics research will be performed simultaneously. Figure 3 contains some information for the half-life measurement, where the filled boxes correspond to the nuclei with known half-lives, and opens are for the missing half-lives. Worldwide efforts have been devoted for half-life measurements with various kinds of experimental techniques. One of the critical issues in the experiment is the accumulation of the statistics for the precise measurement of half-life, where the decay time is deduced via the fitting procedure of the decay spectrum. Another issue is the technical difficulties in the particle identification of the produced nuclei, especially for the massive region.

At present, various kinds of experiments have been carried out at GANIL, MSU, GSI, and ISOLDE. For example, GSI has constructed a high precision storage ring ESR, which enables us to measure the masses and their half-lives simultaneously. The GANIL and MSU have established the decay measurement system using position-sensitive silicon detectors, which are used for the implantation of the incident ions as well as the beta-ray detection. The advantage of this scheme is its capabilities of measuring the energy deposited for both the incident ion and associated beta decays in very short time below ms. Thus, the experimental setup using such position sensitive silicon detectors is certainly one of the options for the the half-life measurement with weak beams [10,11].

On the other hand, about $60 \sim 70$ of isotopes with unknown half-lives is expected to be produced at the first beam of the RIBF even with the beam intensity of 1/100 of maximum ($\sim$10 nA of uranium beam). These isotopes will arrive at the end of our beta counting system with mixed condition. Therefore, the operation of beta counting system with faint beam is not feasible from the aspect of efficiency. Besides the option of introducing silicon detector array or the expensive storage ring, it is worth developing a new beta counting system aiming at efficient and simultaneous measurements of the half-lives for rare isotopes under high beam-intensity condition.

3.1. *Development of beam-line detectors*

The fast fragmentation beam contains various kinds of isotopes with different charge states. The particle identification in the beam line is essential, but difficult especially in the massive region. Usually, particle identification is performed with the combination of position (X,Y), energy deposited (ΔE/dx), time-of-flight (TOF), and total energy (E). Because of the operation of the beam line detectors under high beam intensity, measurement of ΔE/dx by standard silicon detector is not realistic due to its weakness in terms of radiation hardness. Recently, high precision ionization chamber (IC) is the devices which has been developed instead of silicon detector at RIKEN [12]. The advantages of this IC is its energy resolution, equivalent to that of silicon detector, even in the beam intensity of above 10^5. Also, it's radiation hardness promises us for a stable operation of experiment for long term. In addition, we have developed a ultra-fast TOF detector with timing resolution of below 7 ps for ^{40}Ar beam at the energies of 95MeV per nucleon and even better for massive nuclei using fast plastic scintillator [13]. The precise measurement of TOF with extended flight through the downstream beam line spectrometer (Zero-degree spectrometer) enables us to improve the separation of the produced fragments.

4. Design and construction of beta counting system

Development of a high efficiency beta counting system is essential for statistical improvement of the half-life measurement for the nuclei far from the stability. The reduction of the backgrounds is also required in the reconstruction of decay events. In general, beta-delayed gamma-ray techniques works well for identification of decay from the nuclei of interest [14]. However, requirement of delayed gamma measurement certainly decreases the statistics of decay events and becomes critical for very neutron-rich nuclei. At the RIBF, severe backgrounds is expected for the half-life measurement in the case of high intensity of mixed beam.

A new beta counting system is designed and constructed for efficient measurement of decay spectrum as well as minimizing the contaminants from various kinds of background including cosmic rays. The apparatus of the beta counting system is shown in Figure 4. The system is comprised of two subsystems. One is the intermediate moving stopper plates attached to the rotating wheel as to stop the incident isotopes. Another is high efficiency position-sensitive scintillation counters for the detection of beta-rays. The details of the subsystems are described below.

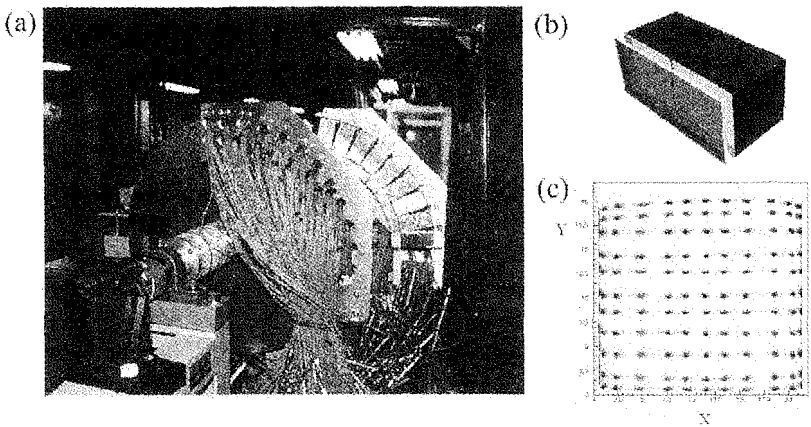

Figure 4. (a) A schematic view of the whole system for half-life measurement using rotating wheel covered by the beta-ray detection system. (b) As a position sensitive beta-ray detectors, a thin scintillator is coupled on the PMT window directly for efficient measurement of beta-rays. (c) Mapping of a position sensitive PMT R8520 irradiated by blue-LED light.

4.1. *Multi-layer stopper foils*

One of the characteristics of this system is its structure of ion stopper plates consisting of multi-layers of thin plates. These layers enable us to separate the isotopic species in the layer depth according to their different stopping range in the material. In fact, simulation study using stopping ion code SRIM combined with a beam transport code MOCADI indicates that nuclei are fairly distributed in the target system, with higher-Z nuclei stopping sooner. The application of the thin materials instead of the silicon detectors is aimed to avoid the potential problem of radiation damage on the detector itself. Furthermore, background decays from the accumulated unstable nuclei could be minimized easily by sweeping the remaining daughter nuclei away as well as increasing the accuracy of position association using rotating disks as is shown in Figure 4.

4.2. *Beta-ray detection system*

A next generation of beta-ray detection system has been developed using a new position sensitive photomultiplier tube (Hamamatsu R8520). Apparatus of the beta-ray detection system is shown in Figure 4(b). A plastic scintillator with thickness of 0.5 mm is directly attached on the PMT win-

dow. The advantage of this beta-ray detection system is its high detection efficiency as well as its high precision position measurement of beta-rays [15]. These features allow us to operate the device under high multiplicity environment with mixed beam condition without suffering the pile-up of decay events. To reduce the total number of readout channels, a resistive network was connected to the PMT anodes for position determination [16,17]. The centroid position of each event is calculated by measuring the pulse heights, and hence the complication due to cross-talk between neighboring anodes could be removed. Rejection of gamma-ray in the beta-ray detector could be achieved by adding additional layer of slow scintillators as phoswich detector.

4.3. *Half-life measurement at RIPS*

Our primary experiment is carried out at the RIKEN Ring Cyclotron (RRC). Figure 5 shows a schematic view of the experimental setup. The neutron-rich nuclei have been produced by the fragmentation of a 63A·MeV $^{86}Kr^{32+}$ beam, of mean intensity 1 eμA, onto a ^{9}Be target of 375 μm thickness. The produced fragments are separated by the RIPS, where a momentum slit and a 60mg/cm^2 Al wedge degrader are used. Four position sensitive parallel-plate avalanche counter PPACs [18] are installed in the beam line and two of them at the F3 are used to measure the trajectory of incoming fast beam. The fragment energy loss, for beam particle identification purposes, is measured using 150 μm silicon detector (SSD). The TOF of fragment is determined by the time difference between two scintillation detectors. The inset of Figure 5 presents a scatter plot between the dE/dx and the the TOF. Our primary experiment shows reasonable capability of particle identification, where the neutron-rich V, Cr, Mn, Fe, Co, and Ni isotopes are clearly identified. The separated fast fragment beam is directed to the beta counting station installed at the end of the beam line, where beam chopper has not been applied during the experiment. As is reported [15,19], the incident ions are implanted on a single layer of active scintillation material. The thickness of the scintillation stopper plate is 0.2 mm in order to separate the charge of incident ions. Several thickness of degraders are installed in front of the beta counting system and are used in order to adjust to stopping range of the target nuclei (^{61}V, ^{63,64}Cr, ^{65,66}Mn, ^{67,68}Fe, and ^{69,70}Co) in the plates. Scintillation light emitted from the active scintillation stopper plate is measured by the downstream position sensitive veto counter via air coupling, so that the stopped position in space is confirmed

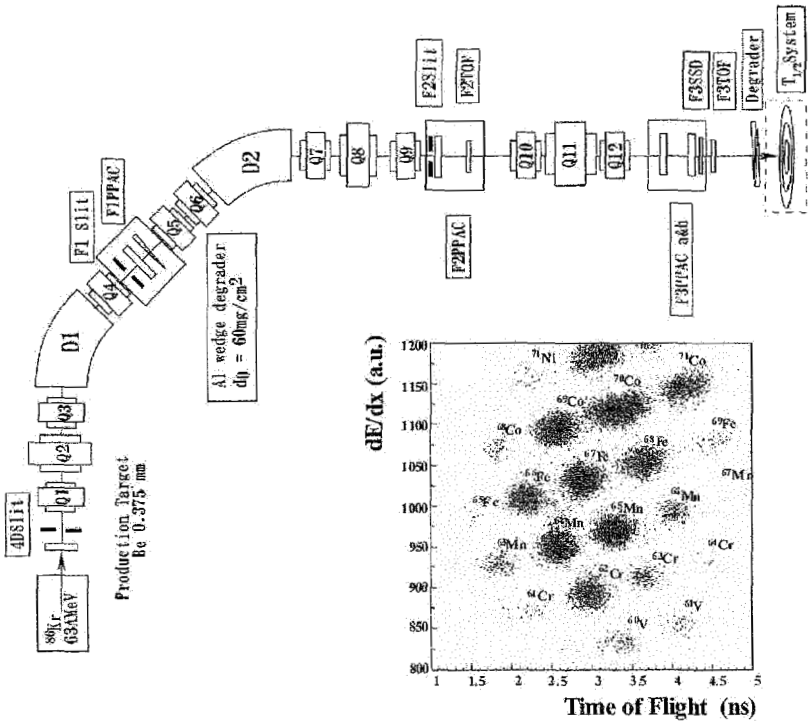

Figure 5. ^{86}Kr beam are impinged on the Be target at the energies of 63 MeV per nucleon. The produced fragments are transported via RIPS spectrometer and implanted on the beta counting system installed at the end of beam line. The capability of particle identification is confirmed using SSD detector and TOF detectors.

directly including the depth.

As the wheel is rotated continuously at the speed of 60 rpm, every nucleus caught in the stopper plate is transported immediately to the beta-ray detection section ($\phi = 10 \sim 100$ °). The beta-rays from these decays are collected by covering both sides of the stopper plates with the position sensitive beta-ray detectors along the rotating direction in ϕ. The event associations between the implanted nuclei and the beta decays are achieved by the precise position measurements of incident nucleus and the beta-decay positions on the stopper plates. Since there are two independent trigger events for the beams and beta-decays, each event is stored in common data taking system with the label of trigger and absolute time stamp generated

by a free-running clock (one pulse per every 100 μs). Decay times are obtained by subtracting the time of a fragment implant from that of its associated beta decay in the offline analysis.

Figure6(a) shows the angle correlation between the decay position and the implanted position in ϕ for ^{65}Mn. A peak at zero indicates that event association is achieved between implanted ions and the decay points. The beta-decay time spectrum in correlation with the implantation of ^{65}Mn is deduced after the careful event association (See Fig.6(b)). The cutoff time after 250 ms is determined by the acceptance of the beta-ray detectors. The half-lives of nuclei are extracted by considering the four parameters in the fitting procedure: the half-lives of the mother and daughter nuclei, the beta detection efficiency, and the background rate over the collecting time. The half-lives of daughter nuclei have been obtained from the experimental values in the reference [20]. The errors in the measured values

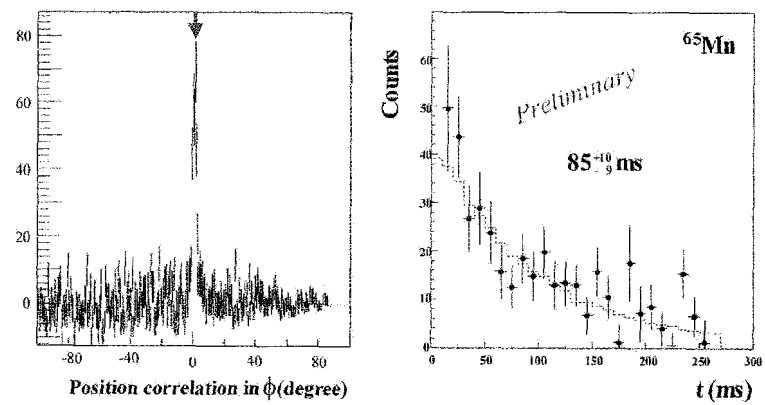

Figure 6. beta-decay spectrum of ^{65}Mn has been deduced with half-life of 85±10ms, consistent with the previous measured values of 89±10ms.

of half-lives are estimated from the chi-square mapping of decay spectra. Our preliminary results of half-lives for the neutron-rich ^{63,64}Cr, ^{65,66}Mn, ^{67,68}Fe, and ^{69,70}Co nuclei are summarized in Table 1. In addition, the results from other experiments [20] and theoretical predictions[21] are listed for comparison. Our results are consistent with the recent values reported from the experiment at GANIL [22]. The discrepancy between the experimental values and the theoretical predictions support the overabundances of ^{64}Ni in certain inclusions of meteorites as is discussed. Partial γ-ray spectra are

also taken for these nuclei by the NaI(Tl) detectors attached beside the β detectors for the β-γ coincidence, though the statistics were not enough for extracting useful information .

Table 1. Preliminary results of half-lives of ^{63,64}Cr, ^{65,66}Mn, ^{67,68}Fe, and ^{69,70}Co nuclei. Also presented are the results from other experiments and theoretical predictions.

RI	$T_{1/2}^{Thiswork}$ (ms)	$T_{1/2}^{Exp.}$ (ms)	$T_{1/2}^{Theo.}$ (ms)
^{70}Co	135 $(^{+11}_{-9})$	120	47.5
^{69}Co	197 $(^{+80}_{-29})$	216	76.6
^{68}Fe	155 $(^{+34}_{-18})$	155	767.3
^{67}Fe	597 $(^{+209}_{-100})$	470	1139
^{66}Mn	103 $(^{+44}_{-33})$	66	23.1
^{65}Mn	85 $(^{+10}_{-9})$	88	28.9
^{64}Cr	61 $(^{+60}_{-19})$	44	153.9
^{63}Cr	161 $(^{+104}_{-91})$	113	96.6

4.4. *Future upgrade of beta counting system*

The beta counting system has been designed for the half-life measurement of short-lived nuclei. However, current system will also suffer the event associations for the long-lived nuclei due to the increase of accidental coincidences. The upgrade of the system is planned by introducing additional coincidences. First of all, an identification capabilities of the beta-rays against the background gamma-rays and the noise from the PMTs will be achieved by adding additional layer of slow scintillator (CaF_2(Eu)). This phoswich structure enables us to measure the energies of beta-rays, where the position information could be maintained by introducing pixel structures (5x5x15 mm^3) of thick scintillators. In addition, the multi-layer of tapes will be introduced instead of rotating wheel in order to increase the cycle time, i.e. to reduce the decay events from the previous cycle of implantation. The depth information could be also extracted by introducing different speed of tape for each layer instead of installing additional detection arrays. Simultaneously, emission probabilities of neutrons and energies of the gamma-rays could be also measurable by installing the high efficiency detectors (Liquid scintillators, ^{3}He gas counters, NaI(Tl), Germanium) along the beta-ray detectors. Certainly, these detectors will provide us for additional information on the nuclei as well as a drastic improvement in the background reduction.

5. Summary

A new accelerator facility RIBF will be ready in 2006 at RIKEN. Its capability of producing neutron-rich nuclei will provide us good opportunities for studying the nuclei related to the r-process. A beta counting system with position sensitive scintillation detectors has been constructed and tested using the existing Ring Cyclotron. Our primary experiment for half-life measurement successfully demonstrates the possibility of reconstructing beta-decay spectra of rare isotopes even with mixed beam. Further upgrades of the detectors are in progress.

5.1. *Acknowledgments*

The authors gratefully acknowledge all of the staff at the RIKEN Ring Cyclotron for insuring smooth operation of the accelerator. This work was supported partially by the President's Special Research Grant at RIKEN

References

1. G.J. Mathews and J.J. Cowan, *Nature* **345**, 491 (1990).
2. B.S. Meyer, *Ann. Rev. Astron. Ap.* **32**, 153 (1990).
3. J.H. Cowan, et al., *Astrophys. J.* **521**, 194 (1999).
4. J. Engel, et al., *Phys. Rev.* **C60**, 014302 (1999).
5. A. Ozawa, et al., *Phys. Rev. Lett.* **84**, 5493 (2000).
6. I. Tanihata, *J. Phys. and Nucl. Part. Phys.* **24**, 1311 (1998).
7. T. Kubo, *Nucl. Instrum. and Meth.* **B204**, 97 (2003).
8. H. Koura, et al. *Nucl. Phys.* **A674**, 47 (2000).
9. K. Suemmerer, B. Blank, *Phys. Rev.* **C61**, 034607 (2000).
10. J.I. Prisciandaro et al., *Phys. Lett* **B510**, 17 (2001).
11. O. Sorlin, et al., *Eur. Phys. J* **A16**, 55 (2003).
12. K. Kimura, et al., *RIKEN Accel. Prog. Rep.* **33**, 176 (2000).
13. S. Nishimura et al, *Nucl. Instrum. and Meth.* **A510**, 377 (2003).
14. P.F. Mantica, et al., *Phys. Rev.* **C67**, 014311 (2003).
15. S. Nishimura et al., *Nucl. Phys. A* **718**, 214c (2003).
16. M.P. Tornai, et al., *IEEE Trans. Nucl. Sci.* **NS-43** (1996).
17. K. Inoue, et al., *Nucl. Instr. and Meth.* **A423**, 364 (1999).
18. H. Kumagai, et al., *Nucl. Instr. and Meth.* **A470**, 562 (2001).
19. M.A. Famiano, Y. Nishi, S. Nishimura, and I. Tanihata, *Nucl. Instrum. and Meth. A* **496**, 248 (2003).
20. T. Horiguchi, T. Tachibana, H. Koura, and J. Katakura, *Chart of the Nuclides* (2000).
21. P. Möller, J.R. Nix, and K.-L. Kratz, *Atomic Data and Nuclear Data Tables* **66**, 131 (1997).
22. O. Sorlin et al., *Nucl. Phys.* **A719**, 193c (2003).

DIRECT MEASUREMENTS OF THE ASTROPHYSICAL (α, n) AND (p, n) REACTIONS BY USING LOW-ENERGY LIGHT NEUTRON-RICH RNB

HIRONOBU ISHIYAMA, HIROARI MIYATAKE, MASA-HIKO TANAKA, YUTAKA WATANABE, NOBUHARU YOSHIKAWA, SUNCHAN JEONG, YOSHITAKA MATSUYAMA, YOSHIHIDE FUCHI, ICHIRO KATAYAMA, TORU NOMURA

Institute of Particle and Nuclear Studies, High Energy Accelerator Research organization (KEK), Tsukuba, Ibaraki, 305-0801 Japan

TAKASHI HASHIMOTO, TOMOKO ISHIKAWA, KOUJI NAKAI

Department of Physics, Tokyo University of Science, Noda, Chiba, 278-8510 Japan

SURANJAN K. DAS, PRANAB K. SAHA, TOMOKAZU FUKUDA

Osaka Electro-Communication University, Neyagawa, Osaka, 572-8530 Japan

KATSUHISA NISHIO, SHINICHI MITSUOKA, HIROSHI IKEZOE, MAKOTO MATSUDA, SHINICHI ICHIKAWA

Japan Atomic Energy Research Institute (JAERI), Tokai, Ibaraki, 319-1195 Japan

TAKESHI FURUKAWA, HIDEAKI IZUMI, TADASHI SHIMODA

Department of Physics, Osaka University, Toyonaka, Osaka, 560-0043

YUTAKA MIZOI

The Institute of Physical and Chemical Research (RIKEN), Wako, Saitama, 351-0198 Japan

MARIKO TERASAWA

Center for Nuclear Study, University of Tokyo, Wako, Saitama, 351-0198 Japan

An experimental program to measure reaction cross sections of (α, n) and (p, n) reactions on light neutron-rich nuclei by using low-energy radioactive nuclear beams is in progress at Tandem accelerator facility of Japan Atomic Energy Research Institute. Exclusive measurements of ^{8}Li(α, n)^{11}B and ^{16}N(α, n)^{19}F reaction cross sections have been performed successfully. Their excitation functions together with the experimental method are presented.

1. Introduction

Where the rapid process takes place has been a long-standing puzzle in the history of theoretical studies of element synthesis in the universe. One of the most probable sites for the r-process often discussed today is the so-called " hot bubble" in the supernova explosion. That is, the r-process is considered to occur in the region between the surface of a pre-neutron star and the outward-moving shock wave during the explosion. The nuclear statistical equilibrium favors abundant free neutrons and alpha particles in this region as long as the relevant temperature is high. When we follow the paper of Ref. [1], even seed nuclei for the r-process can be produced in this region in the early α-capture process at around $T_9 = 3$. When the temperature and density become lower and charged-particle induced reactions almost cease, the usual r-process starts from such seed nuclei produced and a large number of free neutrons. Therefore, nuclear reactions such as (α, n) on light neutron-rich nuclei play an important role as the r-process starting point [1].

However, there is little experimental data on cross sections of reactions on light neutron-rich nuclei. We are therefore proceeding an experimental project to measure systematically cross sections of astrophysical interest for (α, n) and (p, n) reactions on ^{6}He, ^{8}Li, ^{10}Be, ^{12}B, ^{16}N, and ^{20}F using radioactive nuclear beams (RNB) [2, 3] at Tandem accelerator facility of Japan Atomic Energy Research Institute (JAERI). Direct measurements of ^{8}Li(α, n)^{11}B, ^{16}N(α, n)^{19}F and ^{16}N(p, n)^{16}O reaction rates have been already carried out and their analysis are in progress.

The present method of production of low-energy neutron-rich RNB, some characteristics of the detection system as well as the resultant excitation functions of ^{8}Li(α, n)^{11}B and ^{16}N(α, n)^{19}F reactions are presented in this paper.

2. Experiment

2.1. *RNB production*

Because the beam energy available is relatively low, we have decided to produce low-energy neutron-rich beams by using transfer reactions on light targets. In this case, it is important to avoid impurities originating from the primary beam particles [4]. We have utilized a recoil mass separator (RMS) existing at Tandem accelerator facility [5, 6], which consists of two electric dipoles and a magnetic dipole as shown in Fig. 1. The RNB can be separated from the primary beam using the difference of the magnetic and electric rigidities.

The d(^{18}O, ^{16}N)α reaction was chosen for production of ^{16}N-beam. The production target was D_2 gas of 1 atmospheric pressure contained in a 5 cm long chamber separated from the vacuum region with 7.5 μm Havar foils. The typical intensity of the primary $^{18}O^{6+}$-beam of 73 MeV was about 300 enA on the target. The ^{16}N-beam energy was 32 MeV at the exit of the target. The intensity of the secondary beam was then 4.7 kpps at the focal plane of RMS. The contamination of ^{18}O particles in the ^{16}N-beam measured with a ΔE-E telescope at the RMS focal plane was about 1.5%.

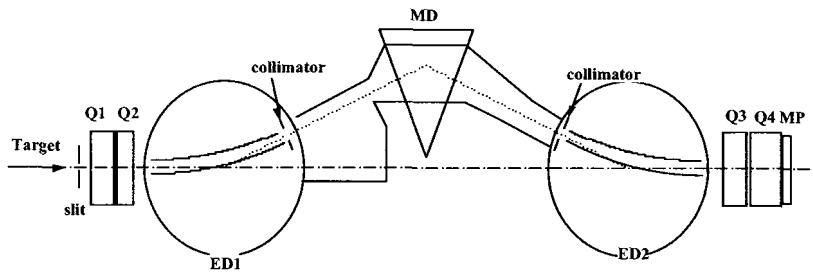

Figure 1. Ion optical configuration of JAERI-RMS. Q, ED, MD, and MP stand for magnetic quadrupole, electric dipole, magnetic dipole, and magnetic multi-pole, respectively.

The beam suppression factor, which was defined as the ratio of the number of ^{18}O particles contained in ^{16}N beam to that in the primary beam, was 2.2 ~10^{-10}. It should be ,however, noted that the ^{16}N-beam consisted of the ground state ($J^{\pi} = 2^-$) and the isomeric state (E_x = 120 keV, $J^{\pi} = 0^-$, $t_{1/2}$ = 5.25 μs). The isomer ratio has been measured to be 35 } 1 % by an independent measurement.

The ^{8}Li-beam has been produced via ^{9}Be(^{7}Li, ^{8}Li) reaction. A 42μm ^{9}Be foil was set at the target position. In order to make the energy resolution of the resultant ^{8}Li-beam better, the target foil was tilted at 40 with respect to the beam axis. The maximum intensity of the primary $^7Li^{3+}$-beam was about 200 enA, its initial energy being 24 MeV. The intensity of ^{8}Li was 4.8 ~10^3 pps /10 enA $^7Li^{3+}$ beam at the focal plane of RMS. Its energy and resolution were 14.6 MeV and 5%, respectively. Although a little amount of ^{6}He particles were mixed in the secondary ^{8}Li–beam obtained, no ^{7}Li impurities were observed. The purity of ^{8}Li-RNB was 99%.

Table 1 lists RNBs so far produced. Concerning the ^{6}He-beam case, the main contaminant was triton, of which the intensity was the same order of magnitude as that of ^{6}He, because their velocity was nearly the same as that of ^{6}He particles.

However, it is no serious problem under the present detector system described later, because tritons can be easily distinguished from ^{6}He.

Table 1. Measured yield and purity of radioactive nuclear beams.

RNB	production reaction	E [MeV]	Intensity [pps/100enA^{-1}]	contamination
^{6}He	d(^{7}Li, ^{6}He)^{3}He	10	5.9 ~10^{3}	t = 42%
^{8}Li	^{9}Be(^{7}Li, ^{8}Li)	14.6	4.8 ~10^{4}	^{6}He = 1%
^{12}B	d(^{11}B, ^{12}B)p	20	2.0 ~10^{4}	^{12}C, ^{11}B < 10 %
^{16}N	d(^{18}O, ^{16}N)α	32	1.6 ~10^{3}	^{18}O = 1.5%

2.2. *Detector system*

The present detector system is schematically shown in Fig. 2. It consists of a beam pick up detector system, a "multi-sampling and tracking proportional chamber" (MSTPC) [7] placed at the focal-plane of RMS, and a neutron detector array, where the first one is composed of a multi-channel plate (MCP) and a parallel plate avalanche counter (PPAC). The absolute energy of RNB is determined by time-of-flight (TOF) information between MCP and PPAC. Then, the RNB is injected into the MSTPC filled with gas of He+CO_2, which works as counter gas and gas target.

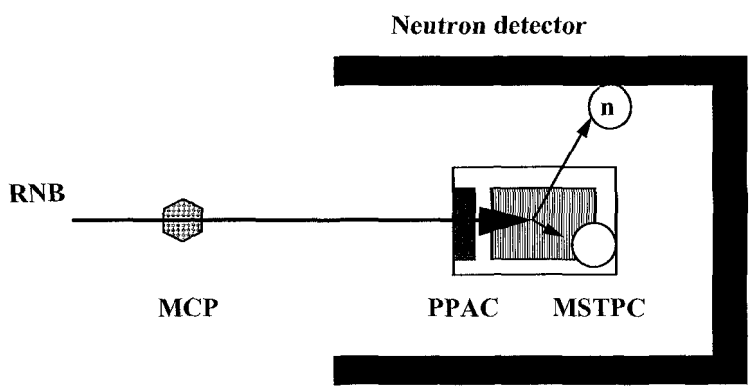

Figure 2. Schematic view of the experimental set-up. The RNB provided from JAERI-RMS is injected into the MSTPC filled with He +CO_2 gas, which acts as counter gas and as gas target. A neutron detector array consisting of 28 plastic scintillators is placed around the MSTPC.

Fig. 3 shows the cross-sectional view of the MSTPC. The MSTPC can measure a three-dimensional track of a charged particle and the energy loss along its trajectory. Electrons produced by the incoming charged particle in the drift space are drifted toward the proportional region consisting of a segmented cathode, 24 pad cells, and anode wires.

The vertical position of a trajectory can be determined by drift time of electrons. The horizontal position is determined by the comparison of signals from the right-hand and left-hand sides of a pad cell divided into 2 electrodes. The position along the beam direction can be determined by the position of the segmented cathode. Of course, the energy loss of each pad can be obtained.

When a nuclear reaction takes place inside the MSTPC, the energy loss (dE/dx) changes largely due to the change of the relevant atomic numbers. Therefore, where the reaction occurs can be determined by detecting the dE/dx change, and the beam energy at the reaction point can be evaluated with the energy loss along the trajectory.

A neutron detector array to detect neutrons emitted from nuclear reactions is placed to surround the MSTPC as much as possible. It consists of 28 pieces of BC408 plastic sintillators, covering 31.2% solid angle of 4 π. The absolute energy of a neutron is obtained by TOF information between the PPAC and the plastic scintillator. The vertical position of the neutron is determined by the position of a plastic sintillator itself, and the horizontal position is evaluated by the time difference of right-hand side and left-hand side signals from a plastic scintillator. The typical efficiency for a 5 MeV neutron measured by using a ^{252}Cf-fission source is about 40%.

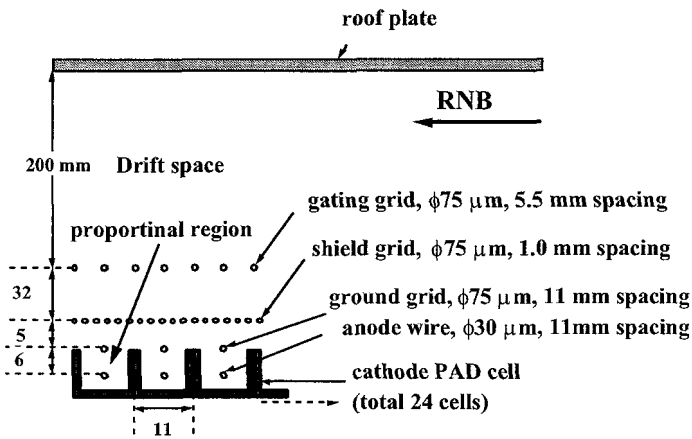

Figure 3. Schematic cross-sectional view of the MSTPC (not scaled).

2.3. *Measurements*

All the experiments to measure cross sections of (α, n) and (p, n) reactions have been carried out at the JAERI tandem facility.

RNB injection rates into the MSTPC for measurements of ^{16}N(α, n) and ^{8}Li(α, n) were 2 ~10^3 pps and 5 ~10^3 pps, respectively. These rates were limited by the present data acquisition system. The trigger for data acquisition was generated by the coincident signal between the PPAC and one of the plastic scintillators. The maximum trigger rate was 20 cps, which was mainly due to accidental coincidences between the injected RNB and background signals of plastic scintillators.

The MSTPC was filled with He + CO_2 (10 %) gas. Gas pressure for measurements of ^{16}N(α, n) and ^{8}Li(α, n) cross sections were 129 Torr and 220 Torr, respectively. Some typical parameters used for the ^{16}N(α, n) measurement are tabulated in Table. 2. Those for the measurement of the ^{8}Li(α, n) reaction are given in ref. [8].

Because the accidental rate mentioned above is far higher than the true event rate, it is necessary to distinguish true events from accidental. It is possible to select true events by comparison with the energy loss between a certain pad and the next pad. The threshold of energy loss difference between the two pads was set at 150 keV for the selection of the ^{16}N(α, n) reaction events by considering the energy loss of the emitted ^{19}F. In the case of the ^{8}Li(α, n) reaction, it was set at 40 keV by considering the energy loss of the emitted ^{11}B. The reaction event thus selected was checked with its kinematical condition by using all information on its reaction energy, scattering angle and energy of ejected nuclei and neutron and was finally accepted. The selected typical event of the ^{16}N(α, n) ^{19}F reaction is shown in Fig. 4.

Table 2. Some typical parameters of the ^{16}N(α, n) measurement.

Parameter	value
electrode of MCP	1.5 μm Mylar, evaporated Au
entrance window of PPAC	2.0 μm Mylar, 40 mm (diameter)
electrode of PPAC	1.5 μm Mylar, evaporated Al
exit window of PPAC	3.5 μm Mylar, 40 mm (diameter)
gas in PPAC	iso-butane, 6 Torr
gas in MSTPC	He + CO_2 (10 %), 129 Torr
roof plate voltage of MSTPC	-1170 V
gating grid voltage (V_0) of MSTPC	-199 V
gating grid voltage ( )ΔV) of MSTPC	40 V
anode wire voltage of MSTPC	790.3 V
length between MSTPC and plastic scintillators	900 mm
size of a typical plastic scintillator	50 ~150 ~1500 mm

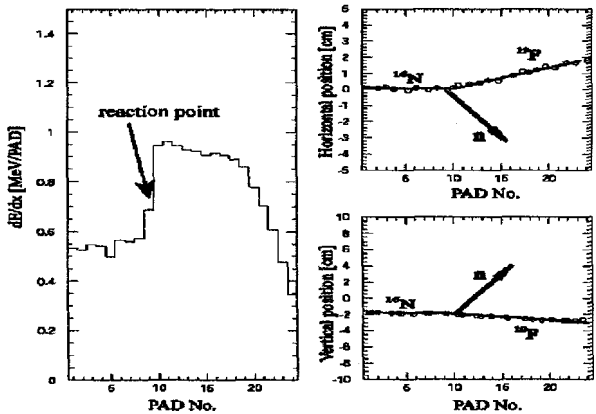

Figure 4. Selected typical event of the $^{16}N(\alpha, n)$ reaction. The left-hand side of the figure shows the dE/dx spectrum. The horizontal axis shows the relative length from the beam injection point inside the MSTPC given by the pad number. One pad corresponds to 11mm. The right-hand shows horizontal and vertical projections of the 3-dimensional particle trajectory. A neutron is detected at the direction marked by arrow.

3. Results

The measured excitation function of the $^{16}N(\alpha, n)^{19}F$ reaction is shown in Fig. 5. Black circles indicate the measured cross sections and the curve shows the theoretical estimation by Fowler [9]. Arrows indicate the Gamow energy region at $T_9 = 2$ and 3.

The excitation function of $^{16}N(\alpha, n)^{19}F$ reaction was determined successfully in the energy region of $E_{cm} = 1.5 - 4.0$ MeV. It is to be noted that the present measured cross sections around the energy region of $T_9 = 3$ are a few times larger than the theoretical estimation.

Fig. 6 shows the measured excitation function of the $^{8}Li(\alpha, n)^{11}B$ reaction. It is still preliminary, because the analysis is not yet complete in various aspects. The given errors are only statistical.

Black circles indicate our experimental cross sections and the other symbols show previous experimental data. Open circles and squares indicate the data by Boyd et al. [10] and Gu et al. [11] based on inclusive measurements without neutron detection. Black triangles indicate the data by Mizoi et al. [12] based on the exclusive measurement using a detector system similar to that in the present

work. Black crosses show cross sections leading to the ground state only obtained by the inversion reaction [13].

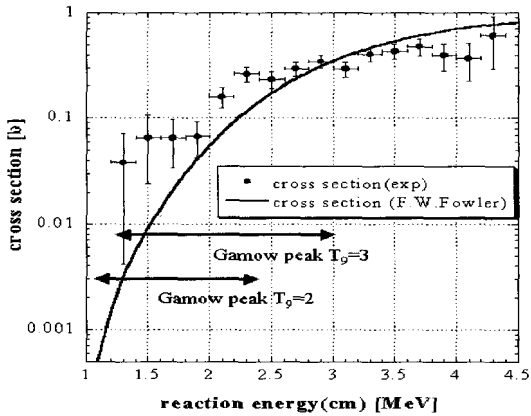

Figure 5. Measured excitation function of $^{16}N(\alpha, n)^{19}F$ reaction. The horizontal axis is the center-of-mass energy and the vertical one is the cross section given in unit of barns.

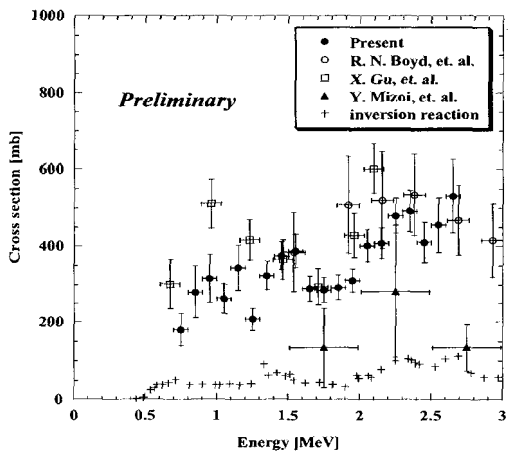

Figure 6. The measured excitation function of $^{8}Li(\alpha, n)^{11}B$ reaction (black circles). The horizontal axis is the center-of-mass energy and the vertical one is the cross section in unit of mb.

It is to be noted that the present result has good statistics compared with the previous data.

In addition, it is possible to obtain branching ratios of neutron decay channels from the compound ^{12}B in our experiment. Excited states of residual ^{11}B are open up to the 8th state (Ex = 8.559 MeV, J^{π} = 3/2$^-$) in our experimental condition. The excitation-energy spectrum of ^{11}B is shown in Fig. 7. The ground and the first excited states are not separated clearly. But the other higher excited states can be seen in this spectrum and positions of measured peaks look consistent with those expected. Its branching ratios will be determined in further analysis.

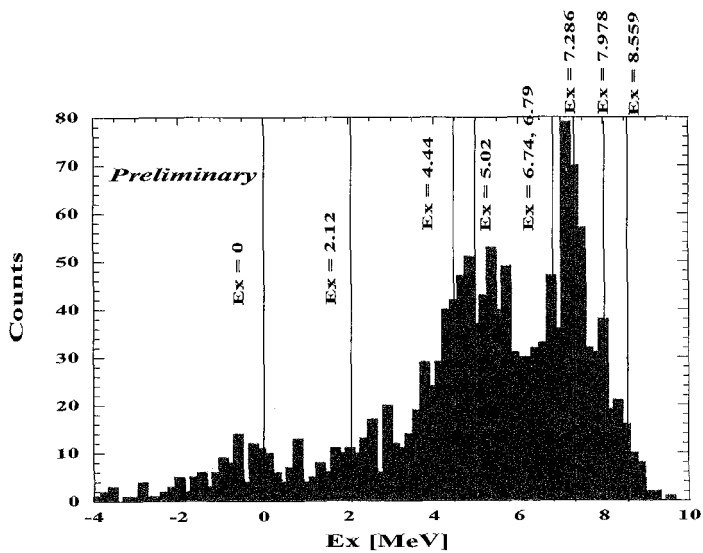

Figure 7. Excitation-energy spectrum of ^{11}B states. The horizontal axis shows the excitation-energy in unit of MeV and the vertical axis shows the number of raw events summed over the energy region from E_{cm} = 0.8 MeV to 2.7 MeV. Each line indicates excitation energy of an ^{11}B state.

4. Summary

Exclusive measurements of reaction rates of (α, n) reactions on light neutron-rich nuclei are in progress using low-energy radioactive nuclear beams. The excitation function of the ^{16}N(α, n) reaction has been measured in the energy region of E_{cm} = 1.5 – 4.0 MeV corresponding to the Gamow energy at T_9 = 2 – 6. In the energy region of T_9 = 3, experimental cross sections obtained are a few

times larger than the theoretical estimation. Preliminary results of the ^{8}Li(α, n) reaction cross sections measured in the energy region of E_{cm} = 0.8 – 2.7 MeV are reported. Further measurement of the same reaction rates below E_{cm} = 0.8 MeV will be carried out soon. Measurements of ^{6}He(α, n), ^{10}Be(α, n) and (p, n), ^{12}B(α, n) and (p, n), ^{20}F(α, n) and (p, n) reactions are also being planned.

Acknowledgments

The authors wish to thank Prof. Y. Tagishi and Dr. T. Komatsubara at University of Tsukuba for their helpful support in the performance test of the MSTPC. We also thank the staff members of the JAERI Tandem facility for their kind operation of the tandem accelerator.

References

1. M. Terasawa, et. al., *Nucl. Phys.* **A688**, 581c(2001).
2. H. Ishiyama, et. al., *Nucl. Phys.* **A718**, 481c-483c (2003).
3. T. Ishikawa, et. al., *Nucl. Phys.* **A718**, 484c-486c (2003).
4. F. D. Becchetti, et. al., *Nucl. Instrum. Meth. Phys. Res.* **B56/57**, 554 (1991).
5. H. Ikezoe, et. al., *Nucl. Instrum. Meth. Phys. Res.* **A376**, 470 (1996).
6. T. Kuzumaki, et. al., *Nucl. Instrum. Meth. Phys. Res.* **A437**, 107 (1999).
7. Y. Mizoi, et. al., *Nucl. Instrum. Meth. Phys. Res.* **A431**, 112 (1999).
8. T. Hashimoto, et. al., to be submitted in *Nucl. Instrum. Meth.*
9. W. A. Fowler, *Astrophy. J. Supp.* **91**,201 (1964).
10. R. N. Boyd, et. al., *Phys. Rev. Lett.* **68**, 1283 (1992).
11. X. Gu, et. al., *Phys. Lett.* **B343**, 31 (1995).
12. Y. Mizoi, et. al., *Phys. Rev.* **C62**, 065801 (2000).
13. T. Paradellis, et. al., *Z. Phys.* **A337**, 211 (1990).

A HYPERNOVA MODEL FOR SN 2003DH/GRB 030329

N.TOMINAGA, J.DENG, K.MAEDA, H.UMEDA, AND K.NOMOTO
Department of Astronomy, University of Tokyo,
Hongo 7-3-1, Bunkyo-ku,
Tokyo 113-0033, Japan
E-mail: ntominaga@astron.s.u-tokyo.ac.jp

P.A.MAZZALI
INAF-Osservatorio Astronomico,
Via Tiepolo, 11,
34131 Trieste, Italy

K.S.KAWABATA
Department of Physical Sciences, School of Science, Hiroshima University,
1-3-1 Kagamiyama, Higashi-Hiroshima,
Hiroshima 739-8526, Japan

GRB 030329 has provided solid evidence for the Gamma-Ray Burst -Supernova connection. Spectral observations showed that GRB 030329 is associated with a hypernova, SN 2003dh. We constructed an ejecta model for SN 2003dh by reproducing the spectra. This model is constructed by combining the models for SNe 1998bw and 1997ef. We named this model COMDH. We found that the energetic model, in which $M_{\rm ej} = 8{\rm M}_\odot$ ($M_{\rm ms} \sim 35 - 40{\rm M}_\odot$), $E_{\rm K} = 4 \times 10^{52}$ ergs, and $M(^{56}{\rm Ni}) = 0.35{\rm M}_\odot$, is also necessary for light curve fitting.

1. Introduction

SN 1998bw/GRB 980425 provided for the first time the evidence that (some) long duration Gamma-Ray Bursts (GRBs) are associated with Supernovae (SNe) [5]. The properties of the GRB, however, were rather unusual. It is very close, with a redshift of z = 0.0085. The estimated isotropic γ-ray energy, $E_{\gamma,{\rm iso}} \sim 8 \times 10^{47}$ erg [5], is then much smaller than that of typical GRBs with known redshifts ($z \sim 1$, $E_{\gamma,{\rm iso}} \sim 10^{52-54}$erg), which makes the GRB an extrodinarily weak one. SN 1998bw is also unusual in its own right. It has broader spectral features and a brighter light curve (LC) than ordinary SNe Ic. These features indicate that SN 1998bw is an

energetic SN, with $E_K \sim 3-5\times10^{52}$ ergs, so it is classified as a "hypernova" [10], [21]. It remained to be clarified if GRB 980425/SN 1998bw belongs to a distinct sub-class of GRBs (e.g., [2]), or it is in fact a typical GRB but dimmed by some secondary effects (e.g., viewing angle; [34]).

The discovery of SN 1998bw/GRB 980425 has thus motivated many investigations into SN signatures in cosmological GRBs. In some GRBs, 'bumps' have been detected in the LCs of optical afterglows (e.g., [3], [6], [4]). Such 'bumps' have been widely interpreted as the emergence of a underlying SN. Alternative explanations, however, are possible which are in principle capable to make a SN-like 'bump' (e.g., dust echoes; [33]). Confirmation of GRB/SN connection has thus waited for spectroscopic evidence of a SN in a (cosmological) GRB afterglow.

GRB 030329 was detected by HETE-2 on March 29, 2003 [28]. It has been extensively observed from unprecedentedly early phases. For about one week after the burst, the spectra of the optical afterglow were characterized by a power-law continuum as expected from the fire-ball model (e.g. [27]). Several days later, however, the spectra deviated noticeably from power-law: a SN emerged in the spectra and was named as SN 2003dh [31], [8]. The early spectra of SN 2003dh were similar to those of SN 1998bw, which suggests that the SN is a very energetic one, i.e. a hypernova [17]. The SN spectra then evolved to become SN 1997ef-like, as shown by the spectra taken with the SUBARU telescope 40 days and 80 days after the burst [12],[13].

We suggest that SN 2003dh is the explosion of a C+O star, and construct an ejecta model for it through spectra and LC fitting. Model parameters, i.e. ejecta mass, explosion energy, and total ^{56}Ni mass, are determined.

2. C+O star models for SNe Ic

H and He layers are supposed to be lost in stellar evolution to expose the C+O core, this core is called C+O star. C+O stars are usually considered as progenitors for SNe Ic [23],[24]. Si and Fe cores are formed in the center of the C+O star. In the SN explosion following the collapse of the Fe core, abundant ^{56}Ni is synthesized which subsequently decays to power the SN LC. SN parameters, like the ejected mass, explosion energy, and total ^{56}Ni mass, can be determined with spectral and LC fitting using exploding C+O star models.

Figure 1 shows density profiles of various exploding C+O star models. Among them, CO138E50 [21] and CO100E18 [18], are the models for

SNe 1998bw and 1997ef, respectively. The former is the explosion of a C+O star of $M_{\rm C+O} \sim 13.8$ M$_\odot$ ($M_{\rm ms} \sim 40$ M$_\odot$) with $\sim 5 \times 10^{52}$ ergs, while the latter is that of a C+O star of $M_{\rm C+O} \sim 10$ M$_\odot$ ($M_{\rm ms} \sim 35$ M$_\odot$) with $\sim 1.8 \times 10^{52}$ ergs.

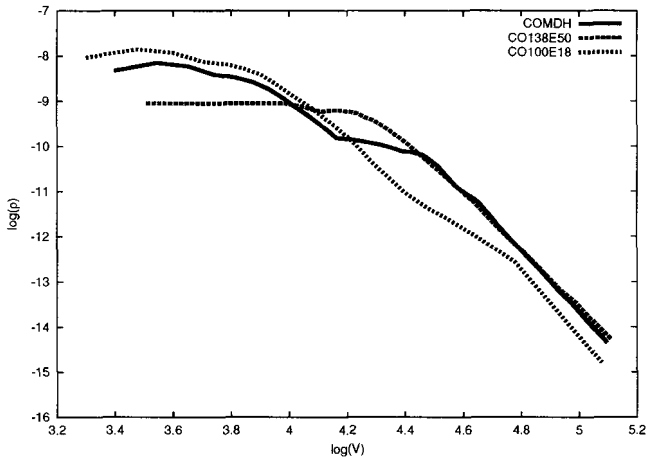

Figure 1. Density profiles of models COMDH (solid line; for SN 2003dh, [20]), CO138E50 (dashed line; for SN 1998bw, [21]), and CO100E18 (dotted line; for SN 1997ef, [18]).

Table 1. Models

Model	$M_{\rm ej}/M_\odot$	$M_{\rm C+O}/M_\odot$	$M_{\rm ms}/M_\odot$	E_{51}	$M(^{56}{\rm Ni})^{\rm a}$
CO100E18 [18]	9.6	10	35	18	0.31
CO138E50 [21]	10.4	13.8	40	50	0.3
COMDH [20]	8.0	10-11	35-40	38	0.35

a Values required to reproduce the peak brightness of SN 2003dh.

Model COMDH was constructed for SN 2003dh. We note that in early phases the spectra of SN 2003dh are similar to those of SN 1998bw, while in late phases they are similar to those of SN 1997ef. Therefore, we used CO100E18/2 for $v < 15000$ km s^{-1}, CO138E50 for $v > 25000$ km s^{-1}, and merged the two models linearly in between [20]. Note CO100E18/2

is a model where the density of CO100E18 is reduced by a factor of two throughout.

In the following sections, we will show that the model COMDH can well reproduce both the spectra of SN 2003dh and its LC.

3. Spectrum Synthesis

We have compared the synthetic spectra of model COMDH with observations at three epochs [20].

The first spectrum was obtained at the MMT on 2003 April 10 [17]. This is $\sim$ 12 days after the GRB, i.e. $\sim$ 10 rest-frame days into the life of the SN, assuming that the SN and the GRB coincided in time. The spectrum is characterized by very broad absorption lines, and it is similar to those of SN 1998bw at a comparable epoch. A good match can be obtained for $\log L[\mathrm{erg}] = 42.83$ and $v(\mathrm{ph}) = 28000$ km s^{-1} (Figure 2). At this epoch, the photosphere is located far outside, and this SN 1998bw-like spectrum is formed in the CO138E50-like part of COMDH.

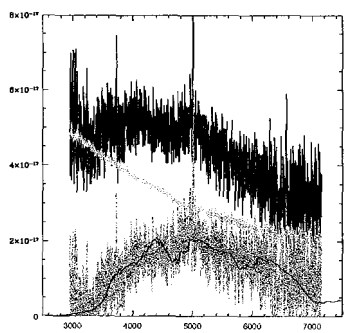

Figure 2. The observed 2003 April 10 spectrum (top, black line), subtracted afterglow spectrum (observed on 2003 April 1, middle, thin gray line), 'net' SN spectrum (bottom, thick gray line), and our synthetic spectrum (bottom, black line).

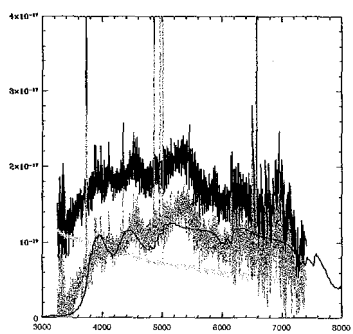

Figure 3. The observed 2003 April 24 spectrum (top, black line), subtracted afterglow spectrum (observed on 2003 April 1, bottom, thin gray line), 'net' SN spectrum (middle, thick gray line), and our synthetic spectrum (middle, black line).

The next spectrum was obtained at the MMT on 2003 April 24 [17]. Its rest-frame epoch is 23 days. At this epoch, the photosphere falls in the joining region. So this spectrum is a good test for the merged model. We

obtained a good match with $\log L[\mathrm{erg}] = 42.79$ and $v(\mathrm{ph}) = 18000$ km s^{-1} (Figure 3).

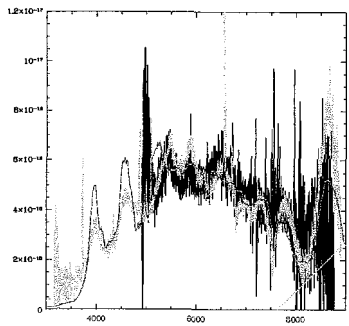

Figure 4. The observed 2003 May 10 spectrum (black line), spectrum of SN 1997ef obtained on 1998 January 1 (thin gray line), and our synthetic spectrum (thick gray line).

Our third spectrum was obtained with Subaru on 2003 May 10 [12], a rest-frame epoch $\sim$ 36 days, and it resembles that of SN 1997ef at a comparable epoch. At this epoch, model COMDH gives a good fit using $\log L[\mathrm{erg}] = 42.43$ and $v(\mathrm{ph}) = 7500$ km s^{-1} (Figure 4). It means that the photosphere has receded deep inside, and that this SN 1997bw-like spectrum is determined by the CO100E18-like part of COMDH.

4. Light Curve Construction

We extracted the SN component from the observed spectra of [17], [12], [13]. The spectrum taken on April 4 was adopted as the fiducial non-SN afterglow (AG) spectrum (following Matheson17 et al. 2003), scaled in flux, and then subtracted from the observations together with a host galaxy component [12]. We adjusted the scaling factor to make the flux between 3200 Å and 3600 Å in the rest frame roughly disappear from the results. This is justified by the fact that type Ib/c SNe, like SNe Ia, always show flux deficiency to the blue of $\sim$ 3600 Å due to line-blanketing (e.g. [18]). The AG flux deduced this way can be fitted using a power-law function of time, $f \approx t^{-\alpha}$, where $\alpha = -2.18 \pm 0.08$. The extrapolated AG flux was subtracted from the spectrum taken on May 10, which does not cover the wavelength range mentioned above.

We derived the absolute V-band LC of SN 2003dh from the decomposed spectra. We then transformed it to the bolometric LC by using the bolometric corrections of SN 1998bw [26], noting their spectral similarity. The bolometric light curves are ploted in the rest frame in Figure 5. Ref. 13 have estimated the SN photometry on June 22 from a spectrum taken with the Subaru telescope. They assumed a negligible AG contribution, while our fitting AG evolution predicts about 27% the total flux at that epoch.

Our LC differs from those reported by refs. 8 and 17, which are also different from one another. It roughly follows that of SN 1998bw before the peak, while it is fainter than SN 1998bw by about 0.6 mag after the peak. Though the likely time of peak is not covered, it is possibly 2 – 5 days earlier than SN 1998bw and the peak brightness may be a bit fainter. The light curve in [8], however, rises much more rapidly, reaches a brighter peak, and then drops much faster, while the one in [17] appears to resemble that of SN 1998bw. It is likely we subtracted more AG flux than ref. 17 did because we intended to avoid the un-physical "blue excess" in the decomposed spectra. Refs. 8 and 17 used a χ-square fitting method to decompose the spectra. We tried that method, only to get a LC similar to the one reported here.

We also constructed another bol LC using BVRI photometry [14]. The LC from the spectra is similar to that from the photometry (figure 5).

5. Light Curve Fitting

Synthetic bolometric LCs were computed using an LTE radiation transfer code and a gray γ-ray transfer code [10]. Generally speaking, γ-rays created in radioactive decays of ^{56}Ni and ^{56}Co can be either absorbed by SN ejecta or escape, as determined by transfer calculations. The heated ejecta material then emits optical photons, which escape from optically thin regions. A constant line opacity of 0.03 cm^2 g^{-1} was assumed in our computation. The whole optical opacity was found to be dominated by electron scattering. The balance between photoionizations and recombinations has been taken into account.

First, we discuss the general dependance of the synthetic light curve on various model parameters. The width of the LC peak, $\tau_{\rm LC}$, can be roughly expressed as $\tau_{\rm LC} \approx A \times {\kappa_{\rm opt}}^{1/2} {M_{\rm ej}}^{3/4} {E_{\rm K}}^{-1/4}$ [1], where $\kappa_{\rm opt}$ is optical opacity and A is a function of the density structure and ^{56}Ni distribution. The rising time of the LC is strongly affected by the ^{56}Ni distribution. If ^{56}Ni is absent from the outer region, γ-rays and optical photons are long

trapped in optically thick regions and hence the LC rises slowly. After the peak and in later phases, the whole ejecta becomes transparent to optical photons. So the decline rate of the LC is mainly determined by the optical depth of the ejecta to γ-rays, which roughly scales as $\kappa_\gamma \rho R \propto M^2 {E_{\rm K}}^{-1} t^{-2}$, where κ_γ is γ-ray opacity.

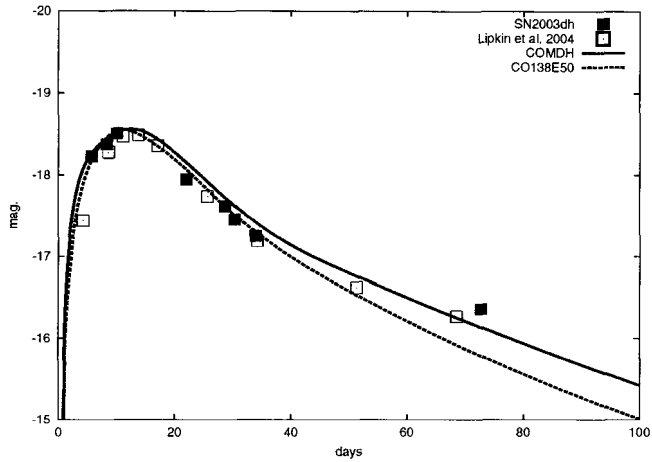

Figure 5. The observed bolometric LC of SN 2003dh (filled suqares; this paper), synthetic LC of the merged model COMDH (solid line), and that of model CO138E50 (dashed line).

We tested two models to fit the LC of SN 2003dh, CO138E50 and COMDH. ^{56}Ni distribution and the total ^{56}Ni mass were treated as free parameters. As shown in Figure 5, both models can reproduce the observed LC peak. This is consistent with the above parameter analysis. The best-fit ^{56}Ni mass for each model is listed in Table 1. The synthetic LC of CO138E50, however, declines faster than observations in later phases. Model COMDH, on the other hand, has a denser core compared with CO138E50 (see Figure 1). The denser core increases the efficiency of γ-ray trappings and results in a LC being brighter and slower in later phases than that of CO138E50.

6. Discussion

We have studied the properties of SN 2003dh and constructed model COMDH for it. We summarize in Figure 6 the model parameters of core-

collapse SNe and hypernovae for comparison [25]. It shows that normal core-collapse SNe occur for stars having main-sequence mass less than ~ 20 $M_\odot$, which probably explode with the canonical kinetic energy of $\sim 1 \times 10^{51}$ ergs and eject ~ 0.1 $M_\odot$ ^{56}Ni [22], [23]. SNe originated from more massive stars can be divided into two branches. One is the hypernova branch, which features high kinetic energy and large ejected ^{56}Ni mass [32]. The other is the faint SN branch, showing low kinetic energy and small ejected ^{56}Ni mass. It is clear that SN 2003dh belongs to the hypernova branch.

Our spectra and LC fitting require a dense core for SN 2003dh. Such a dense core is unlikely the outcome of any realistic 1-D hydrodynamical calculations. Actually, all spherically symmetric explosion models, e.g. CO100E18 and CO138E50 in Figure 1, are very flat inside, and they all have an inner mass-cut defining a 'hole' in the density profile. In 2-D jet-induced explosions, however, a dense core can be formed through accretion along the equatorial direction and the LC declines slowly according to the 2-D hydrodynamical and light curve calculations [16].

References

1. Arnett, W.D., *ApJ* **253** 785 (1982).
2. Bloom, J.S., et al., *ApJ* **508** L21 (1998).
3. Bloom, J.S., et al., *ApJ* **572** L45 (2002).
4. Della Valle, M., et al., *A&A* **406** L33 (2003).
5. Galama, T.J., et al., *Nature* **395** 670 (1998).
6. Garnavich, P.M., et al., *ApJ* **582** 924 (2003).
7. Hatano, K., et al., *BAAS* **198** 3902 (2001).
8. Hjorth, J., et al., *Nature* **423** 847 (2003).
9. Iwamoto, K., et al., *ApJ* **437** L115 (1994).
10. Iwamoto, K., et al., *Nature* **395** 672 (1998).
11. Iwamoto, K., et al., *ApJ* **534** 660 (2000).
12. Kawabata, K.S., et al., *ApJ* **593** L19 (2003).
13. Kosugi, G., et al., *PASJ* in press (2004).
14. Lipkin, Y.M., et al., *ApJ* submitted (2004) (astro-ph/0312594).
15. Maeda, K., et al., *ApJ* **593** 931 (2003).
16. Maeda, K., *PhD thesis*, Univ. of Tokyo (2004).
17. Matheson, T., et al., *ApJ* **599** 394 (2003).
18. Mazzali, P.A., Iwamoto, K., & Nomoto, K., *ApJ* **545** 407 (2000).
19. Mazzali, P.A., et al., *ApJ* **572** L61 (2002).
20. Mazzali, P.A., et al., *ApJ* **599** L95 (2003).
21. Nakamura, T., Mazzali, P.A., Nomoto, K., & Iwamoto, K., *ApJ* **550** 991 (2001).
22. Nomoto, K., et al., *Nature* **364** 507 (1993).
23. Nomoto, K., et al., *Nature* **371** 227 (1994).

24. Nomoto, K., Iwamoto, K., Suzuki, T., *Physics Reports* **256** 173 (1995).
25. Nomoto, K., et al., *Fayer book astrom* (2004).
26. Patat, F., *ApJ* **555** 900 (2001).
27. Piran, T., *Physics Reports* **314** 575 (1999) (astro-ph/9810256).
28. Ricker, G.R., et al., *IAUC* 8101 (2003).
29. Shigeyama, T., & Nomoto, K., *ApJ* **360** 242 (1990).
30. Shigeyama, T., et al., *ApJ* **420** 341 (1994).
31. Stanek, K.Z., et al., *ApJ* **591** L17 (2003) (astro-ph/03041173).
32. Turatto, M., et al., *ApJ* **498** L129 (1998).
33. Waxman, E., & Draine, B.T., *ApJ* **537** 796 (2000).
34. Yamazaki, R., Yonetoku, D., & Nakamura, T., *ApJ* **594** L79 (1998).
35. Zampieri, L., et al., *MNRAS* **338** 711 (2003).

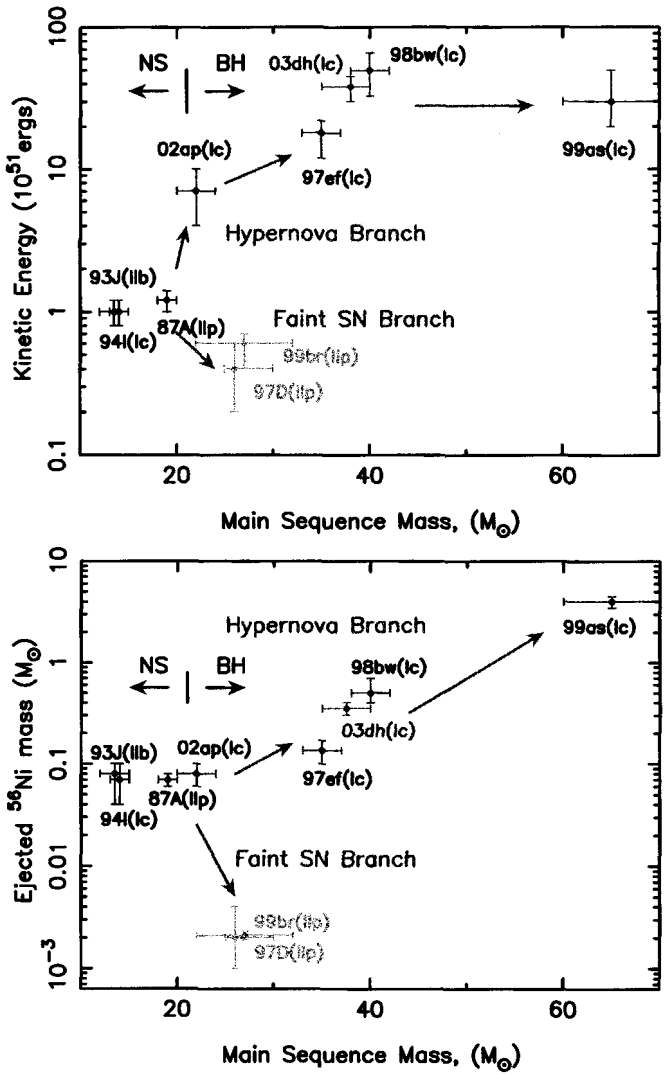

Figure 6. Top panel: main-sequence mass of the progenitors for core-collapse SNe/hypernovae v.s. kinetic energies. Bottom panel: main-sequence mass v.s. total ^{56}Ni mass. The parameters of these SNe were estimated by previous papers (SN II 1987A, [29]; SN IIb 1993J, [30]; SN Ic 1994I, [9]; SN II 1997D, [32]; SN II 1999br, [35]; SN Ic 1997ef, [18]; SN Ic 1998bw, [21]; SN Ic 1999as, [7]; SN Ic 2002ap, [19]; SN Ic 2003dh, [20]).

THE "DARK SIDE" OF GAMMA-RAY BURSTS AND IMPLICATIONS FOR NUCLEOSYNTHESIS OF LIGHT AND HEAVY ELEMENTS

S. INOUE

Max-Planck-Institut für Astrophysik, Garching, Germany
E-mail: inouemu@MPA-Garching.MPG.DE

N. IWAMOTO

Dept. of Astronomy, University of Tokyo, Tokyo, Japan
E-mail: niwamoto@astron.s.u-tokyo.ac.jp

M. ORITO

Research Lab. for Nuclear Reactors, Tokyo Inst. of Tech., Tokyo, Japan
E-mail: orito@nr.titech.ac.jp

M. TERASAWA

Center for Nuclear Study, University of Tokyo, Wako, Saitama, Japan
E-mail: mariko@cns.s.u-tokyo.ac.jp

Recent observational and theoretical advances in studies of gamma-ray bursts (GRBs) indicate that there can be a significant "dark side" to the GRB energy budget: besides the ultrarelativistic jet giving rise to the bright gamma-ray emission, there can be an even greater amount of "dark" energy contained in an accompanying, mildly relativistic outflow. The occurrence of such outflows are strongly supported in theoretical models, particularly for collapsar-type GRB progenitors, and also has been directly confirmed in observations of GRB030329/SN2003dh. This outflow component, which should be more baryon-rich than the GRB jet, can have interesting implications for nucleosynthesis. Inside the outflow, light elements may be produced through reactions similar to big bang nucleosynthesis. Heavy element synthesis by neutron capture can also take place, sometimes by a moderately rapid "n-process" rather than an r-process. The resulting nucleosynthetic products may be observationally relevant for the most metal-poor stars, as well as the companion stars of black hole binary systems.

1. Introduction

Successful generation of GRBs requires the formation of a narrowly-collimated, ultrarelativistic outflow with bulk Lorentz factor $\Gamma \gtrsim 100$, implying very low baryon-loading (e.g.[14]). Since the temperature at the base of the outflow should be of order MeV and the baryons are likely to contain a high fraction of neutrons,[1,19] some production of nuclei starting from free protons and neutrons is expected to occur in the expanding flow. However, as shown in several recent papers,[1,10,18] in the very high entropy and extremely rapid expansion characteristic of GRB jets, nucleosynthesis is limited to only small production of D and ^{4}He, which are difficult to observe.

Nevertheless, most GRB progenitors should also give rise to associated outflows with higher baryon-loads and lower velocities (baryon-rich outflows, or BROs), as discussed in the next section. The lower entropy, slower expansion and higher ejecta mass of BROs compared to GRB jets make them much more interesting from a nucleosynthesis viewpoint. As a first study of nucleosynthesis in BROs associated with GRBs, we have investigated this problem utilizing the simple dynamical framework of the basic fireball model, but incorporating detailed nuclear reaction networks including both light and heavy elements. More details can be found in [6].

2. Evidence for BROs: the "Dark Side" of GRBs

Besides the ultrarelativistic jet giving rise to the conspicuous GRB emission, there is growing evidence, both theoretical and observational, for the existence of different types of BROs which constitute a "dark" component to the GRB energy budget. Theoretically, it is highly probable that different types of "circum-jet winds" of baryon-loaded material surround and coexist with the narrowly collimated GRB jet. In general, the GRB jet production mechanism is likely to act not only on the baryon-poor zones near the jet axis, but also on the more baryon-contaminated, peripheral regions, leading to BROs as a natural byproduct. Models involving core collapse and jet penetration in massive stars[12,27] have recently gained strong support through observations of SN2003dh associated with GRB030329.[5,13] In such models, BROs should be induced through entrainment and mixing with the stellar material. High-resolution numerical simulations of jet-star interaction in collapsars[29] indeed demonstrate the inevitable generation of a peripheral, low Γ outflow containing a significant fraction of the total energy. In generic black hole accretion disk models, baryon-rich winds

may also arise from the outer disk by mechanisms distinct from the GRB jet.[8,11,15,21,24]

Observationally, some interpretations of X-ray flashes (e.g.[28]) and the statistics of afterglow light curve breaks (e.g.[23]) point to the important role of circum-jet BROs. The strongest and most direct evidence yet comes from the observation of a distinct feature in the light curve of the GRB030329/SN2003dh afterglow, which is likely to have been caused by a peripheral outflow with $\Gamma \sim$ a few that dominates the total energy budget.[2] (Thus, GRB-BROs are not exactly "dark", but rather "not so bright".)

Alternatively, BROs may occur without concomitant GRBs as "failed GRBs", potentially with event rates higher than successful GRBs, if the baryon-loading process acts more thoroughly or the the GRB jet-driving mechanism operates less efficiently in the central engine.[28,29] These may possibly be identified with the observed "hypernovae",[16] X-ray flashes,[9] or with some hitherto unrecognized type of transient. Either way, the lower entropy, slower expansion and higher ejecta mass of BROs compared to GRB jets make them much more interesting from a nucleosynthesis viewpoint.

3. Nucleosynthesis in GRB-BROs

We consider a wind fireball, i.e. an adiabatic, thermally-driven and freely-expanding outflow.[17] The key parameters are the luminosity $L = 10^{52}L_{52}\mathrm{erg\ s^{-1}}$, the initial radius $r_0 = 10^7 r_{0,7}\mathrm{cm}$, and the dimensionless entropy $\eta = L/\dot{M}c^2$. The fireball first undergoes an acceleration phase, where the comoving temperature and density decrease exponentially on the initial dynamical timescale $t_{d0} \simeq 0.33\ \mathrm{msec}\ r_{0,7}$. After the internal energy is converted to bulk kinetic energy, there follows a coasting phase where T and ρ_b decrease as power-laws, asymptotically becoming $T = T_0\eta^{-1}(t/t_{d0})^{-2/3}$ and $\rho_b = \rho_{b,0}\eta^{-3}(t/t_{d0})^{-2}$. These formulae are valid for $\eta \gtrsim 1$. Although $\eta \lesssim 1$ (nonrelativistic expansion) may be realized in some progenitor models, here we assume $\eta \geq 2$, corresponding to baryon load mass $M_b \leq 2.8 \times 10^{-2}\mathrm{M}_\odot E_{53}$ for total energy $E = 10^{53}\mathrm{erg}E_{53}$. This may be a reasonable upper limit for relatively baryon-free progenitors such as neutron star mergers[8] or supranovae,[26] and may possibly apply even for the jet production regions of collapsars. The initial electron fraction Y_e is taken to be an additional parameter, in view of the uncertainties in its expected value.[19] We implement nuclear reaction network codes including a large number of light, very neutron-rich nuclei,[25] which play a very crucial

role in the present problem.

Taking fiducial values of $L_{52} = 1$ and $r_{0,7} = 1$, we concentrate on the effect of variations in η and Y_e. Although ^{4}He is the dominant final species besides remaining free nucleons for all cases, interesting amounts of other light elements can also result, particularly deuterium, whose final mass fraction can reach $X_D \simeq 0.02$ (Fig. 1). For $\eta \gtrsim 20$, the reactions mainly occur during the exponential expansion (acceleration) phase, similar to the case of big bang nucleosynthesis. Contrastingly, for $\eta \lesssim 10$, nucleosynthesis proceeds mainly during the power-law expansion (coasting) phase. When $Y_e \lesssim 0.5$, free neutrons remain abundant in the outflow until they start decaying into protons, so that D production can proceed efficiently by subsequent p(n,γ)d reactions at very late times. Other elements such as ^{7}Li, ^{9}Be and ^{11}B can be generated at levels of $X \sim 10^{-8} - 10^{-7}$.

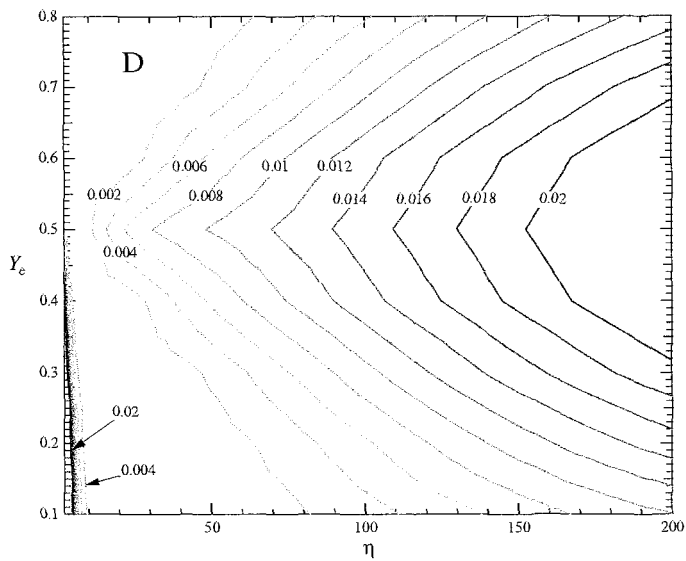

Figure 1. Contours of final abundance by mass fraction of deuterium for different parameter values of η and Y_e.

The synthesis of heavy elements through neutron capture is even more intriguing. The fiducial $\eta = 2$ outflow is characterized by very high entropy ($s/k_B \simeq 2500$), low density ($\rho_{b,0} \simeq 1.5 \times 10^5$g cm^{-3}) and short initial expansion timescale ($t_{d0} \simeq 0.33$ ms), leading to nucleosynthesis which

is markedly different from the better-studied r-process in supernova (SN) neutrino-driven winds (e.g.[22]). The final abundances are shown in Fig. 2. When $Y_e \lesssim 0.4$, considerable reaction flows can occur to high mass numbers, although the peak abundances are at levels of $Y \simeq 10^{-6}$. (Note that the apparent peak at $A \simeq 250$ is an artifact of our neglect of fission.) The abundance patterns do not match the solar distribution and possess peaks in between the solar s- and r-process peaks. This reflects the occurrence of reaction flow paths intermediate between those of the s- and r-processes (Fig. 3), resulting from the balance of neutron captures and β-decays rather than (n,γ)-(γ,n) equilibrium. Such processes have been discussed in previous contexts and called the "n-process".[3] We also note that the neutrons remain abundant after the reactions freeze out until they freely decay, instead of being exhausted by neutron captures.

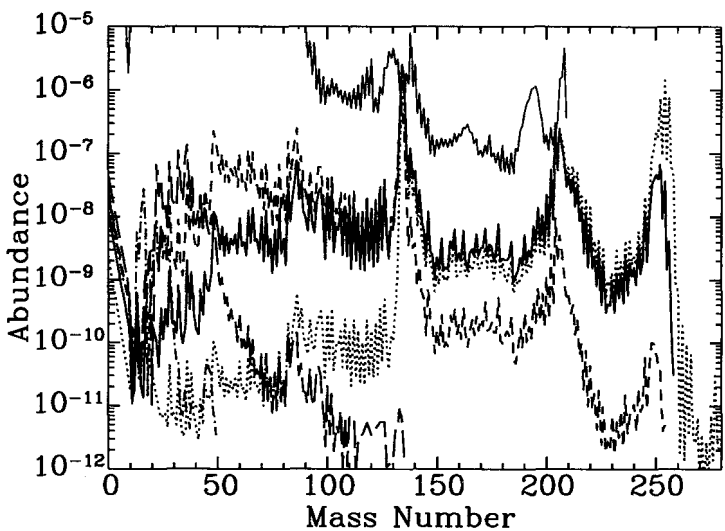

Figure 2. Final abundances as function of mass number, for $\eta = 2$ and $Y_e = 0.1$, 0.3, 0.4, 0.48 and 0.498, represented by the dotted, solid, dashed, long-dashed and dot-dashed curves, respectively. The uppermost, thin solid curve is the solar abundance distribution in arbitrary units.

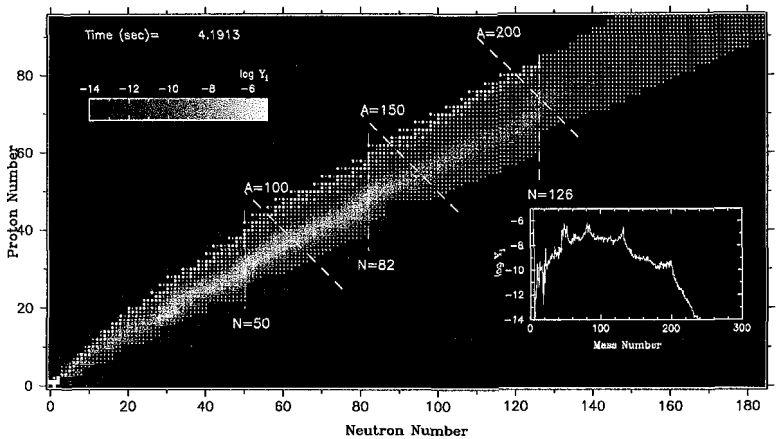

Figure 3. Snapshot of reaction flow in the N (neutron number) - Z (proton number) plane, for $Y_e = 0.3$ at time $t \simeq 4.2$ s. Large and small circles on the grid indicate stable and unstable nuclei, respectively. The inset shows the number fraction of heavy elements as a function of mass number.

4. Observational Implications

The present results of nucleosynthesis in GRB-BROs have interesting observational implications. For our case of $\eta = 2$ and $Y_e \simeq 0.1 - 0.4$, the ejected mass in heavy elements per single GRB-BRO event should be $M_{h,BRO} \sim 10^{-7}$-$10^{-6}\mathrm{M}_\odot$ for $A \gtrsim 100$, comparable to or somewhat less than that expected in r-process elements from a normal core collapse SN.[22] Considering the fact that the abundance patterns are different from solar, and that the intrinsic event rates of (either successful or failed) GRBs are estimated to be less than that for SNe, the contribution of GRB-BROs to the solar/Galactic abundances are unlikely to be large, at least for the conditions treated here (see however [20].)

However, some observable environments may manifest the local abundance pattern of the BRO ejecta. Many facts suggest that chemical evolution in the early Galaxy proceeded inhomogeneously, and also that GRBs are associated with the most massive progenitor stars. If so, these explosions may have dominated at the earliest epochs, so that the BRO nucleosynthetic signature are visible in the most metal-poor stars.[4] Alternatively, both light and heavy element products may be clearly discernible in the companion star of a black hole binary system, where the event that formed

the black hole may have left traces of the explosion ejecta on its surface.[7] High resolution spectroscopic observations of such stars are warranted for detailed studies of their elemental abundance patterns. Such studies should yield important constraints on the value of Y_e, providing us with valuable insight into the innermost regions of GRB sources which are otherwise very difficult to probe.

5. Conclusions and Outlook

From an exploratory study, we have shown that BROs associated with GRBs can be interesting sites for nucleosynthesis of both light and heavy elements, with important observational consequences. We have neglected here various realistic effects that can be potentially important, including fission and proton-rich nuclei, collimation and higher baryon loading, neutrino irradiation, nonthermal spallation, neutron captures on external matter, etc., all of which can be significant, e.g. in the widely discussed collapsar scenario (see [6] for more discussion). Until we arrive at a definitive understanding of the physics of the GRB central engine, construction step by step of increasingly realistic models incorporating these effects and comparison with various observations may help us constrain the unknown properties of the GRB source, as well as to clarify the role of GRB-BROs in the chemical evolution of the Galaxy. It is certain that much interesting work lies ahead.

References

1. A. M. Beloborodov, *Ap.J.* **588**, 931 (2003).
2. E. Berger et al., *Nature* **426**, 154 (2003).
3. J. B. Blake and D. N. Schramm, *Ap.J.* **209**, 846 (1976).
4. N. Christlieb et al. *Nature* **419**, 904 (2002).
5. J. Hjorth et al., *Nature* **427**, 847 (2003).
6. S. Inoue, N. Iwamoto, M. Orito and M. Terasawa, *Ap.J.* **595**, 294 (2003).
7. G. Israelian et al., *Nature* **401**, 142 (1999).
8. H.-T. Janka and M. Ruffert, in *Stellar Collisions, Mergers and their Consequences*, Ed. M. M. Shara (Astron. Soc. of the Pacific), p.333 (2002).
9. R. M. Kippen et al., in *Gamma-Ray Burst and Afterglow Astronomy 2001*, Eds. G. R. Ricker and R. K. Vanderspek (Am. Inst. Phys.), p.372 (2002).
10. M. Lemoine, *A.&Ap.* **390**, L31 (2002).
11. A. I. MacFadyen, in *From Twilight to Highlight: The Physics of Supernovae*, Eds. W. Hillebrandt and B. Leibundgut (Springer), p.97 (2003).
12. A. I. MacFadyen and S. E. Woosley, *Ap.J.* **524**, 262 (1999).
13. T. Matheson et al., *Ap.J.* **599**, 394 (2003).
14. P. Mészáros, *A.R.A.A.* **40**, 137 (2002).

15. R. Narayan, T. Piran and P. Kumar, *Ap.J.* **557**, 949 (2001).
16. K. Nomoto et al., to appear in *Stellar Collapse*, Ed. C. Fryer (astro-ph/0308136).
17. B. Paczyński, *Ap.J.* **363**, 218 (1990).
18. J. Pruet, S. Guiles and G. M. Fuller, *Ap.J.* **580**, 368 (2002).
19. J. Pruet, S. E. Woosley and R. D. Hoffman, *Ap.J.* **586**, 1254 (2003).
20. J. Pruet, R. Surman and G. C. McLaughlin, *Ap.J.* submitted (astro-ph/0309673).
21. J. Pruet, T. A. Thompson and R. D. Hoffman, *Ap.J.* submitted (astro-ph/0309278).
22. Y.-Z. Qian, *Prog. Part. Nuc. Phys.* **50**, 153 (2003).
23. E. Rossi, D. Lazzati and M. J. Rees, *M.N.R.A.S.* **332**, 945 (2002).
24. R. Surman and G. C. McLaughlin, *Ap.J.* submitted (astro-ph/0308004).
25. M. Terasawa et al., *Ap.J.* **562**, 470 (2001).
26. M. Vietri and L. Stella, *Ap.J.* **507**, L45 (1998)
27. J. C. Wheeler, D. L. Meier and J. R. Wilson, *Ap.J.* **568**, 807 (2002).
28. S. E. Woosley, W. Zhang and A. Heger, in *From Twilight to Highlight: The Physics of Supernovae*, Eds. W. Hillebrandt and B. Leibundgut (Springer), p.87 (2003).
29. W. Zhang, S. E. Woosley and A. Heger, *Ap.J.* submitted (astro-ph/0308389).

NUCLEOSYNTHESIS INSIDE GAMMA-RAY BURST ACCRETION DISKS

SHIN-ICHIROU FUJIMOTO

Department of Electronic Control, Kumamoto National College of Technology, Kumamoto 861-1102, Japan; E-mail: fujimoto@ec.knct.ac.jp

MASA-AKI HASHIMOTO

Department of Physics, School of Sciences, Kyushu University, Fukuoka 810-8560, Japan

KENZO ARAI AND RYUICHI MATSUBA

Department of Physics, Kumamoto University, Kumamoto 860-8555, Japan

We investigate nucleosynthesis inside both a gamma-ray burst accretion disk and a wind launched from an inner region of the disk using one-dimensional models of the disk and wind and a nuclear reaction network. Far from a central black hole, the composition of accreting gas is taken to be that of an O-rich layer of a massive star before core collapse. We find that the disk consists of five layers characterized by dominant elements: ^{16}O, ^{28}Si, ^{54}Fe (and ^{56}Ni), ^{4}He, and nucleons, and the individual layers shift inward with keeping the overall profiles of compositions as the accretion rate decreases. ^{56}Ni are abundantly ejected through the wind from the inner region of the disk with the electron fraction $\simeq 0.5$. In addition to iron group, elements heavier than Cu, in particular ^{63}Cu and ^{64}Zn, are massively produced through the wind. Various neutron-rich nuclei can be also produced in the wind from neutron-rich regions of the disk, though the estimated yields have large uncertainties.

1. Introduction

Observational evidences have been accumulated for a connection between gamma-ray bursts (GRBs) and supernovae (SNe): association of SN 1998bw and GRB 980425[1] and SN 2003dh in afterglow of GRB 030329.[2] A *collapsar* model is one of promising scenarios to explain a huge gamma-ray production in GRBs and GRB/SN connections.[3,4] During collapse of massive stars, stellar material greater than several solar masses falls back on a new-born black hole with extremely high accretion rates ($\leq 1 M_{\odot}\,\mathrm{s}^{-1}$).[5]

An accretion disk forms around the hole due to the angular momentum of the fallback material.[3,4,6] In the context of the collapsar model, jet-like explosion driven by neutrino annihilation and nucleosynthesis in the jet has been investigated.[7] Although ^{56}Ni with high velocity ($> 0.1c$) can be massively produced , it is not sufficient for an observed amount in SN 1998bw.[7] In addition to the production via the jet, massive synthesis of ^{56}Ni is also suggested in winds launched from the accretion disk.[3,8] Neutron-rich nuclei may be produced through r-process inside the wind ejected from an inner, neutron-rich region of the disk.[8] In the present paper, we examine nucleosynthesis inside a GRB accretion disk and investigate abundance change through the wind launched from the disk.

2. Disk Model and Input Physics

We construct a steady, axisymmetric model[9,10] of the disk around a black hole of mass M with accretion rates up to $10 M_\odot\,\mathrm{s}^{-1}$. The black hole mass is fixed to be 3 $M_\odot$ and the viscosity parameter is set to be $\alpha_{\rm vis} = 0.1$. Figure 1 shows the profiles of density, ρ, (thick lines) and temperature, T, (thin lines) in the accretion disk for $\dot{M} = 1$ (solid lines), 0.1 (dotted lines), and $0.01 M_\odot\,\mathrm{s}^{-1}$ (dashed lines). These profiles are roughly agreement with the corresponding profiles in another disk model[9] except for the region near the disk inner edge; our density and temperature drop rapidly near the inner edge. This is attributed to our use of the pseudo-Newtonian potential and the zero torque condition at the inner edge.

Chemical composition of accreting gas far from the black hole is set to be that of an O-rich layer of a 20 $M_\odot$ star before core collapse.[11] Once temperatures and densities are evaluated inside the disk, using a nuclear reaction network,[12,13] which includes 463 nuclei up to ^{94}Kr, we follow evolution of the composition in the accreting material during the infall onto the hole. We note that at the inner region of the disk, where $T \geq 9 \times 10^9$K, the composition is in nuclear statistical equilibrium (NSE).[14]

3. Abundance Distribution inside Disks

Figure 2 shows the abundance profiles of representative nuclei inside the disk with $\dot{M} = 0.1 M_\odot\,\mathrm{s}^{-1}$. Far from the black hole $r > 1000 r_{\rm g}$, where $r_{\rm g} = 2GM/c^2$ is the Schwarzschild radius, accreting gas keeps presupernova composition, or that of the O-rich layer, because of low temperatures ($T < 2 \times 10^9$K). As the material falls down, the gas becomes rich in iron-group elements via explosive O-burning, followed by Si-burning. The processed

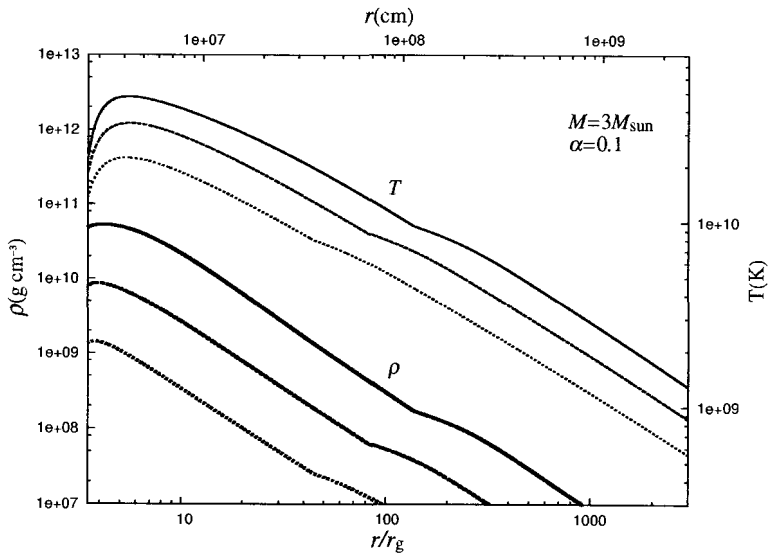

Figure 1. Density and temperature profiles inside the disk with 0.01, 0.1 and $1 M_\odot\,\mathrm{s}^{-1}$.

heavy elements, however, are destroyed to helium, and finally to protons and neutrons through photodisintegrations deep inside the disk. Near the inner edge of the disk, neutrons are the most abundant by electron captures on protons. Considerable amounts of D, T and ^{6}Li exist due to NSE.

For higher accretion rates, the density is higher, the electron capture is more efficient, and consequently the disk becomes more neutron-rich. In fact, the ratios of neutron to proton are 1.33, 3.50 and 10.4 for $\dot{M} = 0.01$, 0.1 and 1 $M_\odot\,\mathrm{s}^{-1}$, respectively, near the inner edge of the disk. Radial profiles of the electron fraction are similar to those in the other authors.[8]

The disk consists of five layers characterized by dominant elements: ^{16}O, ^{28}Si, ^{54}Fe (and ^{56}Ni), ^{4}He, and nucleons. Hereafter, these five layers are referred to as the O-rich, Si-rich, Fe-rich, He-rich, and np-rich disk layers. Figure 3 shows the interfaces of these layers for $\dot{M} = 0.01 - 1 M_\odot\,\mathrm{s}^{-1}$. Temperatures increase with the increasing accretion rate at a given radius, so that the individual layers shift outward, but the overall profiles of composition are preserved. This is because nucleosynthesis inside a disk mainly depends on the temperature distribution of the disk. Averaged mass fractions over the individual layers of 40 abundant nuclei are given in Table 1 for the Fe-rich and He-rich disk layers with $\dot{M} = 0.01$ and 0.1 $M_\odot\,\mathrm{s}^{-1}$. We find that the averaged abundances of the individual disk layers are not

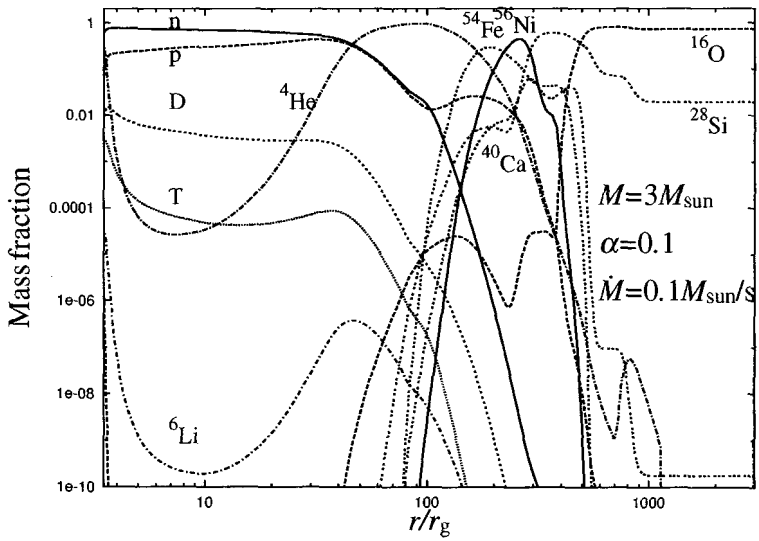

Figure 2. Abundance profiles of representative nuclei inside the disk with $0.1 M_{\odot}\,s^{-1}$.

significantly changed as the accretion rates.

4. Chemical Composition of Disk Winds

4.1. ^{56}Ni *in Winds*

During accretion onto a black hole, some fractions of accreting gas could be ejected through winds from an accretion disk. Possible processes driving the wind are magnetical centrifugal force[15] and viscosity.[3] Abundances of ejecta through the wind change via decay processes as well as charged particle and capture processes because of high densities and temperatures of the ejecta. The abundances hence depend not only on initial conditions of the ejecta (abundances, density, temperature, and so on) but also on hydrodynamics of the wind. Detailed dynamics of the wind is, however, still uncertain. We therefore adopt a simple hydrodynamical model of the wind,[16] where the gasses are assumed to be adiabatic and freely expanding. The ejection velocity $v_{\rm ej}$ is set to be $10^{-4} - 0.1 v_{\rm K}$ with the Keplerian velocity $v_{\rm K}$ at the ejection radius $r_{\rm ej}$ of the disk. The density and temperature of the wind are initially taken to be those of the disk at $r_{\rm ej}$. We note that the entropy per baryon are 10–20 in units of the Boltzmann constant and that the non-relativistic entropies are always larger than the relativistic ones in

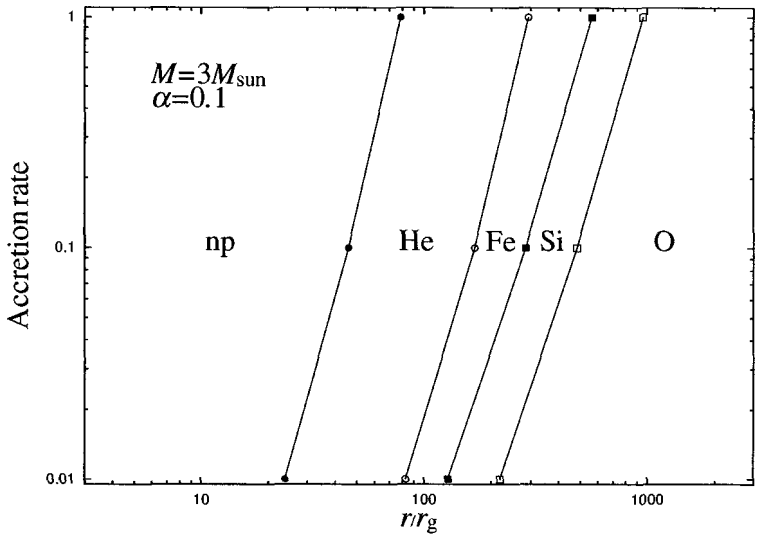

Figure 3. Interfaces of various layers . The disk consists of five layers characterized by dominant elements: ^{16}O, ^{28}Si, ^{54}Fe (and ^{56}Ni), ^{4}He, and nucleons.

the ejecta. The adiabatic index is accordingly taken to be 5/3.

Using density and temperature evolution calculated with the above wind model, we can evaluate change in abundances of the ejecta from an initial composition which is the same as in the accretion disk at $r_{\rm ej}$, with similar post-processing calculations to those in accretion disks. We have calculated abundance change through wind launched from the inner region ($r_{\rm ej} \leq 200 r_g$) of the disk with $\dot{M} = 10^{-4} - 0.1 M_\odot\,{\rm s}^{-1}$. In briefly, the abundances through the winds ejected from the O-rich and Si-rich disk layers are found to be not largely changed from those of the disk. On the other hand, for the winds from the He-rich and np-rich disk layers, the composition is largely altered from that of the disk.

In Figure 4, we show the mass fractions of ^{56}Ni inside the winds from the accretion disk with $\dot{M} = 0.01 M_\odot\,{\rm s}^{-1}$. The abscissa is the radius from which the wind is launched. The abundances are evaluated at the time when $T_{\rm ej} \simeq 5 \times 10^8$K. Abundant radioactives have not decayed significantly until the epoch. We find that the winds from the np-rich disk layer are abundant in ^{56}Ni, as suggested by the several authors.[3,8] We also find that ^{56}Ni is the most abundant in the ejecta from not only the np-rich layer but also the He-rich and Fe-rich layers and inner parts of the Si -rich layer. The smallness

Table 1. Averaged abundances in the Fe and He layer of the disk before decay.

Fe-rich disk layer				He-rich disk layer			
$0.01 M_\odot\,\mathrm{s}^{-1}$		$0.1 M_\odot\,\mathrm{s}^{-1}$		$0.01 M_\odot\,\mathrm{s}^{-1}$		$0.1 M_\odot\,\mathrm{s}^{-1}$	
elem.	X	elem.	X	elem.	X	elem.	X
Fe54	2.47E-01	Ni56	2.59E-01	He4	6.68E-01	He4	6.29E-01
Ni56	1.67E-01	Fe54	1.82E-01	Fe54	5.12E-02	Fe54	5.49E-02
Co55	1.13E-01	Co55	1.17E-01	p	4.34E-02	p	4.08E-02
Ni58	7.22E-02	Ni58	6.10E-02	Fe56	3.58E-02	Fe56	3.60E-02
He4	6.77E-02	Ni57	5.12E-02	n	3.18E-02	n	3.04E-02
Ni57	4.58E-02	Si28	4.68E-02	Fe55	2.68E-02	Fe55	3.02E-02
Si28	4.28E-02	He4	4.58E-02	Mn53	1.88E-02	Mn53	2.13E-02
S32	3.88E-02	S32	4.18E-02	Co57	1.40E-02	Co57	1.62E-02
Fe52	2.41E-02	Fe52	3.26E-02	Cr52	1.37E-02	Cr52	1.49E-02
Fe53	2.19E-02	Fe53	2.22E-02	Ni58	1.27E-02	Ni58	1.45E-02
Ca40	1.95E-02	Ca40	2.12E-02	Mn54	1.07E-02	Mn54	1.41E-02
Fe55	1.79E-02	Ar36	1.82E-02	Cr50	6.81E-03	Cr50	8.35E-03
p	1.75E-02	Co56	1.47E-02	Co56	5.92E-03	Co56	7.81E-03
Ar36	1.72E-02	p	1.33E-02	Co55	5.62E-03	Co55	7.31E-03
Co56	1.64E-02	Fe55	1.31E-02	Ni59	5.56E-03	Ni59	6.94E-03
Cr50	1.38E-02	Cr50	1.03E-02	Ni60	4.92E-03	Cr51	5.57E-03
Co57	1.08E-02	Mn51	9.36E-03	Cr51	4.27E-03	Ni60	5.50E-03
Mn51	9.54E-03	Co57	8.30E-03	Fe57	4.18E-03	Mn55	5.28E-03
Mn53	9.46E-03	Mn53	6.85E-03	Mn55	4.16E-03	Fe57	5.22E-03
Fe56	5.96E-03	Fe56	3.84E-03	Co58	2.99E-03	Co58	4.05E-03
Ni59	4.48E-03	Ni59	3.74E-03	Mn52	2.62E-03	Mn52	3.85E-03
Mn52	3.65E-03	Mn52	3.29E-03	Ni57	2.33E-03	Ni57	3.20E-03
Cr48	2.49E-03	Cr48	3.07E-03	Cr53	2.22E-03	Fe53	2.92E-03
Cr49	2.05E-03	Cr49	1.99E-03	Fe53	1.98E-03	Cr53	2.89E-03
Cr51	1.20E-03	Cr51	9.56E-04	V49	1.35E-03	V49	2.04E-03
Ni60	1.12E-03	V47	8.37E-04	V51	1.32E-03	Mn51	1.88E-03
Cr52	1.03E-03	Ni60	8.04E-04	Co59	1.32E-03	V51	1.74E-03
V47	8.03E-04	Cu59	7.94E-04	Fe58	1.29E-03	Co59	1.73E-03
Cu59	6.08E-04	Cr52	6.81E-04	Mn51	1.21E-03	Fe58	1.70E-03
Mn54	6.08E-04	Co54	5.66E-04	Si28	1.04E-03	Si28	1.38E-03
K39	3.85E-04	Mn54	5.03E-04	Ni56	9.70E-04	Ni56	1.35E-03
Co54	3.81E-04	Ti44	3.80E-04	Cr54	9.19E-04	V50	1.28E-03
Ti46	3.51E-04	Cu60	3.71E-04	V50	7.93E-04	Cr54	1.22E-03
Ti44	3.45E-04	K39	2.92E-04	S32	7.85E-04	S32	1.04E-03
Cu60	3.11E-04	Ti46	2.81E-04	Ni61	7.63E-04	Ni61	1.03E-03
Co58	3.03E-04	Co58	2.61E-04	Ti48	6.17E-04	V48	9.49E-04
V48	2.43E-04	V48	2.59E-04	Mn56	5.64E-04	Mn56	9.44E-04
Cl35	2.14E-04	V49	1.75E-04	V48	5.11E-04	Ti48	8.85E-04
V49	1.95E-04	Ti45	1.59E-04	Ti46	4.36E-04	Cr49	6.41E-04
Cu61	1.51E-04	Cl35	1.56E-04	Cr49	3.88E-04	Ti46	6.29E-04

of ^{56}Ni in the ejecta from $10r_g$ is attributed to efficient neutron capture on iron peak elements. The electron fraction, Y_e, is initially 0.4830 in the ejecta. ^{56}Ni is consequently largely depleted through neutron capture,

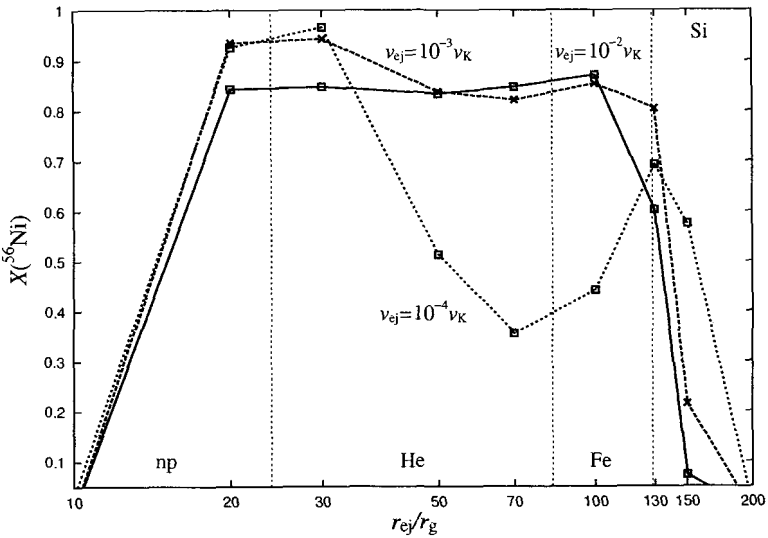

Figure 4. Mass fraction of ^{56}Ni of winds ejected from various disk radii and various ejection velocities.

while more neutron rich nuclei, such as ^{58}Ni, ^{60}Ni, and ^{64}Zn, are abundantly synthesized. On the other hand, in the ejecta launched from $20r_g$ (Y_e is 0.4994 initially), neutron capture on iron peak elements is less efficient in the ejecta. The mass fraction of neutrons in the ejecta from $10r_g$ is larger than that of protons by 0.034, which is too small to conduct r-process successfully.

4.2. *Chemical Composition of Winds*

We average abundances in winds ejected from the inner region ($r \leq 50r_g$) of the disk to estimate the yields through the winds from the disk. The averaging procedure is the same as in our previous study[13] but included with a weight of $1 - \exp(-r_{ej}/50r_g)$, (or 0, whichever is smaller than 0), which means more massive ejection from smaller disk radius less than $50r_g$. Figure 5 shows the yields via the winds from the disk with $\dot{M} = 0.001$, 0.01, and $0.05M_\odot\,\mathrm{s}^{-1}$. The total mass of ejecta is set to be $1M_\odot$.[3] The profiles of yields are similar for different $\dot{M}$, but the ejected masses heavier than Cu are larger for higher $\dot{M}$. This is due to the neutron richness of inner regions of the disk. It should be noted that appreciable amounts of ^{63}Cu and ^{64}Zn can be produced through the winds from the disk without

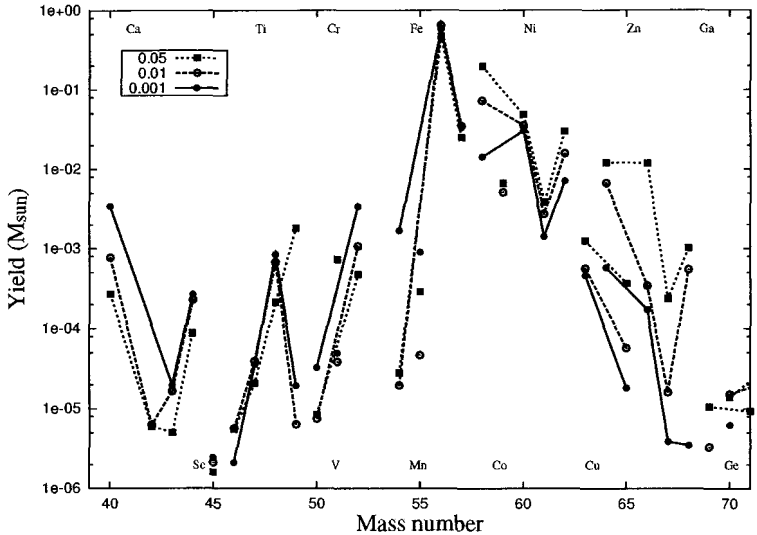

Figure 5. Yields through the wind ejected from the disk with 0.001 (filled circles with solid line), 0.01 (circles with dashed line), and $0.05 M_\odot\,\mathrm{s}^{-1}$ (squares with dotted line) after decay when the total mass through the wind is $1 M_\odot$.

neutron-rich regions (for $0.001 M_\odot\,\mathrm{s}^{-1}$).

4.3. *Chemical Composition of Winds from Neutron-rich Regions of Disks*

We investigate abundances in winds from neutron-rich regions of the disk with $\dot{M} \geq 0.1 M_\odot\,\mathrm{s}^{-1}$. We use the same procedure as in §4.1 but with the larger nuclear reaction network which includes various neutron-rich nuclei. Figure 6 shows the abundances in the wind after decays for the representative case: the wind launched from $r_{\rm ej} = 10 r_{\rm g}$ of the accretion disk with $\dot{M} = 0.1 M_\odot\,\mathrm{s}^{-1}$. The electron fraction and the entropy per baryon are initially 0.30 and $13.1 k_{\rm B}$, respectively. The ejection velocities of the wind are taken to be $0.01 v_{\rm K}$ (solid line) and $0.001 v_{\rm K}$ (dotted line). We find that neutron-rich nuclei are abundantly synthesized in the winds. More massive nuclei can be produced in the slower wind. This is because slower winds have enough time for nuclei to capture neutrons. Nuclei with mass numbers $\simeq 120$ and 180 are abundant for cases with $v_{\rm ej} = 0.01 v_{\rm K}$ and $0.001 v_{\rm K}$, respectively. For faster winds than $0.1 v_{\rm K}$, on the other hand, light elements are dominant. The abundances in the winds from neutron-rich regions of

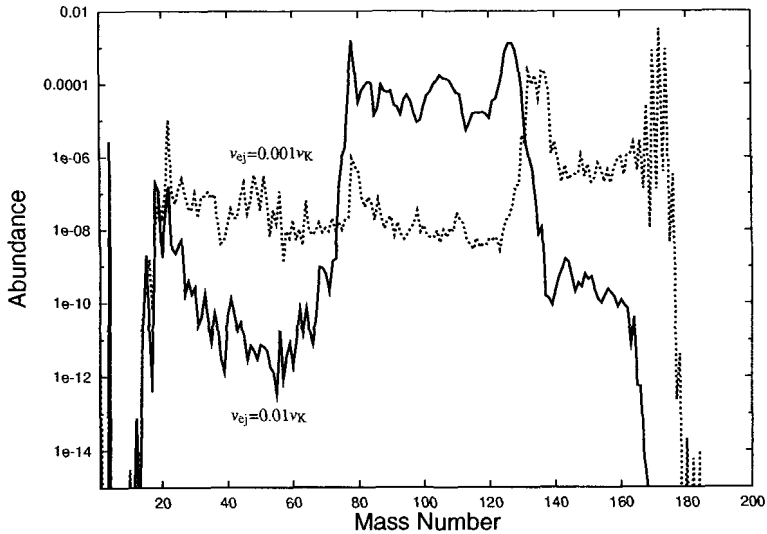

Figure 6. Abundances in the wind ejected from $r_{ej} = 10r_g$ of the disk with $\dot{M} = 0.1M_\odot\,s^{-1}$. The ejection velocities of the wind are taken to be $0.01v_K$ (solid line) and $0.001v_K$ (dotted line).

the disk are sensitive to the ejection velocity as well as the electron fraction. Although the electron fractions are comparable to or less than that of the disk in our wind model, the fractions may increase to be larger than 0.5 if the wind is driven via viscosity.[17] The abundances are likely to strongly depend on hydrodynamics of the wind. The yields from the neutron-rich disk therefore are still uncertain.

5. Summary

We have investigated nucleosynthesis inside the accretion disk associated with GRBs and inside winds launched from an inner region of the disk using the one-dimensional disk and wind models and the nuclear reaction network. The initial composition of accreting gas is taken to be that of an O-rich layer of a 20 $M_\odot$ star before the core collapse. We have found that the disk consists of five layers characterized by dominant elements: ^{16}O, ^{28}Si, ^{54}Fe (and ^{56}Ni), ^{4}He, and nucleons, and the individual layers shift inward with keeping the overall profiles of compositions as the accretion rate decreases. ^{56}Ni are abundantly ejected through the wind from the Fe-rich, He-rich and nucleon-rich disk layers with the electron fraction $\simeq 0.5$.

In addition to iron group elements, heavier elements than Cu, in particular ^{63}Cu and ^{64}Zn, are massively produced via the wind. Various neutron-rich nuclei can be produced through the wind from neutron-rich regions of the disk in our simple wind model, though the estimated yields have large uncertainties.

References

1. T. Galama et al., *Nature* **395**, 670 (1998).
2. J. Hjorth et al., *Nature* **423**, 847 (2003).
3. A. I. MacFadyen and S. E. Woosley, *Astrophys. J.* **524**, 262 (1999).
4. A. I. MacFadyen, S. E. Woosley and A. Heger, *Astrophys. J.* **550**, 410 (2001).
5. S. E. Woosley and T. A. Weaver, *Astrophys. J. S.* **101**, 181 (1995).
6. S. Mineshige, H. Nomura, M. Hirose, K. Nomoto and T. Suzuki, *Astrophys. J.* **489**, 227 (1997).
7. S. Nagataki, A. Mizuta, S. Yamada, H. Takabe and K. Sato, *Astrophys. J.* **596**, 401 (2003).
8. J. Pruet, S. E. Woosley and R. D. Hoffman, *Astrophys. J.* **586**, 1254 (2003).
9. T. Di Matteo, R. Perna and R. Narayan, *Astrophys. J.* **579**, 706 (2002).
10. K. Kohri and S. Mineshige, *Astrophys. J.* **577**, 311 (2002).
11. M. Hashimoto, *Prog. Theor. Phys.* **94**, 663 (1995).
12. S. Fujimoto, K. Arai, R. Matsuba, M. Hashimoto, O. Koike and S. Mineshige, *Publ. Astron. Soc. Japan* **53**, 509 (2001).
13. S. Fujimoto, M. Hashimoto, O. Koike, K. Arai and R. Matsuba, *Astrophys. J.* **585**, 418 (2003).
14. D. D. Clayton, 1968, *Principles of Stellar Evolution and Nucleosynthesis* (New York: MacGraw-Hill)
15. F. Daigne and R. Mochkovitch, *Astron. Astrophys.* **388**, 189 (2002).
16. C. Freiburghaus et al., *Astrophys. J.* **516**, 381 (1999).
17. J. Pruet, T. A. Thompson and R. D. Hoffman, *Astrophys. J.* appeared (2004) (astro-ph/0309278).

DIRECT MEASUREMENT OF THE ASTROPHYSICAL REACTION $^{14}O(\alpha,P)^{17}F$

M. NOTANI, S. KUBONO, T. TERANISHI, S. MICHIMASA, K. UE, J.J. HE, M. TAMAKI AND S. SHIMOURA

Center for Nuclear Study, University of Tokyo (CNS), RIKEN Branch, 2-1 Hirosawa, Wako, Saitama 351-0198, Japan

Y. YANAGISAWA AND T. MINEMURA

RIKEN (The Institute of Physical and Chemical Research), 2-1 Hirosawa, Wako, Saitama 351-0198, Japan

H. IWASAKI

Department of Physics, University of Tokyo, 7-3-1 Hongo, Bunkyo, Tokyo 113-0033, Japan

H. BABA

Department of Physics, Rikkyo University, 3-34-1 Nishi-Ikebukuro, Toshima, Tokyo 171-8501, Japan

N. HOKOIWA, Y. WAKABAYASHI, T. SASAKI, T. FUKUCHI AND Y. GONO

Department of Physics, Kyushu University, 6-10-1 Hakozaki, Fukuoka 812-8581, Japan

A. ODAHARA

Nishinippon Institute of Technology, Fukuoka 800-0394, Japan

ZS. FÜLÖP

Institute of Nuclear Research (ATOMKI), PO Box 51, H-4001 Debrecen, Hungary

E.K. LEE AND K.I. HAHN

Department of Science Education, Ewha Woman's University, Seoul 120-750,

South Korea

J.Y. MOON, C.C. YUN, J.H. LEE AND C.S. LEE
Department of Physics, Chung-Ang University, Seoul 156-756, South Korea

S. KATO
Department of Physics, Yamagata University, Yamagata 990-8560, Japan

The stellar reaction $^{14}O(\alpha,p)^{17}F$, that critically determines the onset of the high-temperature rp-process, has been studied through a direct measurement with a low-energy radioactive ^{14}O beam and a gaseous helium target cooled down to 30 K. The reaction cross section was measured by means of a thick target technique in the energy range of $E_{c.m.}(^{14}O+\alpha)$ = 0.8-3.8 MeV. The $^{14}O(\alpha,p)^{17}F^*$ reaction leading to the first excited state in ^{17}F was identified for the first time, suggesting an increase of about 50% for the stellar reaction rate through resonances at around 7.1 MeV in ^{18}Ne

1. Introduction

In explosive astrophysical events such as novae and X-ray bursts, the proton-rich nuclei interact further with protons and alpha particles on a short time scale relative to the beta decay. The nucleosynthetic process from the hot-CNO cycle to the heavy elements along the proton-rich side of the valley of stability is called the rp-process. As a starting point of the rp-process, nuclear reactions on the breakout process from the hot-CNO cycle are of much interesting in the field of nuclear astrophysics[1]. At high temparature, the $^{14}O(\alpha,p)^{17}F$ $(p,\gamma)^{18}Ne$ $(\alpha,p)^{21}Na$ reaction sequence can provide a path into the rp-process. Hydrogen burning of ^{14}O is inhibited since ^{15}F is particle unbound, and significant amount of ^{14}O may be accumulated due to the relatively long half-life of the beta decay ($t_{1/2}$ = 71 s) in the hot-CNO cycle. Thus the $^{14}O(\alpha,p)^{17}F$ reaction is essential to understand the breakout process.

However, this reaction was studied only via indirect methods and time-reverse reaction so far. Since the reaction is mainly resonant, it depends on the properties of intermediate states in the compound nucleus ^{18}Ne. The properties of these levels have been investigated[2,3,4,5,6] by measuring the resonance energies with other reactions and by estimating widths and spin assignments from the mirror nucleus ^{18}O. The $^{14}O(\alpha,p)^{17}F$ reaction rate at low temperatures is believed to be dominated by a resonance corresponding to a 1^- state at E_x = 6.15 MeV in ^{18}Ne. In addition to the

6.15-MeV state, several states at E_x = 7.0–7.5 MeV may contribute to the reaction rate at higher temperatures up to 3×10^9 K, and this topic motivated a novel research via the time-reverse ^{17}F(p,α)^{14}O reaction with a radioactive ^{17}F beam[7,8]. This reaction, however, only provides values for the partial widths for proton decay to the ground states of ^{17}F. Since the proton decay to the first-excited $1/2^+$ state in ^{17}F at E_x = 0.495 MeV would also contribute to the astrophysical yield, these proton widths have to be determined experimentally.

A direct measurement of the cross section for the ^{14}O(α,p)^{17}F reaction is difficult because, in addition to a low-energy radioactive ^{14}O beam, it also requires using a long ^{4}He gas target. This difficulty has been overcome by the combination of a newly-developed low-energy in-flight RI beam separator and a cold helium gas target. The measurement was performed with a thick target method[9,10].

In this paper, we report the results of a direct measurement of the nuclear reaction ^{4}He(^{14}O,p)^{17}F using the ^{14}O beam in conjuction with a cold gaseous helium target. The energy spectrum of protons from the helium target was measured and the reaction cross section for the ^{14}O(α,p)^{17}F was deduced from the spectrum. By comparing with the results in the experiments using time-reversed reaction, the reaction leading to the first excited state in ^{17}F was identified for the first time.

2. Experimental Setup

The experiment was performed using the CNS radioactive ion beam separator (CRIB)[11], which was recently installed by CNS, in the RIKEN accelerator facility. The CRIB has been developed as an extensive low-energy RI beam separator of in-flight type. Figure 1 shows the experimental setup of the measurement. A primary beam of ^{14}N was accelerated up to an energy of 8.4A MeV at the RIKEN AVF cyclotron with K = 70. The maximum intensity of the beam was 300 pnA. The primary beam bombarded a CH_4 gas target with a thickness of 1.3 mg/cm^2. The target gas was confined in a small chamber with entrance and exit windows. The gas pressure was 1.0 atm and Havar foils of thickness of 2.2 μm were used for the windows. A secondary beam of ^{14}O was produced by the ^{1}H(^{14}N,^{14}O)n reaction.

The secondary ^{14}O particles were separated in the CRIB. An energy degrader of 10-μm thick Mylar foil was installed at the momentum dispersive focal plane (F1) to remove background light ions from the secondary beam. A holizontal slit was set after the degrader to separate the ^{14}O particles at

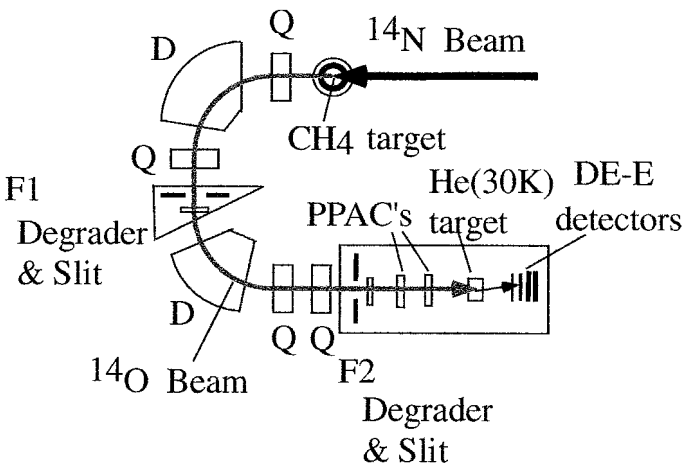

Figure 1. Schematic view of the experimental setup used for the measurement of the $^{14}O(\alpha,p)^{17}F$ reaction cross section.

a mean energy of 6.40A MeV with the momentum acceptance of 1%.

At the achromatic focal plane (F2) of CRIB, a series of detectors and a secondary target were installed after an energy degrader of 7.5-μm thick tantalum foil in a vacuum chamber. The setup consisted of two parallel-plate avalanche counters (PPAC's)[12], a secondary target of helium gas with a thickness of 3.57 mg/cm^2, and a silicon-detector stuck with thicknesses of 0.02, 0.07, 1.5 and 1.5 mm. The secondary beam was monitored with two PPAC's during the data taking. Particle identification was performed for each event on the basis of time of flight (TOF) between the two PPAC's. The purity of the ^{14}O beam was 85% at F2.

The ^{14}O beam bombarded a novel helium gas target, which operates at 30 K, offering ten times larger density than at room temperature. This design results in compactness and makes it possible to effectively apply the thick target method. The helium gas at a pressure of 0.6 atm was confined in a 50-mm long gas cell with two windows of 2.2-μm thick Havar foils. The effective thickness of ^{4}He was about 3.1 mg/cm^2. The target was chosen as thin as possible, being large enough to stop the ^{14}O nuclei in it. The reaction products emitted from the helium target were identified by the ΔE-E method, using the telescope of four silicon detectors located at 0°. The energy deposit in each detector was measured, where the energy of each detector was calibrated using proton beams produced through the CRIB

facility.

3. Result and Discussion

The ^{4}He(^{14}O,p)^{17}F reaction was measured with a ^{14}O beam at the incident energy of 43 MeV on the helium gas target. One can deduce the reaction cross sections from the energy spectrum of protons emitted from the target, because the proton energy is a function of the center-of-mass energy of ^{14}O+α system due to the ^{14}O-ion energy loss in the target. The protons from the helium gas target were detected by the silicon telescope. Assuming the final state of ^{17}F is ground state, the cross sections for the ^{14}O(α,p)^{17}F reaction were obtained in the region of $E_{\mathrm{c.m.}}(^{14}\mathrm{O}+\alpha) = 0.8$–$3.8$ MeV. The result is presented in Fig. 2. Eight resonances are evident in the data which correspond to previously observed states in ^{18}Ne at the 6.15, 6.29, 7.05, 7.12, 7.35, 7.62, 7.95 and 8.30 MeV[2,3]. The eight arrows with the labels of excitation energy in Fig. 2 indicate the location of these resonances. The rate for the breakout reactions is dominated by the resonance parameters for the 1^- state at 6.15 MeV at around the temparature $T_9 = 1$, while the contributions from the three higher-lying resonances start to dominate the reaction rate in the temparature range $T_9 \geq 3$[13]. In addition, we newly observed a peak at around 1.5 MeV of the ^{14}O-α center-of-mass energy. The ^{18}Ne levels in the energy region have been investigated by means of indirect method, however, the peak observed newly in our experiment has not been observed. Thus we could not assign the new peak to any of the known levels in ^{18}Ne.

The new peak would be a transition to the excited state in ^{17}F. Figure 3 shows the level scheme of ^{18}Ne. The first excited state of ^{17}F is located at excitation energy of 0.495 MeV from the ground state. The new peak was observed at the excitation energy to be 0.5-MeV lower than the 7.10-MeV level. Thus one could understand it to be at around 7.15 MeV the ^{14}O(α,p)^{17}F* reaction leading to the $1/2^+$ first-excited state in ^{17}F, which goes through resonances at around 7.1 MeV. The dashed arrow shows the transition to the excited state in ^{17}F.

The result of this experiment demonstrated the usefulness of the low-energy radioactive ^{14}O beam and the cold helium gas target for a direct measurement of the ^{14}O(α,p)^{17}F reaction. Due to the contribution from the excited state in ^{17}F, the reaction cross sections were found to differ from that obtained by the time-reverse reaction[7,13]. This branch may increase the ^{14}O(α,p)^{17}F astrophysical reaction rate [8]. For instance, a calculation

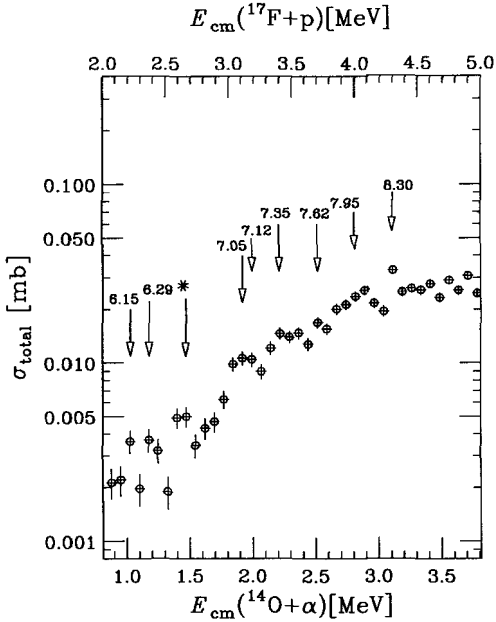

Figure 2. Measured cross sections for the $^{14}O(\alpha,p)^{17}F$ reaction. The arrows with labels of excitation energy indicate the location of known states in ^{18}Ne, and the asterisk mark is the new one.

of the stellar reaction rate was presented in Ref. [13]. The contribution from the 7.05 MeV becomes the main component of total reaction rate over the temperature of $T_9 = 2.0$ K. The present result would change the result of calculation. The cross section of the excited state over that of the ground excited state in ^{17}F would suggest a 50% increase for the $^{14}O(\alpha,p)^{17}F$ reaction rate through resonances at around 7.1 MeV in ^{18}Ne. In order to make a calculation of the stellar reaction rate, one should take into account the enhancement of reaction rate due to the path to the excited state in ^{17}F.

4. Summary

In summary, the astrophysical $^{14}O(\alpha,p)^{17}F$ reaction, which is important in various steller environments such as X-ray bursts, has been measured directly for the first time, by using a radioactive ^{14}O beam. The present experiment has shown that the combination of a low-energy RI beam and

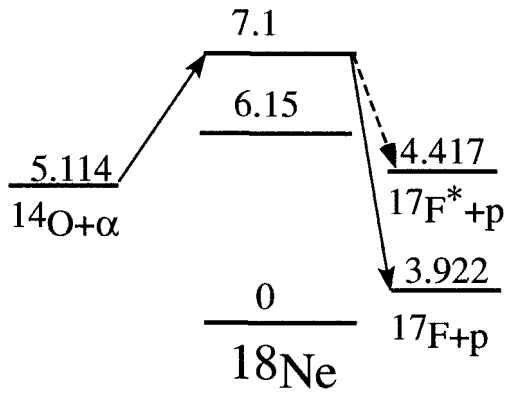

Figure 3. Level Scheme of ^{18}Ne. The dashed line arrow shows a transition to the excited state of ^{17}F

cold helium gas target can be used for the study of (α,p) reactions. The measured cross section was found to differ from a prediction based on an indirect measurement, and a direct measurement with time-inverse reaction since the observed channel was limited to the branch to the ^{17}F ground state alone. A proton decay from the ^{18}Ne levels at $E_x = 7.05$ and 7.12 MeV to the first-excited state in ^{17}F has been measured. This result would suggest an increase of 50% for the ^{14}O$(\alpha,p)^{17}$F reaction rate via the resonances around 7.1 MeV and might affect the senario of ignition phase of X-ray burst.

References

1. R.K. Wallace and S. E. Woosley, Astrophys. J., Suppl. Ser. 45, (1981) 389.
2. K.I. Hahn et al., Phys. Rev. C 54, (1996) 1999.
3. S.H. Park et al., Phys. Rev. C 59, (1999) 1182.
4. M. Wiescher et al., Astrophys. J. 316, (1988) 162.
5. M. Wiescher, J.Görres, and F.-K. Thielemann, Astrophys. J. 316, (1988) 384.
6. C. Funck, B. Grund, and K. Langanke, Z. Phys. A 332, (1989) 109.
7. B. Harss et al., Phys. Rev. Lett 82, (1999) 3964.
8. J.C. Blackmon et al., Nucl. Phys. A 688, (2001) 142.
9. K.P. Artemov et al., Sov. J. Nucl. Phys. 52, (1990) 408.
10. S. Kubono et al., Nucl. Phys. A 693, (2001) 221.
11. Y. Yanagisawa et al., RIKEN Accel. Prog. Rep. 34, (2001) 183.
12. H. Kumagai et al., Nucl. Instrum. Meth. A 470, (2001) 562.
13. B. Harss et al., Phys. Rev. C 65, (2002) 035803.

ELASTIC RESONANCE SCATTERING OF ^{23}Mg+p

T. TERANISHI*, S. KUBONO*, J.J. HE, M. NOTANI, T. FUKUCHI, S. MICHIMASA AND S. SHIMOURA
Center for Nuclear Study (CNS), University of Tokyo, RIKEN campus, 2-1 Hirosawa, Saitama, Japan
E-mail: teranisi@cns.s.u-tokyo.ac.jp

S. NISHIMURA AND M. NISHIMURA
Institute of Chemical and Physical Research (RIKEN)

Y. WAKABAYASHI, N. HOKOIWA AND Y. GONO
Department of Physics, Kyushu University, Japan

A. ODAHARA
Nishinippon Institute of Technology, Japan

H. ISHIYAMA, Y.X. WATANABE, T. HASHIMOTO, T. ISHIKAWA, M.H. TANAKA AND H. MIYATAKE
IPNS, KEK, Japan

J.Y. MOON, J.C. KIM AND C.S. LEE†
Chung-Ang University, Korea

V. GUIMARÃES AND R.F. LIHITENTHALER
Department of Nuclear Physics, São Paulo University, Brazil

H. BABA
Department of Physics, Rikkyo University, Japan

K. SATO, T. KAWAMURA AND S. KATO
Department of Physics, Yamagata University, Japan

The ^{23}Mg+p elastic resonance scattering was observed by using a low-energy radioactive-ion beam of ^{23}Mg to study resonance levels in ^{24}Al. Resonance patterns were found in the excitation function of the elastic scattering. New information on spin-parities and widths of the ^{24}Al levels may help understand the stellar ^{23}Mg(p,γ)^{24}Mg reaction rates. Another data of the ^{24}Mg+p resonance scattering, taken simultaneously in the present experiment, confirmed the present experimental technique.

1. Introduction

Recently, low-energy radioactive-ion beams at around 5 MeV/nucleon were developed at Center for Nuclear Study (CNS), University of Tokyo. The secondary beams were produced by using low-energy heavy-ion primary beams bombarding targets of light elements. After the production-target position, the secondary particles were separated by an in-flight magnetic separator, called CRIB[1,2]. So far, low-energy beams of more than ten radioactive nuclides have been produced by CRIB. With these beams, experiments for resonance scattering[3] and direct/resonance reactions[4] are being performed mainly for nuclear astrophysics.

The present paper reports the most recent experiment of ^{23}Mg+p elastic resonance scattering performed at the CNS facility. The excitation function of ^{23}Mg+p was measured to identify resonance levels in ^{24}Al above the proton threshold of E_x = 1.871 MeV. Spin-parity (J^π) values were not precisely assigned to many of these resonance levels before. There were almost no experimental data on widths (Γ) of the resonance levels in ^{24}Al[5]. Updating the data table of ^{24}Al levels is necessary not only for nuclear structure study but also for nuclear astrophysics. Some of the levels above the proton threshold may play important roles in the stellar reaction of ^{23}Mg(p,γ)^{24}Al, which is one of breakout paths from the Ne-Na cycle[6]. The present experiment aimed at deducing new information on J^π and Γ for these levels from the excitation function of ^{23}Mg+p.

2. Experiment

The ^{23}Mg+p experiment was performed in inverse kinematics with a secondary ^{23}Mg beam and a proton target. The ^{23}Mg beam was produced by

*Work partially supported by Grant-in-Aid for Science Research from the Japan Ministry of Education, Culture, Sports, and Technology under the contract numbers 13440071 and 14740156.

†Work partially supported by the Joint Research Program under the Korea-Japan Basic Science Promotion Program (KOSEF 2002-JR015).

the ^{24}Mg(d,t)^{23}Mg reaction in inverse kinematics. The primary beam of ^{24}Mg was accelerated by an AVF cyclotron up to 7.5 MeV/nucleon with an intensity of 60 pnA. The deuterium gas target had a thickness of 0.33 mg/cm^2 confined in a cell by two Havar window foils of 2.2 μm. After the particle separation by CRIB, the ^{23}Mg secondary beam had an energy of 4.0 MeV/nucleon and an intensity of 3.2×10^4 particles/sec, which was 12% of the total intensity. A major contaminant in the beam was ^{24}Mg with an energy of 3.5 MeV/nucleon originated from scattering of the primary beam at beam pipes and inner walls of the separator magnets. This ^{24}Mg contaminant was utilized to measure a spectrum of known resonance levels in the ^{24}Mg+p (^{25}Al) system simultaneously with the ^{23}Mg+p data of interest.

The setup for the elastic scattering measurement consisted of two parallel-plate avalanche counters (PPACs)[7] as beam counters, a polyethylene ($(CH_2)_n$) sheet as a proton target, and two sets of silicon detector for recoil protons. The PPACs were set upstream of the proton target and used to tag beam particles on an event-by-event basis. The beam incident angle and reaction position on the target were determined by the hit positions at the two PPACs. The beam nuclides of ^{23}Mg and ^{24}Mg were identified by the time-of-flight between the two PPACs to make the spectra of ^{23}Mg+p and ^{24}Mg+p, respectively.

A thick-target technique[8,9] was used to measure the excitation function efficiently. The thickness of the polyethylene target was chosen to be 8.2 mg/cm^2, which was a little larger than the stopping range for the beam particles. Utilizing energy-loss process of the beam in the target, a wide range of center-of-mass energy ($E_{\rm CM}$) was scanned without changing the beam energy before the target. While the beam particles were completely stopped in the target, most of the recoil protons went out from the target with small energy losses.

The recoil protons were detected by the silicon detector sets at laboratory angles of $\theta_{\rm LAB} = 0°$ and 17°. Each set consisted of ΔE and E layers with thicknesses of 75 and 1500 μm, respectively. Protons were identified with the information of ΔE, E, and timing. The $E_{\rm CM}$ and center-of-mass angle ($\theta_{\rm CM}$) were determined by measuring the energy and angle of proton. At $\theta_{\rm LAB} = 0°$, the proton energy is roughly four times of $E_{\rm CM}$. An $E_{\rm CM}$ resolution of 30 keV (FWHM) was easily achieved because of this kinematic factor and a silicon detector resolution of about 100 keV (FWHM).

A carbon target was also used to measure the background contribution to the proton spectrum from C atoms in the $(CH_2)_n$ target. The proton

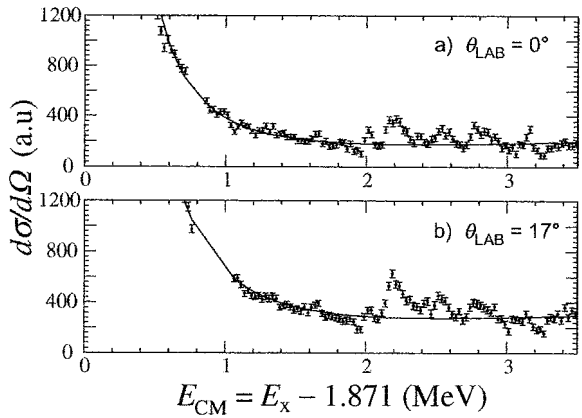

Figure 1. Preliminary result of the excitation function for the ^{23}Mg+p elastic scattering at a) $\theta_{LAB} = 0°$ and b) 17°. The solid curves represent cross sections for the potential (Rutherford + hard-sphere) scattering.

spectrum with the C target was subtracted from that with the $(CH_2)_n$ target to deduce the excitation function of proton elastic scattering.

In the excitation function, a resonance level can be identified as an interference pattern of potential scattering and resonance scattering. The energy, Γ, and J^π of the level may be deduced from an R-matrix analysis for the interference pattern. The angle of $\theta_{LAB} = 0°$ corresponds to $\theta_{CM} = 180°$, where the Coulomb-potential scattering amplitude is minimum. Therefore, angles around $\theta_{LAB} = 0°$ are suitable for observing resonance contributions.

3. Results

Preliminary spectra of ^{23}Mg+p at $\theta_{LAB} = 0°$ and 17° are shown in Figure 1. The solid line represents cross sections deduced from the Rutherford and hard-sphere scattering amplitudes. Deviation of the experimental cross sections from the solid line is seen above about $E_{CM} = 1.6$ MeV both at 0° and 17°. Those deviation patterns are similar and indicating existence of several resonance levels. A small bump at $E_{CM} = 1.6$ MeV and two peaks at 2.0 and 2.2 MeV may be attributed to three levels. The spectral pattern above $E_{CM} = 2.4$ MeV is possibly due to three or more resonance levels. Some of the peaks seem to be consistent with the latest compilation of ^{24}Al levels[5]. Quantitative analysis of these patterns is in progress. Some J^π

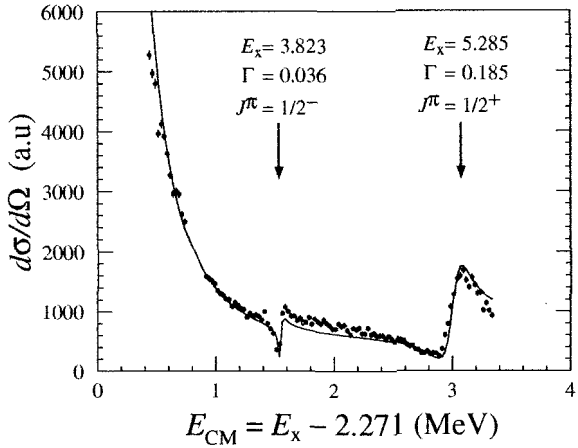

Figure 2. Preliminary result of the excitation function for the elastic scattering of protons on ^{24}Mg stable nucleus at $\theta_{LAB} = 0°$. The solid curve represents a tentative result of an R-matrix fit.

values will be newly determined by an R-matrix analysis. The Γ for these levels will be also evaluated for the first time. For example, the clearest peak at $E_{CM} = 2.2$ MeV has $\Gamma \sim 60$ keV according to a preliminary analysis.

The ^{24}Mg+p data, taken simultaneously with the ^{23}Mg+p data, is useful to check the energy calibration of the silicon detectors and analysis procedures. Figure 2 shows the result of ^{24}Mg+p excitation function, covering $E_x = 2.7$–5.6 MeV in ^{25}Al. The spectrum clearly shows resonance shapes due to two known levels in ^{25}Al at $E_x = 3.823$ and 5.285 MeV with $\Gamma = 0.036$ and 0.185 MeV, respectively[5]. The solid curve in Fig. 2 represents a result of R-matrix analysis and agrees well with the experimental data. There are many other known levels in the present spectral range. However, their contributions to the spectrum are not clear because most of their widths are known to be less than 10 keV[5], which is smaller than the energy resolution of about 30 keV (FWHM).

4. Summary

The excitation function of the ^{23}Mg+p elastic scattering was measured by using a low-energy ^{23}Mg beam and a thick proton target. The resonance patterns seen in the excitation function are under analysis and will provide new information on J^π and Γ of the resonance levels in ^{24}Al. To extract

the resonance contribution to the ^{23}Mg(p,γ)^{24}Mg reaction rates, one has to know the gamma widths, which are unable to be deduced from the present experiment. However, the information from the present experiment will help further study on this stellar reaction. The validity of the ^{23}Mg+p data was proven by the calibration spectrum of ^{24}Mg+p, which was measured simultaneously by using the same experimental setup. Measurement and analysis of other resonance-scattering experiments on proton-rich unstable nuclei are in progress[10,11] or being planned with interests in nuclear astrophysics and nuclear structure study.

References

1. T. Teranishi et al., *Nucl. Phys.* **A718**, 207c (2003).
2. S. Kubono et al., *Eur. Phys. J.* **A13**, 217 (2002).
3. T. Teranishi et al., *Phys. Lett.* **B556** 27 (2003).
4. M. Notani et al., in this proceedings.
5. P.M. Endt, *Nucl. Phys.* **A633**, 1 (1998).
6. S. Kubono et al., *Nucl. Phys.* **A588** 521 (1995), and references therein.
7. H. Kumagai et al., *Nucl. Instrum. and Methods* **A470**, 562 (2001).
8. K.P. Artemov et al., *Sov. J. Nucl. Phys.* **52**, 408 (1990).
9. S. Kubono, *Nucl. Phys.* **A693**, 221 (2001), and references therein.
10. J.J. He et al., in this proceedings.
11. J.Y. Moon et al., in this proceedings.

RESONANCE STATES IN ^{22}Mg, ^{26}Si FOR REACTION RATES IN THE RP-PROCESS

Y. SHIMIZU, K. HATANAKA, G.P.A. BERG, M. WIESCHER[a], H. SCHATZ[b], T. ADACH[c], A.D. BACHER[d], C.C. FOSTER[d], K. FUJITA, H. FUJITA, Y. FUJITA[c], J. GÖRRES[a], CH. HERMAN[e], J. KAMIYA, Y. SAKEMI, Y. SHIMBARA, E.J. STEPHENSON[d], T. WAKASA[f], AND M. YOSOI[g]

Research Center for Nuclear Physics (RCNP), Ibaraki, Osaka 567-0047, Japan
[a] *University of Notre Dame, Notre Dame, Indiana 46556, USA*
[b] *NSCL and Dept. of Physics, and Astronomy, MSU, East Lansing, MI 48824, USA*
[c] *Department of Physics, Osaka University, Toyonaka, Osaka 560-0043, Japan*
[d] *Indiana University Cyclotron Facility, Bloomington, Indiana 47408, USA*
[e] *Department of Physics, Ohio State University, Columbous, Ohio 43210, USA*
[f] *Department of Physics, Kyushu University, Hakozaki, Fukuoka 812-8581, Japan*
[g] *Department of Physics, Kyoto University, Sakyo, Kyoto 606-8502, Japan*

Motivated by the need of spectroscopic data to better understand the astrophysical rp-process, we developed a new experimental method using the Grand Raiden magnet spectrometer to study proton rich nuclei with α and ^{3}He induced reactions. The results of the ^{24}Mg(^{4}He,^{6}He)^{22}Mg reaction at 205 MeV and 0° are presented, showing states relevant for resonant reaction rate calculations of the proton capture ^{21}Na$(p,\gamma)^{22}$Mg and ^{18}Ne$(\alpha,p)^{21}$Na reaction which controls the break-out of the hot CNO cycles at X-ray burst conditions. In addition, the results of the ^{28}Si(^{4}He,^{6}He)^{26}Si reaction are presented, showing states relevant to the production rate of ^{26}Al in its ground state which provides models of the explosive hydrogen burning process in novae and supernovae.

1. Introduction

Explosive nuclear hydrogen burning at high temperature conditions on the surface of accreting white dwarfs is dominated by the hot CNO cycles[1]. Explosive hydrogen burning on the surface of accreting neutron stars leads to considerably higher temperatures and break-out from the hot CNO cycles triggers the rp-process[2,3]. Network calculations are well capable of qualitatively reproducing characteristics of these phenomena. Their quantitative interpretation, however requires a better understanding of the nuclear pro-

cesses during these explosive events by the measurement of reaction rates and structure of unstable, proton rich nuclei[4].

Even though new facilities are now able to directly measure relevant reaction rates by using radioactive beams and reversed kinematics, measurements will also benefit from level structure information with excitation energies in the resonance regions of interest. In order to study the precise level structure of relevant nuclei, a good energy resolution is required. The advantage of the (^{4}He,^{6}He) reaction is its possibility to achieve high resolution.

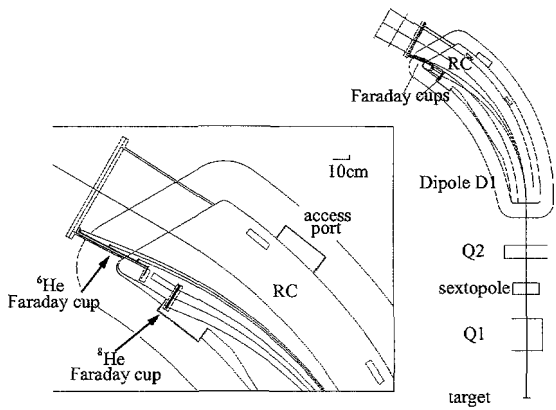

Figure 1. Detailed configuration of new Faraday cups installed inside, near the exit of the first dipole magnet of the Grand Raiden spectrometer.

2. Experiment

The measurements were performed at the Research Center for Nuclear Physics (RCNP), Osaka University by using a 205 MeV ^{4}He beam from the $K = 400$ RCNP ring cyclotron and the Grand Raiden spectrometer[5] placed at 0°. The extracted beam from the ring cyclotron was transported to the West Experimental Hall via the WS beamline[6]. In order to stop and integrate the current of the beam, a new Faraday cups were installed inside, near the exit of the first dipole magnet of the Grand Raiden spectrometer (see Figure 1). The reaction products continue to travel through the spectrometer and are measured in a focal plane detector system, consisting of two vertical drift chambers (VDC) that allow the determination

of the horizontal and vertical positions and angles in the focal plane. Three plastic scintillators, 1 mm, 10 mm, and 10 mm thick, mounted behind the VDC system allowed particle identification, time of flight measurements, and light particle rejection. Typical beam particle currents were 200 enA. For best vertical scattering angle definition the spectrometer was used in overfocus mode which allows reconstruction of the vertical component of the scattering angle from the measured vertical position in the focal plane.

For good resolution in momentum and horizontal scattering angle component, full dispersion matching[7] was applied. While these are newly developed standard procedures, the energy spread in the 0.7 mg/cm^2 target, the large Q-value, and limitations in the angle definition have limited the best resolution to 60 keV so far.

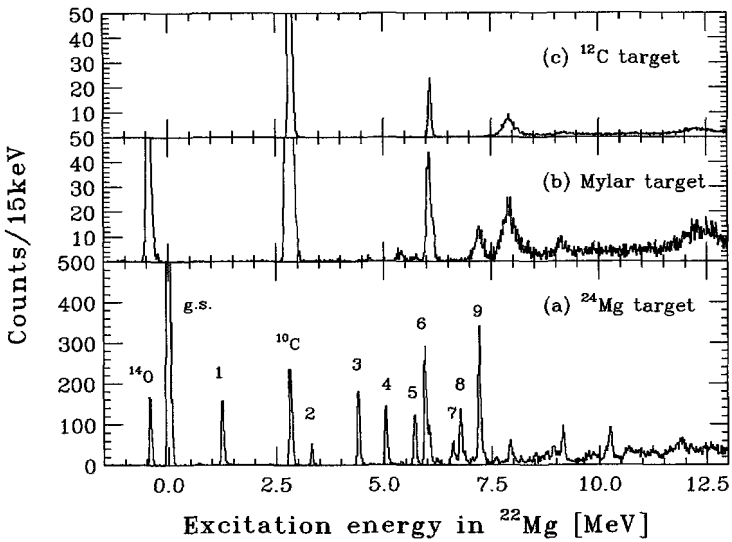

Figure 2. Measured ^{22}Mg, ^{10}C, and Mylar spectrum with angle cut 0 ° - 1° and resolution of 60 keV

3. Data Analysis

In all of the runs we observed ^{6}He and other light particles in the detector. The energy lost in the scintillator, and the time of flight information built by the scintillator and the rf signal of the AVF cyclotron were used for particle identification. The horizontal position and angle in focal plane were

also used to correct time of flight information. Since most of background particles didn't come from the target, two-dimensional gates in the time of flight signal and the horizontal position or angle in focal plane allowed us to separate each particle group clearly. The final ^{6}He spectrum is shown in Figure 2(a).

Thin self-supporting enriched ^{24}Mg and ^{28}Si foils with a thickness of 0.7 mg/cm^2 were used as the target. Target contaminations of ^{12}C and ^{16}O were observed. In order to subtract contaminant yields, mylar and carbon target were used. Figure 2 shows the ^{22}Mg, ^{12}C, and Mylar spectra measured at the same spectrometer setting. The ^{14}O yields was obtained by subtracting ^{10}C from the (^{4}He, ^{6}He) spectrum on the Mylar target. The background was estimated by normalizing ^{14}O and ^{10}C ground state yields.

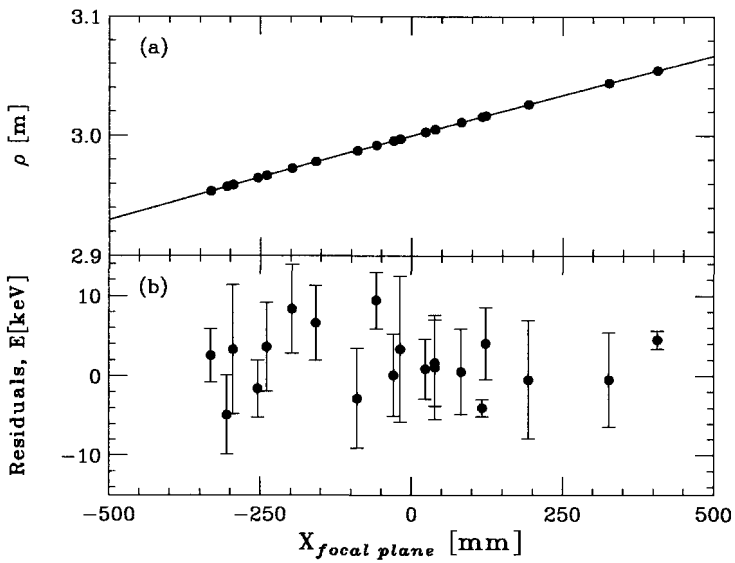

Figure 3. Energy calibration in whole the focal plane; fit (above), and residuals (below). ρ is calculated from kinematics and magnetic field.

In order to calibrate the particle momentum, all well separated known low-lying levels[8] in ^{22}Mg labeled g.s. and 1-9 were used at two magnetic field settings to calibrate whole the focal plane. We observed twenty isolated levels in the focal plane. Figure 3(a) shows the relation between the focal pale position and the bending radius ρ which was calculated from kinematics and magnetic field. The calibration is linear with a small quadratic

term. Energy of the particles was calculated by this relation. Almost all of these states have excitation energies that are known to better than 10 keV (see Figure 3(b)). The standard deviation of the calibration is 9 keV.

4. Excitation energies in ^{22}Mg

Figure 4 shows the measured energy spectra of the ^{24}Mg(^{4}He,^{6}He)^{22}Mg reaction at several scattered angles around α-threshold. The resolution of measurement was 56, 64, and 80 keV at 0°-1°, 1°-2°, and 2°-3°, respectively. Our measured ^{22}Mg excitation energies above 6 MeV are summarized in Table 1 and compared to results of the previous measurement[9]. Errors shown in Table 1 resulted from uncertainties in the peak fitting procedure. For most levels our results agree with previously reported excitation energies. Energy levels above 8.14 MeV are relevant for rate calculations of the ^{18}Ne(α,p)^{21}Na reaction which controls the break-out of the hot CNO cycles above 0.8 GK.

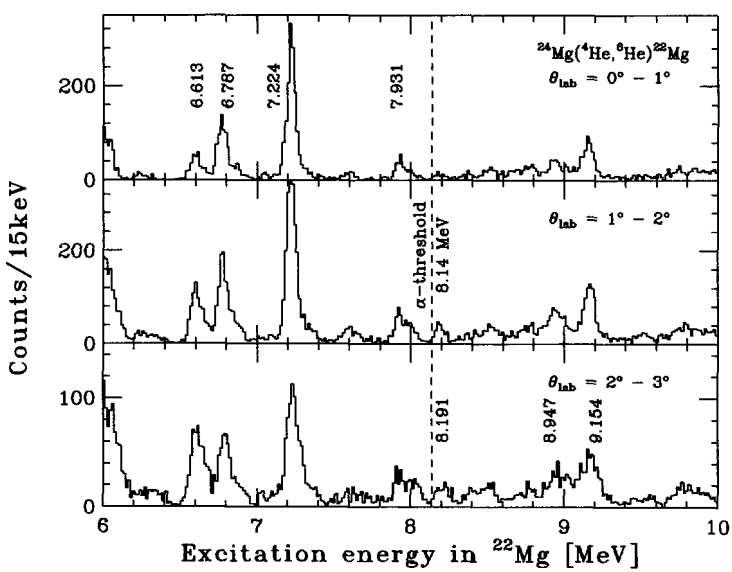

Figure 4. Excitation energy of ^{22}Mg spectrum at several scattered angles. The dashed line shows α-threshold (E_x = 8.14 MeV).

Table 1. Energy levels of ^{22}Mg, in units of keV

this work	E_x[9]	this work	E_x[9]	this work	E_x[9]
6046 ± 4	6041 ± 11	8384 ± 8	8396 ± 15		10078 ± 24
6246 ± 7	6255 ± 10	8521 ± 5	8547 ± 18	10165 ± 4	10090 ± 29
6605 ± 3	6606 ± 11	8685 ± 6	8613 ± 20	10262 ± 3	10297 ± 25
6774 ± 2	6767 ± 20	8791 ± 5	8754 ± 15	10404 ± 7	10429 ± 26
6876 ± 6	6889 ± 10	8947 ± 4	8925 ± 19	10609 ± 5	10570 ± 25
7070 ± 8			9066 ± 18	10711 ± 4	10660 ± 31
7224 ± 2	7169 ± 11	9154 ± 3	(9172 ± 23)		10750 ± 31
	7402 ± 13		(9248 ± 20)	10872 ± 4	10844 ± 38
7604 ± 7	7674 ± 11		9329 ± 18	11003 ± 5	10980 ± 31
	7784 ± 18	9526 ± 10	9533 ± 24	11125 ± 5	11135 ± 40
7931 ± 5	7964 ± 16	9748 ± 6	9712 ± 21	11236 ± 5	
8006 ± 8	8062 ± 16	9861 ± 6	9827 ± 44	11347 ± 5	
8191 ± 8	8203 ± 23	9972 ± 6	9924 ± 28	11540 ± 5	

5. Excitation energies in ^{26}Si

Figure 5 shows the measured energy spectra of the ^{28}Si(^{4}He,^{6}He)^{26}Si reaction at several scattered angles around p-threshold. The resolution of measurement was 60, 64, and 64 keV at 0°-1°, 1°-2°, and 2°-3°, respectively. Our measured ^{26}Si excitation energies are summarized in Table 2 and compared to results of the previous measurement[10]. Errors shown in Table 2 resulted from uncertainties in the peak fitting procedure. For most levels our results agree with previously reported excitation energies. However, we cannot see the state at 5.515 MeV reported by (p,t) measurements[10]. This suggests that the state has an unnatural parity, because (^{4}He,^{6}He) reaction cannot excite a state with unnatural parity, but (p,t) reaction can excite it. Energy levels above 5.518 MeV are relevant to the production rate of ^{26}Al in its ground state which provides a valuable constraint on models used to understand the explosive hydrogen burning process in novae and supernovae.

6. Summary and Conclusion

Excitation energies of ^{22}Mg and ^{26}Si were measured by (^{4}He, ^{6}He) reaction on ^{24}Mg and ^{26}Si targets, respectively, at an incident energy of E_α = 205 MeV. Excitation energies were determined up to 12.5 MeV. The lateral

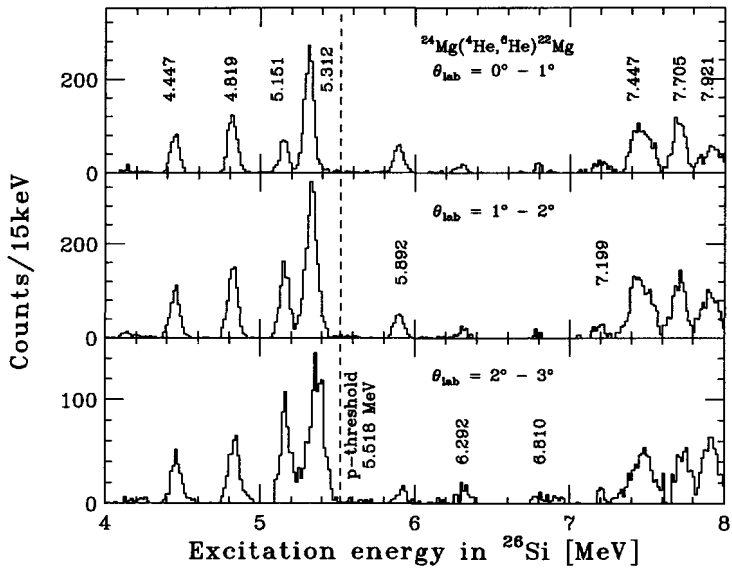

Figure 5. Excitation energy of ^{26}Si spectrum at several scattered angles. The dashed line shows p-threshold (E_x = 5.518 MeV).

Table 2. Energy levels of ^{26}Si, in units of keV

this work	E_x[10]	this work	E_x[10]	this work	E_x[10]
1793 ± 3	1795.9	5892 ± 4	5916 ± 2	8570 ± 4	
2785 ± 2	2783.5	6292 ± 8	6300 ± 4	8806 ± 5	
3337 ± 3	3332.5		6380 ± 4	8952 ± 7	
	3756 ± 2	6810 ± 8	6787 ± 4	9067 ± 5	
4138 ± 11	4138 ± 1		7019 ± 10	9247 ± 8	
	4211 ± 16	7199 ± 6	7160 ± 5	9374 ± 7	
4447 ± 4	4445 ± 3	7447 ± 2	7498 ± 4	9607 ± 9	
4819 ± 3	4805 ± 2	7705 ± 3	7687 ± 22	9802 ± 7	
5151 ± 4	5145 ± 2	7921 ± 3	7900 ± 22	9917 ± 2	
5312 ± 2	5291 ± 3	8282 ± 6		10070 ± 8	
	5515 ± 5	8431 ± 6		10294 ± 7	

and angular dispersion matching was applied to the beam optics. The spectrometer was used in the overfocus mode. For ^{22}Mg excitation energies, we observed new levels around α-threshold. Several of these levels are

important for radiative proton capture reactions on ^{21}Na occurring in a classic nova stellar explosion. For ^{26}Si excitation energies, we observed new levels around the α-threshold. We cannot see the state at 5.515 MeV which reported by the previous (p,t) measurement[10]. Our result suggests that this state has an unnatural parity.

In future works, the spin and parity will be assigned to the measured levels which are necessary by the Network calculation. We have measured angular distributions of these levels. They will be compared with a DWBA calculation. Now Network calculation based on our results is in progress.

7. Acknowledgments

We thank the RCNP staff for their support during the experiment. We also wish to thank Professor H. Toki for his encouragements throughout the work. This experiment was performed under Program No. E163 and E187 at the RCNP.

References

1. S. Starrfield *et al.*, Ap. J. Suppl. **127**, (2000) 485.
2. R.K. Wallace and S.E. Woosley, Ap. J. Suppl. **45**, (1981) 389.
3. H. Schatz, L. Bildsten, A. Cumming, and M. Wiescher, Ap. J. **524**, (1999) 1014.
4. H. Schatz, J. Görres, H. Herndl, N.I. Kaloskamis, E. Stech, P. Tischhauser, M. Wischer, A. Bacher, G.P.A. Berg, T.C. Black, S Choi, C.C. Foster, K. Jiang, and E.J. Stephenson, Phys. Rev. Let. **79**, (1997) 3845.
5. M. Fujiwara, H. Akimune, I. daito, H. Fujimura, Y. Fujita, K. Hatanaka, H. Ikegami, I. Katayama, K. Nagayama, N. Matsuoka, S. Morinobu, T. Noro, M. Yoshimura, H. Sakaguchi, Y. Sakemi, A. Tamii, and M. Yosoi, Nucl. Instrum. Meshodos Phys. Res. A **422**, 484 (1999).
6. T. Wakasa, K. Hatanaka, Y. Fujita, G.P.A. Berg, H. Fujimura, H. Fujita, M. Itoh, J. Kamiya, T. Kawabata, K. Nagayama, T. Noro, H. Sakaguchi, Y. Shimbara, H. Takeda, K. Tamura, H. Ueno, M. Uchida, M. Uraki, and M. Yosoi, Nucl. Instrum. Methods Phys. Res. A **482**, 79 (2002).
7. Y. Fujita, K. Hatanaka, G.P.A. Berg, K. Hosono, N. Matsuoka, S. Morinobu, T. Noro, M. Sato, K. Tamura, and H. Ueno, Nucl. Instrum. Methods Phys. Res. B **126**, 274 (1997).
8. P.M. Endt, Nucl. Phys., **A521**, (1990) 1.
9. A.A. Chen, R. Lewis, K.B. Swartz, D.W. Visser, and P.D. Parker, Phys. Rev. C **63**, 065807 (2001).
10. D.W. Bardayan, J.C. Blackmon, A.E. Champagne, A.K. Dummer, T. Davinson, U. Greife, D. Hill, C.Iliadis, B.A. Johnson, R.L. Kozub, C.S. Lee, M.S. Smith, and P.J. Woods, Phys. Rev. C **65**, 032801 (2002).

THE ^{21}Na$(p,\gamma)^{22}$Mg REACTION FROM $E_{CM} = 200$ TO 850 KEV IN EXPLOSIVE STELLAR EVENTS

S. BISHOP[*], J. M. D'AURIA, A. CHEN[†], D. HUNTER[‡], M. LAMEY, W. LIU AND C. WREDE[§]
Simon Fraser University, Burnaby, British Columbia, Canada

R. E. AZUMA AND J. D. KING
University of Toronto, Toronto, Canada

L. BUCHMANN, D. HUTCHEON, A. M. LAIRD[¶], A. OLIN, D. OTTEWELL AND J. ROGERS
TRIUMF, Vancouver, British Columbia, Canada

M. L. CHATTERJEE
Saha Institute of Nuclear Physics, Calcutta, India

S. ENGEL
Ruhr-Universität, Bochum, Germany

D. GIGLIOTTI AND A. HUSSEIN
University of Northern British Columbia, Prince George, British Columbia, Canada

U. GREIFE AND C. C. JEWETT
Colorado School of Mines, Golden, Colorado, USA

J. JOSÉ
Institut d'Estudis Espacials de Catalunya, CSIC/UPC, Barcelona, Spain

S. KUBONO AND S. MICHIMASA
University of Tokyo, Tokyo, Japan

R. LEWIS AND P. PARKER
Yale University, New Haven, CT, USA

The long-lived radioactive nuclide ^{22}Na ($t_{1/2}$ = 2.6 y) is, in principle, an astronomical observable for understanding the physics processes of oxygen-neon novae. Production and abundance yields of ^{22}Na in these events are dependent to the hitherto unknown rate of the ^{21}Na(p,γ)^{22}Mg reaction. Using a high intensity radioactive ^{21}Na beam at the TRIUMF–ISAC facility, direct measurements of the strengths of six potentially astrophysically important resonances have been made at center of mass energies in the range: E_{cm} = 200 to 850 keV. Reported herein are preliminary results obtained for these strengths and their respective contributions to the ^{21}Na(p,γ)^{22}Mg stellar reaction rate.

1. Introduction

Explosive steller events, such as classical novae and X-ray bursts, are two astrophysical sites wherein the "burning" of heavy elements can proceed by way of successive proton capture on radioactive nuclei. The high temperatures and densities within the burning zones of these events are such that radiative proton capture rates can exceed the competing beta decay rates of the reactant radioactive nuclei. Novae are presently understood to be the result of a thermonuclear runaway (TNR) across the surface of a white dwarf star within a binary star system. The densities and temperatures within the TNR allow proton capture on the seed nuclei comprising the white dwarf surface, resulting in the production of intermediate mass nuclides that are ejected into the interstellar medium (ISM). The mechanism for an X-ray burst event is considered to be essentially that of a novae event, with the important distinction that the underlying progenitor of the explosion is a neutron star. However, material is not ejected into the ISM due to the high escape velocity of neutron stars.

Nova temperatures and densities are such that, given Coulomb barrier constraints, the proton capture reaction flow predominantly occurs along the periphery of the proton-rich side of the valley of stability. With a neutron star as the underlying progenitor for X-ray bursts, burning zone temperatures and densities can be at least an order of magnitude greater than in novae, resulting in a reaction flow occurs further removed from the valley of stability, even merging with the proton drip-line beyond A = 38 [1,2,3]. Figure 1 shows our present understanding of the level scheme

*Present address: Heavy Ion Nuclear Physics Laboratory, RIKEN, Wako, Saitama, Japan, bishop@rarfaxp.riken.jp
†Present address: McMaster University, Hamilton, Ontario, Canada
‡Present address: Langara College, Vancouver, British Columbia, Canada
§present address: Yale University, New Haven, CT. USA
¶Present address: University of York, York, England

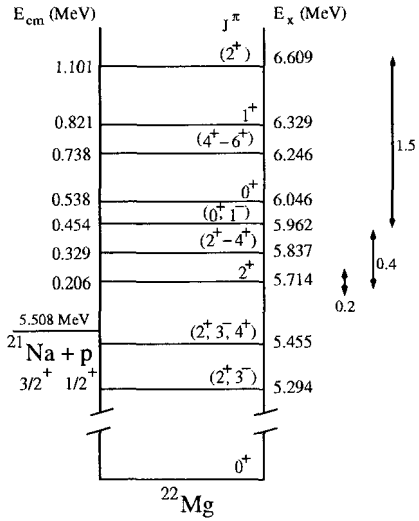

Figure 1. Level scheme of the ^{22}Mg nucleus showing the excitation energies and presumed spin assignments of the states of astrophysical interest. Gamow windows for ^{21}Na + p burning are depicted on the right for some burning temperatures (in GK) typical of ONe novae or X-ray bursts. See text for discussion on the Q-value used.

of ^{22}Mg above the proton threshold [4,5,6,7,8]. In the ^{22}Mg system, three resonances at E_x = 5.714, 5.837, and 5.962 MeV can contribute to the ^{21}Na(p,γ)^{22}Mg reaction rate at oxygen-neon novae temperatures ($T \leq 0.5\times 10^9$ K), as shown in figure 1 by the Gamow windows. Within oxygen-neon nova, production of the astronomical observable ^{22}Na is sensitive to the resonant reaction rate, and thus, to the strengths of these three resonances.

Resonances in ^{22}Mg at E_x = 6.046, 6.248, and 6.323 MeV, in addition to the aforementioned state at 5.962 MeV, can contribute to the ^{21}Na(p,γ)^{22}Mg rate for X-ray burst events, as indicated by the Gamow window in figure 1. Detailed X-ray burst calculations [3,9] indicate that ^{21}Na(p,γ)^{22}Mg is the predominant nuclear path from the CNO cycle through the NeNa mass region and beyond, stressing the role of this reaction in the evolution of an X-ray burst.

Reported herein are the experimental measurements of resonance strength for the six aforementioned resonances. These resonance strengths have been determined from the thick target yield measurements using the DRAGON facility at TRIUMF–ISAC. From these measurements, the respective contributions of these resonances to the resonant stellar

^{21}Na$(p,\gamma)^{22}$Mg reaction rate are determined.

2. Resonant Stellar Reaction Rate and Yield

The resonant stellar reaction rate per particle pair for a narrow resonance, in units of cm^3 s^{-1} mol^{-1}, is given by [10],

$$N_{\rm A}\langle\sigma v\rangle = 1.54 \times 10^{11}(\mu T_9)^{-3/2}\omega\gamma \, \exp\left(-11.605\frac{E_{\rm R}}{T_9}\right) , \qquad (1)$$

with $N_{\rm A}$ Avogadro's number; μ the reduced mass, in amu, of the compound system; T_9 the temperature in units of GK; $\langle\sigma v\rangle$ the thermally averaged nuclear cross section; $E_{\rm R}$ the resonance energy, and $\omega\gamma$ the resonance strength. The resonance strength is defined by,

$$\omega\gamma \equiv \frac{2J_{\rm R}+1}{(2J_{\rm p}+1)(2J_{21}+1)}\,\frac{\Gamma_{\rm p}\Gamma_\gamma}{\Gamma} , \qquad (2)$$

with $J_{\rm R}$, $J_{\rm p}$, and J_{21} the spins of the resonance, proton, and ground state of ^{21}Na, respectively, and where $\Gamma_{\rm p}$ and Γ_γ are, respectively, the partial proton and partial gamma widths of the resonance. Lastly, $\Gamma = \Gamma_{\rm p} + \Gamma_\gamma$. Thus, it is seen from Eq. 1 that the resonant stellar reaction rate is directly proportional to the strength of the resonance into which radiative proton capture is occurring. Therefore, a measurement of $\omega\gamma$ for resonances in the compound system, of known energy, provides the resonant stellar reaction rate.

The strengths of narrow ($\Gamma \ll E_{\rm R}$) resonances can be obtained from measurements of thick target yields *viz* [11],

$$Y(\infty) = \frac{\lambda^2}{2}\frac{m_{21}+m_{\rm p}}{m_{\rm p}}\left(\frac{1}{\rho}\frac{dE}{dx}\right)^{-1}\omega\gamma . \qquad (3)$$

Here λ is the de Broglie wavelength of the reduced mass of the compound system, and $dE/\rho dx$ is the density-scaled stopping cross section of ^{21}Na in H_2 gas. Both of these quantities are to be evaluated at the resonance energy. A measurement, therefore, of thick target yield provides the resonance strength when the stopping cross section is known.

3. Experimental Facilities

This reaction study was done at the ISAC radioactive ion beam facility at TRIUMF, located in Vancouver, Canada, using a nominal ^{21}Na beam intensity of $\sim 10^8$ ^{21}Na per second.

The DRAGON (Detector of Recoils And Gammas Of Nuclear reactions) facility, situated in the ISAC experimental hall, consists of four main components: a differentially pumped, recirculating, windowless hydrogen gas target; a BGO γ-detector array; an electromagnetic mass separator (EMS); and a final focus heavy ion detector system. It has been designed to measure heavy ion radiative proton capture reactions at sub-Coulomb barrier energies in inverse kinematics.

The DRAGON gas target consists of an aluminum target box in which is housed a windowless target cell, with an effective gas column length of 11.2 ± 0.2 cm. Situated on the downstream side of the target cell, a silicon detector positioned at 30° to the beam axis, continuously detected elastically scattered protons as a means to determine the integrated beam on target for each experimental run. Surrounding the gas target box is a γ-detector array comprised of 30 BGO crystals in a tightly packed geometry. The array covers approximately 90% of 4π solid angle, as viewed from the center of the gas cell. The array detects and records the energy of γ-rays above a pre-selected hardware energy threshold of 2 MeV. The detection of a γ-ray with energy above this energy threshold "gates-on" a TDC module whose gate width was set approximately times the nominal time of flight of ^{22}Mg recoils from the gas target to the final focal plane. The stop signal for this TDC was either provided by the closure of its gate, or by a "stop signal" created by the arrival of a heavy ion in the final focal plane detector. Data from this experiment were therefore acquired in two modes: coincidence mode, via time of flight coincidence between the γ-detector array and the final focal plane detector, or singles mode, whereby ^{22}Mg fusion recoils are observed in the data of the final focal plane detector without the detection of a corresponding reaction γ-ray. Further details on the design of the facility can be found elsewhere [12], as can information detailing the experimental method [13].

Following the gas target is a double–stage electromagnetic mass separator (EMS), 21 m in length from the center of the target cell to the location of the final focal plane detector. Each stage consists of a magnetic dipole bender and an electrostatic dipole bender. Fusion recoil and beam particles exit the gas target populate a distribution of charge states caused by electronic charge exchange collisions with the hydrogen molecules. In the first stage of the separator, a momentum dispersed focus downstream of the first magnetic dipole (MD1) allowed passage of both beam and recoil ions of a *known* charge state through the remainder of the separator. The charge state chosen was the one for the fusion recoil, ^{22}Mg, of highest prob-

ability at the particular energy of the reaction. Recoils and beam particles of charge states different from the selected charge state had their transmission blocked by a combination of vertical and horizontal slits. The charge state selection was based on results from previous charge state studies [14,15]. The known charge state and momentum of the ^{22}Mg recoils permits proper selection of fields for the transmission optics and benders in the remainder of the EMS. A final focal plane double sided silicon strip detector (DSSSD) at the end of DRAGON was employed to detect and measure the energy of the heavy ion particles.

4. Data and Results

Results for the measured resonance strengths for the first six states above proton threshold in ^{22}Mg (figure 1) are summarized below. All results, with the exception of that 206 keV resonance data, are preliminary.

4.1. *206 keV Resonance*

Details on the results of the resonance strength measurement of this state can be found elsewhere [16,13]. On the basis of a thick target yield curve (Fig. 4 of Bishop *et al.* [16]), the energy of this resonance was found to be at 205.7 ± 0.5 keV, not 212 keV previously implied by the literature. This new resonance energy implies a new proton threshold [16] for ^{21}Na$(p,\gamma)^{22}$Mg , as shown in figure 1. An efficiency corrected thick target yield of $(5.76 \pm 0.88) \times 10^{-12}$ was obtained for this resonance and the ^{21}Na stopping cross section in H_2 gas was measured to be $(8.18 \pm 0.41) \times 10^{-14}$ eV $\cdot$ cm^2/atom; implying, by equation 3, a strength $\omega\gamma = 1.03 \pm 0.16_{\rm stat} \pm 0.14_{\rm sys}$ meV [16,13].

4.2. *329 keV Resonance*

No ^{22}Mg heavy ion events were observed in coincidence with the expected γ-rays [17] from the decay of this state. The study employed a ^{21}Na beam with an energy of 360 keV/u and a nominal gas target pressure of 8 Torr. Energy loss through the gas target was such that the reaction location would have been within $\approx$ 1 cm of the gas target centre, where the γ-array efficiency is highest. Figure 2 shows the coincidence γ-ray energy versus ^{22}Mg heavy ion time of flight (TOF) through the 21 m long DRAGON mass separator. The box indicates the expected TOF for ^{22}Mg; no events are observed. An upper limit on the strength of this state has been determined to be $\omega\gamma \leq 0.29$ meV [13].

4.3. *454 keV Resonance*

This resonance was observed in a series of runs at a ^{21}Na beam energy of 490 keV/u and a nominal gas target pressure of 8 Torr. Figure 3 shows coincidence data of ^{22}Mg heavy ion TOF versus ^{22}Mg heavy ion energy. The region enclosed by the dashed box denotes heavy ion events clustered around a specific TOF. There are 19 heavy ion events in total, but a wider cut energy in the region of accidental coincidences gave an estimate that 6 of the 19 events should be accidental. The beam on target was determined to be 4.9×10^{13} giving an efficiency corrected thick target yield of 1.4×10^{-12} and a strength $\omega\gamma = 0.70 \pm 0.19_{\text{stat}}$ meV.

4.4. *538 and 740 keV Resonances*

Data for both of these resonances were analyzed in singles mode, as mass separation with DRAGON at these energies was sufficient to isolate fusion recoil events from the background ^{21}Na events. Figure 4 shows singles heavy ion events, as recorded by the DSSSD detector at the final focal plane of DRAGON, for the reaction study of the 530 keV resonance in ^{22}Mg. Three gas target pressures were chosen in the study of this resonance: 4.8, 7.6 and 8.1 Torr. A beam energy of 570.2 keV/u was chosen. The region

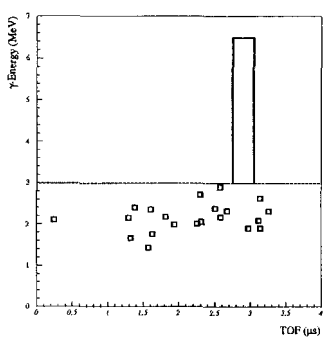

Figure 2. Coincidence spectrum of coincident γ-ray versus ^{22}Mg heavy ion time of flight of all experimental runs for the ^{22}Mg resonance at $E_{\text{R}} = 329$ keV. No yield is observed.

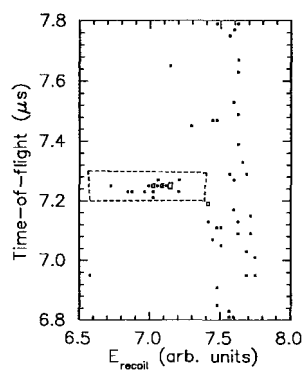

Figure 3. Coincident ^{22}Mg heavy ion energy versus time of flight of all experimental runs for the ^{22}Mg resonance at $E_{\text{R}} = 454$ keV.

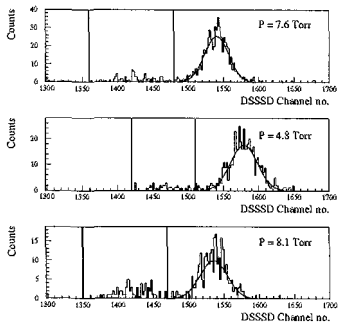

Figure 4. DSSSD singles data for the ^{22}Mg resonance level at $E_{\mathrm{R}} = 538$ keV. The top panel shows the ^{22}Mg heavy ion energy distribution (between vertical lines) for runs taken at a target pressure of 7.6 Torr, $E_{\mathrm{beam}} = 570$ keV/u. The "leaky beam" peak, with Gaussian fit, is also shown. Similarly for the central and bottom panel, with respective target pressure shown.

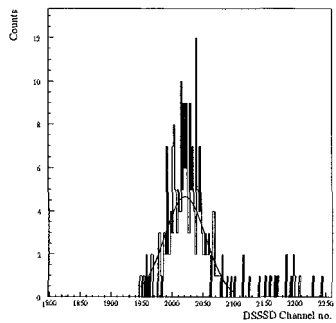

Figure 5. DSSD ^{22}Mg heavy ion singles data for the ^{22}Mg resonance level at $E_{\mathrm{R}} = 740$ keV. The prominent peak, with Gaussian fit, is comprised of ^{22}Mg events. The few events above channel 2100 are ^{21}Na background beam events.

bounded by the vertical lines in each panel of figure 4 denotes the ^{22}Mg recoil events; the events fitted by the Gaussian curves are background ^{21}Na beam particles. The total number of ^{22}Mg heavy ion events is 183 with at total ^{21}Na beam on target of $(2.79 \pm 0.30) \times 10^{13}$. The stopping cross section was measured to be $(9.06 \pm 0.44) \times 10^{-14}$ eV $\cdot$ cm^2/atom. The efficiency corrected yield for this resonance is $(2.19 \pm 0.15) \times 10^{-11}$, implying a strength $\omega\gamma = 11.5 \pm 0.8$ meV.

Recoil data for the ^{22}Mg resonance at 740 keV were taken with a beam energy of 774.7 keV/u and a gas target pressure of 7.8 Torr. Shown in figure 5 are the ^{22}Mg heavy ion energy spectrum from the DSSSD. The region fitted by the Gaussian contains the ^{22}Mg recoil events: a total of 216 ^{22}Mg events were measured for a total beam on target of $(1.67 \pm 0.07) \times 10^{12}$. The stopping cross section at this energy was measured to be $8.74 \pm 0.39 \times 10^{-14}$ eV $\cdot$ cm^2/atom. The efficiency corrected thick target yield is $(3.18 \pm 0.21) \times 10^{-10}$ resulting in a strength for this state of $\omega\gamma = (2.19 \pm 0.15) \times 10^2$ meV.

4.5. *820 keV Resonance*

Yield data for this resonance was taken at ^{21}Na beam energies 20 keV above and below the resonance energy. At these beam energies, complete ^{21}Na mass separation occurred, allowing singles data mode yield analysis. The measured yield curve of this broad resonance is shown in figure 6 along with a least squares fit of a thick target yield curve to the data [13]. The extracted width and strength for this resonance, as determined by the fit, were $\Gamma = 16.1 \pm 2.8$ keV and $\omega\gamma = 555.7 \pm 76.7$ meV.

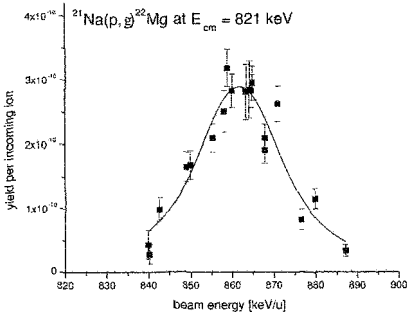

Figure 6. Thick target yield data for the ^{22}Mg resonance level at $E_R = 820$ keV. The curve is a least squares fit to the data.

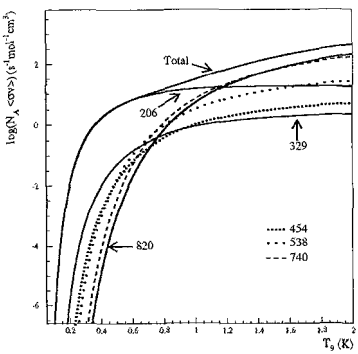

Figure 7. Total resonant stellar reaction rate for ^{21}Na(p,γ)^{22}Mg , along with the component rates.

5. Conclusion

Figure 7 shows the result of our direct ^{22}Mg resonance strength measurements. It is evident from the figure that, for nova temperatures, only the ^{22}Mg state at $E_R = 205.7$ keV contributes, whereas the states at 329 and 454 keV are negligible across the entire temperature range of novae and X-ray bursts. The resonances at 740 and 820 keV can be seen to contribute almost equally to X-ray burst events. Further details on the implications of these results can be found in other papers [16,13].

References

1. A. E. Champagne and M. Wiescher, *Annu. Rev. Nucl. Part Sci.* **42**, 39 (1992).

2. F. Käppler, F. K. Thielemann, and M. Wiescher, *Annu. Rev. Nucl. Part. Sci.* **48**, 175 (1998).
3. H. Schatz et al., *Astrophys. J.* **524**, 1014 (1999).
4. N. Bateman et al., *Phys. Rev. C* **63**, 035803 (2001).
5. S. Michimasa et al., *Eur. Phys. J. A* **14**, 275 (2002).
6. J. A. Caggiano et al., *Phys. Rev. C* **66**, 15804 (2002).
7. A. A. Chen et al., *Phys. Rev. C* **63**, 065807 (2001).
8. P. Endt, *Nucl. Phys.* **521**, 1 (1990)
9. H. Schatz et al., *Phys. Rev. Lett.* **86**, 3471 (2001).
10. W. A. Fowler, G. R. Caughlan and B. A. Zimmerman, *Ann. Rev. Astron. Astrophys.* **5**, 525 (1967).
11. W. A. Fowler, C. C. Lauritsen and T. Lauritsen *Rev. Mod. Phys.* **20**, 236 (1948).
12. D. A. Hutcheon et al., *Nucl. Inst. & Meth. In Phys. Res. A* **498**, 190 (2003).
13. J. M. D'Auria et al., *Phys. Rev. C* (2004): to be submitted.
14. W. Liu, Master's thesis, Simon Fraser University, Burnaby, BC, Canada (2001), URL: http://www.triumf.ca/dragon/docs/wenjiethesis.pdf.
15. W. Liu et al., *Nucl. Inst. & Meth. In Phys. Res. A* **496**, 198 (2003)
16. S. Bishop et al., *Phys. Rev. Lett.* **90**, 162501 (2003).
17. C. E. Rolfs et al., *Nucl. Phys.* **191**, 209 (1972).

VII. Nuclear Equation of State and Neutron Stars

This page intentionally left blank

NEUTRON STAR MATTER WITH IN-MEDIUM MESON MASS

C. H. HYUN, M. H. KIM, S. W. HONG
Department of Physics and Institute of Basic Science, Sungkyunkwan University, Suwon 440-746, Korea

B. K. JENNINGS
TRIUMF, 4004 Wesbrook Mall, Vancouver, British Columbia, Canada V6T 2A3

We investigate the properties of the neutron star matter with the relativistic mean field models. We incorporate in quantum hadrodynamics and quark-meson coupling models a possible reduction of meson masses in nuclear matter. The equation of state for neutron star matter is calculated at the matter densities up to 4 times the nuclear saturation density. We find that the equation of state and the composition of the matter are sensitive to the behavior of meson masses in medium.

1. Introduction

The state of matter at extremely hot or dense condition is one of the most fundamental questions in physics. Terrestrial nuclei of heavy elements provide a glimpse at such extreme states but there are far-more-extreme states in our universe. Neutron star, which is a huge nucleus, is one example of such an extreme state of matter. The state of matter can be characterized by the equation of state (EoS). From the microscopic point of view the EoS is determined by how the constituent particles of the matter interact. For nuclei or the neutron star, constituent particles are the nucleons and they interact through meson exchanges. Therefore the state of matter at extreme conditions can be understood when we have enough knowledge about the properties of the nucleon and the mesons and how they interact.

In the early 90's, Brown and Rho argued the scaling of hadron masses in dense medium in terms of the scale invariance of the effective lagrangian [1]. They showed that the ratios of the in-medium masses of the nucleon, $\sigma-$, $\omega-$ and $\rho-$mesons to their respective masses in free space are approximately equal to each other at around the nuclear saturation density. Afterwards, variation of the hadron masses in medium was calculated in the framework

of QCD-sum rule [2] and the quark-meson-coupling (QMC) model [3]. In Refs. 2 and 3, masses of ρ and ω mesons were calculated at the nuclear saturation density ρ_0, and similar amount of mass reduction from the free mass, $m^*_{\rho,\omega}/m_{\rho,\omega} \simeq 0.8$ was predicted. Experimentally, microscopic properties of hadrons as well as the state of matter at hot or dense environment have been investigated in the relativistic heavy-ion collisions. Indications of possible meson mass reduction in the nuclear matter were reported through the dileptonic decay of ρ and ω mesons in the CERES/NA45 [4] and KEK-PS E325 [5] experiments.

Motivated by these previous theoretical and experimental studies, in this work we take into account the reduction of meson masses in the nuclear models such as quantum hadrodynamics (QHD) and QMC, and we will apply these models to the neutron star matter. The models are calibrated to the bulk properties of nuclear matter at the saturation density, such as saturation density ρ_0 ($= 0.17$ fm^3), binding energy E_B ($= 16.0$ MeV), symmetry energy $a_{\rm sym}$ ($= 32.5$ MeV) and compression modulus K ($200 \sim 300$ MeV). We take into account the effect of meson mass changes in the following ways. First, we use the meson mass in free space without any medium modification as usually done in most works. Secondly, we adopt the Brown-Rho (BR) scaling law [1],

$$\frac{m^*_N}{m_N} \simeq \frac{m^*_\sigma}{m_\sigma} \simeq \frac{m^*_\omega}{m_\omega} \simeq \frac{m^*_\rho}{m_\rho} \tag{1}$$

and assume that the scaling can be expressed by a simple function of density. The models that incorporate the BR scaling are denoted by the abbreviation "BR". Thirdly, we consider the QMC type models and treat the heavy mesons (ρ and ω) as meson bags (denoted by "MB") composed of a quark and an anti-quark [6]. In these cases, the mass of heavy mesons are calculated self-consistently within the framework of the QMC. We apply these different models for nuclear matter to the neutron star matter and see how the reduction of meson masses in matter may influence the EoS of the neutron star matter.

In Sec. 2, we briefly describe the models and show the parameters of the models and the resultant properties of nuclear matter at the saturation density. In Sec. 3, we apply the various models fixed in Sec. 2 to the neutron star matter, show the results of the calculations and discuss the implications to the properties of the neutron star. Conclusions are drawn in Sec. 4.

2. Models for Nuclear Matter and the Parameters

In this work we will consider 5 different models. We refer to them as QHD, QHD-BR; MQMC, MQMC-BR and MQMC-MB. The parameters for each model will be determined to produce known saturation properties ρ_0 and E_B. The symmetry energy $a_{\rm sym}$ is used in determining the $\rho - N$ coupling constant $g_{\rho N}$ at the saturation density.

2.1. *QHD*

The lagrangian for QHD in the mean field approximation reads

$$\begin{aligned} L^{\rm MF}_{\rm QHD} = \bar{\psi}_N[i\gamma^\mu\partial_\mu - (m_N - g_{\sigma N}\,\bar{\sigma}) - g_{\omega N}\,\gamma^0\,\bar{\omega}_0 - \frac{1}{2}\,g_{\rho N}\,\gamma^0\,\bar{b}_{03}\,\tau_3]\psi_N \\ -\frac{1}{2}m_\sigma^2\,\bar{\sigma}^2 - \frac{1}{3}m_N\,b\,(g_{\sigma N}\,\bar{\sigma})^3 - \frac{1}{4}c\,(g_{\sigma N}\,\bar{\sigma})^4 \\ +\frac{1}{2}m_\omega^2\,\bar{\omega}_0^2 + \frac{1}{2}m_\rho^2\,\bar{b}_{03}^2. \end{aligned} \tag{2}$$

The masses m_N, m_σ, m_ω and m_ρ refer to the values in free space, 939, 550, 783 and 770 MeV, respectively. The effective mass of the nucleon is defined as

$$m_N^*(\text{QHD}) \equiv m_N - g_{\sigma N}\,\bar{\sigma}. \tag{3}$$

The meson fields are determined from the equations of motion in the mean field approximation ;

$$\bar{\sigma} = \frac{g_{\sigma N}}{m_\sigma^2}\,\rho_s - \frac{m_N}{m_\sigma^2}\,b\,g_{\sigma N}^3\,\bar{\sigma}^2 - \frac{1}{m_\sigma^2}\,c\,g_{\sigma N}^4\,\bar{\sigma}^3, \tag{4}$$

$$\bar{\omega}_0 = \frac{g_{\omega N}}{m_\omega^2}\,\frac{1}{3\pi^2}\sum_{N=n,p} k_N^3 = \frac{g_{\omega N}}{m_\omega^2}\,\rho, \tag{5}$$

$$\bar{b}_{03} = \frac{g_{\rho N}}{m_\rho^2}\,\frac{1}{3\pi^2}\sum_{N=n,p} I_{N3}k_N^3 = \frac{1}{2}\,\frac{g_{\rho N}}{m_\rho^2}\,(\rho_p - \rho_n) \tag{6}$$

where I_{N3} is 1/2 (-1/2) for the proton (neutron).

$$\rho_s = \frac{1}{\pi^2}\sum_{N=n,p}\int_0^{k_N} \frac{m_N^*}{\sqrt{k^2 + m_N^{*2}}}\,k^2\,dk \tag{7}$$

is the scalar density and k_N is the Fermi momentum of the nucleon at a given density.

2.2. *QHD-BR*

We now consider the meson mass changes in matter and adopt the model proposed in Ref. 7 where the BR-scaling law is incorporated in the original QHD. The model lagrangian reads

$$L^{\rm MF}_{\rm QHD-BR} = \bar{\psi}_N[i\gamma^\mu\partial_\mu - (M^*_N - g_{\sigma N}\,\bar{\sigma}) - g^*_{\omega N}\,\gamma^0\,\bar{\omega}_0 - \frac{1}{2}g_{\rho N}\,\gamma^0\,\bar{b}_{03}\,\tau_3]\psi_N$$
$$-\frac{1}{2}m^{*2}_\sigma\,\bar{\sigma}^2 + \frac{1}{2}m^{*2}_\omega\,\bar{\omega}^2_0 + \frac{1}{2}m^{*2}_\rho\,\bar{b}^2_{03}. \tag{8}$$

The BR-scaling law is parametrized as [7]

$$\frac{M^*_N}{m_N} = \frac{m^*_\sigma}{m_\sigma} = \frac{m^*_\omega}{m_\omega} = \frac{m^*_\rho}{m_\rho} = \left(1 + y\frac{\rho}{\rho_0}\right)^{-1}. \tag{9}$$

The effective mass of the nucleon is defined as

$$m^*_N(\text{QHD-BR}) = M^*_N - g_{\sigma N}\,\bar{\sigma}. \tag{10}$$

(Note the use of M^*_N in place of m_N of Eq. (3).) In Ref. 7, $g_{\omega N}$ is also assumed to vary with density as $g^*_{\omega N}/g_{\omega N} \simeq m^*_\omega/m_\omega$ at around the saturation density. Then $g^*_{\omega N}$ scaling is expressed as

$$\frac{g^*_{\omega N}}{g_{\omega N}} = \left(1 + z\frac{\rho}{\rho_0}\right)^{-1}. \tag{11}$$

The parameters for the QHD and QHD-BR models and the resulting properties at the saturation are summarized in Tab. 1.

Table 1. Parameters and the saturation properties for the QHD and QHD-BR models. The subscript M for m^*_M/m_M refers to σ, ω and ρ mesons.

Model	$g_{\sigma N}$	$g_{\omega N}$	$g_{\rho N}$	$b\times 100$	$c\times 100$	y	z	m^*_N/m_N	m^*_M/m_M	K
QHD	8.11	8.36	7.85	0.3478	1.328	·	·	0.773	1.0	310.8
QHD-BR	5.38	15.38	6.33	·	·	0.28	0.31	0.667	0.781	264.5

2.3. *MQMC*

In the QMC model, interactions between the nucleons (bags) are mediated by the exchange of mesons which couple with the quarks that constitute the bags [8]. The mean field lagrangian for non-overlapping spherical bags in dense matter can be written as

$$L^{\rm MF}_{\rm QMC} = \bar{\psi}_q[i\gamma^\mu\partial_\mu - (m^0_q - g^q_\sigma\,\bar{\sigma}) - g^q_\omega\,\gamma^0\,\bar{\omega}_0 - \frac{1}{2}g^q_\rho\,\gamma^0\,\bar{b}_{03}\,\tau_3 - B] \times \theta_V(R-r)\psi_q$$
$$-\frac{1}{2}m^2_\sigma\,\bar{\sigma}^2 + \frac{1}{2}m^2_\omega\,\bar{\omega}^2_0 + \frac{1}{2}m^2_\rho\,\bar{b}^2_{03}, \tag{12}$$

where $q = u,\ d$ since only nucleons are considered in this work. The effective mass of the nucleon in the QMC is given by

$$m_N^*(\mathrm{QMC}) = \sqrt{\left(E_{bag}^N\right)^2 - \sum_q \frac{x_q^2}{R^2}}, \tag{13}$$

$$E_{bag}^N = \sum_q \frac{\Omega_q}{R} - \frac{Z_N}{R} + \frac{4}{3}\pi R^3 B_0, \tag{14}$$

$$\Omega_q = \sqrt{x_q^2 + R^2 m_q^{*2}}, \quad (m_q^* = m_q^0 - g_\sigma^q \bar{\sigma}). \tag{15}$$

x_q is the eigen energy of the quarks in the bag determined by the boundary conditions at $r = R$. Z_N is a phenomenological constant that incorporates the effects not explicitly taken into account, including zero-point motion.

It is well known that the scalar and the vector potentials obtained from the QMC model are much smaller than those from the QHD. As a result, the spin-orbit potential becomes too weak to explain the spin-orbit splittings in finite nuclei and the spin observables in nucleon-nucleus scattering. To circumvent these shortcomings, a density dependent bag constant was introduced [9]. The QMC model with a density dependent bag constant is called the modified QMC (MQMC) model. We adopt the direct coupling model of Ref. 9 where the bag constant reads

$$B = B_0 \left(1 - g_\sigma^B \frac{4}{\delta} \frac{\bar{\sigma}}{m_N}\right)^\delta. \tag{16}$$

$\bar{\sigma}$ value is determined from the self-consistency condition (SCC)

$$\bar{\sigma} = 3 \frac{g_\sigma^q}{m_\sigma^2} \rho_s \left[C_N(\bar{\sigma}) + \frac{g_\sigma^B}{g_\sigma^q} \frac{E_{bag}^N}{m_N^*} \frac{16\pi}{9} R^3 \frac{B}{m_N} \left(1 - \frac{4}{\delta} \frac{g_\sigma^B \bar{\sigma}}{m_N}\right)^{-1} \right] \tag{17}$$

where

$$C_N(\bar{\sigma}) = \frac{E_{bag}^N}{m_N^*} \left[\left(1 - \frac{\Omega_q}{E_{bag}^N R}\right) S(\bar{\sigma}) + \frac{m_q^*}{E_{bag}^N} \right] \tag{18}$$

and

$$S(\bar{\sigma}) = \frac{\Omega_q/2 + R\, m_q^* (\Omega_q - 1)}{\Omega_q (\Omega_q - 1) + R\, m_q^*/2}. \tag{19}$$

B_0 and Z_N are fitted to reproduce the free nucleon mass with the stability condition

$$\left.\frac{\partial\, m_N^*}{\partial\, R}\right|_{R=R_0} = 0 \tag{20}$$

Table 2. Parameters and the saturation properties from MQMC-type models. The subscript M denotes σ, ω and ρ mesons for MQMC-BR. For MQMC-MB, M refers to ω and ρ mesons.

Model	g_σ^q	g_ω^q	g_σ^B	g_ρ^q	y	m_N^*/m_N	m_M^*/m_M	K
MQMC	1.0	2.71	6.81	7.89	·	0.783	1.0	285.5
MQMC-BR	1.0	2.31	5.51	6.09	0.28	0.758	0.781	591.5
MQMC-MB	1.0	1.77	5.44	8.15	·	0.852	0.861	324.1

where m_N^* is evaluated by Eq. (13) but with B_0 replaced by B. We choose $R_0 = 0.6$ fm and obtain $B_0^{1/4} = 188.1$ MeV and $Z_N = 2.030$. g_σ^B and δ, g_σ^q and g_ω^q are adjusted to produce saturation properties and reasonable values of K and m_N^*. g_ρ^q is fitted for the symmetry energy to be reproduced.

2.4. *MQMC-BR*

We now incorporate the BR-scaling law in the MQMC model (hence, the name MQMC-BR). Meson masses are assumed to satisfy

$$\frac{m_\sigma^*}{m_\sigma} = \frac{m_\omega^*}{m_\omega} = \frac{m_\rho^*}{m_\rho} = \left(1 + y\frac{\rho}{\rho_0}\right)^{-1}. \tag{21}$$

The scaling parameter y is determined to satisfy the BR-scaling law, Eq. (1) with m_N^* given by Eq. (13), which depends on $\bar{\sigma}$. The lagrangian for this model can be obtained by replacing the meson masses in Eq. (12) with the asterisked ones in Eq. (21).

2.5. *MQMC-MB*

Vector mesons may be treated as bags composed of a quark and an anti-quark. In this case, the parameters B_0, R_0 and Z_M ($M = \rho$, ω) for the meson bags can differ depending on the species of mesons, but for simplicity we fix B_0 and R_0 as those values for the nucleon and treat only Z_M as a free parameter for each meson [6]. Then the effective mass of each meson can be written as

$$m_M^* = \sqrt{\left(E_{bag}^M\right)^2 - 2\frac{x_q^2}{R^2}}, \tag{22}$$

$$E_{bag}^M = 2\frac{\Omega_q}{R} - \frac{Z_M}{R} + \frac{4}{3}\pi R^3 B. \tag{23}$$

Z_M is fixed so that m_M^* defined as in Eq. (22) in free space recovers the mass of the free ω and ρ mesons. $Z_\omega = 0.7904$ and $Z_\rho = 0.8154$ are obtained. The lagrangian for the model can be written by replacing the meson masses in Eq. (12) by m_M^* in Eq. (22). The parameters that can produce the saturation at ρ_0 are listed in Tab. 2.

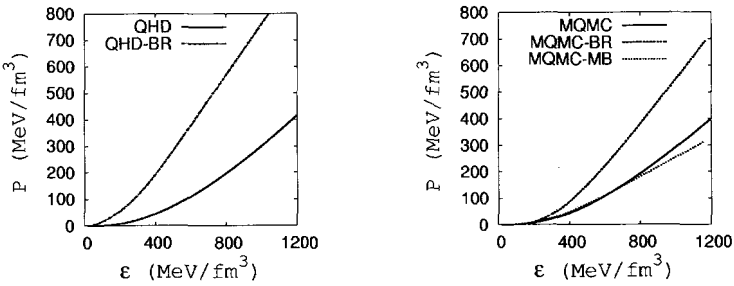

Figure 1. EoS from the 5 different models.

3. Application of the Models to Neutron Star Matter

We now apply the above five models calibrated at the saturation density to the neutron star matter.

3.1. *EoS*

The energy density and the pressure in the QHD model read

$$\varepsilon = \frac{1}{2}m_\sigma^2\,\bar{\sigma}^2 + \frac{1}{3}m_N\,b\,(g_{\sigma N}\,\bar{\sigma})^3 + \frac{1}{4}c\,(g_{\sigma N}\,\bar{\sigma})^4 + \frac{1}{2}m_\omega^2\,\bar{\omega}_0^2 + \frac{1}{2}m_\rho^2\,\bar{b}_{03}^2 + \frac{1}{\pi^2}\sum_{N=n,p}\int_0^{k_N}\sqrt{k^2+m_N^{*2}}\;k^2dk + \frac{1}{\pi^2}\sum_l\int_0^{k_l}\sqrt{k^2+m_l^2}\;k^2dk, \quad (24)$$

$$P = -\frac{1}{2}m_\sigma^2\,\bar{\sigma}^2 - \frac{1}{3}m_N\,b\,(g_{\sigma N}\,\bar{\sigma})^3 - \frac{1}{4}c\,(g_{\sigma N}\,\bar{\sigma})^4 + \frac{1}{2}m_\omega^2\,\bar{\omega}_0^2 + \frac{1}{2}m_\rho^2\,\bar{b}_{03}^2 + \frac{1}{3\pi^2}\sum_{N=n,p}\int_0^{k_N}\frac{k^4}{\sqrt{k^2+m_N^{*2}}}dk + \frac{1}{3\pi^2}\sum_l\int_0^{k_l}\frac{k^4}{\sqrt{k^2+m_l^2}}dk. \quad (25)$$

The energy density and the pressure of the QHD-BR model can be obtained from Eq. (24) and Eq. (25), respectively, by removing the cubic and quartic self-interaction terms of the $\sigma-$meson and replacing the free meson masses with the scaled ones given in Eq. (21). The energy density and the pressure of the MQMC-type models can be obtained by using $g_{\sigma N} = 3g_\sigma^q$, $g_{\omega N} = 3g_\omega^q$ and $g_{\rho N} = g_\rho^q$ together with proper replacement of meson masses in Eqs. (24) and (25). The resulting EoS curves for each model are shown in Fig. 1. If the pressure exerted by nuclear repulsion is strong, the matter becomes more incompressible, which corresponds to a large K value and a stiff EoS. The EoS's of the QHD, MQMC and MQMC-MB models whose K's are

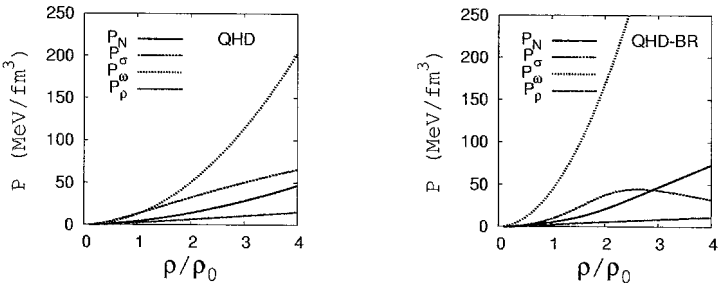

Figure 2. Comparison of the magnitude of σ, ω, ρ and the nucleon contributions to the pressure for the QHD (left) and the QHD-BR (right). Definitions of P_i's are given in the text. Nucleon, σ, ω and ρ contributions are represented by solid, dashed, dotted and dot-dashed lines, respectivley.

close to each other (310.8, 285.5 and 324.1 MeV, respectively) show similar behaviors at the energy densities considered here.

The EoS of the BR scaling models (QHD-BR and MQMC-BR) turns out to be stiffer than the EoS from other models. This behavior can be understood by observing that the repulsive contribution from the $\omega-$meson is augmented at high densities while the attraction caused by the $\sigma-$meson is not strong enough to cancel the repulsion.

In Fig. 2 we compare the magnitude of σ, ω, ρ and N contributions to the pressure P. Each contribution (P_i ; $i = \sigma$, ω, ρ, N) is defined as

$$P_\sigma = \frac{1}{2} m_\sigma^{*2} \bar{\sigma}^2, \quad P_\omega = \frac{1}{2} m_\omega^{*2} \bar{\omega}_0^2, \quad P_\rho = \frac{1}{2} m_\rho^{*2} \bar{b}_{30}^2,$$

$$P_N = \frac{1}{3\pi^2} \sum_{N=n,p} \int_0^{k_N} \frac{k^4}{\sqrt{k^2 + m_N^{*2}}} \, dk.$$

Then the total pressure is

$$P \simeq -P_\sigma + P_\omega + P_\rho + P_N,$$

ignoring the cubic and quartic self-interaction terms of the σ-meson. For the QHD, P_σ is non-negligible compared to P_ω in the density region considered here. Since σ-meson contributes to the pressure negatively, P_σ reduces P substantially for QHD, which leads to a sizable softening of the EoS. On the contrary, P_ω of QHD-BR is about 3 times larger than that of QHD, but P_σ of QHD-BR is more or less similar to that of the QHD. Thus the softening of the EoS by P_σ in QHD-BR is relatively negligible as the density becomes high, and consequently the EoS of QHD-BR is stiffer than that of QHD.

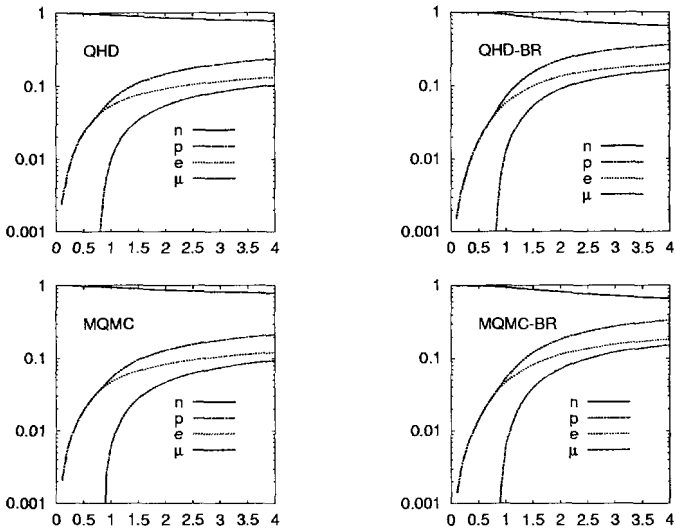

Figure 3. Particle (n, p, e, μ) fractions calculated by different models are plotted against neutron star matter densities. Horizontal axis represents ρ/ρ_0. The figure for MQMC-MB is somewhat similar to that of MQMC and so not included.

3.2. *Composition*

The composition of the neutron star matter is represented by the numbers of particles divided by the total baryon number. The number of each kind of particles is determined by the charge neutrality and chemical equilibrium. The results are shown in Fig. 3. The compositions obtained from the QHD and MQMC models are very similar to each other. The number of the protons is slightly enhanced in the BR models.

4. Conclusion

In this work, we have investigated the properties of the neutron star matter by incorporating the reduction of meson masses in medium. We have explored various models at the hadron and the quark levels. The BR-scaling of mesons in matter is considered for the QHD and MQMC models. MQMC-MB treats the heavy mesons as well as the nucleons consistently in terms of the MIT bag model. The EoS and particle fractions of the models were calculated. The EoS of BR-scaled models are stiffer than that of the models with the constant-meson masses, and the fraction of the proton increases slightly for the BR-scaled models.

Acknowledgements

This work was partially supported by Korea Research Foundation (Grant No. 2002-042-C00014).

References

1. G. E. Brown and M. Rho, Phys. Rev. Lett. **66** (1991) 2720.
2. T. Hatsuda and S. H. Lee, Phys. Rev. **C 46** (1992) R34.
3. K. Saito, K. Tsushima and A. W. Thomas, Phys. Rev. **C 55** (1997) 2637.
4. G. Agakichiev *et al.*, Phys. Lett. **B 422** (1998) 405.
5. K. Ozawa *et al.*, Phys. Rev. Lett. **86** (2001) 5019.
6. K. Saito and A. W. Thomas, Phys. Rev. **C 51** (1995) 2757.
7. C. Song, G. E. Brown, D.-P. Min and M. Rho, Phys. Rev. **C 56** (1997) 2244.
8. P. A. M. Guichon, Phys. Lett. **B 200** (1988) 235.
9. X. Jin and B. K. Jennings, Phys. Rev. **C 54** (1996) 1427.

SCREENING EFFECT IN QUARK-HADRON MIXED PHASE

T. TATSUMI

Department of Physics, Kyoto University,
Kyoto 606-8502, Japan
E-mail: tatsumi@ruby.scphys.kyoto-u.ac.jp

D. N. VOSKRESENSKY

Moscow Institute for Physics and Engineering,
Kashirskoe sh. 31, Moscow 115409, Russia

Possibility of the structured mixed phases at first order phase transitions in neutron stars is reexamined by taking into account the charge screening effect. The Maxwell construction is shown to be not conflicted with the Gibbs conditions once the Coulomb potential is properly taken into account. Taking the hadron-quark deconfinement transition as an example, we explicitly demonstrate a mechanical instability of the geometrical structure of the structured mixed phase by the charge screening effect. In this case we have effectively the picture given by the Maxwell construction.

1. Introduction

It is now commonly accepted that various phase transitions may occur in compact star interiors or during the gravitational collapse from progenitor stars. Possibilities of the meson (pion and kaon) condensations and the hadron-quark deconfinement transition at high-density matter or the liquid - gas transition at subnuclear density have been studied by many authors. These phase transitions may have some implications to compact star phenomena, and it has been expected that recent progress in observations might reveal such new forms of matter.

Such phase transitions are of the first order in most cases and the Maxwell construction has been applied to get the equation of state (EOS) in phase equilibrium; there appears a separation of spatially bulk phases in the mixed-phase with the equal pressure. Glendenning demonstrated a possibility of the structured mixed phases (SMP) in such systems by invoking the proper treatment based on the Gibbs conditions [1], where the charge

density as well as the baryon-number density are inhomogeneous. Subsequently, many authors have demonstrated energetic preference of SMP and its existence in a wide density region, disregarding effects of inhomogeneity of the particle configurations and/or the electric field [2]. The geometrical structure of SMP looks like droplets, rods or slabs as in the nuclear pasta phase [3,4].

The Gibbs conditions require the pressure balance and the equality of the chemical potentials between two phases, denoted by I and II, for phase equilibrium [5]. [a] For a multi-component system with more than one chemical potential, as is common in neutron-star matter, we must impose the equality condition for each chemical potential in order to fulfill the condition of the physico-chemical equilibrium. More definitely, we, hereafter, consider the charge chemical potential (μ_Q) and the baryon-number chemical potential (μ_B) respecting two conservation laws in neutron-star matter: $\mu_Q^I = \mu_Q^{II}$ and $\mu_B^I = \mu_B^{II}$. On the other hand, the first condition is not fulfilled in the Maxwell construction, since the *local* charge neutrality is implicitly imposed, while only the *global* charge neutrality must be satisfied. When we naively apply the Gibbs conditions instead of the Maxwell construction, we can see that there appears SMP in a wide density region and there is no constant-pressure region in EOS.

SMP, if exists, may have phenomenological implications on compact stars through e.g., glitches, neutrino opacity, gamma-ray burst or mass of hybrid stars.

In this talk we address a controversial issue about the relevance of SMP, by taking the hadron-quark deconfinement transition as an example [6]. We shall see that the Debye screening effects greatly modify the mechanical stability of SMP. In the absence of SMP we effectively recover the picture of phase equilibrium given by the Maxwell construction where two bulk phases are separated without spoiling the Gibbs conditions.

2. Bulk calculations and finite-size effects

Consider SMP consisting of two phases I and II, where we assume spherical droplets of phase I with the radius R to be embedded in the matter of phase II and two phases are clearly separated by sharp boundaries. We divide the whole space into the equivalent Wigner-Seitz cells with the radius R_W (see Fig.1). The volume of the cell is $V_W = 4\pi R_W^3/3$ and that of the droplet is $V = 4\pi R^3/3$.

[a] We consider here matter at zero temperature

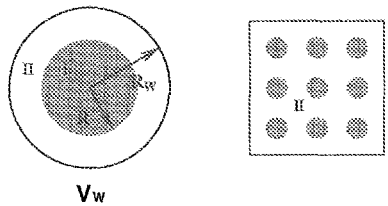

Figure 1. Equal droplets of the phase I embedded in the phase II (right panel), and the geometrical structure of the Wigner-Seitz cell (left panel)

A bulk calculation proceeds as follows [3]. For a given volume fraction factor $f = (R/R_W)^3$, the total energy E may be written as the sum of the volume energy E_V, the Coulomb energy E_C and the surface energy E_S,

$$E = E_V + E_C + E_S. \tag{1}$$

We further assume, for simplicity, that baryon number (ρ_B^α) and charge (ρ_Q^α) densities are uniform in each phase α, $\alpha = I, II$. Then, E_V can be written as $E_V/V_W = f\epsilon^I(\rho_B^I) + (1-f)\epsilon^{II}(\rho_B^{II})$ in terms of the energy densities ϵ^α, $\alpha = I, II$. The surface energy E_S may be represented as $E_S/V_W = f \times 4\pi\sigma/R$ in terms of the surface tension σ. The Coulomb energy E_C is given by

$$E_C/V_W = f \times \frac{16\pi^2}{15}\left(\rho_Q^I - \rho_Q^{II}\right)^2 R^2. \tag{2}$$

The optimal value of R_D is determined by the minimum condition,

$$\left.\frac{\partial(E/V_W)}{\partial R}\right|_f = 0, \tag{3}$$

for a given f (see Fig. 2). Since E_V does not depend on R, we can *always* find a minimum as a result of the competition between the Coulomb and the surface energies, satisfying the well-known relation, $E_S = 2E_C$.

However, such bulk calculations have been proved to be too crude for the discussions of SMP. Instead, a careful consideration of the interface of two phases is required. As a defect of the bulk calculations they ignore the *finite size effects*. In particular, they have the inconsistent treatment of the Coulomb potential; they do not use the Poisson equation, so that the charge density profiles are assumed ab initio to be constants and the Coulomb potential is assumed to be $1/r$. If one properly solves the Poisson equation, one should have the screening effect as a result of the rearrangement of the

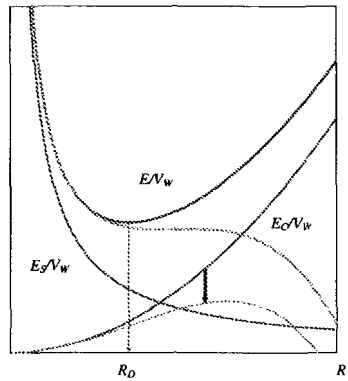

Figure 2. Schematic view of the total energy and each contribution in the bulk calculations (solid curves). Screening effect reduces the Coulomb energy, shown by the thick arrow.

charge-density distribution. Hence, the radius R_D should be not too large, compared with the Debye screening length $\lambda_D^{-2} = \sum_i (\lambda_D^i)^{-2}$,

$$1/\lambda_D^{i2} = 4\pi Q_i \frac{\partial \rho_{ch}}{\partial \mu_i}, \tag{4}$$

in order the above treatment to be justified, the suffix i runs over the particle species. Otherwise, the Coulomb energy is reduced by the screening effect, which should lead to a *mechanical instability* of SMP in some cases (Fig. 2). In the case of the hadron-quark deconfinement transition, $\lambda_D^q \simeq$ 5fm and λ_D^p, λ_D^e are of the same order as λ_D^q, for a typical density with $\mu_B \simeq 1$GeV. We shall see in the following that R_D is typically of the same order as $\lambda_D \sim \lambda_D^q$, and the mechanical stability of the droplet is much affected by the screening effect.

3. Mechanical instability of the geometrical structure of SMP

3.1. *Thermodynamic potential for hadron - quark deconfinement transition*

In the following we consider thermodynamics for non-uniform systems. The situation is the same as described in Fig. 1: the phase I in the domain D^I consists of u, d, s quarks and electrons and the phase II in the domain D^{II} neutrons, protons and electrons. These phases should be clearly separated

by the narrow boundary layer D_S with the width $\sim d_s \leq 1$ fm due to the non-perturbative effect of QCD. We treat such narrow boundary as the sharp one (∂D) with the surface tension parameter $\sigma_{\rm QCD}$ by using the bag model picture, while the value of $\sigma_{\rm QCD}$ is poorly known. We shall see that the Debye screening length λ_D is much longer than d_s and thereby the introduction of the sharp boundary should be reasonable [b].

Then, the thermodynamic potential per cell is given by a density functional [7],

$$\Omega = E[\rho] - \mu_i^{\rm I} \int_{D^{\rm I}} d\vec{r}\rho_i^{\rm I} - \mu_i^{\rm II} \int_{D^{\rm II}} d\vec{r}\rho_i^{\rm II}, \tag{5}$$

where $E[\rho]$ is the energy of the cell and consists of four contributions:

$$E[\rho] = \int_{D^{\rm I}} d\vec{r}\epsilon^{\rm I}_{\rm kin+str}[\rho_i^{\rm I}] + \int_{D^{\rm II}} d\vec{r}\epsilon^{\rm II}_{\rm kin+str}[\rho_i^{\rm II}] + 4\pi R^2\sigma_{\rm QCD} + E_V. \tag{6}$$

The first two terms are given by the kinetic and strong interaction energies, and the Coulomb interaction energy E_V is expressed in terms of particle densities,

$$E_V = \frac{1}{2}\int d\vec{r}\, d\vec{r}' \frac{Q_i\rho_i(\vec{r})Q_j\rho_j(\vec{r}')}{\mid \vec{r} - \vec{r}' \mid}, \tag{7}$$

with Q_i being the particle charge ($Q = -e < 0$ for the electron).

The equations of motion are given by $\delta\Omega/\delta\rho_i^\alpha = 0$ and written as

$$\mu_i^\alpha = \frac{\partial\epsilon^\alpha_{\rm kin+str}}{\partial\rho_i^\alpha} - N_i^{{\rm ch},\alpha}V^\alpha(\vec{r}), \quad N_i^{{\rm ch},\alpha} = Q_i^\alpha/e, \tag{8}$$

with the electric potential $V^\alpha(\vec{r})$:

$$V(\vec{r}) = -\int d\vec{r}' \frac{eQ_i\rho_i(\vec{r}')}{\mid \vec{r} - \vec{r}' \mid} \equiv \begin{cases} V^{\rm I}(\vec{r}), & \vec{r} \in D^{\rm I} \\ V^{\rm II}(\vec{r}), & \vec{r} \in D^{\rm II} \end{cases}. \tag{9}$$

Thus chemical potentials μ_i^α for charged particles have values depending on the electric state of the phase as well as on its chemical composition. Actually it is sometimes called the *electro-chemical potential* to stress this fact [5].

[b] This treatment is also similar to the *Gibbs geometrical surface* [5].

3.2. *Gauge invariance*

The thermodynamic potential enjoys the invariance under a gauge transformation, $V(\vec{r}) \to V(\vec{r}) - V^0$ and $\mu_i^\alpha \to \mu_i^\alpha + N_i^{\mathrm{ch},\alpha} V^0$, with an arbitrary constant V^0. Hence the chemical potential μ_i^α acquires physical meaning only *after gauge fixing* [c] .

Here we reconsider the Gibbs conditions and the Maxwell construction. As has been mentioned, on the first glance the Maxwell construction looks as contradicting the Gibbs conditions, especially the equilibrium condition for the charge chemical potential $\mu_Q (= \mu_e)$ in our context. However, correctly speaking, when we say $\mu_e^I \neq \mu_e^{II}$ within the Maxwell construction, it means nothing but the difference in the electron number density n_e in two phases, $n_e^I \neq n_e^{II}$; this is because $n_e = \mu_e^3/(3\pi^2)$, if the Coulomb potential is *absent*. Once the Coulomb potential is taken into account, using eq. (8), n_e can be written as

$$n_e^\alpha = \frac{(\mu_e^\alpha - V^\alpha)^3}{3\pi^2}. \tag{10}$$

Thus we may have $\mu_e^I = \mu_e^{II}$ and $n_e^I \neq n_e^{II}$ simultaneously, with the *different values of* V, $V^I \neq V^{II}$ (see Fig. 3).

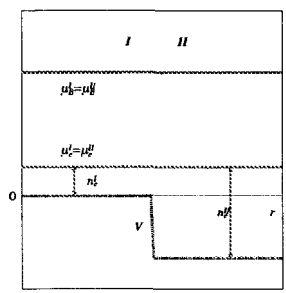

Figure 3. Relation between the charge chemical potential $\mu_Q (= \mu_e)$ and the electron number density n_e in the presence of the Coulomb potential V. Fulfilling the Gibbs conditions, $\mu_B^I = \mu_B^{II}$, $\mu_e^I = \mu_e^{II}$, we can change n_e in two phases as in the Maxwell construction, if V changes from one phase to another.

Applying Laplacian (Δ) to the l.h.s. of eq. (9) we recover the Poisson

[c] Note that $V = 0$ is a conventional choice in the usual treatment of uniform matter, while any constant is possible there.

equation ($\vec{r} \in D^\alpha$),

$$\Delta V^\alpha(\vec{r}) = 4\pi e^2 \rho^{\mathrm{ch},\alpha}(\vec{r}) \equiv 4\pi e Q_i^\alpha \rho_i^\alpha(\vec{r}). \tag{11}$$

The charge density $\rho^{\mathrm{ch},\alpha}(\vec{r})$ as a function of $V^\alpha(\vec{r})$ is determined by the equations of motion (8). Thus eq. (11) is a nonlinear differential equation for $V^\alpha(\vec{r})$. The boundary conditions are

$$V^{\mathrm{I}} = V^{\mathrm{II}}, \quad \nabla V^{\mathrm{I}} = \nabla V^{\mathrm{II}}, \quad \vec{r} \in \partial D, \tag{12}$$

where we have neglected a small contribution of the surface charge accumulated at the interface of the phases. We also impose the condition, $\nabla V^{\mathrm{II}} = 0$, at the boundary of the Wigner-Seitz cell, which implies that each cell must be charge neutral.

3.3. *Results*

The Debye screening parameter is introduced by the Poisson equation, if one expands the charge density in $\delta V^\alpha(\vec{r}) = V^\alpha(\vec{r}) - V^\alpha_{\mathrm{ref}}$ around a reference value V^α_{ref}. Then eq. (11) renders

$$\Delta \delta V^\alpha(\vec{r}) = 4\pi e^2 \rho^{\mathrm{ch},\alpha}(V^\alpha(\vec{r}) = V^\alpha_{\mathrm{ref}}) + (\kappa^\alpha(V^\alpha(\vec{r}) = V^\alpha_{\mathrm{ref}}))^2 \delta V^\alpha(\vec{r}) + ..., \tag{13}$$

with the *Debye screening* parameter,

$$(\kappa^\alpha(V^\alpha(\vec{r}) = V^\alpha_{\mathrm{ref}}))^2 = 4\pi e^2 \left[\frac{\partial \rho^{\mathrm{ch},\alpha}}{\partial V}\right]_{V^\alpha(\vec{r}) = V^\alpha_{\mathrm{ref}}} = 4\,\pi Q_i^\alpha Q_j^\alpha \left.\frac{\partial \rho_j^\alpha}{\partial \mu_i^\alpha}\right|_{V^\alpha(\vec{r}) = V^\alpha_{\mathrm{ref}}}. \tag{14}$$

Then we calculate contribution to the thermodynamic potential of the cell up to $O(\delta V^\alpha(\vec{r}))^2$. The "electric field energy" of the cell (7) can be written by way of the Poisson equation (13) as

$$E_V = \int_{D^{\mathrm{I}}} d\vec{r} \epsilon_V^{\mathrm{I}} + \int_{D^{\mathrm{II}}} d\vec{r} \epsilon_V^{\mathrm{II}} = \int_{D^{\mathrm{I}}} \frac{(\nabla V^{\mathrm{I}}(\vec{r}))^2}{8\pi e^2} d\vec{r} + \int_{D^{\mathrm{II}}} \frac{(\nabla V^{\mathrm{II}}(\vec{r}))^2}{8\pi e^2} d\vec{r} \tag{15}$$

that is, in the case of unscreened approximations, usually called the Coulomb energy. Besides the terms given by (15), there are another contributions arising from effects associated with the inhomogeneity of the electric potential profile, through implicit dependence of the particle densities on $V^{\mathrm{I,II}}(\vec{r})$. We will call them "correlation terms", $\omega^\alpha_{\mathrm{cor}} = \epsilon^\alpha_{\mathrm{kin+str}} - \mu_i^\alpha \rho_i^\alpha$.

We obtain the corresponding correlation contribution to the thermodynamic potential $\Omega_{\mathrm{cor}} = \int_{D^{\mathrm{I}}} d\vec{r} \omega^{\mathrm{I}}_{\mathrm{cor}} + \int_{D^{\mathrm{II}}} d\vec{r} \omega^{\mathrm{II}}_{\mathrm{cor}}$:

$$\omega^\alpha_{\mathrm{cor}} = \epsilon^\alpha_{\mathrm{kin+str}}(\rho_i^\alpha(V^\alpha_{\mathrm{ref}})) - \mu_i^\alpha \rho_i^\alpha(V^\alpha_{\mathrm{ref}}) - \rho^{\mathrm{ch},\alpha}(V^\alpha_{\mathrm{ref}}) V^\alpha_{\mathrm{ref}}$$
$$+ \frac{V^\alpha_{\mathrm{ref}} \Delta V^\alpha(\vec{r})}{4\pi e^2} + \frac{(\kappa^\alpha(V^\alpha_{\mathrm{ref}}))^2 (\delta V^\alpha(\vec{r}))^2}{8\pi e^2} + ..., \tag{16}$$

where we also used eqs. (13) and (14). In general $V_{\rm ref}^{\rm I} \neq V_{\rm ref}^{\rm II}$ and they may depend on the droplet size. Their proper choice should provide appropriate convergence of the above expansion in $\delta V(\vec{r})$. Taking $V_{\rm ref}^{\rm I} = V_{\rm ref}^{\rm II} = V_{\rm ref} = const$ we find

$$\omega_{\rm cor}^{\alpha} = \frac{(\kappa^{\alpha}(V_{\rm ref}))^2 (V^{\alpha}(\vec{r}) - V_{\rm ref})^2}{8\pi e^2}, \tag{17}$$

except an irrelevant constant.

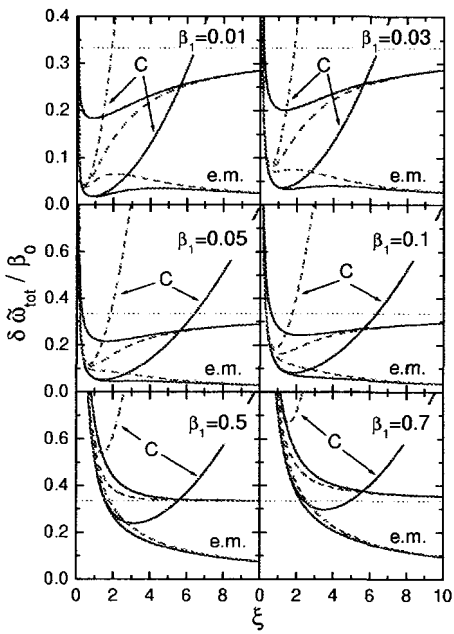

Figure 4. Dimensionless value of the thermodynamic potential per droplet volume. Solid lines are given for $f = 0.5$ and dashed lines for $f = 1/100$. The ratio of the screening lengths of two phases, $\alpha_0 = \lambda_D^I/\lambda_D^{II}$, is fixed as one. ξ is a dimensionless radius of the droplet, $\xi \equiv R/\lambda_D^I$, with $\lambda_D^I \simeq 5$ fm in this calculation. See text for further details.

For given baryon-number chemical potential μ_B and charge chemical potential μ_Q, all the particle chemical potentials μ_i can be represented in terms of μ_B and $\mu_Q(=\mu_e)$ with the help of the chemical equilibrium conditions:

$$\mu_u - \mu_s + \mu_e = 0, \quad \mu_d = \mu_s, \quad \mu_n = \mu_p + \mu_e, \tag{18}$$

in each phase and

$$\mu_B \equiv \mu_n = 2\mu_d + \mu_u, \tag{19}$$

at the boundary.

Then particle number densities ρ_i are represented as functions of μ_B, μ_Q and the Coulomb potential V, due to the equations of motion. Substituting them in the Poisson equation (11), we can solve it with the proper boundary conditions (12); note that $\nabla V = 0$ at the boundary of the Wigner-Seitz cell provides us with another relation between μ_B and μ_Q.

Thus we eventually have the density profiles of all the particles for

given density or the baryon-number chemical potential μ_B. In Fig. 4 we demonstrate the radius (R) dependence of the total thermodynamic potential per droplet volume for the case of spherical droplets,$\delta\widetilde{\omega}_{\rm tot}/\beta_0 = (\widetilde{\epsilon}^{\rm I}_V + \widetilde{\epsilon}^{\rm II}_V + \widetilde{\omega}^{\rm I}_{\rm cor} + \widetilde{\omega}^{\rm II}_{\rm cor} + \widetilde{\epsilon}_{\rm S})/\beta_0$, given by the sum of partial contributions, where tilde denotes each quantity scaled by the droplet volume $V = 4\pi R^3/3$ and β_0 is a typical quantity with the dimension of the energy density[6]. Preparing some wide range for the value of the surface tension parameter σ_{QCD}, $\beta_1 \propto {\sigma_{QCD}}^6$, we present two cases of f, $f = 0.01, 0.5$.

The label "C" is given for reference to show the previous non-selfconsistent case, where the Coulomb potential is not screened see Fig. 2. We can see that only in the limit of $f \ll 1$ and $R \ll \lambda^I_D$, we are able to recover this case. The "e.m." curve shows the partial contribution to the thermodynamic potential, $\widetilde{\epsilon}_{\rm e.m.}/\beta_0 \equiv (\widetilde{\epsilon}_V + \widetilde{\epsilon}_{\rm S})/\beta_0$, ignoring correlation terms. Comparing these curves we can see how the screening effect changes the thermodynamic potential: we can see that the minima at the "e.m." curves disappear already at $\beta_1 > 0.03$, corresponding to unphysically small $\sigma_{QCD} \sim$ several MeV$\cdot$fm^{-2}. However, the correlation energy gives a sizable contribution to allow the minimum for larger value of σ_{QCD}. Consequently, the minimum totally disappears between $\beta_1 = 0.1$ and $\beta_1 = 0.5$, which may be interpreted as $10 < \sigma_{QCD} < 50$(MeV$\cdot$fm^{-2}) in this calculation. Thus we have seen a *mechanical instability* of the droplet for the medium values of σ_{QCD}, which might be in the physically meaningfull range.

4. Summary and Concluding remarks

In this talk we addressed an issue about SMP at the first order phase transitions in multicomponent systems, like in neutron-star matter. We have studied a so called "contradiction" between the Gibbs conditions and the Maxwell construction extensively discussed in previous works. We have demonstrated that this contradiction is resolved if one correctly takes into account the difference in the "meaning" of the chemical potentials used in the two approaches: the different values of the electron chemical potentials in the Maxwell construction and the ones used in the Gibbs conditions do not contradict each other if one properly takes into account the electric field.

We have presented a framework based on the density functional theory to describe thermodynamics in the non-uniform systems. The Coulomb potential is properly included and particle density profiles are consistently determined with the Poisson equation.

Taking the hadron-quark deconfinement transition in high-density matter as an example, we have demonstrated the importance of the Debye screening effect, which is a consequence of the above treatment. With a numerical example, we have seen that the screening effect gives rise to a mechanical instability for realistic values of the surface tension parameter of σ_{QCD}. In this case we may effectively recover the picture given by the Maxwell construction, where the *phase separation* of two bulk phases arises.

Our framework is rather general and it may be applicable to any first order phase transition, e.g. the liquid-gas phase transition at subnuclear density [8].

Acknowledgments

We acknowledge with special thanks contributions of our collaborators, E.E. Kolomeitsev, T. Maruyama, S. Chiba, T. Tanigawa and T. Endo to the results presented in this paper. The present work of T.T. is partially supported by the Japanese Grant-in-Aid for Scientific Research Fund of the Ministry of Education, Culture, Sports, Science and Technology (11640272, 13640282)

References

1. N.K. Glendenning, Phys. Rev. **D46** (1992) 1274; Phys. Rep. **342** (2001) 393.
2. N.K. Glendenning and J. Schaffner-Bielich, Phys. Rev. **C60** (1999) 025803. M. Christiansen and N.K. Glendenning, *astro-ph/0008207*; M. Christiansen, N.K. Glendenning and J. Schaffner-Bielich, Phys. Rev. **C62** (2000) 025804.
3. D.G. Ravenhall, C.J. Pethick and J.R. Wilson, Phys. Rev. Lett. **50** (1983) 2066;
   H. Heiselberg, C.J. Pethick and E.F. Staubo, Phys. Rev. Lett. **70** (1993) 1355.
4. T. Norsen and S. Reddy, Phys.Rev. **C63** (2001) 065804.
5. e.g., E.A. Guggenheim, *Thermodynamics*, (North-Holland pub., 1977).
6. D.N. Voskresenky, M. Yasuhira and T. Tatsumi, Phys. Lett. **B541** (2002) 93, ; Nucl. Phys. **A723** (2003) 291; T. Tatsumi, M. Yasuhira and D.N. Voskresenky, Nucl. Phys. **A718** (2003) 359c.
7. R.G. Parr and W. Yang, *Density-Functional Theory of Atoms and Molecules*, (Oxford U. Press, 1989).
8. T. Maruyama et al., nucl-th/0311076; in this proceedings.

EQUATION OF STATE OF NUCLEAR MATTER, NEUTRON RICH NUCLEI IN LABORATORIES AND PASTA NUCLEI IN NEUTRON STAR CRUSTS

K. OYAMATSU

Department of Media Theories and Production, Aichi Shukutoku University
Nagakute-cho, Aichi-gun, Aichi, 480-1197, Japan
E-mail: oyak@asu.aasa.ac.jp

K. IIDA

The Institute of Physical and Chemical Research (RIKEN)
Hirosawa, Wako, Saitama 351-0198, Japan
E-mail: keiiida@postman.riken.go.jp

The equation of state (EOS) of asymmetric nuclear matter dominates macroscopic properties of neutron rich nuclei in laboratories, and extremely neutron-rich pasta nuclei (rodlike and slablike nuclei and rodlike and spherical nuclear bubbles) in a neutron star crust. The purpose of this study is to identify the most important EOS parameter that governs the radii of neutron-rich laboratory nuclei and the density range of the pasta nuclei. In a simplified Thomas-Fermi method, we calculate the masses and density distributions of neutron-rich laboratory nuclei and pasta nuclei using various EOS's that are consistent with empirical data for masses and radii of stable nuclei, and systematically examine the EOS dependence of the matter radii of laboratory nuclei and the density range of the crustal part including pasta nuclei. It is found that both the calculated matter radii of neutron-rich laboratory nuclei and the calculated density range of the pasta nuclei show a clear dependence on the density symmetry coefficient L, while the dependence on the incompressibility K_0 is much weaker. The density range of the pasta nuclei is found to disappear for extremely large L values. These results suggest that future systematic measurements of the matter radii of neutron-rich nuclei could help deduce the L value, which in turn could give useful information about the presence of pasta nuclei in neutron star crusts.

1. Introduction

The equation of state (EOS) of asymmetric nuclear matter is supposed to mainly determine masses and radii of neutron-rich laboratory nuclei, and the density range of the innermost part of a neutron star crust in which extremely neutron-rich pasta nuclei, i.e., rodlike and slablike nuclei and

rodlike and spherical nuclear bubbles, occur. In this study, we attempt to specify the most important EOS parameter that governs these properties.

The energy per nucleon near the saturation point of symmetric nuclear matter is generally expressed as[1]

$$w = w_0 + \frac{K_0}{18n_0^2}(n-n_0)^2 + \left[S_0 + \frac{L}{3n_0}(n-n_0) + \frac{K_{asym}}{18n_0^2}(n-n_0)^2\right]\alpha^2. \quad (1)$$

Here w_0, n_0 and K_0 are the saturation energy, the saturation density and the incompressibility of symmetric nuclear matter. The neutron excess is defined as $\alpha = 1 - 2x$ using proton fraction x. The parameters S_0 (the symmetry energy), L (the density symmetry coefficient) and K_{asym} characterize the density dependent symmetry energy $S(n)$ at $n \approx n_0$;

$$S_0 = S(n_0), \quad (2)$$

$$L = 3n_0(dS/dn)_{n=n_0}, \quad (3)$$

$$K_{asym} = 9n_0^2(d^2S/dn^2)_{n=n_0}. \quad (4)$$

From Eq. (1), the saturation density n_s and energy w_s of asymmetric nuclear matter with fixed proton fraction are given, up to the second order of α, by

$$n_s = n_0 - \frac{3n_0L}{K_0}\alpha^2, \quad (5)$$

$$w_s = w_0 + S_0\alpha^2. \quad (6)$$

One useful empirical parameter to characterize the saturation of asymmetric nuclear matter is the slope, y, of the saturation line near $\alpha = 0$ ($x = 1/2$).[1] It is expressed as

$$y = -\frac{K_0S_0}{3n_0L}. \quad (7)$$

2. Macroscopic nuclear model

In constructing a macroscopic nuclear model, we begin with a simple expression for the bulk energy per nucleon,[5]

$$w = \frac{3\hbar^2(3\pi^2)^{2/3}}{10m_n n}(n_n^{5/3} + n_p^{5/3}) + (1-\alpha^2)v_s(n)/n + \alpha^2 v_n(n)/n, \quad (8)$$

where

$$v_s = a_1n^2 + \frac{a_2n^3}{1+a_3n} \quad (9)$$

and

$$v_n = b_1 n^2 + \frac{b_2 n^3}{1 + b_3 n} \tag{10}$$

are the potential energy densities for symmetric nuclear matter and pure neutron matter, and m_n is the neutron mass. Here, replacement of the proton mass m_p by m_n in the proton kinetic energy makes only a negligible difference. Equation (8) can well reproduce the microscopic calculations of symmetric nuclear matter and pure neutron matter by Friedman and Pandharipande[3] and of asymmetric nuclear matter by Lagaris and Pandharipande[4]. Furthermore the expression can also reproduce phenomenological Skyrme Hartree-Fock and relativistic mean field EOS's.

We determine the parameters included in Eqs. (9) and (10) in such a way that they reproduce data on radii and masses of *stable* nuclei. In the limit of $n \to n_0$ and $\alpha \to 0$ ($x \to 1/2$), expression (8) reduces to the usual form (1).[2] The parameter b_3, which controls the EOS of matter at large neutron excess and high density, has little effect on the saturation properties of nearly symmetric nuclear matter. We will thus set b_3 as a typical value 1.586 fm^3, which was obtained by one of the authors[5] in such a way as to reproduce the neutron matter energy of Friedman and Pandharipande.[3]

We describe a spherical nucleus of proton number Z and mass number A within the framework of a simplified version of the extended Thomas-Fermi theory.[5] We first write the total energy of a nucleus as a function of the density distributions $n_n(\mathbf{r})$ and $n_p(\mathbf{r})$ according to

$$E = \int d^3r n(\mathbf{r}) w\left(n_n(\mathbf{r}), n_p(\mathbf{r})\right) + F_0 \int d^3r |\nabla n(\mathbf{r})|^2 + \frac{e^2}{2} \int d^3r \int d^3r' \frac{n_p(\mathbf{r}) n_p(\mathbf{r}')}{|\mathbf{r} - \mathbf{r}'|} + N m_n + Z m_p, \tag{11}$$

where the first, second and third terms on the right hand side are the bulk energy, the gradient energy with an adjustable constant F_0, and the Coulomb energy, respectively. The symbol $N = A - Z$ denotes the neutron number. Here we neglect the contribution to the gradient energy from $|\nabla(n_n(\mathbf{r}) - n_p(\mathbf{r}))|^2$; this contribution makes only a little difference even in the description of extremely neutron-rich nuclei, as clarified in the context of neutron star matter.[5]

For the present purpose of examining the macroscopic properties of nuclei such as masses and radii, it is sufficient to characterize the neutron and proton distributions for each nucleus by the central densities, radii and surface diffuseness different between neutrons and protons, as in Ref. 5.

We thus assume the nucleon distributions $n_i(r)$ $(i = n, p)$, where r is the distance from the center of the nucleus, as

$$n_i(r) = \begin{cases} n_i^{\rm in}\left[1 - \left(\dfrac{r}{R_i}\right)^{t_i}\right]^3, & r < R_i, \\ n_i^{\rm out}, & r \geq R_i. \end{cases} \tag{12}$$

Here R_i roughly represents the nucleon radius, t_i the relative surface diffuseness, and $n_i^{\rm in}$ the central number density. The density of the outside nucleon gas, $n_i^{\rm out}$, is greater than zero for nuclei in the inner crust of a neutron star while it is zero for laboratory nuclei. The proton distribution of the form (12) can fairly well reproduce the experimental data for stable nuclei such as ^{90}Zr and ^{208}Pb.[5]

3. Optimal relations among EOS parameters

The EOS parameters a_1–b_2 and F_0 are determined from masses and radii of stable nuclei in the same way as in Ref. 5 using the empirical values for nine nuclei on the smoothed β-stability line ranging $25 \leq A \leq 245$ (see Table A.1 in Ref. 5, which is based on Refs. 6, 7). For fixed slope y and incompressibility K_0, such a comparison is made by a usual least squares fitting, which gives rise to an optimal set of the parameters a_1–b_3 and F_0. Here, we set y and K_0 as -1800 MeV fm^3 $\leq y \leq -200$ MeV fm^3 and 180 MeV $\leq K_0 \leq 360$ MeV; the numerical results for n_0, w_0, S_0, L and F_0 are obtained for about 200 combinations of y and K_0. All of them reproduce the input nuclear data almost equally.

As shown in Fig. 1, we find an empirical correlation between S_0 and L,

$$S_0 \approx B + CL, \tag{13}$$

with $B \approx 28$ MeV and $C \approx 0.075$. A similar result, $B = 29$ MeV and $C = 0.1$, was obtained from various Hartree-Fock models with finite-range forces by Farine et al..[8]

The saturation energy of symmetric nuclear matter, w_0, always takes on a value of -16.0 ± 0.5 MeV. There is a weak correlation between n_0 and K_0 as shown in Fig. 2. This is a feature which was found among non-relativistic phenomenological Skyrme Hartree-Fock EOS's (see Fig. 4 of Ref. 9).

In Fig. 3, the uncertainties in L and K_0 is represented as a band, which reflects the constraint on (y, K_0). In this band, L increases with increasing

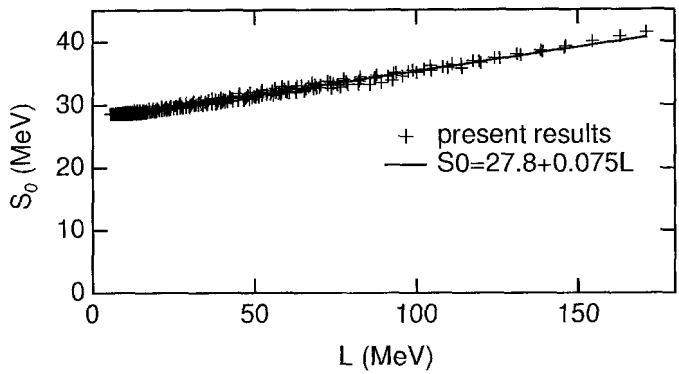

Figure 1. The empirical correlation between S_0 and L.

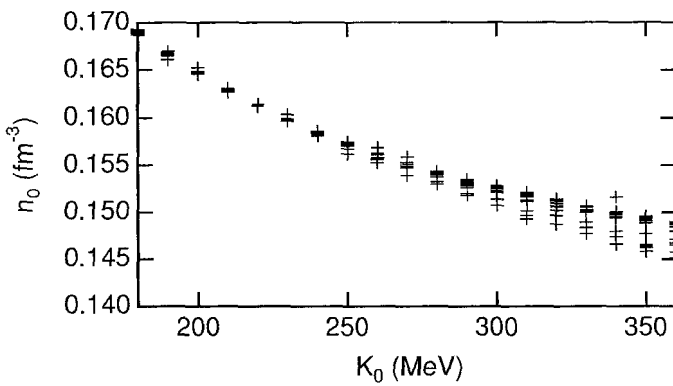

Figure 2. The empirical correlation between n_0 and K_0.

y for fixed K_0. The upper bound ($y = -200$ MeV fm^3) reaches a large value of L, which increases with increase in K_0.

Figure 4 shows nine typical EOS's that correspond with points A-I in Fig. 3. The EOS reasonably covers phenomenological EOS's of contemporary use. For example, the SIII EOS in non-relativistic theory is quite similar to EOS I and TM1 EOS in the relativistic mean field is between EOS B and C.

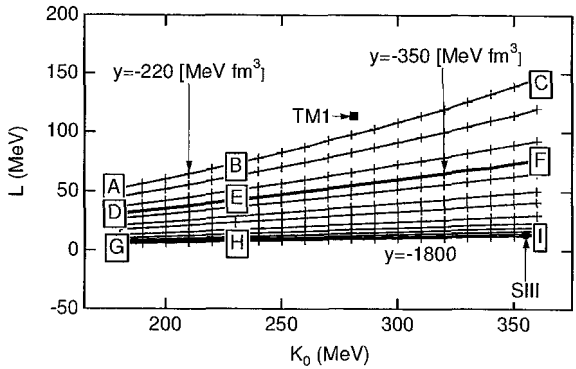

Figure 3. The optimum (L, K_0) values. The symbols A-I correspond to EOS A-I in Fig. 4.

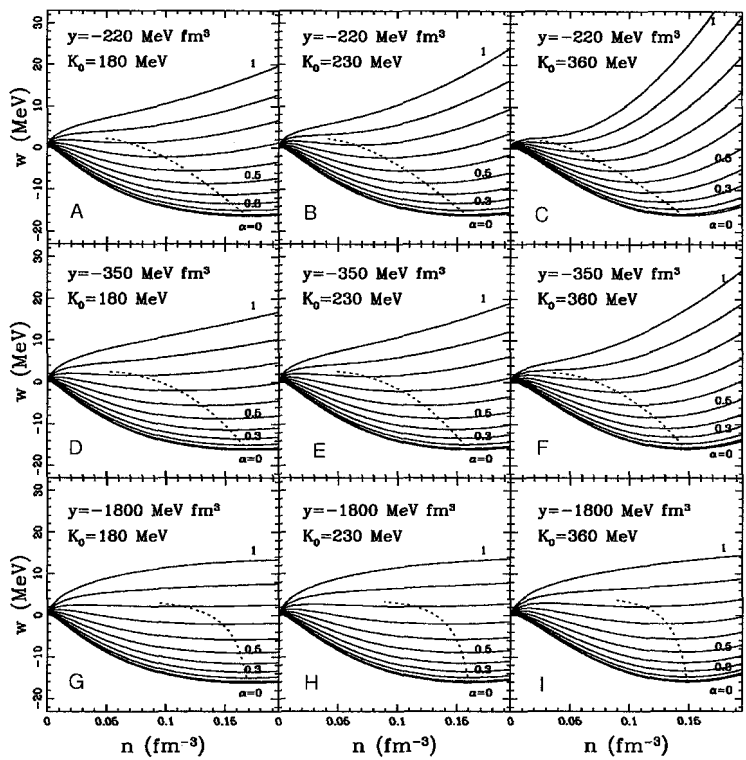

Figure 4. Nine typical EOS's corresponding to points A-I in Fig. 3.

4. Neutron rich nuclei in laboratories

Using the systematically obtained EOS's, we calculate radii and masses of neutron rich nuclei, and examine how they depend on the EOS parameters in Eq. (1). Figures 5 and 6 show that the mass and matter radius of neutron rich ^{80}Ni ($Z/A = 0.35$) have clear dependence on L. Some points in Fig. 6 scatter appreciably due probably to small numerical errors in w_0 but the neutron separation energy shows clearer dependence on L.

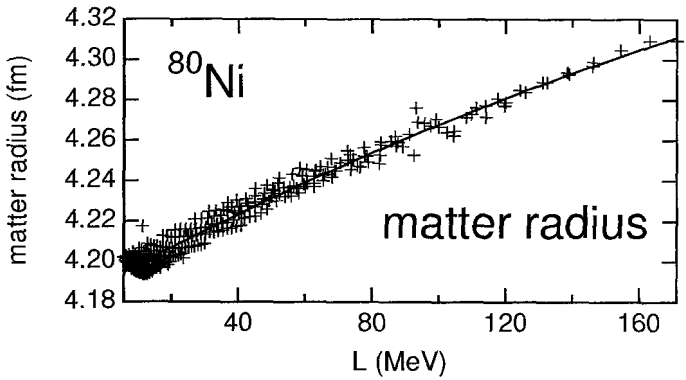

Figure 5. Matter radius of ^{80}Ni.

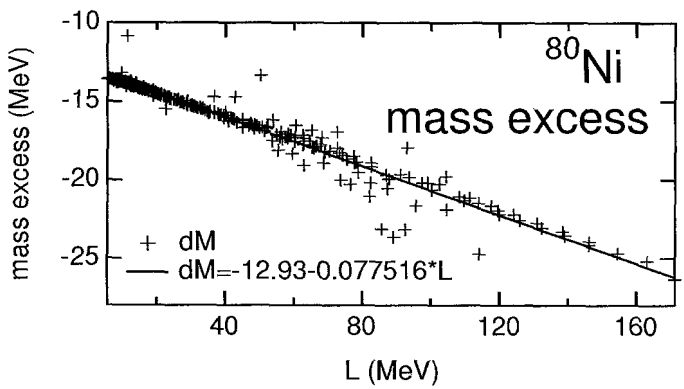

Figure 6. Mass excess of ^{80}Ni.

5. Nuclei in neutron star crusts

A good estimate of the crust-core boundary density is obtained from a stability analysis against proton clustering.[10] In this analysis, we calculate the energy change when small variations of particle densities are imposed on a uniform liquid of protons, neutrons and electrons. The estimate of the boundary density, $n(Q)$, is defined as the lowest density where the system is stable against the small density modulations. Figure 7 shows that $n(Q)$ is obviously dependent on L.

In the inner edge of a neutron star crust, there may or may not exist pasta nuclei (rodlike and slablike nuclei and rodlike and spherical nuclear bubbles). The existence is conjectured to depend on the asymmetric nuclear matter EOS. We calculate pasta nuclei using the nine typical EOS's in Fig. 4 to see this dependence. The result of a preliminary calculation is shown in Fig. 8. From Figs. 4 and 8, we see that the density range becomes narrower as the L value increases. For EOS C, which has extremely large L and K_0, the density range disappears so that pasta nuclei do not exist.

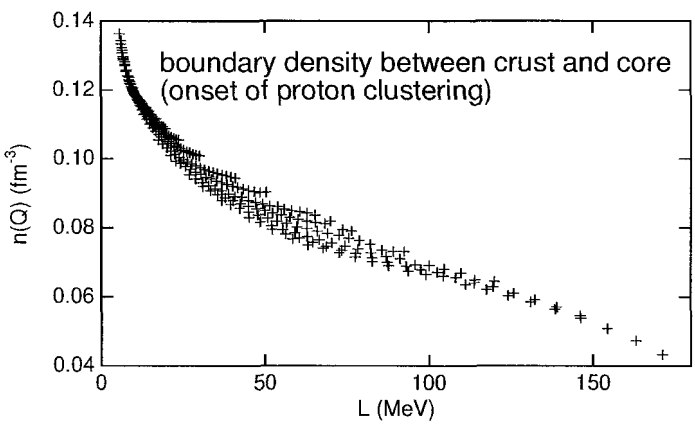

Figure 7. An estimate of the crust-core boundary density.

6. Summary

About 200 sets of the EOS parameters are systematically obtained from fitting to masses and radii of stable nuclei using a simplified Thomas-Fermi model paying attention to large uncertainties in K_0 and L values.

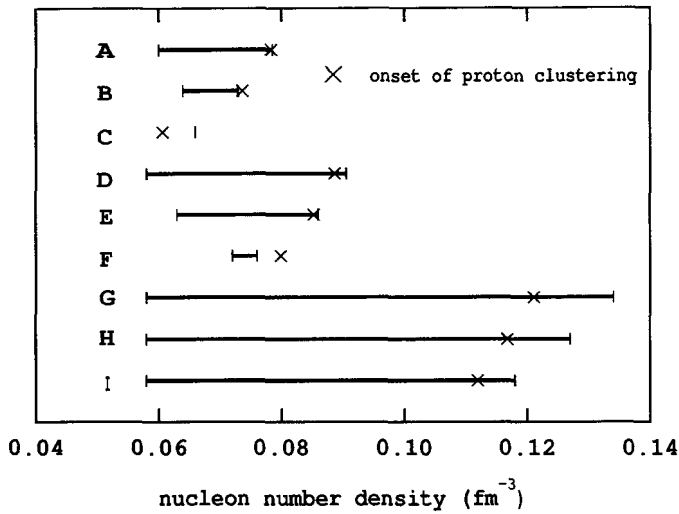

Figure 8. The density range of pasta nuclei.

As for symmetric nuclear matter, the saturation density n_0 has a weak K_0 dependence while the saturation energy, w_0, is essentially constant.

There is a strong correlation between S_0 and L : $S_0 \approx 28 + 0.075L$ (MeV). Although the L value can not be determined from stable nuclei, the empirical upper bound of L is found to be an increasing function of K_0. This is a consequence of the empirical constraint on the slope of the saturation line. Taking the uncertainties in L and K_0 into account, we systematically obtain various asymmetric matter EOS's which reasonably cover typical Skyrme Hartree-Fock EOS's and relativistic mean field EOS's.

For neutron rich nuclei in laboratories, we find that the matter radii and masses have clear L dependence almost independent of K_0. For nuclei in a neutron star crust, the boundary density between the core and the crust has clear L dependence. The density range of pasta nuclei becomes narrower with L, and vanishes with the largest L value. From these results, we conclude that future systematic measurements of the matter radii of neutron-rich nuclei could help deduce the L value, which in turn could give useful information about the presence of pasta nuclei in neutron star crusts.

References

1. K. Oyamatsu, I. Tanihata, Y. Sugahara, K. Sumiyoshi, H. Toki, Nucl. Phys. A 634 (1998) 3.
2. K. Oyamatsu and K. Iida, Prog. Theor. Phys. 109 (2003) 631.
3. B. Friedman, V.R. Pandharipande, Nucl. Phys. A 361 (1981) 502.
4. I.E. Lagaris, V.R. Pandharipande, Nucl. Phys. A 369 (1981) 470.
5. K. Oyamatsu, Nucl. Phys. A 561 (1993) 431.
6. M. Yamada, Prog. Theor. Phys. 32 (1964) 512.
7. H. de Vries, C.W. de Jager, C. de Vries, At. Data Nucl. Data Tables 36 (1987) 495.
8. M. Farine, J.M. Pearson, B. Rouben, Nucl. Phys. A 304 (1978) 317.
9. J.P. Blaizot, Phys. Rep. **64**, 171 (1980).
10. C.J. Pethick, D.G. Ravenhall, C.P. Lorenz, Nucl. Phys. A 584 (1995) 675.

COULOMB SCREENING EFFECT ON THE NUCLEAR-PASTA STRUCTURE

TOSHIKI MARUYAMA[1], TOSHITAKA TATSUMI[2],
DMITRI N. VOSKRESENSKY[3], TOMONORI TANIGAWA[4,1],
SATOSHI CHIBA[1], TOMOYUKI MARUYAMA[5]

1 Advanced Science Research Center, Japan Atomic Energy Research Institute, Tokai, Ibaraki 319-1195, Japan

2 Department of Physics, Kyoto University, Kyoto 606-8502, Japan

3 Moscow Institute for Physics and Engineering, Kashirskoe sh. 31, Moscow 115409, Russia

4 Japan Society for the Promotion of Science, Tokyo 102-8471, Japan

5 BRS, Nihon University, Fujisawa, Kanagawa 252-8510, Japan

Using the density functional theory (DFT) with the relativistic mean field (RMF) model, we study the non-uniform state of nuclear matter, "nuclear pasta". We self-consistently include the Coulomb interaction together with other interactions. It is found that the Coulomb screening effect is significant for each pasta structure but not for the bulk equation of state (EOS) of the nuclear pasta phase.

1. Introduction

One of the most interesting features of low-density nuclear matter is the possibility of the existence of non-uniform structures, called "nuclear pastas".[1] At low densities, nuclei in matter are expected to form the Coulomb lattice embedded in the neutron-electron seas, so as to minimize the Coulomb interaction energy. On the other hand, another possibility has been discussed: the stable nuclear shape may change from sphere to cylinder, slab, cylindrical hole, and to spherical hole with increase of the matter density, and "pastas" are eventually dissolved into uniform matter at a certain nucleon density close to the saturation density, $\rho_s \simeq 0.16$ fm^{-3}. The existence

of such "pasta" phases, instead of the ordinary crystalline lattice of nuclei, would modify several important processes in supernova explosions by changing the hydrodynamic properties and the neutrino opacity in the supernova matter. Also expected is the influence of the "pasta" phases on star quakes of neutron stars and pulsar glitches via the change of mechanical properties of the crust matter.

Several authors have investigated the low-density nuclear matter using various models. [1–8] Roughly speaking, the favorable nuclear shape is determined by a balance between the surface and the Coulomb energies, as has been shown by previous studies, where the rearrangement effect on the density profile of the charged particles, especially electrons, by the Coulomb interaction is discarded. However, the proper treatment of the Coulomb interaction should be very important, as it is demonstrated in Ref. 9; the screening of the Coulomb interaction by the charged particles may give a large effect on the stability of the geometrical structures.

We have been recently exploring the effect of the Coulomb screening in the context of the structured mixed phases in various first order phase transitions such as hadron-quark deconfinement transition, kaon condensation and liquid-gas transition in nuclear matter. We treat the nuclear "pasta" phases as a part of our project, since they can be considered as structured mixed phases during the liquid-gas transition in nuclear matter.

Our aim here is to study the nuclear "pasta" structures by means of a mean field model, which includes the Coulomb interaction in a proper way, and we figure out how the Coulomb screening effect modifies the previous results without it.

2. Density Functional Theory with the Relativistic Mean-field Model

To study the non-uniform nuclear matter, we follow the density functional theory (DFT) with the relativistic mean field (RMF) model.[10] The RMF model with fields of mesons and baryons is rather simple for numerical calculations, but realistic enough to reproduce main nuclear matter properties. In our framework, the Coulomb interaction is properly included in the equations of motion for nucleons, electrons and the meson mean fields, and we solve the Poisson equation for the Coulomb potential $V_{\rm Coul}$ self-consistently with them. Thus the baryon and electron density profiles, as well as the meson mean fields, are determined in a way fully consistent with the Coulomb potential. Note that our framework can be easily extended to

other situations. For example, if we take into account meson condensations, which are likely realized in a high-density region, we should only add the relevant meson field terms. In Ref. 11 we have included the kaon degree of freedom in such a treatment to discuss kaon condensation in high density regime.

To begin with, we present the thermodynamic potential of the form,

$$\Omega = \Omega_B + \Omega_M + \Omega_e, \tag{1}$$

$$\Omega_B = \int d^3r \left[\sum_{i=p,n} \left(\frac{2}{(2\pi)^3} \int_0^{k_{Fi}} d^3k \sqrt{m_B^{*\,2} + k^2} - \rho_i \nu_i \right) \right], \tag{2}$$

$$\Omega_M = \int d^3r \left[\frac{(\nabla\sigma)^2 + m_\sigma^2\sigma^2}{2} + U(\sigma) - \frac{(\nabla\omega_0)^2 + m_\omega^2\omega_0^2}{2} - \frac{(\nabla\rho_0)^2 + m_\rho^2\rho_0^2}{2} \right], \tag{3}$$

$$\Omega_e = \int d^3r \left[-\frac{1}{8\pi e^2} (\nabla V_{\rm Coul})^2 - \frac{(V_{\rm Coul} - \mu_e)^4}{12\pi^2} \right], \tag{4}$$

where $\nu_p = \mu_B - \mu_e + V_{\rm Coul} - g_{\omega N}\omega_0 - g_{\rho N}\rho_0$, $\nu_n = \mu_B - g_{\omega N}\omega_0 + g_{\rho N}\rho_0$, $m_B^* = m_B - g_{\sigma N}\sigma$, and $U(\sigma) = \frac{1}{3}bm_B(g_{\sigma N}\sigma)^3 + \frac{1}{4}c(g_{\sigma N}\sigma)^4$. Here we used the local-density approximation for nucleons and electrons, while one still should carefully check its validity. The introduction of the density variable is meaningful, if the typical length of the nucleon density variation inside the structure is larger than the inter-nucleon distance, which we assume to be fulfilled. We must also keep in mind that the approximation is broken down for small structure sizes, since quantum effects become prominent there. For the sake of simplicity we also omitted nucleon and electron density derivative terms. If the nucleon length scale were shorter than lengths of changes of the meson mean fields, one could not introduce the derivatives of the nucleon density but could simplify the problem introducing the corresponding contribution to the surface tension. In the given case (when we suppressed the derivative terms mentioned above) the resulting nucleon density follows the changes of the meson mean fields. However, even in this case the presence of the derivative terms (of the same order as for other fields) could affect the numerical results. Here we consider large-size pasta structures and simply discard the density variation effect, as a first-step calculation, while it can be incorporated in the quasi classical way by the derivative expansion within the density functional theory.[10] The parameters are set to reproduce the nuclear-matter saturation properties. From the variational principle, $\frac{\delta\Omega}{\delta\phi_i(\mathbf{r})} = 0$ ($\phi_i = \sigma, \rho_0, \omega_0, V_{\rm Coul}$) or

$\frac{\delta\Omega}{\delta\rho_i(\mathbf{r})} = 0 (i = n, p, e)$, we get the coupled equations of motion as

$$-\nabla^2\sigma + m_\sigma^2\sigma = -\frac{dU}{d\sigma} + g_{\sigma N}(\rho_n^{(s)} + \rho_p^{(s)}) \tag{5}$$

$$-\nabla^2\omega_0 + m_\omega^2\omega_0 = g_{\omega N}(\rho_p + \rho_n) \tag{6}$$

$$-\nabla^2\rho_0 + m_\rho^2\rho_0 = g_{\rho N}(\rho_p - \rho_n) \tag{7}$$

$$\nabla^2 V_{\rm Coul} = 4\pi e^2 \rho_{\rm ch} \quad (\text{charge density } \rho_{\rm ch} = \rho_p + \rho_e) \tag{8}$$

$$\mu_n = \mu_B = \sqrt{k_{Fn}^2 + m_B^{*\,2}} + g_{\omega N}\omega_0 - g_{\rho N}\rho_0 \tag{9}$$

$$\mu_p = \mu_B - \mu_e = \sqrt{k_{Fp}^2 + m_B^{*\,2}} + g_{\omega N}\omega_0 + g_{\rho N}\rho_0 - V_{\rm Coul} \tag{10}$$

$$\rho_e = -(\mu_e - V_{\rm Coul})^3/3\pi^2. \tag{11}$$

Note that first, the Poisson equation (8) is a highly nonlinear equation for $V_{\rm Coul}$, since $\rho_{\rm ch}$ in r.h.s. includes it in a complicated way, and secondly, the Coulomb potential always enters the equation through the gauge invariant combination, $\mu_e - V_{\rm Coul}$.

To solve the above coupled equations numerically, we use the Wigner-Seitz cell approximation: the space is divided into equivalent cells with some geometrical symmetry. The shape of the cell changes: sphere in three dimensional (3D) calculation, cylinder in 2D and slab in 1D, respectively. Each cell is charge-neutral and all the physical quantities in a cell are smoothly connected to those of the neighbor cell with zero gradients at the boundary. The cell is divided into grid points ($N_{\rm grid} \approx 100$) and the differential equations for fields are solved by the relaxation method with constraints of given baryon number and charge neutrality.

3. Bulk Property of Finite Nuclei

Before applying our framework to the problem of the pasta phases in nuclear matter, we check how it can describe finite nuclei. In this calculation, the electron density is set to be zero and the boundary condition or the charge-neutrality condition is not imposed. However, we assumed the spherical shape of nuclei. In Fig. 1 (left panel) we show the density profiles of some typical nuclei. We can see how well our framework may describe the density profiles of these nuclei. To get a better fit, especially around the surface region, we might need to include the derivative terms, as we have mentioned. Fine structures seen in the empirical density profiles, which come from the shell effects (see, e.g., a proton density dip at the center of a light ^{16}O nucleus), cannot be reproduced by the mean field approach. By imposing the

beta equilibrium, the most stable proton ratio can be obtained for a given mass number. Figure 1 (right panel) shows the mass-number dependence of the binding energy per nucleon and the proton ratio. We can see that the bulk properties of finite nuclei (density, binding energy and proton ratio) are satisfactorily reproduced for our present purpose.

Note that we should adjust a slightly smaller value of the sigma mass than that one usually uses, i.e. 400 MeV, to get such a good fit. If we used the popular value of $m_\sigma \approx 500$ MeV, finite nuclei would be overbound by about 3 MeV per nucleon. Although the actual value of the sigma mass (or the omega mass) has little relevance for infinite nuclear matter, it is important for finite nuclei and other non-uniform nucleon systems, since the meson mass characterizes the interaction range and consequently affects, e.g., the nuclear surface property.

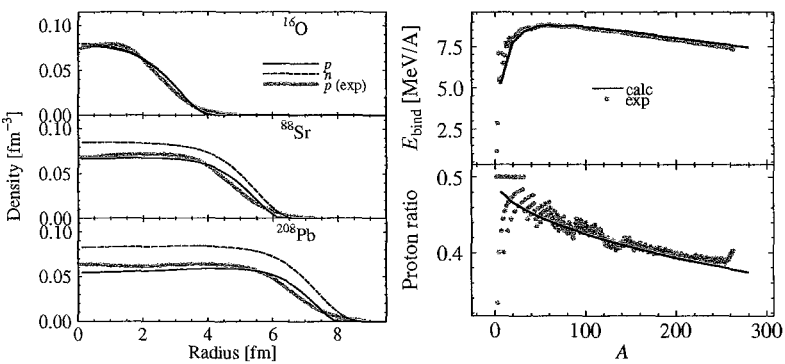

Figure 1. Left: the density profiles of typical nuclei. The proton densities (solid curves) are compared with the experiment. Right: the binding energy per nucleon and the proton ratio of finite nuclei.

4. Nuclear "Pasta" at Sub-nuclear Densities

It is widely accepted that the "pasta" structure is realized basically due to the balance of the Coulomb energy and the surface tension. However, the electron density has been always treated as an uniform background in the standard treatments. Here we study the nuclear "pasta" structure within our framework, which consistently treats the Coulomb potential and the electron distribution.

4.1. *Symmetric Nuclear Matter and the Coulomb Screening Effect*

First, we focus on symmetric nuclear matter (relevant to supernova matter at the initial stage of collapse) where the Coulomb screening effect by electrons is expected to be large. Figure 2 shows some typical density profiles in the Wigner-Seitz cells. The geometrical dimension of the cell is denoted as "3D" (three dimensional), etc. The horizontal axis in each panel denotes the radial distance from the center of the cell, and the boundary is indicated by the hatch. The nuclear "pasta" structures are clearly seen. Note that the electron density profile becomes no more uniform due to the Coulomb screening.

The phase diagram of the matter structure is shown in Fig. 3 (left). The size of the cell $R_{\rm cell}$ is optimized with precision of 1 fm, and the lowest energy configurations are chosen among various geometrical structures. In the figure, there never appears the spherical-hole configuration. This is one of the consequences of the Coulomb screening effect. It should be noted that appearance of the pasta structures is also sensitive to the choice of the effective interaction, as discussed by Oyamatsu et al.[12]

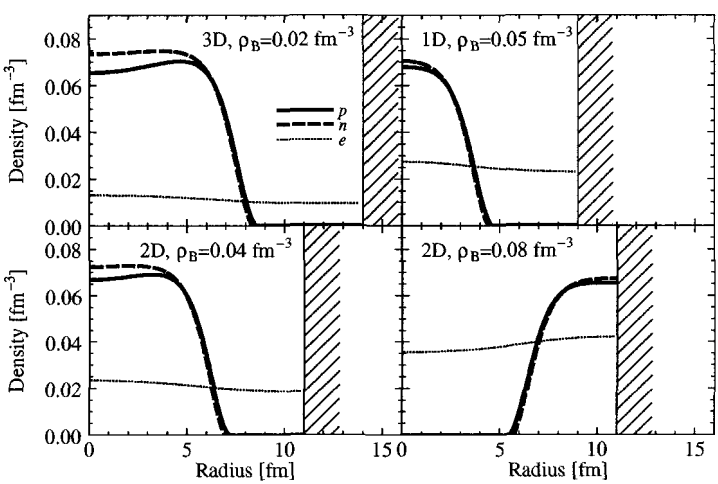

Figure 2. Examples of the density profiles in the cell for symmetric nuclear matter (droplet, rod, slab, and tube).

To elucidate the Coulomb screening effect, there are two possible ways:

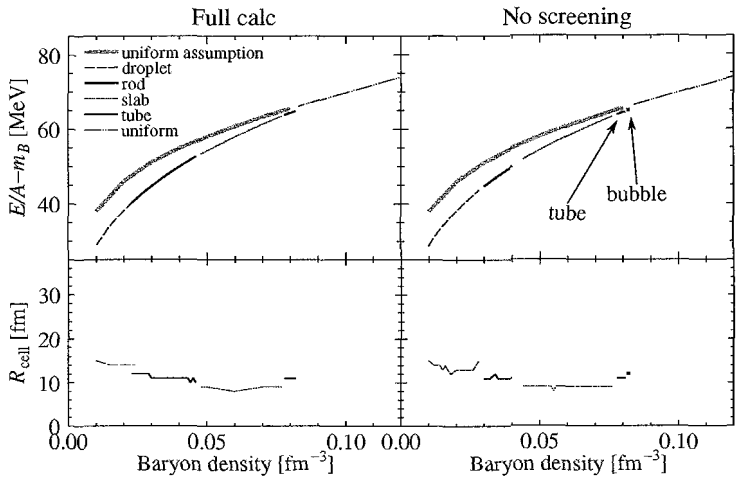

Figure 3. Left: the binding energy per nucleon and the cell size of symmetric nuclear matter. Right: the same as the left panel with the uniform electron distribution.

one is to compare our results with those given by solving the equations of motion for fields and the density profiles neglecting the Coulomb potential V_{Coul}. Then the Coulomb energy is calculated by the use of the density profiles thus determined and finally added to the total energy, as in the simple bulk calculations. The optimum cell size is determined by this total energy including the Coulomb energy. The other way is to compare our results with those given by only discarding $V_{\rm Coul}$ in r.h.s. of the Poisson equation, while keeping it in other equations of motion. It is equivalent to the assumption of the *uniform* electron density distribution, which has been used in the previous studies;[3–8] there protons interact with each other and may form a non-uniform structure through the balance between the nuclear surface tension and the Coulomb interaction in a *uniform* electron background. Thus the density rearrangement effect is partially taken into account for protons, while it is completely neglected for electrons. The first way may be standard to extract the Coulomb effect and to compare our full calculation with the bulk one; actually this way has been taken in the context of kaon condensation[11] or hadron-quark deconfinement transition.[9] However, we don't take the first way and dare to take the second way here to compare our results with the previous ones given by the uniform-electron calculation.

We show in the right panel of Fig. 3 the results without the Coulomb screening (uniform-electron calculation). The region of each structure (droplet, rod, etc.) is different from that given by the full calculation. Especially, the "bubble" (spherical hole) appears in this case. Since the appearance of various geometrical structures and their region depend on the very subtle energy difference, the Coulomb screening has a significant influence on the sequence of the different pasta phases.

Comparing the case of uniform matter with the case of the pasta phases, one can see that the non-uniform structures reduce the energy. However, the Coulomb screening effect on the bulk EOS (difference between left and right panels of Fig. 3) is rather small.

4.2. *Nuclear Matter in Beta Equilibrium*

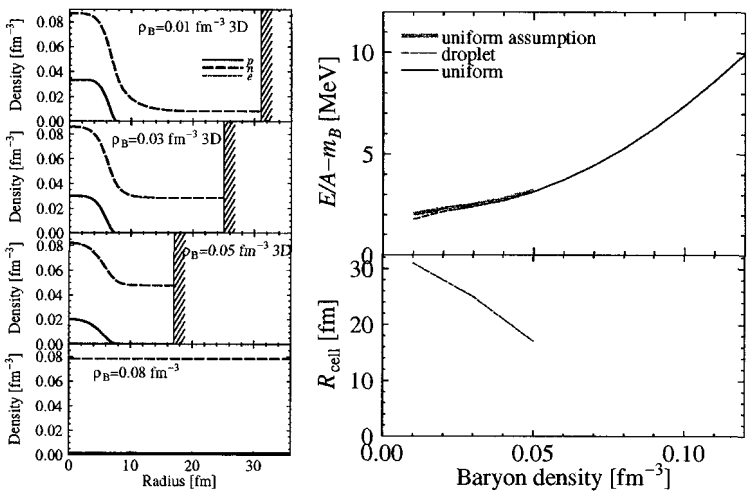

Figure 4. Left: examples of the density profiles of nuclear matter in beta equilibrium. The electron density is too small to see clearly. Right: the binding energy per nucleon and the cell size.

Next, we discuss the nuclear matter in beta equilibrium, which is relevant to stable neutron stars. Figure 4 (left) shows the density profiles at several densities. Only the case for three dimensional (3D) geometrical structure is shown, since 2D and 1D cases are energetically unfavored in our calculation. One can see the proton-enriched droplets embedded into

the neutron sea at low densities. The EOS with the 3D phases is shown in the right panel of Fig. 4. In the beta equilibrium nuclear matter the effect of the non-uniform structure becomes much less compared to that for symmetric nuclear matter. Since the electron fraction is small, the Coulomb screening effect should not be remarkable.

5. Summary and Concluding Remarks

We have discussed the low-density nuclear matter structures "nuclear pastas" and elucidated the Coulomb screening effect. Using a self-consistent framework based on DFT and RMF, we took into account the Coulomb interaction in a proper way and numerically solved the coupled equations of motion to extract the density profiles of nucleons.

First we have checked how realistic our framework is by calculating the bulk properties of finite nuclei as well as the saturation properties of nuclear matter, and found it can describe both features satisfactorily.

In symmetric nuclear matter, we have observed the "nuclear pasta" structures with various geometries at sub-nuclear densities. The appearance of the pasta structures significantly lowers the energy, i.e. softens the EOS, while the energy differences between various geometrical structures are rather small. So the Coulomb screening effect and the rearrangement of the charge density can affect such changes of geometrical structures in spite of that its absolute value is rather small in comparison with nuclear interaction energy.

By comparing the results with and without the Coulomb screening, we have seen that the self-consistent inclusion of the Coulomb interaction changes the phase diagram. In particular one of the pasta configurations appears only when the Coulomb screening is switched off in our calculation. The effects of the Coulomb screening on the EOS, on the other hand, was found to be small.

We have also studied the structure of nuclear matter in beta equilibrium. There we have observed only proton-enriched droplet in the neutron sea. No other geometrical structures like rod, slab, etc. appeared.

Detailed discussions about the Coulomb screening effect on the nuclear pasta phases will be reported elsewhere.

References

1. D. G. Ravenhall, C. J. Pethick and J. R. Wilson, *Phys. Rev. Lett.* **27**, 2066 (1983).

2. M. Hashimoto, H. Seki and M. Yamada, *Prog. Theor. Phys.* **71**, 320 (1984).
3. R. D. Williams and S. E. Koonin, *Nucl. Phys.* **A435**, 844 (1985).
4. K. Oyamatsu, *Nucl. Phys.* **A561**, 431 (1993).
5. C. P. Lorentz, D. G. Ravenhall and C. J. Pethick, *Phys. Rev. Lett.* **25**, 379 (1993).
6. K. S. Cheng, C. C. Yao and Z. G. Dai, *Phys. Rev.* **C55**, 2092 (1997).
7. T. Maruyama, K. Niita, K. Oyamatsu, T. Maruyama, S. Chiba and A. Iwamoto, *Phys. Rev.* **C57**, 655 (1998). T. Kido, T. Maruyama, K. Niita and S. Chiba, *Nucl. Phys.* **A663-664**, 877 (2000).
8. G. Watanabe, K. Iida and K. Sato, *Nucl. Phys.* **A676**, 445 (2000); G. Watanabe, K. Sato, K. Yasuoka and T. Ebisuzaki, *Phys. Rev.* **C66**, 012801 (2002).
9. D.N. Voskresensky, M. Yasuhira and T. Tatsumi, *Phys. Lett.* **B541**, 93 (2002); *Nucl. Phys.* **A723**, 291 (2003); T. Tatsumi and D. N. Voskresensky, this proceedings (nucl-th/0312114).
10. *Density Functional Theory*, ed. E. K. U. Gross and R. M. Dreizler, Plenum Press (1995).
11. T. Maruyama et al., this proceedings.
12. K. Oyamatsu et al., this proceedings.

VIII. Stellar Abundance, Galactic Chemical Evolution and Nucleo-Cosmochronology

This page intentionally left blank

MEASUREMENTS OF LI AND EU ISOTOPE ABUNDANCES IN METAL-DEFICIENT STARS

WAKO AOKI

National Astronomical Observatory of Japan
2-21-1, Osawa, Mitaka, Tokyo, 181-8588 Japan
E-mail: aokiwako@nao.ac.jp

Measurements of isotope abundances give quite strong constraints on nucleosynthesis models. High resolution spectrographs recently mounted on large telescopes enable us to measure isotope abundances for several elements in metal-deficient stars. We report on the measurements of isotope abundances for Europium and Lithium using the 8.2m Subaru Telescope.

1. Measurements of isotope abundances in stellar photospheres

Measurements of chemical abundances in stellar photospheres have been giving valuable information to understand the nucleosynthesis processes in the universe. The measurements are made by the detailed analysis of stellar spectra obtained with high resolution spectrograph using model stellar photospheres. The analyses are generally made for *elemental* abundances rather than *isotopic* ones, because the spectral lines are basically determined by the chemical nature rather than the mass of the nuclei.

For this reason, the prediction by nucleosynthesis models are usually reduced to the *elemental* abundances to compare with observed chemical abundances measured for stars. An exception is the isotope composition in solar system material, most of which can be measured by the analysis of meteorites. Measurements of *isotope* abnundacnes for stars give quite strong constraints on nucleosynthesis models.

Though the measurements of isotope abundances in stellar photospheres are difficult, there are some opportunities (Table 1). One is to use molecular spectra, which are sometimes significantly affected by the difference of mass of the nuclei[1]. For instance, carbon isotope ratios ($^{12}C/^{13}C$) has been measured for a number of cool stars in field stars in our Galaxy as well as those in clusters from the analyses of spectra of carbon-bearing molecules (e.g.,

Table 1. Measurements of isotope fractions in stellar photospheres

isotopes	features	objects	references
$^{6}Li/^{7}Li$	Li I 6708 Å	metal-deficient stars	5,6,7
$^{12}C/^{13}C$	CH, CN, CO, C_2	cool stars	9,10,11
$^{16}O/^{17}O/^{18}O$	OH	cool stars	12
$^{24}Mg/^{25}Mg/^{26}Mg$	MgH 5130 Å	metal-deficient stars	13,2
$^{28}Si/^{29}Si/^{30}Si$	SiO	cool stars	15
Ba (even/odd)	Ba II 4554 Å	metal-deficient stars	14,16
$^{151}Eu/^{153}Eu$	Eu II 4205 Å etc.	metal-deficient stars	17,18,19

CH, CN, CO). The carbon isotope ratio is a quite useful indicator of the evolutionary stages of giant stars. Recent analysis of MgH lines have made a rapid progress in the understanding of magnesium isotope abundances (^{24}Mg, ^{25}Mg, and ^{26}Mg) in field and globular cluster stars (e.g., Yong et al.[2]). These results have impact on the interpretation of the wavelength shifts of Mg resonance lines found in some quasar absorption systems[3,4], which is sometimes interpreted as an evidence of the time variation of the fine structure constant. Oxygen and silicon isotope abundances have been measured for cool stars using molecular spectra in near infrared ranges (see references in Table 1).

The atomic spectra of light elements are also affected by the difference of the mass of the nuclei. The isotope shifts of hydrogen lines are well known, and are measured in many astronomical objects including quasar absorption system (e.g., Kirkman et al.[20]). The third lightest element lithium also shows a rather large isotope shifts in the resonance line at 6708 Å. The measurements of Li isotope abundances are discussed in section 3.

The other possibility is to make use of the hyperfine splitting found in heavy elements. The behavior of hyperfine splitting is different between isotopes of an element in general, and the difference sometimes enables us to estimate the isotope ratios by the detailed profile analysis of absorption lines in stellar spectra. Magain & Zhao[14] analyzed the absorption profile of the Ba II 4554 Å resonance line to estimate the isotope components in the metal-deficient ([Fe/H]~ -2.5) star HD 140283. Since Ba has 7 stable isotopes, it is very difficult to determine the isotope fractions. However, production of ^{138}Ba dominates in the s-process, while isotopes with odd mass number (^{135}Ba and ^{137}Ba) as well as ^{138}Ba are yielded by r-process. For this reason, the ratio of the contribution by r- and s-processes to the Ba in a star can be estimated from the analysis of the Ba line profile. Their result suggested that a significant part of the Ba in HD140283 is produced by the s-process. This is a surprising result because only a small contribution of s-process is expected for stars with such low metallicity.

The Ba isotope fractions in this object is still in controversy (e.g., Lambert et al.[16]).

Recently, analyses of Eu lines were made for some metal-deficient stars. Our recent studies are reported in section 2.

Measurements of the isotope abundances require very high quality spectra, because the analysis is usually based on the detailed profile fitting of spectra calculated using model stellar photosphere to observed ones. The spectral resolution of $R \sim 100,000$ (3km s^{-1}) or higher is desirable to fully resolve the stellar spectra which are intrinsically broadened by thermal motion and turbulence in the photosphere with several km s^{-1}. In order to obtain high signal-to-noise spectra with such high spectral resolution, large telescopes (e.g., the ESO Very Large Telescopes, the Subaru Telescope) and high resolution spectrographs are required. In this paper, we report the recent isotope measurements based on the high resolution spectra obtained with the High Dispersion Spectrograph (HDS[21]) of the 8.2m Subaru Telescope.

2. Eu isotopes in very metal-deficient stars

Eu has two isotopes with odd mass number (^{151}Eu and ^{153}Eu). The effect of hyperfine splitting is significant in both isotopes, but the degree of the splitting is quite different. Hence, this element is an ideal case to measure isotope ratios. An accurate line list including hyperfine splitting was recently provided by Lawler et al.[22], and, using this line list, Eu isotope ratios were measured for three metal-deficient stars by Sneden et al.[17].

2.1. *Eu isotopes produced by r-process*

Figure 1 shows observed spectra of the Eu II 4205 Å line for three stars[19]. HD 6268 (top panel) is known to have moderate enhancements of neutron-capture elements whose elemental abundance pattern is well explained by the r-process nucleosynthesis[23]. The wavelengths and relative strength of the hyperfine components for ^{151}Eu and ^{153}Eu are shown in the top panel. Since the hyperfine splitting of ^{151}Eu is much more significant than that of the other isotope, in particular in the bluer part of the absorption profile, the isotope ratios can be estimated from the profile analysis. The dotted, solid, and dashed lines show the synthetic spectra calculated using model photospheres for three different isotope fractions (fraction of ^{151}Eu (fr(^{151}Eu)) is set to be 0.38, 0.48, and 0.58). The χ^2 fitting of these synthetic spectra to observed one derives fr(^{151}Eu) to be 0.48 ± 0.04. The

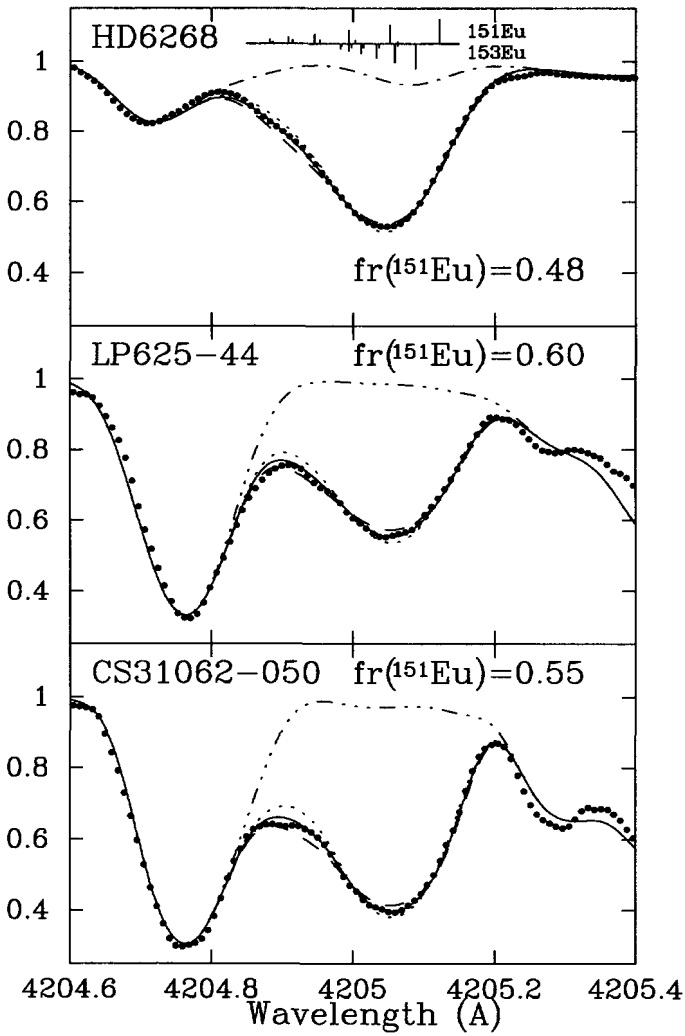

Figure 1. Comparison of the observed spectra (dots) and synthetic ones (lines) for the Eu II 4205 Å line. The name of the object and the adopted fr(^{151}Eu) value are presented in each panel. The solid line shows the synthetic spectra for the adopted fr(^{151}Eu); the dotted and dashed lines show those for ratios which are smaller and larger by 0.10 in fr(^{151}Eu), respectively. The dot-dashed lines show the synthetic spectra for no Eu. The wavelengths and relative strength of the hyperfine components for ^{151}Eu and ^{153}Eu are shown in the top panel.

uncertainty includes the 3σ confidence level of the fitting and errors caused by uncertainties of continuum level, line position, and Eu total abundance.

The result perfectly agrees with that of solar-system material[24]. Since 95% of the Eu in solar-system material is expected to originate from the r-process[25], this ratio well represents that of the r-process component in the solar system. Similar analysis were also made for other three r-process-element-enhanced stars[18] including CS 31082–001 in which uranium was detected by Cayrel et al.[26] (see also Honda [27]). These results and those by Sneden et al.[17] show that the Eu isotope ratios in stars with excesses of r-process elements are consistent with that in solar system material within the errors. The remarkable agreement of *elemental* abundance patterns of these objects with that of solar-system r-process component was found by previous studies (see references of Honda[27]). The analysis of Eu isotopes confirm for the first time this agreement in *isotope* level.

2.2. *Eu isotopes produced by s-process: a new probe of ^{151}Sm branching*

The other two stars shown in Figure 1 (LP 625–44 and CS 31062–050) are very metal-deficient ([Fe/H]~ -2.5), but have large excesses of s-process elements[28,29]. These excesses are explained by the mass transfer across binary systems containing AGB stars which have already evolved to white dwarfs. Indeed, variation of radial velocity has been confirmed for these two stars, indicating they have unseen companions which are presumably white dwarfs. Even though about 95 % of Eu in *solar system material* is believed to originate from r-process, and this element is sometimes refereed to as 'r-process element', the majority of the Eu in these two metal-deficient stars are estimated to originate from the s-process from the abundance patterns of elements between Ba and Eu [28,29].

The ^{151}Eu fractions derived for LP 625–44 and CS 31062–050 are 0.60 and 0.55, respectively, with uncertainties of about ± 0.05. This is the first estimate of the Eu isotope fractions produced by s-process, because that can not be estimated from solar system material in which r-process contribution is dominant. These values are higher than found in solar-system material (fr(^{151}Eu)=0.478). However, they agree well with the predictions of recent s-process models by Arlandini et al.[25], who deduced fr(^{151}Eu)=0.541 and 0.585 from their best-fit stellar and classical models, respectively.

The Eu isotope fractions are quite useful as a probe of ^{151}Sm branching of s-process nucleosynthesis (Figure 2). For ^{151}Sm, whose half-life is about 90 years, the β-decay rate is strongly dependent on temperature, while the neutron capture rate is not. This makes the ^{151}Sm branching an excellent

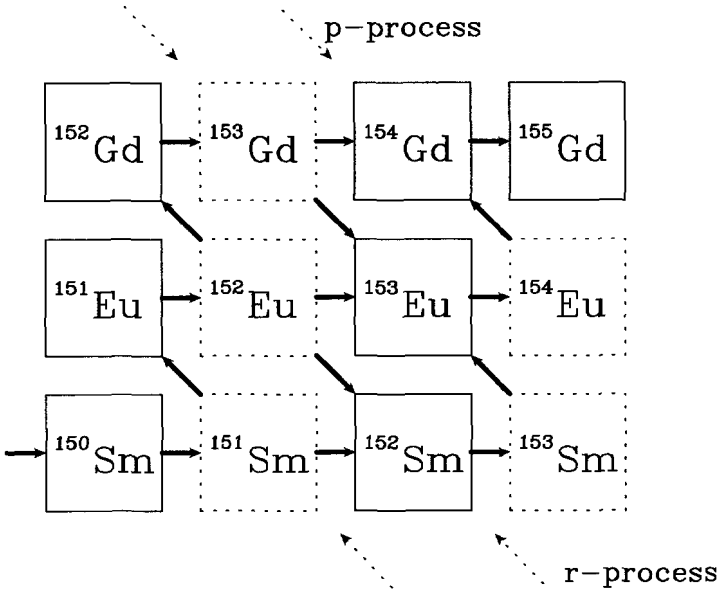

Figure 2. The s-process reaction path around the ^{151}Sm branching. Unstable nuclei are shown by boxes with dotted lines.

thermometer[30]. Previously, this branching has been analyzed using the ^{152}Gd and ^{154}Gd isotope ratios in solar-system material, which are believed to be significantly affected by this branching (e.g., Beer et al.[31]; Wisshak et al.[30]). One difficulty in this approach is that these Gd isotopes are affected by a small amount of contamination from the p-process, though they are shielded from the r-process.

We have made an analysis using the thermally pulsed s-process models, using updated reaction rates (see Aoki et al.[19]). Figure 3 shows the fr(^{151}Eu) values calculated by our model. They are plotted as a function of neutron density ($N_{\rm n}$) for four temperatures (kT = 10, 15, 20, and 30 keV). Also shown for comparison by the hatched area is the fr(^{151}Eu) range deduced for the s-process-element-enhanced star LP 625–44 (the upper panel) and CS 31062–050 (the lower panel). As can be seen in this figure, the fr(^{151}Eu) value is rather sensitive to the ambient temperature and neutron density during the s-process.

The fr(^{151}Eu) value is maximized in the range of neutron density from $N_{\rm n} = 5\times\ 10^7$ to 10^9 cm^{-3}. For $N_{\rm n} > 10^7$ cm^{-3}, the branching factor at ^{151}Sm is higher than 0.9, and the nuclear flow bypasses ^{151}Eu. In this

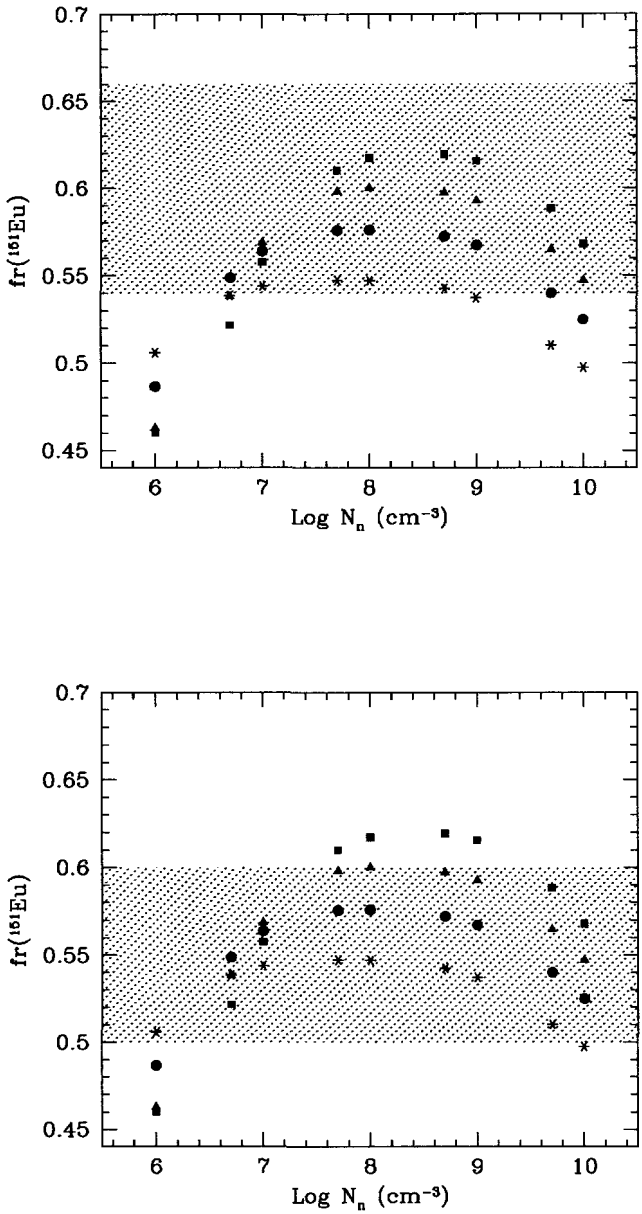

Figure 3. The fr(^{151}Eu) values calculated for four temperatures (squares: $kT = 30$ keV, triangles: 20 keV, circles: 15 keV, and asterisks: 10 keV) as a function of neutron density ($N_{\rm n}$). The upper and lower panels compare the calculations with the observed results for LP 625–44 and CS 31062–050, respectively.

case, the fr(^{151}Eu) value decreases with increasing neutron density by the effect of branching at ^{153}Sm. In contrast, in the range of low neutron density ($N_n < 10^7$ cm^{-3}), the nuclear flow passes ^{151}Eu and ^{152}Gd, and the electron-capture on ^{153}Gd is comparable with, or faster than, the neutron capture, which contributes to the production of ^{153}Eu. This results in the decrease of fr(^{151}Eu) with decreasing neutron density in the low ($N_n \lesssim 10^7$ cm^{-3}) range (see Aoki et al.[19] for more details).

The comparison of the calculations with the observational results indicates that s-processes with high neutron density ($\log N_n \gtrsim 9$) and low temperature ($kT \lesssim 20$ keV), or those with quite low neutron density ($N_n < 10^7$cm^{-3}), are not allowed for LP 625-44 (the upper panel of Figure 3). For CS 31062–050 (the lower panel), the process with high temperature ($kT \gtrsim 30$ keV) and medium neutron density ($10^8 \lesssim N_n \lesssim 10^9$cm^{-3}) is not allowed. These are new constraints on s-process nucleosynthesis provided by the Eu isotope analysis.

Recent models of AGB stars show that the abundance patterns of nuclei in branchings are affected by the s-process both during the thermal pulses and between pulses (e.g., Arlandini et al.[25]). The reaction which provides neutron in the former phase is ^{22}Ne$(\alpha, n)^{25}$Mg, which produces a neutron density as high as 10^8–10^{10} cm^{-3}. In the interpulse phase, ^{13}C$(\alpha, n)^{16}$O is assumed to be the neutron source reaction, which leads to a lower neutron density ($N_n \sim 10^7$ cm^{-3}).

Though the uncertainties in measurements are still large, the comparison of observational results with model calculations in Figure 3 suggests that the contribution of s-process with low temperature *between* the thermal pulses is large in CS 31062–050, while the process *during* thermal pulse plays an important role in LP 625–44. This suggests the s-processes contributed to these two stars occurred in quite different conditions. It should be noted that their Pb/Ba abundance ratios are significantly different[28,29]. The low Pb/Ba ratio of LP 625–44 cannot be explained by standard AGB models with low metallicity (e.g. Busso et al.[32]), and another model for a possible s-process during the thermal pulse was proposed by Iwamoto et al.[33]. Further studies for Eu isotopes as well as elemental abundances with higher accuracy are clearly desirable to understand the s-process nucleosynthesis in very metal-deficient AGB stars.

It should also be noted that, before deriving a clear conclusion, more accurate reaction rates for isotopes around the branching point are required. Indeed, our first analysis using previous neutron-capture rate of ^{151}Sm which is about 50% higher than that used in the present work re-

sults in lower ^{151}Eu fractions by 0.05-0.08. New experiments to determine the neutron capture cross section of ^{151}Sm are highly desirable to fix ratios of ^{151}Eu/^{153}Eu and also ^{152}Gd/^{154}Gd.

3. Li isotopes

A number of studies have been made to accurately determine lithium abundances in metal-deficient main-sequence stars to constrain the big-bang nucleosynthesis (see Coc et al.[34]). There are two stable isotopes of this element (^{6}Li and ^{7}Li), and ^{7}Li is believed to be dominant in most stars (the isotope ratio in solar system material is ^{6}Li/^{7}Li = 0.08). The plateau found in the abundance of this element in most metal-deficient stars has been interpreted as the result of ^{7}Li production in the big bang nucleosynthesis.

However, the value of the ^{7}Li abundance plateau ($\log\epsilon$ (^{7}Li) $\sim$ 2.2) is by 0.4-0.5 dex lower than that expected from the standard bin-bang nucleosynthesis model constrained by the recent measurements of cosmic microwave background radiation by WMAP and the cosmic D/H ratios [34]). An important uncertainty in observational data is a possible depletion of Li in the stellar photosphere from its original value. Since ^{6}Li is more easily destroyed during stellar evolution than ^{7}Li, the depletion of ^{7}Li will be excluded if ^{6}Li is detected in the same object. This is the cosmological interest to search for ^{6}Li in metal-deficient main-sequence stars.

In addition, the origin of ^{6}Li in very metal-deficient stars is still unclear, while the major producer of their ^{7}Li would be the big bang nucleosynthesis. The spallation of heavier nuclei by cosmic-rays provided by supernova explosions only explains the ^{6}Li in higher metallicity. Recently, Suzuki & Inoue[35] proposed shocks produced by the formation of the large scale structure of the Galaxy as a new source of cosmic-ray. The metallicity dependence of Li isotope ratios is expected to be a key to understand the origin of ^{6}Li (see references in Table 1).

^{6}Li has been first detected by Smith et al.[5] for the metal-deficient ([Fe/H]= -2.2) star HD84937. Subsequent studies determined the ^{6}Li/^{7}Li isotope ratios to be about 0.05 for a few objects with similar metallicity.

We have started an observational program using the Subaru Telescope to measure ^{6}Li/^{7}Li ratios to extend the study to lower metallicity. As the first sample of this program, we obtained a very high quality spectrum (R = 95,000 and S/N = 1000) of the bright subgiant HD140283, which has the lowest metallicity ([Fe/H]= -2.5) among the objects for which Li isotopes have been tried to measure to date. The detailed profile analysis

for the Li I 6708 Å line showed no evidence of ^{6}Li in this object, and determined a quite low upper limit on the Li isotope ratio (^{6}Li/^{7}Li$<$ 0.026). The low upper-limit of ^{6}Li/^{7}Li may indicate a decrease of ^{6}Li at the lowest metallicity. However, unfortunately, this object may be sufficiently cool that ^{6}Li was affected by internal processes of the star itself, even though ^{7}Li and Be abundances show no depletion compared with other stars with similar metallicity.

In order to derive a clear conclusion, we also have obtained high quality spectra for several main-sequence stars with lower metallicity. Measurements of Li isotopes for larger sample of metal-deficient main-sequence stars are ongoing using the ESO VLT. The behavior of Li isotopes in lowest metallicity will be soon revealed by these intensive studies.

Acknowledgments

Figure 3 was provided by N. Iwamoto who carried out the s-process model calculations.

References

1. Herzberg, G., 'Molecular Spectra and Modecular Structure. I., Spectra of Diatomic Molecules', Van Nostrand Reinhold Company, New York (1950)
2. Yong, D., Lambert, D. L., & Ivans, I. I., ApJ, 599, 1357 (2003)
3. Ashenfelter, T. P., Mathews, G. J., & Olive, K. A., ApJL, in press
4. Otsuki, K. et al. 2004, this volume
5. Smith, V. V., Lambert, D. L., & Nissen, P., ApJ, 408, 262 (1993)
6. Smith, V. V., Lambert, D. L., & Nissen, P., ApJ, 506, 405 (1998)
7. Nissen, P. E., Lambert, D. L., Primas, F., & Smith, V. V., A&A, 348, 211 (1999)
8. Cayrel, R., Spite, M., Spite, F., Vangioni-Flam, E., Cassé, M., & Audouze, J., A&A, 343, 923 (1999)
9. Sneden, C., Pilachowski, C. A., & Vandenberg, D. A., ApJ, 311, 826 (1986)
10. Lambert, D. L., Gustafsson, B., Eriksson, K., Hinkle, K. H., ApJS, 62, 373 (1986)
11. Aoki, W., & Tsuji, T., A&A, 317, 845 (1997)
12. Harris, M. J., Lambert, D. L. & Smith, V. V., ApJ, 292, 620 (1985)
13. McWilliam, A., Lambert, D. L., MNRAS, 230, 573 (1988)
14. Magain, P. & Zhao, G., A&A, 268, L27 (1993)
15. Tsuji, T., Ohnaka, K., Hinkle, K. H., & Ridgeway, S. T., A&A, 289, 469 (1994)
16. Lambert, D. L., Allende Prieto, C., MNRAS, 335, 325 (2002)
17. Sneden, C., Cowan, J. J., Lawler, J. E., Burles, S., Beers, T. C. & Fuller, G. M., ApJ, 566, L25 (2002)

18. Aoki, W., Honda, S., Beers, T. C., & Sneden, C., ApJ, 586, 506 (2003a)
19. Aoki, W., Ryan, S. G., Iwamoto, N., Beers, T. C., Norris, J. E., Ando, H., Kajino, T., Mathews, G. J., & Fujimoto, M. Y., ApJ, 592, L67 (2003b)
20. Kirkman, D., Tytler, D., Suzuki, N., O'Meara, J. M., & Lubin, D., ApJS, 149, 1 (2003)
21. Noguchi, K., Aoki, W., Kawanomoto, S., et al., PASJ, 54, 855 (2002)
22. Lawler, J. E., Wickliffe, M. E., Den Hartog, E. A. & Sneden, C., ApJ, 563, 1075 (2001)
23. Honda, S.. Aoki, W., Kajino, T., Ando, H., Beers, T. C., Izumiura, H., Sadakane, K., Takada-Hidai, M. 2004, submitted to ApJ
24. Anders, E. & Grevesse, N., Geochem. Cosmochim. Acta, 53, 197 (1989)
25. Arlandini, C., Käppeler, F., Wisshak, K., Gallino, R., Lugaro, M., Busso, M. & Straniero, O., ApJ, 525, 886 (1999)
26. Cayrel, R. et al., Nature, 409, 691 (2001)
27. Honda, S. 2004, *this volume*
28. Aoki, W., Ryan, S.G., Norris, J.E., Beers, T.C., Ando, H., Iwamoto, N., Kajino, T., Mathews, G. J. & Fujimoto, M.Y., ApJ, 561, 346 (2001)
29. Aoki, W., Ryan, S. G., Norris, J. E., Beers, T. C., Ando, H., & Tsangarides S., ApJ, 580, 1149 (2002b)
30. Wisshak, K., Voss, F., Käppeler, F., Guber, K., Kazakov, L., Kornilov, N., Uhl, M., & Reffo, G., Phys. Rev. C, 52, 2762 (1995)
31. Beer, H., & Macklin, R.L., ApJ, 331, 1047 (1988)
32. Busso, M., Gallino, R., & Wasserburg, G. J., ARAA, 37, 239 (1999)
33. Iwamoto, N., Kajino, T., Mathews, G. J., Fujimoto, M. Y., Aoki, W. 2004, ApJ, in press
34. Coc, A. et al. 2004, this volume
35. Suzuki, K. T. & Inoue, S., ApJ, 573, 168 (2002)

SPECTROSCOPIC STUDIES OF R-PROCESS ELEMENTS IN VERY METAL-POOR STARS WITH SUBARU/HDS*

S. HONDA, W. AOKI, T. KAJINO AND H. ANDO
National Astronomical Observatory of Japan
2-21-1,
Osawa Mitaka, Tokyo, Japan
E-mail: honda@optik.mtk.nao.ac.jp

T. C. BEERS
Department of Physics and Astronomy, Michigan State University

SUBARU/HDS GROUP

We present the abundance analyses for the neutron-capture elements in very metal-poor stars based on the high-quality spectra obtained with the Subaru Telescope High Dispersion Spectrograph. Our study covers elements from light neutron-capture nuclei to the heaviest ones. The abundance patterns of elements around Ba and Eu are quite similar to that of the r-process component in solar-system material, suggesting the origin of neutron-capture elements is r-process in these metal-poor stars. However, the abundance ratios between Sr and Ba show a very large scatter. Th/Eu ratios also show a scatter, even though that is much smaller than the scatter found in Sr/Ba. These results provide a quite useful constraints on r-process modeling and will be useful to search for the sites of this process.

1. Introduction

Metal-poor stars are believed to be born in the early era of the Galaxy, and their chemical composition would be determined by a small number of nucleosynthetic events. This indicates that we can learn the individual nucleosynthesis processes from the detailed analyses of chemical abundances for metal-poor stars. These studies also provide important information to understand the evolution of early Galaxy.

Studies of chemical compositions for rather large samples of metal-poor

*Based on data collected at subaru telescope, which is operated by the national astronomical observatory of japan.

stars, based on high dispersion spectroscopy, have been made in the past decade (e.g., McWilliam et al.[1], Ryan et al.[2], Burris et al.[3], Cayrel et al.[4], Honda et al.[5]). These studies have shown the existence of large star-to-star scatters in the abundances of neutron-capture elements at low metallicity. These scatters are usually interpreted as results of the spatial inhomogeneity of the chemical composition of interstellar matter in the early Galaxy [6,7].

Some stars show large excesses of neutron-capture elements. Detailed abundance studies for these objects show that the abundance patterns of heavy neutron-capture elements are quite similar. For example, Sneden et al.[8] found the abundance pattern of CS 22892-052 is well in agreement with that of the solar-system r-process component.

A recent progress in the observational studies is that the measurements of chemical abundances have been extended to elements covering wide ranges in atomic number. Sneden et al.[8] succeeded in the clear detection of Th ($Z = 90$) line in that star. Since Th is a radioactive element with a half-life of about 14 Gyr, it can be used as a cosmochronometer if it's initial abundance is accurately estimated. They reported the age of this star to be 15 Gyr $\pm$ 4 using the Th/Eu ratio, assuming that the initial Th/Eu ratio is the same as that in solar-system material. On the other hand, another recent study of the very metal-poor star CS 31082-001 shows higher Th/Eu ratio than estimated value from the solar-system one[9,10]. These results indicate further studies for the heaviest elements like Th are very useful to understand the r-process nucleosynthesis and to apply the abundances of these elements to chronometry.

2. Observations

We have obtained high-resolution ($R \simeq$ 50,000 or 90,000), high-quality (S/N $>$ 100) spectra of 22 very metal-poor stars ([Fe/H] $\leq$ -2.5) with the High Dispersion Spectrograph (HDS; [11]) fabricated for the 8.2m Subaru Telescope. The spectra cover the wavelength range from 3500 to 5100 Å; equivalent widths were measured for isolated lines of numerous elemental species, including the α elements, the iron-peak elements, and the light and heavy neutron-capture elements.

For some strong lines, as well as lines contaminated by other absorption features, a spectral synthesis technique is required. Our analysis underscores the importance of obtaining accurate line data, including hyperfine splitting, for use in abundance studies of these heavy elements.

3. Results and Discussion

We have confirmed the large star-to-star scatter in the abundance of neutron-capture elements relative to iron (e.g., $\simeq$ 3 dex for Ba/Fe) for observed stars with [Fe/H] < -2.5 (Figure 1). Large scatters are also found in the abundance ratios of almost all neutron-capture elements with $Z \leq 56$.

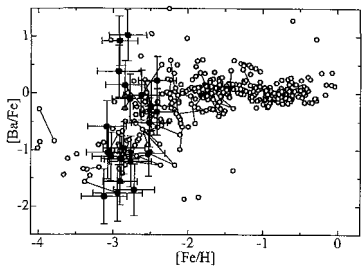

Figure 1. [Ba/Fe] values as a function of [Fe/H]. Our results are shown by filled circles with error bars, while results by previous studies (compilation of literature data taken from Norris et al.[12], McWilliam [13], and Burris et al.[3]) are shown by open circles.

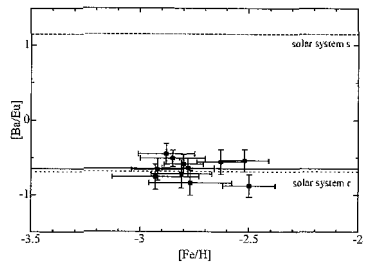

Figure 2. [Ba/Eu] as a function of [Fe/H] for our sample. The solid line indicates mean value of our [Ba/Eu]. The dotted line indicates the [Ba/Eu] of the r-process compotnent in the solar system, while the dashed line means that of the s-process-component in the solar system.

In order to distinguish the contributions of the r- and s-process to these stars, we here investigate the Ba/Eu ratio (Figure 2). The Ba/Eu ratios produced by r- and s-process are quite different. The Ba to Eu ratios in metal-poor stars observed in our program are nearly equal to that of the solar system r-process component (Figure 2). It means that the Ba nuclei in very metal-poor stars have been mostly produced by the r-process. We note that this is partially due to our sample selection. In order to study the r-process in the early Galaxy, we selected some r-process-element-enhanced stars known from the previous studies, and excluded stars known to show excesses of s-process elements from our sample.

Among these stars, we selected seven stars with excesses of r-process elements to discuss the chemical abundance patterns of neutron-capture elements in detail. As expected from the Ba/Eu ratios, these stars show similar abundance patterns of neutron-capture elements around Ba ($Z = 56$) and Eu ($Z = 63$). For each of the seven stars with detectable r-process elements, we use the solar-system r-process abundance pattern as a template to compare the heavy-element abundances of the stars on a common

scale. There is an agreement between the observed abundance pattern of the elements with $56 \leq Z \leq 70$ for these very metal-poor stars and the solar system r-process pattern (Figure 3). On the other hand, the abundance ratios of the light neutron-capture elements ($38 \leq Z \leq 46$) exhibit a rather large dispersion.

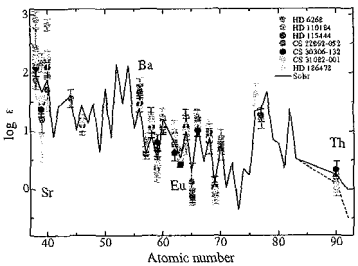

Figure 3. Scaled abundances in our objects compared with the solar system r-process abundance. The dashed line indicates the present solar-system-r-process abundance.

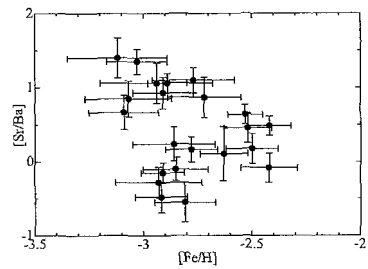

Figure 4. [Sr/Ba] as a function of [Fe/H] for our sample. The scale of the horizontal-axis, the vertical-axis are the same as Figure 2.

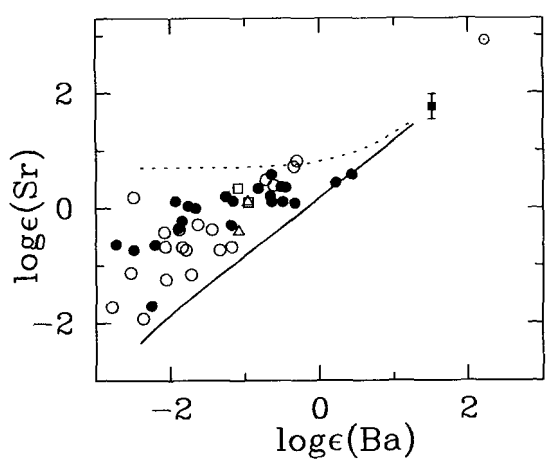

Figure 5. Correlation between abundances of Sr and Ba for objects with [Fe/H]$\lesssim -2.5$ from McWilliam et al.[1] (open circles), Burris et al.[3] (squares), Johnson & Bolte[14] (triangles), and the present work (filled circles). The filled square indicates the values of the r-process component of solar-system material.

By way of contrast, situation is very different in the chemical abundances for lighter and heavier elements. First we discuss about the lighter neutron-capture elements, which would be represented by Sr (Z = 38). To investigate the correlation between Sr and Ba in the same way as that between Ba and Eu, Figure 4 shows the ratio [Sr/Ba] for the stars in our sample as a function of [Fe/H]. The scatter in [Sr/Ba] is very large as compared with [Ba/Eu]. That seems to be larger at lower metallicity, but the dependence on metallicity is not clear. However, there is a correlation between the *scatter* in Sr abundance and the abundance of Ba, as shown in Figure 5. Namely, all Ba-enhanced stars have high Sr abundances, while stars with low (or normal) Ba abundances show a scatter larger than 2 dex. The solid and dotted lines in the figure show the enrichment of Sr and Ba with a constant Sr/Ba ratio for the two cases of initial abundances of Sr and Ba (high and low Sr abundances, respectively). This result suggests that there are at least two processes to enrich Sr in the early Galaxy: one enriches Sr without Ba production, and the other enriches both Sr and Ba. From the astrophysical point of view, it is very important to understand whether these two processes occurred in a single event (e.g., supernova explosion) or in two different sites (e.g., two supernovae by two progenitors with different mass).

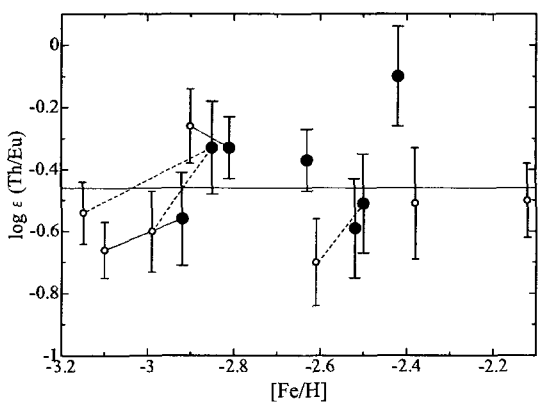

Figure 6. Th/Eu ratios as a function of [Fe/H].

Abundance ratios of heavier neutron-capture elements (e.g., Th) relative to others (e.g., Eu) also provide strong constraints on the r-process

modeling. Th II 4019Å is detected in seven stars in our sample. The results (Th/Eu ratios) are plotted in Figure 6. Previous studies of Th abundances for several metal-poor stars reported that the Th/Eu ratios are quite similar to that in solar-system value, if the Th abundances in metal-poor stars are corrected for the decay of Th in 12-15 Gyr. However, the abundances of Th are slightly higher than the values expected from the solar system r-process pattern in a few metal-poor stars (e.g., CS 30306-132). Th/Eu ratios show a dispersion of about 0.5 dex in our sample (Figure 6). This result indicates the ages of some objects are only a few Gyr, if we assume the initial Th/Eu abundance ratio is the same as that of the solar system. These are too short as the ages of very metal-poor stars, which are believed to be formed in the early Galaxy. We interpret this result that the universality of the abundance pattern of the neutron-capture elements can not be extended to Th ($Z = 90$). This is an expected result from the theoretical models which predict that the production of these heaviest elements is quite sensitive to the condition in the r-process site. Further abundance studies for larger sample will better constrain these models.

References

1. McWilliam, A, Preston, G. W., Sneden, C, AJ **109**, 27 (1995).
2. Ryan, S. G., Norris, J. E., Beers, T. C., ApJ **471**, 254 (1996).
3. Burris, D. L., Pilachowski, C. A., Armandroff, T. E., Sneden, C., Cowan, J. J., & Roe, H ApJ **544**, 302 (2000).
4. Cayrel, R. et al. A&A in press.
5. Honda, S. et al. ApJS in press.
6. Primas, F. in this volume.
7. Ishimaru, Y. in this volume.
8. Sneden, C., McWilliam, A., Preston, G. W., Cowan, J. J., Burris, D. L., & Armosky, ApJ **467**, 819 (1996).
9. Cayrel et al., Nature, 409, 691 (2001)
10. Hill, V. et al. A&A **387**, 560 (2002).
11. Noguchi, K., et al. PASJ **54**, 855 (2002).
12. Norris, J. E., Ryan, S. G., & Beers, T. C. ApJS **107**, 391 (1996).
13. McWilliam, A. AJ **115**, 1640 (1998).
14. Johnson, J. A., & Bolte, M. ApJ **554**, 888 (2001).

LIGHT ELEMENTS PRODUCED BY TYPE IC SUPERNOVAE

K. NAKAMURA AND T. SHIGEYAMA

Research Center for the Early Universe, Graduate School of Science, University of Tokyo, Bunkyo-ku, Tokyo 113-0033, Japan

E-mail: nakamura@resceu.s.u-tokyo.ac.jp, shigeyama@resceu.s.u-tokyo.ac.jp

Recent observations of extremely metal-poor stars suggest that the primary spallation process dominated the light element (Li,Be,B) nucleosynthesis in the early galaxy. To investigate the energy spectra of SN ejecta which mainly consist of C/O, we have performed numerical calculations of type Ic supernova explosions using a relativistic hydrodynamic code with realistic numerical models for massive stars and a realistic equation of states. Moreover, we estimate the yields of light elements by spallation reactions using the energy spectra from our numerical calculations together with empirical cross sections of the reactions. We find that the adiabatic index becomes larger than 4/3 in a mild explosion and the acceleration of ejecta becomes more efficient. We also find that not only highly energetic explosions like SN 1998bw but also normal Ic SNe explosions significantly accelerate their outermost layers beyond the threshold energy of spallation reactions. On the other hand, the accelerated ejecta lose their energy because of interactions with the interstellar neutral atoms before they undergo spallations with the interstellar H and/or He. Though the abundance ratios such as Li/Be and Be/B are compatible with observations, none of type Ic supernovae (SNe Ic) could be main sources of light elements in the Galactic halo, as long as most of the interstellar atoms are not ionized. If 99 % of the interstellar H are ionized, SNe Ic like SN 2002ap can be candidates of light element sources.

1. Introduction

Recent observations of extremely metal-poor stars suggest that, in the early galaxy, the LiBeB nucleosynthesis was dominated by the primary spallation process rather than the secondary [1]. In this light, the yields of LiBeB produced by the spallation reactions between SNe Ic ejecta and the interstellar H and He are estimated [2] under the assumptions of a simple density distribution and the constant adiabatic index. These yields led to a conclusion that SNe Ic significantly contribute to light element nucleosythesis. The adiabatic index is, however, not constant and varies depending on the physical conditions. We use a relativistic hydrodynamic code with real-

istic numerical models for massive stars and a realistic equation of states including both the thermal radiation and ideal gas and estimate the yields of light elements. We also solve the transfer equation to take into account the energy loss of ejecta by ionizing the interstellar H I atoms.

In the following sections, we describe our relativistic hydrodynamic code in the Lagrangian form (§2) and initial conditions (§3). Then we show the result in §4. In §5, we solve the transfer equation and estimate the yields of light elements.

2. Equations

We have constructed a numerical code for relativistic hydrodynamics with a Lagrangian coordinate [3].

Since we are concerned with spherically symmetric explosions, we will write the equations of relativistic hidrodynamics (RHD) of a perfect fluid in the 1-dimensional spherical coordinate system.

$$\frac{d(1/\rho W)}{dt} - 4\pi \frac{\partial (r^2 v)}{\partial m} = 0, \tag{1}$$

$$\frac{d(hWv)}{dt} + 4\pi r^2 \frac{\partial p}{\partial m} + \frac{GM_r}{r^2} = 0, \tag{2}$$

$$\frac{dQ}{dt} + 4\pi \frac{\partial (r^2 pv)}{\partial m} = 0, \tag{3}$$

where t denotes the time, v the radial velocity, G the gravitational constant and M_r the mass included within radius r. ρ, p, W and h denote the proper rest-mass density, the pressure, the fluid Lorentz factor, and the specific enthalpy, respectively. The specific enthalpy is given by

$$h = 1 + \varepsilon + \frac{p}{\rho}, \tag{4}$$

where ε is the specific internal energy. Q is defined by

$$Q = \frac{\rho h W^2 - p - \rho W}{\rho W} - \frac{GM_r}{r}. \tag{5}$$

The Lagrangian coordinate m is related to r through

$$\partial m = \frac{4\pi r^2}{V} \partial r. \tag{6}$$

The gravity is included in the weak limit where no general relativistic effect is prominent. The pressure is described as the sum of the radiation pressure and the gas pressure:

$$p = \frac{a}{3}T^4 + \frac{k\rho T}{\mu m_p}. \tag{7}$$

Here a denotes the radiation constant, T the temperature, k the Boltzmann constant, μ the mean molecular weight, and m_p the mass of proton. The specific internal energy ε is given by

$$\varepsilon = \frac{aT^4}{\rho} + \frac{3kT}{2\mu m_p}. \tag{8}$$

Here we will introduce two kinds of adiabatic indices, γ_1 and γ_2 defined by

$$\gamma_1 = \left(\frac{d\ln p}{d\ln \rho}\right)_S, \tag{9}$$

$$\gamma_2 = \frac{p}{\rho\varepsilon} + 1. \tag{10}$$

To obtain the energy distribution of the ejecta above the threshold energies for cosmic-ray spallation reactions, our models have the masses of the outermost layers well below $10^{-9}M_\odot$.

When we calculate the explosion of a star, we need to set the boundary conditions at the center and the outer edge of the star. The boundary conditions at the outer edge are

$$\begin{aligned} p_{imax+1/2} &= 0, \\ v_{imax+1/2} &= v_{imax}, \end{aligned} \tag{11}$$

where $imax$ is the zone number corresponding to the outermost layer. At the center, which corresponds to the zone interface $i = 1/2$, we consider an imaginary zone $i = 0$, where the physical quantities are given by

$$\begin{aligned} p_0 &= p_1 \\ \rho_0 &= \rho_1 \\ v_0 &= -v_1, \end{aligned} \tag{12}$$

to keep the symmetry with respect to the center.

3. Initial conditions

We consider three models of massive stars immediately before the core collapse [4,5,6]. These stars are originated from $12-40M_{\odot}$ main-sequence stars. They are thought to have undergone intense stellar winds and lost their H-rich and He envelopes. As a result, the stellar surfaces mainly consist of carbon and oxygen at explosion. These three models have corresponding real type Ic supernovae as shown in Table 1. These stars have become fairy compact with radii less than the solar radius. This compactness results in higher pressures at the shock breakout compared with explosion of a star with an extended envelope if the explosion energies per unit ejecta mass are the same. To initiate explosions, we first replace the central Fe core with the point mass located at the center. Then we release the energy in the innermost several zones in the form of thermal energy (or pressure) and trace the evolution of physical quantities. The calculations are stopped when the ejecta keep expanding homologously. The parameters of each model are tabulated in Table 1.

Table 1. Parameters of Stellar Models.

$M_{\rm ms}$ ($M_{\odot}$)	M_* ($M_{\odot}$)	R_* ($R_{\odot}$)	$M_{\rm ej}$ ($M_{\odot}$)	$M_{\rm O}$ ($M_{\odot}$)	$E_{\rm ex}$ ($\times 10^{51}$ergs)	SN
-40	15	0.29	13	10	30	1998bw
20-25	4.6	0.32	2.9	2.1	4	2002ap
12-15	2.4	0.24	0.99	0.66	1	1994I

Note: $M_{\rm ms}$ is the stellar mass on main sequence epoch, M_* and R_* are the stellar mass and radius at core collapse, $M_{\rm ej}$ is the mass of ejecta, $M_{\rm O}$ is the mass of oxygen in the ejecta, $E_{\rm ex}$ is the explosion energy, and SN is the corresponding real supernova.

4. The Energy Distributions

Calculating acceleration of stellar envelopes, we obtain the energy distribution of ejecta for each model. Now, we verify the assumptions of the simple stellar model and constant adiabatic index ($\gamma_1 = \gamma_2 = 4/3$) adopted by the previous work [2].

Figure 1 shows the energy distributions of ejecta for SN 1998bw model calculated from the fitting formula [2] and from our numerical code. Three lines show a good agreement at the high energy region. This means that the adiabatic index is close to 4/3 when the explosion is furious and that the simple density distribution they assumed is good.

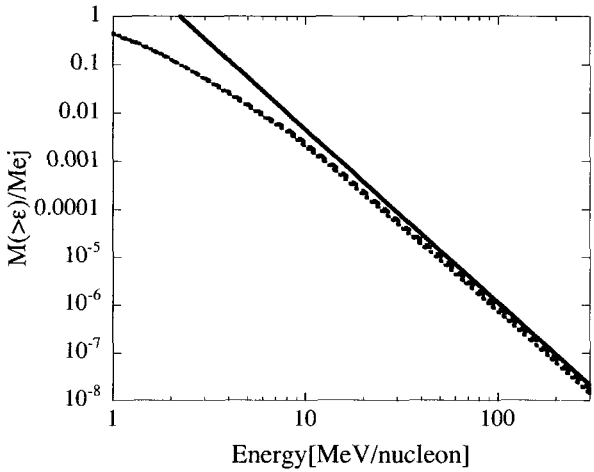

Figure 1. The energy distribution of ejecta for SN1998bw model with $E_{\rm ex} = 3 \times 10^{52}$ ergs. The solid line represents the fitting formula of Fields et al. 2002. The result of our numerical calculation with the constant (4/3) adiabatic index is shown by the dotted line. The dashed line shows the result with the variable adiabatic index. These two lines are hardly distinguishable in this plot.

On the other hand, when the explosion is mild (ex. $E_{\rm ex} = 3 \times 10^{51}$ ergs), our result shows a significant deviation from their fitting formula (Figure 2). If $E_{\rm ex}/M_{\rm ej}$ is small, the adiabatic index would be bigger than 4/3 and the acceleration could become more efficient.

In fact, the adiabatic index defined by equation (9) in the outermost layers becomes bigger than 4/3 when $E_{\rm ex}/M_{\rm ej}$ is relatively small (Figure 3).

5. Light Element Nucleosynthesis

5.1. *Transfer Equation*

The accelerated particles lose their energy when they collide with neutral atoms in the interstellar medium and ionize them. We use the ionization energy loss rate of element i in the ejecta through hydrogen gas, ω_i (MeV/nucleon/s), of the form [7]

$$\omega_i = Z_{{\rm eff},i}^2 \times 1.82 \times 10^{-13} n_{\rm H\,I}/A_i \times \left\{1 + 0.0185 \ln \beta H(\beta - 0.01)\right\} \frac{2\beta^2}{10^{-6} + 2\beta^3}, \quad (13)$$

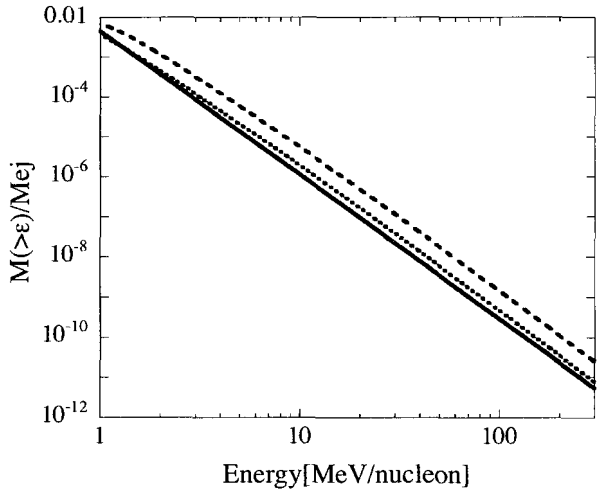

Figure 2. The energy distribution for SN 1998bw model with $E_{\rm ex} = 3 \times 10^{51}$ ergs. The solid, dotted and dashed lines are for the same case as in Figure 1. Our result for the case of variable adiabatic index show a significant deviation from the fitting formula of Fields et al. 2002.

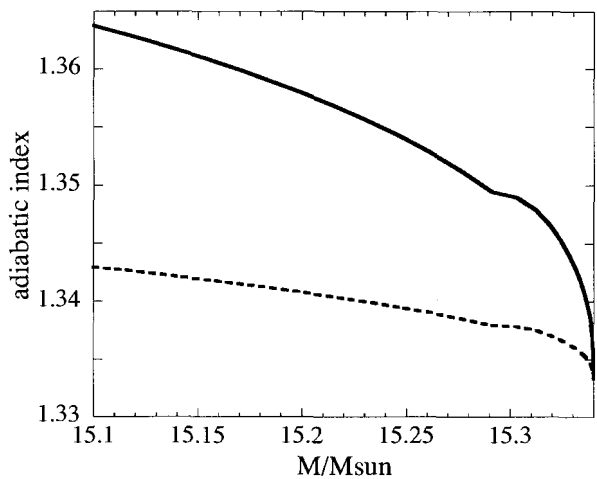

Figure 3. The distributions of adiabatic index for SN1998bw model with $E_{\rm ex} = 3 \times 10^{51}$ ergs (solid line) and 3×10^{52} ergs (dashed). Each line is that of just after shock breakout.

where $n_{\rm H\,I}$ is the number density of neutral hydrogen in the interstellar medium, $\beta = v/c$ and $H(x)$ denotes the Heaviside step function. The effective charge $Z_{{\rm eff},i}$ is expressed as

$$Z_{{\rm eff},i} = Z_i\left\{1 - 1.034\exp\left(-137\beta Z_i^{-0.688}\right)\right\}, \tag{14}$$

where Z_i is the atomic number of the element i in the ejecta.

We use the leaky-box model [8] and the transfer equation for the mass of the element i with an energy per nucleon ϵ at time t, $F_i(\epsilon, t)$, is written as

$$\begin{aligned}\frac{\partial F_i(\epsilon,t)}{\partial t} =& \frac{\partial[\omega_i(\epsilon)F_i(\epsilon,t)]}{\partial\epsilon} \\ &- \left(\frac{F_i(\epsilon,t)}{\Lambda_{\rm esc}} + \frac{F_i(\epsilon,t)}{\Lambda_{n,i}}\right)\rho v_i(\epsilon),\end{aligned} \tag{15}$$

where Λ's are the loss lengths in g cm^{-2}, ρ denotes the mass density of the interstellar medium, $v_i(\epsilon)$ the velocity of the element i with an energy per nucleon of ϵ. $\Lambda_{\rm esc}$ is due to escape from a given system (we assume $\Lambda_{\rm esc} = 100$ g cm^{-2} according to Suzuki & Yoshii 2001 [9]), and $\Lambda_{n,i}$ due to spallation reactions. The latter is expressed as

$$\Lambda_{n,i}(\epsilon) = \frac{n_p m_p + n_{\rm He} m_{\rm He}}{n_p \sigma_{p,i}(\epsilon) + n_{\rm He}\sigma_{{\rm He},i}(\epsilon)}. \tag{16}$$

Here the total cross sections of spallation reactions between particle i and proton or He are denoted by $\sigma_{p,i}$ or $\sigma_{{\rm He},i}$, respectively. The mass of He is denoted by $m_{\rm He}$. The number densities of proton and He in the interstellar medium have been introduced as n_p and $n_{\rm He}$ and we assume that the interstellar medium is uniform and neutral: $n_p = n_{\rm H\,I} = 1\,{\rm cm}^{-3}$ and $n_{\rm He} = 0.1\,{\rm cm}^{-3}$.

Equations (15) for C and O are numerically solved with initial conditions given by the energy distribution presented in the previous section:

$$F_i(\epsilon, 0) = -X_i(\epsilon)\frac{dM(>\epsilon)}{d\epsilon}. \tag{17}$$

Here $X_i(\epsilon)$ denotes the mass fraction of the element i with an energy per nucleon of ϵ. Equations (15) are implicitly integrated with respect to time.

Through the ionization energy loss, the energy spectrum of ejecta becomes harder as time passes as shown in Figure 4. The effect of $\Lambda_{\rm esc}$ is negligible in our calculations. Ionizations reduce the energies of most particles below the threshold energies for the spallation reactions before the particles escape from the system.

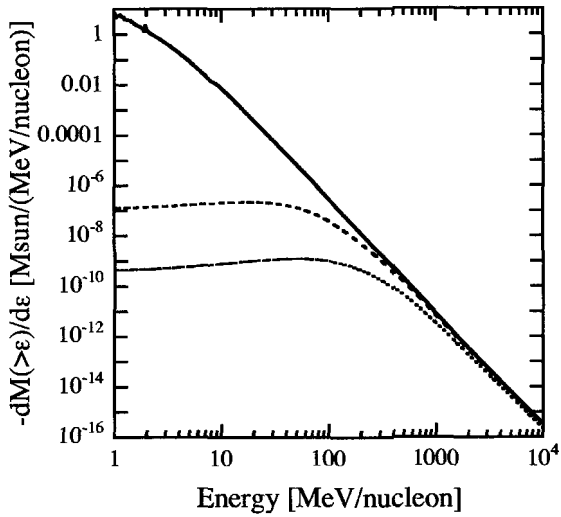

Figure 4. The attenuation of mass spectra of oxygen for SN1998bw model with $E_{ex} = 3 \times 10^{52}$ ergs. The solid line is that of just after shock breakout, dashed line is at $t = 1$ Myr, and dotted line is at $t = 5$ Myr.

5.2. *Yields of Light Elements*

Light elements (LiBeB) are produced through the spallation reactions; C, O + H, He $\rightarrow {}^{6,7}$Li, ^{9}Be, ^{10,11}B. The yield of a light element l via the $i + j \rightarrow l + \cdots$ reaction is estimated by

$$\frac{dN_l}{dt} = n_j \int_{\epsilon_{\min}}^{\epsilon_{\max}} \sigma_{i,j}^{l}(\epsilon) \frac{F_i(\epsilon, t)}{A_i m_p} v_i(\epsilon) d\epsilon, \tag{18}$$

where N_l is the number of the produced light element l, n_j the number density of interstellar H or He, $\sigma_{i,j}^{l}$ the cross section of $i + j \rightarrow l + \cdots$ reaction, A_i the mass number of the element i. The integration with respect to energy is carried out between the minimum and maximum energies per nucleon in the ejecta obtained from our numerical calculations, which are denoted as $\epsilon_{\min}$ and $\epsilon_{\max}$, respectively. We use the empirical formula [10] for the cross sections.

Table 2 summarizes the results. Since the ratios of elements are determined solely by the energy distribution of the injected materials and the energy distributions of all the calculated models have a similar shape, the models give similar isotopic ratios: ^{7}Li/^{6}Li$\sim$1.4 and ^{11}B/^{10}B$\sim$ 3.1. The B isotopic ratio observed in meteorites is 4.05$\pm$0.05. Thus some different

Table 2. Yields of Light Elements ($10^{-7} M_{\odot}$).

Model	^{6} Li	^{7} Li	^{9} Be	^{10} B	^{11} B
SN1998bw	2.38	3.31	0.999	4.38	13.4
SN2002ap	0.0841	0.114	0.0348	0.152	0.464
SN1994I	0.0140	0.0190	0.00578	0.0253	0.0776

sites are responsible for B isotopes in the solar system.

The element ratio B/Be$\sim$ 17.8 from our models can explain this ratio on the surfaces of some halo stars because the average ratio of halo stars are thought to be 20--25 and some halo stars like HD94028 show fairly low ratio as $\sim$ 14. The solar value 35.5 again suggests that B in the solar system must have been synthesized in different sites.

The element abundances of Be are determined for more stars than those of the other light elements Li and B. The observed mass ratios of Be/O on the surfaces of stars [11] range from $\sim 10^{-9}$ to $\sim 2 \times 10^{-8}$. Our result (Be/O $\sim 0.87 \times 10^{-9} - 1.0 \times 10^{-8}$) is in good agreement with this observation.

The observed number ratio Be/H has a value $\sim 10^{-12}$ at [Fe/H]~ -1.5 which is the maximum value of [Fe/H] attained by halo stars of the Galaxy [11]. A chemical evolution model for the Galactic halo [12] suggests that $\sim$ 10 % of a proto-cloud had been converted into stars before the cloud was broken up by supernovae. Thus the mass fraction of massive stars with the initial mass $> 10 M_{\odot}$, that eventually explode as supernovae, is $\sim$ 1.8 % provided that the initial mass function was the Salpeter's one. These values indicate that the yield of Be per unit supernova mass is $M_{\rm Be}/M_{\rm SN} \sim 3.8 \times 10^{-9}$ in the halo. The corresponding values for the three models in Table 2 are 2.5×10^{-9} (SN 1998bw), 1.7×10^{-10} (SN 2002ap), and 4.8×10^{-11} (SN 1994I). Therefore these supernovae cannot be the main production site for Be if all H atoms in the ISM are neutral. The element abundance ratios B/Be from the present models consistent with those for Galactic halo stars indicate that these supernovae cannot explain B in the halo. From the similar argument with observed number ratios Li/H on the surfaces of metal-poor stars, SNe Ic cannot produce the observed amount of Li as long as the ISM is not ionized.

To partially take into account the effects of ionization on the energy distribution of the cosmic-rays from SNe Ic, we have calculated the light element yields when the density of neutral H is $n_{\rm H\,I} = 0.1 n_p$ and $0.01 n_p$ i.e., 90 % and 99% of H atoms are ionized. Table 3 summarizes the results

for SN 1998bw model with $E_{\rm ex} = 3 \times 10^{52}$ ergs. The mass ratio ^{7}Li/^{6}Li slightly decreases with increasing degree of ionization.

Table 3. Yields of Light Elements for various degree of ionization ($10^{-7} M_\odot$).

Degree of ionization	^{6} Li	^{7} Li	^{9} Be	^{10} B	^{11} B
0.00	2.38	3.31	0.999	4.38	13.4
0.90	21.7	29.4	9.05	39.7	123
0.99	154	184	63.0	271	846

6. Conclusion

We investigate the acceleration of the outermost layers of SNe Ic and find that the adiabatic index could be bigger than 4/3 if $E_{\rm ex}/M_{\rm ej}$ is relatively small. It makes the acceleration of ejecta more efficient and not only highly energetic explosions like SN 1998bw but also normal SN Ic explosions significantly accelerate their outermost layers beyond the threshold energy of spallation reactions. However, if the most of interstellar atoms are neutral, the accelerated elements rapidly lose their energy when they collide with interstellar atoms and ionize them, and normal SNe Ic could not be the main source of light elements.

References

1. Duncan, D. K., Lambert, D. L., & Lemke, M., *ApJ* **401**, 584 (1992)
2. Fields, B. D., Daigne, F., Cassé, M., & Vangioni-Flam, E., *ApJ* **581**, 389 (2002)
3. Martí, J. M., & Müller, E., *J. Comput. Phys.* **123**, 1 (1996)
4. Nakamura, T. et al., *ApJ* **550**, 991 (2001)
5. Mazzali, P. A. et al., *ApJ* **572**, L61 (2002)
6. Iwamoto, K. et al., *ApJ* **437**, L115 (1994)
7. Schlickeiser, R., *in Cosmic ray astrophysics / Reinhard Schlickeiser, Astronomy and Astrophysics Library; Physics and Astronomy Online Library. Berlin: Springer. 2002, XV* (2002)
8. Meneguzzi, M., Audouze, J., & Reeves, H., *A&A* **15**, 337 (1971)
9. Suzuki, T. K. & Yoshii, Y., *ApJ* **549**, 303 (2001)
10. Read, S. M. & Viola, V. E., *Atomic Data and Nucl. Data Tables* **31**, 359 (1984)
11. Boesgaard, A. M. e al., *AJ* 117, 1549 (1999)
12. Tsujimoto, T., Shigeyama, T., & Yoshii, Y., *ApJ* **519**, L63 (1999)

SUPERNOVA NEUTRINOS AND THEIR INFLUENCE ON NUCLEOSYNTHESIS: LIGHT ELEMENTS AND R-PROCESS ELEMENTS

TAKASHI YOSHIDA

Astronomical Data Analysis Center, National Astronomical Observatory of Japan

Department of Astronomy, Graduate School of Science, University of Tokyo

MARIKO TERASAWA

Center for Nuclear Study, Graduate School of Science, University of Tokyo

TOSHITAKA KAJINO

National Astronomical Observatory of Japan and The Graduate School for Advanced Studies

Department of Astronomy, Graduate School of Science, University of Tokyo

Advanced Science Research Center, Japan Atomic Energy Research Institute

KOHSUKE SUMIYOSHI

Numazu College of Technology

The influence of the neutrino luminosity on the nucleosynthesis of the light elements ^{7}Li and ^{11}B and the r-process heavy elements in Type II Supernovae is investigated. Common models of the neutrino luminosity, which are parameterized by the total energy E_ν and decay time τ_ν, are adopted to understand both processes. The supernova explosion of a 16.2 $M_\odot$ star, which corresponds to SN 1987A, is calculated and the light element synthesis is pursued by postprocessing. The ejected masses of ^{7}Li and ^{11}B are roughly proportional to E_ν but are insensitive to τ_ν. As for the r-process, the same models of neutrino luminosity are adopted in the neutrino-driven wind models of a 1.4 $M_\odot$ neutron star. The r-process is affected through the peak neutrino luminosity, which relates to E_ν/τ_ν. An unsolved problem of the overproduction of ^{11}B in the galactic chemical evolution is discussed. The total neutrino energy should be smaller than 1.2×10^{53} ergs to avoid the overproduction of ^{11}B, which is too small to accept compared to 3.0×10^{53} ergs deduced from the observation of SN 1987A. We here propose to reduce the temperature of $\nu_{\mu,\tau}$ and $\bar{\nu}_{\mu,\tau}$ to 6.0 MeV/k in a model with $E_\nu \sim 3 \times 10^{53}$ ergs and $\tau_\nu = 9.0$ s. This modification is shown to resolve the overproduction problem of ^{11}B while still preserving a successful r-process abundance pattern.

1. Introduction

The neutrino interactions induced by a huge amount of neutrinos emitted during supernova explosions can change chemical compositions of some elements in the supernovae. There are two nucleosynthesis processes affected by the neutrino interactions: the light element synthesis in the outer He-rich layer [1-5] and the r-process in a "hot bubble" region just above a proto neutron star [6-9]. Since these nucleosynthesis processes occur in different sites in the supernova ejecta, they were investigated individually using different sets of the supernova neutrinos. For the light element synthesis, the average energies of the supernova neutrino spectra were set to be 25 MeV for $\nu_{\mu,\tau}$ and $\bar{\nu}_{\mu,\tau}$ and 13 MeV for $\nu_{\rm e}$ and $\bar{\nu}_{\rm e}$ [1-5]. For most cases of the r-process calculations, they were set to be about 30 MeV for $\nu_{\mu,\tau}$ and $\bar{\nu}_{\mu,\tau}$, 20 MeV for $\bar{\nu}_{\rm e}$ and 10 MeV for $\nu_{\rm e}$ [7-9]. Thus, we should investigate both of the processes using *common* supernova neutrino models.

Supernova explosions contribute the production of ^{7}Li and ^{11}B during the Galactic Chemical Evolution (GCE) [10-13]. Supernova contribution of the ^{11}B amount is determined to reproduce meteoritic ^{11}B/^{10}B ratio (=4.05, [14]) at the solar metallicity. Since ^{10}B is produced by the Galactic cosmic rays (GCRs) and the ^{11}B/^{10}B ratio obtained from the GCRs is 2.5 (e.g., [10]), supernova contribution of ^{11}B is needed. However, the ^{11}B amount evaluated from supernova nucleosynthesis models by [2] is overproduced by a factor of 2.5 to 5.6 compared to that evaluated from the GCE models [10-13]. Although the characteristics of the supernova neutrinos affect not only the light element nucleosynthesis but also the r-process, the dependence of the supernova neutrinos on these nucleosynthesis processes has not precisely investigated. Thus, we should find supernova neutrino models appropriate for both of the GCE of ^{11}B and the r-process abundance pattern.

We investigate the dependence of the supernova neutrinos on the synthesis of the light elements and the r-process heavy elements using common supernova neutrino models. We discuss supernova neutrino models appropriate for the ^{11}B amount in the GCE and the r-process abundance pattern. In this proceeding, we present summary of our present study. More details are discussed in Yoshida, Terasawa, Kajino, and Sumiyoshi [15].

2. Calculations

We use common sets of the supernova neutrinos for the light element synthesis and the r-process. The neutrino luminosity L_{ν_i} ($\nu_i = \nu_{\rm e}, \nu_\mu, \nu_\tau$ and their antiparticles) at a radius r is assumed to be the same for all neutrino

Table 1. The adopted parameter sets of neutrino luminosity models.

Model	E_ν (ergs)	τ_ν (s)	$L_{\nu_i,0}$ (ergs s^{-1})	$L_{\nu_i,\mathrm{half}}$ (ergs s^{-1})	$L_{\nu_i,\mathrm{end}}$ (ergs s^{-1})	t_{end} (s)
	$T_{\nu_{\mu,\tau}} = T_{\bar{\nu}_{\mu,\tau}} = 8.0$ MeV/k, $T_{\nu_e} = 3.2$ MeV/k, and $T_{\bar{\nu}_e} = 5.0$ MeV/k.					
LL	1.0×10^{53}	3.0	5.56×10^{51}	4.42×10^{51}	3.50×10^{51}	1.39
LS	1.0×10^{53}	1.0	16.67×10^{51}	7.64×10^{51}	3.50×10^{51}	1.56
HL	3.0×10^{53}	3.0	16.67×10^{51}	7.64×10^{51}	3.50×10^{51}	4.68
	$T_{\nu_{\mu,\tau}} = T_{\bar{\nu}_{\mu,\tau}} = 6.0$ MeV/k, $T_{\nu_e} = 3.2$ MeV/k, and $T_{\bar{\nu}_e} = 5.0$ MeV/k.					
MLL	3.0×10^{53}	9.0	5.56×10^{51}	4.42×10^{51}	3.50×10^{51}	4.16

flavors and to decrease exponentially with a decay time τ_ν

$$L_{\nu_i} = \frac{1}{6}\frac{E_\nu}{\tau_\nu} \exp\left(-\frac{t - r/c}{\tau_\nu}\right) \Theta(t - r/c), \tag{1}$$

where E_ν is the total neutrino energy, c is the speed of light, and $\Theta(x)$ is the step function defined by $\Theta(x) = 1$ for $x \geq 0$ and 0 for $x < 0$.

We set the total neutrino energy E_ν and the decay time of the neutrino luminosity τ_ν as parameters. We vary E_ν between 1.0×10^{53} and 6.0×10^{53} ergs. We set τ_ν as 1 s and 3 s. The neutrino energy spectra are assumed to obey Fermi distributions with zero chemical potential. We set the temperature of $\nu_{\mu,\tau}$ and $\bar{\nu}_{\mu,\tau}$ as 8.0 MeV/k and set those of ν_e and $\bar{\nu}_e$ as 3.2 MeV/k and 5.0 MeV/k, respectively. The corresponding average energies of $\nu_{\mu,\tau}$ and $\bar{\nu}_{\mu,\tau}$, ν_e, and $\bar{\nu}_e$ are 25 MeV, 10 MeV, and 16 MeV.

For the light element synthesis, we pursued the shock propagation of the supernova explosion using a spherically symmetric PPM code [16,17]. The presupernova structure is adopted from 14E1 model in [18] corresponding to SN 1987A. The explosion energy and the mass cut are set to be 1×10^{51} ergs and 1.61 $M_\odot$. Detailed nucleosynthesis was calculated by postprocessing using a nuclear reaction network consisting of 291 species of nuclei [15].

To evaluate the total ejected mass of each isotope $M_{eject,i}$ of the r-process elements for a given neutrino luminosity model, we simulate a set of three neutrino driven wind models with constant and different neutrino luminosities. Then, we sum up the results using the following formulation:

$$M_{eject,i} = \left(\frac{\dot{M}_{0,i} + \dot{M}_{\mathrm{half},i}}{2} + \frac{\dot{M}_{\mathrm{half},i} + \dot{M}_{\mathrm{end},i}}{2}\right)\frac{t_{\mathrm{end}}}{2}, \tag{2}$$

where $\dot{M}_{0,i}$, $\dot{M}_{\mathrm{half},i}$, and $M_{\mathrm{end},i}$ are the mass ejection rates of isotope i obtained from the calculation for three constant L_{ν_i}: $L_{\nu_i,0}$, $L_{\nu_i,\mathrm{half}}$, and $L_{\nu_i,\mathrm{end}}$, and t_{end} is the time when L_{ν_i} is 3.5×10^{51} ergs s^{-1} (see Table 1).

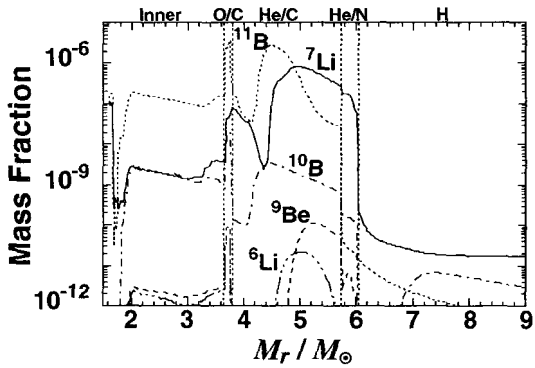

Figure 1. Distribution of the mass fractions of the light elements (Li, Be, and B) in the case of $E_\nu = 3 \times 10^{53}$ ergs and τ_ν=3.0 s. The mass fraction of ^{7}Li means the sum of the mass fractions of ^{7}Li and ^{7}Be. The mass fraction of ^{11}B means the sum of the mass fractions of ^{11}B and ^{11}C.

We followed the evolution of neutrino driven winds using an implicit numerical code for general-relativistic and spherically symmetric hydrodynamics [19] used in [15]. As an initial condition, we put the surface material on a 1.4 $M_\odot$ neutron star [9]. As an outer boundary condition, we set the pressure to be 1×10^{20} dyn cm^{-2} for all simulations.

3. Results

3.1. *The Ejected Masses of ^{7}Li and ^{11}B*

Figure 1 shows the mass fraction distribution of the light elements in the case of $E_\nu = 1 \times 10^{53}$ ergs and $\tau_\nu = 3$ s. This figure indicates that ^{7}Li and ^{11}B are mainly produced in the outer He-layer, especially in the ranges of $4.6M_\odot \leq M_r \leq 5.8M_\odot$ and $4.2M_\odot \leq M_r \leq 5.0M_\odot$, respectively. The amounts of ^{6}Li, ^{9}Be, and ^{10}B are much smaller than those of ^{7}Li and ^{11}B. The main production processes of ^{7}Li and ^{11}B in the He-layer are ^{4}He$(\nu, \nu' p)^3$H$(\alpha, \gamma)^7$Li$(\alpha, \gamma)^{11}$B, ^{4}He$(\nu, \nu' n)^3$He$(\alpha, \gamma)^7$Be(e^-, ν_e) ^{7}Li, and ^{12}C$(\nu, \nu' p)^{11}$B. At higher temperatures in the inner region of the He-layer, a ^{11}B$(\alpha, n)^{14}$N reaction also occurs. All these reaction sequences are triggered by neutrino spallations and are followed by α-captures.

Figures 2*a* and 2*b* show the ejected masses of ^{7}Li and ^{11}B, respectively, as a function of the total neutrino energy E_ν. We see two clear features of the ejected masses of ^{7}Li and ^{11}B: one is that they are almost proportional

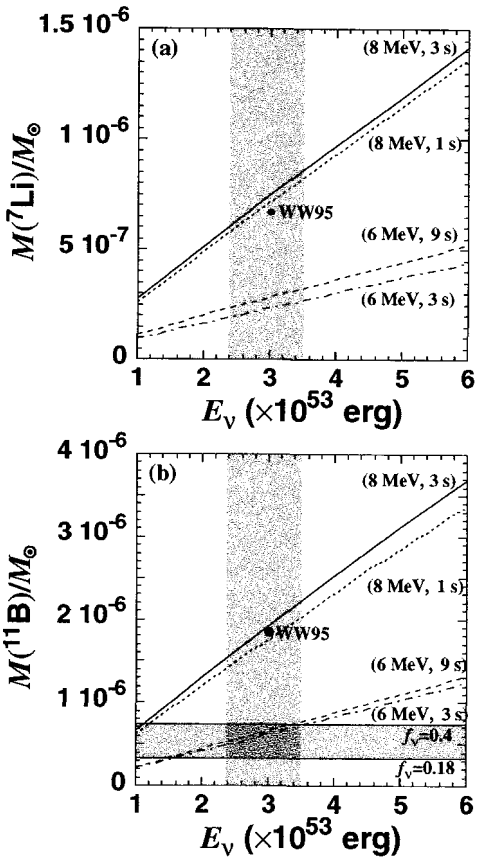

Figure 2. Ejected masses of ^{7}Li (a) and ^{11}B (b) as a function of the total neutrino energy E_ν. The solid and dotted lines show the ejected masses in the cases of τ_ν=3 and 1 s, respectively. The point denoted by WW95 shows the ejected mass given by the S20A model in [2]. The shaded region denoting the ^{11}B mass in (b) is determined from the GCE models (see Eq. (3)). The shaded region denoting the range of the total neutrino energy is determined from the gravitational energy of a 1.4 $M_\odot$ neutron star (see Eq. (4)). The dashed and dot-dashed lines show the ejected masses in the cases of τ_ν=9 s and 3 s for $T_{\nu_{\mu,\tau}} = T_{\bar{\nu}_{\mu,\tau}}$=6 MeV/$k$ (see §4).

to the total neutrino energy E_ν and the other is that they are insensitive to the decay time of the neutrino luminosity τ_ν.

The proportionality of the ejected masses of ^{7}Li and ^{11}B to E_ν arises from the properties of their synthesis processes, i.e., the ν-process and the α-capture reactions. The reaction rates of the ν-process reactions are pro-

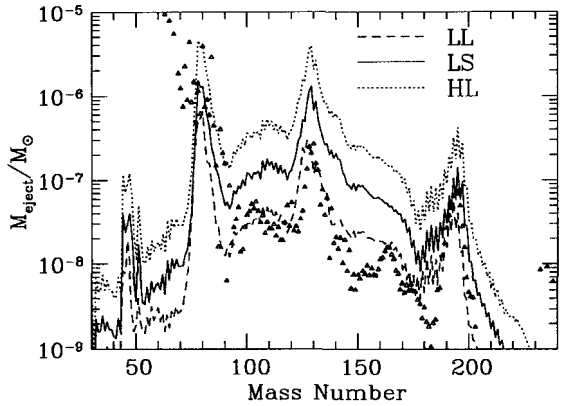

Figure 3. Isotopic distribution of ejected mass as a function of mass number. The dashed, solid, and dotted lines indicate the results of the LL, LS, and HL models (see Table 1). Triangles show the solar r-process abundance [20] shifted to the value of the LL model at the second peak.

portional to E_ν. On the other hand, the reaction rates of the α-capture reactions do not depend on the neutrino luminosity. The amounts of seed nuclei of ^{7}Li and ^{11}B, i.e., ^{4}He and ^{12}C, are determined by the composition of the presupernova star and are independent of the neutrino luminosity.

We turn to the insensitivity of the ejected masses of ^{7}Li and ^{11}B to the decay time of the neutrino luminosity. In the ^{7}Li and ^{11}B production regions, the ^{7}Li and ^{11}B mass fractions do not strongly depend on the decay time. All neutrinos promptly pass through the region before the shock arrival and ^{7}Li and ^{11}B are not effectively processed even after the shock arrival. Only inside the ^{7}Li and ^{11}B abundant region, the ^{7}Li and ^{11}B mass fractions are affected by the decay time. However, they are much smaller despite the difference of the decay time in such a region.

We compare the ejected masses of ^{7}Li and ^{11}B in the case of $E_\nu = 3 \times 10^{53}$ ergs and $\tau_\nu = 3$ s to those of S20A model in [2]. Figures 2*a* and 2*b* show that our result well agrees with that of [2]. Thus, we can conclude that the difference of the temperatures of ν_e and $\bar{\nu}_e$ scarcely affects the ejected masses of ^{7}Li and ^{11}B.

3.2. *The r-Process Abundance Pattern*

The total isotopic distribution of the ejected mass of the r-process elements is presented as a function of mass number in Fig. 3 for the three sets of

neutrino luminosities listed in Table 1. The dashed line, solid line, and dotted line indicate the cases with *low* E_ν and *long* τ_ν (LL model), *low* E_ν and *short* τ_ν (LS model), and *high* E_ν and *long* τ_ν (HL model), respectively. The third peak elements are synthesized in all three models. However, the height of the peak and the ejected mass of these elements differ largely.

We compare the result of the LL model to that of the LS model to investigate the dependence of the ejected mass distribution on the decay time. Figure 3 shows that the ejected mass in the LS model is larger than that in the LL model. It is known that the mass ejection rate increases as fast as the luminosity increases [21]. Thus, the mass ejection at high luminosity is dominant in the whole wind and the total ejected mass is mainly determined by the peak neutrino luminosity. The peak neutrino luminosity in the LS model with the short decay time is larger than that of the LL model with the long decay time because of a common total neutrino energy. Thus, a shorter decay time leads to a larger ejected mass.

Figure 3 also shows that the abundance ratio of the third- to second-peak elements in the LL model is larger than in the LS model. In both models, the efficiency for producing the third-peak elements is higher for $L_{\nu_i,\mathrm{end}}$ than for $L_{\nu_i,0}$ and $L_{\nu_i,\mathrm{half}}$. Thus, it seems that lower neutrino luminosity model provides large third- to second-peak element ratio (see [15] for details).

Next, we compare the results of the LL and HL models in Fig. 3 to investigate the E_ν dependence. Compared to the result of the LL model, the total ejected mass is larger and the abundance ratio of the third- to second-peak elements is smaller for the HL model. This is due to lower peak neutrino luminosity of the LL model.

We compare the results of the HL and LS models. Figure 3 shows that the ejected mass in the HL model is larger and that the abundance pattern is exactly the same in these two models. In these models, $L_{\nu_i,0}$, $L_{\nu_i,\mathrm{half}}$, and $L_{\nu_i,\mathrm{end}}$ depend only on E_ν/τ_ν and, their values and the corresponding mass ejection rates are exactly the same (see Table 1 and Eq. (2)). Thus, the key quantity is the neutrino luminosity for determining the r-process abundance pattern in our study.

In summary, lower peak luminosity is preferable for obtaining a successful r-process abundance pattern. Figure 3 also shows the solar r-process abundance pattern in [20] shifted to the value of the LL model at the second peak. We can conclude that the LL model is the best among our adopted three models to reproduce the solar r-process abundance pattern.

4. Discussion on the Galactic Chemical Evolution

Recent studies on the GCE have indicated that the ^{11}B amount evaluated from supernova nucleosynthesis models [2] is overproduced by a factor of 2.5 to 5.6 compared to that evaluated from the GCE models. Several studies on the GCE of the light elements have introduced a reduction factor f_ν at the ratio of the amount of ^{11}B determined in a GCE model to that evaluated from the result in [2]. The factor f_ν has been evaluated as 0.40 [10], 0.18 [11], 0.28 [12], and 0.29 [13]. Since the factor f_ν still depends on the GCR treatment, we set an acceptable range of the factor f_ν to be

$$0.18 \leq f_\nu \leq 0.40. \tag{3}$$

The range of the corresponding ejected mass of ^{11}B is drawn by a shaded region in Fig. 2*b*. We see that the total neutrino energy satisfying the corresponding ^{11}B mass range is smaller than 1.2×10^{53} ergs.

The total neutrino energy is well approximated by the gravitational energy of a neutron star because about 99% of the gravitational energy is released as supernova neutrinos when the supernova explosion occurs. The relation between the gravitational energy and the gravitational mass of a neutron star was evaluated in [22]. Using their relation, the total neutrino energy for a 1.4 $M_\odot$ neutron star turns out to be

$$2.4 \times 10^{53}\,\text{ergs} \leq E_\nu \leq 3.5 \times 10^{53}\,\text{ergs}. \tag{4}$$

This range is drawn by shaded regions in Figs. 2*a* and 2*b*. The obtained range is clearly much higher than the energy satisfying the GCE of ^{11}B.

In order to solve such inconsistency, we change the temperature of $\nu_{\mu,\tau}$ and $\bar{\nu}_{\mu,\tau}$ from 8 MeV/k to 6 MeV/k and reset the decay time of the neutrino luminosity. Although supernova neutrino spectra have not been precisely determined, some recent studies showed the neutrino temperature to be smaller than 8 MeV/k [23,24]. For the r-process calculations, we set the MLL model where $E_\nu = 3.0 \times 10^{53}$ ergs and τ_ν=9.0 s (see Table 1). The LL model is the most favorable for explaining the solar r-process abundance pattern. However, the total neutrino energy of it is outside the range of Eq. (4). The MLL model satisfies the appropriate total neutrino energy and preserves a low peak neutrino luminosity.

The dashed lines in Figs. 2*a* and 2*b* indicate the ejected masses of ^{7}Li and ^{11}B in the case of $T_{\nu_{\mu,\tau}} = T_{\bar{\nu}_{\mu,\tau}} = 6$ MeV/k and $\tau_\nu = 9.0$ s. The result in the case of $\tau_\nu = 3.0$ s is also shown (Fig. 2, dot-dashed line). The ejected mass of ^{11}B is successfully in the range required from the GCE models ([10-13]). This range clearly overlaps with the range of Eq. (4). Thus, we

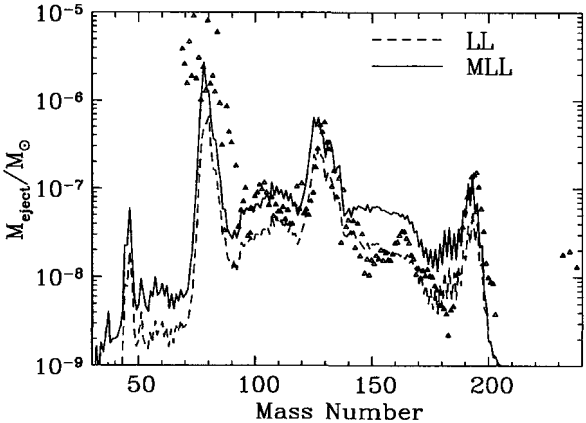

Figure 4. Isotopic distribution of ejected mass as a function of mass number. The solid and dashed lines refer to the MLL and LL models. Stars show the solar r-process abundances [20] shifted to the value of the MLL model at the second peak.

can conclude that the ejected mass of ^{11}B required from the GCE models is reproduced with the appropriate range of E_ν when $T_{\nu_{\mu,\tau}} = T_{\bar{\nu}_{\mu,\tau}} = 6$ MeV/k and $\tau_\nu = 9.0$ s. The ejected masses of ^{7}Li and ^{11}B are

$$2.3 \times 10^{-7} M_\odot \leq M(^7\mathrm{Li}) \leq 3.1 \times 10^{-7} M_\odot,$$

$$5.2 \times 10^{-7} M_\odot \leq M(^{11}\mathrm{B}) \leq 7.4 \times 10^{-7} M_\odot.$$

We also show the distribution of the ejected mass of the r-process elements in the MLL model ($E_\nu = 3 \times 10^{53}$ ergs, $\tau_\nu = 9.0$ s, see Table 1) in Fig. 4. The mass distribution in the LL model is also shown for comparison. Stars indicate the solar r-process abundances shifted to the value of the MLL model at the second peak. We see that the third- to second-peak ratio of the MLL model is slightly larger than that of the LL model. We therefore conclude that a lower neutrino temperature is preferable for not only light elements but also heavy r-process elements.

5. Summary

We investigated the dependence of the supernova neutrino models on the nucleosynthesis of the light elements and r-process heavy elements using common supernova neutrino models. We also obtained the ejected masses of the light elements and the abundance distribution of the r-process elements appropriate for the current studies on the GCE. We summarize our findings.

First, the ejected masses of ^{7}Li and ^{11}B are roughly proportional to the total neutrino energy E_ν whereas they are insensitive to the decay time of the neutrino luminosity τ_ν.

Second, the distribution of the ejected masses of the r-process heavy elements mainly depends on the peak neutrino luminosity, which is proportional to E_ν/τ_ν. A lower neutrino luminosity is preferred for reproducing the solar r-process abundance ratio of the third- to second-peak elements.

Third, the supernova neutrino model with $T_{\nu_{\mu,\tau}} = T_{\bar{\nu}_{\mu,\tau}} = 6$ MeV/k rather than 8 MeV/k is preferable for the ^{11}B amount during GCE and the r-process abundance pattern. The preferred total neutrino energy and the decay time are $E_\nu \sim 3.0 \times 10^{53}$ ergs and $\tau_\nu = 9.0$ s.

Extensive studies of the neutrino spectra and their effect on the light element production are under way [25].

References

1. S. E. Woosley, et al., *Astrophys. J.* **356**, 272 (1990).
2. S. E. Woosley and T. A. Weaver, *Astrophys. J. Suppl.* **101**, 181 (1995).
3. T. Yoshida, H. Emori, and K. Nakazawa, *Earth Planets Space* **52**, 203 (2000).
4. T. Yoshida, K. Nakazawa, and H. Emori, *Earth Planets Space* **52**, 361 (2000).
5. T. Yoshida, H. Emori, and K. Nakazawa, *Earth Planets Space* **53**, 767 (2001).
6. Y.-Z. Qian and S. E. Woosley, *Astrophys. J.* **471**, 331 (1996).
7. K. Otsuki, et al., *Astrophys. J.* **533**, 424 (2000).
8. M. Terasawa, et al., *Astrophys. J.* **562**, 470 (2001).
9. M. Terasawa, et al., *Astrophys. J.* **578**, L137 (2002).
10. B. D. Fields, et al., *Astrophys. J.* **540**, 930 (2000).
11. R. Ramaty, et al., in Proc. IAU Symp. 198, *The Light Elements and Their Evolution*, ed. L. da Silva, M. Spite, and J. R. de Medeiros (Cambridge: Cambridge Univ. Press), 51 (2000).
12. R. Ramaty, et al., *Astrophys. J.* **534**, 747 (2000).
13. A. Alibés, J. Labay, and R. Canal, *Astrophys. J.* **571**, 326 (2002).
14. E. Anders and N. Grevesse, *Geochim. Cosmochim. Acta* **53**, 197 (1989).
15. T. Yoshida, M. Terasawa, T. Kajino, and K. Sumiyoshi, *Astrophys. J.* **600**, 204 (2004).
16. P. Colella and P. R. Woodward, *J. Comput. Phys.* **54**, 174 (1984).
17. T. Shigeyama, et al., *Astrophys. J.* **386**, L13 (1992).
18. T. Shigeyama and K. Nomoto, *Astrophys. J.* **360**, 242 (1990).
19. S. Yamada, *Astrophys. J.* **475**, 720 (1997).
20. F. Käppeler, H. Beer, and K. Wisshak, *Rep. Prog. Phys.* **52**, 945 (1989).
21. S. E. Woosley, et al., *Astrophys. J.* **433**, 229 (1994).
22. J. M. Lattimer and M. Prakash, *Astrophys. J.* **550**, 426 (2001).
23. E. S. Myra and A. Burrows, *Astrophys. J.* **364**, 222 (1990).
24. R. Buras, et al., *Phys. Rev. Lett.* **90**, 1101 (2003).
25. T. Yoshida and T. Kajino, *in preparation* (2004).

CONSTRAINTS ON GLOBULAR CLUSTER FORMATION AND EVOLUTION FROM MAGNESIUM ISOTOPE RATIOS AND R-PROCESS ELEMENTAL ABUNDANCES

K. OTSUKI, G. J. MATHEWS, AND T. ASHENFELTER

Center of Astrophysics and JINA, University of Notre Dame
225 Nieuwland Science Hall, University of Notre Dame,
Notre Dame, IN 46556, USA
E-mail: kotsuki@nd.edu, gmathews@nd.edu, tashenfe@nd.edu

We studied Mg isotope ratios in globular-cluster stars using a simple supernova-induced self-enrichment model. Our basic idea is to explain the observed Mg isotope ratios by the contribution from an early generation of intermediate-mass stars. Although our model produces some Mg isotopic abundance variation, not enough heavier Mg isotopes (^{25}Mg and ^{26}Mg) were formed unless star formation occurs in low density regions behind the super shell. In our model, the 1st generation of AGB stars could not affect heavier Mg isotopes if we assume contamination occurs in the super shell. We also discuss neutron-capture elements in M15 using the same model. It appears difficult to explain current observational results by cloud-collision models. If we assume the r-process occurs in low-mass supernovae, (e.g., ONeMg supernovae), our self-enrichment model can reproduce the observed [Ba/Fe] scatter.

1. Introduction

Halo globular clusters are the oldest Galactic objects. The metallicity, [Fe/H], of stars in the same cluster has the same value within 0.1dex. This implies that, after the cluster formed, the stars in the cluster have not experienced explosive nucleosynthesis events which produce Fe. This seems to imply that all stars in a cluster form from the same material at the same time.

However, star-to-star abundance variations for light elements (C, N, O, Na, Al) have been observed (e.g., Refs. 4, 13). Quite recently a Mg isotope ratio scatter for globular cluster giants in NGC6752 was also reported[22]. There are two kinds of theoretical models to explain this scatter: evolutionary and primordial scenarios. The evolutionary scenarios explain star-to-star abundance variations with internal stellar processes. These variations

arise when stars become red giants with convective envelopes. In the primordial scenario, the abundance variations were imprinted when the stars formed. In this case, the abundance variations appear in main sequence stars.

Although there have been many studies of globular cluster formation and evolution, each model has its uncertainties, and these are still controversial. We wish to construct a globular cluster formation model which is consistent with observation both chemically and dynamically. In this paper, we discuss the Mg isotope ratio and the r-process elements in globular cluster stars.

2. Mg isotope ratio in NGC 6752

The origin of neutron-rich Mg isotopes in metal-deficient stars is still a mystery. In the early Galaxy, Mg is mainly produced by Type II supernovae. Although current Type II supernovae nucleosynthesis models[21] eject ^{24}Mg about two orders of magnitude higher than heavier isotopes, observed heavier Mg isotopes in metal-deficient stars are quite high. Type I SNe can produce Mg also, but they cannot produce heavier isotopes because of neutron deficiency[18]. Novae produce heavier Mg isotopes, but it seems unlikely that nucleosynthesis in novae affect metal-deficient stars.

Recently, it was proposed that low-metallicity intermediate-mass stars can produce heavier Mg isotopes during their AGB phase[14]. ^{14}N makes ^{22}Ne via α-capture, and ^{22}Ne makes heavier Mg isotopes via ^{22}Ne(α, n)^{25}Mg and ^{22}Ne(α, γ)^{26}Mg. If the temperature is high enough for extended convective envelopes, a significant amount of heavy Mg isotopes can be ejected. Unfortunately, this production is still uncertain because of the strong dependence of the nuclear reaction. Yong et al. reported a scatter in the Mg isotope ratio in the globular cluster NGC 6752 [22]. In NGC 6752 giants, ^{25}Mg and ^{26}Mg isotope ratios are higher than theoretically calculated metal-poor SN ejecta (e.g., Ref. 21). In addition, these isotope ratios vary for each star (Fig.1). They suggest that this scatter could be a primordial effect because correlations of the Mg isotopic abundances with stellar evolutionary status were not found. To investigate how these heavier isotopes were formed and what the origin of this scatter is, we calculated contributions of heavier Mg isotopes from intermediate mass stars using a simple self-enrichment model.

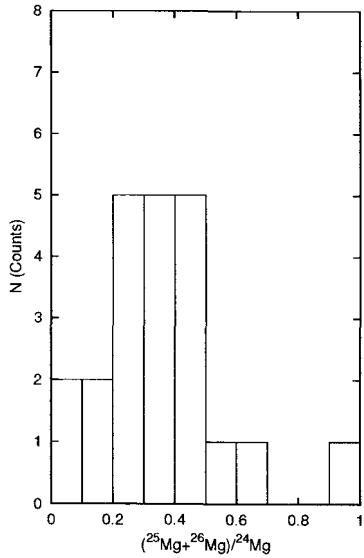

Figure 1. Observed Mg isotope ratio in NGC 6752 from Yong et al.(2003).

3. Theoretical calculations

3.1. *A model for globular cluster formation*

Although recent cloud-cloud collision models are thought to be reliable, it is difficult to account for such primordial abundance variations using them. This is because their abundance variations should be reset to reproduce same [Fe/H] for each star within the cluster. For this study, we assume a simple supernovae-induced self-enrichment model based upon familiar models studied by many researchers[2 20 10].

Our model starts at the point when a very massive object explodes at the center of a metal-free proto-globular cluster cloud and the first generation of stars are formed with some mass distribution. SNe of the first generation induce formation of the second generation of stars, i.e., those are observed today. Second generation supernovae then blow off the remaining gas in a cluster. To reproduce uniform [Fe/H], all supernovae must form a super shell and the ejected material must be mixed completely in that shell before the second generation of stars is formed.

We can consider two possible AGB contributions: contamination from the first generation of AGB stars and contamination from the second gen-

eration. The former is a primordial scenario, while the latter is an evolutionary scenario. We consider the primordial scenario here because (1) There are no correlations of Mg isotopic abundance with stellar evolutionary status[22], and (2) for other light elements, abundance variations were observed in main sequence stars[4 5].

For this model, if star formation continues until the first generation of AGB stars ejects the heavier Mg isotopes, a super shell can be contaminated without changing [Fe/H]. In this case, star formation must continue over $\sim 10^7$ years. Hydrodynamic calculations of cloud and shell formation are necessary to estimate a super-shell lifetime correctly. Nevertheless one can estimate this lifetime from the sound crossing time of a proto-globular cluster cloud $\tau = r/c_s = r(\mu m/\gamma kT)$. For a 10 pc cloud of at temperature of 100 k, the sound crossing time is indeed $> 10^7$ yrs. Hence,we assume here that a super shell can exist long enough to be contaminated by AGB stars.

3.2. *Our calculation*

For the first generation stars, the star formation rate is assumed to be

$$\Psi(t) = (E_{vms} + M_{sw1})/\delta t,$$

where E_{vms} is ejected material from the initial pair creation supernova (PCSN), M_{sw1} is the mass of material swept up by the PCSN, and δt is the period of star formation. We assume that subsequently, the star formation rate for the second generation stars at time t is:

$$\Psi(t) = \epsilon \times (\int E_j(t)dt + M_{sw2})/\delta t,$$

where ϵ is the star formation efficiency and $E_j(t)$ is the mass of ejected material from supernovae exploding before the second generation of stars were formed. M_{sw2} is the mass swept up into super shell at t. In this calculation, ejected material is mixed with the shell completely before stars form. We consider the following four IMF cases[12 9 3](Fig. 2):

$$\phi_1(m) = m^{-1.35} \quad (1)$$

$$\phi_2(m) = (1 + m/13.2)^{-1.35} \quad (2)$$

$$\phi_3(m) = (1 - \exp(-m/2)) \times m^{-1.35} \quad (3)$$

$$\phi_4(m) = \exp(-13.2/m) \times m^{-1.35}. \quad (4)$$

ϕ_1 is the regular Salpeter IMF, ϕ_2 and ϕ_3 are top-heavy IMFs suggested by Larson for early generation star formation. ϕ_4 emphasizes intermediate

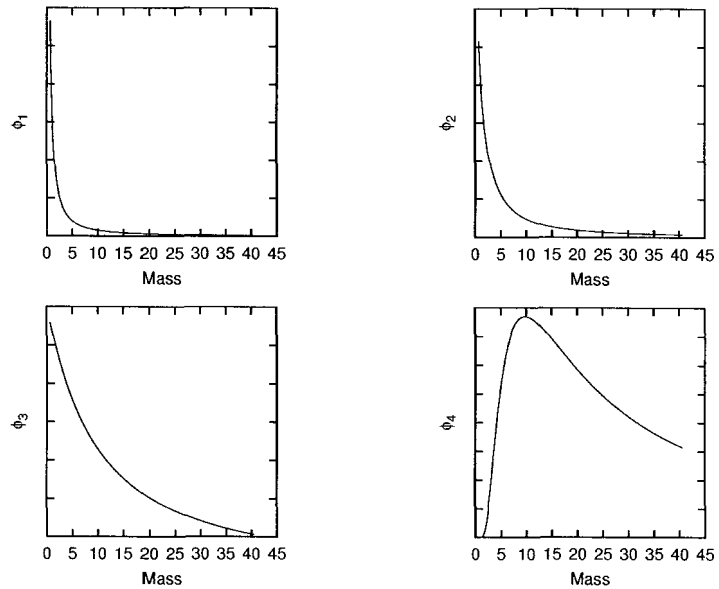

Figure 2.
The initial mass functions (IMFs), $\phi_1(m) = m^{-1.35}$, $\phi_2(m) = (1 + m/13.2)^{-1.35}$, $\phi_3(m) = (1 - \exp(-m/2)) \times m^{-1.35}$, $\phi_4(m) = \exp(-13.2/m) \times m^{-1.35}$. The vertical axis shows stellar masses in unit of solar mass.

mass stars. For all of our calculations, we assume a star formation efficiency of $\epsilon = 0.01$ and an initial globular cluster cloud mass of $10^7 M_\odot$. M_{sw} was chosen for each calculation to reproduce a reasonable metallicity of a globular cluster, [Fe/H] $= -1.5 \sim -2$.

We use stellar yields of Ref. 21,11 for Type II supernovae ($40M_\odot \leq M \leq 9M_\odot$), Ref. 11 for ONeMg supernovae ($8M_\odot \leq M \leq 6M_\odot$), and Ref. 11,8 for intermediate mass stars ($5M_\odot \leq M$). For ejecta from very massive objects which collapsed as PCSN, we use the yields of Ref. 6.

3.3. *Results*

Fig. 3 shows heavier Mg isotope ratios in the super shell from our calculations. ^{25}Mg and ^{26}Mg abundances increase with time after the AGB stars start ejecting material. We assume the second generation stars form at 30 Myr. After this time, [Fe/H] in the shell is almost unchange. Fig. 4 shows the relative number of stars with various isotope ratios. These stars show

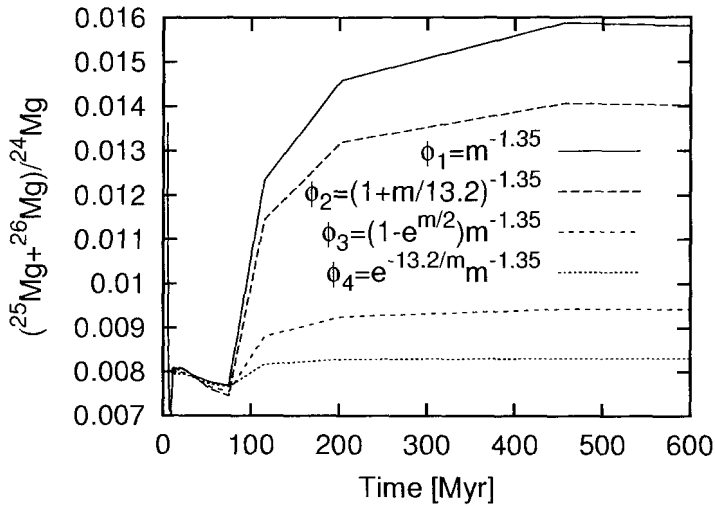

Figure 3. The Mg isotopes in super shell.

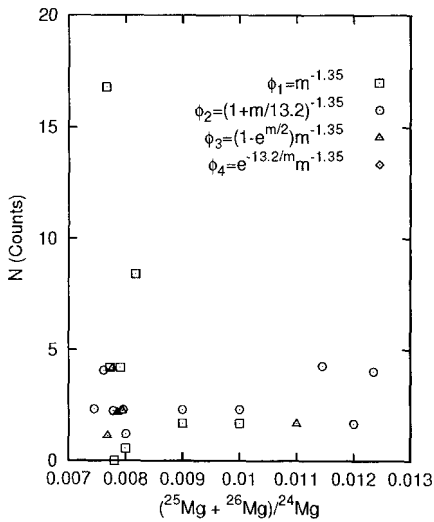

Figure 4. The Mg isotope ratios for each star. The vertical axis is number of stars normalized (by 21) for comparison with Fig.1.

abundance variations, but the amount of heavier Mg isotope is insufficient to reproduce observational data. This is because the ejected material was overdiluted in the super shell.

However, in this calculation, we have ignored the dynamics of the super shell. If we consider the time evolution of the super shell, the density profile of the star forming region should change with time and contamination from AGB stars in lower density regions can be possible. We also calculated another case assuming two orders of magnitude lower density in the star forming region. In these cases, heavier Mg isotopes formed sufficiently. Therefore, if star formation occurs behind the expanding super shell as might be expected due to the AGB lifetime and if the first generation AGB stars eject heavier Mg isotopes after the shell passes, enough contamination from the first generation AGB stars should be possible. A more detailed study including shell dynamics is currently in progress.

4. Neutron capture elements in globular clusters

Elements heavier than iron are mainly produced via neutron capture processes, the r(apid)-process and s(low)-process. The neutron capture elemental abundances for M15 giants were reported in Ref. 1,15,16, and 17. Sneden et al. concluded that those neutron capture elements in M15, at least heavier than Ba ($Z \geq 56$), are pure r-products because their abundances are consistent with a pure r-process synthesis pattern[15]. However, large spreads in the [Ba/Fe] and [Eu/Fe] ratios in M15 giants were reported in Ref. 16. These spreads are similar to the scatters observed in metal-deficient field stars. For the field stars, these scatters are explained by a summation of the yields of different nucleosynthesis events (e.g., r-process nucleosynthesis in different progenitor supernovae [19] [7]). If the neutron capture elements in M15 are pure r-process products, this will be a strong constraint for globular cluster formation models.

Although the origin of r-process elements is still uncertain, they were probably formed in core-collapsed supernovae. If Ba and Eu in M15 are pure r-process elements, their scatter cannot be explained by an evolutionary scenario. This means cloud-collision globular cluster formation models face a serious problem.

On the other hand, our model can avoid this problem if the r-process occurs in ONeMg supernovae. Since ONeMg supernovae do not form Fe and such lighter supernovae explode later, ejecta from ONeMg supernovae should not be completely mixed within the super shell material. This model

is consistent with the model of Ref. 7, which explains the similar scatter in field halo stars with r-process nucleosynthesis in ONeMg (or heavier) supernovae.

Since [Ba/Eu] ratios of M15 giants are higher than that of a pure r-process abundance[16], we still cannot dismiss possible s-process effects on these abundances. In this case, evolutionary scenarios also could reproduce the scatter and cloud-collision models may still be reasonable. For further discussion, more precise spectroscopic data for other elemental abundances (including lighter elements) are necessary.

Acknowledgments

This work was supported in part by JSPS, and in part by DOE Nuclear Theory Grant DE-FG02-95ER40934 and JINA.

References

1. B. J. Armosky, C. Sneden, G.E. Langer and R.P. Kraft *AJ***108**,1364 (1994).
2. M. A. Beasley, D. Kawata, F. P. Pearce, D.A.Forbes and B. K. Gibson *ApJ***596**, L187 (2003).
3. V. Bromm, R. P. Kudritzki and A. Loeb *ApJ*,**552**, 464 (2001)
4. R. G. Gratton, P. Bonifacio, A. Bragaglia et al. *A&A***369**, 87 (2001).
5. F. Grundahl, M. Briley, P. E. Nissen and S. Feltzing *A&A***385**, L14 (2002).
6. A. Heger and S. E. Woosley *ApJ***567**, 532 (2002).
7. Y. Ishimaru and S. Wanajo *ApJ***511**,L33 (1999).
8. A.I. Karakas and J.C. Lattanzio *PASA***20**, 279 (2003).
9. R. B. Larson *MNRAS***301**, 569 (1998).
10. e.g. G. Parmentier, E. Jehin, P. Magain, C. Neuforge, A. Noels and A. A. Thoul *A&A***352**, 138 (1999), A. Thoul, A. Jorissen, S. Goriely, E. Jehin, P. Margain, A. Noels and G. Parmentier *A&A***383**, 491 (2002).
11. L. Portinali, C. Chiosi, and A. Bressan *A&A***334**, 505 (1998).
12. L. Saleh, T. C. Beers and G.J. Mathews *submitted to ApJ*
13. M. D. Shetrone
14. L. Siess, M. Livio and J. C. Lattanzio *ApJ***570**, 329 (2002).
15. C. Sneden, J. Johnson, R. P. Kraft, G. H. Smith, J. J. Cowan and M. S. Bolte, *ApJ***536**, L85 (2000).
16. C. Sneden, R. P. Kraft, M. D. Shetrone, G. H. Smith, G. E. Langer and C. F. Prosser*AJ* **114**, 1964 (1997).
17. C. Sneden, C. A. Pilachowski and R. P. Kraft *ApJ* **120**, 1351 (2000).
18. F.-K. Thielemann, K. Nomoto and K. Yokoi *A&A***158**, 17 (1986).
19. T. Tsujimoto, T. Shigeyama and Y. Yoshii *Ap&SS* **281**, 221 (2002).
20. M. Vietri and E. Pesce *ApJ***442**, 618 (1995).
21. S. E. Woosley and T. A. Weaver *ApJS***101**, 181 (1995).

22. D. Yong, F. Grundahl, D. L. Lambert, P. E. Nissen and M. D. Shetrone *A&A* **402**, 985 (2003).

Poster Session

This page intentionally left blank

COULOMB DISSOCIATION OF ^{23}Al - STUDY OF THE ^{22}Mg(p,γ)^{23}Al REACTION -

T. GOMI[1], T. MOTOBAYASHI[2], Y. ANDO[1], N. AOI[2], H. BABA[1], K. DEMICHI[1], Z. ELEKES[2], N. FUKUDA[2], ZS. FÜLÖP[3], U. FUTAKAMI[1], H. HASEGAWA[1], Y. HIGURASHI[2], K. IEKI[1], N. IMAI[2], M. ISHIHARA[2], K. ISHIKAWA[4], N. IWASA[5], H. IWASAKI[6], S. KANNO[1], Y. KONDO[4], T. KUBO[2], S. KUBONO[7], M. KUNIBU[1], K. KURITA[1], Y. U. MATSUYAMA[1], S. MICHIMASA[7], T. MINEMURA[2], M. MIURA[4], H. MURAKAMI[1], T. NAKAMURA[4], M. NOTANI[7], S. OTA[8], A. SAITO[1], H. SAKURAI[6], M. SERATA[1], S. SHIMOURA[7], T. SUGIMOTO[4], E. TAKESHITA[1], S. TAKEUCHI[2], Y. TOGANO[1], K. UE[6], K. YAMADA[1], Y. YANAGISAWA[2], K. YONEDA[9], AND A. YOSHIDA[2]

[1] *Department of Physics, Rikkyo University, Tokyo 171-8501, Japan*
[2] *RIKEN (Institute of Physical and Chemical Research), Saitama 351-0198, Japan*
[3] *Institute of Nuclear Research of the Hungarian Academy of Science (ATOMKI), 4001 Debrecen Hungary*
[4] *Department of Physics, Tokyo Institute of Technology, Tokyo 152-8551, Japan*
[5] *Department of Physics, Tohoku University, Miyagi, 980-8578, Japan*
[6] *Department of Physics, University of Tokyo, Tokyo 113-0033, Japan*
[7] *Center of Nuclear Study (CNS), University of Tokyo, Saitama 351-0198, Japan*
[8] *Department of Physics, Kyoto University, Kyoto 606-8502, Japan*
[9] *National Superconducting Cyclotron Laboratory, Michigan state University, East Lansing, Michigan 48824*

We have performed a Coulomb dissociation experiment of ^{23}Al to study the stellar ^{22}Mg(p,γ)^{23}Al reaction. The radiative width of the first excited state in ^{23}Al , which can affect the resonant reaction rate, is determined experimentally for the first time.

1. Introduction

At the high temperature and high density attained during Ne-rich novae, the reaction flow is characterized by the NeNa and MgAl cycles, which results in a significant production of ^{22}Na. Attempts of observing the characteristic ^{22}Na activities with satellite telescopes have been performed[1],

and estimates of the production yield have been also made by thermonuclear calculations[2,3,4,5]. For reliable arguments on the ^{22}Na synthesis, uncertainties of the nuclear reaction cross sections employed in the calculations should be reduced. ^{22}Na is produced via the reaction sequence, ^{20}Ne(p,γ)^{21}Na(p,γ)^{22}Mg ($\beta^+\nu$)^{22}Na, and is depleted by the ^{22}Na(p,γ) process. The yield of ^{22}Na might be further reduced if an escape from the reaction sequence strongly takes place via the ^{22}Mg(p,γ)^{23}Al reaction. It is expected that the resonant capture through the first excited state of ^{23}Al, which is located at 405 keV above the proton threshold[6], contributes significantly to the astrophysical reaction rate. However, there is no experimental data for the strength of this resonant capture. We performed a Coulomb dissociation experiment to determine the radiative width Γ_γ of this resonant state in ^{23}Al.

2. Experiment

The experiment was performed at the RIPS facility in RIKEN. The secondary beam of ^{23}Al at 50 MeV/nucleon was produced by a projectile fragmentation of 135 MeV/nucleon ^{28}Si in a ^{9}Be target. The beam of ^{23}Al bombarded a Pb target. The products of the breakup reaction, ^{22}Mg and a proton, were detected respectively using silicon counter telescopes and a plastic scintillator hodoscope located respectively 50 cm and 3 m downstream of the target. The schematic view of the experimental setup is shown in Fig. 1. The telescope consisted of four layers of 0.5 mm thick silicon detectors, and provided ΔE-E information of the products ^{22}Mg. We used position-sensitive silicon detectors with strips of 5 mm width for the first and second layers to obtain information on the scattering angles of the reaction products. Single-element silicon detectors were used for the third and fourth layers. The hodoscope, constituted of two layers of plastic scintillators (5 mm and 60 mm thick), afforded TOF-ΔE-E information for the proton which penetrated the silicon telescope. A stack of sixty-eight NaI(Tl) scintillators was placed around the target to measure de-excitation γ rays from bound excited states of ^{22}Mg. To select the breakup events through the first excited state in ^{23}Al, we deduced the relative energy of the reaction products measured in coincidence. The momentum vectors of the particles were determined from their energies combined with the hit positions on the silicon telescope.

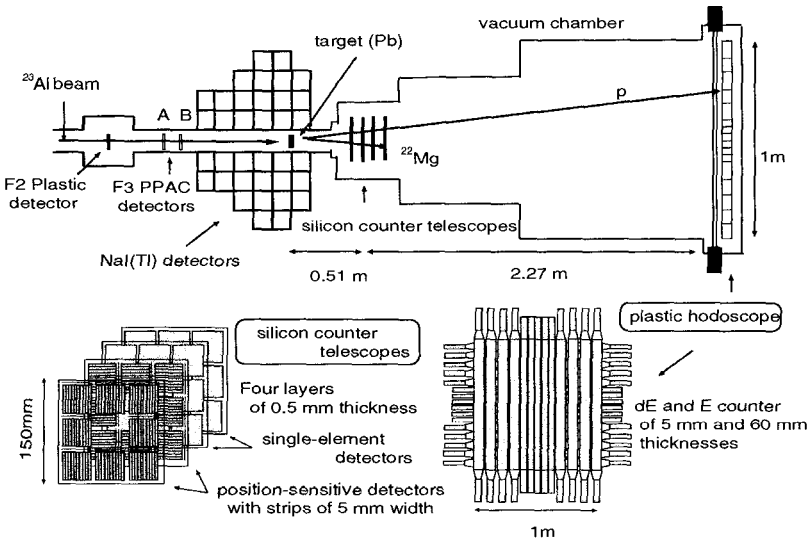

Figure 1. Schematic view of the experimental setup

3. Results

The relative energy spectrum obtained for the ^{208}Pb(^{23}Al,^{22}Mg p)^{208}Pb reaction is shown in Fig. 2. We deduced this spectrum by subtracting the contribution of the dissociation processes leading to bound excited states in ^{22}Mg using the information from the γ-ray detector array. Therefore, this spectrum is for the process in which ^{23}Al disintegrates to the ground state of ^{22}Mg through excited states in ^{23}Al. In this spectrum, the first excited state of ^{23}Al corresponds to the peak around 400 keV. Supposing that the spins and parities of ^{23}Al for the ground and the first excited states are $5/2^+$ and $1/2^+$, respectively, we obtained the radiative width $\Gamma_\gamma = 7.2 \times 10^{-7}$ eV with an error of 30%, which is compatible with the value predicted by J.A. Caggiano *et.al.* [6].

In order to evaluate the influence of the ^{22}Mg(p,γ)^{23}Al reaction on the network calculation for thermonuclear runaway, we considered the competition with β decay of ^{22}Mg. Considering the temperature and density condition predicted by nova models[7], the main reaction flow favors the β decay rather than the proton capture on ^{22}Mg. Since the resonant strength was only known as the theoretical calculations and has not been measured be-

fore experimentally, our experimental data greatly reduces the uncertainty of the astrophysical rate of the ^{22}Mg(p,γ)^{23}Al reaction.

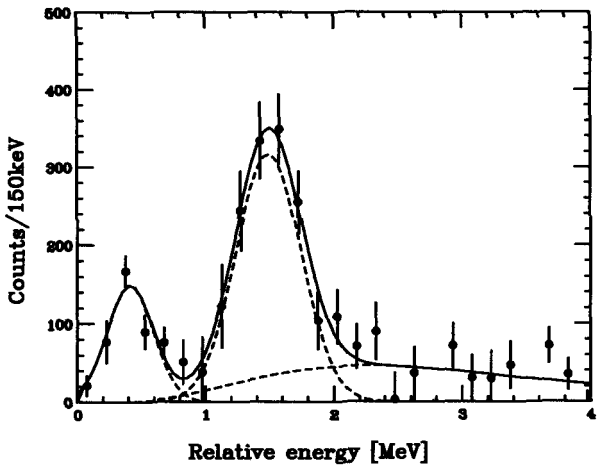

Figure 2. Relative energy spectrum obtained for the ^{208}Pb(^{23}Al, ^{22}Mg p)^{208}Pb reaction. The solid curve represents the result of a fitting with two Gaussian functions and a distribution assuming a nonresonant component. The dashed curves show each component.

References

1. A.F. Iyudin, *et al.*, Astron. Astrophys. **300**, 422 (1995).
2. M. Politano, *et al.*, Astrophys. J. **448**, 807 (1995).
3. S. Starrfiled, *et al.*, Nucl. Phys. A **621**, 495 (1997).
4. J. Jose, *et al.*, Astrophys. J. **494**, 680 (1998).
5. J. Jose, *et al.*, Astrophys. J. **520**, 347 (1999).
6. J.A. Caggiano, *et al.*, Phys. Rev. C **64**, 025802 (2001).
7. C. Iliadis *et al.*, Astrophys. J. Supp. **142**, 105 (2002).

INVESTIGATION OF RESONANT STATES IN ^{23}AL USING A RADIOACTIVE BEAM OF ^{22}MG ON A PROTON TARGET

J. J. HE, S. KUBONO, T. TERANISHI, M. NOTANI, S. MICHIMASA
Center of Nuclear Study (CNS), University of Tokyo, RIKEN Campus, Wako, Saitama 351-0198, Japan

H. BABA
Department of Physics, Rikkyo University, Toshima, Tokyo 171-8501, Japan

S. NISHIMURA, M. NISHIMURA, Y. YANAGISAWA
The Institute of Physical and Chemical Research (RIKEN), 2-1 Hirosawa, Wako, Saitama 351-0198, Japan

N. HOKOIWA, M. KIBE, Y. GONO
Department of Physics, Kyushu University, 6-10-1, Hakozaki, Fukuoka 812-8581, Japan

J. Y. MOON, J. H. LEE, C. S. LEE
Department of Physics, Chung-Ang University, Seol 156-756, Korea

H. IWASAKI
Department of Physics, University of Tokyo, 7-3-1 Hongo, Bunkyo-ku, Tokyo 113-0033, Japan

S. KATO
Department of Physics, Yamagata University, Yamagata 990-8560, Japan

Resonant states in ^{23}Al related to the astrophysical ^{22}Mg(p, γ) reaction, were firstly investigated by using the resonant elastic scattering of ^{22}Mg+p with a low-energy radioactive-ion beam of ^{22}Mg at 4.38 MeV/nucleon and a thick $(CH_2)_n$ target. A new resonant state at 2.99-MeV was observed in the spectrum of recoil protons.

1. Introduction

The astrophysical ^{22}Mg (p, γ) ^{23}Al reaction plays an important role in the hot Ne-Na cycle during the early stage of the *rp* process. It possibly influences the production of a γ emitter ^{22}Na in Ne-rich novae [1 - 3]. Previously, excited states in ^{23}Al were studied via the ^{24}Mg(^{7}Li, ^{8}He)^{23}Al reaction [2, 3] and a β-delayed-proton-decay study of ^{23}Si [4]. In the present study, we aimed at directly

investigating proton resonant states in ^{23}Al using the resonant elastic scattering of ^{22}Mg RI beam on a proton target.

2. Experimental procedure

The experiment was performed by using the CNS radioactive ion beam separator (CRIB) [5, 6]. A primary beam of $^{20}Ne^{8+}$ was accelerated up to 8.11 MeV/nucleon by an AVF cyclotron (K = 70) with an average intensity of 200 pnA and bombarded a ^{3}He gas target (0.36 mg/cm^2). A ^{22}Mg secondary beam was produced from the ^{3}He (^{20}Ne, ^{22}Mg)n reaction. Furthermore, a ^{21}Na RI beam was produced simultaneously. Both of them were used in the experiment. The experimental results with ^{21}Na beam will be discussed elsewhere.

The experimental setup is shown in Fig. 1. At the momentum dispersive focal plane (F1) a 5.4-μm-thick Mylar foil was used to eliminate the light-ion background from the secondary beam. After energy degradation, those of ^{22}Mg particles with a momentum spread of ±0.48% with respect to the central orbit were selected by a horizontal slit.

On the achromatic focal plane (F2), a scattering setup was installed [7] (Fig. 1). The setup consists of two parallel-plate avalanche counters (PPACs), a polyethylene $(CH_2)_n$ target (7.9-mg/cm^2) and three sets of ΔE-E silicon telescope. The PPACs were used for measuring the timing signals and the two-dimensional-position signals of the particles. The ^{22}Mg particles were identified by using TOF between the two PPACs in conjunction with the RF signal provided by the AVF cyclotron in an event-by-event mode. The average intensity of ^{22}Mg was 5.2×10^3 particles/s. The major contaminant was ^{20}Ne caused by scattering of the primary beam on the inner walls of the magnets. As for the ^{22}Mg beam on the $(CH_2)_n$ target, the beam spot widths were 15 mm (FWHM) horizontally and 11 mm (FWHM) vertically. The energy of ^{22}Mg was 4.38 MeV/nucleon with a width of 0.12 MeV/nucleon (FWHM) just before the target.

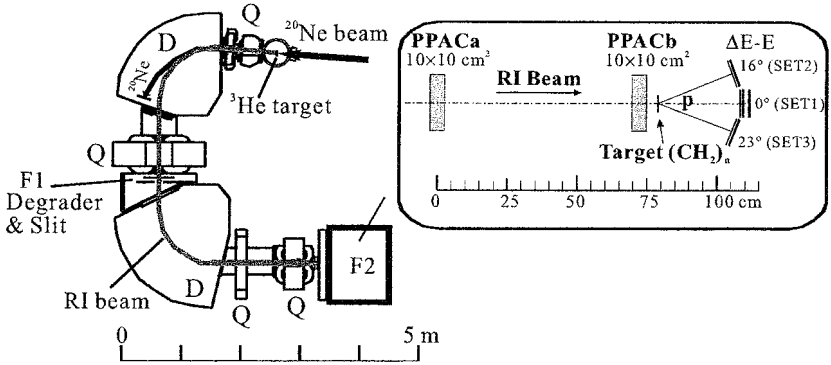

Fig. 1: Experimental setup for CRIB and scattering measurement.

In the following description, the ΔE-E telescopes at angles of θ_{lab} = 0°, 16° and 23° are referred to as SET1, SET2 and SET3, respectively. In this proceeding, we only report the result of SET1. As for SET1, a double-sided-strip (16×16 strips) ΔE was used to determine the two dimensional positions, while for ΔE (in SET2 and SET3), only horizontal x strips were used. The resolution (FWHM) of the scattering angle was 1.0°, 1.4° and 1.3° in respective cases.

The protons were clearly identified by using ΔE-E and E_p-TOF information, where E_p is the summation of proton energies measured by the ΔE and E detectors, and TOF is the time-of-flight between PPACb (see Fig. 1) and ΔE detector. The overall energy resolution of E_p was determined mainly by the energy resolution of the ΔE-E detector system and the energy straggling of particles in the target. The proton energies E_p were calibrated by using the secondary proton beams separated by CRIB at several energy points.

We aim at identifying the proton resonant states in the compound nucleus ^{23}Al. Therefore, we need to know the center-of-mass energy (E_{cm}) instead of the proton energy E_p. The E_{cm} was reconstructed by taking into account the kinematics of ^{22}Mg + p and the energy loss of particles (including ^{22}Mg and proton) in the target. The resolution of E_{cm} deduced from those of E_p and θ_{lab} was in the range of 20 – 45 keV. The systematic errors of E_{cm} were in the range of 15 – 25 keV, which mainly came from those of E_p, (exactly speaking, from the uncertainties of proton energy calibration). The proton threshold in ^{23}Al is known to be 0.123 MeV [2], and therefore the excitation energy in ^{23}Al is E_x = E_{cm} + 0.123 MeV.

Experimental data with a C target (9.3 mg/cm^2) was also acquired in a separate run to evaluate the background contribution from the reactions of ^{22}Mg with C atoms in the $(CH_2)_n$ target. The proton spectrum with the C target had a wide bump shape but no sharp structure. The yield ratio of these two proton spectra [with $(CH_2)_n$ and C targets] was normalized by the number of beam particles and by the target thickness per unit beam energy loss in the corresponding target. Consequently, the spectrum of a pure proton target was deduced by subtracting the spectrum of normalized C-target from that of $(CH_2)_n$-target accordingly.

3. Experimental results

After the background subtraction, the experimental proton spectrum of the ^{22}Mg + p scattering at θ_{lab} = 0° (θ_{cm} = 180°) is shown in Fig. 2. The arrows indicate the excitation energies in ^{23}Al. Several resonant structures can be seen in the spectrum. According to the current analysis, the 2.99-MeV state is a new resonant state in ^{23}Al, which was not observed in the previous experiments. The

other states indicated in the figure were not assigned yet. The corresponding resonant energies, spin-parities and widths are being analyzed with an R-matrix code SAMMY-M6-BETA [8]. In addition, the inelastic scattering might be involved in the spectrum, that is, the compound nucleus ^{23}Al de-excited into a proton and the first excited state (2^+, 1.25 MeV) in ^{22}Mg, which is also under careful evaluation comparing with the proton spectra at other scattering angles.

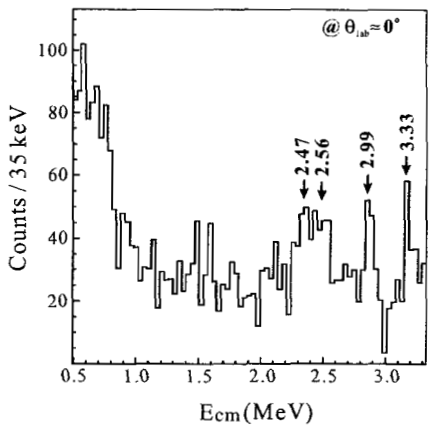

Fig. 2. Experimental proton spectrum for the ^{22}Mg + p elastic scattering at θ_{lab} = 0° (SET1).

Acknowledgments

We would like to thank the CNS/RIKEN staff members for their operation of the ion source and the cyclotron. This work is partially supported by Grant-in-Aid for Science Research from the Japan Ministry of Education, Culture, Sports, and Technology under the contract number 13440071 and 14740156, and also by the Joint Research Program under the Korea-Japan Basic Science Promotion Program (KOSEF 2002-JR015).

References

1. A. F. Iyudin *et al.*, *Astron. Astrophys.* **300**, 422 (1995).
2. M. Wiescher *et al.*, *Nucl. Phys.* **A484**, 90 (1988).
3. J. A. Caggiano *et al.*, *Phys. Rev.* **C64**, 025802 (2001).
4. B. Blank *et al.*, *Z. Phys.* **357**, 247 (1997).
5. S. Kubono *et al.*, *Eur. Phys. J* **A13**, 217 (2002).
6. T. Teranishi *et al.*, *Phys. Lett.* **B556**, 27 (2003).
7. J. J. He *et al.*, *CNS Ann. Rep.* **2002**, 1 (2003).
8. N. M. Larson, ORNL/TM-9179/R5 (October 2000)

PRELIMINARY ANALYSES OF OXYGEN ABUNDANCES IN METAL-POOR STARS OBSERVED WITH OAO/HIDES

M. TAKADA-HIDAI
Liberal Arts Education Center, Tokai University,
Kitakaname, Hiratsuka, Japan 259-1292
E-mail: masath@keyaki.cc.u-tokai.ac.jp

N. CHIYO AND Y.-J. SAITO
Physics Department, Tokai University,
Kitakaname, Hiratsuka, Japan 259-1292

Y. TAKEDA
National Astronomical Observatory,
Mitaka, Tokyo, Japan 181-8588

Preliminary LTE and non-LTE (NLTE) analyses of oxygen (O) abundances were carried out for the 19 metal-poor stars and the two normal stars, Procyon and the Sun, based on high-resolution, high-signal-to-noise spectra obtained with OAO/HIDES as well as on the ELODIE spectral database. The forbidden lines [O I] 6300/6363 Å were analyzed on LTE assumption, while the triplet lines O I 7772–5 Å were corrected for NLTE effects. Our main results are: (1) NLTE [O/Fe] derived from the triplet lines distribute almost flat with an average of $\sim$ 0.75 dex in the range of [Fe/H]< -1, while those from the forbidden lines seem to show an increasing trend with decreasing [Fe/H], which must be confirmed by a further detailed study. (2) The triplet-line NLTE [O/Fe] are systematically larger than the forbidden-line [O/Fe] by an average of $\sim$ 0.35 dex in the range of $-2 <$[Fe/H]< 0.

1. Introduction

There have been intensive debates concerning the behavior of oxygen abundances in metal-poor stars: increasing or flat trend with decreasing metallicity. To try to solve the contraversial issue, the O abundances have been investigated based on the various line data of UV and IR OH, forbidden [O I], and permitted O I triplet. Especially, extensive analyses have been carried out for [O I] 6300/6363 Å and O I 7772–5 Å triplet lines. Very recently, Nissen et al. (2002) studied O abundances for metal-poor dwarfs

and subgiants and found that the [O I] 6300 Å line and the triplet lines give consistent results with [O/Fe] increasing quasi-linearly with decreasing [Fe/H], based on the agreement between LTE abundances from [O I] and NLTE ones from the triplet.

To explore the behavior of O and the consistency of abundances between the forbidden and triplet lines in metal-poor giants, we analyzed the [O I] 6300/6363 Å and O I 7772–5 Å triplet lines observed for our sample of metal-poor stars with $-3 <$[Fe/H]< -0.5 as well as the Sun and Procyon. The preliminary results obtained so far are presented.

2. Observations

The sample stars are listed in Table 1, which are almost common with those observed by Takada-Hidai et al. (2004) to study the behavior of sulfur in metal-poor stars. The observations of the triplet lines were made with HIDES (High Dispersion Echelle Spectrograph) equipped on the 1.88-m telescope at the OAO (Okayama Astrophysical Observatory), while the [O I] lines of a few stars were also observed with HIDES, since they are not included in the ELODIE database (Soubiran et al. 1998). Resolution is $\sim$ 50000 and signal-to-noise ratios range from 100 to 525 (mostly 200 – 450).

3. Measurements and Analyses

Equivalent widths of the [O I] lines were measured mostly on ELODIE spectra, and those of the triplet lines on HIDES spectra. Model atmospheres were adopted from Takada-Hidai et al. (2004). The WIDTH9 code written by R.L. Kurucz was used to derive abundances. The [O I] 6300/6363 Å lines were analyzed adopting the gf-values from Allende Prieto et al. (2001). The contribution of Ni I 6300.34 Å line was *not* corrected for the O abundances derived from [O I] 6300 Å line. In this sense, our results of the [O I] lines are preliminary, since the contribution of the Ni I line is significant ($\sim$ 0.1 dex) in the Sun, though its effect becomes very small in halo stars with the range of [Fe/H]< -1, yielding the differences of less than 0.04 dex (Nissen et al. 2002). The abundance results are shown in column (7) of Table 1.

LTE analyses of the triplet lines were performed using the gf-values of Wiese et al. (1996), and NLTE analyses were made using NLTE corrections calculated by Takeda (2003). The NLTE results are given in column (8) of Table 1.

Table 1. Preliminary Oxygen Abundances Derived from Forbidden and Triplet Lines.

Star	$T_{\rm eff}$ (K)	log g	[Fe/H]	ξ (km s^{-1})	[Fe II/H]	log O Forbdn	log $O_{\rm NLTE}$ Triplet	[O/Fe] Forbdn	[O/Fe] Triplet	δ[O/Fe] (Forb)−(Trip)
(1)	(2)	(3)	(4)	(5)	(6)	(7)	(8)	(9)	(10)	(11)
HD 4306	5000	2.88	−2.70	1.6	−2.58	7.69:	7.39	1.39:	1.14	0.25:
HD 6833	4430	1.68	−1.00	1.1	−0.79	8.18	8.39	0.03	0.35	−0.32
HD 26297	4380	0.77	−1.65	1.5	−1.80	7.42	7.60	0.34	0.57	−0.23
HD 61421	6400	3.93	−0.05	1.5	−0.01	8.59	9.10	−0.28	0.28	−0.56
HD 73394	4440	1.38	−1.40	1.6	−1.50	7.83	7.99	0.45	0.66	−0.21
HD 76932	5820	4.05	−0.95	1.0	−1.00	8.16	8.49	0.28	0.66	−0.38
HD 88609	4570	0.75	−2.65	2.1	−2.83	6.86	6.61	0.81	0.61	0.20
HD 106516	6180	4.28	−0.70	1.2	−0.90	<8.27	8.71	<0.29	0.78	< −0.49
HD 108317	5310	2.77	−2.35	1.9	−2.36	7.44	7.24	0.92	0.77	0.15
HD 122563	4650	1.36	−2.65	1.9	−2.53	<6.45	6.88	<0.10	0.58	< −0.48
HD 140283	5830	3.67	−2.55	1.9	−2.42	7.66:	7.08	1.20:	0.67	0.53:
HD 148816	5860	4.07	−1.00	1.6	−0.76	8.37	...	0.25	...	...
HD 165195	4190	0.96	−2.15	1.7	−1.88	7.27	7.77	0.27	0.82	−0.55
HD 165908	5920	4.09	−0.55	1.2	−0.69	8.39	8.60	0.20	0.46	−0.26
HD 187111	4310	1.09	−1.85	1.5	−1.74	7.65	8.01	0.51	0.92	−0.41
HD 199191	5030	2.73	−0.70	1.6	−0.87	8.84:	8.26	0.83:	0.30	0.53:
HD 201891	5900	4.19	−1.10	1.4	−1.20	<8.00	...	<0.32	...	...
HD 216143	4540	1.78	−2.15	2.1	−2.09	7.48	7.70	0.69	0.96	−0.27
HD 221170	4570	1.37	−2.10	1.6	−2.03	7.37	7.54	0.52	0.74	−0.22
BD+37°1458	5570	3.36	−2.15	1.9	−2.08	8.02:	7.45	1.22:	0.70	0.52:
Sun	5780	4.44	0.00	1.2	0.00	8.88	8.83	0.00	0.00	0.00

4. Preliminary Results

We adopted [Fe II/H] from Takada-Hidai et al. (2004) and used them for estimates of [O/Fe], which is listed in Table 1. The [O/H] values of the [O I] and triplet lines were estimated by subtracting a corresponding solar value, respectively, and then each [O/Fe] values were estimated as given in columns (9) and (10) of Table 1. To see a consistency between the abundances from the [O I] and triplet lines, the differences δ[O/Fe]=[O/Fe]$_{\rm Forb}$−[O/Fe]$_{\rm Trip}$ are also shown in column (11) of Table 1.

A careful inspection of [O/Fe] and δ[O/Fe] derived from the forbidden and the triplet lines reveals: (1) that the values of NLTE [O/Fe] of the triplet lines distribute almost flat with an average of $\sim$ 0.75 dex in the range of [Fe/H]< -1, while those of the [O I] lines seem to show an increasing trend with decreasing [Fe/H], and (2) that the triplet-line NLTE [O/Fe] are systematically larger than the forbidden-line [O/Fe] by an average of $\sim$ 0.35 dex in the range of $-2 <$[Fe/H]< 0.

These preliminary results should be confirmed by the further detailed studies of the forbidden lines, taking into account of influence with the blend of Ni I line and with CO molecule.

Acknowledgments

We would like to thank the staff of OAO for the help with observations. M. T.-H. acknowledges partial finacial support from JSPS (C-2, No. 13640246) as well as Tokai University. This research has made use of the SIMBAD database, operated at CDS, Strasbourg, France.

References

1. C. Allende Prieto, D. L. Lambert and M. Asplund, *ApJ.* **556**, L63 (2001).
2. P. E. Nissen, F. Primas, M. Asplund and D. L. Lambert, *A&A* **390**, 235 (2002).
3. C. Soubiran, D. Katz and R. Cayrel, *A&AS* **133**, 221 (1998).
4. M. Takada-Hidai, Y.-j. Saito, Y. Takeda, S. Honda, K. Sadakane, S. Masuda and H. izumiura, *to be submitted to PASJ*, (2004)
5. Y. Takeda, *A&A* **402**, 343 (2003).
6. W. L. Wiese, J. R. Fuhr and T. M. Deters, *J. Phys. Chem. Ref. Data, Monograph* **No. 7**, (1996).

SUPERNOVA EXPLOSION ENERGY WITH RELATIVISITIC EOS INCLUDING HYPERON

CHIKAKO ISHIZUKA[†],
Department of Physics, Hokkaido University, Sapporo, Japan

AKIRA OHNISHI,
Department of Physics, Hokkaido University, Sapporo, Japan

KOHSUKE SUMIYOSHI,
Numazu College of Technology, Numazu, Japan

SHOICHI YAMADA
Department of Science and Engineering, Waseda University, Tokyo, Japan

In the framework of RMF containing the full baryon octet [1] , we have made the EOS table at high densities combined with the relativistic nuclear EOS table [2] at lower densities. Both parts of the table is based on the TM1 parameter [3] of RMF, then the table covers wide range of nuclear densities, from $10^{5.1}$g/cc to $10^{15.4}$g/cc, smoothly. As a sample calculation by using this new EOS table, we perform 1-dim. spherical hydrodynamical calculation [4] with the relativistic EOS of supernova matter including hyperons and discuss the EOS dependence of the explosion energy. For the most attractive Σ potential case, we find that hyperons increase the explosion energy by about 4 % in the case of $15M_{\odot}$ model. We also show the element composition around core bounce, where $\rho \sim 1.6\rho_0$. At this density, hyperons can appear due to finite temperature effects. Although the hyperon ratio is small, it leads to the reduction of pressure by around 3 %. In this paper, we discuss the mechanism of hyperon admixture, and progenitor mass dependence on hyperon ratio.

* This work is supported by the Grant-in Aid for Scientific Research (15540243) of the Ministry of Education, Science, Sports and Culture of Japan.
[†]E-mail : chikako@nucl.sci.hokudai.ac.jp

1. Introduction

One feature behind this work is the fact that successful supernova explosion of massive star has not been achieved in spite of various discussions about its dynamics and micro-physics inputs of hydro-dynamical calculations. Then, a lot of improvements have been considered for numerical calculations of the explosion. In the following sentences, we briefly introduce major ideas about the input physics. As a macro physics, hydro-dynamics with ration and convection are considered. Another aspect of the improvements is radioactive transport or general relativity. Added to that, recently, MHD driven explosion has attracted interest. On the other hand, as for the micro physics, weak interaction, ν-interaction rate with matter or ν-oscillation, are important. Especially nuclear physics such as the equation of state (EOS) of hadronic matter and many body effects on ν-reaction rate cannot be considered by itself. The obtained results by using these inputs give us knowledge of chemical evolution of the universe, formation of compact objects, or acceleration of high energy particles.

As you may know, in neutron stars or supernova explosions of massive stars, hyperons are expected to emerge and to soften EOS. Recent experiments provide us useful information on hyperons. For example, we know that Λ and Ξ potentials at ρ_0 are -28 MeV and -14 ~ -16 MeV, respectively. However, there has been no work on supernova explosion with relativistic EOS including hyperons.

2. Construction of relativistic EOS table with hyperons

We made an EOS table in the framework of relativistic mean field (RMF). Our table is based on a Lagrangian [1] which includes full baryon octet (n, p, Λ, Σ^-, Σ^0, Σ^-, Ξ^-, Ξ^0). The baryon potentials are as follows;

$$U_\Lambda^{(N)} = U_\Sigma^{(N)} = -30 \text{ MeV}, \; U_\Xi^{(N)} = -28 \text{ MeV},$$
$$U_\Xi^{(\Xi)} \sim U_\Lambda^{(\Xi)} \sim U_\Xi^{(\Lambda)} \sim 2U_\Lambda^{(\Lambda)} \sim -40 \text{ MeV}.$$

As described before, Λ is attractive and we take here attractive Σ-N interaction. As for Σ, its potential has large ambiguity. For instance, the potential is the same order of Λ in old conjecture, while recent several researches suggest the repulsive Σ. Then we can assume that the Σ potential is between -30 MeV and 150 MeV.

This table follows Shen et al.'s style [2], which is relativistic EOS of nuclear matter and is used in calculations of core collapse supernova and it is also based on the same parameter set of TM1 [3]. The table gives thermo-dynamical variables as a function of electron ratio Ye, baryon density n_B, and temperature T.

These variables cover the following ranges:

- $Ye = 0 \sim 0.56$
- $Log_{10}n_B = 5.1 \sim 15.5$ [g/cc]
- $T = 0 \sim 100$ [MeV]

As we mentioned earlier, our table includes full baryon octet at high densities and it is combined with their relativistic nuclear EOS at lower densities than ρ_0. Therefore, it is useful for studies of supernova physics because this covers hadronic properties which we need in a calculation of core collapse.

3. Application to Hydro-dynamical calculation

At the end of the stellar evolution, an iron core is formed at the center of the pre-SN star. The inner core bounces due to a hard core of nuclear force after gravitational collapse. Then as a sample calculation using our table, we perform hydro-dynamical simulation of 1-dim. spherical explosion by using the numerical code developed by our collaborators (see ref.[4] for details). The code assumes a adiabatic explosion by shock propagation. For pre-supernova model of massive stars, we use the model provided by Woosley. In this calculation, 11, 12, 13, 15, 18 and 20 M_o progenitor models are assumed in order to see hyperon effects not at neutron star cooling state but at the early stage of core bounce, although the delayed type explosion with ν transport are usually supported for these stellar masses.

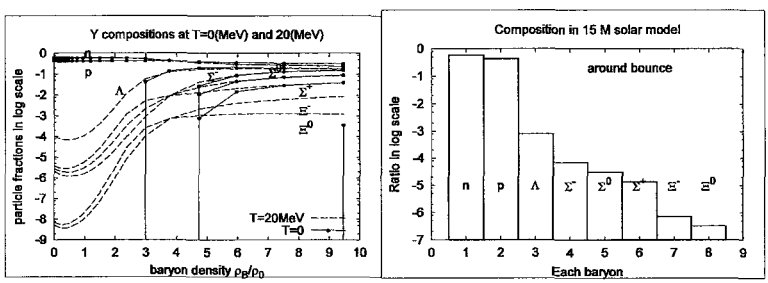

Figure 1. The left panel shows the hyperon fractions at Ye~0.42 and T=20MeV (dashed line) and those at T=0 MeV (dotted solid line). The right panel shows the ratios of each baryons normalized by baryon density $1.6\rho_0$ at central mass mesh around core bounce (Ye, ρ_B, T) = (0.42, $1.6\rho_0$, 22 MeV) in the case of the initial configuration of 15 M_o pre-supernova model..

As a result, the progenitor mass dependence on hyperon ratio is small, then we concentrate on 15 M_o model in this paper. The density trajectory shows that densities based on EOS with hyperon are suppressed compared to that with EOS without hyperons just outside of the center of the core behind shock front, though the central density is almost same in the case of both tables. Here, the

central density is about $1.6\rho_0$. This is why the shock waves at this moment reach up to only central part of the core. In the region behind the shock, temperature rises very quickly. Then hyperon appears by finite temperature effect and EOS becomes soft.

In a usual treatment of the core collapse, hyperon effect is considered to be negligible during core bounce because the matter density does not reach to $2\sim3\rho_0$ at which hyperon appearance is expected to start in cold dense matter. However, in the left panel of Fig.1, you can see that Λ, $\Sigma_{-,0,+}$ can be already seen just above the normal density in T=20 MeV case, while no hyperons appear until density rises a few times of the normal density at T=0 Mev.

As a sample plot of hadronic distributions, we show hyperon compositions of a central mass mesh around core bounce in the right panel of Fig.1. The main component of hyperons at this mesh point is Λ and Σ is smaller than Λ by one order. Ξ's contribution can be considered to be negligible in this model.

After simple evaluation, we find that the hyperons reduced 3% of the pressure at the center and increase a explosion energy about 4%, where the explosion energy follows a definition in ref.[4]. The explosion energy based on EOS table without hyperon is $1.52\text{x}10^{51}$erg and that with hyerons is $1.57\text{x}10^{51}$erg.

Thus hyperons result in percent order changes even if their amounts are quite small. These results may facilitate the explosion with ν-transport.

In the future work, we should compare results based on several parameter set of EOS, since the hyperon potential in nuclear matter is still ambiguous. Then we will perform a simulation with neutrino transport by using this EOS table in near future after the extension of our table for $U_\Sigma(\rho_0) = -30 \sim +30$ MeV.

References

1. J. Schaffner and I. Mishustin, *Phys. Rev.* **C53**, 1416 (1996).
2. H. Shen, H. Toki, K. Oyamatsu and K. Sumiyoshi, *Prog. Theor. Phys.* **100**, 1013 (1998).
3. Y. Sugahara, H. Toki, *Nucl. Phys.* **A579**, 557 (1994).
4. K. Sumiyoshi, H. Suzuki, S. Yamada, H. Toki, *Nucl. Phys.* **A** accepted (2003).

THE p-PROCESS IN CORE COLLAPSE SUPERNOVAE: INFLUENCE OF DIFFERENT EXPLOSION ENERGIES AND METALLICITIES

N. IWAMOTO, H. UMEDA AND K. NOMOTO

Department of Astronomy, School of Science, University of Tokyo, Hongo 7-3-1, Bunkyo-ku, Tokyo 113-0033, JAPAN
E-mail: niwamoto@astron.s.u-tokyo.ac.jp

We present results of p-process nucleosynthesis in core collapse supernovae (SNe). We focus on the influence of different explosion energies and metallicities on p-process yields. We find that overproduction factors have a strong sensitivity on peak temperatures and that the distribution of normalized mean overproduction factors is robust to changing the explosion energy and metallicity. Our results indicate that (1) the contribution to the galactic evolution of p-nuclei from stars with $Z \lesssim Z_{\odot}/20$ reduces significantly, and (2) more massive ($M \gtrsim 25M_{\odot}$) and energetic SNe may be a dominant production site of the p-nuclei.

1. Introduction

The p-nuclei are neutron-deficient, rare isotopes of elements with atomic number $Z \geq 34$. Most of them are bypassed from the neutron capture s-process paths and shielded from β-decay after the freeze-out of the r-process. Many investigations have been performed and have found that the most promising site is the O/Ne layer in core collapse supernovae (SNe)[1,2,3] (see Ref. 4 for a recent review). However, some shortcomings have been reported. The most important one is that ^{92,94}Mo, ^{96,98}Ru and ^{138}La are relatively underproduced.[5,6] The other problem was also addressed that the p-nuclei are produced much less than oxygen which is the main products in SNe.[3,7] In this work, we calculate p-process nucleosynthesis in core collapse SNe and investigate influences of different explosion energies and metallicities on the yields of p-nuclei. Models with masses of 15, 25 and $40M_{\odot}$ and metallicities of $Z = 0.02$ and 0.001 are evolved from main sequence to Fe core collapse stage, and exploded with explosion energies of $E_{51} = E/10^{51}$ ergs $= 1$ and 20 (1 and 20 foe), except for the $15M_{\odot}$ models because in $M \lesssim 20M_{\odot}$ explosion energy is considered to be almost unchanged ($\sim 10^{51}$

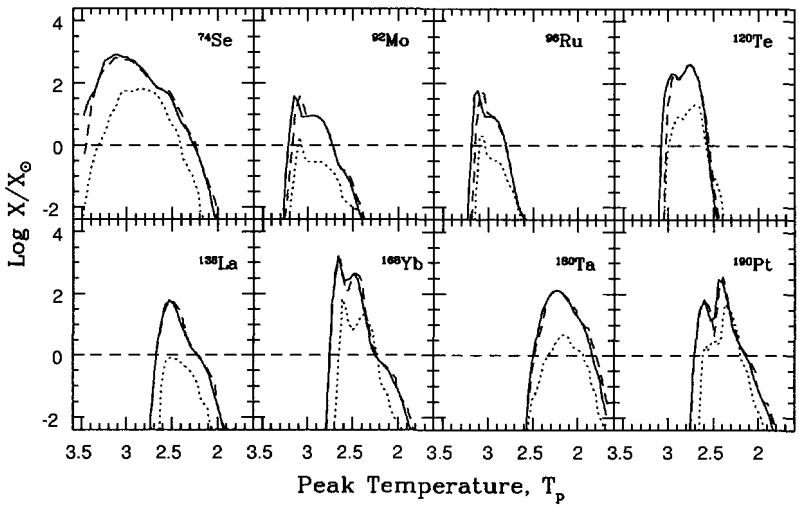

Figure 1. Overproduction factors of some p-nuclides in the $25M_{\odot}$ models with (E_{51}, Z) = (1, 0.001), (1, 0.02), and (20, 0.02), indicated by dotted, dashed and solid lines, respectively, are shown as a function of T_p.

ergs).[8] The s-process nucleosynthesis during core He burning is calculated to obtain seed abundances of elements with atomic number higher than 30. For lighter elements we adopted abundances at presupernova stage. In our nuclear reaction network, we consider 1752 nuclides and most of the reaction rates are taken from REACLIB.[9]

2. Results

We use time variations of temperature and density at layers with peak temperatures T_p (in units of 10^9 K) in the range of 1.7-3.5 where a typical condition for the production of p-nuclei holds after shock wave passes through these layers (so-called p-process layer, hereafter PPL). The production is driven by photodisintegration on stable heavy nuclei. The main contributions come from neutron emitting (γ, n) reactions. In addition, (γ, p) and (γ, α) reactions also play an important role to create rare p-nuclei. We find that the production of p-nuclei strongly depends on the T_p in Figure 1 (cf., Ref. 3). We obtain that a higher explosion energy causes the region related with the p-process to shift outward and extend in mass.[10] For example, the mass regions of the PPL are 1.97-2.80$M_{\odot}$ and 2.87-4.63$M_{\odot}$ for $25M_{\odot}$, solar metallicity models with E_{51} = 1 and 20, respectively. In the 20 foe

models the p-nuclei are synthesized under conditions with lower density and faster expansion timescale. As a result, the small difference in the distribution of overproduction factors $(X_i/X_{i,\odot})$ can be seen in the solar metallicity models in Fig. 1. However, the difference in the density and expansion timescale is not so critical as to influence the overall p-process nucleosynthesis. The influence of different stellar masses on the overproduction factors in the same metallicity and explosion energy models is also small in the temperature ranges in which the p-nuclei are efficiently produced, though somewhat large differences for light p-nuclei ^{74}Se, ^{78}Kr and ^{84}Sr can be recognized, resulting from the different initial seed abundance distributions. The dependence of the overproduction factors on T_p in the $Z = 0.001$ models are relatively similar to that in solar metallicity models, but produced abundances are low by a factor of $\sim$ 10-100 due to small amounts of seed nuclei.

Here we define mean overproduction factor $< F_i >$ in the form

$$< F_i >= \sum_{n>1} \frac{1}{2}(f_{i,n} + f_{i,n-1})(M_n - M_{n-1})/M_{PPL},$$

where n is the mesh number, $f_{i,n}$ $(= X_{i,n}/X_{i,\odot})$ the overproduction factor for each nuclide, and M_{PPL} the total mass of the PPL. Therefore, $< F_i >$ stands for a degree of enhancement of p-nuclides in the PPL. We also use the overproduction factor averaged over 35 p-nuclei F_0 to represent an average enhancement of p-nuclides in the PPL.

In Figure 2 the distribution of $< F_i > /F_0$ has the same feature as in previous works that ^{92,94}Mo, ^{96,98}Ru, ^{113}In, ^{115}Sn and ^{138}La are severely deficient. The overall distribution is robust to changes of explosion energy and metallicity. This is because the p-nuclei are made in the almost same peak temperature range (see Fig. 1). In contrast, F_0 varies significantly in the different metallicity models. For $Z = 0.001$ models we obtain very low overproduction factors of F_0 =2-3, resulting from low seed abundances. Therefore, this implies that the contribution to the galactic evolution of p-nuclei from core collapse SNe with $Z \lesssim 0.001$ is very small since the p-process yields largely depend on the initial amount of heavy seed nuclei.

In high explosion energy models the mass region where the complete and incomplete Si burnings take place moves outward and extends.[10] Thus, the oxygen layer becomes narrow in mass and the resultant ejected oxygen mass also decreases. In addition, F_0 becomes large since a wide mass region is related to the p-process as mentioned above. As a consequence, we infer that the p-process nucleosythesis in SNe with high mass $(M \gtrsim 25M_\odot)$ and

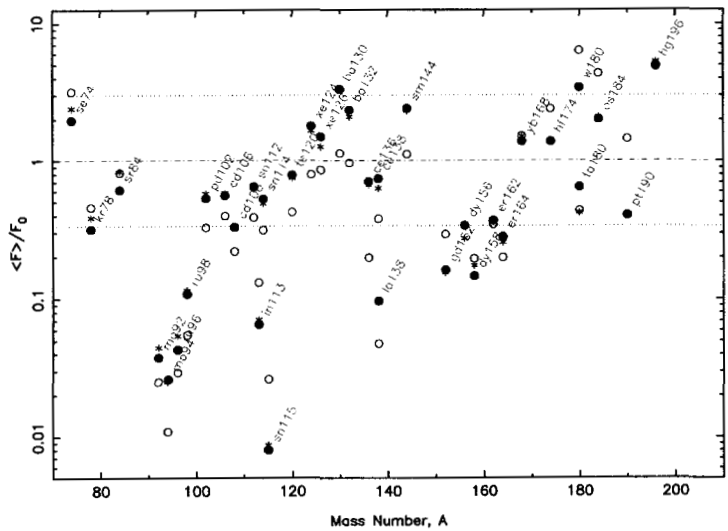

Figure 2. Values of normalized mean overproduction factor $< F_i > /F_0$ for the $25M_\odot$ models with (E_{51}, Z, F_0) = (1, 0.001, 2.22), (1, 0.02, 49.3), and (20, 0.02, 54.4), indicated by open and filled circles, and asterisks, respectively. The dotted horizontal lines designate the range within a factor of 3 from the average enhancement F_0.

high explosion energy relieves the crucial problem that the yield of the p-nuclei is relatively low, in comparison with that of oxygen.[3,7] We note that other production sites and processes[6,11,12,13] should be investigated to explain the abundance pattern of p-nuclides in the solar system.

References

1. S. Woosley and W. M. Howard, *ApJS* **36**, 285 (1978)
2. M. Rayet, N. Prantzos and M. Arnould, *A&A* **227**, 271 (1990)
3. N. Prantzos, M. Hashimoto and K. Nomoto, *A&A* **234**, 211 (1990)
4. M. Arnould and S. Goriely, *Phys. Rep.* **384**, 1 (2003)
5. V. Costa et al., *A&A* **358**, L67 (2000)
6. S. Goriely et al., *A&A* **375**, L35 (2001)
7. M. Rayet et al., *A&A* **298**, 517 (1995)
8. K. Nomoto et al., astro-ph/0308136 (2003)
9. F. -K. Thielemenn, private communication (1995)
10. T. Nakamura et al., *ApJ* **555**, 880 (2001)
11. W. M. Howard and B. S. Meyer, *Nuclei in the Cosmos 2*, 575 (1993)
12. S. Goriely et al., *A&A* **383**, L27 (2002)
13. S. Fujimoto et al., *ApJ* **585**, 418 (2003)

A COMPARISON BETWEEN AN ULTRA-RELATIVISTIC *AU+AU* COLLISION AND THE PRIMORDIAL UNIVERSE

JENS SÖREN LANGE*

Institut für Kernphysik†, Johann Wolfgang Goethe-Universität, August-Euler-Straße 6, 60486 Frankfurt/Main, Germany

Ultra-relativistic nucleus-nucleus collisions create a state of matter of high temperature and small baryo-chemical potential, which is similar to the thermodynamical conditions in the primordial universe. Recent analyses of *Au+Au* collisions at RHIC revealed the temperature, size and density of the system. Thus, a comparison to the primordial universe can be attempted. In particular, two observables shall be investigated, namely *(1)* the temperature at baryon freeze-out ($t\simeq$10 fm/c in the *Au+Au* collision) and *(2)* the matter density at the partonic stage ($t\leq$1 fm/c).

At the Relativistic Heavy Ion Collider (RHIC) at Brookhaven National Laboratory, New York, USA, gold nuclei collide at a maximum center-of-mass energy $\sqrt{s}$=200 GeV. The STAR experiment is one of four experiments [1], which investigate novel QCD phenomena at high density and high temperature in these collisions. The main STAR subdetector is a midrapidity ($|\eta|\leq$1.6) Time Projection Chamber [2] (TPC, R=2 m, L=4 m) with $\simeq$48,000,000 pixels. In 3 years of data taking, high statistics ($10^6\leq N\leq 10^7$ events on tape) for *Au+Au*, *p+p* and *d+Au* at $\sqrt{s}$=200 GeV and *Au+Au* at $\sqrt{s}$=130 GeV were recorded[a]. Fig. 1 shows a RHIC *Au+Au* collision.

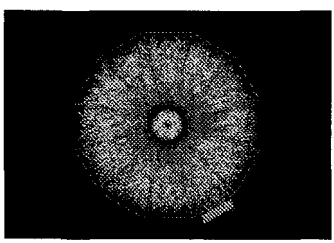

Figure 1. RHIC *Au+Au* collision at $\sqrt{s}$=200 GeV, recorded at the STAR experiment.

1. Comparison of the Temperature

Generally, in a thermalized system, inclusive particle transverse mass spectra can be described by a Boltzmann distribution $dN/dm_T \sim m_T \exp(-(m_T-m)/T)$ [3], where N denotes the particle yield. The transverse mass is defined as $m_T=\sqrt{p_T^2+m^2}$. By using dN/dm_T for $\pi^{\pm}$, $K^{\pm}$, protons and antiprotons, the freeze-out temperature in an *Au+Au* collision was determined to be T= 89±10 MeV [4], which corresponds to $T=(1.03\pm0.12)\cdot10^{12}$ K. This temperature can be compared to other systems (Tab. 1). An interesting difference is, that an *Au+Au* collision is matter dominated all the time. In the universe, there has been at first a radiation dominated time period ($T\geq$1 eV), followed by a matter dominated period ($T\leq$1 eV). Both periods differ in

*Email soeren@bnl.gov.

†currently on sabattical leave to
Brookhaven National Laboratory, Upton, New York 11973, USA

[a]The *p+p* and *d+Au* data set serve as reference.

the time dependence of the temperature, i.e. $T\sim 1/t^{1/2}$ vs. $T\sim 1/t^{2/3}$, respectively. For a $Au+Au$ collision, the time dependence can be derived by a simple thermodynamical ansatz $E/N\sim$T and $N/V\sim T^3\sim 1/t$, which leads to a flatter time dependence $T\sim 1/t^{1/3}$ (using total energy E, particle number N and volume V). The above mentioned temperature T_{kin}=89±10 MeV refers to *kinetic* freeze-out, i.e. the termination of elastic rescattering. The temperature of the earlier *chemical* freeze-out (i.e. the termination of ineleastic rescattering) is higher T_{chem}=156±6 MeV [4]. As it does not depend upon the particle density, the *chemical* freeze-out temperature is a universal quantity, i.e. identical for the $Au+Au$ collisions and the primordial universe.

2. Comparison of the Size

The size[b] of the fireball in a $Au+Au$ collision was measured precisely by $\pi^{\pm}\pi^{\pm}$ interferometry [7], i.e. in the beam direction R_{long}=5.99±0.19(stat.) ±0.36(syst.), and perpendicular to the beam direction R_{out}=5.39±0.18 (stat.)±0.28(syst.). This size corresponds to the time of pion freeze-out ($t\simeq$10 fm/c). As the fireball is expanding (Sec. 3), the size is a function of time. What was the size of the universe, when it had a temperature of T=100 MeV (corresponding to hadronic freeze-out) ? As shown in Fig. 2, hadronic freeze-out is believed to have occured in the primordial universe at $t\sim 10^{-3}$ s. As inflation is believed to have occured at 10^{-36} s$\leq t\leq 10^{-33}$ s, it can be concluded, that during baryonic freeze-out the universe had already macroscopic dimensions, i.e. a horizon distance of $R\sim$10 km.

3. Comparison of the Expansion Velocity

As mentioned in Sec. 1, inclusive particle m_T spectra for a $Au+Au$ collision can be fitted by a Boltzmann distribution. This ansatz is only approximately true, as it neglects kinetic terms, i.e. the inverse logarithmic slope is not only proportional to $1/T$, but $1/T+1/2mv^2$. Only for light particles the approximation $m\simeq 0$ holds. If treated more quantitatively [4], an expansion velocity can be extracted from a simultaneous fit to π, K and p spectra. The result is β=0.59±0.05 with $v=\beta$c. For the universe, at the time of baryon freeze-out with a horizon distance of $R\simeq$10 km (corresponding to $T\simeq$100 MeV), the expansion rate had been slower than the speed of light by a very large factor $1/M^2_{Planck}\simeq 10^{19}$ [8]. In addition, the topology of the primordial universe might have been very different from the topology of a RHIC collision. The general relativity line element $ds^2\sim dr^2/(1\text{-}k)$ contains a curvature $k=2GM/Rc^2$, using the gravitational constant G. M and R

[b] Note that a priori R_{long} and R_{out} are measurements of homogenity lengths, which then are interpreted as system size.

denote the mass and the size of the system, respectively. Even though the universe appears to be flat (k=0) in the present, the inflation model still allows a primordial non-flat geometry [9]. For a singularity at t=0, one would have to assume k=+1 for the period before inflation. In that case, the universe would have been a 3-dim sphere curved into the 4^{th} dimension, and thus infinite for an observer inside the universe. A particle travelling into one direction, finally - due to the curvature - comes back to the point, where it started. The system is closed. The RHIC collision topology is not a sphere, because the two initial state Au nuclei are moving along the beam axis with the speed of light. Thus, the system has a cylindrical component. Additionally, in case of the RHIC collision, space time is not curved. According to [10], one can estimate k=10^{-22}. Hence, the system is geometrically flat and thermodynamically open, and any particle can escape.

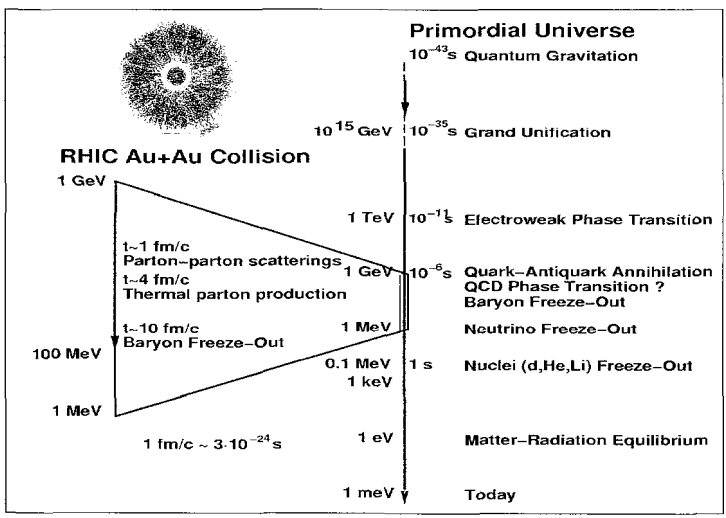

Figure 2. Timeline of an Au+Au collision (left) and the primordial universe [5] [6] (right).

4. Comparison of the Matter Density

For a RHIC Au+Au collision, the spatial matter density, i.e. the number of partons per volume ρ=$N_{partons}/V$ can be estimated by a Bjorken ansatz [11]. If assuming that initial and final entropy are equal, the number of partons at $t \leq 1$ fm/c is equal to the measured number of final state hadrons N_{hadron}. The volume can be calculated by inserting the fireball

radius (Sec. 2) into a cylindrical volume (due to Lorentz boost in the beam direction), i.e. $\rho \simeq dN_{parton}/dy \cdot 1/(\pi R^2 t)$ using the Lorentz invariant rapidity y. For this ansatz, highest densities are expected early in the collision (singularity for $t \to 0$). For t=0.2 fm/c the matter density is $\rho \simeq 20/\mathrm{fm}^3$, which corresponds to $\simeq 15 \times \rho_o$, the density of cold gold nuclei. At this high density, hadrons are definitely non-existent. In Tab. 2, the density is compared to other systems. What was the size of the universe at $\rho = 15\rho_o$? For the scenario of inflation, an initial universe mass $M \simeq 25$ g is generally assumed. For inflation from an initial radius of $R_i = 10^{-40}$ m to a final radius of R_f=1 m, the density would change from $\rho_i \simeq 10^{118}$ kg/cm^3 (at $t \simeq 10^{-36}$ s) to $\rho_f \simeq 10^{-19}$ kg/cm^3 (at $t \simeq 10^{-33}$ s). Thus, RHIC density was achieved *during* inflation. In non-inflation models, the size of the universe in the Planck epoch ($t \simeq 10^{-43}$ s) is $R \simeq 10^{-5}$ m. To achieve RHIC density, one would hypothetically[c] have to fill it with $m \simeq 3600$ kg gold. If the initial mass were less, RHIC density would never have been achieved.

Table 1. Comparison of the temperatures in various systems.

$1.4 \cdot 10^{34}$ K	Planck temperature
$1.0 \cdot 10^{12}$ K	*Au*+*Au* collision
10^9 K	sun (core)
$15 \cdot 10^6$ K	supernova
$55 \cdot 10^6$ K	plasma fusion
$4 \cdot 10^6$ K	laser fusion

Table 2. Comparison of the density in various systems.

$2 \cdot 10^{17}$ kg/cm^3	*Au* nuclear density
$30 \cdot 10^{17}$ kg/cm^3	*Au*+*Au* collision
$\sim$20,000 kg/cm^3	*Au* atomic density (solid)
$\sim$1000 kg/cm^3	metallic hydrogen
$1.1 \cdot 10^{-26}$ kg/cm^3	universe critical density

References

1. For a RHIC overview see `http://www.bnl.gov/rhic/`
2. M. Anderson at al., *Nucl. Inst. Meth.* **A499**(2003)659
3. J. S. Lange, *Nucl. Phys.* **A718**(2003)367
4. The STAR Collaboration, nucl-ex/0310004, subm. *Phys. Rev. Lett.*
5. `http://en.wikipedia.org/wiki/Timeline_of_the_Big_Bang`
6. D. H. Lyth, Introduction to Cosmology, 1993, astro-ph/9312022
7. The STAR Collaboration, *Phys. Rev. Lett.* **87**(2001)082301, nucl-ex/0107008
8. K. Kajantie, European School of High-Energy Physics, CERN-97-03, p. 261
9. A. H. Guth, *Phys. Rev. D***23**(1981)347
10. W. Busza, R. Jaffe, J. Sandweiss, F. Wilczek, *Rev. Mod. Phys.* **72**(2000)1125
11. J.D. Bjorken, Phys. Rev. **D27**(1983)140
12. S. Hawking, Mon. Not. R. Astro. Soc. **152**(1971)75

[c]Even before the existence of mass in the context of *particle* mass, mass can be defined in the context of a *gravitational* horizon mass $m = 6c^3 t/G$ [12].

KAON CONDENSATION AND THE NON-UNIFORM NUCLEAR MATTER

TOSHIKI MARUYAMA[1], TOSHITAKA TATSUMI[2],
DMITRI N. VOSKRESENSKY[3], TOMONORI TANIGAWA[4,1],
SATOSHI CHIBA[1], TOMOYUKI MARUYAMA[5]

1 Advanced Science Research Center, Japan Atomic Energy Research Institute, Tokai, Ibaraki 319-1195, Japan

2 Department of Physics, Kyoto University, Kyoto 606-8502, Japan

3 Moscow Institute for Physics and Engineering, Kashirskoe sh. 31, Moscow 115409, Russia

4 Japan Society for the Promotion of Science, Tokyo 102-8471, Japan

5 BRS, Nihon University, Fujisawa, Kanagawa 252-8510, Japan

Non-uniform structures of the mixed phase during the first-order kaon condensation, using the density functional theory with the relativistic mean-field model. Including the Coulomb potential and applying the Gibbs conditions in a proper way, we numerically determine the density profiles of nucleons, electrons and condensed kaons The importance of the Coulomb screening effects is elucidated and thereby we suggest that the Maxwell construction is effectively justified.

1. Introduction

There have been discussed various phase transitions in nuclear matter, like liquid-gas transition, meson condensations, hadron-quark deconfinement transition, etc. In most cases they exhibit the first-order phase transitions. In the first-order phase transition with more than one chemical potential, which is relevant for neutron-star matter, the structured mixed phase may be expected in the wide density range due to the Gibbs conditions for the phase equilibrium[1].

At densities where kaon condensation may occur, it has been suggested

that the structured mixed phase appears as a result of the first-order phase transition (FOPT). If this is the case, we can expect the geometrical structures in nuclear matter similar to the "pasta" phases at sub-nuclear densities.[2] For the first-order phase transitions with more than one chemical potential, the Maxwell construction (*coexisting separate phases* with the local charge neutrality) does not necessarily fulfill the Gibbs conditions for the phase equilibrium,

$$T^{\rm I} = T^{\rm II}, \quad P^{\rm I} = P^{\rm II}, \quad \mu_B^{\rm I} = \mu_B^{\rm II}, \quad \mu_e^{\rm I} = \mu_e^{\rm II}; \tag{1}$$

the last condition for the electron (charge) chemical potential is *violated*, $\mu_e^{\rm I} \neq \mu_e^{\rm II}$. When we naively apply the Gibbs conditions to the FOPT with more than one chemical potential, we expect there is no equal-pressure region seen in the Maxwell construction case and the *structured mixed phase* is realized instead in a wide density range in the EOS, where charge density as well as baryon density are no more uniform.[1]

However, it has been suggested in recent papers that the Maxwell construction may still have a physical meaning by taking the hadron-quark matter transition as an example: the density region of the structured mixed phase is largely limited by the *Coulomb screening effect*, and results based on the Gibbs conditions become very close to the Maxwell construction curve.[3] The aim of this paper is to clarify the Coulomb screening effect on the structure of matter in the first-order kaon condensation. Note that the uneasy relation, $\mu_e^{\rm I} \neq \mu_e^{\rm II}$, means nothing but the difference in the electron number between two phases, once the Coulomb potential is properly introduced.[3]

2. Kaon Condensation in High-density Matter

We use the density functional theory (DFT) with a relativistic mean field (RMF) model [4] in our study. We numerically solve the coupled equations of motion for meson fields (sigma, omega, rho and kaon), nucleon fields and electron field consistently with the Coulomb potential. Our framework and its ability are reported in detail by Maruyama et al.[5] With this framework we can satisfy the Gibbs conditions in a proper way.

If Glendenning's claim is correct, the structured mixed phase develops in a wide density range from well below to well above the critical density of the first-order kaon condensation. Then nuclear matter should exhibit the similar structure change to the nuclear "pasta" phases[5]: the kaonic droplet, the hole, and the uniform kaonic matter; actually we observe such structures in our calculation (see Fig. 1). Note that the present result

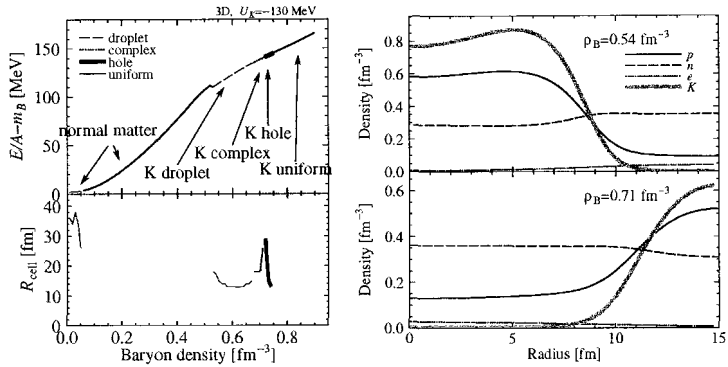

Figure 1. Left: the binding energy per nucleon and the cell size of nuclear matter in beta equilibrium. Right: the density profiles of kaonic matter. Droplet (upper panel) and hole (lower panel) configuration.

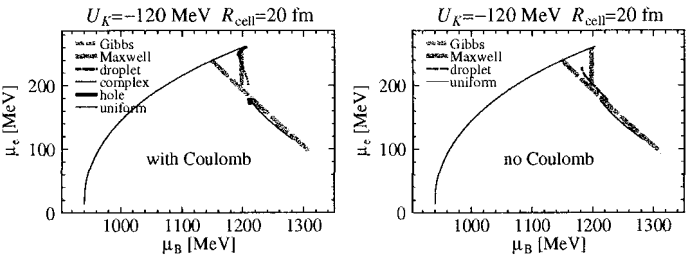

Figure 2. Phase diagram in the chemical potential plane. The cell radius is fixed to 20 fm. Left: full calculation. Right: the Coulomb potential is discarded to determine the matter structure. Curves by Gibbs conditions and Maxwell construction are also drawn in panels for comparison; both curves are calculated without the Coulomb interaction.[6]

is only for three dimensional calculation; we only considered the spherical configurations for the Wigner-Seitz cell. The "complex" configuration seen in the diagram only means not a simple droplet or a hole structure but *something like a shell shape or a hybrid structure of droplet and hole.* So we may not expect such configuration to be realized, when two or one dimensional geometrical structure is taken into account for the Wigner-Seitz cell.

To demonstrate the Coulomb screening effect on the kaonic mixed phase, we show in Fig. 2 the phase diagrams in the μ_B-μ_e plane with and without the Coulomb interaction. In the latter calculation the Coulomb potential

is discarded in determining the density profile and the Coulomb energy calculated using the density profile thus determined is finally added to the total energy. Though we cannot definitely say now, the curve without the Coulomb interaction is similar to the one given by the Gibbs conditions and the curve with the Coulomb interaction to the one given by the Maxwell construction. If we look at the density profile, the local charge neutrality is more achieved in the case with the Coulomb interaction. These results suggest that the Maxwell construction is effectively meaningful due to the Coulomb screening.

3. Summary and Concluding Remarks

We have discussed how the geometrical structure of the kaonic mixed phase changes during the phase transition. Using a self-consistent framework based on DFT and RMF, we took into account the Coulomb interaction in a proper way. We have seen how the self-consistent inclusion of the Coulomb interaction changes the phase diagram. Note that it becomes more remarkable in the case of kaon condensation than that of the nuclear pastas;[5] the density range of the structured mixed phase is largely limited and thereby the phase diagram becomes similar to that given by the Maxwell construction. The density profiles there also suggest the phase separation of two bulk matters. Although the importance of such a treatment has been demonstrated for the quark-hadron matter transition,[3] one of our new findings here is that we could figure out the peculiar role of the screening effect without introducing an "artificial" input for the surface tension; remember that we need to introduce a sharp boundary and its surface tension by hand as in discussing the quark-hadron mixed phase. Using the present results we can numerically extract the surface tension as well.

References

1. N. K. Glendenning, *Phys. Rev.* **D46**, 1274 (1992).
2. T. Norsen and S. Reddy, *Phys. Rev.* **C63**, 65804 (2001).
3. D. N. Voskresensky, M. Yasuhira and T. Tatsumi, *Phys. Lett.* **B541**, 93 (2002); Nucl. Phys. **A723**, 291 (2003); T. Tatsumi and D. N. Voskresensky, this proceedings.
4. *Density Functional Theory*, ed. E. K. U. Gross and R. M. Dreizler, Plenum Press (1995).
5. T. Maruyama et al., nucl-th/0311076; this proceedings.
6. N. K. Glendenning and J. Schaffner-Bielich, *Phys. Rev.* **C60**, 25803 (1999).

STUDY OF PROTON RESONANCES IN ^{26}SI AND ^{27}P BY THE ELASTIC SCATTERING OF ^{1}H(^{25}AL,P)^{25}AL, ^{1}H(^{26}SI,P)^{26}SI

J. Y. MOON, C. S. LEE, J. H. LEE and C. C. YUN
Chung-Ang University, Korea

J. C. KIM and M. YOUN
Seoul National University, Korea

S. KUBONO, T. TERANISHI, J. J. HE and M. NOTANI
Center for Nuclear Study, Graduate School of Science, University of Tokyo, Japan

S. NISHIMURA and M. NISHIMURA
RIKEN, Japan

V. GUIMARÃES and R. F. LIHITENTHALER
Instituto de Física, Universidade de São Paulo, Brazil

S. KATO
Yamagata University, Japan

The observational space map of 1.809-MeV gamma rays - coming from the decay of ^{26}Al - taken by COMPTEL requires the sources and their nucleosynthetic activity to be unveiled. One suggestion for the observation is the explosive hydrogen burning process which occurs in novae or X-ray bursts. Two capture reactions such as ^{25}Al(p,γ)^{26}Si and ^{26}Si(p,γ)^{27}P are of great importance in the production of 1.809-MeV gamma rays. Resonance states within the Gamow window should be precisely known to determine their reaction rates. As for the latter reaction, only a few levels in ^{27}P have been known above the proton threshold in comparison with many levels known in its mirror nucleus ^{27}Mg. We studied proton resonances in ^{26}Si and ^{27}P by the elastic scattering at low energies, respectively using low-energy ^{25}Al and ^{26}Si radioactive ion beams available from the CRIB facility at CNS, University of Tokyo. We carried out an experiment to investigate proton resonances in ^{26}Si up to $E_{C.M.}$ = 3.016 MeV, especially to determine the resonance parameters of the states at E_x = 7.019 and 8.120 MeV. We also measured the elastic scattering of p + ^{26}Si up to $E_{C.M.}$ = 3.290 MeV.

1. Introduction

The nine-year survey of COMPTEL aboard CGRO (Compton Gamma-Ray Observatory) has updated the all-sky map of 1.809-MeV gamma rays. The gamma rays are produced by the β^+-decay of ^{26}Al(g.s.) to the first excited state of ^{26}Mg, followed by deexcitation to its ground state. Knowledge of their sources is still unclear though massive stars, novae and X-ray bursts have been assumed to be possible sites. Therefore, information on the resonance states in relevant nuclei such as energy, spin and parity, is crucial to understanding production of the gamma-ray emitter ^{26}Al(g.s.) at the stellar condition and further clarifying knowledge of the sources. In thermonuclear runaway under the explosive hydrogen burning, the ^{25}Al(p,γ)^{26}Si reaction hinders production of ^{26}Al(g.s.). In spite of previous experimental measurements of the resonance states in ^{26}Si, several relevant states could not be clearly identified. Especially, the astrophysically important 3^+ state with the resonance energy (E_R) = 0.427 MeV could not be seen [1], nor definitely identified [2]. On the other hand, the ^{26}Si(p,γ)^{27}P reaction prevents ^{26m}Al from being produced. It has been suggested that high-temperature novae ($T \geq 0.4$ GK) may be hot enough to establish an equilibrium between ^{26}Al(g.s.) and ^{26m}Al [3]. Thus, study of the resonance states in ^{27}P is necessary to determine the reaction rate of proton capture on ^{26}Si. Only one state at 1.199 MeV above the proton threshold has been reported to date [4]. In the present experiment, we investigated the resonance states in ^{26}Si and ^{27}P using the inverse elastic scattering of ^{1}H(^{25}Al,p)^{25}Al and ^{1}H(^{26}Si,p)^{26}Si in a thick-target method.

2. Experimental procedure

The radioactive ion beams used in the present experiment were obtained by the CNS radioactive ion beam separator (CRIB) housed at RIKEN campus of the University of Tokyo. The ^{24}Mg^{8+} primary beam, accelerated by the K = 70 AVF cyclotron, was bombarded on a ^{3}He gas target at 7.434 A·MeV. The thickness of the ^{3}He gas target was 0.32 mg/cm^2. The ^{25}Al and ^{26}Si radioactive ion beams were simultaneously produced via ^{3}He(^{24}Mg,n)^{26}Si*(p)^{25}Al and ^{3}He(^{24}Mg,n)^{26}Si, respectively. These two beams were used for measurement of the elastic scattering of ^{1}H(^{25}Al,p)^{25}Al and ^{1}H(^{26}Si,p)^{26}Si in inverse kinematics. The radioactive ion beams were identified by using the time-of-flight (TOF) between the two parallel plate avalanche counters (PPAC's) in an achromatic focal plane (F2) together with the beam energy and TOF between the production target and the

PPAC on F2 plane. A slit on the momentum-dispersive focal plane (F1) enhanced beam purity. In addition, an energy degrader of the 2.6 μm mylar was used to provide another particle separation. The beams were finally bombarded on a polyethylene (CH_2) experimental target with the thickness of 8.24 mg/cm^2, being fully stopped in the target. To detect the recoiled protons, two sets of the silicon counter telescope consisting of a position-sensitive silicon detector (PSD) of 75 μm and a surface-barrier silicon detector (SSD) of 1500 μm were installed at 0° and 17°. They were used as ΔE-E telescopes to identify particles. In the second set at 17°, another SSD was added to reject high-energy protons. The thick-target method was employed to cover a wide range of excitation energy in ^{26}Si and ^{27}P. Beam energies on the target were 3.4407 A·MeV for ^{25}Al and 3.9575 A·MeV for ^{26}Si, respectively. With such experimental settings, we could study ^{26}Si up to E_x = 8.8243 MeV and ^{27}P up to E_x = 4.7109 MeV above the proton threshold. Measurement with a pure carbon target was done to subtract a carbon contamination from the proton spectrum of CH_2 target. The energy calibration of the detectors was done with the protons whose energies were determined by the CRIB magnetic settings.

Table 1. Specification of the radioactive ion beams (on target) used in the present work.

	Energy (A·MeV)	Intensity (kcps)	Purity (%)
^{25}Al	3.44	9.325	4.72
^{26}Si	3.95	1.573	0.7

3. Preliminary results

Data analysis was started just before the conference. Proton spectra shown in Figure 1 are presented as preliminary results. For the ^{25}Al + p spectrum (Figure 1(a)), candidates for several resonance states are observed but with weak intensity. We could not identify the 3^+ unnatural parity state with E_R = 0.427 MeV because the target was too thick for the recoiled proton to escape. Nuclear structure quantities such as spin-parity and energy will be determined with the future R-matrix analysis. For the ^{26}Si + p spectrum, we have also seen several peaks though statistics are not good (Figure 1(b)). Now data analysis is in progress.

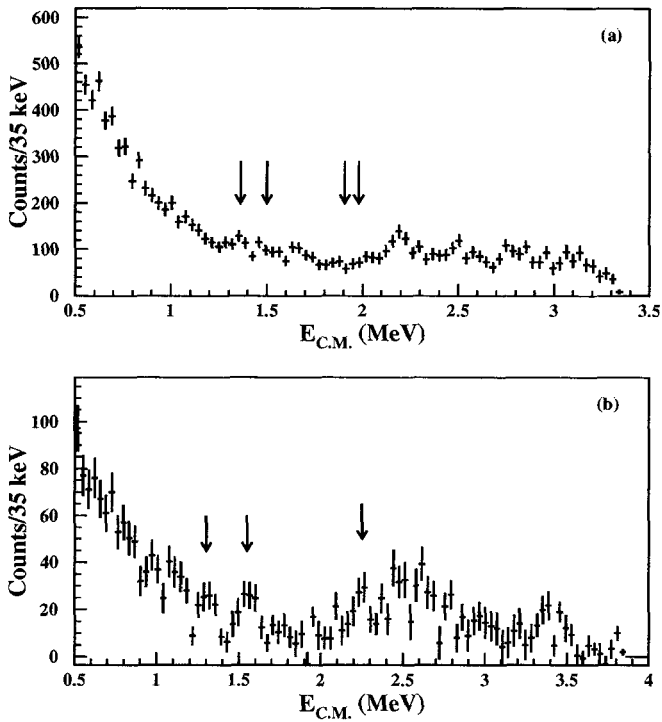

Figure 1. Energy spectra in the-center-of-mass (C.M.) system for the protons recoiled from the inverse elastic scattering of (a) ^{25}Al + p and (b) ^{26}Si + p. Both spectra were obtained from the detectors at 17°. Candidates for resonance states of interest are marked by arrows.

References

1. D. W. Bardayan et al., *Phys. Rev.* **C65**, 032801(R) (2002).
2. J. A. Caggiano et al., *Phys. Rev.* **C65**, 055801 (2002).
3. A. Coc, M.-G. Porquet and F. Nowacki, *Phys. Rev.* **C61**, 015801 (1999).
4. J. A. Caggiano et al., *Phys. Rev.* **C64**, 025802 (2001).

DUST FORMATION AND EVOLUTION IN THE EARLY UNIVERSE

TAKAYA NOZAWA AND TAKASHI KOZASA

Division of Earth and Planetary Sciences, Graduate School of Science, Hokkaido University, Sapporo 060-0810, Japan
E-mail: nozawa@ep.sci.hokudai.ac.jp, kozasa@ep.sci.hokudai.ac.jp

HIDEYUKI UMEDA, KEIICHI MAEDA AND KEN'ICHI NOMOTO

Department of Astronomy, School of Science, University of Tokyo, Bunkyo-ku, Tokyo 113-0033, Japan
E-mail: umeda@astron.s.u-tokyo.ac.jp, maeda@astron.s.u-tokyo.ac.jp, nomoto@astron.s.u-tokyo.ac.jp

We have investigated the formation of dust grains in the ejecta of Population III supernova; core collapse supernovae with the progenitor mass $M_{\rm pr}$ ranging from 13 to 30 $M_\odot$ and pair-instability supernovae with $M_{\rm pr} = 170$ and 200 $M_\odot$. In this paper, we report the amount of dust grains formed in the ejecta of Population III supernovae, and discuss the time evolution of dust-to-gas mass ratio and metallicity in the primordial universe.

1. Introduction

The recent observations have confirmed the presence of large amounts of dust grains even at $z > 6$ (e.g., Bertoldi et al. 2003). Dust grains absorb stellar light and re-emit it by thermal radiation, which heavily depend on the chemical composition, size and amount of dust grains. Therefore, dust grains in the early universe play a crucial role on deduction of the star formation rate (SFR) and the initial mass function (IMF) from the relevant observations.

The recent sub-millimeter observations toward the supernova remnant Cas A (Dunne et al. 2003) and Kepler (Morgan et al. 2003) by SCUBA have revealed the thermal radiation from cold dust, and suggested that dust grains of a few $M_\odot$ had condensed in the ejecta. At $z > 5$, the formation sites of dust grains are considered to be confined to supernovae because of their short life time of progenitors. In addition to ordinary core collapse su-

pernovae (CCSNe), the recent theoretical investigations have claimed that stars more massive than 100 $M_\odot$ populate the first generation (e.g. Bromm, Coppi and Larson 2002) and end up as pair-instability supernovae (PISNe, e.g. Umeda and Nomoto 2002).

Thus, to clarify the chemical composition, size and amount of dust grains in the primordial interstellar space, we performed the calculations of dust formation in the ejecta of Population III CCSNe with the progenitor mass $M_{\rm pr}$ ranging from 13 to 30 $M_\odot$ and PISNe with $M_{\rm pr} = 170$ and 200 $M_\odot$. In the calculation, for the elemental composition in the ejecta, we consider the two extreme cases; unmixed and uniformly mixed case. For the details of models and results of calculations, see Nozawa et al. (2003).

In this paper, we report the dependence of mass of dust grains formed in the ejecta on the progenitor mass (Section 2), and then discuss the time evolution of dust-to-gas mass ratio and metallicity in the early universe, employing a closed-box model (Section 3).

2. The amount of dust grains formed in the ejecta of Population III supernovae

Figure 1 shows the total mass of dust grains formed in the ejecta as a function of the progenitor mass. Figure 1a is for CCSNe and Figure 1b for PISNe; the solid line for the unmixed ejecta and the dashed line for the mixed ejecta. Total mass of dust grains increases with increasing the progenitor mass, and is larger in the mixed ejecta than in the unmixed ejecta, because more oxygen atoms are locked into dust grains in the mixed ejecta. The ratio of dust mass to progenitor mass ranges from 0.02 to 0.05 for CCSNe and from 0.15 to 0.3 for PISNe, and increases with increasing progenitor mass. This implies that a large amount of dust grains would be produced in the early universe, if Population III stars were very massive.

3. Time evolution of dust-to-gas mass ratio and metallicity

On the basis of dust yields obtained in the unmixed case, we calculate the time evolution of dust-to-gas mass ratio D ($= M_{\rm dust}/M_{\rm gas}$) and metallicity in the gas phase $Z_{\rm gas}$, employing a closed-box model. The details of calculation will be given by Nozawa et al. (2004, in preparation). For the IMF, we adopt the Salpeter-like IMF ($\phi(m) \propto m^{-1.35}$), but consider two types of mass range; one is the conventional Salpeter IMF with the mass range of $0.1M_\odot < m < 100M_\odot$ and, the other is the top-heavy IMF with $100M_\odot < m < 500M_\odot$ since the first generation stars are considered to be

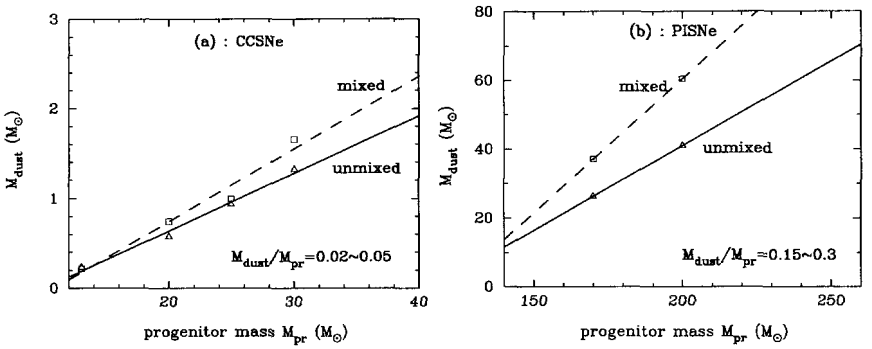

Figure 1. Total mass of dust grains formed in the unmixed (triangles) and mixed (squares) ejecta vs. progenitor mass $M_{\rm pr}$ (a) for CCSNe and (b) for PISNe; the solid line for the unmixed ejecta and dashed line for the mixed ejecta.

very massive (e.g. Bromm, Coppi and Larson 2002). For simplicity, the SFR is assumed to be constant and given by $\psi(t) = M_{\rm gas}/\tau_{\rm sf}$, where $\tau_{\rm sf}$ represents timescale of star formation. Also, we do not consider the effect of destruction of dust grains.

For the conventional Salpeter IMF (Fig. 2a), the increase of heavy elements in the interstellar space becomes prominent at $t = 4$–5×10^6 yr after the onset of star formation. When $\tau_{\rm sf} = 10^8$ yr (high SFR), metallicity $Z_{\rm gas}$ reaches 10^{-3} at $t = 2 \times 10^7$ yr. The dust-to-gas mass ratio is a factor of 3–4 smaller than metallicity for a given $\tau_{\rm sf}$ because the mass fraction of heavy elements locked into dust grains in the ejecta of CCSNe is 0.2–0.25.

For the top-heavy IMF (Fig. 2b), dust grains rapidly increase at $t = 2.2 \times 10^6$ yr. At $t = 2 \times 10^7$ yr, metallicity is more than 10^{-2}, 10^{-3} and 10^{-4} for $\tau_{\rm sf} = 10^8$, 10^9 and 10^{10} yr, respectively. Note that the difference between D and $Z_{\rm gas}$ is small in comparison with that for Salpeter IMF, because the mass fraction of heavy elements locked into dust grains in the ejecta of PISNe is ~ 0.35. Furthermore, the dust-to-gas mass ratio and the metallicity for the top-heavy IMF are about an order of magnitude larger than for the Salpeter IMF for a given $\tau_{\rm sf}$.

Hirashita and Ferrara (2002) suggest from their study of galaxy evolution that dust destruction has little influence on the amount of dust grains during the early evolution. In fact, we can neglect the effect of dust destruction until $t = 2 \times 10^7$ yr, except for the case of $\tau_{\rm sf} = 10^8$ yr for the top-heavy IMF. However, it should be noted that the effect of destruction of dust grains must be taken into account during the early phase, depending on the SFR and the IMF.

From these results, we can conclude that the time evolution of dust-to-gas mass ratio and metallicity in the early universe strongly depend on the SFR and the IMF. In order to estimate the SFR and the IMF in the early universe, it is necessary to observe not only the metallicity but also the dust-to-gas mass ratio at high z. Also, we must construct the more realistic models taking into account the effect of dust destruction.

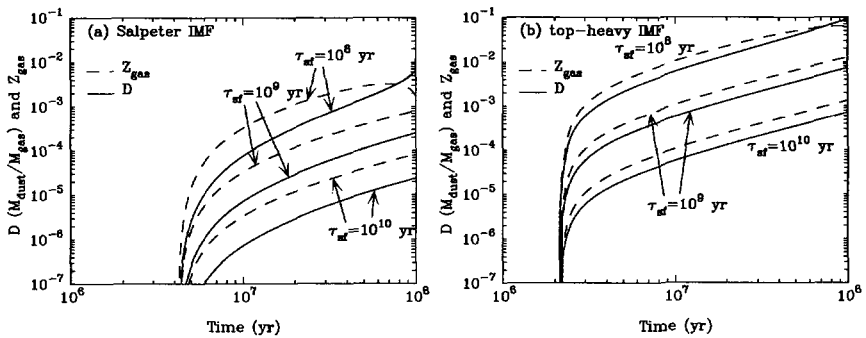

Figure 2. Time evolution of dust-to-gas mass ratio D (solid) and metallicity $Z_{\rm gas}$ (dashed) in the early universe, employing a closed-box model; (a) for the Salpeter IMF and (b) for the top-heavy IMF.

Acknowledgments

This work has been supported in part by a Grant-in-Aid for Scientific Research from the Japan Society for the Promotion of Sciences (13640229).

References

1. F. Bertoldi, C. L. Carilli, P. Cox, X. Fan, M. A. Strauss, A. Beelen, A. Omont and R. Zylka, *Astron. Astrophys.* **406**, L55 (2003).
2. L. Dunne, S. A. Eales, R. J. Ivison, H. Morgan and M. G. Edmunds, *Nature* **424**, 285 (2003).
3. H. Morgan, L. Dunne, S. A. Eales, R. J. Ivison and M. G. Edmunds, *Astrophys. J.* **597**, L33 (2003).
4. V. Bromm, P. S. Coppi and R. B. Larson, *Astrophys. J.* **564**, 23 (2002).
5. H. Umeda and K. Nomoto, *Astrophys. J.* **565**, 385 (2002).
6. T. Nozawa, T. Kozasa, H. Umeda, K. Maeda and K. Nomoto, *Astrophys. J.* **598**, 785 (2003).
7. T. Nozawa, H. Hirashita, T. Takeuchi and T. Kozasa, in preparation (2004).
8. H. Hirashita and A. Ferrara, *Mon. Not. R. Astron. Soc.* **337**, 921 (2002).

QUASI-FREE PROTON-PROTON ELASTIC SCATTERING IN THE TROJAN HORSE FRAMEWORK

M.G. PELLEGRITI[1,2], C. SPITALERI[1,2], A. MUSUMARRA[1,2], L. CALABRETTA [2], S. CHERUBINI[3], A. DI PIETRO[2], P. FIGUERA[2], R.G. PIZZONE[2], S. ROMANO[1,2], S. TUDISCO [1,2], A. TUMINO[1,2]

[1] *Dipartimento di Metodologie Chimiche e Fisiche per l'Ingegneria, Università di Catania, Italy*

[2] *Laboratori Nazionali del Sud, INFN, Catania, Italy*

[3] *Ruhr-Universität Bochum, Bochum, Germany*

The behaviour of the quasi-free p-p elastic cross section was investigated by using the Trojan Horse Method and the $^2H(p,pp)n$ reaction. This reaction has been recently studied at Laboratori Nazionali del Sud, INFN, Catania at a proton beam energy of 6 MeV. The extracted two-body cross section is compared with the free p-p one at relative enegies where the free p-p cross section is sensitive to the Coulomb interaction.

1. Introduction

The Trojan Horse Method (THM) [1,2,3,4,5,6,7] is an indirect method for nuclear astrophysics, based on a three-body reaction quasi-free mechanism, that allows cross section measurements at energy far below the Coulomb barrier. It is possible to extract a two-body cross section $(a + b \rightarrow c + C)$ from a measured three-body one $(a + A \rightarrow c + C + x)$ where the chosen nucleus A has a high probability to be clusterized into $x \oplus b$ and x behaves as a spectator to the process. If the reaction energy is higher than the Coulomb barrier in the entrance channel of the three-body reaction, the two-body interaction can be considered as taking place inside the nuclear field.

Therefore, in this picture, the extracted two-body cross section refers to the nuclear interaction only, the Coulomb barrier being already overcome in the entrance channel [4].

The present paper reports on the application of this method to the p-p scattering, the simplest case where the Coulomb suppression can be tested. The p-p cross section is well-known, its energy trend has been observed to

be very similar to that of n-n or p-n systems ($\approx 1/v$) except at low proton energies where it shows a deep minimum (E_{lab} = 382.43 keV, $\theta_{cm} = 90^o$) due to the interference between the nuclear and the Coulomb scattering amplitudes [8].

So, if one extracts the p-p cross section, under the THM assumptions from a suitable three-body one, like the $^2H(p,pp)n$ reaction, this extracted cross section is expected to show Coulomb suppression effects. For this reason, the $^2H(p,pp)n$ reaction was studied at Laboratori Nazionali del Sud (LNS), INFN, Catania, at proton energy higher than the p+d Coulomb barrier and such that the p-p relative energy in the exit channel is in the region of the deep minimum.

Thus, the extracted cross results can be compared both with the free p-p cross section which contains all Coulomb effects and with the n-n cross section that is sensitive to the nuclear interaction only.

2. Experimental set-up

A kinematically complete experiment was carried out at the LNS. The 15 MV Tandem provided a 6 MeV proton beam with a current of about 2 nA. The target consisted of a deuterated polyethylen film, 178 $\mu g/cm^2$ thick. Proton-proton coincidences were measured by two Position Sensitive Detectors placed at roughly symmetrical angles with respect to the beam direction: $16.2^o < \theta_{p1} < 24^o$ and $15.6^o < \theta_{p2} < 23.4^o$. The investigated proton-proton relative energy, E_{12}, ranges from 0.3 to 0.8 MeV.

3. Analysis and conclusions

The quasi-free mechanism for the $^2H(p,pp)n$ reaction has been already studied in Valcovic et al. [9] at a beam energy ranging from 4.5 to 13 MeV, where the Plane Wave Impulse Approximation (PWIA) has been used to reproduce the data.

The 3-body cross section can be written, in PWIA, as a product of the phase space factor, the momentum distribution of the spectator inside the deuteron, and the two-body cross section [9].

The PWIA approach was used for the application of the THM in [2,3,4,5]. By measuring the three-body cross section, it is possible to extract the p-p two-body cross section by dividing it for the momentum distribution of the neutron inside the deuteron and the phase space factor.

The extracted cross section is shown in Fig. 1 a) as a function of the proton-proton relative energy. The experimental data are compared with

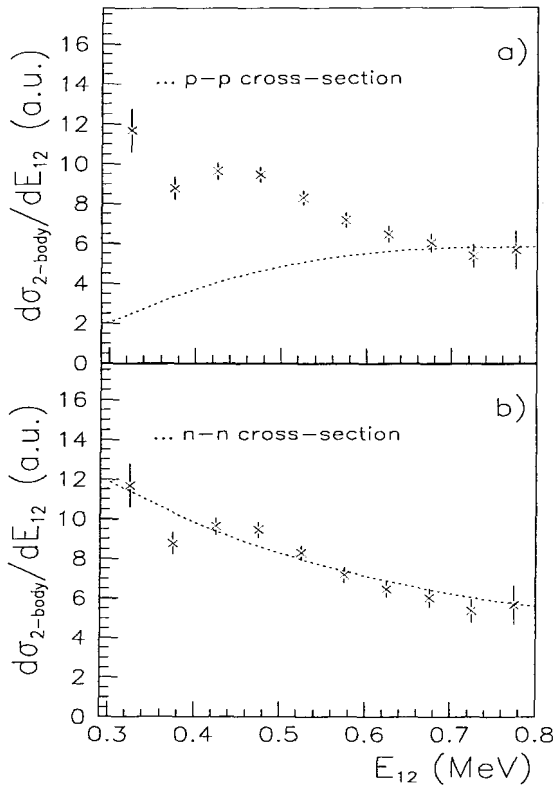

Figure 1. In (a) the extracted two-body cross section is plotted together with the free proton-proton cross section (dashed line). In (b), the extracted two body cross section is plotted together with the neutron-neutron cross section

the free p-p cross section at the corresponding center-of-mass energies and angular ranges. For the free p-p cross section [10], the l=0 phase shift has been calculated in the Jackson and Blatt formalism [11] by using the Foldy et al. parameters [12]: $-R/a = 3.704$ and $r_o = 2.76$ fm where a is the scattering lenght, r_o is the effective range, and R is equal to $\frac{\hbar^2}{me^2}$. The free p-p cross section and the extracted 2-body cross section are normalized with each other under the hypothesis that at relative energies above the proton-proton Coulomb barrier ($\approx$ 550 keV), they must be in agreement within

experimental errors. For this normalization, the disagreement between data and the free p-p cross section at lower energies is again evident. In order to take into account just the nuclear part of the interaction the extracted two-body cross section has been also compared with the n-n cross section.

The n-n cross section has been expressed by using the *effective-range theory* where the scattering lenght and the effective range (a = -16.6 fm, r_o = 2.9 fm) are from [13]. The normalization has been done at higher energies and again the cross section is plotted in arbitrary units (Fig. 1 b)). Here the agreement between data and n-n cross section is farly good.

These results seems to confirm the THM predictions because we have observed that the Coulomb interaction is suppressed for this THM extracted cross section. This represents an important starting-point for further investigations both on the experimental side (e. g. the absolute values of the cross section) and the theoretical one (e. g. detailed analysis from a microscopic point of view or in the framework of direct reactions).

References

1. G. Baur, *Phys. Lett.* **B178**, 35 (1986).
2. S. Cherubini, V. N. Kondratyev, M. Lattuada, C. Spitaleri, D. Miljanić, M. Zadro, G. Baur, *Ap.J.* **457**, 855 (1996).
3. G. Calvi, S. Cherubini, M. Lattuada, S. Romano, C. Spitaleri, M. Aliotta, G. Rizzari, M. Sciuto, R.A. Zappalà, V.N. Kondratyev, D. Milianič, M. Zadro, G. Baur, O.Yu. Goryunov, A.A. Shvedov *Nucl. Phys.* **A621**, 139c (1997).
4. C. Spitaleri,M. Aliotta, S. Cherubini, M. Lattuada, D. Miljanić, S. Romano,N. Soić, M. Zadro, R. A. Zappalà, *Phys. Rev.* **C60**, 055802 (1999).
5. C. Spitaleri, M. Aliotta, M. Lattuada, R.G. Pizzone, S. Romano, A. Tumino, C. Rolfs, L. Gialanella, F. Strieder, S. Cherubini, A. Musumarra, D. Miljanic, S. Typel, H.H. Wolter, *Eur. Phys. J.* **15**, 181 (2000).
6. C. Spitaleri, S. Typel, R.G. Pizzone, M. Aliotta, S. Blagus, M. Bogovac, S. Cherubini, P. Figuera, M. Lattuada, M. Milin, D. Milianič, A. Musumarra, M.G. Pellegriti, D. Rendic, C. Rolfs, S. Romano, N. Soic, A. Tumino, H.H. Wolter, M. Zadro, *Phys. Rev.* **C63**, 055801 (2001).
7. S. Typel, H.H. Wolter, *Few-Body Systems* **29**, 7 (2000).
8. J.E. Brolley, J.D. Seagrave, J.G. Beery, *Phys. Rev.* **135**, B1119 (1964).
9. V. Valković, D. Rendić, V.A. Otte, W. von Witsch, G. C. Phillips, *Nucl. Phys.* **A166**, 547 (1971).
10. R.D. Evans, The Atomic Nucleus, *McGraw-Hill Book Company* (1955).
11. J. D. Jackson, J. M. Blatt, *Rev. Mod. Phys.* **22**, 77 (1950).
12. L.L. Foldy, E. Eriksen, *Phys. Rev.* **98**, 775 (1955)
13. R.J. Slobodrian, *Rep. Prog. Phys.* **34**, 175 (1971).

QUANTITATIVE ESTIMATE OF THE REACTION DEPENDENCE OF THE R-PROCESS NUCLEOSYNTHESIS

TAKA. SASAQUI AND T. KAJINO

National Astronomical Observatory and
The Graduate University for Advanced Study,
2-21-1 Osawa, Mitaka, Tokyo 181-8588, Japan,
and
Department of Astronomy, University of Tokyo,
7-3-1 Hongo, Bunkyo-ku, Tokyo 113-0033, Japan.
E-mail: sasaqui@th.nao.ac.jp

K. OTSUKI AND G. J. MATHEWS

Center for Astrophysics and Department of Physics,
University of Notre Dame,
Notre Dame, IN 46556, U.S.A

T. NAKAMURA

Department of Physics,
Tokyo Institute of Technology,
2-12-1, O-Okayama Meguro-ku, Tokyo 152-0033, Japan

Very massive stars $\geq 8M_{\odot}$ culminate their evolution by supernova (SN) explosions which are presumed to be most viable candidate for the astrophysical site of heavy r-process nucleosynthesis. In an explosive circumstances of the neutrino-driven winds in gravitational core-collapse Type II SNe, not only heavy neutron-rich nuclei but also light unstable nuclei play the significant roles. We first studied in this article the efficiency and sensitivity of the SN r-process nucleosynthesis to many relevant nuclear reaction rates. Our adopted theoretical method and formulae are very effective, and their successful power has already been established in theoretical studies of the missing solar neutrino problem. We also adopted two different models of the neutrino-driven winds in order to study the dependence of our result on wind models. In this study we found quantitatively that several specific nuclear reactions on light neutron-rich nuclei take very critical keys to the final nucleosynthesis yields of r-process elements [1]. Our numerical result of the sensitivity analysis emphasizes and motivates the importance of future experiments aimed at unambiguously determining the nuclear reaction rates that most strongly affect the SN r-process abundance. It would in turn serve to constrain physical and environmental conditions for successful r-process nucleosynthesis in exploding Type II SNe.

1. Introduction

The r-process abundance can change significantly with the change of some specific reaction rates. Among a number of reactions studied in our calculation, the three reactions, $\alpha(\alpha n, \gamma)^9$Be, $\alpha(t, \gamma)^7$Li, and ^{7}Li(n, $\gamma)^8$Li, prove to be especially important to the production of r-process elements, though the reaction rates are comparatively well known by experiment (Figure 1).

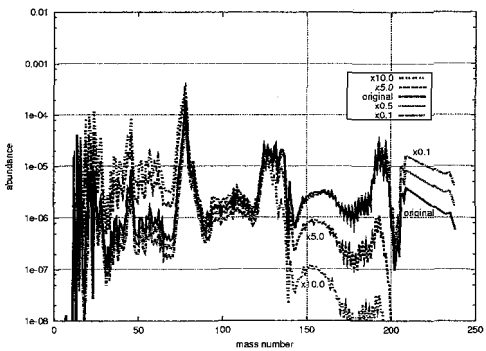

Figure 1. Dependence of final abundance yield on the reaction rates of $\alpha(\alpha n, \gamma)$ ^{9}Be. This is a final yield produced in the SN explosion model. The results are shown in the case of changing of original rate by a factors 10, 5.0, 0.5 and 0.1, respectively.

2. Estimate of Sensitivity

2.1. *Definition of Reaction Sensitivity*

In order to formulate the reaction sensitivity of the r-process nucleosynthesis, we first define the r-process yield at the 2nd and 3rd abundance peaks,

$$Y_{\rm 2nd} = Y(129) + Y(130) + Y(131), \tag{1}$$

$$Y_{\rm 3rd} = Y(194) + Y(195) + Y(196), \tag{2}$$

where $Y(A) = \frac{n(A)}{\rho N_{AV}}$ denotes the number fraction of element which has mass number A, $n(A)$ is the number density, ρ is the mass density of the gas, and N_{AV} is Avogadro's number. We adopt the following formulation [?],

$$Y_{\rm 2nd} = Y_{\rm 2nd}(0) \prod_i \left(\frac{S_i}{S_i(0)} \right)^{\sigma_i}, \tag{3}$$

$$Y_{3\mathrm{rd}} = Y_{3\mathrm{rd}}(0) \prod_i \left(\frac{S_i}{S_i(0)} \right)^{\sigma_i}, \tag{4}$$

where $S_i = N_{AV} < \sigma(E)v >$ is the thermonuclear reaction rate for each reaction. $S_i(0)$ is the 'standard' value for each reaction i, thus $Y_r(0)(r = 2\mathrm{nd}$ or $3\mathrm{rd})$ is the r-process yield for these $S_i(0)$ values. The power index σ_i, which is mathematically defined by $\sigma_i = \partial(\frac{\log Y_r}{Y_r(0)})/\partial(\frac{\log S_i}{S_i(0)})$, is hereafter called 'sensitivity' parameter of the r-process yield associated with the i-th nuclear reaction. It is one of our goals to derive σ_i values. If σ_i is equal to unity, the production of the yield is linearly dependent on this thermonuclear reaction rate. The larger the $|\sigma_i|$ is, the stronger reaction sensitivity the r-process shows. Note, however, that $\sigma_i = 0$ does not mean that the r-process is totally independent of the i-th nuclear reaction. Although one can conclude that the sensitivity is negligible by definition, this occurs when the collision time of the reaction, $t_{coll} = (n(A)\sigma v)^{-1}$, is extremely smaller than the expansion time scale of the neutrino-driven wind.

2.2. *Hydrodynamics*

In this work, we choose a spherical steady-state flow model for the neutrino-driven wind [2, 3, 4]. This flow is one of the accepted models which lead to successful r-process. For the present application the hydrodynamic flow can be deduced from the following non-relativistic equations:

$$4\pi r^2 \rho v = \dot{M}, \tag{5}$$

$$\frac{1}{2}v^2 - \frac{GM}{r} + N_A \mathrm{kT} s_{rad} = E, \tag{6}$$

$$s_{rad} = \frac{11\pi^2}{45\rho N_A} \left(\frac{\mathrm{k}T}{\hbar c} \right)^3, \tag{7}$$

where $\dot{M}$ is the rate at which matter is ejected by neutrino heating on the surface of the proto-neutron star, and k is the Boltzmann constant. In equation (6), the total energy E is fixed by the boundary condition on the asymptotic temperature T_b

$$E = N_A S \mathrm{kT}_b.$$

For simplicity in the present work, we utilize an adiabatic, constant entropy wind rather than to compute the neutrino heating explicitly [5]. This is adequate for our purpose which is to sketch the difference of the abundance.

This model has four parameters, which are the neutron-star mass, the entropy (constant), the boundary temperature, and mass loss rate. We set the entropy per baryon to be $S/k = 300$. Since the expansion time scale of the wind is small, it is proper enough to treat the flow as a steady state.

3. Calculated Result

We carried out the network calculation and obtained the final abundance of the r-process. The individual reaction rate is changed in the range $10^{-1} \leq \frac{\delta S_i}{S_i(0)} \leq 10$ in order to derive the sensitivity parameter σ_i formulated in section 2.1. These results are showed in Figure 2. The numbers shown in Figure 2 mean sensitivity parameter values. We now study more details of sixteen reactions because they are thought to be especially important so far [1].

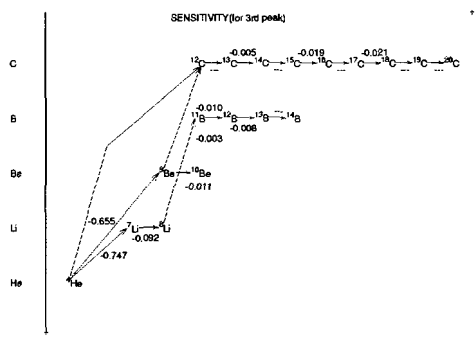

Figure 2. The sensitivity of each reaction to the 3rd peak element. The number means the value of sensitivity. This is one part of the results. See our paper in details.

References

1. Sasaqui, T., Otsuki, K., Kajino, T., Mathews, G.J. and Nakamura, T., *Astrophys. J.*(2004), submitted.
2. Qian, Y.-Z., and Woosley, S.E., *Astrophys. J.* **471**(1996)331.
3. Takahashi, K. & Janka, H.-T. 1997, Proc. I. C., Origin of Matter and Evolution of Galaxies in the Universe '96, on 1997 Eds.
4. Otsuki, K., Tagoshi, H., Kajino, T., & Wanajo, S., *Astrophys. J.*, **533** , 424 (2000)
5. Wanajo, S., Kajino, T., Mathews, G. J., and Otsuki, K., *Astrophys. J.* **554**(2001)578.

NEUTRON EXPERIMENT FOR THE STUDY OF Re/Os COSMOCHRONOMETER

M.SEGAWA[1†], Y.NAGAI[1], T.SHIMA[1], H.MAKII[1], K.MISHIMA[1], H.UEDA[1], H.TEMMA[1], T.MASAKI[1], M.IGASHIRA[2], T.OHSAKI[2], T.SHIZUMA[3] AND T.HAYAKAWA[3]

1 Research Center for Nuclear Physics, Osaka University, 10-1 Mihogaoka, Ibaraki, Osaka 567-0047, Japan

2 Research Laboratory for Nuclear Reactors, Tokyo Institute of Technology, O-okayama, Meguro, Tokyo 152-8550, Japan

3 Japan Atomic Energy Research Institute, 2-4 Shirakatashirane, Toukaimura, Ibaraki 319-1195, Japan

We should clarify several problems for the Re-Os pair to be used as one of the good cosmochronometers. First, since ^{187}Os is formed and depleted by sequential neutron capture in stars, the effects should be corrected. Second, ^{187}Os is depleted by the neutron capture process through the excited state at 10keV. It is very important to find a proper way to correct for the s-process contribution in deducing the age of the Galaxy. In order to correct for the effect mentioned above and to determine the age of the universe, we are planning to measure the neutron capture cross section of the first excited state ($E_{excited}$ = 10 keV) of ^{187}Os is one of the key parameters in deduceing the age of the Galaxy using the Re-Os cosmochronometer. In order to deduce the cross section we are preparing various detectors using a newly developed experimental method. In these paper I briefly describe our experimental methods to accurately determine the neutron caprute cross section of the first excited state of ^{187}Os.

1. Introduction

The age determination of the universe has been an interesting subject so far the following three different methods have been used to deduce the age. First one is to use the Hubble constant, and second one is to use the age of the stars in globular clusters, and third one is to use long-lived radioactive species. Among these methods the nuclear approach is unique, since one can deduce the age of the Galaxy accurately if one can construct proper models for the s- and r-process nucleosynthesis. The age of the universe can be obtained by adding the time interval between the Big-Bang and the start of the Galatic first generation star

† segawa@rcnp.osaka-u.ac.jp

formation. The age of an old star can be estimated by measuring the decay rate of the abundance of a long-lived nucleus in the star during a certain period. If the old star would be one of the oldest stars in the galaxy, the life would give the lower limit of the life of our galaxy [1]. It has been considered that Re-Os pair can be one of the good cosmochronometers, since it has unique features as discussed below. First, ^{187}Re is produced by only r-process and the half life is quite long 42.3±1.3Gyr [2]. Second, ^{186}Os is the s-only isotope. Therfore, ^{187}Os is produced not only by the decay of ^{187}Re but also by slow neutron capture process by ^{186}Os. Hence, principally if we know the production rate by the s-process neutron capture of ^{186}Os and the loss rate of ^{187}Os, we could obtain the amount of the decay product of ^{187}Re using the well known relation, $\sigma(^{186}\mathrm{Os})N(^{186}\mathrm{Os}) = \sigma(^{187}\mathrm{Os})N(^{187}\mathrm{Os})$. Here, $\sigma(^{A}\mathrm{Os})$ and $N(^{A}\mathrm{Os})$ stand for the neutron capture cross section and the observed abundance of Os with mass number A, respectively. Consequently, we could deduce the age of the Galaxy. However, there is a problem which should be clarified. Namely, there exists the excited state at 10 keV in ^{187}Os (Fig.1). The state could be significantly populated at the stellar temperature, and therefore ^{187}Os is depleted by the neutron capture process through the excited state. Here it is very important to find a proper way to correct for the the loss rate of ^{187}Os through the excited state in deducing the age of the Galaxy [3,4,5,6,7]. In order to correct for the effect mentioned above and to determine the age of the universe we are planning to measure both the neutron capture cross sections and neutron inelastic cross sections of ^{186}Os, ^{187}Os, ^{188}Os and ^{189}Os using a newly developed experimental method.

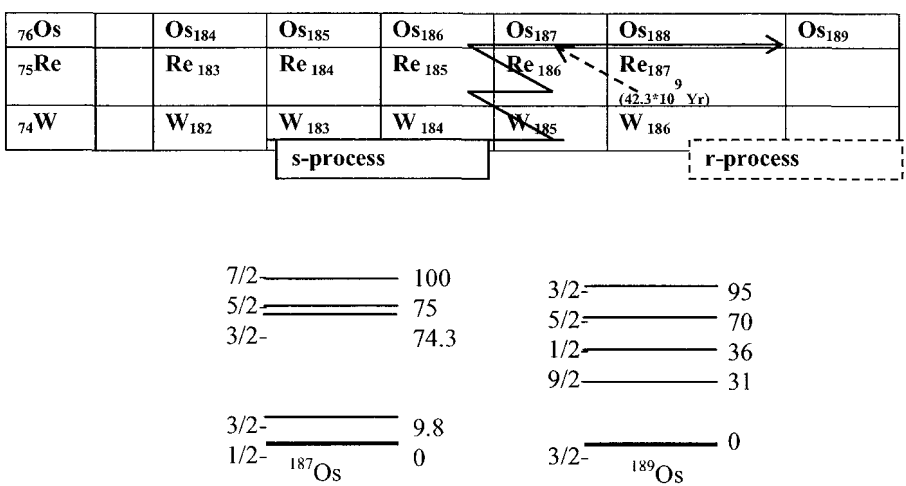

Fig.1 Partial level scheme of ^{187}Os and ^{189}Os

2. Experimental Method

2.1. *Neutron Source*

Fast keV neutrons are produced by the ^{7}Li(p,n) reaction using the proton provided from the pelletron accelerator of the Research Laboratory for Nuclear Reactors at Tokyo Institute of Technology. We use several neutron energies for the (n,γ) and (n,n') experiments on Os isotopes. Since ^{189}Os has the second excited state at 74.3 keV, the incident neutron energy should be adjusted not to exceed the energy of the state.

2.2. *Detecting System*

2.2.1 Cross section measurement of (n,γ) reactions on Os isotopes

We use the anti-compton NaI(Tl) spectrometers for detecting gamma rays from the neutron capture reaction of Os isotopes (Fig.2). Each spectrometer consists of a central NaI(Tl) detector with a diameter of 9 inches and a length of 8 inches and an annular NaI(Tl) detector with a diameter of 13inches and a length of 11inches. Each spectrometer is enveloped by Pb and borated paraffin blocks to attenuate background gamma rays and neutrons.

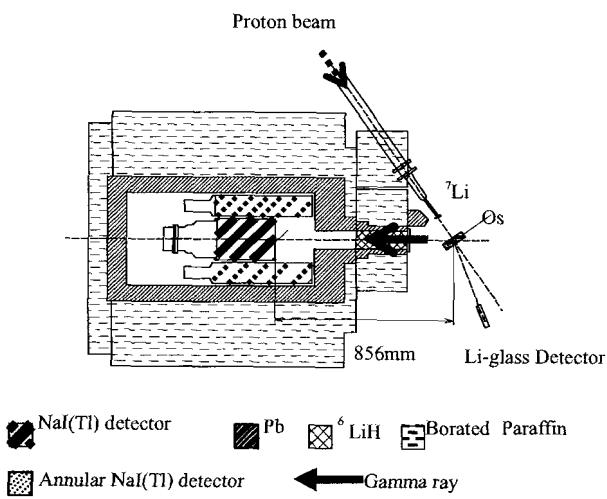

Fig.2 Schematic view of the experimental set up

2.2.2 Cross section measurement of (n,n') reactions on Os isotopes

We use a Li-glass detector for detecting inelastically scattered neutrons from Os isotopes. There are four main Li-glass detectors with a diameter of 50mm and a thickness of 10 mm. The discrimination between neuron and gamma ray backgrounds can be made by their pulse heights. The detectors are enveloped by borated paraffin blocks to attenuate neutron backgrounds to measure the inelastic neutrons free from gamma ray backgrounds.

3. Conclusion

We are now making test experiments to measure both the neutron capture cross sections and neutron inelastic cross sections of ^{186}Os, ^{187}Os, ^{188}Os and ^{189}Os using a newly developed method to derive the age of the Galaxy. We hope that we could determine the age within an uncertainty of one billion year.

References

1. D. D. Clayton, *Astrophys. J.* **139**, 637 (1964).
2. M. Linder et al., *Geochim. Cosmochim. Acta.* **53**, 1597 (1989).
3. R. R. Winters, *Astron. Astrophys.* **171**, 9 (1987).
4. J. C. Brown, *Phys. Rev.* **C23**, 1434 (1981).
5. M. J. Harris, *Astrophy. Space. Sci.* **77**, 357 (1981).
6. S. E. Woosley, *Astrophys. J.* **233**, 411 (1979).

RECENT NUCLEAR ASTROPHYSICS DATA ACTIVITIES AT ORNL*

MICHAEL S. SMITH, DANIEL W. BARDAYAN, JEFFERY C. BLACKMON
Physics Division, Oak Ridge National Laboratory, Oak Ridge, TN, USA

RICHARD A. MEYER
RAME' Inc., Teaticket, MA, USA

KYUNGYUK CHAE, MICHAEL W. GUIDRY, W. RAPHAEL HIX, ERIC J. LINGERFELT, ZHANWEN MA, JASON P. SCOTT
Department of Physics & Astronomy, Univ. of Tennessee, Knoxville, TN, USA and Physics Division, Oak Ridge National Laboratory, Oak Ridge, TN, USA

RAYMOND L. KOZUB
Physics Department, Tennessee Technological Univ., Cookeville, TN, USA

Recent measurements with radioactive beams at ORNL's Holifield Radioactive Ion Beam Facility (HRIBF) have prompted the evaluation of a number of reactions involving unstable nuclei needed for stellar explosion studies. We discuss these evaluations, as well as the development of a new computational infrastructure to enable the rapid incorporation of the latest nuclear physics results in astrophysics models. This infrastructure includes programs that simplify the generation of reaction rates, manage rate databases, and visualize reaction rates, all hosted at a new website **www.nucastrodata.org**.

1. Nuclear Data Evaluations for Stellar Explosion Studies

Information on proton-rich unstable nuclei is needed to understand nova explosions occurring on the surface of white dwarf stars and X-ray bursts on the surface of neutron stars. Recent measurements with radioactive beams at ORNL's Holifield Radioactive Ion Beam Facility (HRIBF)[1] have prompted the evaluation of a number of reactions involving unstable nuclei,

*ORNL is managed by UT-Battelle, LLC, for the U.S. Department of Energy under contract DE-AC05-00OR22725.

and the associated level structures, that are necessary to probe the details of these spectacular astrophysical explosions. A number of reactions are also being investigated to prepare for possible future measurements at HRIBF.

Recent reactions and nuclei being assessed at ORNL include:

- ^{18}F(p,α)^{15}O and ^{18}F(p,γ)^{19}Ne and the level structure of ^{19}Ne above the ^{18}F + p threshold; a first paper on this evaluation is complete[2], and a longer paper updated with recent results from a ^{18}F(d,p)^{19}F measurement is in progress
- ^{14}O(α,p)^{17}F and the level structure of ^{18}Ne above the ^{14}O + α and ^{17}F + p thresholds; R-matrix fits to the measurements of four different reaction yields are currently being made[3]
- ^{33,34}Cl(p,γ)^{34,35}Ar and the level structure of ^{34,35}Ar above the ^{33,34}Cl + p thresholds, for a future HRIBF measurement
- ^{30}P(p,γ)^{31}S and the level structure of ^{31}S above the ^{30}S + p threshold; this work includes results from a recent HRIBF measurement of ^{32}S(p,d)^{31}S

The results of these evaluation – new cross sections and level schemes – will be converted into new thermonuclear reaction rates using software tools discussed below.

2. Strategies for Future Nuclear Astrophysics Data Activities

Measurements and theoretical descriptions of nuclei and their interactions provide a foundation for sophisticated models of stellar explosions, as well as for other astrophysical systems ranging from the Big Bang to the inner workings of our own Sun. In many instances, the ability of astrophysical models to accurately describe the latest, spectacular observations of the cosmos strongly depends on the input nuclear data, and more extensive and precise nuclear data is required for advances in astrophysics. However, to be utilized for astrophysical studies, state-of-the-art nuclear measurements and theoretical calculations have to be *appropriately processed* for input into astrophysics simulation codes. This requires *dedicated efforts* in data compilation, evaluation, processsing, dissemination, and coordination. Unfortunately, the current worldwide effort in nuclear astrophysics data does not meet the data needs of the astrophysics community. As a result, the latest nuclear measurements or model calculations are frequently not utilized in studies of the very astrophysical puzzles that motivated their

generation. The situation is getting worse as more nuclear measurements are being made but not incorporated into reaction rate libraries and other astrophysical datasets that are in the public domain.

Fortunately, there are a number of strategies that will enable a more effective utilization of nuclear physics information in astrophysics simulations. These include the development of software to facilitate the connection between the nuclear laboratory and stellar models, as well as initiatives to boost evaluation manpower in this field. For example, at ORNL we are creating a new *computational infrastructure* for nuclear astrophysics data. This suite of computer codes will expedite the incorporation of nuclear physics information into astrophysical simulation codes. Available on-line through a web browser, a simple point-and-click interface will guide users to convert input nuclear structure and reaction information – the products of evaluation activities – into thermonuclear reaction rates in a variety of popular formats, including that of the widely-used REACLIB library[4] which contains over 60000 rates. The interface will also enable users to easily access and manage databases – for example, to insert a new reaction rate into an online reaction rate library, as well as to create, merge, store, document, and share custom rate libraries. This functionality will hopefully make it possible for the community to replace multiple, proprietary versions of REACLIB that each have different, partial reaction rate updates with frequently updated public releases – making the intercomparison of results from different astrophysics simulations easier.

The infrastructure will also enable users to easily visualize rate libraries with **Rateplotter**, the first easy-to-use, interactive, platform-independent, graphical user interface to REACLIB-format rate libraries. This program, viewable through a web browser or as a stand-alone application, enables users to plot multiple rates, access rate parameters, add new rates and plot them, and create rate versus temperature tables, all through a point-and-click graphical user interface based on the chart of the nuclides. To host this new infrastructure for nuclear astrophysics data, a new website has been launched: **www.nucastrodata.org**. In addition to the components described above, this site features an extensive list of nuclear datasets (over 60 so far) important for nuclear astrophysics studies available from around the world. It is designed to help users navigate through these datasets, as well as to publicize them to the research community. This site and its new infrastructure have a strong potential to become a valuable asset for the nuclear astrophysics research community.

Even with the new computational infrastructure discussed above, more

manpower will still be needed for evaluations. Some of this may come from appeals for volunteer work from the nuclear astrophysics research community. Exploiting the overlap between the nuclear data and nuclear astrophysics communities[5] is another approach to increasing evaluation manpower. To make these approaches work, communication is crucial. First, the benefits of evaluations need to be clearly elucidated to enlist additional evaluators. Next, strong lines of communication between evaluators are needed, both nationally and internationally, to share expertise and to help avoid unnecessary duplications of effort. Third, a robust dialogue between evaluators and astrophysical modelers, the end users of the nuclear data, is vital to ensure that evaluations are focused on the most important reactions and nuclei.

Such enhanced communications, as well as other data activities, would be greatly facilitated by the establishment of a Nuclear Astrophysics Data Coordinator, whose duties would also include: maintaining and updating a central WWW site linking relevant datasets; modifying datasets for compatibility with astrophysical codes; and improving data accessibility via the creation of indices, search capabilities, graphical interfaces, bibliographies, error checking, plotting tools, and other enhancements. Other activities could include encouraging and helping coordinate evaluation activities; establishing and maintaining a nuclear astrophysics email distribution list; publicizing new nuclear astrophysics meetings, experimental results, and publications; and establishing and maintaining a priority list of important nuclear reactions and properties that require further study. It would also be beneficial for the Coordinator to maintain an active research program using nuclear astrophysics data to ensure the data activities truly fulfill the needs of data users. The establishment of a Coordinator would have a strong positive impact on nuclear astrophysics research efforts worldwide with only a modest investment.

References

1. Stracener, D.W., *Nucl. Inst. Meth.* **B204**, 42 (2003).
2. Shu, N. *et al.*, *Chin. Phys. Lett.* **20**, 1470 (2003).
3. Blackmon, J.C. *et al.*, *Nucl. Phys.* **A718**, 127 (2003).
4. F.-K. Thielemann et al., *Adv. Nuclear Astrophysics* **525**, 1 (1987); http://quasar.physik.unibas.ch/~tommy/adndt.html#reaclib.
5. M.S. Smith *et al.*, U.S. Nuclear Data Program Astrophysics Task Force Report, unpublished (1995); http://www.phy.ornl.gov/astrophysics/data/task/taskforce_report.html.

NUCLEOSYNTHESIS IN EXTREMELY METAL POOR STARS AND THE ORIGIN OF THE MOST METAL-POOR STAR HE0107-5240

T. SUDA,* M. AIKAWA,† T. NISHIMURA AND M. Y. FUJIMOTO
Department of Physics, Hokkaido University,
Sapporo 060-0810, Japan
E-mail: suda@astro1.sci.hokudai.ac.jp, aikawa@nucl.sci.hokudai.ac.jp,
nishimura,fujimoto@astro1.sci.hokudai.ac.jp

We discuss the origin of the most metal poor star HE0107-5240 which is recently observed. The discovery of the extremely low metalicity of [Fe/H]$= -5.3$ has a great importance for our understanding of early universe. As seen in the other extremely metal poor stars, the star exhibits peculiar abundance pattern at the surface compared with the solar one. At present, it is known that HE0107-5240 shows not only large enhancement of carbon ([C/Fe] $= 4.0$) and nitrogen ([N/Fe] $= 2.3$), but mildly enhanced sodium ([Na/Fe] $= 0.8$)[1,2]. Though large enhancement of carbon and nitrogen in the metal poor stars at the red giant branch has already confirmed theoretically by [3], its ratio is not in agreement with the observation. Therefore, the simple scenario of the remnant of a single low mass Pop III star is abandoned. Moreover, the enhancement of oxygen has also been reported ([O/Fe] $= 2.4 \pm 0.5$, Beers *et al.* 2003, private communication). On the other hand, only an upper bound is given for the important s-process element Ba ([Ba/Fe] < 0.8)[2].

In discussing the origin of HE0107-5240, it is important to consider separately (a) the source of iron group elements, (b) the source of light elements such as α-rich elements, C and O, and the secondary elements,

*Meme Media Laboratry, Hokkaido University
†Meme Media Laboratry, Hokkaido University

N and Na, and (c) the source of s-process elements. It is reasonable to suppose that the origin of the metals in HE0107-5240 should be the consequence of pollution from the mother cloud where the star was born, not of the printinity that the star has already retained them in its birth. The discussion about the source of iron group elements is beyond the scope of this paper and we simply give a reference on the whole discussion[4].

On the origin of other elements, we presented a scenario that HE0107-5240 belongs to binary system and suffered a mass trnasfer event from more massive companion[4], since the single star evolution of $0.8M_{\odot}$ model cannot achieve the observed abundance ratio of carbon and nitrogen (C/N $\sim$ 150). This binary scenario gives reasonable account to the source of light elements such as C, N, O, and Na as well as the source of s-process elements. In this paper, we focus on the nucleosynthesis in the helium flash convective zone of massive ($1.2 \lesssim M/M_{\odot} \lesssim 3.0$) AGB companion evolved from main sequence phase with primordial composition.

A major characteristics of metal-free and extremely metal poor star is the engulfment of hydrogen by the helium flash convection at the early phase of thermal puslating AGB. As a result of small amount of hydrogen mixing into the helium convection, the convection splits into two, outer one driven by the hydrogen burning and the inner one by the helium burning. Before the split of convection, some of mixed hydrogen, captured by ^{12}C, goes inward and is incorporated into the inner helium convection as ^{13}N and/or ^{13}C. These nuclei help to burn in the helium convection and to produce neutron via $^{13}\mathrm{C}(\alpha, n)^{16}\mathrm{O}$.

We computed the progress of nucleosynthesis during the helium shell flash, induced by the mixing of ^{13}C, by the same one-zone approximation as used by [5]. The model parameters of shell flashes are taken from the computation of the evolution of $2.0M_{\odot}$ star and we treat the amount of mixed ^{13}C as the parameter in our computation. Figure 1 shows the progress of nucleosynthesis consequent on the mixing of ^{13}C, set at $^{13}\mathrm{C}/^{12}\mathrm{C} = 10^{-3}$, at the peak of shell flash.

As soon as ^{13}C is mixed, it rapidly reacts with helium to produce neutrons. The delivered neutrons are mainly captured by ^{12}C owing to the absence of other competent absorbers. This enriches ^{16}O by the reactions of $^{12}\mathrm{C}(n, \gamma)^{13}\mathrm{C}(\alpha, n)^{16}\mathrm{O}$ and ^{17}O by $^{16}\mathrm{O}(n, \gamma)^{17}\mathrm{O}$. ^{20}Ne is also produced via $^{17}\mathrm{O}(\alpha, n)^{20}\mathrm{Ne}$. The newly formed ^{20}Ne captures and consumes neutrons to further yield Na and Mg isotopes. The resultant abundances relative to carbon agree well with those of HE0107-5240 for light elements.

As for the heavy s-process elements, its production depends on whether

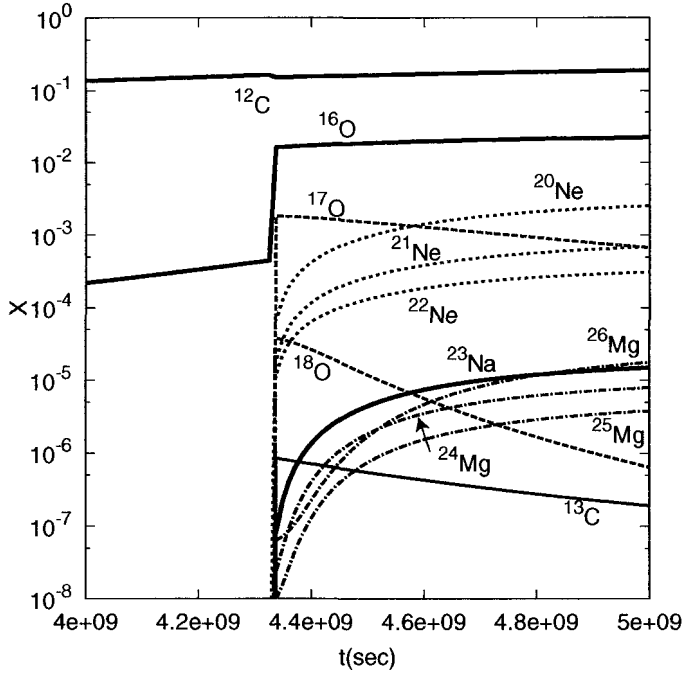

Figure 1. Progress of the neutron capture reactions, triggered by the mixing of ^{13}C into the helium flash convection for the model of the amount of mixing $^{13}C/^{12}C = 10^{-3}$. The instantaneous mixing of ^{13}C is assumed at the peak stage of helium burning rate. The model parameters of helium shell flash are taken from the $2M_{\odot}$ star model calculated by our stellar evolution code.

the seed nuclei are processed in the helium convective zone, which is roughly estimated by the number of neutrons absorbed by the nuclei as shown in Figure 2. Since the neutron exposure is small for small amount of mixing, seed nuclei for s-process are little produced, for most of neutrons are absorbed by the abundant byproducts of neutron source reactions, such as Ne, Na, Mg, and their neutron-rich progenies. Therefore, s-process enhancement should not be detected if HE0107-5240 belongs to a binary system of a first generation object. On the other hand, if HE0107-5240 is a second generation star or a first star that the neutron irradiative region is polluted by the accretion of metals and by the intrusion of surface convection, the s-process nucleosynthesis proceeds with the preexisting iron-group elements

as seed nuclei, to yield the s-process isotopes.

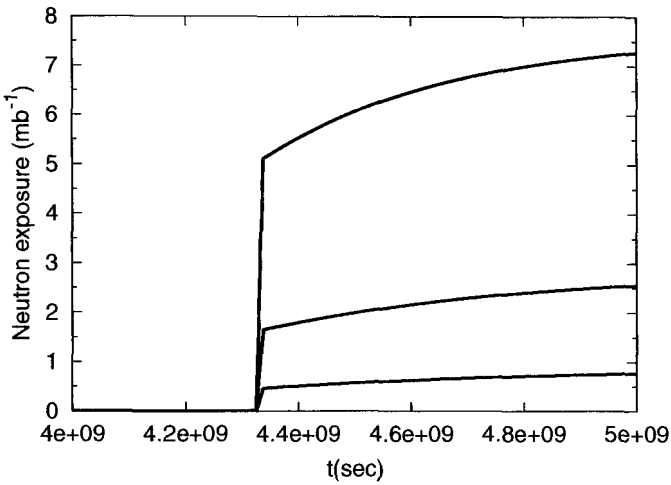

Figure 2. Number of neutrons captured by nuclei in the helium shell flash convective region. Each line corresponds the degree of mixing, $^{13}C/^{12}C = 10^{-4}$, 10^{-3}, 10^{-2} from bottom to top in the figure.

In conclusion, it is crucial to determine the abundances of s-process elements in order to confirm the origin of HE0107-5240. In particular, it is important to derive the abundance of heavier s-process element like Pb or Bi, because the neutrons per seed nuclei should be very large in the helium convective zones under the very metal-poor circumstances and heavy s-process elements are likely to be produced.

References

1. N. Christlieb, M. S. Bessell, T. C. Beers, B. Gustafsson, A. Korn, P. S. Barklem, T. Karisson, M. Mizuno-Wiedner, & S. Rossi, *Nature*, **419**, 904, (2002)
2. N. Christlieb, B. Gustafsson, A. Korn, P. S. Barklem, T. C. Beers, M. S. Bessell, T. Karisson, and M. Mizuno-Wiedner, *Astro-ph/0311173*, (2003)
3. M. Y. Fujimoto, Y. Ikeda, and I. Iben, Jr., *ApJ Letters*, **529**, L25, (2000)
4. T. Suda, M. Aikawa, M. N. Machida, M. Y. Fujimoto, and I. Iben, Jr., *ApJ submitted*
5. M. Aikawa, M. Y. Fujimoto, and K. Kato, *ApJ*, **560**, 937, (2001)

THE NUCLEAR RESPONSES FOR DOUBLE BETA NEUTRINOS AND DOUBLE SPIN ISOSPIN RESONANCES BY USING OF DOUBLE CHARGE EXCHANGE HEAVY ION REACTION

K.TAKAHISA, H. AKIMUNE[1], H. EJIRI, H. FUJIMURA, M. FUJIWARA, K. HARA,H. HASIMOTO, K. HATANAKA, T. ITAHASI, T. KAWABATA, K.KAWASE, Y.KOREEDA, N. MAEHARA, S. MORDECHAI[2], Y. NAGAI, K. NAKANISHI, S. NINOMIYA, T. SHIMA, M. TANAKA[3], S. UMEHARA[4], S. UMISEDO, H.P. YOSHIDA, S. YOSHIDA[4], M. YOSHIMURA AND M. YOSOI[5]

Research Center for Nuclear Physics, Osaka University, Mihogaoka 10-1,Ibaraki,Osaka,567-0047 Japan,
Konan University[1],
Ben-Gurion University of the Negev[2],
Kobe Tokiwa Jr. College[3],
Department of Physics, Osaka University[4],
Department of Physics, Kyoto University[5]

To study double spin-isospin responses in view of the ββν decays, double charge-exchange nuclear reactions have measured at RCNP. We have succeeded to measure the double charge exchange reaction by means of heavy ion reaction. From these experiments, we conclude that the (^{11}B,^{11}Li) reaction at 70 **MeV**/nucleon is a good spectroscopic tool. We believe that the reaction can be well applied to the study of pure spin-flip nuclear responses in higher-excited regions including DGT and higher ΔL excitations.

1. Introduction

Double beta decays (ββ) are of current interest in view of particle, astro and nuclear physics[1,2]. Neutrino-less double beta decays (0νββ), which require the neutrino helicity mixing, are sensitive to the Majorana masses of light and heavy neutrinos(ν), right-left mixings of weak currents, and to SUSY-neutrino couplings, and others beyond the standard theory. Finite ν-masses give contributions to non-baryonic hot dark matters in the universe.

Nucleon (quark) sectors of double beta decays include mainly double spin-flip and double isospin flip nuclear weak responses. The nuclear spin-isospin operator $\sigma\tau$ results in the broad GTR (Gamow Teller resonance) and double GT ones (DGTR). Recently, ββν responses have been analyzed in terms of couplings of single particle-hole GT states and GTR. Here DGTR play crucial roles for the ββν responses.

Double giant resonances are of great interest to see resonance features at high excitation energy regions. DGTR standing on the GTR, however, have not well studied. It is shown that nuclear weak responses relevant to the isospin and isospin-spin mode are investigated by studying strong processes of charge-exchange (isospin-flip) spin-flip nuclear reaction. Actually, charge-exchange

(^{3}He,t) reactions with $Ei(^3He)$ = 450**MeV** are used to study isospin spin responses for ββ-nuclei. The charge-exchange reactions at the intermediate energy excite preferentially the isospin spin modes.

Therefore, we start the studies of double spin-isospin responses in view of the ββν decays. The double isospin spin giant resonances are investigated by means of double charge-exchange nuclear reactions at RCNP.

2. Double charge exchange reaction

In the (π^+,π^-) double charge exchange reaction, GDR*IAS (Giant Dipole Resonance built on isobaric analog states) and DIAS (Double Isobaric Analogue State) and DGDR (Double Giant Dipole Resonance) were discovered[3]. But, pion has zero spin, therefore pion could not excite the spin flip DGTR excitations. About heavy ion double charge exchange reaction, search of DGTR was done by using of ^{24}Mg(^{18}O,^{18}Ne)^{24}Ne reaction[4] on the 100 **MeV**/nucleon at NSCL-MSU and 76 **MeV**/nucleon at GANIL. However, there were large statistical uncertainties. Heavy ion single charge exchange reaction, such as (^{3}He,t) and (^{6}Li,^{6}He),(^{12}C,^{12}N) reaction was studied on GT strength at RCNP, et al.[5-7]

3. The (^{11}B,^{11}Li) reaction

The (^{11}B,^{11}Li) reaction is one of the most lightest heavy ion double charge exchange reaction. Research and Development of the (^{11}B,^{11}Li) reaction was started at RCNP by using of NEOMAFIOS (ECR ion source, 10G*Hz*, a permanent magnet as a mirror magnet).

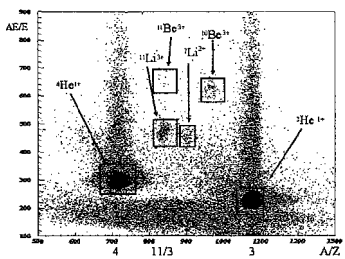

Figure 1. Particle identification of the scattered ^{11}Li particle by using the drift time and energy loss technique.

The (^{11}B,^{11}Li) double charge exchange reaction was carried out by using of ^{11}B (*Ei* = 758 **MeV**) beam by RING-cyclotron. The spectrometer Grand Raiden will be set at 0 degree with equal horizontal and vertical opening angles of 30 **mr** each. The full solid angle is 1.6 **msr** which will be divided later on by

software cuts. The $^{11}B^{5+}$ beam enters the spectrometer at this angle but will be deflected because of its lower magnetic rigidity into an internal Faraday cup in the first dipole (D1) magnet of the Grand Raiden spectrometer. The thin foil was attached to reduce the ($^{11}B^{5+}$,$^{11}B^{3+}$) reaction. We can clearly identify the scattered ^{11}Li particle by using the drift time and energy loss technique (Fig.1.). Therefore, the (^{11}B,^{11}Li) reaction has been shown possible.

4. $^{13}C(^{11}B,^{11}Li)$ reaction

We have measured the ^{13}C(^{11}B,^{11}Li)^{13}O reaction (Fig.2.). The sharp peak of ^{13}O ground state has clearly seen (69 }13*nb/sr*). The energy calibration of the spectrometer has made by this peak. The resolution of this peak has clearly explained by beam resolution and difference of energy loss inside the target. Compare to $^{13}C(\pi^+,\pi^-)$ reaction (140**MeV**), the cross section of G.S. is smaller about 40%. Inelastic energy revel (25**MeV**) and GDR*IAS were seen.

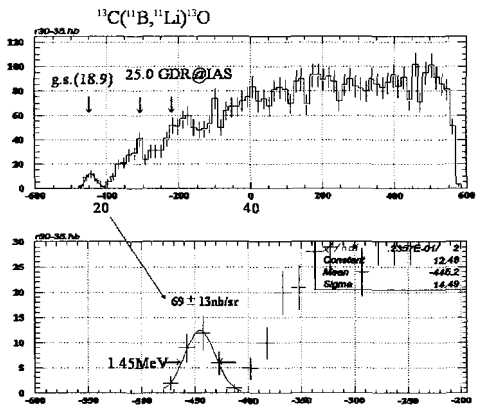

Figure 2. The $^{13}C(^{11}B,^{11}Li)^{13}O$ reaction. The upper graph shows the excitation function. We can clearly see the grand state peak of ^{13}O nucleus in lower graph. The width of this peak has clearly explained.

5. ^{56}Fe ($^{11}B,^{11}Li$) reaction

The experimental data of $^{56}Fe(\pi^+,\pi^-)$ (**ΔT**=2,**ΔS**=0) reaction existed[3]. In this reaction, DIAS and GDR*IAS were observed. Meanwhile, ^{56}Fe(^{11}B,^{11}Li) (**ΔT**=2,**ΔS**=2) reaction is possible to excite not only DIAS and GDR*IAS ,but also DGTR. About ^{56}Fe nuclei, theoretical calculation about DGTR is available. The peak excitation energy of DGTR was estimated about 25.6**MeV** and focus. The preliminary result of the ^{56}Fe(^{11}B,^{11}Li) reaction (Fig.3.) was shown the

similar spectrum of $^{56}Fe(\pi^+,\pi^-)$ reaction in the DIAS and GDR*IAS region. The DGTR region of $^{56}Fe(^{11}B,^{11}Li)^{58}Ni$ shows the forward angle peak.

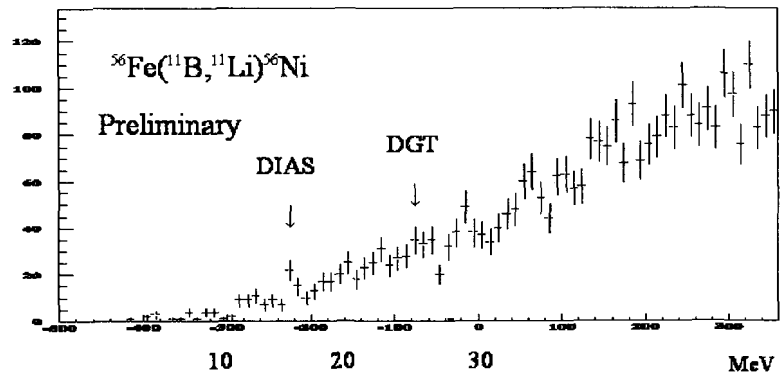

Figure 3. The $^{56}Fe(^{11}B,^{11}Li)$ reaction. We can clearly see the peak of DIAS. The excitation energy of DGT is estimated about 25.6**MeV**.

6. Discussion and Conclusion

We have established the $(^{11}B,^{11}Li)$ reaction. The energy calibration has made by the G.S. of $^{13}C(^{11}B,^{11}Li)^{13}O$ reaction. The DGTR region of $^{56}Fe(^{11}B,^{11}Li)^{58}Ni$ shows the forward angle peak. Compare to the (π^+,π^-)reaction, we can see not only the DIAS and GDR*IAS but also other component such as DGTR. From these facts we conclude that the $(^{11}B,^{11}Li)$ reaction at 70 **MeV**/nucleon is a good spectroscopic tool. We believe that the reaction can be well applied to the study of pure spin-flip nuclear responses in higher-excited regions including DGTR and higher **ΔL** excitations. The setup enables us to get information on the double spin exchange response about double beta decay nuclei.

References

1. H.Ejiri et al. , *Int.J.Mod.Phys.E.*VOL.**6**(1997)1
2. H.Ejiri et al. , *J.Phys.Soc.Japan Lett.***65**(1996)7
3. S.Mordechai et al..,*Int. Jour. of Mod. Phys. E,* Vol.**3** No.**1**(1994)39
4. J.Blomgren et al.. *Phys.. Lett.* **B362** (1995)34.
5. M.Fujiwara et al. , *Nucl.Phys.* **A599**(1996)223c
6. N.Anantaraman et al..,*Phys.Rev* **44** (1991)398
7. F.Osterfield et al.. *Phys.. Rev.* **C45** (1992)2854.

NEWAGE PROJECT —DARK MATTER DETECTION WITH AN ADVANCED GASEOUS TRACKING DEVICE*

A. TAKEDA, T. TANIMORI, H. KUBO, K. MIUCHI, T. NAGAYOSHI, Y. OKADA, R. ORITO, A. TAKADA

Department of Physics, Graduate School of Science, Kyoto University
Kitashirakawa-Oiwake, Sakyo-ku, Kyoto 606-8502, Japan

Measuring the distribution of nuclear recoil angles is said to be one of the most reliable methods to identify a positive sign of weakly interacting massive particles (WIMPs) which are leading candidates for the cold dark matter. We evaluated the detection feasibility with CF_4 gas for spin-dependent (SD) interactions and Xe gas for spin-independent (SI) interactions taking into account the performance of the μ-TPC which is an existing three-dimensional tracking detector. We consequently found that the μ-TPC filled with CF_4 gas can reach the best sensitivity of the current experiments for SD interactions with even a $0.3\,m^3 \cdot$ year of exposure at Kamioka Observatory (2700 m.w.e.). We also found it is possible to explore the theory regions predicted by minimal supersymmetric extensions of the standard model (MSSM) via SD and SI interactions with a sufficient exposure ($\sim 300\,m^3 \cdot$ year).

1. Introduction

Owing to the motion of the solar system around the galactic center, the velocity distribution of weakly interacting massive particles (WIMPs) is expected to show an asymmetry like a wind of WIMPs[1]. Among the many attempts to detect this WIMP-wind by measuring the recoil angles[2,3,4,5], gaseous detectors are one of the most appropriate devices because of their fine spatial resolution[4]. We have studied the detection feasibility of WIMP-wind via spin-dependent (SD) interactions using carbon tetrafluoride (CF_4) gas and spin-independent (SI) interactions using Xe gas. In particular, fluorine was found to be one of the best nuclei for the SD coupled WIMP search[6,7].

*This work is supported by a Grant-in-Aid Scientific Research of the Japan Ministry of Education, Culture, Science, Sports, Technology; Ground Research Announcement for Space Utilization promoted by Japan Space Forum; and Grant-in-Aid for the 21st Century COE "Center for Diversity and Universality in Physics".

In this paper, the calculated detection possibility of the WIMP-wind using an existing three-dimensional (3D) tracking detector (μ-TPC) is described[8].

2. μ-TPC: advanced gaseous tracking device

The μ-TPC which is a gas TPC with a micro pixel chamber (μ-PIC) read out has been developed for measuring 3D tracks of charged particles with fine spatial resolutions[9,10,11,12]. A μ-PIC is a gaseous two-dimensional (2D) imaging detector with a pitch of 400 μm manufactured using printed circuit board (PCB) technology. With PCB technology, large area detectors can potentially be mass-produced. We developed a prototype of the $10 \times 10\,\mathrm{cm}^2$ μ-PIC whose electrode structure were optimized using 3D simulators so that the high gas gain and good gain uniformity could been achieved[13]. The left and right panels of Fig.1 show a schematic view of the μ-PIC and an obtained X-ray image, respectively.

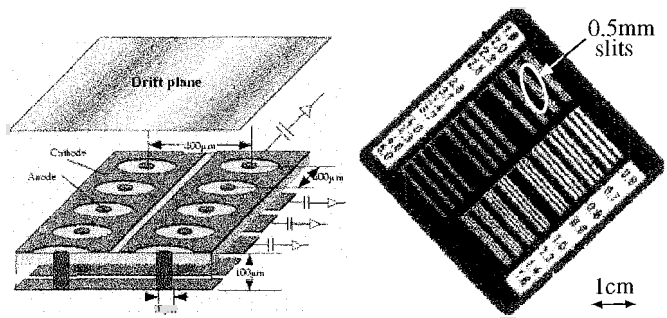

Figure 1. Schematic view of the μ-PIC (left) and X-ray image of the test chart (right).

We developed a prototype of the $10 \times 10 \times 8\,\mathrm{cm}^3$ volume μ-TPC, and 3D tracks of the recoil protons (500 keV–1 MeV) were successfully obtained (Fig.2). The distance between track points shown in Fig.2 was restricted by the clock of the electronics (20 MHz), which we will soon increase to more than 50 MHz. Since the electron tracks are much more winding and have a smaller energy deposition (dE/dx) than those of protons as clearly shown in Fig.2, the electron tracks are known to be discriminated with high efficiency[14].

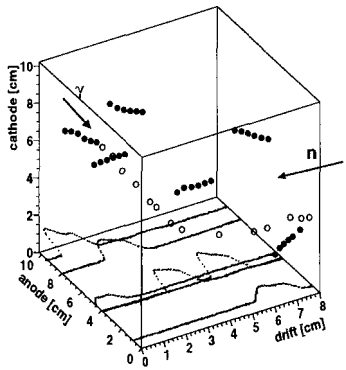

Figure 2. Obtained 3D proton tracks (closed circles) and their Bragg curves shown in the cathode=0 plane. A typical electron track is also shown by open circles.

3. WIMP-wind detection with μ-TPC

Taking into account the tracking capability of the prototype μ-TPC and measured neutron flux at Kamioka Observatory[15], we calculated the detection sensitivities of WIMP-wind[8]. We assume that the track length and dE/dx threshold of a μ-TPC as a WIMP-wind detector are 3 mm and 10 keV/cm, respectively. From the calculated energy deposition of the F ion and the scaled track length of the measured value[16], we consequently knew that 25 keV F ion has a range of roughly 3 mm in 20 Torr of CF_4. We also knew that 25 keV Xe ion has a range of roughly 3 mm in 5 Torr of Xe. The left and right panels of Fig.3 show the SD and SI 3σ detection sensitivities, respectively.

A prototype μ-TPC as a WIMP detector with a detection volume $30 \times 30 \times 30\,\mathrm{cm}^3$ is now being manufactured. Since the fundamental manufacturing technology is already established, a large volume detector ($\sim 1\,\mathrm{m}^3$) for the underground measurement will soon be available.

4. Conclusion

We found that μ-TPC filled with CF_4 gas is a promising device for the WIMP-wind detection via SD interactions. With even a $0.3\,\mathrm{m}^3 \cdot$ year of exposure at Kamioka Observatory, it is expected that the best sensitivity of the current experiments can be achieved. Moreover, it is expected that the sensitivities of μ-TPC as WIMP detector can explore the MSSM region for SD and SI interactions with a sufficient exposure ($\sim 300\,\mathrm{m}^3 \cdot$ year).

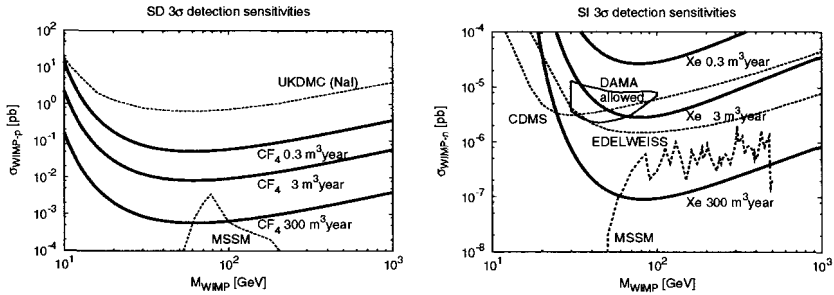

Figure 3. Estimated SD (left) and SI (right) 3σ detection sensitivities at Kamioka Observatory for three exposures shown by thick solid lines. Limits from the UKDMC experiment[17] are shown by a thin dotted line (left). Limits from other experiments[18,19] are shown by thin dotted lines, and DAMA's allowed region[20] is shown by a closed contour (right). Theory regions predicted by minimal supersymmetric extensions of the standard model (MSSM)[21] are also shown in a thin dotted lines (left and right).

References

1. D.N. Spergel *et al.*, Phys. Rev. D **37** (1988) 1353.
2. P. Belli *et al.*, Nuovo Cimento C **15** (1992) 475; R. Bernabei *et al.*, Eur. Phys. J. C **28** (2003) 203.
3. K.N. Buckland *et al.*, Phys. Rev. Lett. **73** (1994) 1067.
4. D.P. Snowden-Ifft *et al.*, Nucl. Instrum. Methods A **498** (2003) 155.
5. Y. Shimizu *et al.*, Nucl. Instrum. Methods A **496** (2003) 347; H. Sekiya *et al.*, Phys. Lett. B **571** (2003) 132.
6. J.I. Collar *et al.*, Phys. Rev. Lett. **85** (2000) 3083.
7. K. Miuchi *et al.*, Astropart. Phys. **19** (2003) 135; A. Takeda *et al.*, Phys. Lett. B **572** (2003) 145.
8. T. Tanimori *et al.*, Phys. Lett. B **578** (2004) 241.
9. A. Ochi *et al.*, Nucl. Instrum. Methods A **471** (2001) 264; **478** (2002) 196.
10. T. Nagayoshi *et al.*, Nucl. Instrum. Methods A **513** (2003) 277.
11. H. Kubo *et al.*, Nucl. Instrum. Methods A **513** (2003) 94.
12. K. Miuchi *et al.*, IEEE Trans. Nucl. Sci. **50** (2003) 825.
13. M. Bouianov *et al.*; T. Nagayoshi *et al.* in preparation.
14. K. Miuchi *et al* , to appear in Nucl. Instrum. Methods A, physics/0308097.
15. A. Minamino, University of Tokyo (private communication).
16. G.L. Cano, Phys. Rev. **169** (1968) 277.
17. N.J.C. Spooner *et al.*, Phys. Lett. B **473** (2000) 330.
18. CDMS Collaboration, Phys. Rev. Lett. **84** (2000) 5699.
19. EDELWEISS Collaboration, Phys. Lett. B **545** (2002) 43.
20. R. Bernabei *et al.*, astro-ph/0307403; Phys. Lett. B **424** (1998) 195; **450** (1999) 448; **480** (2000) 23.
21. J. Ellis, A. Ferstl, and K.A. Olive, Phys. Rev. D **63** (2001) 065016.

WHAT IS THE REAL ORIGIN OF PRESOLAR-NOVA GRAINS?*

MARIKO TERASAWA

Center for Nuclear Study, University of Tokyo, Hirosawa, Wako, Saitama 351-0198; mariko@cns.s.u-tokyo.ac.jp

NOBUYUKI IWAMOTO

Department of Astronomy, University of Tokyo, Hongo, Bunkyo-ku, Tokyo 113-0033

We investigate important reactions and reaction paths in order to reproduce the isotopic ratios of characteristic elements, C, N, and Si, in presolar SiC grains from novae. We find that the N-isotopic ratio strongly depends on the temperature profile in a nova explosion. By using this temperature dependence, we obtain a favorable temperature profile during a nova outburst. Moreover, the calculated $^{30}Si/^{28}Si$ ratio is high compared with the observational data of presolar nova grains. We also find that this overproduction of ^{30}Si can be avoided if the reaction rate of $^{30}P(p,\gamma)^{31}S$, which is experimentally still unknown, could increase by a factor of a few tens around the temperature of $\sim 3 \times 10^8$ K.

1. Introduction

Grains with specific isotopic ratios different from the solar are called 'presolar grains'. It has been considered that these presolar grains contain a lot of information about the site of the nucleosynthesis before the formation of the solar system [1,2]. Understanding the origin of these grains gives us an insight of not only the synthesized site but also the chemical evolution of the Galaxy [3].

The presolar grains are classified into some groups based on their isotopic ratios. In this investigation, we specifically focus on the so-called 'nova grains', which were discovered and reported by Amari et al. [4]. Although they inferred a production site as novae from the fact that the isotopic ratios are $^{12}C/^{13}C$ of 4-9, $^{14}N/^{15}N$ of 5-20, high $^{26}Al/^{27}Al$, close-to-solar $^{29}Si/^{28}Si$, and a little excess in $^{30}Si/^{28}Si$, the real origin of nova grains is still questionable. This is because ratios calculated by hydrodynamical models are largely different from analyzed data, and the ratios could not be realized by adopting any nova models [4]. Their results showed that extra mixing of ejected material with close-to-solar matter is needed more than 95% after nucleosynthesis ended. However, it is also likely that 'nova grains' come from only nova ejecta without such a high mixing rate.

* This work is supported by the fellowship of the Japan Society for Promotion of Science (JSPS).

Therefore, we re-explore reaction paths during nova nucleosynthesis in detail. As a result, we find the ideal profile of temperature in order to reproduce the grain data of $^{12}C/^{13}C$, $^{14}N/^{15}N$, and $^{29}Si/^{28}Si$. It is also showed that the $^{30}Si/^{28}Si$ ratio can be explained, if the reaction rate of an experimentally unknown reaction, $^{30}P(p,\gamma)^{31}S$, changes by a factor of a few tens. Note that we exclude $^{26}Al/^{27}Al$ ratio from consideration, since the data of $^{26}Al/^{27}Al$ have a large uncertainty [4].

2. Calculations and Parameters for Nova Explosions

We adopt the one-zone model for nova explosions [5]. When the temperature at the bottom of the envelope (T_b) is given, the temperature and density structures in the envelope are determined by a WD mass (M_{WD}) and an envelope mass (M_{env}). We assume an outburst on an ONe white dwarf (WD) because of the overabundance of ^{30}Si isotope in nova grains. We change the values of M_{WD} between $1.15M_{\odot}$ and $1.35\ M_{\odot}$, and M_{env} between $10^{-5.5}\ M_{\odot}$ and $10^{-3.0}\ M_{\odot}$. These parameter ranges are necessary to eject the envelope [5]. We have to mention that this one-zone model may not be appropriate near the last phase of the nova outburst, since the envelope is implicitly assumed to be fully convective. Therefore we assume temperature and density profiles to decay exponentially during the late phase.

It has been generally assumed that the dredged-up matter from the ONe WD is mixed with the accreted matter from a companion star. The mixing fraction, X_{WD}, presents the portion of the dredged-up matter in the mixed-matter. A larger value of X_{WD} means that novae contain a larger amount of heavy elements. We also treat the mixing fraction as a parameter, whose ranges are between 0.1 and 0.8.

3. Results

Nucleosynthesis separately occurs in lower and upper regions of the bottle-neck nuclei with the mass number of A = 19, which have a small proton separation energy. Each region is related with CNO elements and heavier elements than Ne. So, we can discuss conditions necessary to reproduce the data of nova grains in each region, separately. In this paper, we first explain how the temperature profile is restricted from the temperature dependence of C- and N-isotopic ratios and secondly we show results from Si-isotopic ratios (for details see Terasawa and Iwamoto [6]). We note that these necessary conditions change slightly with values of X_{WD}, since different values of X_{WD} mean different initial abundances. Here, we will show an ideal condition in the case of $X_{WD} = 0.8$.

In nova explosions, T_b becomes high enough to exceed 2×10^8 K, so that Hot-CNO cycle (HCNO) occurs. In the HCNO cycle, $^{15}N(p,\alpha)^{12}C$ is the key reaction to determine C and N ratios because of its high reaction rate. The strong dependence of the reaction rate on the temperature changes rapidly the ^{15}N

abundance with temperature. Therefore, ^{15}N is transformed to ^{12}C under the condition with relatively high temperature as soon as ^{15}O decays into ^{15}N. On the other hand, when the temperature is relatively low, ^{15}N remains and thus the $^{14}N/^{15}N$ ratio becomes low. This dependence of the reaction on the temperature can give a strong constraint on the profile of temperature evolution after ^{15}N is made by the β-decay of ^{15}O, that is, at the late phase of explosions. In order to leave an appropriate amount of ^{15}N, it is needed to synthesize ^{15}O abundantly at the early phase before the β-decay of ^{15}O. For this, it is important that the peak temperature exceeds $\sim 2.8 \times 10^8$ K. As we described before, since ^{15}O should decay in the condition with relatively low temperature below $\sim 2 \times 10^8$ K, the decreasing time from the peak to $\sim 2 \times 10^8$ K is necessary to be about the β-lifetime of ^{15}O, 120 sec. Moreover, it is necessary that the temperature is kept in a range from $\sim 2 \times 10^8$ K to $\sim 10^8$ K in order to preserve the nuclear flow from ^{15}N to ^{12}C. The duration is favorable to be several thousands of seconds.

As for Si-isotopic ratios, Amari et al. [4] also reported that the $^{29}Si/^{28}Si$ and $^{30}Si/^{28}Si$ ratios are almost the same as the solar. However, both analytical and hydrodynamical studies [4,5] have showed a large enhancement of ^{30}Si relative to ^{28}Si by about a factor of 10. In ONe nova models with high peak temperatures, the reactions which change the abundances of Si isotopes are known to be the following eight reactions, $^{20}Ne(p, \gamma)^{21}Na$, $^{23}Na(p, \gamma)^{24}Mg$, $^{23}Mg(p, \gamma)^{24}Al$, $^{28}Si(p, \gamma)^{29}P$, $^{29}Si(p, \gamma)^{30}P$, $^{29}P(p, \gamma)^{30}S$, $^{30}P(p, \gamma)^{31}S$, and $^{31}P(p,\alpha)^{28}Si$ [7]. Since only the $^{30}Si/^{28}Si$ ratio is large compared with grain data, it is favorable that the ^{30}Si abundance reduces as the ^{29}Si abundance remains unchanged.

Among above eight reactions, the reaction of $^{30}P(p,\gamma)^{31}S$ has large and direct effects on only ^{30}Si abundance [8]. This is because the flow from ^{28}Si to heavier elements does not go through ^{29}Si, and ^{30}Si are made by β^+-decay of ^{30}P at the late phase. If the reaction rate of $^{30}P(p,\gamma)^{31}S$ becomes larger by a few tens, the flow to heavier elements becomes faster. The remaining abundance of ^{30}P decreases by a few tens. As a result, ^{30}Si abundance reduces and the Si-isotopic ratios in the nova grains can be reproduced. Moreover, since there has been no reliable reaction rate for $^{30}P(p,\gamma)^{31}S$ due to the lack of experimental knowledge, the uncertainty is still a factor of 100 up and down [7]. Accordingly, it is quite possible that the reaction rate could be a factor of a few tens higher than the current rate.

Thus, when its reaction rate becomes higher by a few tens at the temperature around 3×10^8 K, a good fit is obtained with Si-isotopic ratios measured in nova grain candidates. For example, we can see a good agreement, $^{12}C/^{13}C = 7.74$ and $^{14}N/^{15}N = 5.56$, in the case of an explosion with $M_{WD} = 1.3M_\odot$, $M_{env} = 2.5 \times 10^{-5}$ $M_\odot$, and $X_{WD} = 0.8$. The reaction rate of $^{30}P(p,\gamma)^{31}S$ is multiplied by 20.

At the end, we describe shortly the dependence of temperature profiles on the value of X_{WD}. We find that it is necessary for the temperature to reach $\sim 3.5 \times 10^8$ K in order to make sufficient ^{29}Si in the case of $X_{WD} = 0.4$. This constraint is more rigorous than that from the N-isotopic ratio. Thus, synthesis of Si isotopes

imposes a constraint on the peak temperature. When a larger value of X_{WD} is adopted, the initial abundance of ^{28}Si becomes higher. Then, the peak temperature is allowed to be low. Actually, the peak temperature of $\sim 2.8 \times 10^8$K suffices in the case of $X_{WD} = 0.8$.

4. Discussions

We have to mention that the most remarkable difference between hydrodynamical models and our one-zone models is made at the late phase of outbursts because of different treatments for convection. However we recognize that abundances of ^{12}C, ^{13}C and ^{15}N strongly depend on the temperature profile at the late phase. Previous hydrodynamical simulations showed the lower values of C- and N-isotopic ratios than nova grains [4]. Based on their results and our results in which temperature remains relatively high even at the late phase, the inner and narrow regions in the envelope may be preferable to form the nova grains. Therefore, nova grains may be seldom found though nova frequency is relatively high in our Galaxy (30 ± 10 yr^{-1}).

Acknowledgments

One of the authors (MT) would like to thank Prof. S. Kubono for useful discussions.

References

1. E. Anders and E. Zinner, *Meteoritics*, **28**, 490 (1993)
2. E. Zinner, *Meteoritics and Planetary Science*, **33**, 549 (1998)
3. T. J. Bernatowicz and R. Cowsik, *American Institute of Physics Conference Series*, **402**, 451 (1997)
4. S. Amari, X. Gao, L. R. Nittler, E. Zinner, J. Jose, M. Hernanz and R. S. Lewis, *ApJ*, **551**, 1065 (2001)
5. S. Wanajo, M. Hashimoto and K. Nomoto, *ApJ*, **523**, 409 (1999)
6. M. Terasawa and N. Iwamoto, *submitted to ApJL* (2004)
7. C. Iliadis, A. Champagne, J. Jose, S. Starrfield, and P. Tupper, *ApJS*, **142**, 105 (2002)
8. J. Jose, A. Coc, and M. Hernanz, *ApJ*, **560**, 897 (2001)

AMD+GCM STUDY OF STRUCTURE OF CARBON ISOTOPES*

G. THIAMOVA†, N. ITAGAKI, T. OTSUKA
Department of Physics, University of Tokyo, Hongo, Tokyo 113-0033, Japan

K. IKEDA
The Institute of Physical and Chemical Research (RIKEN), Wako, Saitama, 351-0198, Japan

The ground state properties of the carbon isotopes are investigated using the extended version of the Antisymmetrized Molecular Dynamics (AMD) Multi Slater Determinant method. We can reproduce reasonably well many experimental data for ^{12}C-^{22}C. In this contribution we present a systematic calculation of binding energies, energies of the 2^1_+ states and B(E2) transition strengths.

1. Introduction

The AMD method is very suitable for the description of light systems where both shell-model and cluster structures can appear because it is free from any model assumption concerning the wave functions.

The extended version of the AMD method adopted in this work corresponds to the combination of AMD and the Generator Coordinates Method (GCM) [1]. The initial GCM basis functions are prepared in such a way that they correspond to several properly chosen r.m.s. radii constraints, close to the experimental values.

The mixing amplitudes of these Slater determinants are determined by diagonalization of the Hamiltonian matrix. In this way suitable basis for the GCM calculations can be obtained. The theoretical details of the method are explained in [2].

2. Results

The Hamiltonian and the effective nucleon-nucleon interaction used is the same as in [3]. The calculations are performed with 45 and 60 basis functions for

* This work is supported by Grant-in Aid for Scientific Research (13740145) and by The Japanese Society for Promotion of Science under the contract No

† On leave of absence from the Nuclear Physics Institute, Czech Academy of Sciences, Prague-Rez, Czech Republic.

even-even and even-odd isotopes, respectively. The details concerning the basis functions can be found in [2].

The binding energies are presented in Fig.1. In general, good agreement is obtained in all the studied region The binding energy of ^{12}C is smaller than the experimental value. It is partially due to the Majorana parameter M=0.6, fitted to the binding energy of ^{16}O and known to produce underbinding of ^{12}C. On the other hand, the spin-orbit term seems to be too strong and thus the 3-alpha component in the ground state wave function is too small. This is also reflected in the smaller B(E2) transition strength (see below).

To describe a halo nucleus ^{15}C is a real challenge for the AMD methods. Here we do not reproduce the ground state spin $1/2^+$. This is mainly due to the simple interaction with no tensor term and strong spin-orbit term. However, in [2] we have adopted a better description of the s-orbit for the odd neutron and the excitation energy of the $1/2^+$ decreased considerabely.

The systematics of the excitation energies of the 2^+_1 states clearly supports the idea about N=16 magic number, reflected by large 2^+_1 energy of ^{22}C. The $(d_{5/2})^6$ subshell closure predicted by our calculation but not seen experimentally is again due to the stronger spin-orbit term, which pushes the $d_{5/2}$ orbit down in energy. A comparison is made with an AMD calculation [4] with weaker spin-orbit term and modified Volkov interaction MV1.

The B(E2) transition strengths (Fig.3) are compared with the experimental data and the shell-model values [5] obtained with effective charges. Smaller B(E2) value for ^{12}C reflects most probably smaller 3-alpha component in the ground state wave function due to stronger spin-orbit term. In ^{16,18}C protons construct almost closed shell-model configuration so the B(E2) value is very small. Proton contribution is recovered again in ^{20}C. The very small B(E2) value for ^{16}C has been measured recently [6] and is successfully reproduced by our model.

3. Summary

We have performed a systematic AMD+GCM calculation of structure of carbon isotopes ^{12}C-^{22}C. We can reproduce fairly well a lot of experimental data. Here we present the systematic calculation of binding energies, 2^+_1 energies and B(E2) strengths. Even though the effective interaction is simple and there are indications that the spin-orbit term is too strong it should not change the qualitative results of this analysis. From the systematics of 2^+_1 energies a clear support for the N=16 magic number is given. B(E2) value of ^{12}C is smaller due to stronger-spin orbit term. Very small B(E2) value for ^{16}C is successfully reproduced by our model.

References

1. N. Itagaki and S. Aoyama, *Phys. Rev.* **C61**, 024303 (2000).
2. G. Thiamova, N. Itagaki, T. Otsuka and K. Ikeda, *to be published.*
3. N. Itagaki and S. Okabe, *Phys. Rev.***C61**, 044306 (2000)
4. Y. Kanada-En'yo and H. Horiuchi,, *Prog. Theor.Phys..Suppl.* **142**, 205 (2001).
5. R. Fujimoto, PhD thesis, University of Tokyo, 2002
6. N. Imai and Z. Elekes, private communication

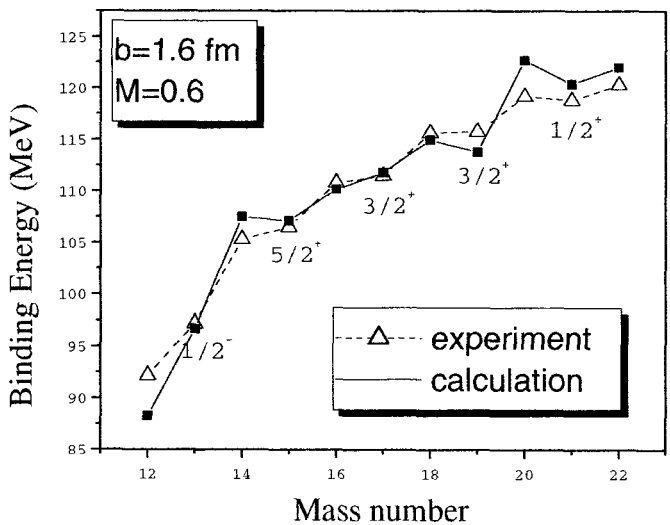

Figure 1. Experimental and calculated binding energies of ^{12}C -^{22}C.

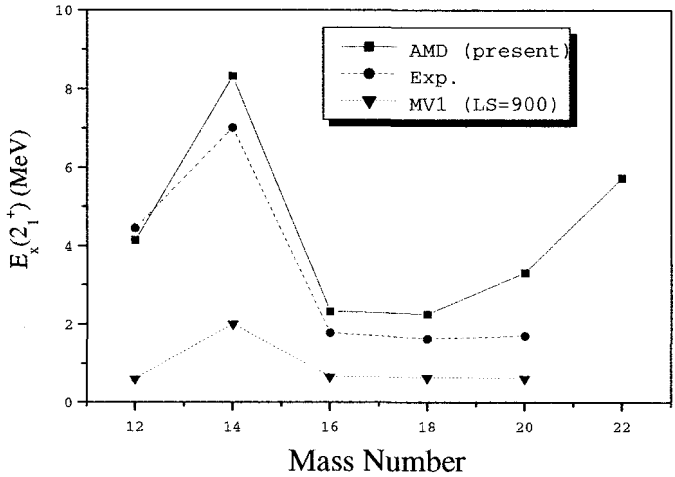

Figure 2. Experimental and calculated energies of the 2^+_1 states. A comparison is made with an AMD calculation with the MV1 interaction and weaker spin-orbit term.

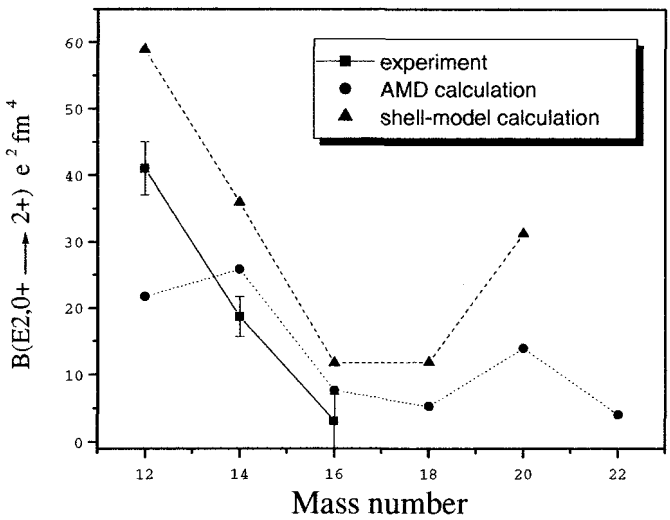

Figure 3. Experimental and calculated B(E2) transition strengths.

STUDY OF THE $^{26}Si(p,\gamma)^{27}P$ REACTION BY THE COULOMB DISSOCIATION METHOD

Y. TOGANO[1], T. GOMI[1], T. MOTOBAYASHI[2], Y. ANDO[1], N. AOI[2], H. BABA[1], K. DEMICHI[1], Z. ELEKES[3], N. FUKUDA[2], ZS. FÜLÖP[3], U. FUTAKAMI[1], H. HASEGAWA[1], Y. HIGURASHI[2], K. IEKI[1], N. IMAI[2], M. ISHIHARA[2], K. ISHIKAWA[4], N. IWASA[5], H. IWASAKI[6], S. KANNO[1], Y. KONDO[4], T. KUBO[2], S. KUBONO[7], M. KUNIBU[1], K. KURITA[1], Y. U. MATSUYAMA[1], S. MICHIMASA[7], T. MINEMURA[2], M. MIURA[4], H. MURAKAMI[1], T. NAKAMURA[4], M. NOTANI[7], S. OTA[8], A. SAITO[1], H. SAKURAI[6], M. SERATA[1], S. SHIMOURA[7], T. SUGIMOTO[4], E. TAKESHITA[1], S. TAKEUCHI[2], K. UE[6], K. YAMADA[1], Y. YANAGISAWA[2], K. YONEDA[9], AND A. YOSHIDA[2]

[1] *Department of Physics, Rikkyo University, Tokyo 171-8501, Japan*
[2] *RIKEN (Institute of Physical and Chemical Research), Saitama 351-0198, Japan*
[3] *Institute of Nuclear Research of the Hungarian Academy of Science (ATOMKI), 4001 Debrecen Hungary*
[4] *Department of Physics, Tokyo Institute of Technology, Tokyo 152-8551, Japan*
[5] *Department of Physics, Tohoku University, Miyagi, 980-8578, Japan*
[6] *Department of Physics, University of Tokyo, Tokyo 113-0033, Japan*
[7] *Center of Nuclear Study (CNS), University of Tokyo, Saitama 351-0198, Japan*
[8] *Department of Physics, Kyoto University, Kyoto 606-8502, Japan*
[9] *National Superconducting Cyclotron Laboratory, Michigan state University, East Lansing, Michigan 48824*

The Coulomb dissociation of ^{27}P was studied experimentally using ^{27}P beams at 57 MeV/nucleon with a lead target. The gamma decay width of the first excited state in ^{27}P was extracted for astrophysical interest. A preliminary result is consistent with the value estimated on the basis of a shell model calculation by Caggiano *et al.*

1. Introduction

Observation of galactic γ rays using the satellite equipped with γ telescope indicates an intense ^{26}Al distribution throughout the galactic plane [1]. The $^{26}Si(p,\gamma)^{27}P$ reaction is one of the key reactions in nucleosynthesis of ^{26}Al in novae. The production of ^{26}Al mainly depends on the reaction sequence

^{24}Mg(p,γ)^{25}Al($\beta^+\nu$)^{25}Mg(p,γ)^{26}Al. This production sequence can be bypassed by ^{25}Al(p,γ)^{26}Si(p,γ)^{27}P. It has been suggested that higher temperature novae ($T_9 \approx 0.4$) may be hot enough to establish an equilibrium between the isomeric state and the ground state of ^{26}Al [2]. Thus, ^{26}Si destruction by proton capture is important to determine the amount of the ground state of ^{26}Al produced by the equilibrium, since the isomeric level of ^{26}Al would be fed by the ^{26}Si β decay. The ^{27}P production in novae is dominated by resonant capture via the first excited state in ^{27}P at 1.2 MeV, because the state is close to the Gamow window. However, there is no experimental information about the strength of resonant capture in this reaction. Therefore, we aimed at determining experimentally the gamma decay width of the first excited state in ^{27}P.

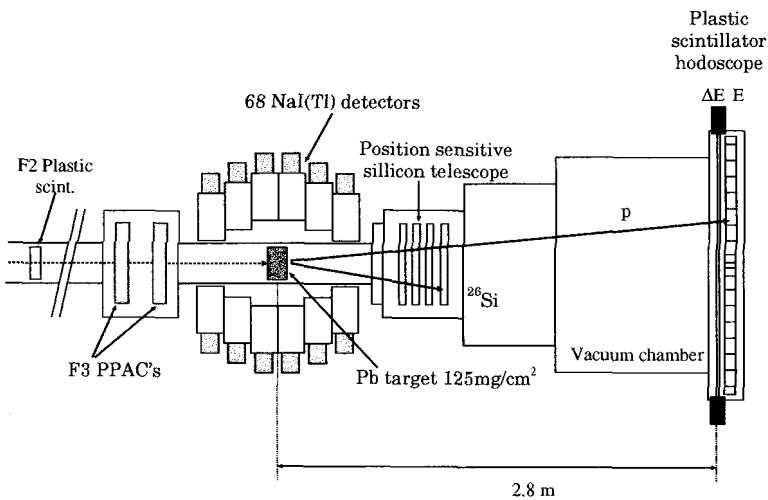

Figure 1. Schematic view of the experimental setup.

2. Experimental Setup

The experiment was performed at the RIPS [3] beam line at the RIKEN Accelerator Research Facility. A secondary beam of ^{27}P at 57 MeV/nucleon was produced by the fragmentation of 115 MeV/nucleon ^{36}Ar beams on a 300 mg/cm^2 thick ^{9}Be target. The ^{27}P beam bombarded a 125 mg/cm^2 thick lead target. A typical intensity and resultant purity were 1.5 kcps

and 1%, respectively. A schematic view of the setup is shown in Fig. 1. Products of the breakup reaction, ^{26}Si and proton, were detected in coincidence using a position sensitive silicon telescope and a plastic scintillator hodoscope. The hit positions of the products and the kinetic energy of ^{26}Si were measured using the position-sensitive silicon telescope located 50 cm downstream of the target. The silicon telescope consisted of two layers of silicon detectors with strips of 5mm width and two layers of single-element silicon detectors. The time of flight of the proton was determined by the plastic scintillator hodoscope placed 2.8 m downstream of the target. The hodoscope consisted of 5-mm-thick ΔE and 60-mm-thick E plastic scintillators. The momentum vectors of the products were determined by combining their energies and hit positions on the position-sensitive silicon telescope. The relative energy between ^{26}Si and proton was extracted from the measured momentum vectors of products.

3. Results and Discussions

The relative energy spectrum is shown in Fig. 2. Peaks were observed at 0.34 MeV and 0.8 MeV which correspond respectively to the known first and the second excited state at 1.2 MeV and 1.6 MeV in ^{27}P [4].

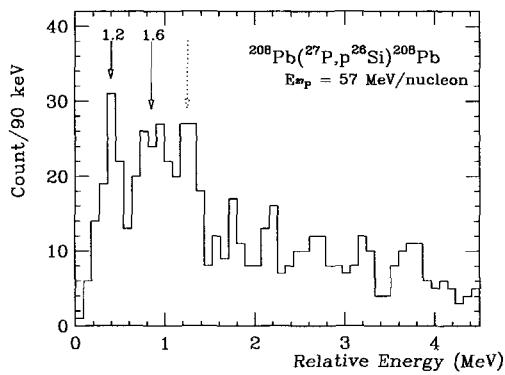

Figure 2. Preliminary relative energy spectrum of the ^{208}Pb(^{27}P,p^{26}Si)^{208}Pb reaction. The peak at 0.34 MeV corresponds to the first excited state in ^{27}P at 1.2 MeV.

We determined preliminarily the cross section for the first excited state of ^{27}P to be 5 mb with a statistical error of about 25%. Supposing the spin and the parity of the first excited state in ^{27}P is $3/2^+$ from the level

scheme of mirror nucleus ^{27}Mg, the transition between the first excited state and the ground state ($1/2^+$) is by the M1/E2 multipolarities. Since the E2 component was strongly enhanced in the Coulomb dissociation [5], the experimental cross section is exhausted via the E2 excitation. To extract the total gamma decay width, the M1 component was estimated using the mixing ratio, E2/M1 = 0.048 from the mirror transition in ^{27}Mg [6]. The gamma decay width of the first excited state was determined preliminarily to be 3.5 $\pm$ 0.6 meV. This result is consistent with the value estimated on the basis of a shell model calculation [4]. It indicates that the ^{26}Si(p,γ)^{27}P reaction does not contribute significantly to the amount of the ground state of ^{26}Al in novae.

4. Summary

We determined experimentally the gamma decay width of the first excited state in ^{27}P. The obtained width is 3.5 $\pm$ 0.6 meV, showing consistency with the shell model calculation. This value indicates that this reaction does not play an important role to control the amount of ^{26}Al in novae.

References

1. N. Prantzos and R. Diehl, *Phys. Rep.* **267**, 1 (1995).
2. A. Coc, M.-G. Porquet, and F. Nowacki, *Phys. Rev.* C **61**, 015801 (1999).
3. T. Kubo *et al.*, *Nucl. Instr. Meth.* **B70**, 309 (1992).
4. J. A. Caggiano *et al.*, *Phys. Rev.* C **64**, 025802 (2001).
5. T. Motobayashi *et al.*, *Phys. Rev. Lett.* **73** 2680 (1994).
6. M. J. A. de Voigt *et al.*, *Nucl. Phys.* **A186**, 365 (1972).

THE TROJAN HORSE METHOD APPLIED TO THE ASTROPHYSICALLY RELEVANT PROTON CAPTURE REACTIONS ON Li ISOTOPES

A. TUMINO, C. SPITALERI, A. MUSUMARRA, M. G. PELLEGRITI, R. G. PIZZONE, A. RINOLLO AND S. ROMANO

Dipartimento di Metodologie Chimiche e Fisiche per l'Ingegneria, Universitá di Catania and Laboratori Nazionali del Sud - INFN
Via S. Sofia, 44
95123 Catania, ITALY
E-mail: tumino@lns.infn.it

L. PAPPALARDO

Texas AM University,
College Station, TEXAS-USA

C. BONOMO, A. DEL ZOPPO, A. DI PIETRO, P. FIGUERA

Laboratori Nazionali del Sud - INFN, Catania, ITALY

M. LA COGNATA, L. LAMIA

Centro Siciliano di Fisica Nucleare e Struttura della Materia, Catania and Laboratori Nazionali del Sud - INFN, Catania, ITALY

S. CHERUBINI AND C. ROLFS

Ruhr Universitaet,
Bochum, GERMANY

S. TYPEL

GSI mbH,
Darmstadt, GERMANY

The ^{7}Li(p,α)^{4}He ^{6}Li(d,α)^{4}He and ^{6}Li(p,α)^{3}He reactions was performed and studied in the framework of the Trojan Horse Method applied to the d(^{7}Li,$\alpha\alpha$)n, ^{6}Li(^{6}Li,$\alpha\alpha$)^{4}He and d(^{6}Li,α^{3}He)n three-body reactions respectively. Their bare astrophysical S-factors were extracted and from the comparison with the behavior of the screened direct data, an independent estimate of the screening potential was obtained.

1. General Introduction

Measurements of Li abundances contribute to the study of different fields as Big Bang nucleosynthesis, cosmic ray physics and stellar structure. Within these fields the knowledge of thermonuclear reaction rates for reactions producing or destroying Li isotopes turns out to be very important. However, due to the Coulomb barrier suppression in the entrance channel and to the electron screening at very low energy, the determination of the relevant astrophysical bare nucleus S(E) factor can be carried out only through the extrapolation from the higher energies [1,2]. A complementary way to get the bare nucleus $S_b(E)$ factor is given by the Trojan Horse Method (THM), which allows to measure the energy dependence of $S_b(E)$ down to the astrophysical energies free of Coulomb suppression and electron screening effects [3,4,5,6,7,8]. The $S_b(E)$ information for the two-body reaction of interest is carried out from the quasi-free contribution of a suitable three-body reaction, where the projectile/target (the so called Trojan Horse nucleus) is clusterised in terms of the two-body projectile/target and another particle which plays the role of spectator to the process. In order to overcome the Coulomb barrier, the three-body reaction takes place at high energy. Then this energy is compensated for by the binding energy of the two clusters inside the Trojan Horse nucleus, in such a way that the two-body reaction can take place even at very low sub-Coulomb energies [7].

2. Experimental details and results

The THM was applied to the d(^{7}Li,α α)n, ^{6}Li(^{6}Li,α α)^{4}He and d(^{6}Li,α ^{3}He)n three-body reactions in order to study the astrophysically relevant ^{7}Li(p,α)^{4}He ^{6}Li(d,α)^{4}He and ^{6}Li(p,α)^{3}He two-body reactions [3,4,5,6,7,8]. The three-body reactions were performed in kinematically complete experiments and the experimental set-ups were optimized in order to cover the angular regions where the quasi-free process is expected to be favored. The two-body cross sections were then extracted from the three-body coincidence yields within a spectator momentum window ranging from -30 to +30 MeV/c. Note that the deduced two-body cross sections are the nuclear part alone, this being the main feature of the THM. In order to deduce the experimental S(E) factors from the standard definition, the nuclear cross sections were multiplied by the proper transmission coefficient $T_l(E)$. The extracted S(E) factors for the three reactions are shown in figs. 1 (^{7}Li(p,α)^{4}He), 2(^{6}Li(d,α)^{4}He), 3(^{6}Li(p,α)^{3}He) (full dots) superimposed to direct data from ref. [1,2] (open symbols). The normalization to the direct

data was performed in an energy region were screening effects on the direct measurements are negligible. At energy above E~100 keV the agreement between the two sets of data is quite good, while they disagree at lower energies as expected, thus fully supporting the validity of the THM. Once parameterized the two behaviors, it was possible to get also independent estimates of the screening potential for the Li+H isotopic pair. The resulting values for the three reactions, together with the S(0) parameters extracted from second order polynomial fits/R-matrix calculations on the data are reported in Table 1. Values from direct experiments are also quoted. Our results affected by smaller uncertainties than direct data agree with both the extrapolated S(0) and U_e direct estimates. Moreover our U_e estimates confirm within the experimental errors the isotopical independence of the screening potential. The large discrepancy (about a factor 2) with the adiabatic limit (186 eV) is still present.

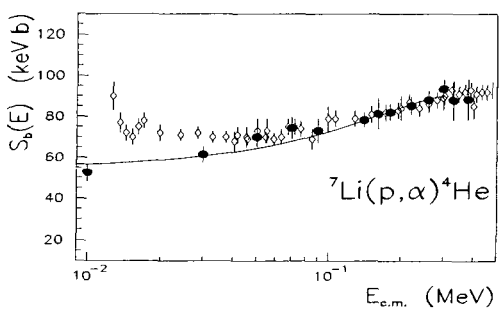

Figure 1. S(E) factor for the ^{7}Li(p,α)^{4}He reaction. Full dots represent THM data, *open symbols refer to direct data of ref.*[1]. *The solid line is the result of a second order* polynomial expansion which gives the S(0) value reported in Table 1.

Table 1. S(0) and U_e values from THM and direct experiments for ^{7}Li(p,α)^{4}He ^{6}Li(d,α)^{4}He and ^{6}Li(p,α)^{3}He reactions.

	S(0) THM [MeV b]	S(0) Dir. [MeV b]	U_e THM [eV]	U_e Dir. [eV]
^{7}Li+p→ α+α	0.055±0.003	0.058	330±40	300±160
^{6}Li+d→ α+α	16.9±0.5	17.4	340±50	330±120
^{6}Li+p→ α+^{3}He	3.00±0.19	2.97	450±100	440±160

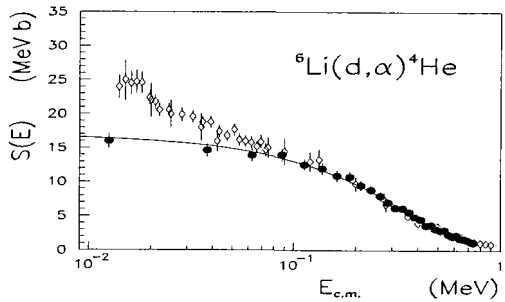

Figure 2. S(E) factor for the ^{6}Li(d,α)^{4}He reaction. Same description as fig.1.

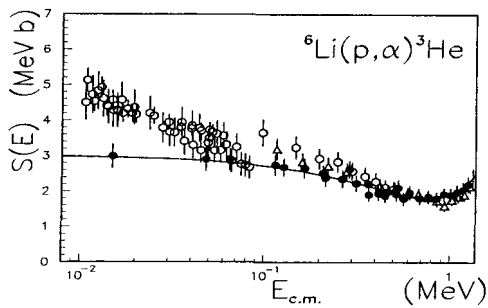

Figure 3. S(E) factor for the ^{6}Li(p,α)^{3}He reaction. Same description as fig.1

References

1. S. Enstler et al., *Z. Phys.* **A342**, 471 (1992).
2. C. Angulo et al., *Nucl. Phys.* **A656**, 3 (1999).
3. C. Spitaleri et al., *Phys. Rev.* **C60**, 55802 (1999).
4. C. Spitaleri et al., *Eur. Phys. Journ.* **A7** 181 (2000).
5. C. Spitaleri et al., *Phys. Rev.* **C63** 055801 (2001).
6. M. Lattuada et al., *ApJ* **562** 1076 (2001).
7. A. Tumino et al., *Phys. Rev.* **C67** (2003).
8. A. Tumino et al., *Nucl. Phys.* **A718**, 499 (2003).

NEUTRON SKIN AND EQUATION OF STATE IN ASYMMETRIC NUCLEAR MATTER

SATOSHI YOSHIDA

Science Research Center, Hosei University 2-17-1 Fujimi, Chiyoda, Tokyo 102-8160, Japan

HIROYUKI SAGAWA

Center for Mathematical Sciences, the University of Aizu Aizu-Wakamatsu, Fukushima 965-8580, Japan

Neutron skin thickness of stable and unstable nuclei are studied by using Skyrme Hartree-Fock (SHF) models and relativistic mean field (RMF) models in relation with the pressure of EOS in neutron matter. We found a clear linear correlation between the neutron skin sizes in heavy nuclei, ^{132}Sn and ^{208}Pb and the pressure of neutron matter in both SHF and RMF, while the correlation is weak in unstable nuclei ^{32}Mg and ^{44}Ar.

1. Equation of state and pressure for neutron matter

The size of the neutron skin thickness will give an important constraint on the pressure of the equation of state (EOS), which is an essential ingredient for the calculation of the properties of neutron stars [1]. The pressure P of neutron matter is defined as the first derivative of Hamiltonian density by the neutron density,

$$P = \rho_n^2 \frac{d}{d\rho_n}\left(\frac{H}{\rho_n}\right) \tag{1}$$

where H is the Hamiltonian density of neutron matter $H(\rho_n, \rho_p = 0)$. In this Hamiltonian density for infinite nuclear matter, the derivative terms and Coulomb term are neglected. Whereas the spherical symmetry is assumed in finite nuclei. The neutron skin is defined by the difference between the root mean square neutron and proton radii,

$$\delta_{np} = \sqrt{\langle r^2 \rangle_n} - \sqrt{\langle r^2 \rangle_p}. \tag{2}$$

Fig. 1(a) shows the neutron equations of state for our different parameter sets, while the pressure of neutron matter is plotted as a function of

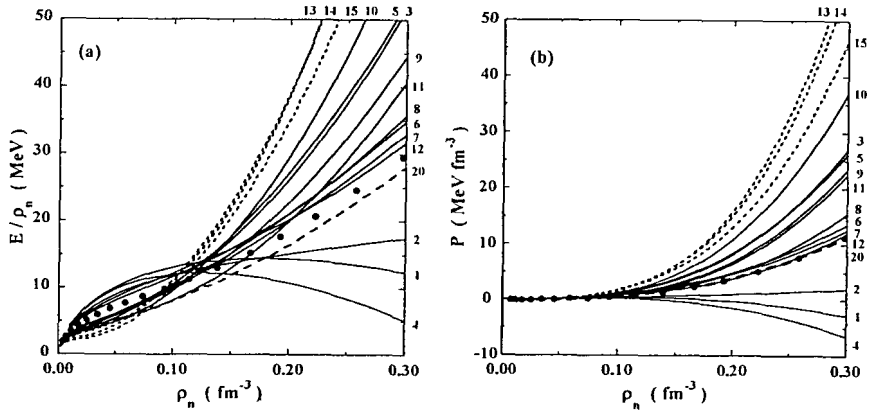

Figure 1. (a) The neutron equations of state are shown for the 12 parameter sets of the SHF model (solid lines) and 3 parameter sets of the RMF model (dashed lines). Filled circles correspond to the variational calculations using the v_{14} nucleon-nucleon potential and a phenomenological three-nucleon interaction, while the long-dashed curve corresponds to the SGII interaction. (b) The pressure of neutron matter as a function of neutron densities. The numbers are a shorthand notation for the different interactions: 1 for SI, 2 for SII,3 for SIV, 4 for SVI, 5 for Skya, 6 for SkM, 7 for SkM*, 8 for SLy4, 9 for MSkA, 10 for SkI3, 11 for SkI4, 12 for SkX, 13 for NLSH, 14 for NL3, 15 for NLC, 20 for SGII.

neutron density in Fig. 1(b). In Figs. 1(a) and 1(b) the solid and dotted lines show the results with SHF and RMF models, respectively. We present results obtained with 13 SHF parameter sets (SI, SIII-IV, SVI, Skya, SkM, SkM*,SkI3, SkI4, MSkA, SLy4, SkX, SGII) and 3 RMF parameter sets (NL3, NLSH, NLC). We plot the results obtained with SGII in Figs. 1(a) and 1(b), since the SGII interaction gives almost equivalent results to those of the variational calculations using the v_{14} nucleon-nucleon potential together with a phenomenological three nucleon-interaction [2]. In Figs. 1(a) and 1(b) one can see large variations among different parameter sets. A general feature is that the RMF curves exhibit a much larger curvature than do the SHF curves, some of which even have negative curvature. Figs. 1(a) and 1(b) show that results obtained with the SGII and SkX parameter sets are almost equivalent to the results of the variational calculations.

Next, we study the relation between the neutron skin thickness of finite nuclei and the pressures of neutron matter at $\rho_n = 0.1$ fm^{-3}. Results for the pressures at $\rho_n = 0.1$ fm^{-3} and are given in Figs. 2(a) and 2(b), respectively. The properties of nuclear matter at high densities are important

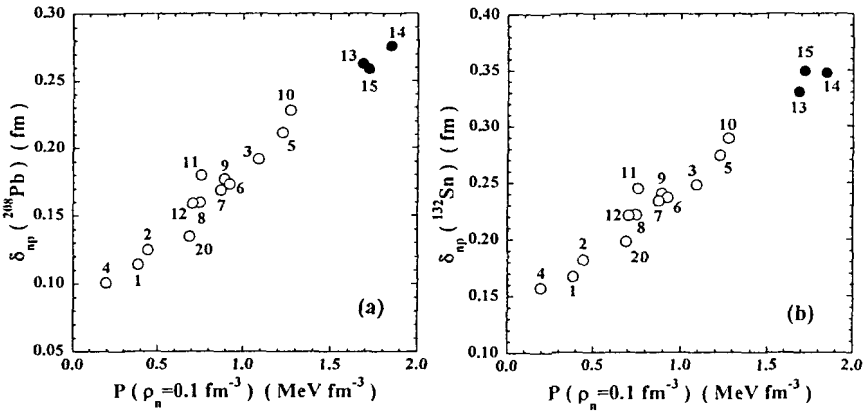

Figure 2. The correlations between the pressures of neutron matter at $\rho_n = 0.1$ fm^{-3} and the neutron skin thickness obtained with the SHF (open circles) and RMF (filled circles) parameter sets. (a) the result for ^{208}Pb. (b) the result for ^{132}Sn. See the caption to Fig. 1 for details.

for a unified description of neutron stars, from the outer crust down to the dense core [3]. Clear linear correlations are found between the neutron skin thickness δ_{np} and the pressure P of ^{208}Pb and ^{132}Sn in Figs. 2(a) and 2(b), respectively, with the parameter sets of the SHF and RMF models used in Figs. 1(a) and 1(b). We checked that there are same linear correlations at not only $\rho_n = 0.1$ fm^{-3} but also $\rho_n = 0.2$ fm^{-3}. In general, the RMF pressures are larger than those of SHF models, and the RMF models give the larger neutron skin thickness. Thus, experimental δ_{np} values would provide important constraints on the parameters used in SHF and RMF models.

We also study the relation between the pressure and the neutron skin thickness of several other nuclei, namely ^{32}Mg, ^{38}Ar, ^{44}Ar, ^{100}Sn, ^{138}Ba, ^{182}Pb and ^{214}Pb obtained in SHF + BCS calculations. In Fig. 3, ^{38}Ar (filled triangles), ^{138}Ba (crosses) and ^{208}Pb (filled circles) are stable nuclei, whereas ^{32}Mg (reversed open triangles), ^{44}Ar (open triangles), ^{132}Sn (open diamonds) and ^{214}Pb (open squares) are neutron-rich nuclei. The two nuclei ^{100}Sn (filled diamonds) and ^{182}Pb (open circles) are neutron-deficient. This figure shows, in general, that the higher the 3rd component of the nuclear isospin $T_z = (N - Z)/2$ is, the steeper the slope of the line is. This isospin rule does not hold in ^{32}Mg. This is because the effect of the neutron-proton Fermi energy disparity dominates the increase in the neutron radii of neutron-rich light nuclei while the pressure plays a minor role, although

the absolute magnitude of δ_{np} is the largest in Fig. 3. The configuration mixing might play an important role in determining the neutron and proton radii in ^{32}Mg. However,the correlation between the neutron skin thickness and the pressure might not be changed by configuration mixing.

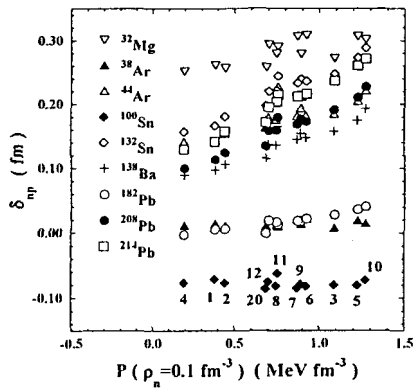

Figure 3. The correlations between the pressures of neutron matter and the neutron skin thickness of ^{32}Mg(reversed open triangles),^{38}Ar(filled triangles),^{44}Ar(open triangles),^{100}Sn(filled diamonds), ^{132}Sn (open diamonds),^{138}Ba(crosses),^{182}Pb(open circles), ^{208}Pb(filled circles),^{214}Pb(open squares) for the pressure at $\rho_n = 0.1$ fm^{-3} obtained by SHF parameter sets. See the caption to Fig. 1 for details.

2. Summary

We studied relations between the neutron skin thickness and the pressure of the EOS in neutron matter obtained in SHF and RMF models. A strong linear correlation between the neutron skin thickness and the pressure of neutron matter as given by the EOS is obtained for stable nuclei such as ^{132}Sn and ^{208}Pb. On the other hand, the correlations between the two quantities in unstable nuclei such as ^{32}Mg and ^{44}Ar are found to be weaker. We pointed out that in general the pressure derived from the RMF model is much higher than that obtained from the SHF model. Also the neutron skin thickness of both stable and unstable nuclei is much larger in the RMF models than in the SHF models for stable nuclei. Thus, experimental data on the neutron skin thickness gives critical information both on the EOS pressure in neutron matter and on the relative merits of the various parameter sets used in mean-field models [4].

References

1. C.J. Horowitz and J. Piekarewicz, *Phys. Rev. Lett.* **86**, 5647 (2001).
2. B. Friedman, and V.R. Pandharipande, *Nucl. Phys.* **A361**, 502 (1981).
3. G. Baym, H.A. Bethe and C.J. Pethick, *Nucl. Phys.* **A175**, 225 (1971).
4. S. Yoshida and H. Sagawa, *Phys. Rev.* **C69**, (2004) to be published

SUPERNOVA MIXING MODELS FOR ISOTOPIC RATIOS OF PRESOLAR GRAINS

TAKASHI YOSHIDA

Astronomical Data Analysis Center, National Astronomical Observatory of Japan, Tokyo 181-8588, Japan
E-mail: takashi.yoshida@nao.ac.jp

MASA-AKI HASHIMOTO

Department of Physics, School of Sciences, Kyushu University, Fukuoka 810-8560, Japan

How many isotopic ratios of individual presolar grains from supernovae agree with those of the mixtures of Type II supernova ejecta with appropriate mixing ratios is investigated. Detailed nucleosynthesis during the evolution and supernova explosion of a 4 $M_\odot$ He star is calculated by postprocessing. Using the obtained supernova ejecta, two cases of mixtures are considered with artificial mixing ratios: one consists of the Si/S, O/Ne, He/C, and He/N layers and the other consists of the Ni, Si/S, He/C, and He/N layers. The isotopic ratios of $^{12}C/^{13}C$, $^{14}N/^{15}N$, $^{26}Al/^{27}Al$, $^{29}Si/^{28}Si$, $^{30}Si/^{28}Si$, and $^{44}Ti/^{48}Ti$ are chosen from eleven SiC grains and four low density graphite ones which contain evidence for the original presence of the short-lived isotope ^{44}Ti. For one SiC X grain and one low density graphite grain, four isotopic ratios are reproduced by the corresponding mixtures. For ten SiC X and low density graphite grains, three isotopic ratios of the grains agree with those of the mixtures. Most of the mixtures reproducing the isotopic ratios of the grains are rich in the composition of the He/N layer. The characteristics of the mixtures are found to be $0.1 < Si/C < 1$ and $Ti/C < 0.1$.

1. Introduction

SiC X, low density graphite grains, and a part of Si_3N_4 have been identified as a supernova origin. These grains have excesses of ^{28}Si and some of them have evidence for the original presence of the short-lived isotope ^{44}Ti. For most of the grains the isotopic ratios of C, N, Al, and Si have been measured and those of O, Ca, and Ti were also measured for smaller number of grains (review in [1]). The isotopic ratios of the grains have been compared with those predicted from supernova nucleosynthesis models. The comparison has indicated that large scale mixing of the supernova ejecta is required for

Table 1. Presolar grains from supernovae adopted in the present study.

Group	Grains	Ref.
Group 1	KJGM2-66-3, 2-243-9, 2-290-2, 4-205-12, 4-271-3, X2	[7]
Group 2	KJC58, 59, 72, 74, KJD57	[3]
Group 3	KE3a-321, 322, KE3c-242, KFA1f-302	[7]

reproducing the isotopic ratios of the grains. Recently, the isotopic ratio distributions of supernova models have been compared quantitatively with those of low density graphite grains [2] and SiC X grains [3]. However, they mainly took into account the distribution of the isotopic ratios of the grains and they did not consider the reproduction of the isotopic ratios of individual grains. In the present study, we investigated how many isotopic ratios of individual presolar grains from supernovae are reproduced by the mixtures with the corresponding appropriate mixing ratios. We show precise results in the submitted article [4]. In this proceeding, we discuss the characteristics of the mixtures reproducing the isotopic ratios of the grains.

2. Supernova Model

In order to construct a model of supernova ejecta, we calculated the evolution and explosion of a massive star. We used a 4 $M_\odot$ He star model in [5] for the stellar evolution and a spherically symmetric hydrodynamical model in [6] for the supernova explosion. The 4 $M_\odot$ He star model corresponds to a 15 $M_\odot$ ZAMS star. We set the explosion energy of 1×10^{51} ergs and the mass cut of 1.41 $M_\odot$ for the supernova explosion. Then, we calculated detailed nucleosynthesis by postprocessing using the nuclear reaction network consisting of 515 species of nuclei from n, H, to Zr [4].

We divided the supernova ejecta into seven layers: the Ni, Si/S, O/Si, O/Ne, C/O, He/C, and He/N layers. We considered two cases of four-layer mixtures: the case A consists of the Si/S, O/Ne, He/C, and He/N layers and the case B consists of the Ni, Si/S, He/C, and He/N layers. We investigated appropriate mixing ratios of both cases of the mixtures for reproducing the isotopic ratios of the individual presolar grains from supernovae.

3. Data of Presolar Grains from Supernovae

We selected 15 SiC X grains and low density graphite grains having evidence for the original presence of the short-lived isotope ^{44}Ti as presolar grains from supernovae. The adopted grains are classified into three groups and listed in Table 1. For the grains in Groups 1 and 3 we considered six isotopic

ratios of $^{12}C/^{13}C$, $^{14}N/^{15}N$, $^{26}Al/^{27}Al$, $^{29}Si/^{28}Si$, $^{30}Si/^{28}Si$, and $^{44}Ti/^{48}Ti$. For the grains in Group 2 we considered three isotopic ratios of $^{29}Si/^{28}Si$, $^{30}Si/^{28}Si$, and $^{44}Ti/^{48}Ti$. For KJD57, we also considered $^{26}Al/^{27}Al$ ratio.

4. Results and Discussion

We investigated how many isotopic ratios of individual grains are reproduced by the mixtures with the corresponding appropriate mixing ratios. We assumed the C/O ratio of the mixtures of the supernova ejecta between 1.0 and 2.0. Here we summarize main results. Details of the analysis procedure and the results are described in [4].

We found that four isotopic ratios of one SiC X grain, KJGM2-243-9, and one low density graphite grain, KE3c-242, agree with those of the mixtures with the corresponding appropriate mixing ratios. For KJGM2-243-9, the mixtures of case A reproduce $^{12}C/^{13}C$, $^{26}Al/^{27}Al$, $^{29}Si/^{28}Si$, $^{44}Ti/^{48}Ti$ and $^{12}C/^{13}C$, $^{26}Al/^{27}Al$, $^{30}Si/^{28}Si$, $^{44}Ti/^{48}Ti$. The mixture of case B reproduces $^{12}C/^{13}C$, $^{26}Al/^{27}Al$, $^{30}Si/^{28}Si$, $^{44}Ti/^{48}Ti$. For KE3c-242, the mixture of case A reproduces $^{14}N/^{15}N$, $^{29}Si/^{28}Si$, $^{30}Si/^{28}Si$, $^{44}Ti/^{48}Ti$. Three isotopic ratios are reproduced by the mixtures with the corresponding mixing ratios of case B for one grain in Group 1, five grains in Group 2, and three grains in Group 3. For two grains in Group 2, three isotopic ratios, i.e., all measured isotopic ratios are reproduced by the mixtures of cases A and B. Thus, about a half of the isotopic ratios are reproduced by the mixtures with appropriate mixing ratios for most of the grains. We note that we have several possibilities of the mixtures reproducing the isotopic ratios for some of the grains. The reproduced isotopic ratios depend on the C/O ratio and the mixing ratios of the mixtures.

We discuss two characteristics of the mixtures reproducing the isotopic ratios of individual grains: the mixing ratios and the ratios of Si/C and Ti/C. The mixing ratios of the mixtures reproducing three or four isotopic ratios of individual grains are shown in Figure 1a. Points at a value of the horizontal axis corresponds to the mixing ratios of each mixture. We see that the mixing ratio of the He/N layer is more than 90% for most of the mixtures reproducing the isotopic ratios of SiC X grains (Groups 1 and 2). The mixing ratio of the inner layers, i.e., the Ni, Si/S, and O/Ne layers, are of order or less than 0.01. Thus, the He/N layer is the main component of the mixtures. This characteristic is seen in both of the cases A and B. On the other hand, the mixtures reproducing the isotopic ratios of low density graphite grains (Group 3) contain approximately equal contributions from

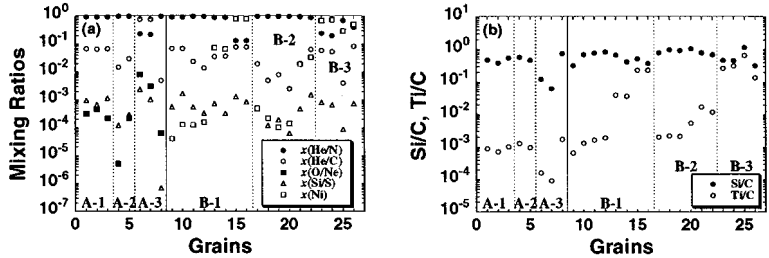

Figure 1. The mixing ratios (a) and the Si/C and Ti/C ratios (b) of the mixtures reproducing three or four isotopic ratios of individual grains. Notation "A" or "B" indicates the composition case of the mixtures. The number attached to the notation indicates the group of the corresponding grains (see section 3).

the Ni or He/C layer and the He/N layer.

The ratios of Si/C and Ti/C in the mixtures are shown in Figure 1b. The Si/C ratio of most of the mixtures is between 0.1 and 1.0. This characteristic is seen in the mixtures of both of the cases and of all groups. We seem that the Si/C ratio of the mixtures depends on the C/O ratio (see [4] for details) : it decreases with increase in the assumed C/O ratio. On the other hand, the Ti/C ratio of the mixture reproducing the isotopic ratios of SiC X grains is smaller than 0.1. The small Ti/C ratio is due to small mixing ratios of the Ni and Si/S layers. In some mixtures (mainly corresponding to Group 3), the Ti/C ratio is of order 0.1. The mixtures also show large mixing ratio of the Ni layer. Thus, the large Ti/C ratio is due to the contribution from the Ni layer.

T. Y. is supported by Research Fellowships of the Japan Society for the Promotion of Science for Young Scientists (12000289).

References

1. E. Zinner, *Annu. Rev. Earth Planet. Sci.* **26**, 147 (1998).
2. C. Travaglio, R. Gallino, S. Amari, E. Zinner, S. E. Woosley, and R. S. Lewis, *Astrophys. J.* **510**, 325 (1999).
3. P. Hoppe, R. Strebel, R. Eberhardt, S. Amari, and R. S. Lewis, *Meteoritics & Planet. Sci.* **35**, 1157 (2000).
4. T. Yoshida and M. Hashimoto, *Astrophys. J.*, in press (2004).
5. K. Nomoto and M. Hashimoto, *Phys. Rep.* **163**, 13 (1988).
6. T. Shigeyama, K. Nomoto, H. Yamaoka, and F.-K. Thielemann, *Astrophys. J.* **386**, L13 (1992).
7. L. R. Nittler, S. Amari, E. Zinner, S. E. Woosley, and R. S. Lewis, *Astrophys. J.* **462**, L31 (1996).

SYMPOSIUM PROGRAM

The Origin of Matter and Evolution of Galaxies 2003

November 17

S. Kubono (CNS), Chair

Opening
H. Sakai (CNS)
Review and Scope
G. J. Mathews* (U. Notre Dame)

Big Bang Cosmology and Primordial Nucleosynthesis

T. Kajino (NAOJ), Chair

A. Coc* (CSNSM):
Updated Big Bang Nucleosynthesis Compared to WMAP Observations and the Abundance of Light Elements
K. Ichiki (U. Tokyo):
Decaying Cold Dark Matter and Cosmological Microwave Background Anisotropies
K. Kohri (Osaka U.):
Hadronic Decay of SUSY Particle and Destruction of Light Elements

Observations: X-Rays, Cosmic Rays and Meteoritic Anomalies I

M. Takada-Hidai (Tokai U.), Chair

R. Diehl* (MPE):
Nuclear Astrophysics with the INTEGRAL Observatory
S. Amari* (Washington U.):
Probing the Galactic Chemical Evolution of Si and Ti with Presolar SiC Grains

Observations: X-Rays, Cosmic Rays and Meteoritic Anomalies II

K. Nomoto (U. Tokyo). Chair

K. Matsushita* (TUS):
XMM Observations of Metal Abundances in the Intracluster Medium
F. Primas* (ESO):
Chemical Signatures of the First Stellar Generations
Y. Ishimaru (Ochanomizu U.):
What Do Metal-Poor Stars Tell?: Origin of O-Zn and r-Process Elements

Weak Interaction, Neutrinos, dark matter

K. Nomoto (U. Tokyo). Chair

B. Balantekin* (U. Wisconsin):
Neutrino Experiments and Implications for r-Process Nucleosynthesis

H. Ejiri* (JASRI/Spring8):
Prospective of double beta Experiments and Neutrons

Y. Inoue (U. Tokyo):
Current Status of Tokyo Dark Matter Experiment

Evolution and Nucleosynthesis in Stars, and cross sections - hydro static burning I

I. Tanihata (RIKEN), Chair

R. Tribble* (Texas A&M U.):
Recent Results for Proton Capture S factors from Measurements of Asymptotic Normalization Coefficients

T. Nakamura* (TITECH):
Neutron Capture Cross Section of ^{14}C Studied by Intermediate-Energy Coulomb Dissociation

short talks for poster presentations

T. Kishida (RIKEN), Chair

T. Gomi (Rikkyo U.):
Coulomb Dissociation of ^{23}Al - Study of the ^{22}Mg(p,γ)^{23}Al Reaction-

J. He (CNS):
Elastic Scattering of ^{22}Mg and ^{21}Na RI Beams on an H Target

M. Takada-Hidai (Tokai U.):
Preliminary Analyses of Oxygen Abundances in Halo Stars

C. Ishizuka (Hokkaido U.):
Supernova Explosion Energy and Composition with Relativistic EoS Including Hyperon

J. S. Lange (Frankfurt U.):
Possible Implications of RHIC Results for the Big Bang

J. Y. Moon (Chung-Ang U.):
Study of Proton Resonances in ^{26}Si and ^{27}P by the Elastic Scattering of ^{1}H(^{25}Al, p)^{25}Al, ^{1}H(^{26}Si, p)^{26}Si

T. Nozawa (Hokkaido U.):
Dust Formation and Evolution in the Early Universe

M. G. Pellegriti (U. Catoyyio):
Quasi-Free Proton-Proton Elastic Scattering in the THM Framework

T. Sasaqui (U. Tokyo):
Reaction Sensitivity of r-Process Nucleosynthesis

M. Segawa (Osaka U.):
Neutron Experiment for the Study of Re/Os Cosmochronometer

T. Suda (Hokkaido U.):
Nucleosynthesis in Extremely Metal Poor Stars and the Origin of the Most Metal-poor Star HE0107-5240
S. Sukhoruchkin (PNPI):
The Combined Study of Nuclear Masses and Eecitations
K. Takahisa (Osaka U.):
Nuclear Responses for Double Beta Neutrinos and Double Spin Isospin Resonances by Using of the Heavy Ion Reaction
A. Takeda (Kyoto U.):
NEWAGE Project -Dark Matter Detection with an Advanced Gaseous Tracking Device-
Y. Tchuvilsky (Moscow State U.):
Structural Forbiddenness of Heavy Fusion and Nucleosynthesis in Iron Maximum Region
G. Thiamova (U. Tokyo):
Systematic Study of Structure of Neutron-Rich Carbon Isotopes with the Antisymmetrized Molecular Dynamics Plus Generator Coordinate Method
Y. Togano (Rikkyo U.):
Study of the ^{26}Si(p,γ)^{27}P Reaction via the Coulomb Dissociation
A. Tumino (U. Catoyyio):
The Trojan Horse Method Applied to the Astrophysically Relevant Proton Capture Reactions on Li Isotopes

welcome party

November 18

Evolution and Nucleosynthesis in Stars, and cross sections - hydro static burning II

M. Terasawa (CNS), Chair

H. Umeda* (U. Tokyo):
Pop III Black-Hole-Forming Supernovae and the Abundance Pattern of Extremely Fe-Poor Stars
T. Ohkubo (U. Tokyo):
Evolution, Explosion, and Nucleosynthesis of Pop III Super-Massive Stars
C. Spitaleri* (U. Catoyyio):
The Trojan Horse Method in Nuclear Astrophysics
N. Iwamoto* (U. Tokyo):
s-Process in Metal-Poor Massive Stars

Evolution and Nucleosynthesis in Stars, and cross sections - hydro static burning III

T. Otsuka (U. Tokyo), Chair

T. Hayakawa (JAERI):
^{186}Re Isomer Contribution to ^{187}Re-^{187}Os Cosmochronometer

T. Shima (Osaka U.):
Direct Measurement of the E1 and E2 Cross Sections of the $^{12}C(\alpha,\gamma)^{16}O$ Reaction at $E_{c.m.}$ =1.3-1.5MeV

Nuclear data and Nuclear Physics I

T. Otsuka (U. Tokyo), Chair

W. Nazarewiz* (U. Tennessee):
Microscopic Nuclear Structure Relevant to Nuclear Astrophysics

RIKN, CNS Tour

Nuclear data and Nuclear Physics II

T. Motobayashi (RIKEN), Chair

P. Descouvemont* (ULB):
Theoretical Models in Nuclear Astrophysics

P. Moller* (LANL):
Global Calculations of Fission Barriers and Beta-Decay Properties of Neutron-Rich Nuclei

K. Morita* (RIKEN):
Synthesis of Super Heavy Elements

K. Ogata (Kyushu U.):
Determination of S_{17} Based on CDCC Analysis of ^{8}B Dissociation

Novae, Supernovae, and Explosive Nucleosynthesis, GRB Models and Nuclearphysics parameters I

K. Sumiyoshi (NCT), Chair

S. Wanajo* (Sophia U.):
The r-Process in Supernova Explosions from the Collapse of ONeMg Cores

T. Yamasaki (Kyoto U.):
Effects of Rotation on the Propagation of Supernova Shock and Nucleosynthesis

S. Nishimura* (RIKEN):
Experimental Study of r-Process Nuclei and the Future at RIBF

H. Ishiyama (KEK):

Direct Measurements of the Astrophysical (α, n) and (p, n) Reaction Cross Sections of Light Neutron-Rich Nuclei by Using Low-Energy RNBs

N. Tominaga (U. Tokyo):
The Model of Type Ic Hypernova SN2003dh/GRB030329

S. Inoue (MPA):
The "Dark Side" of Gamma-Ray Bursts and Implications for Nucleosynthesis of Light and Heavy Elements

S. Fujimoto (KNCT):
Nucleosynthesis inside Gamma-Ray Burst Accretion Disks

Poster session

November 19

Novae, Supernovae, and Explosive Nucleosynthesis, GRB Models and Nuclearphysics parameters II

R. Tribble (Texas A&M U.), Chair

M. Smith* (ORNL):
Stellar Explosion Studies with Radioactive Beams at ORNL

M. Notani (CNS):
Direct Measurement of the Astrophysical Reaction $^{14}O(\alpha,p)^{17}F$

T. Teranishi* (CNS):
Elastic Resonance Scattering of $^{23}Mg+p$

Y. Shimizu (Osaka U.):
Resonance States in ^{22}Mg, ^{26}Si for Reaction Rates

Novae, Supernovae, and Explosive Nucleosynthesis, GRB Models and Nuclearphysics parameters III

Y. Nagai (Osaka U.), Chair

S. Bishop (RIKEN):
The $^{21}Na(p,\gamma)\,^{22}Mg$ Reaction from E_{cm} = 200 to 850 KeV in Explosive Stellar Events

M. Terasawa* (CNS):
Neutrino Effects before, during and after the Freezeout of the r-Process Nucleosynthesis

S. Nagataki* (U. Tokyo):
High-Energy Neutrinos Produced by Interactions of Relativistic Protons in Shocked Pulsar Wind

Nuclear Equation of State and Neutron Stars

B. Balantekin (U. Wisconsin), Chair

C. H. Hyun (Sungkyunkwan U.):
Neutron Star Matter with in-Medium Meson Mass
T. Tatsumi (Kyoto U.):
Screening effect at Quark-Hadron Mixed Phase
K. Oyamatsu (ASU):
Equation of State of Nuclear Matter, Neutron Rich Nuclei in Laboratories, and Pasta Nuclei in Neutron Star Crusts
T. Maruyama (JAERI):
Coulomb Screening Effect on the Nuclear-Pasta Structure

Stellar Abundance, Galactic Chemical Evolution and Nucleo-Cosmochronology
G. J. Mathews (U. Notre Dame), Chair

W. Aoki* (NAOJ):
Measurements of Li and Eu Isotope Abundances in Metal-Deficient Stars
S. Honda (NAOJ):
Spectroscopic Studies of r-process Elements in Very Metal-Poor Stars with Subaru/HDS
K. Nakamura (U. Tokyo):
Roles of Relativistic Supernova Ejecta in Nucleosynthesis of Light Elements, Li, Be, B
T. Yoshida (NAOJ):
Light Element and r-Process Element Syntheses through the ν-Process in Supernova Explosions
K. Otsuki (U. Notre Dame):
Constraints on Globular Cluster Formation and Evolution from Mg Isotope Ratios and r-Process Elemental Abundances

Concluding
T. Kajino (NAOJ)

Poster presentation with no oral presentation:
N. Iwamoto (U. Tokyo):
p-Process Nucleosynthesis in Core Collapse Supernovae
T. Maruyama (JAERI):
Kaon Condensation and the Structured Mixed Phase
M. Smith (ORNL):
Recent Nuclear Astrophysics Data Activities at ORNL
S. Sukhoruchkin (PNPI):
Compilations of Resonance Parameters in Reactions with Neutrons and Charged Particles
M. Terasawa (CNS):
What Is the Real Origin of Presolar-Nova Grain?

This page intentionally left blank

List of Participants

Amari, Sachiko
Physics Department
Washington Univ.
St.Louis
MO63130,USA
sa@wuphys.wustl.edu

Aoki, Wako
Natonal Astromonical Observatory of Japan
2-21-1 Osawa,Mitaka
Tokyo 181-8588
Japan
aoki.wako@nao.ac.jp

Aumann, Thomai
GSI
Planker str.1
D-64291Darmstadt
Germany
t.aumann@gsi.de

Balantekin, Baha Akif
Department of Physics
Univ. Wisconsin
1150 University Avenue Madison
WI 53726
USA
baha@nucth.physics.wisc.edu

Bishop, Shawn
Simon Fraser Univ.
445 East 35 Ave,
Vancouver,vsw101
Canada
bishop@triumf.ca

Claudio, Spitaleri
Itoly and LNS-INFW
University Catoyyio
Via S.Sofia,44
95133 catania
Italy
spitaleri@lns.infw.it

Coc, Alain
CSNSM
Bat 104
F-91405 Orsay Campus
France
coc@csnsm.in2p3.fr

Descouvemont, Pierre
Universite Libre de Bruxelles
CP229
B1050 Bruxelles
Belgium
pdesc@ulb.ac.be

Diehl, Roland L
MPE Garching, Germany
Max Planck Institut fuer
extraterrestrische Physik
Giessenbachstr. 1
D-85741 Garching
Germany
rod@mpe.mpg.de

Ejiri, Hiro
JASRI/Spring-8
Kouto-1-1-1,Mikazuki chou
Hyogo 679-5198
Japan
ejiri@spring8.or.jp

Endo , Tomoki
Kyoto Univ.
Kitashirakawa-Oiwake-cho,
Sakyo-ku, Kyoto 606-8502, Japan
Japan
endo@ruby.scphys.kyoto-u.ac.jp

Fujikawa, Hisashi
University of Tokyo
7-3-1 Hongo,Bunkyo-ku
Tokyo 113-0033
Japan
sequence@rf7.so-net.ne.jp

Fujimoto, Shin-ichiro
Kumamoto National College of
Technology
2659-2 Suya,Nishigoshi,Kikuchi
Kumamoto 861-1102
Japan
fujimoto@ec.knct.ac.jp

Gibelin, Julien
Heavy ion nuclear physics
RIKEN
2-1 Hirosawa, Wako
saitama 351-0198
Japan
gibelin@rarfaxp.riken.go.jp

Gomi, Tomoko
Heavy ion nuclear physics
RIKEN
2-1 Hirosawa Wako
Saitama 351-0198
Japan
gomi@ne.rikkyo.ac.jp

Hayakawa, Takehito
Japan Atomic Energy Research
Institute
Naka,Toukai,Shirakata-Shirane 2-4
Ibaraki 319-1195
Japan
hayakawa@jball4.tokai.jaeri.go.jp

He, Jianjun
Center for Nuclear Study(CNS)
University of Tokyo
2-1Hirosawa,Wako
Saitama 351-0198
Japan
he@cns.s.u-tokyo.ac.jp

Honda, Satoshi
Natonal Astromonical Observatory of
Japan
2-21-1,Osawa,Mitaka
Tokyo 181-8588
Japan
honda@optik.mtk.nao.ac.jp

Hong, Seung-Woo
Department of Physics
Sungkyunkwan University
300 Cheon Cheon Dong,Jang An Gu
Suwon 440-76
Korea
swhong@skku.ac.kr

Hyun, Chang Ho
Institute of Basic Science
Sungkyunkwan University
Cheon Cheon Dong,Jang An Gu
Suwon 440-76
Korea
hch@color.skku.ac.kr

Ichiki, Kiyotomo
National Astronomical Observatory
2-21-1, Osawa, Mitaka
Tokyo, 181-8588
Japan
ichiki@th.nao.ac.jp

Ikeda, Nobuo
Faculty of Engineering
Kyushu Univ.
Hakozaki 6-10-1
Fukuoka 812-0053
Japan
nikeda@nucl.kyushu-u.ac.jp

Inoue, Susumu
Max-Planck-Institut fuer Astrophysik
Karl-Schwarzschild-Str. 1,Postfach 1317
85741 Garching
Germany
inouemu@mpa-garching.mpg.de

Inoue, Yoshizumi
International Center for Elementary Particle Physics
University of Tokyo
7-3-1 Hongo,Bunkyo-ku
Tokyo 113-0033
Japan
berota@icepp.s.u-tokyo.ac.jp

Ishihara, Masayasu
RIKEN
2-1 Hirosawa, Wako
saitama 351-0198
Japan
ishihara@rarfaxp.riken.go.jp

Ishikawa, Tomoko
Tokyo University of Science
Kagurazaka 1-3,Shinjuku
162-8601 Tokyo
Japan
tomoko@post.kek.jp

Ishimaru, Yuhri
Department of Physics
Ochanomizu University
2-1-1 Otsuka,Bunkyo
Tokyo 112-8610
Japan
ishimaru@phys.ocha.ac.jp

Ishiyama, Hironobu
IPNS,KEK
1-1 Oho
Tsukuba-shi,300-0801
Japan
hironobu.ishiyama@kek.jp

Ishizuka, Chikako
Division of Physics
Hokkaido Univ.
Kita 10-jo , Nishi 8-chome , Kita-ku
Sapporo 060-0810
Japan
chikako@nucl.sci.hokudai.ac.jp

Iwamoto, Nobuyuki
University of Tokyo
7-3-1 Hongo,Bunkyo-ku
Tokyo 113-0033
Japan
niwamoto@astron.s.u-tokyo.ac.jp

Iwanami, Tomoko
Heavy ion nuclear physics
RIKEN
2-1 Hirosawa, Wako
saitama 351-0198
Japan

Kajino, Toshitaka
Natonal Astromonical Observatory of Japan
2-21-1,Osawa,Mitaka
Tokyo 181-8588
Japan
kajino@th.nao.ac.jp

Kanungo, Rituparna
RI Beam Science Laboratory
RIKEN
2-1 Hirosawa, Wako
saitama 351-0198
Japan

Kimura, Sachie
INFN-LNS
Via S. Sofia n.62
95123 Catania
Italy
kimura@lns.infn.it

Kishida, Takashi
Heavy ion nuclear physics
RIKEN
2-1 Hirosawa, Wako
saitama 351-0198
Japan
kishida@rarfaxp.riken.go.jp

Kohri, Kazunori
Department of Earth and Space Science
Osaka University
Graduate School of Science Osaka University
Toyonaka OSAKA 560-0043
Japan
kohri@vega.ess.sci.osaka-u.ac.jp

Koura, Hiroyuki
Japan Atomic Energy Research Institute
Naka,Toukai,Shirakata-Shirane 2-4
Ibaraki 319-1195
Japan
koura@riken.jp

Kubono, Shigeru
Center for Nuclear Study(CNS)
University of Tokyo
2-1 Hirosawa, Wako
Saitama 351-0198
Japan
kubono@cns.s.u-tokyo.ac.jp

Kurata-Nishimura , Mizuki
RIKEN
2-1 Hirosawa, Wako
Saitama 351-0198
Japan
mizuki@riken.go.jp

Kusakabe, Motohiko
University of Tokyo
7-3-1 Hongo,Bunkyo-ku
Tokyo 113-0033
Japan
s22003@astron.s.u-tokyo.ac.jp

Lange, Jens-Soeren
Brookhaven National Laboratory
Bldg.510 c/o STAR Experiment
Upton
Frankfurt University
New York 11973-5000
USA
soeren@bnl.gov

Madokoro, Hideki
RIKEN
2-1 Hirosawa, Wako
saitama 351-0198
Japan
madokoro@postman.riken.jp

Maruyama, Toshiki
Japan Atomic Energy Research Institute
Naka,Toukai,Shirakata-Shirane 2-4
Ibaraki 319-1195
Japan
maru@hadron02.tokai.jaeri.go.jp

Mathews, Grant J.
Department of Physics
University of Notre Dame
Notre Dame, IN, 46556
USA
gmathews@nd.edu

Matsunami, Yoshiyuki
Tokyo Inst. Of Technology
2-12-1 O-Okayama,Meguro
Tokyo 152-8551
Japan
matunami@geo.titech.ac.jp

Matsushita, Kyoko
Department of Physics
Tokyo University of Science
Kagurazaka 1-3,Shinjuku
162-8601 Tokyo
Japan
matusita@rs.kagu.tus.ac.jp

Minemura, Toshiyuki
RIKEN
2-1 Hirosawa, Wako
saitama 351-0198
Japan
minemura@riken.jp

Moller, Peter
Nuclear theory
Los Alamos National Laboratory
LosAlamos
NM87545
USA
moller@moller.lanl.gov

Moon, Jun Yung
Department of Physics
Chung-Ang University
221 Huksuk-dong,dongjak-ku
Seoul, 156-756
Korea
jymoon7@hanmail.net

Morita, Kosuke
RIKEN
2-1 Hirosawa, Wako
saitama 351-0198
Japan
morita@rarfaxp.riken.jp

Motobayashi, Tohru
Heavy ion nuclear physics
RIKEN
2-1 Hirosawa, Wako
saitama 351-0198
Japan

Nagai, Yasuki
Osaka University
1-1 Yamadaoka Suita
Osaka 565-0871
Japan
nagai@rcnp.osaka-u.ac.jp

Nagataki, Shigehiro
Department of Physics
University of Tokyo
7-3-1 Hongo,Bunkyo-ku
Tokyo 113-0033
Japan
nagataki@utap.phys.s.u-tokyo.ac.jp

Nakamura, Takashi
Department of Physics
Tokyo Inst. Of Technology
2-12-1 O-Okayama,Meguro
Tokyo 152-8551
Japan
nakamura@ap.titech.ac.jp

Nakamura, Ko
Research Center for the Early Universe
University of Tokyo
7-3-1 Hongo,Bunkyo-ku
Tokyo 113-0033
Japan
nakamura@resceu.s.u-tokyo.ac.jp

Nazarewicz, Witold
Department of Physics & Astronomy
University of Tennessee
401 Nielsen Physics
Knoxville, Tennessee 37996
USA
witek@utk.edu

Nishimura, Shunji
RI Beam Science Laboratory
RIKEN
2-1 Hirosawa, Wako-shi
saitama 350-0198
Japan
nishimu@rarfaxp.riken.go.jp

Nomoto, Kenichi
University of Tokyo
7-3-1 Hongo,Bunkyo-ku
Tokyo 113-0033
Japan
nomoto@astron.s.u-tokyo.ac.jp

Notani, Masahiro
Center for Nuclear Study(CNS)
University of Tokyo
2-1 Hirosawa, Wako
saitama 351-0198
Japan
notani@riken.jp

Nozawa, Takaya
Division of Earth and Planetary Sciences
Hokkaido Univ.
N10 W8,Kita-ku
060-0810 Sapporo
Japan
nozawa@ep.sci.hokudai.ac.jp

Ogata, Kazuyuki
Kyushu Univ.
Hakozaki 6-10-1,Higashi-ku,Fukuoka city
Fukuoka 812-8581
Japan
kazu2scp@mbox.nc.kyushu-u.ac.jp

Ohkubo, Takuya
University of Tokyo
7-3-1 Hongo,Bunkyo-ku
Tokyo 113-0033
Japan
ohkubo@astron.s.u-tokyo.ac.jp

Otsuka, Takaharu
University of Tokyo
7-3-1 Hongo,Bunkyo-ku
Tokyo 113-0033
Japan
Otsuka@phys.s.u-tokyo.ac.jp

Otsuki, Kaori
University of Notre Dame
225 Nieuwland Science Hall
Motre Dame,IN46530
USA
kotsuki@nd.edu

Oyamatsu, Kazuhiro
Aichi Shukutoku University
Nagatake-cho,Aichigun
Aichi,480-1197
Japan
oyak@asu.aasa.ac.jp

Pellegriti, Maria Grazia
Laboratori Nazionali del Sud-INFN and Universit de Catania
Via S.Sofia,44
95123 Catania
Italy
pellegriti@lns.infn.it

Primas, F.
European Southern Observatory
Karl-Schwarzschild Strasse 2
D-85748 Garching bei Muenchen
Germany
fprimas@eso.org

Saito, Akito
Heavy Ion Nuclear Physics Laboratory
RIKEN
2-1 Hirosawa, Wako
saitama 351-0198
Japan
akito@rarfaxp.riken.jp

Sakai, Hideyuki
Center for Nuclear Study(CNS)
University of Tokyo
2-1 Hirosawa, Wako
saitama 351-0198
Japan
sakai@cns.s.u-tokyo.ac.jp

Sasaqui, Takahiro
National Astronomical Observatory
2-21-1, Osawa, Mitaka
Tokyo, 181-8588
Japan
sasaqui@th.nao.ac.jp

Segawa, Mariko
RCNP, Osaka University
10-1, Mihogaoka, Ibaraki
Osaka, 567-0047
Japan
segawa@rcnp.osaka-u.ac.jp

Shima, Tetsushi
Research Center for Nuclear Physics
Osaka University
10-1, Mihogaoka, Ibaraki
Osaka 567-0047
Japan
shima@rcnp.osaka-u.ac.jp

Shimizu, Youhei
Research Center for Nuclear Physics
Osaka University
Onoharanishi 1-8-17-105,Mino
Osaka 562-0032
Japan
yshimizu@rcnp.osaka-u.ac.jp

Shimoura, Susumu
Center for Nuclear Study(CNS)
University of Tokyo
2-1 Hirosawa, Wako
saitama 351-0198
Japan

Shinkai, Hisaaki
Computational Astrophysics Group
Institute of Physical & Chemical Research
RIKEN
2-1 Hirosawa, Wako
saitama 351-0198
Japan
hshinkai@riken.jp

Smith, Michael Scott
ORNL Physics Division
Oak Ridge National Laboratory
MS-6354,Bldg.6025
Oak Ridge, TN 37831-6354
USA
msmith@mail.phy.ornl.gov

Suda, Takuma
Hokkaido Univ.
Kita 10-jo , Nishi 8-chome , Kita-ku
Sapporo 060-0810
Japan
suda@astro1.sci.hokudai.ac.jp

Sukhoruchkin, Sergey Ivanovich
Petersburg Nuclear Physics Institute
188300 Gatchina
Leningrad District
Russia
sergeis@mail.pnpi.spb.ru

Sumiyoshi, Kohsuke
Numazu College of Technology
Ooka3600,Numazu
Shizuoka 410-8501
Japan
sumi@numazu-ct.ac.jp

Tachibana, Takahiro
Waseda University Senior High School
3-31-1 Kamishakujii,Nerimaku
Tokyo,177-0044
Japan
ttachi@waseda.jp

Takada-Hidai, Masahide
Libral Arts Education Center
Tokai Univ.
1117 Kitakaname,Hiratsuka
259-1292
Japan
hidai@keyaki.cc.u-tokai.ac.jp

Takahisa, Keiji
Research Center for Nuclear Physics
Osaka University
10-1,Mihogaoka,Ibaraki-shi
Osaka 567-0047
Japan
takahisa@rcnp.osaka-u.ac.jp

Takano, Masatoshi
Advanced Research Institute for Science and Engineering
Waseda University
3-4-1 Okubo,Shinjuku-ku
Tokyo 169-8555
Japan
takanom@waseda.jp

Takeda, Atsushi
Cosmic-Ray Group,Department of Physics
Kyoto University
Oiwakecho,Kitashirakawa, Sakyo-ku
Kyoto, 606-8502
Japan
takeda@cr.scphys.kyoto-u.ac.jp

Takeuchi, Kazuko
Center for Nuclear Study(CNS)
University of Tokyo
2-1 Hirosawa, Wako
saitama 351-0198
Japan
takeuti@cns.s.u-tokyo.ac.jp

Tanihata, Isao
RIKEN
2-1 Hirosawa, Wako
saitama 351-0198
Japan

Tatsumi, Toshitaka
Department of Physics
Kyoto University
Oiwakecho,Kitashirakawa, Sakyo-ku
Kyoto, 606-8502
Japan
tatsumi@ruby.scphys.kyoto-u.ac.jp

Tchuvil'sky, Yurii
Skobeltsyn Institute of Nuclear Physics
Moscow State University
119992,Moscow
Russia
TCHUVL@nucl-th.sinp.msu.ru

Teranishi, Takashi
Center for Nuclear Study(CNS)
University of Tokyo
2-1 Hirosawa, Wako
saitama 351-0198
Japan
teranisi@cns.s.u-tokyo.ac.jp

Terasawa, Mariko
Center for Nuclear Study(CNS)
University of Tokyo
2-1 Hirosawa, Wako
saitama 351-0198
Japan
mariko@cns.s.u-tokyo.ac.jp

Thiamova, gabriela
Department of Physics
University of Tokyo
Hongo 7-3-1,Bunkyo-ku
Tokyo 113-0033
Japan
thiamova@tkyntm.phys.s.u-tokyo.ac.jp

Togano, Yasuhiro
Rikkyo Univ.
3-34-1 Nishi-ikebukuro,Toshima
Tokyo 171-0021
Japan
toga@ne.rikkyo.ac.jp

Tominaga, Nozomu
Department of Astronomy
University of Tokyo
Hongo 7-3-1,Bunkyo-ku,
Tokyo 113-0033
Japan
ntominaga@astron.s.u-tokyo.ac.jp

Torii, Hisayuki
RIKEN
2-1 Hirosawa, Wako
saitama 351-0198
Japan
htorii@bnl.gov

Tribble, Robert E
Cyclotron Institute
Texas A&M University
College Station
TX 77843
USA
tribble@comp.tamu.edu

Tumino, Aurora
Laboratori Nazionali del Sud-INFN
Via S.Sofia,44
95123 Catania
Italy
tumino@lns.infn.it

Umeda, Hideyuki
University of Tokyo
7-3-1 Hongo,Bunkyo-ku
Tokyo 113-0033
Japan
umeda@astron.s.u-tokyo.ac.jp

Vladimir, Rykov
RIKEN
2-1 Hirosawa, Wako
saitama 351-0198
Japan
rykov@bnl.gov

Wakabayashi, Yasuo
Kyushu Univ. (CNS)
2-1 Hirosawa, Wako
saitama 351-0198
Japan
bayashi@cns.s.u-tokyo.ac.jp

Wanajo, Shinya
Department of Physics
Sophia University
7-1 Kioi-cho,Chiyoda-ku
Tokyo 102-8554
Japan
wanajo@sophia.ac.jp

Yakiv, Pavlenko V
Main astronomical observatory of
national academy of sciences
Zabolotnoho 27
Kyiv_127,03680
Ukraine
yp@mao.kiev.ua

Yamasaki, Tatsuya
Kyoto University
Oiwakecho,Kitashirakawa, Sakyo-ku
Kyoto, 606-8502
Japan
yamasaki@kusastro.kyoto-u.ac.jp

Yano, Yasushige
RIKEN
2-1 Hirosawa, Wako
saitama 351-0198
Japan
yyano@riken.go.jp

Yoshida, Satoshi
Hosei University
2-17-1 Fujimi,Chiyoda-ku
Tokyo 102-8160
Japan
s_yoshida@i.hosei.a.jp

Yoshida, Takashi
Department of Astronomy
University of Tokyo
7-3-1 Hongo,Bunkyo-ku
Tokyo 113-0033
Japan
tyoshida@astron.s.u-tokyo.ac.jp

This page intentionally left blank

AUTHOR INDEX